Active Tectonics and Seismic Hazard in Central Asia

Roberta Wilkinson

Thesis submitted to the University of Oxford
for the degree of Doctor of Philosophy

Michaelmas term, 2023

Department of Earth Sciences
Linacre College
Supervisors:
Prof. Richard Walker, Dr. Simon Daout, Prof. Barry Parsons

Declaration of Authorship

The contents of this thesis are all my own work except where otherwise stated. Detailed statements of authorship can be found at the end of each chapter. The views expressed in this thesis are mine and not necessarily those of any other person unless so attributed.

Abstract

Active Tectonics and Seismic Hazard in Central Asia

Roberta Wilkinson

University of Oxford

Michaelmas Term, 2023

In this thesis, I investigate the behaviour of active faults near major cities in Central Asia, to better understand the seismic hazard they pose. First, I explore past and potential earthquakes on the Zailisky Range Front fault, which lies at the northern boundary of the Tian Shan mountains and runs beneath Almaty, Kazakhstan's largest city. I present the first paleoseismic trench on the fault, which reveals two earthquakes of at least M_W ~6.6 – 6.7. The penultimate earthquake occurred at 9.5 ± 0.8 ka and the most recent event between 8.4 – 2.6 ka. I use high resolution digital elevation data to map and measure fault scarps along the ~300 km of the range front. Scarp heights are consistent with ruptures of at least M_W ~6.5 – 6.7 for the most recent event or events. A tentative mapping of fault segmentation and the historical record of the 1887 M_W ~7.2 – 7.7 Verny earthquake indicate that the fault is capable of rupturing in larger events. I estimate Quaternary slip rates of ~0.1 – 0.4 mm/yr. A higher geodetic slip rate derived from published GNSS velocities (1.9 ± 0.7 mm/yr) indicates deformation is accommodated by several parallel structures, some of which may be unmapped.

The second study region is the northern part of the Tajik basin close to Dushanbe, Tajikistan's capital. I present ~130 m resolution surface velocity maps of the Tajik basin from a Multi-Temporal InSAR analysis of ~5 years of Sentinel-1 data. The rate maps show aseismic slip on several faults associated with an evaporite horizon. The right-lateral Ilyak fault is creeping at ~ 6.7 – 8.7 mm/yr in the east and ~ 4.2 – 4.5 mm/yr in the west. The rate decreases from east to west as slip transfers to the basin thrust sheets. There are no signals indicative of strain accumulation at depth across the Ilyak fault in the

surface velocity maps, but moderate earthquakes in the basement suggest that deformation around a locked fault may be obscured by the sedimentary cover. Finally, using satellite-derived elevation models, I document geomorphic evidence for an active thrust fault within the Dushanbe Trough which may be capable of producing a M_W 7.0 – 7.2 earthquake based on the mapped length, highlighting the need for field studies to determine its seismic potential. The research presented in this thesis highlights the seismic hazard posed to major cities in Central Asia and the need for further research to better characterise the active faults.

Extended Abstract

This thesis explores the active tectonics of two study regions in Central Asia, aiming to gain insights into how faults behave within continental interiors. The research is focused on faulting near major population centres. It is motivated by a need to improve the mapping and understanding of seismogenic structures for qualitative and quantitative hazard assessment. On the continents, deformation tends to be distributed over complex networks of faults with relatively low slip rates and long recurrence intervals. Therefore, seismological records alone do not adequately reflect the full range of behaviour, locations or the extents of active structures. In this thesis, I utilise a suite of other techniques to study fault behaviour, including paleoseismology, tectonic geomorphology and Multi-Temporal InSAR.

I begin, in Chapter 1, by describing the characteristics of intracontinental faulting and the tectonics of Central Asia. I set out the motivations behind this research, and I introduce the two study regions which are the focus of this thesis. The first study region (Chapters 2 and 3) is the Zailisky Range Front fault at the northern edge of the Tian Shan mountains near Almaty, Kazakhstan's largest city. This area is dominated by thick-skinned thrust faulting. Here, I aim to map the extent of fault activity, to find out when the last earthquakes occurred and their magnitudes, and to estimate the rate of deformation across the range front. The second study region (Chapter 4) is the northern part of the Tajik Basin and the Dushanbe Trough, near Dushanbe, the capital city of Tajikistan, which is dominated by east-west shortening across a thin-skinned fold and thrust belt. In this region, I aim to map the active faults, to determine the extent to which they are locked or creeping, and to understand how strain is partitioned between them.

Chapter 2 explores past and potential earthquakes on the Zailisky Range Front fault. I present the first paleoseismic trench on the fault, revealing evidence of two paleo-earthquakes which ruptured the

eastern end of the fault along its northern fault strand in the last ~10 kyrs. Offset sedimentary units in the trench were sampled and ages were obtained by luminescence dating (IRSL) to construct an earthquake chronology. The timing of the penultimate earthquake is well constrained to 9.5 ± 0.8 ka (2σ uncertainty) with ~0.7 m of slip, corresponding to a magnitude of at least M_W ~6.6. The timing of the most recent event (MRE) is less well constrained because there is a large gap in age between the sampled sediments that pre- and post-date the earthquake. The MRE occurred at some point between 8.4 – 2.6 ka (95.4% probability range) and slipped ~1.3 m, corresponding to an earthquake of at least M_W ~6.7. These earthquakes might have been significantly larger than the magnitude estimates if not all of the coseismic slip reached the surface. The results suggest that there are thousands of years of inactivity between earthquakes on this fault, consistent with observations from several other major faults in the Tian Shan. To contextualise the findings from the trench, I also map and measure scarps along the ~300 km of active faulting on the range front. I utilise high resolution digital elevation datasets derived from drone surveys, field GPS surveys and satellite imagery. I analyse data from ~33 sites, many of which I visited in the field. I find that the smallest scarps are ~0.2 – 1.0 m high, which I infer to be the minimum offset in the most recent event or events along the range front. Assuming a fault dip between 30 - 60°, these scarp heights correspond to slip of ~0.2 – 2.0 m and magnitudes of at least M_W ~6.5 – 6.7, consistent with the findings from the trench. From my geomorphic mapping, I also document evidence of uplift in the foreland within the Kazakh platform.

Much of the Zailisky Range Front and its scarps are eroded, covered by loess, or urbanised, making the level of continuity of the fault difficult to ascertain. I tentatively map a possible fault segmentation, with segment lengths on the order of ~40 – 120 km which could correspond to earthquakes of at least M_W ~7.0 – 8.0. I find no strong evidence which would rule out the possibility of large ruptures tens to hundreds of kilometres long. Whilst these geomorphological estimates are uncertain, an historical event confirms that high-magnitude events are possible on or very close to the range front: the 1887

M_W ~7.2 – 7.7 Verny earthquake occurred close to Almaty and may have ruptured the Zailisky Range Front fault, although no surface ruptures have been found. This chapter builds on the evidence of previous studies demonstrating that the Zailisky Range Front fault is a significant source of seismic hazard, particularly due to its location beneath many of the towns along the range front including Almaty, and its proximity to major infrastructure including the Big Almaty Canal. Further trenching studies are needed to build a robust earthquake chronology and an understanding of the extent and magnitude of the faulting along the entire length of the fault.

Building on the findings of Chapter 2, in Chapter 3 I estimate deformation rates across the Zailisky Range Front. I use new luminescence dating (IRSL) results and previously published loess ages to calculate Quaternary slip rates for several field sites on different strands of the Zailisky Range Front fault. I also identify errors in previously published calculations of the Quaternary slip rate, including an over-estimation of the tectonic offset, and an extrapolation of regional terrace ages based on unsupported assumptions. I recalculate one of the previously published rates using an updated methodology. The new and reassessed Quaternary slip rates are between ~0.1 – 0.4 mm/yr, based on deposits from ~10 – 60 ka. Using published GNSS velocities, I also derive a geodetic shortening rate of 1.3 ± 0.4 mm/yr between the Zailisky Alatau mountains and the Kazakh Platform, corresponding to a slip rate of 1.9 ± 0.7 mm/yr. The difference between the geodetic and Quaternary slip rates demonstrates that the fault strands sampled at the slip rate sites accommodate only a small proportion of the total slip. I infer that deformation is distributed across multiple parallel structures which might include faults or folds within the Kazakh Platform. Further slip rate measurements and denser GNSS coverage is needed to determine the relative distribution of strain between different structures and to identify unmapped active faults.

Chapter 4 is concerned with the active deformation in the Tajik basin, with a focus on the Dushanbe Trough in Tajikistan and the Ilyak strike-slip fault. I present surface velocity maps of the Tajik basin with a spatial resolution of ~130 m and an uncertainty of < 1 mm/yr, produced using a bespoke Multi-Temporal InSAR approach with ~5 years of Sentinel-1 acquisitions. The rate maps have a significantly higher resolution than previous datasets, revealing aseismic slip and slip partitioning which were not previously apparent. The Ilyak fault is slipping aseismically to very shallow depths along an evaporite horizon. The right-lateral strike-slip rate is ~ 6.7 – 8.7 mm/yr in the east of the Ilyak fault and ~ 4.2 – 4.5 mm/yr in the west. Slip decreases from east to west due to the partitioning of slip onto the folds and thrusts of the basin, and most prominently onto the Karchitau thrust. Despite moderate earthquakes within the basement beneath the Ilyak fault, including a destructive M5.5 event in 1989, no signals indicative of strain accumulation at depth are apparent in the surface velocity maps. However, evidence of deformation at depth may be absent from the surface measurements because of the mechanical decoupling of the basement and sedimentary cover across an evaporitic décollement horizon. Alternatively, the fast aseismic slip at shallow depths on the Ilyak fault could be obscuring smaller signals from the basement. Therefore, our data cannot rule out the presence of potentially hazardous active faults at depth near Dushanbe. The rate maps also show evidence of aseismic deformation on the Babatag, Surkhu and Vakhsh thrust sheets, and the possible isostatic uplift of the southwestern part of the Tian Shan mountains. Finally, using high resolution Digital Elevation Models derived from satellite data, I document scarps in the young alluvium of the Dushanbe Trough. The geomorphic evidence is consistent with an active south-dipping thrust fault beneath the city of Dushanbe which may be capable of rupturing in a M_W 7.0 – 7.2 earthquake based on the remotely mapped length (~45 km), highlighting the need for field investigations to determine its seismic potential.

In Chapter 5, I summarise the conclusions of this research. Each study demonstrates that there are active faults in close proximity to major population centres in Central Asia which could produce

destructive earthquakes. By combining paleoseismology, tectonic geomorphology and geodetic measurements, I map, measure and characterise faults which are poorly constrained by seismology data. However, questions remain regarding the possible magnitudes of future earthquakes and the locations and extents of some significant active structures. Further research is needed in both regions to comprehensively understand the hazard. Possible research directions include further trenching of the Zailisky Range Front, the deployment of dense seismic arrays around the Ilyak fault, and sampling and trenching of the Dushanbe Trough thrust.

Acknowledgements

I would like to thank my supervisors for their guidance throughout my PhD. Thank you to Richard Walker for his support, scientific insights and for helping me to tailor my project to my interests. I am grateful to Simon Daout for teaching me InSAR techniques, and for interesting and detailed discussions about the results. I would like to thank Barry Parsons for helping me to shape the direction of my research early on in the project. Many thanks also to my examiners, Bob Hilton and Ekbal Hussain, for their helpful comments on this thesis.

I would also like to acknowledge several colleagues whose help and support has been invaluable. I am grateful to Christoph Grützner for his collaboration – for sharing data, for many insightful discussions, and for accompanying me on my first field season. Aidyn Mukambayev was instrumental in enabling the field work on the Zailisky Range Front. I thank him for his time, patience, unparalleled hospitality, and for hunting for fault scarps with me. I am grateful to Ed Rhodes and Andrew Ivester for the time they took to teach me about luminescence dating and for the helpful discussions about the results.

I would also like to thank the many colleagues in the Oxford COMET group and the wider scientific community who have accompanied me on fieldwork, shared their scientific and technical insights, supported me or shown an interest in my work: Wendy Tsai, JD Dianala, Nick Dodds, Qi Ou, Alex Lipp, Neill Marshall, Ben Johnson, Ruth Amey, John Elliott, Kanatbek Abdrakhmatov, Tamarah King, Ian Pierce, Julie Boulliung, Gulkaiyr Tilek Kyzy, Sultan Baikulov, Austin Elliott, Sam Wimpenny, Camilla Penney and Jack McGrath. Thank you also to the field support teams in Kazakhstan and Kyrgyzstan, in particular Russlan for his careful driving and Ainagul for her cooking – but most of all for getting a massive spider out of my tent. Thank you to my proof-readers: Rebecca, Wendy, Neill, Alex, Matthew and Mum. Many thanks also to Kathryn for her help and guidance.

I am very grateful for the support of my friends over the past few years and months, with special mentions to Laura, Alex, Matthew, Rebecca, GK, Poppy, Ricky, and Matt L for their unwavering friendship and solidarity. Finally, to my Mum, my sister, and my Grandma – thank you for everything, this thesis is dedicated to you.

Table of Contents

Chapter 1

Introduction

1.1. Background and Motivation

1.1.1. Deformation, Earthquakes and Seismic Hazard on the Continents

In oceanic lithosphere, deformation and associated earthquakes tends to occupy narrow fault zones along the plate boundaries, with slip rates on the order of tens to hundreds of millimetres per year (Jackson and McKenzie, 1988; England and Jackson, 2011). The situation is strikingly different on the continents, where deformation is distributed across complex networks of faults, spanning broad zones hundreds to thousands of kilometres wide (Figure 1.1-1; Molnar and Tapponnier, 1975; McKenzie and Jackson, 1983; Jackson and McKenzie, 1988; Thatcher, 2009; England and Jackson, 2011). With a large number of active faults simultaneously accommodating strain, slip rates on individual faults within these zones of continental deformation tend to be on the order of a few millimetres per year or less (McKenzie and Jackson, 1983; England and Jackson, 2011).

The complexity of continental deformation creates challenges for mapping major active structures. As slip rates tend to be low, long periods of hundreds or thousands of years can pass between large earthquakes, meaning that historical and instrumental seismic records are insufficient to identify hazardous faults (England and Jackson, 2011; Liu and Stein, 2016; Grützner et al., 2017a). Additionally, in the long gaps between earthquakes, erosion and deposition can destroy or degrade evidence of active faulting (Bilham, 2014). Limited information on active faults, long earthquake recurrence intervals, and uneven distribution of scientific and financial resources globally (among

other factors) have resulted in a lack of awareness of and preparedness for large earthquakes in many intracontinental settings (England and Jackson, 2011; Liu and Stein, 2016). Furthermore, due to the increased availability of water around faults or from their associated mountain ranges, many population centres within the continents are built near to or on top of major active structures (Jackson, 2008). As a result of these factors, there have been many more fatalities from intracontinental earthquakes than those on plate boundaries (Figure 1.1-2), with the number of deaths from $M_W > 7.5$ events typically on the order of tens of thousands and likely to increase with rising populations (England and Jackson, 2011; Bilham, 2014).

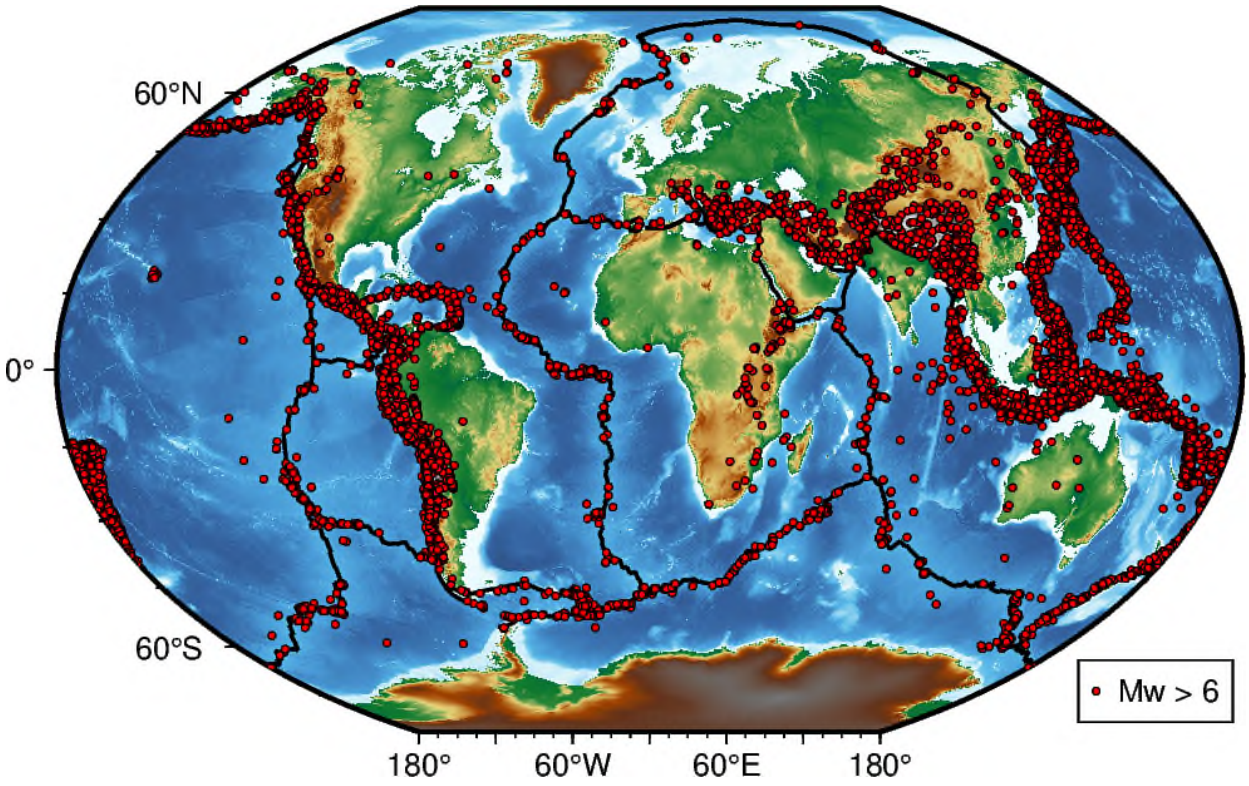

Figure 1.1-1. Global earthquakes larger than magnitude 6 between 1904 to 2020 from the ISC-GEM Catalogue (Bondár et al., 2015; Di Giacomo et al., 2015; Di Giacomo, Engdahl and Storchak, 2018). Black lines = major plate boundaries (U.S. Geological Survey, 2023).

And yet, intracontinental faults remain relatively understudied compared to fast moving plate boundaries such as the San Andreas fault and North Anatolian fault, which have been extensively and

mapped and measured both in the field and using satellite data (e.g. Segall, 2002; Şengör et al., 2005; Fraser, Vanneste and Hubert-Ferrari, 2010; Gizzi, 2015). England and Jackson (2011) argued that "knowledge that underpins earthquake resilience in Japan or California must be transferred to countries in which earthquakes regularly inflict huge death tolls".

In this thesis I aim to address, at least in some small part, the knowledge gaps regarding active faults in the intracontinental region of Central Asia, to improve the identification and understanding of potentially hazardous structures close to big cities. Whilst regional seismicity provides vital context for these studies, this thesis utilises a suite of other techniques to overcome the limitations of seismic catalogues and the specific challenges of characterising deformation in continental interiors. With techniques from paleoseismology and tectonic geomorphology, I assess fault behaviour over timescales of thousands to hundreds of thousands of years. I use geodetic methods (GPS and InSAR) to map and measure decadal deformation over zones of faulting to identify and characterise active structures. Whilst formal seismic hazard assessment or modelling is beyond the scope of this thesis, I aim to provide evidence and analyses which will help towards constraining the underlying parameters of such models, such as potential earthquake size, precise locations and extents of active faults, slip rates, and recurrence intervals (Youngs and Coppersmith, 1985; Wesnousky, 1986; Liu and Stein, 2016). I also aim to address broader hazard-related questions such as the extent to which faults are locked or slipping aseismically (Harris, 2017). Whilst the findings of this thesis contribute to this knowledge base and demonstrate that there are significant sources of seismic hazard in the study region which must be addressed, an important conclusion of all Chapters is that further research is required to comprehensively understand the hazard.

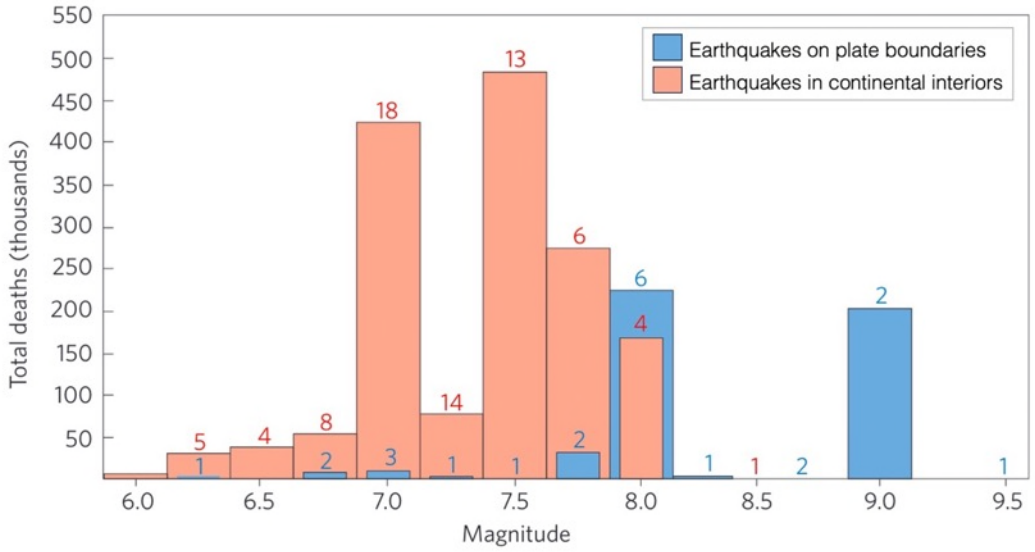

Figure 1.1-2. Earthquake deaths over the century before ~2011 in continental interiors and on plate boundaries binned by earthquake magnitude, modified after England and Jackson (2011). The number of earthquakes in each bin (bin width = 0.25) is given above each bar.

1.1.2. Tectonic Setting of Central Asia

The active tectonics of Central Asia are largely driven by the northwards collision of the Indian continent into Asia (Figure 1.1-3). The India-Asia collision began at ~50 Ma (e.g. Green et al., 2008; Bouilhol et al., 2013) and since ~5Ma its convergence rate has been ~35 mm/yr (Royer, Gordon and Horner-Johnson, 2006; Thatcher, 2009). The resulting deformation is a wide belt of uplift and extrusion across Asia, including the uplift of the Tibetan plateau, directly north of the collision zone (Molnar and Tapponnier, 1975; Avouac and Tapponnier, 1993). Further to the northwest, the relatively rigid and undeformed Tarim Basin separates the Tibetan Plateau from the Tian Shan, a >2500 km long active mountain belt spanning Central Asia, from China in the east to Uzbekistan in the west (Figure 1.1-3; Avouac and Tapponnier, 1993; Jolivet et al., 2010). The Tian Shan is actively shortening in the N-S direction by up to ~20 mm/yr and has hosted some of the largest continental earthquakes on record, including the 1889 M_W ~7.9 – 8.3 Chilik earthquake, despite slow slip rates on individual

active faults (Kondorskaya et al., 1982; Bindi et al., 2014; Abdrakhmatov et al., 2016; Zubovich et al., 2016; Grützner et al., 2017b; Krüger, Kulikova and Landgraf, 2017; 2018; Wu et al., 2023).

To the west of the Tarim basin, the high plateau of the Pamir mountains is sandwiched between the Southern Tian Shan and the western syntaxis of the Indian Plate (Figure 1.1-3; Zubovich et al., 2010; Sippl et al., 2013). Analyses of the seismicity beneath the Pamir and neighbouring Hindu Kush indicate the presence of subducted material, but its exact nature and origin is disputed (Hamburger et al., 1992; Burtman and Molnar, 1993; Sippl et al., 2013; Schurr et al., 2014; Kufner et al., 2018). The Pamir mountains exhibit strike-slip faulting on the eastern and western edges and thrusting on the northern margin, but E-W extension dominates in the interior, suggesting a process of gravitational collapse (Sippl et al., 2013; Schurr et al., 2014; Rutte et al., 2017). The Tajik Basin lies to the west of the Pamir and to the south of the southwestern end of the Tian Shan. Due to its collapse, the Pamir is extruding into the Tajik Basin, inducing E-W shortening of the basin's sedimentary cover and the formation of a rather spectacular fold and thrust belt (Schurr et al., 2014; Rutte et al., 2017; Kufner et al., 2018; Gągała et al., 2020).

This thesis is concerned with two regions on opposite sides of the Tian Shan mountains. At the northern boundary of the Western Tian Shan, I focus on the Zailisky Range Front, which is shortening slowly in the N-S direction along thick-skinned thrust faults (red box in Figure 1.1-3; Grützner et al., 2017b). At the southeastern end of the Tian Shan, I focus on the northern part of the Tajik Basin fold and thrust belt, which is dominated by thin-skinned E-W deformation on a combination of thrusts, folds and strike-slip faults (blue box in Figure 1.1-3; Gągała et al., 2020). Detailed introductions to these study regions can be found in Chapters 2 and 4. Through these contrasting tectonic settings, I explore the wide range of possible fault behaviours in continental interiors. Furthermore, to enhance the utility of this thesis for assessing hazard, each study region was chosen due to the proximity of the

active faults to a major city: Almaty, Kazakhstan's largest city, lies on the Zailisky Range Front, and Dushanbe, Tajikistan's capital, is situated at the northern edge of the Tajik Basin.

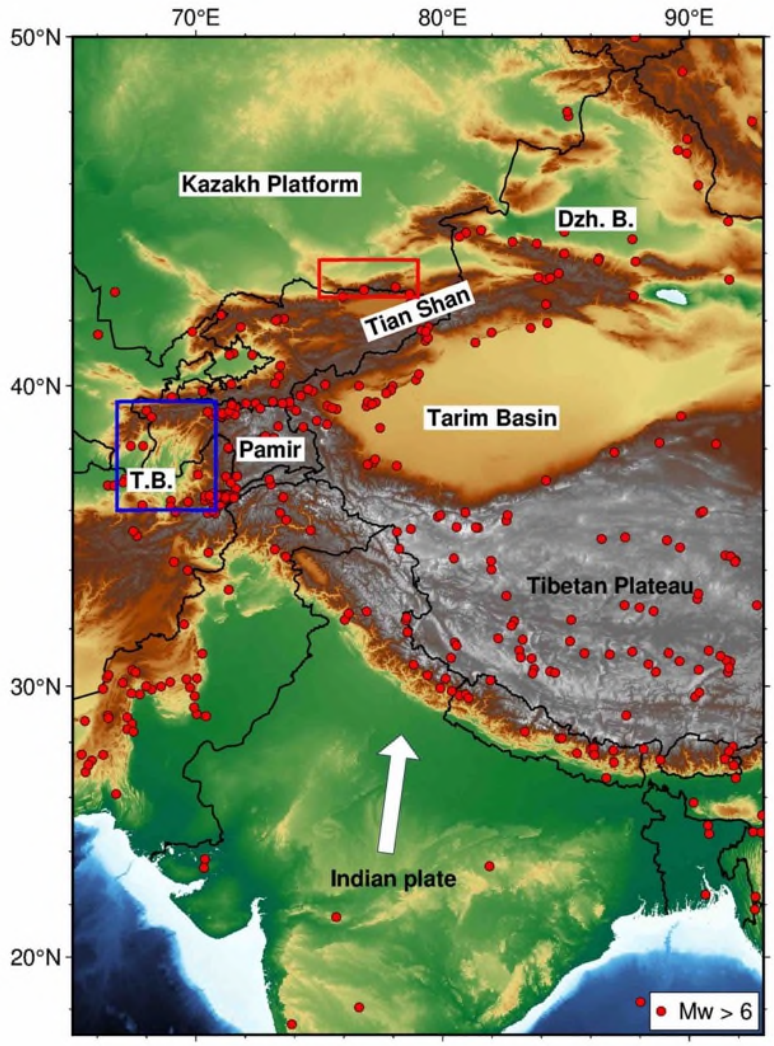

Figure 1.1-3. Overview of the India-Asia collision and major tectonic features of Central Asia (white label boxes). Red box = Zailisky Range Front study region (Chapters 2 and 3). Blue box = Tajik Basin study region (Chapter 4). Dzh. B. = Dzhungarian Basin. T.B. = Tajik Basin. Red circles = earthquakes larger than magnitude 6 between 1904 to 2020 from the ISC-GEM Catalogue (Bondár et al., 2015; Di Giacomo et al., 2015; Di Giacomo, Engdahl and Storchak, 2018). Black lines = political boundaries.

1.1.3. The Seismic Cycle

A simple conceptual model of the seismic cycle was developed by Harry Fielding Reid after the San Francisco earthquake of 1906: in the time between earthquakes (the interseismic phase) far field motion causes the accumulation of strain around a locked fault until, at a critical threshold, the two sides quickly slip past each other producing an earthquake (the coseismic phase; Reid, 1910; Wright, 2002). However, we now know that there are additional complexities to fault behaviour, including transient rapid deformation after earthquakes (post-seismic phase; Wright, 2002; Ingleby and Wright, 2017). Furthermore, some faults tend to release some or all strain by slipping aseismically (creeping), with explanations for creep including (but not limited to) low friction minerals, high pore fluid pressure, heat flow, and fault geometry (Wesson, 1988; Chen and Bürgmann, 2017; Harris, 2017). Additionally, seismogenic faults are often assumed to be quasi-periodic, with the concept of an average recurrence interval or average recurrence rate regularly used in hazard modelling, but there is mounting evidence to suggest that earthquakes can be clustered in time, particularly in slowly deforming continental interiors (Jackson and Kagan, 2006; Clark and McCue, 2009; Scholz, 2010; Bilham, 2014; Liu and Stein, 2016). The contents of this thesis pertain to the coseismic and interseismic phases of the seismic cycle, and are contextualised with the additional complexities listed here.

1.2. Overview of this Thesis

1.2.1. Thesis Structure

Chapter 2 is a study of the Zailisky Range Front fault near Almaty in Kazakhstan. I present results from the first paleoseismic trench on the range front, yielding the timing and minimum magnitude of the most recent earthquakes. I extend the analysis to the rest of the fault by analysing the geomorphology at ~30 sites using high resolution digital elevation data collected in the field and

derived from satellite imagery. I map fault scarps and measure vertical offsets to estimate minimum magnitudes for the most recent events along the range front, and tentatively map fault segmentation to explore further possible earthquake scenarios.

Chapter 3 aims to quantify the slip rate across the Zailisky Range Front. I obtain new estimates of geological slip rates using Quaternary surface ages, as well as by reassessing previously published rate estimates. I analyse published GNSS velocities to estimate the geodetic shortening rate. By comparing these geological and geodetic rates, I assess the distribution of strain between different structures on the range front.

Chapter 4 is a study of the northern part of the Tajik Basin and the Dushanbe Trough, near the city of Dushanbe in Tajikistan. I present high-resolution surface velocity maps produced with Multi-Temporal InSAR to assess fault behaviour, including to what extent faults are locked or creeping and how slip is partitioned between different structures. I combine this analysis with geomorphic mapping of the Dushanbe Trough to identify further potentially hazardous faults close to the city.

Finally, in Chapter 5 I summarise the conclusions of this thesis and reflect on possible directions for future research.

1.2.2. Miscellaneous Comments

I intend to publish the work of this thesis as peer-reviewed papers. Therefore, the substantive Chapters of this thesis are written in the first-person plural (i.e. ‘we’) for ease of conversion into papers, and to recognise the contributions of the colleagues who will be co-authors. These colleagues are formally acknowledged in each post-chapter statement of authorship. For ease of reading, note that each

Chapter has its own Appendix. In preparation for journal submission, Chapter 4 is written in a paper style and much of the methodology can be found in a Supplementary Methods section in its Appendix.

Maps were prepared using QGIS (QGIS.org, 2023), GMT (Wessel et al., 2019) and PyGMT (https://www.pygmt.org/dev/overview.html). Some map data are copyrighted OpenStreetMap contributors, licensed under the Open Database License (https://www.openstreetmap.org/copyright). These data are freely available from https://www.openstreetmap.org.

Abbreviations and conventions:

kyrs = thousands of years, ka = thousands of years before 2023, BP = years before the middle of 1950.

Chapter 2

Past and Potential Earthquakes on the Zailisky Range Front Fault from Paleoseismology and Tectonic Geomorphology

2.1. Introduction

Almaty, the largest city and former capital of Kazakhstan, lies on the northern range front of the Western Tian Shan mountains (Figure 2.1-1a). Although Almaty has been unaffected by earthquakes over the last century, the piedmont and the mountains to the south of the city are permeated by a complex network of active faults (e.g. Abdrakhmatov et al., 2016; Arrowsmith et al., 2017; Grützner et al., 2017b). These faults hosted three large (M_W > ~7.2) and destructive earthquakes between 1887 – 1911, including the M_W ~7.9 – 8.3 1889 Chilik earthquake which is one of the highest magnitude continental events on record (Bindi et al., 2014; Abdrakhmatov et al., 2016; Arrowsmith et al., 2017; Krüger, Kulikova and Landgraf, 2017; 2018). These events demonstrate the high seismic hazard in the northern ranges of the Western Tian Shan.

However, there are significant challenges in identifying and characterising the major sources of hazard to local populations. With typically slow deformation rates (Zubovich et al., 2010; Wu et al., 2023) and thousands of years of inactivity between events on individual structures (e.g. Landgraf et al., 2016; Grützner et al., 2017a; Ainscoe et al., 2019), seismic records are too short to identify all the active faults in the region or understand their behaviour (Liu and Stein, 2016). Paleoseismology and tectonic geomorphology can be used to extend seismic records, but with up to thousands of years since the last earthquake as well as extensive urbanisation, much of the geomorphic expression of faulting has been degraded or completely destroyed (Grützner et al., 2017a; 2017b). The piedmonts of the northern Tian Shan are also blanketed with loess (wind-blown silt; Fitzsimmons et al., 2017; Dave et al., 2023)

which may have buried or obscured scarps since their formation (Grützner et al., 2017b). Furthermore, the 1887 – 1911 earthquake sequence suggest a clustering of earthquakes in time and space. This implies faults may rupture as part of complex, interconnected networks, posing challenges for defining meaningful earthquake recurrence rates on individual faults (Scholz, 2010; Liu and Stein, 2016).

This study aims to overcome some of these challenges to better characterise one active fault near Almaty by conducting detailed mapping and measurement with high-resolution data. We focus on the Zailisky Range Front fault (ZRF) which runs along ~300 km of the Tian Shan's northern piedmont, including beneath Almaty City (Figure 2.1-1b; Grützner et al., 2017b; Amey et al., 2021). The 1887 M_W ~7.2 – 7.7 Verny earthquake (Bindi et al., 2014; Krüger, Kulikova and Landgraf, 2018) has been attributed to the ZRF, but there are no surface ruptures to confirm this, and other than this event there are no instrumental or historical records of ruptures (Tatevossian, 2007; Grützner et al., 2017b). However, Grützner et al. (2017b) documented recent deformation along the range front, suggesting significant past activity, which warrants further investigation.

In this chapter, we begin with a comprehensive review of the regional tectonics and earthquake history to inform the later discussion of our results. We then present a detailed mapping and description of the location and extent of activity on the ZRF, which we use to estimate past earthquake magnitudes and to identify any segmentation or gaps in the fault which could control the length of a future rupture. To aid the detection of subtle and degraded scarps we utilise high resolution field observations, dGPS (differential Global Positioning System) surveys, and DEMs (Digital Elevation Models). We also present new data from a paleoseismic trench in the east of the ZRF to obtain the first earthquake chronology for the fault. Whilst this study does not provide conclusive answers for all inputs needed in seismic hazard analyses, we contribute to an improved understanding of the underlying parameters, identify areas for further research, and qualitatively assess and highlight aspects of the seismic hazard posed by the ZRF. In addition to its implications for hazard assessment, our work adds to a growing

number of studies in the region which together give an insight into the characteristic behaviours of faults in the Tian Shan.

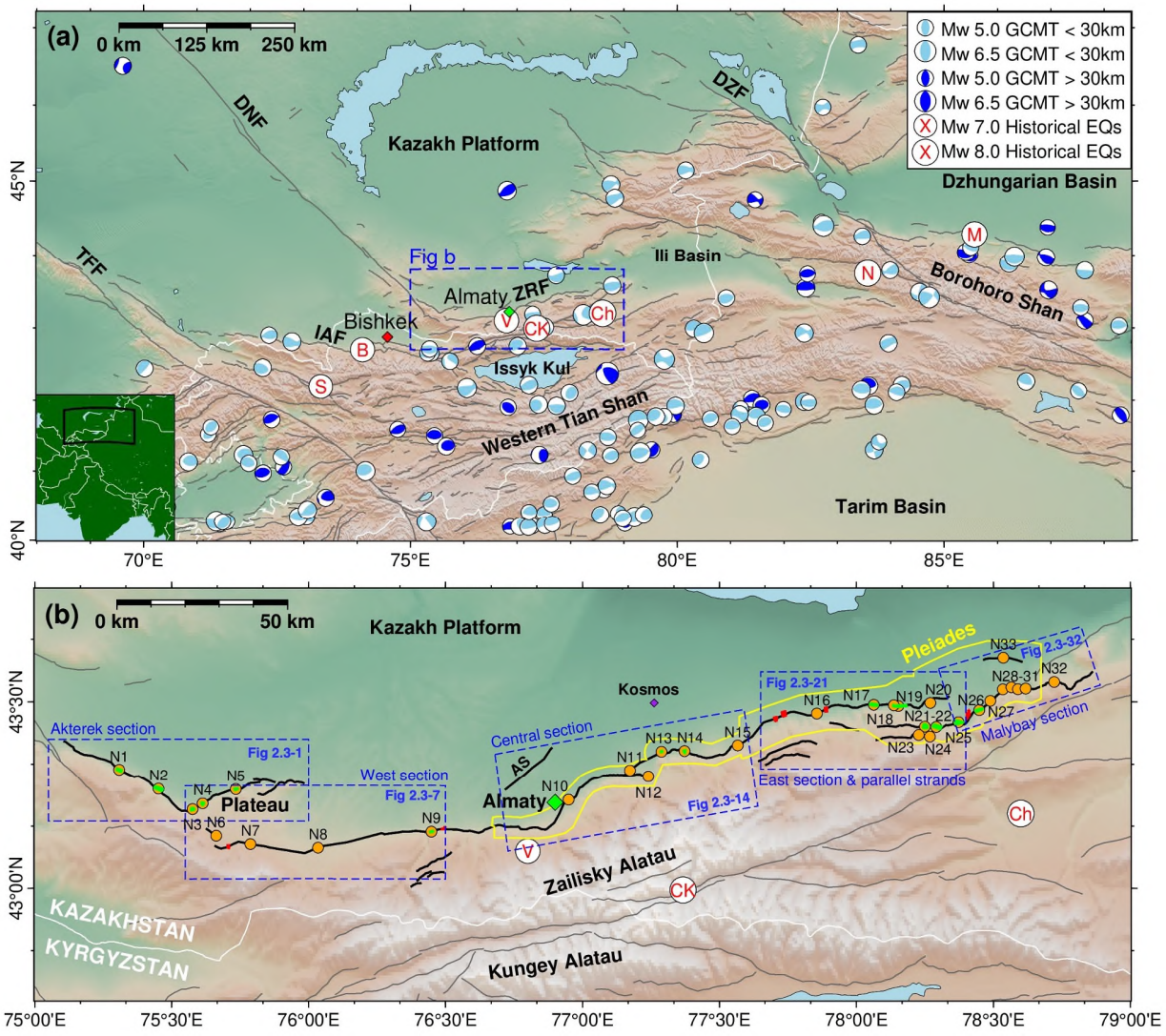

Figure 2.1-1. (a) Overview of Western and Central Tian Shan. Faults (dark grey lines) modified after Zelenin et al. (2022) with mapping from this study. Post-1976 earthquake focal mechanisms from the GCMT catalogue (Dziewonski, Chou and Woodhouse, 1981; Ekström, Nettles and Dziewoński, 2012) are in blue, with earthquakes below 30 km in dark blue and above 30 km in light blue. White circles with red lettering correspond to historical earthquakes: S = 1992 M_W 7.2 Suusamyr (Dziewonski, Chou and Woodhouse, 1981; Ekström, Nettles and Dziewoński, 2012), B = 1885 M_W 6.9 – 7.9 Belovodskoe (Kalmetieva et al., 2009; Krüger, Kulikova and Landgraf, 2018), V = 1887 M_W 7.2 – 7.7 Verny (Kalmetieva et al., 2009; Bindi et al., 2014; Krüger, Kulikova and Landgraf, 2018), CK = 1911 M_W 8.0 Chon Kemin (Kulikova and Krüger, 2015), Ch = 1889 the M_W 7.9 – 8.3 Chilik (Bindi et al., 2014; Krüger, Kulikova and Landgraf, 2017; 2018), N = 1812 M_S 8.0 Nilke (Feng, 1990; Wu et al., 2020; Tsai, 2023), M = 1906 M_W 7.7 Manas (Deng et al., 1996; International Seismological Centre, 2023; Tsai, 2023). Circle size corresponds to earthquake magnitude according to scaling examples shown in legend. Labelled faults: TFF = Talas Fergana fault, IAF = Issyk-Ata fault, DNF = Dzhalair-Naiman

fault, ZRF = Zailisky Range Front fault, DZF = Dzhungarian fault. White lines mark country borders. Green dots show the locations of the cities of Almaty and Bishkek. Background DEM based on SRTM 30 m data (NASA JPL, 2013). (b) Overview map of the Zailisky Range Front. Thick black lines are the Zailisky Range Front faults mapped and measured in this study. Orange circles are sites examined in this study. Small green and red shaded patches correspond to the locations of drone surveys: green indicates surveys in which scarps are present, red indicates surveys in which no scarps were identified. Yellow polygon marks the extent of Pléiades data. Blue boxes correspond to other figures in this study providing overviews of each section. AS = Almaty Splay.

2.1.1. Tectonic Background

The basement rocks of the Tian Shan and their oldest structures originate from a Late Paleozoic accretion of volcanic arcs, accretionary wedges, microcontinents and other terrains during the Variscan Orogeny (Burtman, 1975; Windley et al., 1990; 2007). After a period of relative inactivity, a second phase of orogenesis began in the Cenozoic due to the onset of the India-Asia collision, inducing N-S shortening which continues to the present day (Molnar and Tapponnier, 1975; Windley et al., 1990; Avouac and Tapponnier, 1993). This has produced an ~E-W striking mountain belt, the Tian Shan, >2500 km long and up to 350 km wide, composed of a series of ranges and several interior basins (including Issyk Kul) which are filled predominantly with Tertiary sediments (Figure 2.1-1a; Windley et al., 1990; Jolivet et al., 2010). The Tian Shan is bounded by three rigid blocks with minimal interior deformation: the Tarim Basin to the south, the Kazakh Platform to the northwest and Dzhungarian (or Junggar) Basin to the northeast (Avouac and Tapponnier, 1993; Wu et al., 2023). While the interior of the Tian Shan is dominated by ~E-W striking faults, several ~NW-SE dextral strike-slip faults extend for hundreds of kilometres into the Kazakh Platform and Dzhungarian Basin, including the Talas Fergana fault, Dzhungarian fault and, closest to Almaty, the Dzhalair-Naiman fault (DNF, also referred to as Kindytash in some literature; Campbell et al., 2013; Hollingsworth et al., 2016; Rizza et al., 2019; Tsai et al., 2022; Wu et al., 2023).

Exhumation of the Tian Shan began in the late Oligocene to early Miocene, with evidence for an increase in shortening rates in the late Miocene (Windley et al., 1990; Hendrix, Dumitru and Graham, 1994; Sobel and Dumitru, 1997; Bullen, Burbank and Garver, 2003; Sobel, Chen and Heermance, 2006; Heermance et al., 2008; Charreau et al., 2009; Macaulay et al., 2014). GPS velocities indicate present day shortening of up to ~20 mm/yr across the the Western Tian Shan, as well as up to ~7 – 8 mm/yr of left-lateral shear (Zubovich et al., 2016; Wu et al., 2023). Shortening rates are highest in the west and decrease towards the east, which has been attributed to the clockwise rotation of the Tarim Basin (Avouac et al., 1993; Wu et al., 2023).

The Zailisky Alatau (also known as the Ile or Trans-Ili Alatau) is the most northerly range of the Western Tian Shan, separated from the Kungey (or Kungei) range to the south by the Chon Kemin and Chilik faults (Figure 2.1-1b; Delvaux, Abdrakhmatov and Lemzin, 2001; Selander et al., 2012; Kudriavtseva, 2023). The Zailisky Range Front fault (ZRF), the subject of this study, runs for >300 km along the northern slopes of the Zailisky Alatau between the mountains and the Kazakh Platform. A variety of Palaeozoic rocks make up the basement along the range front, including granites, granodiorites, diorites, and sedimentary strata with interlayered volcanics, but it is within the Quaternary alluvium and fluvial sediments of the piedmont that active faulting is expressed (Parshina, Zolotokrylina and Semenova, 1979; Grützner et al., 2017b). Much of the range front is also blanketed by wind-blown loess which has accumulated over the past few tens to hundreds of kyrs (Grützner et al., 2017b; Dave et al., 2023). From GPS velocities, Wu et al. (2023) estimate 1.9 ± 1.8 mm/yr of shortening and 2.5 ± 1.5 mm/yr of left lateral strike-slip across the northern ranges of the Western Tian Shan. They assign the shortening to the range front fault and the lateral shear to the Chon Kemin fault, a conclusion which we reassess in Chapter 3.

There are only a handful of published studies pertaining to the tectonic geomorphology of the Zailisky Range Front. Tibaldi et al. (1997) mapped apparent NNE-NE striking scarps in the east of Almaty, ~2 – 20 m high with some ~0.5 – 5 m high strands, but it has since been suggested that these offsets are from a river terrace riser rather than a scarp (Grützner et al., 2017b). Selander et al. (2012) examined a small section of the eastern part of the range front to the south of the town of Chilik, mapping faults and folds which deform Quaternary units with offsets of up to 72 ± 30 m in older surfaces. They also report ~3 – 5 m high scarps in the youngest surfaces, but do not document their locations. The first comprehensive mapping of the range front was carried out by Grützner et al. (2017b) who document evidence of active thrust faulting at 11 sites along a ~250 km section of the range front, including scarps beneath Almaty city and Talgar town. They measure scarps with vertical offsets between ~0.5 – 50 m along the range front using a mixture of GPS survey profiles, drone survey DEMs, low resolution satellite DEMs, and approximate estimates of scarp heights from inspection in the field. They also document uplift of the foreland to the northwest of Almaty and infer the presence of blind thrusting or folding beneath the city. Based on their measurements, Grützner et al. (2017b) suggest that scarps with ~2 – 4 m offset ruptured in a single event, corresponding to earthquakes of $M_w > 6.8$. However, they note that they have no direct constraints on whether these are single or multiple event scarps. Grützner et al. (2017b) suggest all of the mapped scarps probably formed in the Holocene based on a qualitative assessment of the degraded scarp morphology, but there are as yet no published studies which provide a dated earthquake chronology for any part of the ZRF. Grützner et al. (2017b) and Selander et al., (2012) estimate slip rates for the ZRF which range from ~0.4 – 2.2 mm/yr. A detailed discussion and reassessment of these estimates can be found in Chapter 3 of this thesis.

At the western end of the ZRF at ~43.41°N, the mountains terminate, giving way to the right-lateral Dzhalair-Naiman fault (DNF) to the northwest (Figure 2.1-1a; Hollingsworth et al., 2016). The DNF is clearly visible in satellite imagery, forming a > 500 km long lineament in the Kazakh Platform, but it

has no historical or instrumental record of earthquakes (Hollingsworth et al., 2016; Wu et al., 2023). There is also limited geomorphic evidence for recent activity, excepting a single preliminary study by Hollingsworth et al. (2016) who documented streams offset by ~80 m and a ~6 m high scarp in Quaternary deposits on the Chokpar segment, a 50 km fault strand ~15 km to the southwest of the main structure. Based on GPS data, Wu et al. (2023) suggest there is 1.6 ± 1.4 mm/yr of right lateral strike slip and no shortening across the DNF. However, this estimate is based on sparse GPS stations, and the step in velocity they measure occurs ~100 km to the east of the surface trace of the DNF. Whilst the DNF is not the subject of this study, we note that it could potentially be another source of seismic hazard to Almaty, and further research is required to determine its earthquake history, rate, and seismic potential.

2.1.2. Regional Earthquakes

The majority of the regional seismicity is located within the Tian Shan and restricted to depths of < 30 km, with occasional deeper events up to ~45 km within the surrounding rigid basins or on their margins (Figure 2.1-1a; Sloan et al., 2011; Alinaghi and Krüger, 2014; Grützner et al., 2017b). Where fault plane solutions are available, most earthquakes have thrust mechanisms with E-W oriented focal planes in addition to a few strike-slip events (Sloan et al., 2011; Grützner et al., 2017b). Three high magnitude events ruptured within the Kungey and Zailisky ranges between 1887 and 1911 (Figure 2.1-1). The first of these events was the 1887 M_W ~7.2 – 7.7 Verny earthquake which had an epicentre on the northern slopes of the Zailisky Alatau, close to the city of Almaty (known at the time as Verny) which was largely destroyed in the earthquake (Kondorskaya et al., 1982; Tatevossian, 2007; Bindi et al., 2014; Krüger, Kulikova and Landgraf, 2018). The rupture caused landsliding, mudflows and cracking on the northern slopes of the Zailisky Alatau and within the mountains (Mushketov, 1890; Bogdanovich et al., 1914; Kondorskaya et al., 1982; Tatevossian, 2007). Contours showing the intensity of environmental effects are elongate rather than circular, consistent with a shallow crustal

source, but no surface ruptures were mapped shortly after the event or in subsequent studies (Mushketov, 1890; Tatevossian, 2007; Grützner et al., 2017b). The absence of scarps associated with the 1887 event might indicate that the earthquake did not rupture the surface, but there are other possible explanations that cannot be discounted. Firstly, the post-event mappers may have failed to distinguish primary scarps from secondary effects in their reporting due the limits of scientific understanding at the time, and any such evidence may have since been destroyed by the development of modern Almaty (Tatevossian, 2007). Kondorskaya et al. (1982) do report 'surface displacement observed in both loose alluvial and dilluvial deposits, as well as in hard rock', but it is unclear where these displacements are located or whether they correspond to primary scarps or secondary effects. Secondly, whilst Bindi et al. (2014) place the epicentre of the 1887 event within Almaty itself, epicentral estimates from other sources and reports of maximum environmental effects are located further south at higher elevations on the northern slopes of the mountains behind Almaty (Kondorskaya et al., 1982; Tatevossian, 2007). If the 1887 coseismic scarps did form at these higher altitudes they would be more inaccessible to mappers and would likely erode more quickly due to the steeper slopes, which could explain why they have not been identified. It is not possible to distinguish between these different explanations and it remains unknown as to whether the 1887 event ruptured the surface (Tatevossian, 2007). Neither can we be certain that the ZRF was the source of the earthquake, although it seems likely due to its reported location.

In 1889 the M_W 7.9 – 8.3 Chilik earthquake ruptured faults in the eastern Kungey range triggering landslides and fissuring (Kondorskaya et al., 1982; Bindi et al., 2014; Abdrakhmatov et al., 2016; Krüger, Kulikova and Landgraf, 2017; 2018). Abdrakhmatov et al. (2016) map ~175 km of scarps with slip of up to 10 m which they suggest formed in the 1889 rupture, although this attribution has not been confirmed by dating (Krüger, Kulikova and Landgraf, 2018). The proposed ruptures form a 'z' shape and are thought to accommodate N-S shortening through a combination of left and right lateral oblique slip across the different faults (Abdrakhmatov et al., 2016). In 1911, the M_W 8.0 Chon Kemin

(or Kebin) earthquake ruptured through the Chon Kemin valley which divides the Kungey and Zailisky ranges, as well as in the Chon Aksu valley within the Kungey range (Figure 2.1-1b; Kulikova and Krüger, 2015; Arrowsmith et al., 2017). According to Kondorskaya et al. (1982), there were at least 450 fatalities and almost 800 buildings were destroyed in Almaty. By digitising and reanalysing seismic records, Kulikova and Krüger (2015) obtain an epicentre of 42.996N° 77.367E° (within the Chon Kemin valley, CK in Figure 2.1-1b) and a thrust mechanism with an east-northeast striking focal plane. Shortly after the earthquake, scarps were documented by Bogdanovich et al. (1914), later by Delvaux, Abdrakhmatov and Lemzin (2001), and most recently by Arrowsmith et al. (2017) who mapped > 155 – 195 km of surface ruptures with an average slip of 3 – 4 m and maximum slip of <14 m in the 1911 event. However, Arrowsmith et al. (2017) infer whether scarps formed in a single or multiple events based on their surface expression alone rather than from paleoseismic data – we note that this introduces significant uncertainties to estimates of slip in the most recent event, as multiple event offsets are not always morphologically distinct from single event scarps. Arrowsmith et al. (2017) also document 13 distinct fault patches, some of which are separated by stepovers of up to ~4 – 10 km.

In addition to these three events within or close to the Zailisky Alatau, several other large earthquakes have ruptured the northern Tian Shan over the last ~200 years. More than 200 km west of Almaty, the 1885 M_W 6.9 – 7.9 Belovodskoe earthquake ruptured the northern range front of Kyrgyz Tian Shan near Bishkek, and is often considered as part of the same sequence as the 1887 – 1991 ruptures (Abdrakhmatov et al., 2016; Patyniak et al., 2017; Krüger, Kulikova and Landgraf, 2018). To the southwest of Belovodskoe in the Kyrgyz Tian Shan, the 1992 M_W 7.2 Suusamyr earthquake (Dziewonski, Chou and Woodhouse, 1981; Ekström, Nettles and Dziewoński, 2012) produced a rather unusual set of surface ruptures for its magnitude: mappers found only ~7 km of segmented scarps separated by gaps of more than 20 km (Ghose et al., 1997; Ainscoe et al., 2019). To the east of the Zailisky Range Front, the 1812 M_S 8.0 Nilke (or Nilka) earthquake (Feng, 1990; Wu et al., 2020) and

the 1906 M_W 7.7 Manas earthquake (Deng et al., 1996; Tsai, 2023) ruptured within the Borohoro Shan, the range lying to the southwest of the Dzhungarian Basin (Figure 2.1-1a). For the 1906 Manas earthquake, it has been suggested that measured surface slip is significantly smaller than expected from an earthquake of this magnitude (Deng et al., 1996; Tsai, 2023).

These historical events provide insights into the range of behaviour of large faults in the Tian Shan. Firstly, several of these earthquakes do not appear to have ruptured the surface with the expected slip or extent we might expect from their magnitudes, implying that empirical scaling relationships between surface rupture parameters and magnitude (e.g. Wells and Coppersmith, 1994; Wesnousky, 2008) might not always apply in this region. Secondly, some of the historical events are spatially and temporally clustered (e.g. the four events between 1885 – 1911), suggesting that traditional models of the seismic cycle with regular recurrence intervals for individual faults may not apply (Liu and Stein, 2016). Liu and Stein (2016) propose that complex, dynamic, interactive behaviour of this nature is typical of slowly deforming regions within continental interiors. Finally, these earthquakes reveal that in contrast to present day instrumental seismicity in the region, the faults of the northern Tian Shan are capable of rupturing in very large events of up to M_W ~8.0 – 8.3. The effects of these historical events included extensive landsliding, mudflows, and fissuring, as well as the destruction of buildings and many fatalities. Most of the range front is blanketed by thick loess (Dave et al., 2023), which is particularly susceptible to landsliding (Zhang and Wang, 2007). A similar earthquake today would be even more destructive, as the city of Almaty has grown dramatically over the last century (including expansion onto the landslide-prone slopes of the mountain front) and now has a population of around 2 million compared to tens of thousands in the late nineteenth century (Amey et al., 2021). Using the Global Earthquake Model's OpenQuake Engine (Pagani et al., 2014), Amey et al. (2021) modelled the impact that the M_W ~7.2 – 7.9 1887 Verny (modelled as M_W 7.3; Bindi et al., 2014; Krüger, Kulikova and Landgraf, 2018), M_W ~7.9 – 8.3 1889 Chilik (Bindi et al., 2014; Krüger, Kulikova and Landgraf, 2017; 2018) and M_W ~8.0 1911 Chon Kemin (Kulikova and Krüger, 2015) earthquakes would have on

present day Almaty, as well as several hypothetical scenarios: two M_W 6.5 events on 25 km long sections of the ZRF beneath Almaty and Talgar, a M_W 6.5 event on a 25 km long splay beneath northern Almaty inferred from folding first mapped by Grützner et al. (2017b), and a M_W 7.7 earthquake deep within the Kazakh Platform based on an expansion of the parameters from a 1979 M_W 5.4 earthquake documented by Sloan et al. (2011) . Of their modelled scenarios, Amey et al. (2021) find the worst impacts are associated with the M_W 6.5 earthquake on the northern splay beneath Almaty, corresponding to ~4,100 ± 3,500 deaths, ~12,300 ± 5,000 collapsed buildings and an economic cost of ~4.7 ± 2.7 Billion USD. This demonstrates that even medium-sized earthquakes can be of great danger along the range front when faults are located directly below populated areas (Amey et al., 2021).

While there are no published paleoseismic studies on the ZRF, Grützner et al. (2017b) dated one deformed surface to ~13.3 – 15 ka, demonstrating that there have been earthquakes on the fault during this period. Excavations elsewhere in the Tian Shan indicate that faults tend to rupture in large but rare earthquakes, with average recurrence intervals of several thousands of years – examples of such behaviour include the Toraigyr fault (Grützner et al., 2017a), the Dzungarian and Lepsy faults (Campbell et al., 2015; Hu et al., 2021; Tsai et al., 2022), the Dushanzi and Manas fault zones (Deng et al., 1996), the Saty fault (Abdrakhmatov et al., 2016), the Suusamyr fault (Ainscoe et al., 2019), and the Chonkurchak fault (Landgraf et al., 2016).

2.2. Methods

2.2.1. Geomorphic Mapping

We map geomorphic evidence of faulting using a range of datasets: Google Satellite imagery in plan-view and visualised in 3D using Google Earth (https://www.google.co.uk/intl/en_uk/earth/), Bing

Aerial Satellite imagery (http://www.bing.com/maps), as well as freely available 30 m digital elevation datasets including the Copernicus GLO-30 DEM (European Space Agency and Airbus, 2022), ALOS World 3D 30 m (Japan Aerospace Exploration Agency, 2021), and SRTM (NASA JPL, 2013). We also utilise higher resolution datasets including DEMs from drone surveys and Pléiades satellite imagery as well as GPS field surveys, all of which are described in detail in the sub-sections below. We study 33 different sites along the range front for which we have varying available data, as detailed in Table 2.2-1. All new elevation datasets presented are available from the author as point clouds upon request.

In our mapping approach, we first map fault scarps in the field or from elevation datasets where we find surface offsets which we infer to be tectonic. At many of these scarp sites we also map the boundaries of alluvial fans or stream terraces, to avoid mistaking erosional or hydrological features for tectonic scarps, and to better understand the earthquake history at the site. Where possible, we tentatively infer relative chronologies for alluvial fans at a given scarp site based on their cross-cutting relationships, depth of incision, level of dissection and (where applicable) relative heights of the fans (Grützner et al., 2017b). At scarp sites which cross larger stream or river valleys, we map terraces based on their relative heights. We map at most 5 different inferred generations of surfaces in addition to modern drainage channels at any given site. We do not correlate our fan mapping between sites due to differences in the resolution of the available data along strike and/or indistinct fan morphologies and uncertainties in cross-cutting relationships. The ages of the different surfaces probably vary along the length of the fault depending on changing sediment and hydrological inputs. Therefore, while we label surfaces as T0 to T5 to indicate their relative ages, this is intended as an internal chronology at an individual site, and surfaces with the same label at different sites should not be taken to be of the same age. We note also that almost all our inferred relative chronologies have not been confirmed by direct dating and as such all are uncertain. Nevertheless, inferred chronologies are included as an aid to interpreting each site and to help future researchers with targeting sampling campaigns.

To infer the location and extent of the fault along the range front, we extend our scarp mapping using larger-scale topographic features. Between scarp sites, we assume the fault is responsible for sharp changes in elevation between the mountains and the piedmont and that the fault trace follows the break in slope, except where it has a clear hydrological origin (such as the edge of an alluvial fan).

Table 2.2-1. Elevation datasets available at each site. The locations of sites N1 – N33 are shown in Figure 2.1-1b. *Dataset published in Grützner et al. (2017b).**Dataset published in Amey et al. (2021).

Site	**Elevation datasets available**			
	Field dGPS survey	**UAV DEM (<0.15 m)**	**Pléiades DEM (~1.5 m)**	**Copernicus GLO-30 DEM (30 m)**
N1		Yes		Yes
N2		Yes		Yes
N3		Yes*		Yes
N4		Yes*		Yes
N5		Yes		Yes
N6				Yes
N7				Yes
N8				Yes
N9		Yes		Yes
N10	Yes**		Yes	Yes
N11	Yes		Yes	Yes
N12	Yes		Yes	Yes
N13		Yes	Yes	Yes
N14		Yes*	Yes	Yes
N15			Yes	Yes
N16			Yes	Yes
N17		Yes	Yes	Yes
N18		Yes*	Yes	Yes
N19		Yes	Yes	Yes
N20		Yes	Yes	Yes
N21		Yes	Yes	Yes
N22		Yes	Yes	Yes
N23			Yes	Yes
N24				Yes
N25		Yes	Yes	Yes
N26		Yes	Yes	Yes
N27			Yes	Yes
N28			Yes	Yes
N29			Yes	Yes
N30			Yes	Yes
N31			Yes	Yes
N32				Yes
N33			Yes	Yes

2.2.1.1. High-resolution Digital Elevation Models

Our highest-resolution DEM datasets are derived from drone surveys. We collected 18 new drone surveys (12 of which contain scarps), adding to the 4 existing surveys of the Zailisky Range Front published by Grützner et al. (2017b). We targeted a range of different sites: Firstly, we surveyed sites where scarps had already been mapped to obtain more detailed measurements. Secondly, we surveyed sites where suspected scarps were visible in satellite imagery but could not be resolved in lower resolution DEMs. Finally, we carried out some speculative surveys of alluvial fans along the expected trace of the fault to check for small scarps not visible in remote imagery or DEMs, covering areas which were too large or inaccessible to comprehensively map on foot. Most of these speculative surveys revealed no scarps when converted into DEMs, but we show the locations of these "null-result" sites as red patches in Figure 2.1-1b.

Photogrammetry surveys were collected using a DJI Phantom 4 drone. For one survey (N19) we placed ground control points (GCPs) throughout the surveyed area, measured their locations with a Promark3 dGPS receiver and base station, and used these as reference points to locate photographed features during survey processing (e.g. Grützner et al., 2017b; Ainscoe et al., 2019). All other surveys were collected with a dGPS receiver (Teokit) attached to the drone instead of GCPs, used in combination with an Emlid Reach RS2 base station for correction of the drone location associated with each photo (e.g. Zhang et al., 2019; Pierce et al., 2022). In each survey we collected between ~150 – 2300 photographs and processed them using Agisoft Metashape software, utilising Structure from Motion (SfM) algorithms to construct a 3-D point cloud from tie points in overlapping photographs (Westoby et al., 2012). We derive DEMs from these point clouds which have resolutions between 5 – 12 cm/pixel. We also analyse drone DEMs from Grützner et al. (2017b) which were processed using a similar methodology and have resolutions of ~10 cm.

We constructed DEMs from Pléiades satellite imagery (available for purchase from https://intelligence.airbus.com/) along the eastern half of the Zailisky Range Front for ~170 km, corresponding to the yellow polygon in Figure 2.1-1b. We processed 12 separate sets of two or three (stereo or tri-stereo) panchromatic images which were acquired by the Pléiades satellite between 2012 – 2020. We processed the images using Agisoft Metashape applying 'Aggressive' Depth Filtering to remove outliers (Agisoft LLC, 2023). We produced point clouds and DEMs with a resolution of < 1.5 m from the Pléiades images.

Whilst SfM techniques can effectively constrain relative elevations, the absolute height of the resulting DEM is often poorly constrained. We find our drone or Pléiades DEMs are offset from global 30 m DEM datasets, so we shift all DEMs up or down by a constant value to align them with the Copernicus GLO-30 DEM before plotting elevation data.

2.2.1.2. dGPS Field Surveys

We present dGPS field surveys at two sites, collected using Emlid Reach RS2 base and rover receivers and processed with Emlid Studio v1.4 software. At site N11 (Section 2.3.3.), we carried out a 'Stop and Go' dGPS survey on foot along a single 70 m long profile perpendicular to the fault scarp. All processed data have 'Fix' solutions, meaning the ambiguities in the position of the rover were successfully resolved using base corrections and have centimetre-level precision (Emlid Studio, 2023). Formal RMS (Root Mean Square) errors are less than 1.5 cm (both lateral and vertical) for all points. At site N12 (Section 2.3.3.), we carried out a kinematic dGPS survey within Talgar town by fixing the rover to our field vehicle and driving it around the road network, recording measurements every ~0.2 seconds. We drove the rover up to 3.5 km from the base station which was left at 43.29N, 77.22E. Most points (61.8%) have 'Fix' solutions indicating cm-level precision (Appendix Figure 2.7-1). Around a third (36.6%) have 'Float' solutions, meaning only some of the positional ambiguities in the

rover position could be resolved, giving sub-meter level precision (Appendix Figure 2.7-1; Emlid Studio, 2023). A small number of points (1.6%) have 'Single' solutions, meaning that base corrections could not be applied and the precision on the order of several metres (Emlid Studio, 2023). We discard points with ‘Single’ solutions due to their low precision. We filter the remaining dGPS measurements by their up, north and east standard deviations, retaining data with standard deviations of less than 10 cm in all 3 directions and discarding the rest. Our data cleaning procedures removed 10% of the dGPS points in total. Upon visual inspection of the data, the obviously erroneous points were removed, such as vertical spikes in elevation above the road surface. As a further quality check, we compare the dGPS survey with 30 m DEM data and find them to be consistent, with dGPS measurements a few metres higher than the DEMs on average (Appendix Figure 2.7-2). We find no time dependent trend in the dGPS data – i.e. no drift in the dGPS measurements as the survey progressed (Appendix Figure 2.7-3).

The surveyed roads largely follow the natural topography, but they are not perfectly smooth and small-scale bumps caused the car to oscillate up and down, introducing some errors in addition to the formal measurement uncertainty. We estimate these errors to be on the order of centimetres to tens of centimetres rather than metres and as such they should not significantly affect our measurements.

2.2.1.3. Scarp Offset Measurement

Average surface slip in an earthquake is a useful proxy for estimating its magnitude (e.g. Wells and Coppersmith, 1994). We therefore measure the vertical displacement (throw) across mapped scarps, which can then be converted to slip by assuming a fault dip. To measure scarp offsets, we draw profiles approximately perpendicular to the fault, adjusting their orientation to ensure they follow geomorphic features rather than cutting across them (Ainscoe et al., 2019). We assume there has been no significant modification of the scarps since their formation, or, in a few cases, we note where scarps may have been modified. We sample elevation data at regular intervals along profile lines: every 15

cm for drone DEMs, every 1.5 m for Pléiades DEMs, and every 30 m for the Copernicus GLO-30 DEM. For dGPS surveys we project the processed and cleaned data onto profile lines and the data resolution is location dependent.

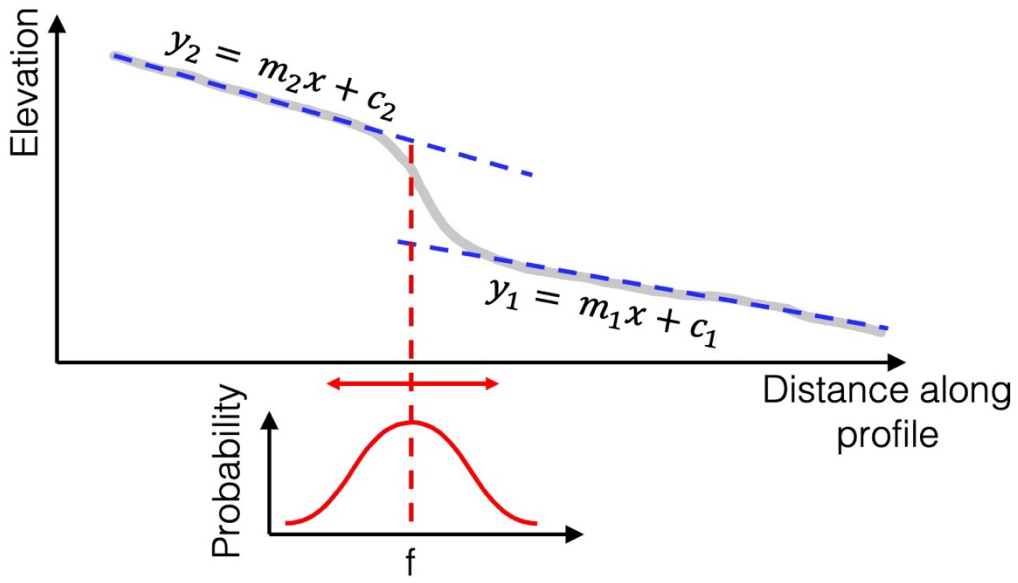

Figure 2.2-1. A schematic diagram of the scarp offset measurement methodology. The thick grey line represents elevation data, with linear slope models shown as blue dashed lines, corresponding to the equations in black. The vertical offset is calculated at location f along the profile (vertical red dashed line), where f is the centre of a range of possible fault locations (horizontal red arrow) that we define manually for each scarp. This range is assumed to represent a 2σ probability range of possible fault locations, normally distributed around f (red curve).

We model footwall and hanging wall surfaces with the linear equations $y_1 = m_1x + c_1$ and $y_2 = m_2x + c_2$ respectively (Figure 2.2-1). Alluvial fans tend to have longitudinal profiles which are concave-upward (Bowman, 2019), but we assume they are approximately linear over short distances for our purposes. However, we allow the hanging wall and footwall models to have different gradients to account for small changes in slope with longitudinal distance. We manually select ranges of points to be used in the modelling of each surface and perform a linear regression to obtain the coefficients m_1, m_2, c_1 and c_2, and their corresponding standard deviations σ_{m_1}, σ_{m_2}, σ_{c_1} and σ_{c_2}. We define a range of possible fault locations and assume this represents a 2σ probability, normally distributed

about the central value, f (Figure 2.2-1). To measure the vertical offset, we calculate the difference in height between the hanging wall and footwall at f:

$$Offset = y_2(f) - y_1(f)$$
$$= (m_2 - m_1)f + (c_2 - c_1). \quad (2.2.1)$$

The formal uncertainty in this offset measurement is

$$\sigma_{offset} = \sqrt{\sigma_{f\Delta m}^2 + \sigma_c^2} \quad (2.2.2)$$

where

$$\sigma_c = \sqrt{\sigma_{c_1}^2 + \sigma_{c_2}^2}, \quad (2.2.3)$$

$$\sigma_{f\Delta m} = |(m_2 - m_2)f| \sqrt{\left(\frac{\sigma_f}{f}\right)^2 + \left(\frac{\sigma_{\Delta m}}{m_2 - m_1}\right)^2}, \quad (2.2.4)$$

and

$$\sigma_{\Delta m} = \sqrt{\sigma_{m_1}^2 + \sigma_{m_2}^2}. \quad (2.2.5)$$

σ_f is the prior uncertainty in fault location and is equal to $\frac{Fault\ range\ in\ x}{4}$ (because the range in fault locations is a 2σ probability range).

In addition to the formal uncertainty for a single offset measurement, several other factors introduce further uncertainty, including the subjective choice of hanging wall and footwall ranges for the model (Grützner et al., 2017a), as well as the azimuth and placement of scarp profile lines. Offsets may also vary along strike even within a short scarp segment due to true variations in slip on the fault. We

attempt to capture some of this additional uncertainty and natural variation by making multiple measurements of a given scarp where possible and reporting a range of vertical offset values. Where only a single scarp offset measurements is made, we report that measurement with its 1σ uncertainty.

2.2.2. Paleoseismic Excavations

We chose a site for paleoseismic trenching at the eastern end of the fault based on scarp mapping by Grützner et al. (2017b), remote investigations using Google Earth and assessment of site accessibility. After excavating the trench (site N19), we cleaned and brushed the eastern wall and created a ~1 x 1 m grid using string. We created an orthophoto of the eastern trench wall using Agisoft Metashape. We photographed the trench wall, logged the stratigraphy and structure, and collected six samples for dating. We also excavated a pit in the hanging wall of a nearby scarp, cleaned, logged and photographed it, and collected two samples for dating. All samples were dated using luminescence dating techniques.

2.2.2.1. Luminescence Dating

This dating method involves measuring luminescence signals accumulated in buried sediments to determine the time since they were last exposed to light, providing an estimate of the age of the surface (Aitken, 1998; Rhodes, 2011). Luminescence dating can be performed on quartz and feldspar grains and is therefore widely applicable (Rhodes, 2011), including to the alluvial and loess deposits of the Zailisky Range Front where we found no material for carbon dating in our paleoseismic excavations.

Luminescence techniques can include the stimulation of samples by heat in thermoluminescence (TL) dating, or by light in Infrared Stimulated Luminescence (IRSL) or Optically Stimulated Luminescence (OSL) dating (Rhodes, 2011). In this thesis we discuss dates obtained from IRSL and OSL, so we outline the principles of both these methods below (Section 2.2.2.1.1). The specific IRSL protocols

used to date feldspars from paleoseismic excavations presented in this chapter are detailed in Section 2.2.2.1.2.

2.2.2.1.1. Background to OSL and IRSL

When a mineral grain is buried, natural environmental radiation (from ^{40}K, ^{238}U, ^{235}U and ^{232}Th, with minor contributions from ^{87}Rb and cosmic rays) causes its electrons to become excited from the valence band to the conduction band, and a small percentage of these excited electrons are trapped in defects within the crystal lattice (Aitken, 1998; Rhodes, 2011). The concentration of trapped electrons increases gradually over ~100 – 100,000 years after burial, but a brief exposure to natural sunlight for ~1 to 100 seconds or heating at 200 to 400 °C releases this trapped charge and resets the accumulated signal to zero, also known as 'bleaching' (Rhodes, 2011; Dave, 2022). The energy stored by these trapped elections is proportional to the total amount of radiation energy absorbed by the grain since it was last bleached, known as the equivalent dose (D_e), with a constant of proportionality dependent on the sample (Aitken, 1998; Rhodes, 2011). Therefore, the age of a grain can be calculated as follows:

$$Age\ (yr) = \frac{D_e\ (Gy)}{D\ (Gy/yr)}$$

where D is the dose rate, the rate at which the grain absorbed energy from environmental radiation during its burial, and Gy is the standard unit of measurement for ionising radiation ($1\ Gy = 1\ J/kg$; Aitken, 1998; Rhodes, 2011).

The D_e is commonly measured using the SAR (Single Aliquot Regenerative-dose) protocol (Murray and Wintle, 2000; 2003): after removing the unstable signal with a preheating step, the sample is stimulated with light causing the trapped electrons to be released and emit photons which are measured with a photomultiplier tube – this is the natural luminescence signal (Rhodes, 2011; Dave, 2022). The sample is then put through repeated cycles of irradiation with a known beta dose (the 'regenerative dose'), brief heating to remove any unstable signal, and stimulation to measure the regenerated

luminescence signal (Rhodes, 2011; Dave, 2022). In each of these SAR cycles, the regenerative dose is varied so that after multiple cycles a growth curve can be constructed from which the equivalent dose is estimated (Figure 2.2-2; Rhodes, 2011; Dave, 2022). There is an upper limit on the age that can be measured for any given sample when it reaches saturation – when all the potential electron traps are full, no further signal can accumulate despite continued exposure to radiation (Rhodes, 2011). The curvature of the growth curve produced in the SAR protocol indicates whether the sample has reached saturation (Figure 2.2-2). To produce finite D_e values, grains must not be at or close to saturation, and they must have sufficient sensitivity (the luminescence signal generated by one unit of applied dose) to produce a measurable signal (Rhodes, 2011). Measuring a few hundred grains commonly produces only a few tens of finite D_e values. This SAR protocol can also be carried out on single grains as opposed to single aliquots (e.g. Rhodes, 2015).

.

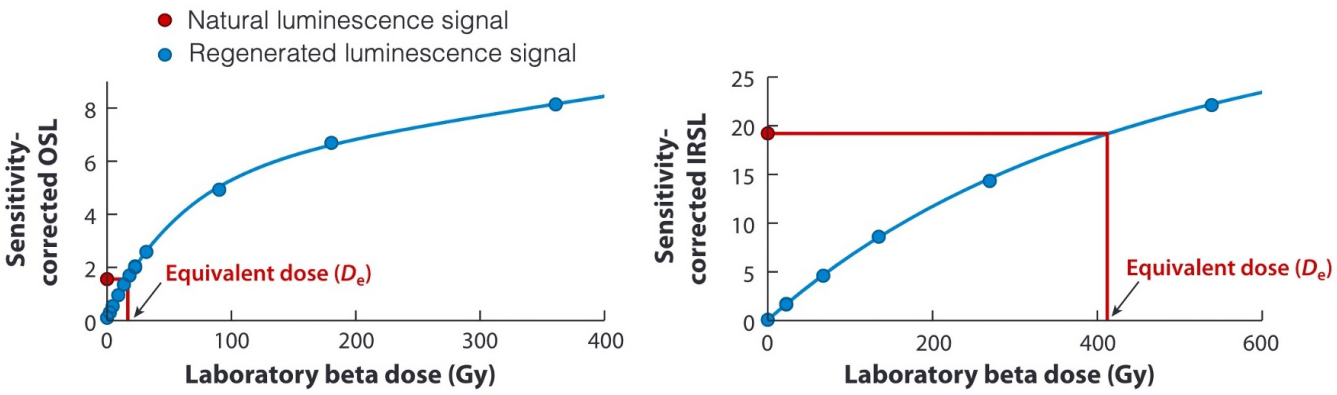

Figure 2.2-2. Modified after Rhodes (2011). Left: OSL growth curve for one aliquot of late Pleistocene fluvial quartz with D_e ~16 Gy. The flattening of the curve shows the approach towards saturation of the electron traps as the regenerative dose is increased, but the natural signal is far from saturation (Rhodes, 2011). Right: An IRSL growth curve with D_e ~400 Gy which does not appear to be approaching saturation in response to the laboratory dosing (Rhodes, 2011).

Some depositional scenarios can lead to incomplete bleaching – for example, if grains are uncovered, transported and deposited at night then the luminescence signal from their previous burial will not be reset to zero (Rhodes, 2011). Even during the day, some environments inhibit light exposure of grains,

such as deep, high-energy fluvial channels (Smedley and Skirrow, 2020). With incomplete bleaching, the D_e will be over-estimated and the sample will appear older than it is (Rhodes, 2011). Big variations in D_e across different aliquots or grains from the same sample may indicate incomplete bleaching, but a meaningful D_e estimate can often still be obtained by applying a minimum age model (Galbraith et al., 1999; Rhodes, 2011).

Recently eroded quartz grains (such as those from mountainous and tectonically active environments like our study area) have particularly low sensitivities (i.e. low luminescence signal brightness) compared to quartz which has been reworked multiple times (e.g. in sand dunes; Rhodes, 2011; Mahan et al., 2022). K feldspars tend to have higher sensitivities, so are a good alternative to quartz in mountainous environments (Rhodes, 2011). However, K feldspars can be affected by a process called 'anomalous fading' in which the luminescence signal rapidly decays due to quantum mechanical tunnelling during burial or storage, producing artificially young ages (Rhodes, 2011; Kitis et al., 2013; Kars et al., 2014). It is common to repeat luminescence readings after storage to check for changes due to fading – if significant differences are identified, fading corrections can be applied (Aitken, 1998; Rhodes, 2011). Anomalous fading can also be mitigated using a post-IR Infrared Stimulated Luminescence (pIR-IRSL) dating approach, in which a low-temperature (e.g. 50 °C) IR bleach is performed to remove the components of the signal most likely to be affected by anomalous fading, before measuring the luminescence signal at a higher temperature (e.g. 225 °C; Buylaert et al., 2009; Rhodes, 2015). Therefore, pIR-IRSL is the approach taken for all new dates presented in this thesis.

The dose rate, D, is calculated from the concentrations of radioactive isotopes in the sampled sediment, the contribution of cosmic radiation (which depends on the sample burial depth), and the sediment's moisture content – interstitial waters absorb some of the radiation such that a 1% change in water content corresponds to a 1% change in dose rate (Aitken, 1998; Rhodes, 2011). In the context of

luminescence dating, very fine sand to fine sand (63 – 250 μm) is referred to as coarse-grained, whilst very fine silt (4 – 11 μm) is referred to as fine-grained (Mahan et al., 2022). Etching coarse-grained samples in acid removes the need to account for alpha irradiation in dose rate calculations (Rhodes, 2011). For fine-grained dating, an alpha efficiency (a-value) is specified to quantify the lower effectiveness of alpha particles in inducing a luminescence signal compared to other forms of radiation (Aitken, 1998; Durcan, King and Duller, 2015).

2.2.2.1.2. IRSL Protocol: 2019 Samples (Site N19)

At site N19, luminescence samples were collected from excavated vertical sections, which were scraped clean before sampling with metal tubes hammered horizontally into the sediment. The outward-facing end of each tube was covered throughout sampling, and upon retrieval of the filled tubes, the exposed inner end was quickly sealed with opaque foil and taped shut to prevent light from entering. The samples were processed under subdued red light in the luminescence laboratory at the Department of Geography at the University of Sheffield, UK. For all samples, the outer 1 – 2 cm of sediment was removed from both ends of each tube to avoid dating any material that was exposed to light. This sediment was weighed, dried in an oven, and then weighed again, in order to determine the percentage moisture content of the sample for dose-rate calculations.

After the removal of the outermost sediment, the remaining sample was wet-sieved and the 90 – 250 μm fraction retained. Grains were treated with 1M HCl to remove carbonate and 30% H_2O_2 to remove organic matter and then rinsed and dried (Ivester et al., 2022). K-feldspars were isolated by density separation with a 2.58 g/cm^3 sodium polytungstate solution in a centrifuge. The feldspar grains were thoroughly rinsed and sieved again, retaining the 125 – 212 μm fraction for measurement. It is common to treat samples with HF at this stage, but we did not implement this step because tests have suggested that it does not make a difference to D_E measurements (Zinke et al., 2017). The

luminescence measurements were made using a Risø TL-DA-20D DASH automated luminescence reader with a the EMD-9107 photomultiplier tube and blue light filters (BG3 and BG39), such that only light emission between ~340 – 470 nm was detected. To minimise the impact of anomalous fading, a single-grain K-feldspar pIR-IRSL SAR protocol (Table 2.2-2) was applied (Buylaert et al., 2009; Thiel et al., 2011) with an initial bleach at 50 °C and post-IR stimulation for luminescence measurement at 225 °C ($pIR_{50}IRSL_{225}$), similar to the protocols described in Rhodes (2015), Grützner et al. (2017a), and Zinke et al. (2017). Between 200 and 600 individual grains were measured from each sample. Grains with measurable D_Es are plotted in Appendix Figure 2.7-4, Appendix Figure 2.7-5, and Appendix Figure 2.7-6. D_E estimates were made using the methods of Rhodes (2015), with an overdispersion parameter of 15% used in the age models for all samples to represent the natural spread in D_E beyond instrumental and analytical error (Mahan et al., 2022). Repetition of the measurements on new grains from each sample after storage to check for anomalous fading yielded no significant change in D_E, so no fading correction was applied.

Table 2.2-2. SAR protocol steps followed for single-grain K-feldspar pIR-IRSL applied to 2019 samples processed in Sheffield, after Rhodes (2015), Grützner et al. (2017a), and Zinke et al. (2017). Note that for some samples the highest dose point was 640 Gy rather than 200 Gy. SG = Single Grain.

SAR step	**Measurement parameters**
1 Beta irradiation	0 (Natural), 20, 6.4, 64, 200, 140, 0, 20 Gy in turn
2 Preheat	60s at 250°C, 5°C s^{-1}
3 SG IR Laser	2.5s 90% power at 50°C
4 SG IR Laser	2.5s 90% power at 225°C
5 Beta test dose	8 Gy
6 Preheat	60s at 250°C, 5°C s-1
7 SG IR Laser Sensitivity measurement	2.5s 90% power at 50°C
8 SG IR Laser Sensitivity measurement	2.5s 90% power at 225°C
9 IR LED Hot bleach	40s IRSL (diodes) at 290°C
Return to 1	

Dose rates were calculated by combining radioisotope concentrations measured by ICP-MS (for U and Th) and IC-OES (for K), an assumed internal K concentration of 12.5% ± 2.5 (Huntley and Baril, 1997), and a burial depth-dependent cosmic dose rate. Interstitial waters absorb environmental radiation and reduce the effective dose reaching the grains, so an attenuation factor was applied in the

dose rate calculation to account for the sediment water content (Mahan et al., 2022). Measured water contents were in the range 1 – 9 % across the samples from site N19, so a uniform water content of 5 ± 5 % was used in all dose rate calculations. As larger grains attenuate more beta radiation, a correction factor was also applied to the beta dose rate based on grain size (Aitken, 1998).

2.2.2.1.3. Modelling Chronologies with OxCAL

To estimate the timings of paleo-earthquakes exposed in our dated trench section, we use OxCal v4.4.4 (Bronk Ramsey, 2009) which uses a Bayesian modelling approach to better constrain chronologies. The model inputs are the ages of *events* with their associated uncertainties, as well as *prior* information including the order of events (the *informative prior*) and the mathematical construct underlying the model (the *uninformative prior*; Bronk Ramsey, 2009). The model uses a Markov Chain Monte Carlo (MCMC) approach to iterate through possible solutions, which are used to construct a *posterior* probability density function (PDF) for the ages of the events (Bronk Ramsey, 2009). A representative age is usually achieved after 100,000 to 1,000,000 iterations, and as a measure of this convergence the model outputs the Convergence Integral parameter (C) which should be > 95% (Bronk Ramsey, 2009). The individual Agreement Index parameter (A) is a statistical measure of the overlap between the measured luminescence age of an individual sample and its modelled OxCal age (Rhodes et al., 2003). The overall Agreement Index parameter ($A_{overall}$) quantifies the agreement between all of the raw age data and the model (Rhodes et al., 2003). For both A and $A_{overall}$, 60% is considered the acceptable minimum value below which the exclusion of samples should be considered (Bronk Ramsey, 1995; 2009; Rhodes et al., 2003).

Approaches to designing an OxCal prior model for paleoseismic trench chronologies vary widely between studies (DuRoss et al., 2011) and references therein). There is more than one valid prior model for a given sampled exposure and the favoured model is a matter of interpretation (Bronk

Ramsey, 2000). Within OxCal, stratigraphic units are input as *phases* (sets of dates with no specified order) which can be put into *groupings* using *boundaries*. A single boundary between groupings models a contiguous transition in which the end boundary of one group is the same as the starting boundary of the next (Table 2.2-3; Bronk Ramsey, 2009). To model groupings that are sequential but not contiguous, the end boundary for the first group must be followed by a separate starting boundary for the second group – this configuration is applicable when there is a hiatus in the deposition (Table 2.2-3; Bronk Ramsey, 2009). Placing no boundaries between phases, thus forming no groupings, assumes that all phases are independent and entirely unrelated to one-another, which usually overestimates the spread of ages if multiple events are modelled (Steier and Rom, 2000; Bronk Ramsey, 2023). Between each set of boundaries, the model applies a uniform prior, assuming groupings are randomly sampled from a uniform distribution unless additional constraints are applied (Bronk Ramsey, 1995; 2009; 2023). Using this framework, we test different model priors (Appendix Section 2.7.3.1.) and justify our preferred approach for the trench in Section 2.4.1.2.1. Where events are tightly constrained by date measurements, we report results as a mean value with 2σ uncertainty. Otherwise, we quote the shortest date range that includes 95.4% of the probability in the posterior PDF (Bronk Ramsey, 2009).

Table 2.2-3. OxCal example SQL codes for contiguous and sequential phase models after (Bronk Ramsey, 2009).

Contiguous phases	**Sequential phases**

Sequence()
{
  Boundary("Start 1");
  Phase("1"){…};
  Boundary("Transition 1/2");
  Phase("2"){…};
  Boundary("Transition 2/3");
  Phase("3"){…};
  Boundary("End 3");
};
	Sequence()
	{
	  Boundary("Start 1");
	  Phase("1"){…};
	  Boundary("End 1");
	  Boundary("Start 2");
	  Phase("2"){…};
	  Boundary("End 2");
	  Boundary("Start 3");
	  Phase("3"){…};
	  Boundary("End 3");
	};

2.3. Geomorphology of the Zailisky Range Front Fault

In this section we document the new evidence for recent activity on the ZRF by describing and mapping scarps and other surface deformation, including detailed analyses of 33 specific sites – we review 11 sites from Grützner et al. (2017b) and present 22 new sites. The smallest and largest offset measurements and key observations from all sites are listed in Appendix Table 2.7-10. We focus on identifying scarps that might have formed in the most recent event (MRE). For the purposes of this analysis we split the range front into six sections with distinct morphologies and levels of scarp abundance or preservation.

2.3.1. Akterek section (N1 to N5)

At the western end of the ZRF between the villages of Kenen (Кенен) and Arkhaly (Арқалы), the mountain front strikes ~NW-SE (Figure 2.3-1). The elevation of the Zailisky Alatau decreases steadily towards the northwest, except for a dip in the relief behind Akterek (Актерек) village, until the range terminates at Kenen. Northwest of Kenen, low-lying hills stretch into the Kazakh Platform, bounded or cut by the sharp trace of the Dzhalair-Naiman fault (Figure 2.1-1a).

We remotely map scarps in the alluvial fans along the ~ 40 km stretch of range front between Kenen and Arkhaly using Google Earth (Figure 2.3-1a). We visited localities N1 and N2 in the field and collected drone surveys. At site N1 we map four generations of fan surface, T1 to T4 from youngest to oldest (Figure 2.3-2). We find scarps in all surfaces except for the youngest fan (T1) which truncates the scarps. We measure distinct vertical offsets in the different fans and find those inferred to be older host larger scarps (Figure 2.3-2; Appendix Figure 2.7-13). The smallest scarp is ~ 2.3 – 2.9 m high within a T2 fan. Within another fan inferred to be of generation T2 a few hundred metres away, we measure a ~3.1 – 4.4 m high scarp. The different scarp heights could be a result of variations in slip magnitude, possibly related to a change in strike, or might indicate that the different T2 surfaces are in

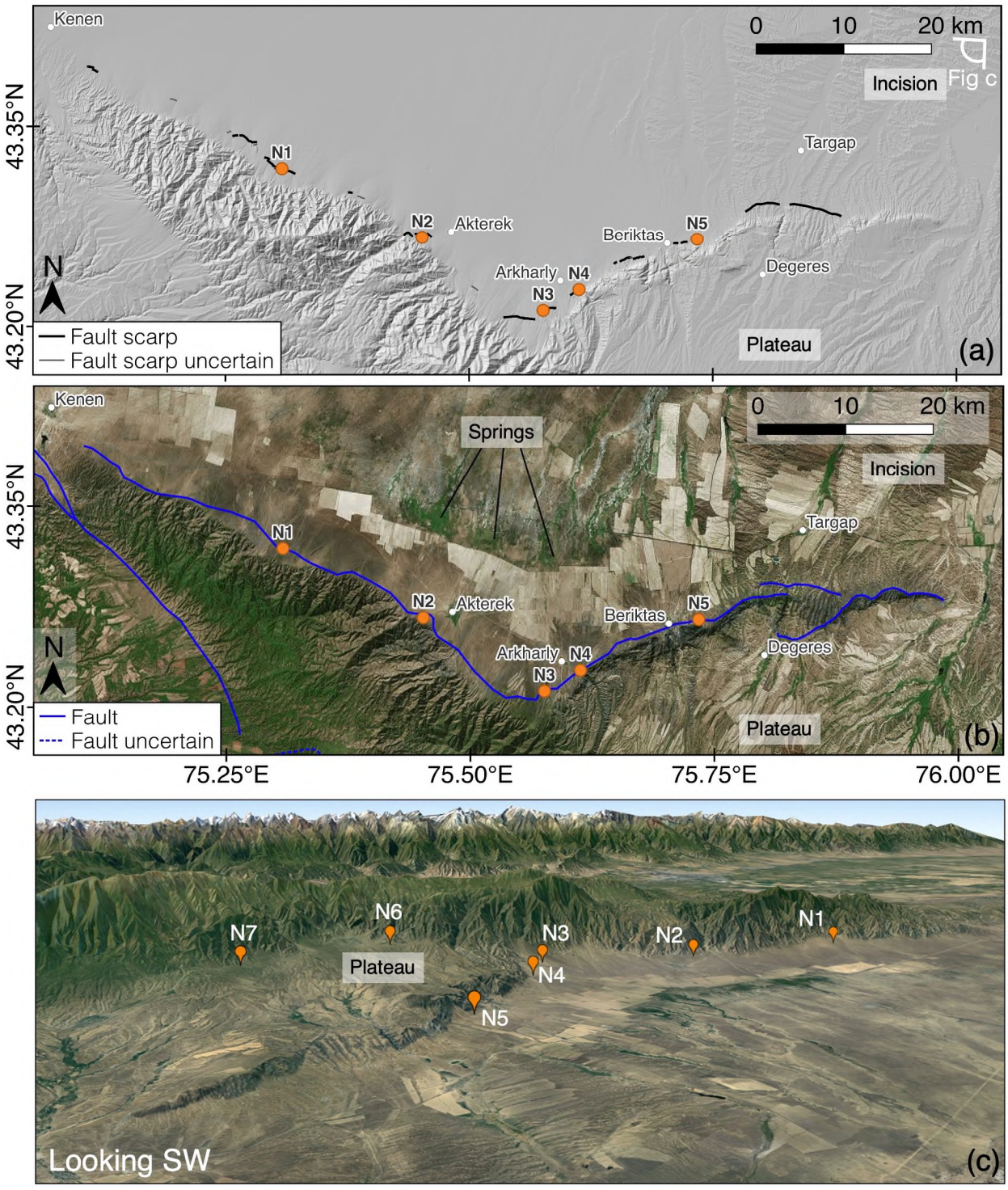

Figure 2.3-1. Overview of Akterek section. Orange data points are sites discussed in the text; white data points are settlements. (a) Scarps mapped in this study overlain on the Copernicus GLO-30 DEM hill shade. (b) Fault mapping overlain on Bing Aerial Imagery (2023 TomTom, Earthstar Geographics SIO). (c) Satellite imagery overlain on 3 x exaggerated topography from Google Earth (2023 Maxar Technologies, 2023 Airbus, Landsat/Copernicus, 2023 CNES/Airbus), 14.87 km eye altitude, looking southwest.

fact of different ages. Scarps in the fans inferred to be of generation T3 and T4 are ~ 8 m and ~14 m high respectively.

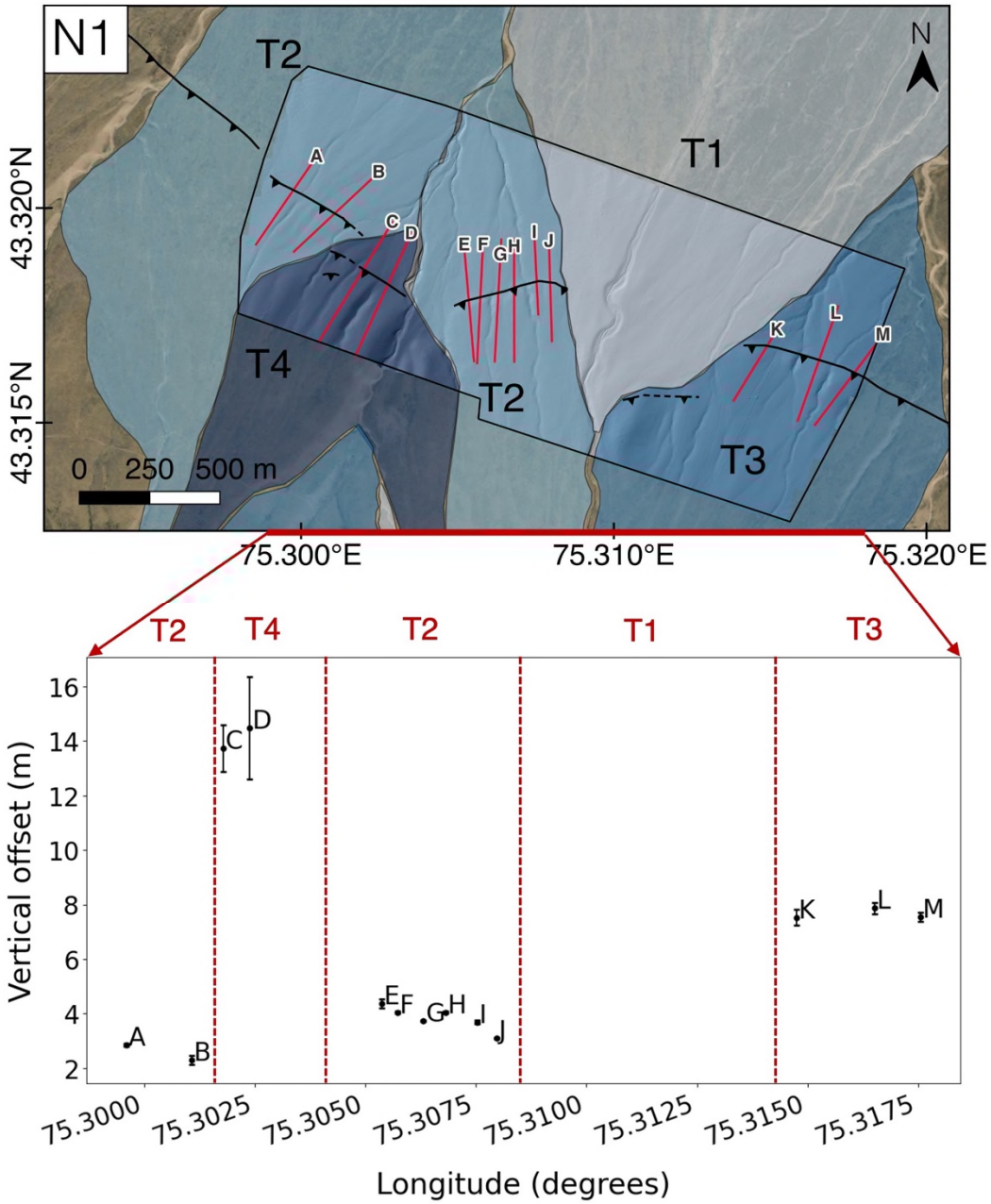

Figure 2.3-2. Site N1. Top: Bing Aerial imagery (2023 TomTom, 2023 Maxar) overlain with hill-shaded drone DEM and alluvial fan mapping of four fan generations (T1-T4, youngest to oldest; different colours indicate different inferred fan ages, darker = older). Profile lines for vertical offset measurement are shown in red, corresponding to Appendix Figure 2.7-13. Bottom: vertical offset measurements plotted by longitude. Dashed lines show approximate transitions between fans of different generations which are labelled in red above the plot.

At site N2 (Figure 2.3-3; Appendix Figure 2.7-14), we also map at least four generations of alluvial fan, T1 to T4, from youngest to oldest (note that relative fan ages reflect a chronology internal to a given scarp site and are not intended to be correlated between sites – see Section 2.2.1. in Methods). We find scarps in T2 and T3 fans only. T4 fans do not cross the mapped fault trace, but the T1 fans appear to truncate it. The smallest scarp is 0.7 ± 0.1m high (profiles L and M), deforming a T2 fan – this scarp might have formed in MRE. A few hundred metres to the east within the same fan we measure scarps of ~1.3– 1.7 m (profiles N to P) – it is again unclear if this scarp formed in more events or can be explained by variations in slip along strike. There is a lot of variation in scarp height between and within fans inferred to be of generation T3: The T3 fan which hosts profiles I, J and K (Figure 2.3-3) is offset by ~ 1.7 – 2.1 m, whilst the larger T3 fan in the east of the site shows significant folding but no measurable vertical offset. In the west of the study area, a T3 fan is offset by a roughly semi-circular fault trace with scarp heights of ~ 3.0 – 7.0 m. Offsets increase with distance from the centre of the fan which is dissected by a younger deposit. The V-shaped pattern of vertical offsets (profiles A to H in Figure 2.3-3) suggests that the fan may have been active whilst the scarp formed, leading to the partial burial or removal of the scarp focussed around a central channel. Whilst site N1 seems to show a correlation between fan age and scarp height, N2 demonstrates that this is not always the case and that the geomorphic expression of faulting can be more complex.

At around 43.20°N, the scarps abruptly turn a corner as the fault branches away from the mountain front, striking ENE for ~35 km and bounding a plateau of uplifted foreland material, elevated by up to ~500 m above the lowlands to the north (Figure 2.3-1). As described in Grützner et al. (2017b), the plateau is composed of incised sediments with basement rocks cropping out along its northern boundary, consistent with uplift by a south-dipping thrust. Grützner et al. (2017b) present two drone-surveyed scarp sites along the plateau-bounding ENE-striking fault section, which correspond to sites N3 and N4 in this study (Figure 2.3-4). Grützner et al. (2017b) map four fan generations (T1 to T4,

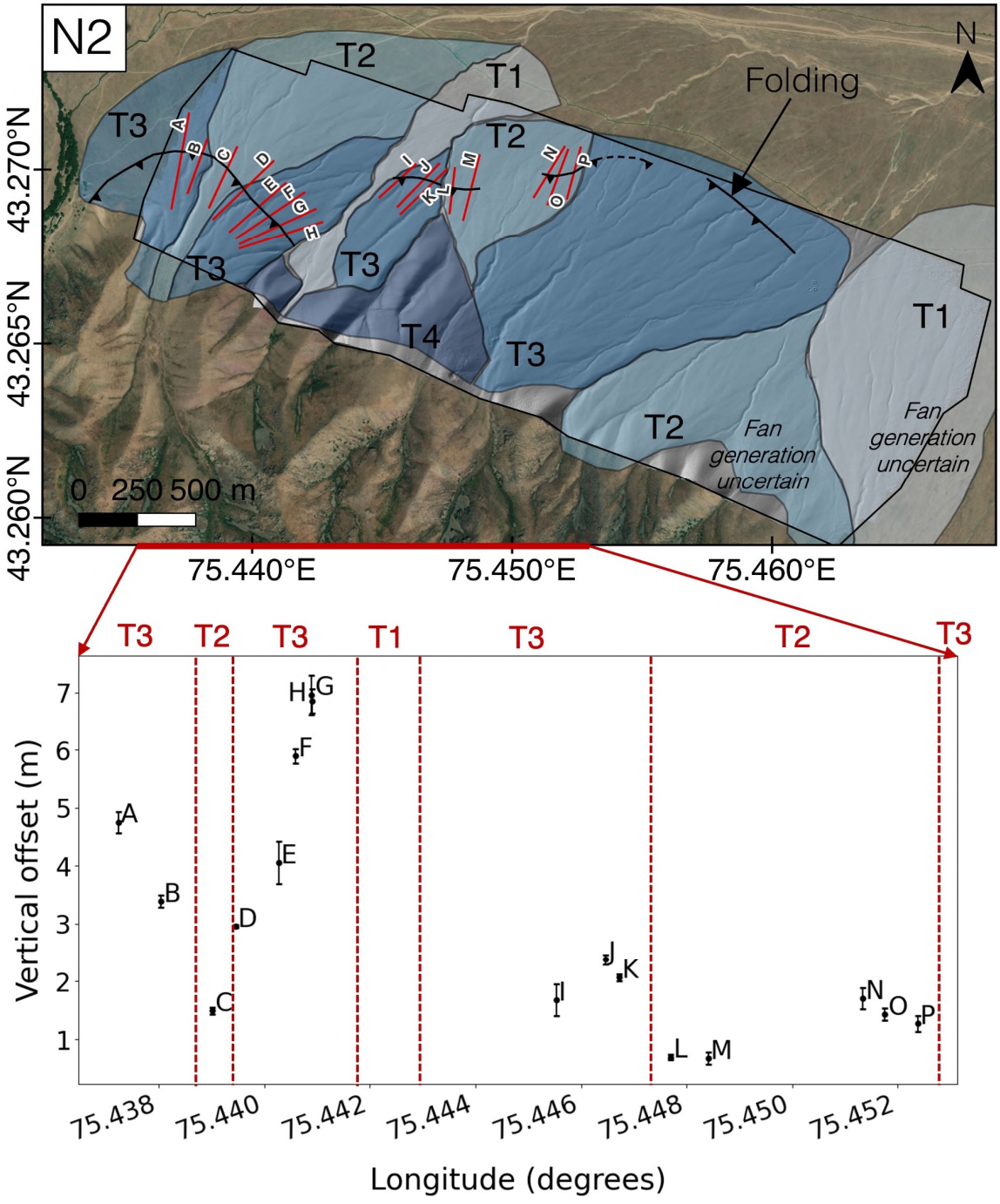

Figure 2.3-3. Site N2. Top: Bing Aerial imagery (2023 TomTom, 2023 Maxar) overlain with hill-shaded drone DEM and alluvial fan mapping of four fan generations (T1-T4, youngest to oldest; different colours indicate different inferred fan ages, darker = older). Profile lines for vertical offset measurement are shown in red corresponding to Appendix Figure 2.7-14. Bottom: vertical offset measurements plotted by longitude. Dashed lines show approximate transitions between fans of different generations which are labelled in red above the plot.

youngest to oldest), and measure vertical offsets of ~2.2 – 2.5 m in T3 at site N3 and ~6 – 8 m in T4 at site N4, with the 8 m measurement being the sum of offsets across two separate scarps of ~7 m and ~1 m. In order to formalise the errors for our analysis, we re-measured these scarps and obtained very similar results of ~1.9 – 2.5 m for T3 at N3 and ~7.7 – 7.8 m for T4 at N4, with the 7.8 m measurement being the sum of ~7.1 m and ~0.7 m scarps (Appendix Figure 2.7-15).

Moving east along the northern edge of plateau, we map further scarps and measure offsets from a drone survey we collected at site N5 (Figure 2.3-5; Appendix Figure 2.7-16) to the east of Beriktas (Бериктас) village. Using our drone DEM, we map discontinuous scarps in the west of the survey. We measure three distinct scarp heights of 8.5 ± 1.0 m (profile A), ~ 2.6 – 2.7 m (profiles B and C), and ~ 0.8 – 1 m (profiles D and E) – the latter scarp might have formed in the MRE. These distinct offsets probably correspond to surfaces of three different ages, but we could not identify sufficient differences in the surfaces to map distinct boundaries. The smallest scarp is very degraded and the subtle change in slope is barely discernible in the field (Figure 2.3-6). This could be due to erosion, or the scarp might have been blanketed with loess.

Around 10 – 15 km to the north of this fault section, there is a strip of vegetation which approximately aligns with the strike of the fault, with streams from the vegetated patches towards the NNE (Figure 2.3-1b, c). These patches might be springs linked to a buried fault in the foreland which is acting as a conduit for fluid flow. However, it is difficult to rule out an anthropogenic cause for their location, such as irrigation.

To summarise, along this fault section we measure a range of scarp heights which sometimes correlate with inferred relative surface ages. The smallest scarps are < 1 m high and might have formed in the MRE. At all sites scarps are truncated by younger fan surfaces, suggesting that a significant amount of time has elapsed since the fault was last active.

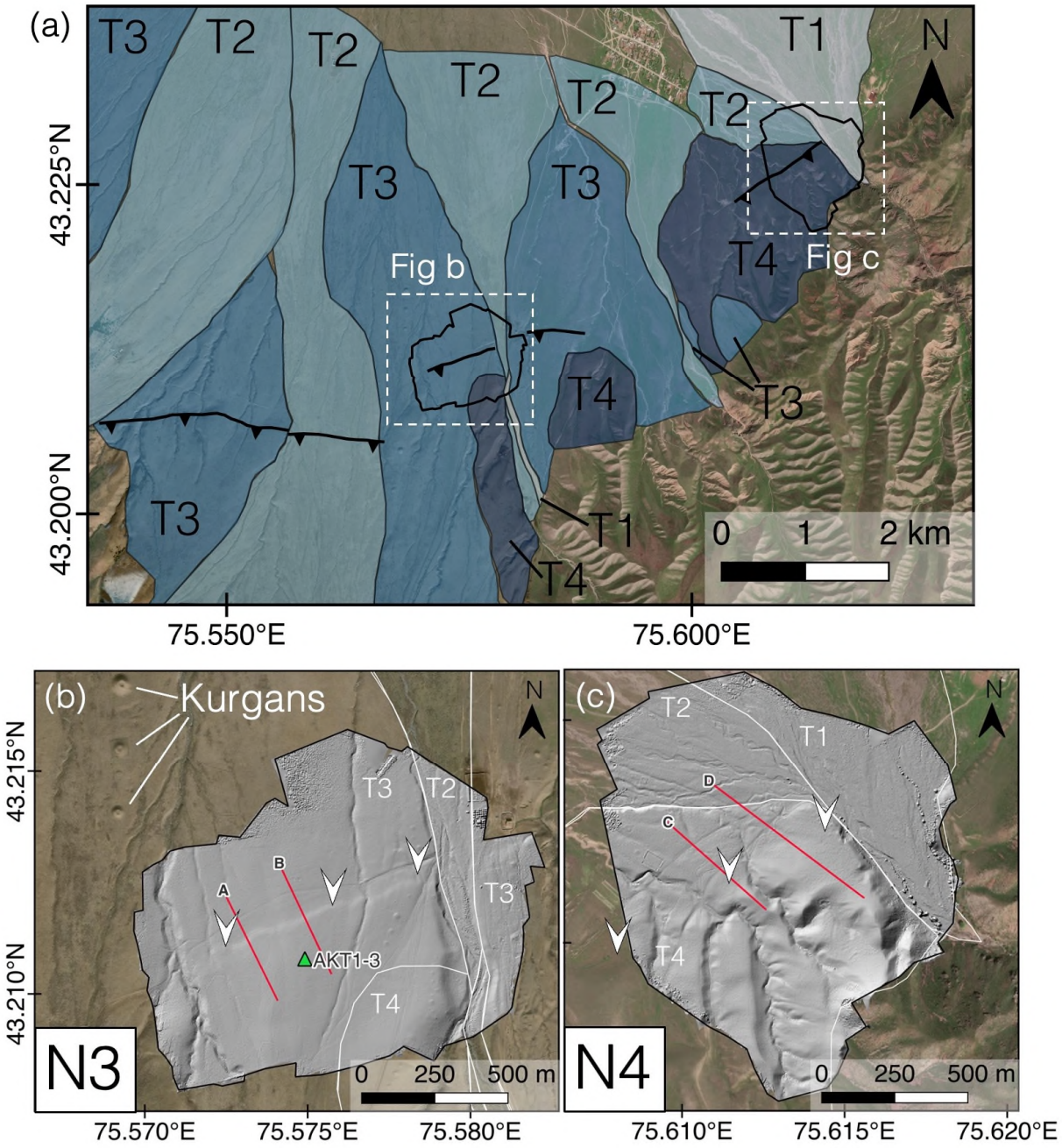

Figure 2.3-4. Overview of sites N3 and N4, corresponding to S1 and S2 in Grützner et al. (2017b). (a) Bing Aerial imagery (2023 TomTom, 2023 Maxar) overlain with alluvial fan mapping of four fan generations (T1-T4, youngest to oldest; different colours indicate different inferred fan ages, darker = older) modified after Grützner et al. (2017b). Figures (b) and (c) show sites N3 and N4 respectively, with Bing Aerial imagery (2023 TomTom, 2023 Maxar) overlain by hill shaded drone DEMs. Red lines are profile locations from Grützner et al. (2017b) which we re-measure (Appendix Figure 2.7-15). White arrows mark scarp location. White lines show the boundaries of the mapped fans. Green triangles show luminescence sampling locations discussed in Chapter 3.

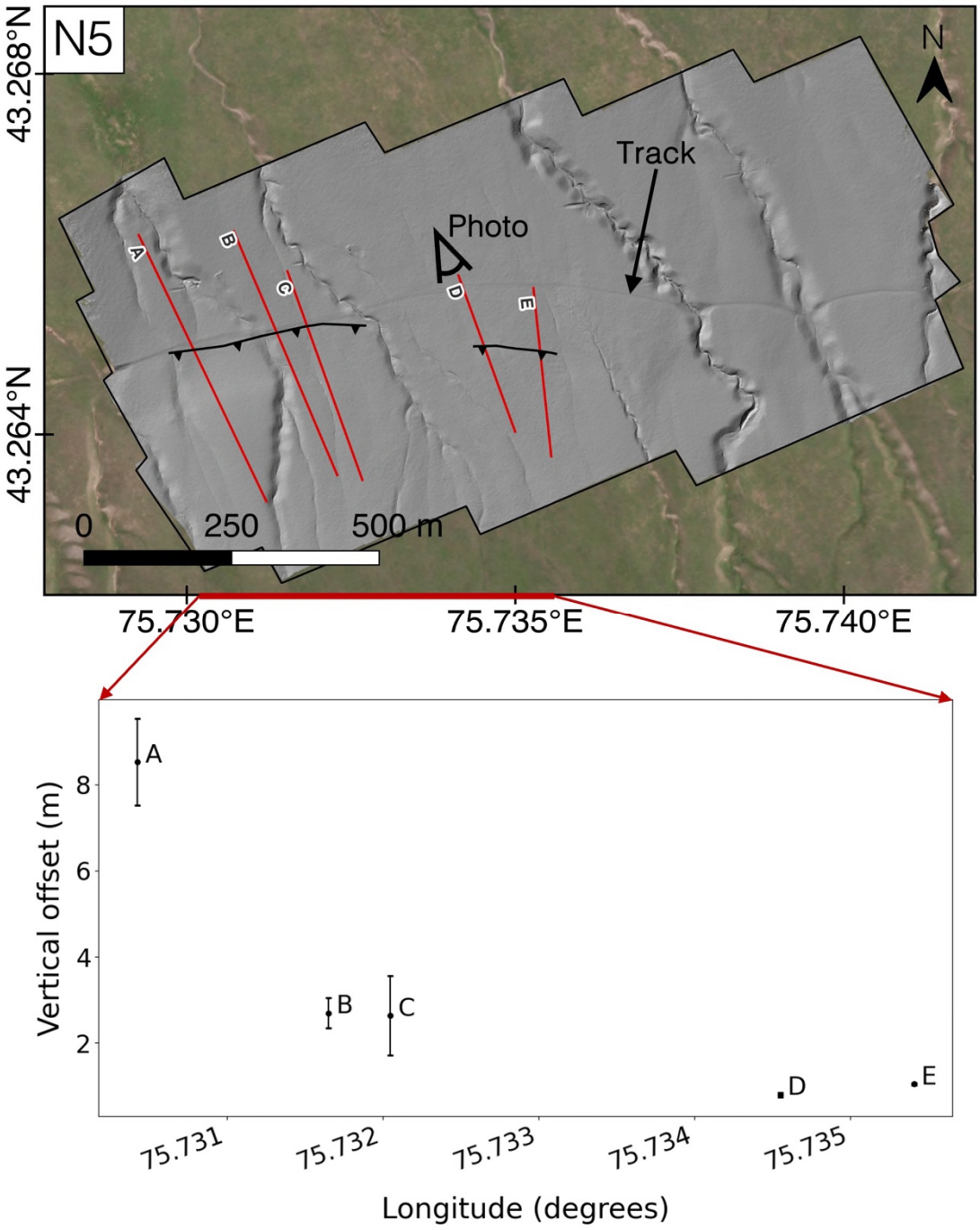

Figure 2.3-5. Site N5. Top: Bing Aerial imagery (2023 TomTom, 2023 Maxar) overlain by hill-shaded drone DEM. Profile lines for vertical offset measurements are shown in red, corresponding to Appendix Figure 2.7-16. Photo viewpoint corresponds to Figure 2.3-6. Bottom: vertical offset measurements plotted by longitude.

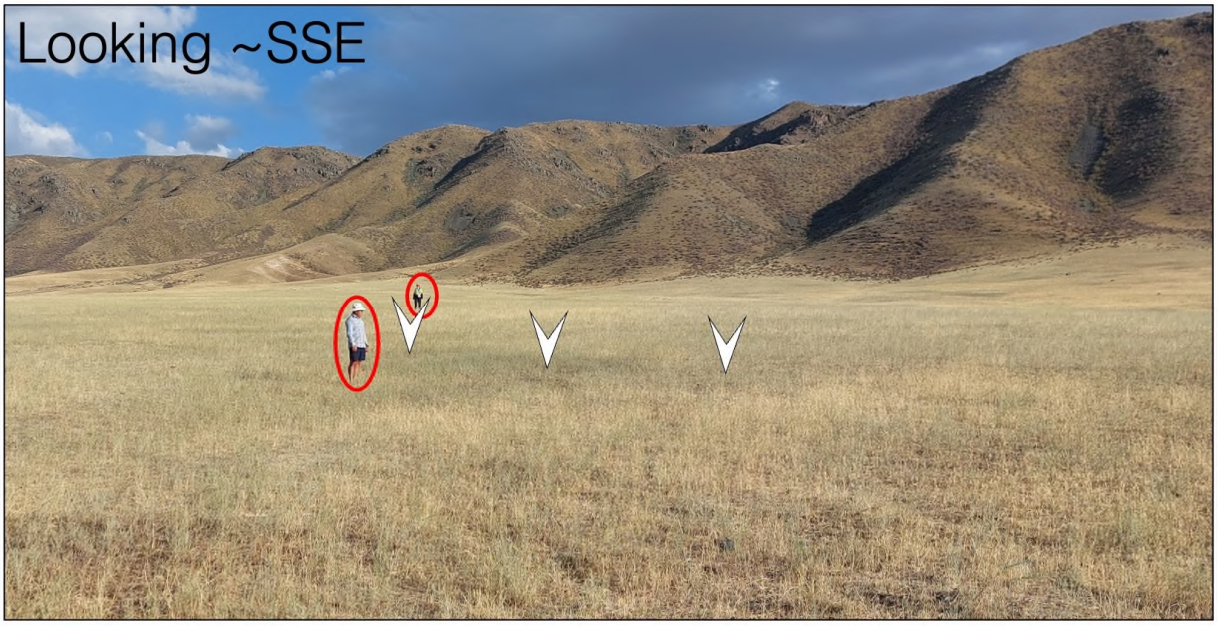

Figure 2.3-6. Photograph of site N5 showing two geologists (encircled) standing on the hanging wall and footwall of a degraded scarp, viewpoint marked in Figure 2.3-5. White arrows mark scarp location.

2.3.2. West Section (N6 – N9)

An uplifted plateau lies between the ENE fault strand which runs through Beriktas and the Zailisky Alatau. The plateau sediments are dissected by many streams and larger river channels, and the alluvial fans we map in this section are more extensive and more deeply incised than those in most other sections of the fault (Figure 2.3-7). This incision probably results from the uplift of the plateau and should not be interpreted as evidence that the fans are older.

On the west side of the plateau to the south of site N3, the Zailisky Alatau strikes ~NW-SE (Figure 2.3-7). The mountain front is initially heavily incised for ~ 5 km and there are no obvious scarps. As the fault approaches the village of Besmoinak (Бесмойнак), a sharp change in elevation at the range front becomes visible again. Around 2 km northwest of Besmoinak at site N6, two small ridges are apparent in the satellite imagery (Figure 2.3-8). The southwest side of the larger ridge is uplifted by around ~ 34 m compared to the northwest side, with the top of the ridge uplifted higher still. This uplift

was probably caused by the range front fault, with erosion or folding producing a ridge rather than a scarp.

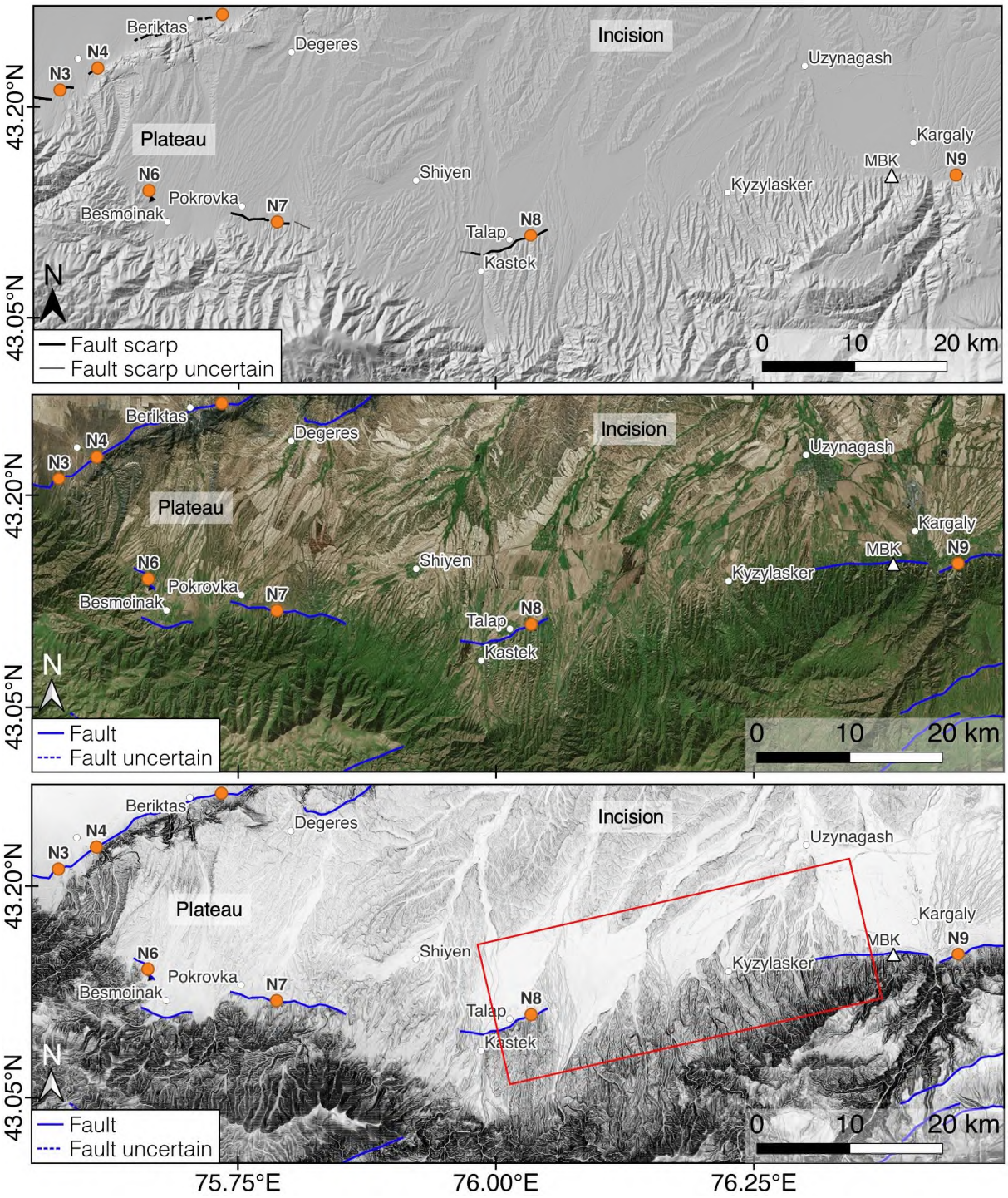

Figure 2.3-7. Overview of West section. Orange data points are sites discussed in the text; white data points are settlements. White triangle shows location of MBK luminescence sample from Fitzsimmons et al. (2017). (a) Scarps mapped in this study overlain on the Copernicus GLO-30 DEM hill shade. (b)

Fault mapping overlain on Bing Satellite Imagery. (c) Fault mapping overlain on slope map derived from Copernicus GLO-30 DEM. Darker colours show steeper slopes. Red box shows the location of Figure 2.3-12.

At ~43.110° latitude near Besmoinak, the Zailisky Alatau begins to strike ~E-W, with a sharp change in elevation at the range front. To the east of Besmoinak younger alluvial fans cross the range front but we identified no fault scarps in them, including within a speculative drone DEM of one of the fans (red patch between N6 and N7 in Figure 2.1-1a). To the south of the village of Pokrovka (Покровка) at site N7, scarps are preserved in a set of older surfaces which lie between two large and heavily incised alluvial fans (Figure 2.3-9). The deformed surfaces host abundant burial mounds – three kurgans in the west of the site were dated as Early Iron Age (A1 in Figure 2.3-10; Bekseitov et al., 2019) and the rest are likely to be of a similar age (Anton Gass, personal communications). Therefore, the fans must have formed before ~ 2.8 – 2.2 kyrs, but are probably significantly older from their morphology. We map scarps across at least three fan generations. We did not survey this site in the field and do not have Pléiades data in this fault section, but the Copernicus GLO-30 DEM yields scarp heights of between 57.3 ± 4.2 m and 9.0 ± 3.3 m, with larger scarps in fans we infer to be older (Figure 2.3-10). We note that smaller scarps would not be discernible in the 30 m DEM.

Scarps stretch from Pokrovka for ~10 km to the east, after which they appear to stop, although the deep incision and erosion of the fan surface and the low resolution of the available data could be masking evidence of deformation. The next scarp we identify is near the villages of Kastek (Кастек) and Talap (Талап) at site N8 (Figure 2.3-11), ~8 km north of the mountains within the piedmont. To the south of this site, the Zailisky Alatau dips in height. We visited N8 in the field and were uncertain whether the offsets were tectonic scarps or erosive contacts from fluvial or fan activity. From our remote mapping of five different fan generations and a modern stream channel, we infer that at least some of the scarp is tectonic in origin (Figure 2.3-11). Fan surfaces of different ages are easily mapped from their distinct levels of incision, evident in the Copernicus GLO-30 DEM and slope map (Figure

2.3-11a and b, respectively). The oldest of the fan (T5) hosts a 118.1 ± 14.1 m high scarp (profile B in Figure 2.3-11d) and a small section of the second oldest fan (T4) is offset by 16.2 ± 1.3. However, there are additional uncertainties in these values because of the extensive incision of the hanging wall and footwall. Robust measurement of scarps along strike is precluded by the deep and frequent drainage channels which cross-cut potential profile lines. The youngest fans and much of T4 do not show any evidence of faulting within the resolution of the 30 m data, although we did not survey them in detail in the field.

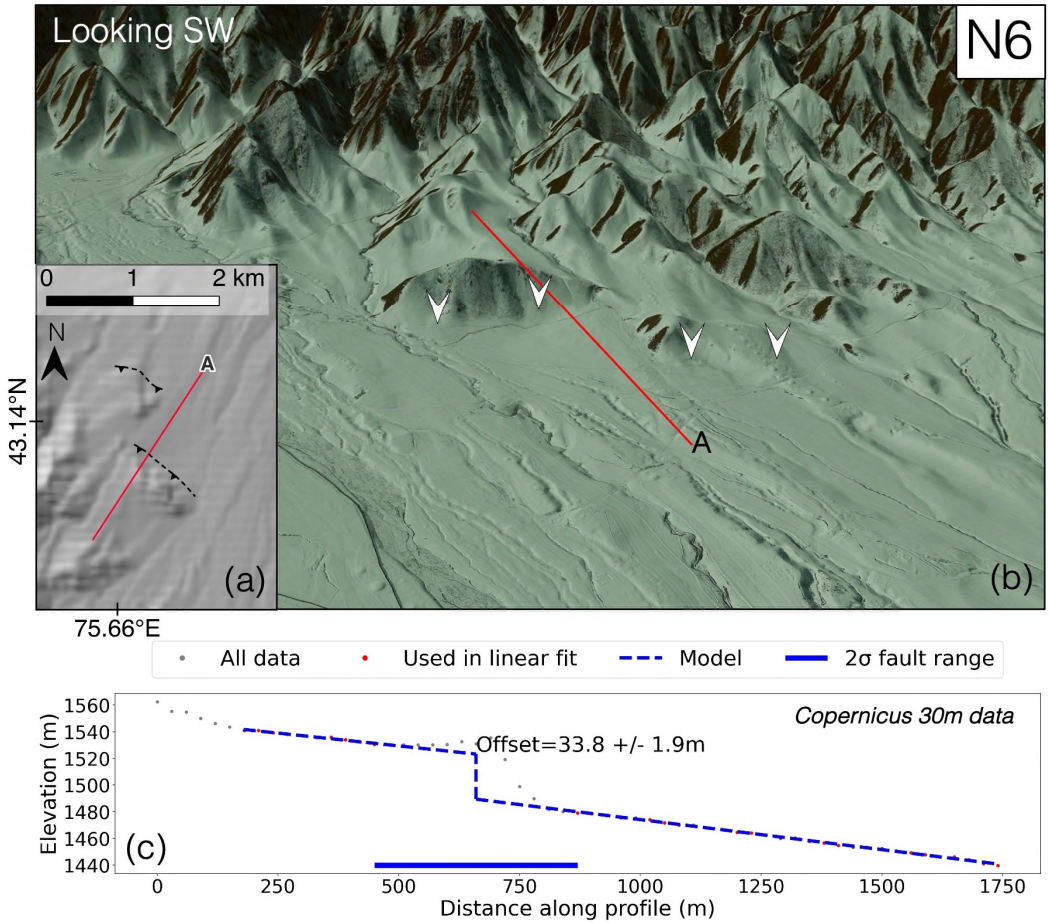

Figure 2.3-8. Site N6 to the northwest of Besmoinak village. (a) Hill-shaded Copernicus GLO-30 DEM. (b) Satellite imagery overlain on 3 x exaggerated topography from Google Earth (2023 Maxar Technologies, Landsat/Copernicus), 5.30 km eye altitude, looking southwest. White arrows mark fault scarps, red line corresponds to profile in (c) measured from Copernicus GLO-30 DEM data sampled every 30 m.

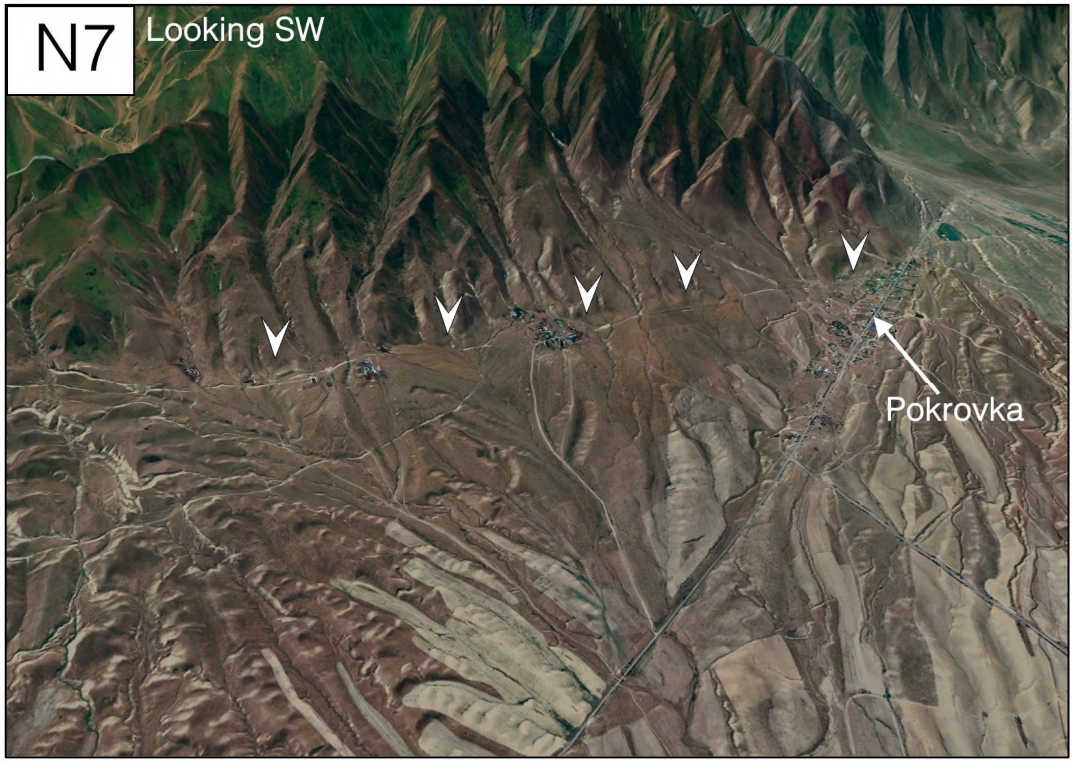

Figure 2.3-9. View of site N7 near Pokrovka. Satellite imagery overlain on 3 x exaggerated topography from Google Earth (2023 CNES/Airbus, Landsat/Copernicus, 2023 Airbus), 7.25 km eye altitude, looking southwest at scarps mapped in Figure 2.3-10. White arrows mark fault scarp.

To the east of N8, the scarp is truncated by a younger (T3) fan (Figure 2.3-12). After this point, for ~27 km to the ENE along strike, we find no scarps nor any continuous sharp change in elevation at the mountain front along which the ZRF could be mapped. However, the slope map, shown in Figure 2.3-12, reveals that much of this section of the range front is occupied by fans which appear to be relatively young (lighter colours in slope map) which cover the expected location of the fault trace for much of this apparent gap. As such, while there appears to be a gap in faulting here, we cannot rule out that the scarps have been covered or eroded by recent deposition.

From around 5 km to the east of the village of Kyzylasker (Кызыласкер) an elevation change at the range front becomes visible again, becoming progressively sharper towards the east, though we do not identify any recent fault scarps for ~ 18 km until the town of Kargaly (Каргалы), formerly Fabrichnyy

(Фабричный; Figure 2.3-7; Figure 2.3-12). To the southeast of Kargaly, Grützner et al. (2017b) identify a fault scarp in alluvial fans on the edge of the mountains which are being actively developed for housing (site N9). They estimate a vertical offset of ~1 m by eye. We conducted a drone survey of the site to obtain a formal measurement of the offset, revealing two scarps and yielding heights of between ~1.3 – 2.6 m, only slightly larger than the estimates from Grützner et al. (2017b) (Figure 2.3-13; Appendix Figure 2.7-18). Significant variations between neighbouring profiles may be related to anthropogenic modification of the surface or modification by channels. We map four ages of surface, T4 to T1, as well as the modern streambed, T0, with the scarp present in the T3 surface only (although the T4 surfaces do not cross the mapped fault trace).

This section of the fault is also characterised by a large zone of incision and relatively high topography which is ~80 km wide and stretches from the mountains to ~50 km into the foreland, extending beyond the northern and eastern edges of the plateau (orange polygon in Figure 2.3-14). There is no indication of increased hydrological input here compared to the rest of the fault – in fact, with relatively low-lying mountains in this section, we might expect there to be less water and sediment input than in the central section of the fault which is fed by glacial meltwaters and erosion of the northern Tian Shan's high peaks. Therefore, we suggest this incision must be related to uplift. We have little evidence to constrain the source of the uplift. There could be a south dipping thrust fault along the northern edge of the incised region ~50 km north of the ZRF, but we cannot tell either way because the topography is truncated by axial drainage which has carved out a shallow ~ENE valley along the northern boundary of the uplifted zone. Alternatively, the uplift could also be the result of folding above a buried thrust fault situated some tens of km to the north of the main range front. The ~35 km-long fault strand which bounds the plateau in the Akterek section is evidence of faulting within the foreland and sits in the centre of the incised sediments. We suggest this could be connected to a buried fault at depth which is causing the wider uplift, similar to the Montello anticline in Italy, for example, where blind thrusting has migrated into the foreland of the eastern Southern Alps (Benedetti et al., 2000; Picotti et al., 2022)

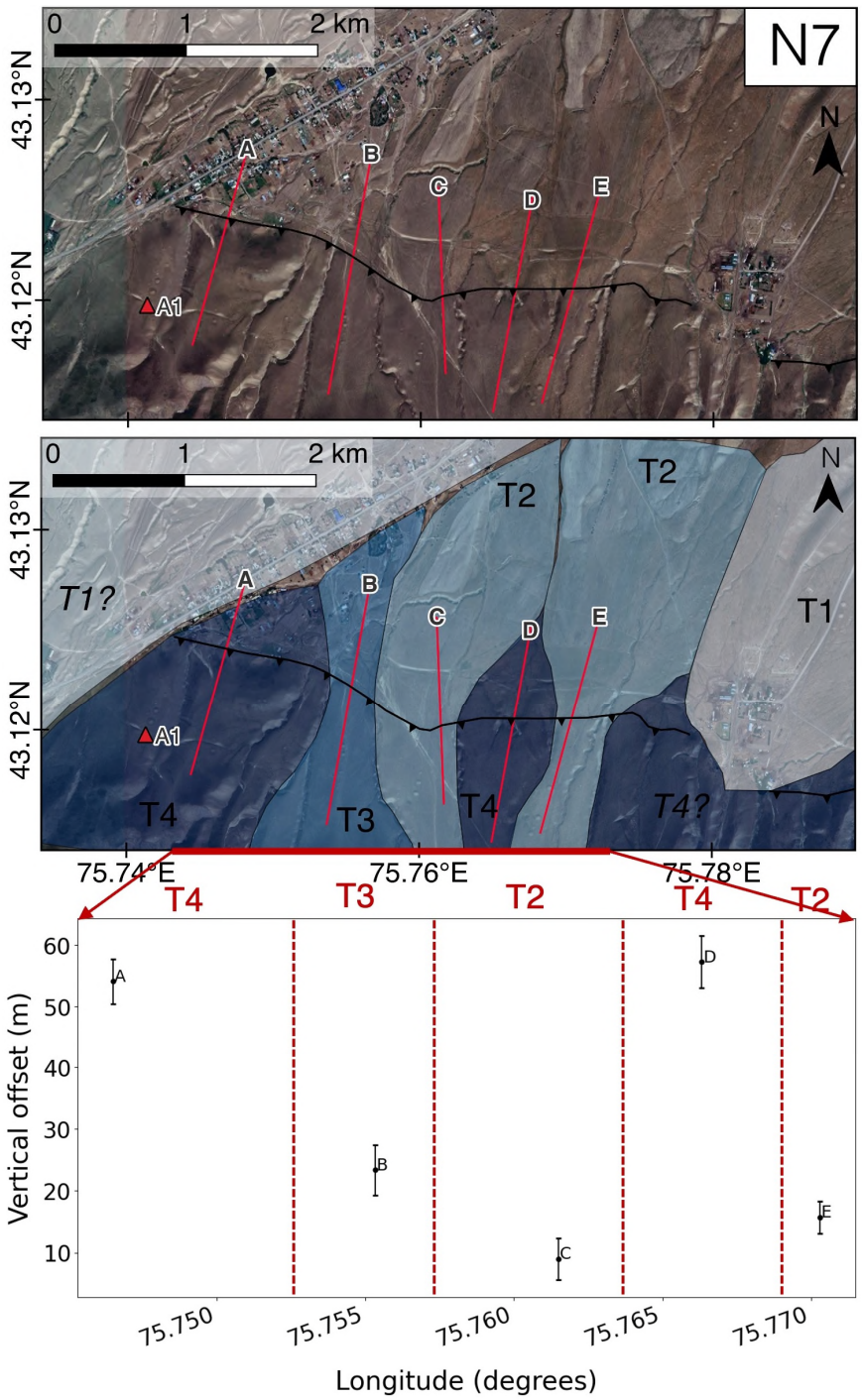

Figure 2.3-10. Site N7 near Pokrovka. A1 is an early Iron Age burial ground (Bekseitov et al., 2019). Top: Google Satellite imagery (2024 Airbus). Profiles correspond to those in Appendix Figure 2.7-17. Middle: Four fan generations overlain on the Google Satellite imagery (2024 Airbus). Bottom: Vertical offset measurements with longitude. Red dashed lines represent transitions between fans of different ages which are labelled above the plot.

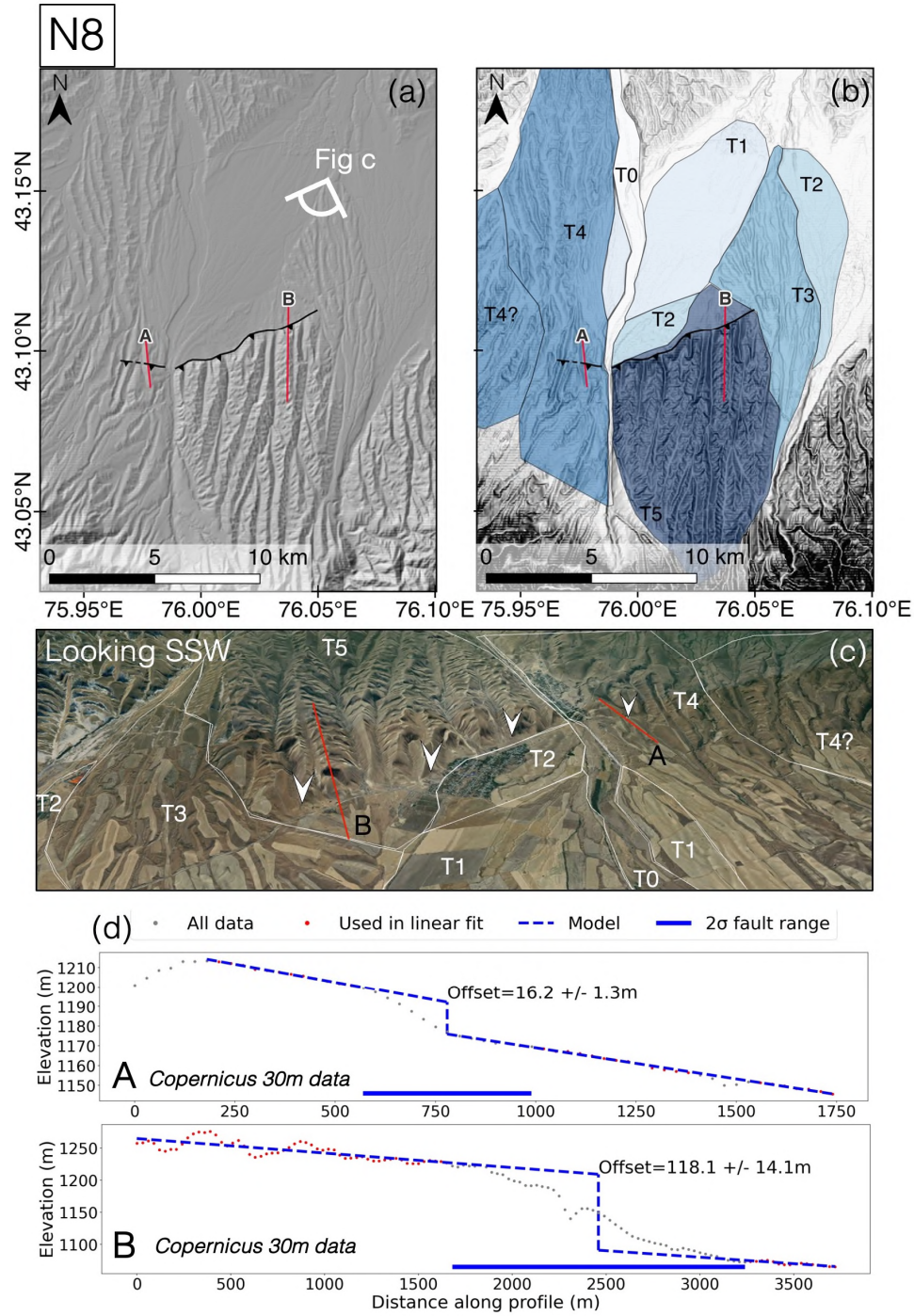

Figure 2.3-11. Site N8 near Kastek and Talap. (a) Hillshade of Copernicus GLO-30 DEM. (b) Slope map derived from Copernicus GLO-30 DEM (darker colours represent steeper slopes), overlain by fan mapping of at least 5 fan generations (T1 – T4) and the modern river channel (T0). (c) Satellite imagery overlain on 3 x exaggerated topography from Google Earth (2023 Maxar Technologies, 2023 Airbus, Landsat/Copernicus, 2023 CNES/Airbus), 7.43 km eye altitude, looking south-southwest. Fan boundaries are marked in white. White arrows mark scarp location. (d) Profiles along lines A and B shown in red in (a), (b) and (c). Data extracted from Copernicus GLO-30 DEM at 30 m intervals.

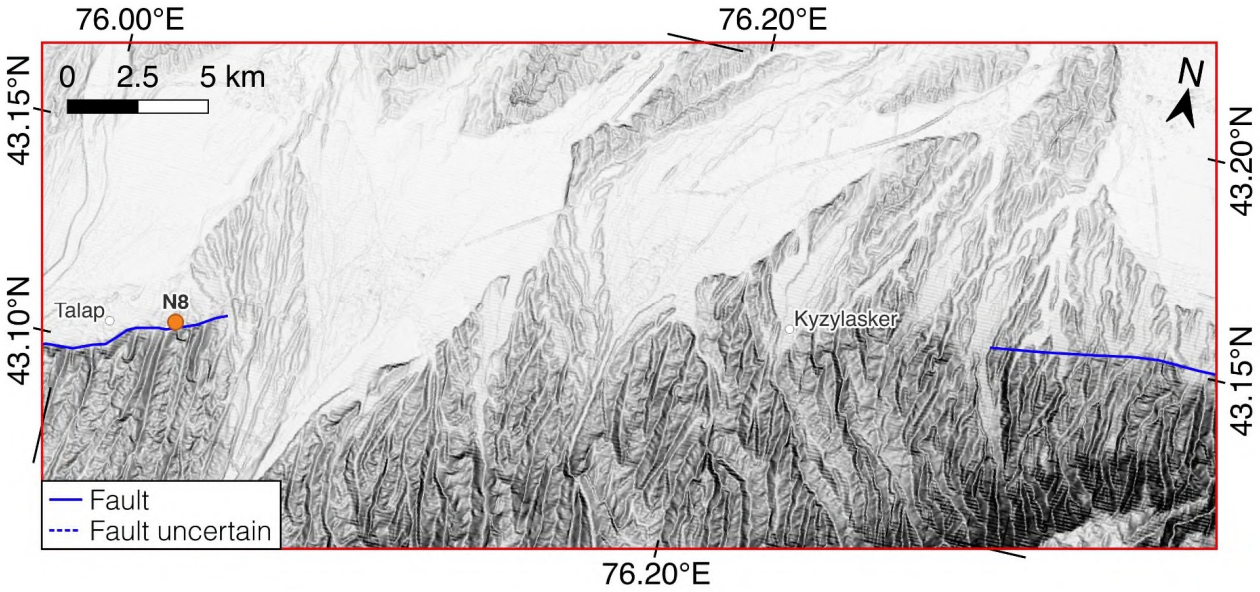

Figure 2.3-12. Slope map of range front to the east of site N8 corresponding to the red box in Figure 2.3-7. Slope map derived from Copernicus GLO-30 DEM. Darker colours show steeper slopes, fault mapping in blue. Older, more incised surfaces have steeper faces and appear darker. Younger, less incised surfaces are flatter and appear lighter. Here, younger surfaces cover much of the expected path of the fault.

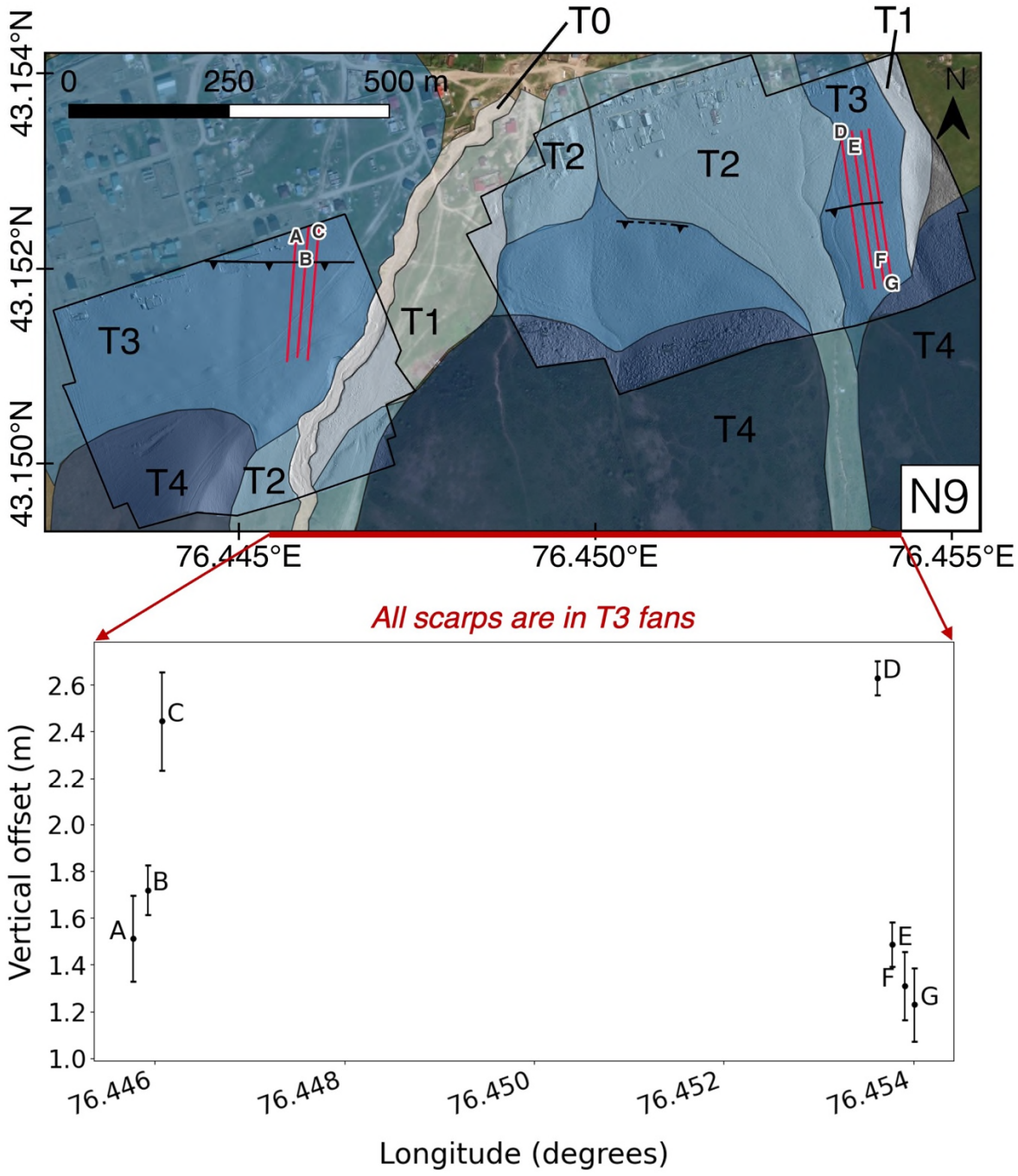

Figure 2.3-13. Site N9, Fabrichnyy/Kargaly, corresponding to site S3 from Grützner et al. (2017b). Top: Hill shade of drone DEM and scarp profiles. Four distinct generations of alluvial fans are mapped (T1-T4), as well as the modern river bed (T0). Bottom: vertical offset measurements plotted by longitude corresponding to profiles in Appendix Figure 2.7-18.

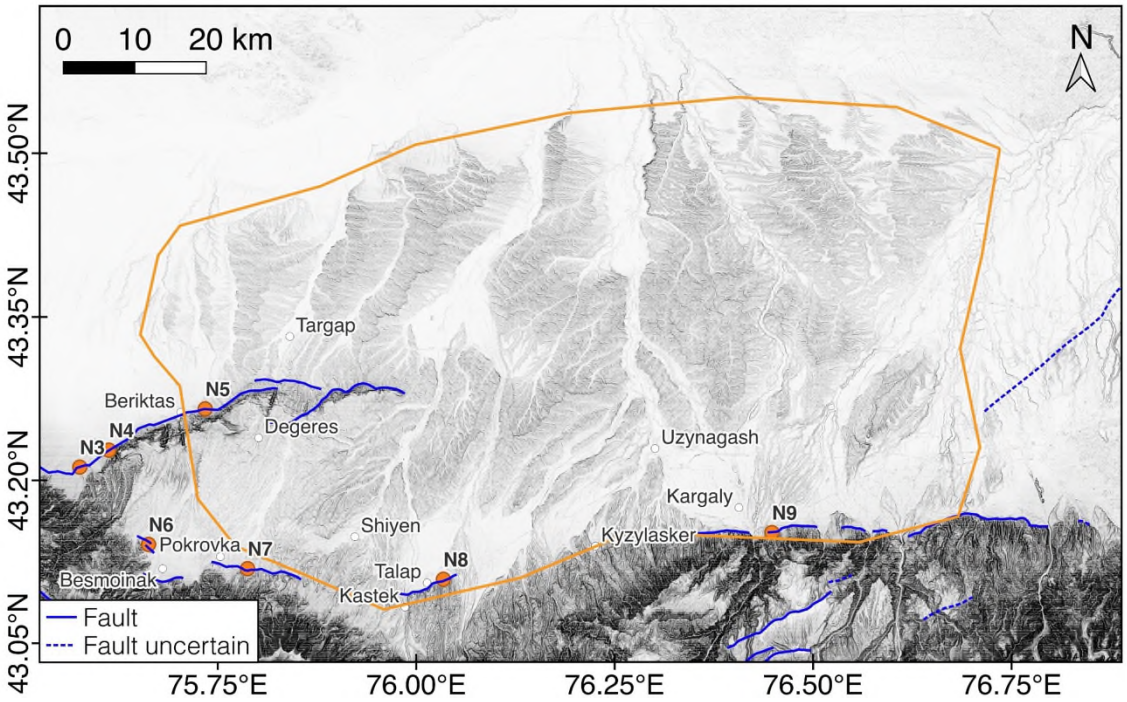

Figure 2.3-14. Fault mapping (blue) and study sites (orange circles) overlain on slope map derived from Copernicus GLO-30 DEM. Darker colours show steeper slopes. Orange polygon marks the region we infer to be a zone of uplift and incision.

2.3.3. Central Section (N10 – N15)

To the east of site N9, the central section of the range front is characterised by a sharp, clearly defined change in elevation between the mountains and the foreland, interrupted by several large alluvial fans which exit from deep gorges in the mountain front (Figure 2.3-15). The drainage here is fed by the snowy and glaciated high mountain catchment which lies to the south. The range front in this section is extensively modified by large settlements and agriculture. From Almaty (Алматы) in the west to Turgen (Тургeн) in the east, a major city and several towns occupy the large alluvial fans, obscuring or limiting access to the likely location of the fault trace. In contrast to the west of the study area, the foreland sediments are not deeply incised except where there is local uplift to the northwest of Almaty (orange polygon in Figure 2.3-15).

Around 50 km east of N9, several fans exit the range front, combining to form the surface upon which the city of Almaty is built. Grützner et al. (2017b) identified a fault scarp within the alluvial fan in the east of the city and measured vertical offsets of ~5 – 7 m using 30 m DEM data (N10; Figure 2.3-16). Amey et al. (2021) measured the same scarp using higher resolution data, testing a range of elevation data sets including Pléiades stereo and tristereo DEMs (1.5 m resolution), SPOT data (4 m resolution) and a GPS field survey. Measurements from the different datasets varied by up to ~1.7 m for a given profile, highlighting the uncertainties in extracting offset measurements and the dependence of the results on the resolution of the data. For our analysis, we use the GPS offset measurements from Amey et al. (2021), which are 2.2 ± 0.5 m, 1.6 ± 0.4 m, 0.7 ± 0.5 m and 1.3 ± 0.1 m from four different profiles lying at least ~700 m apart along strike. The smallest of these measurements could represent the offset in the MRE, but we cannot rule out that the relatively small difference scarp heights along strike reflects variation in slip rather than a different number of events.

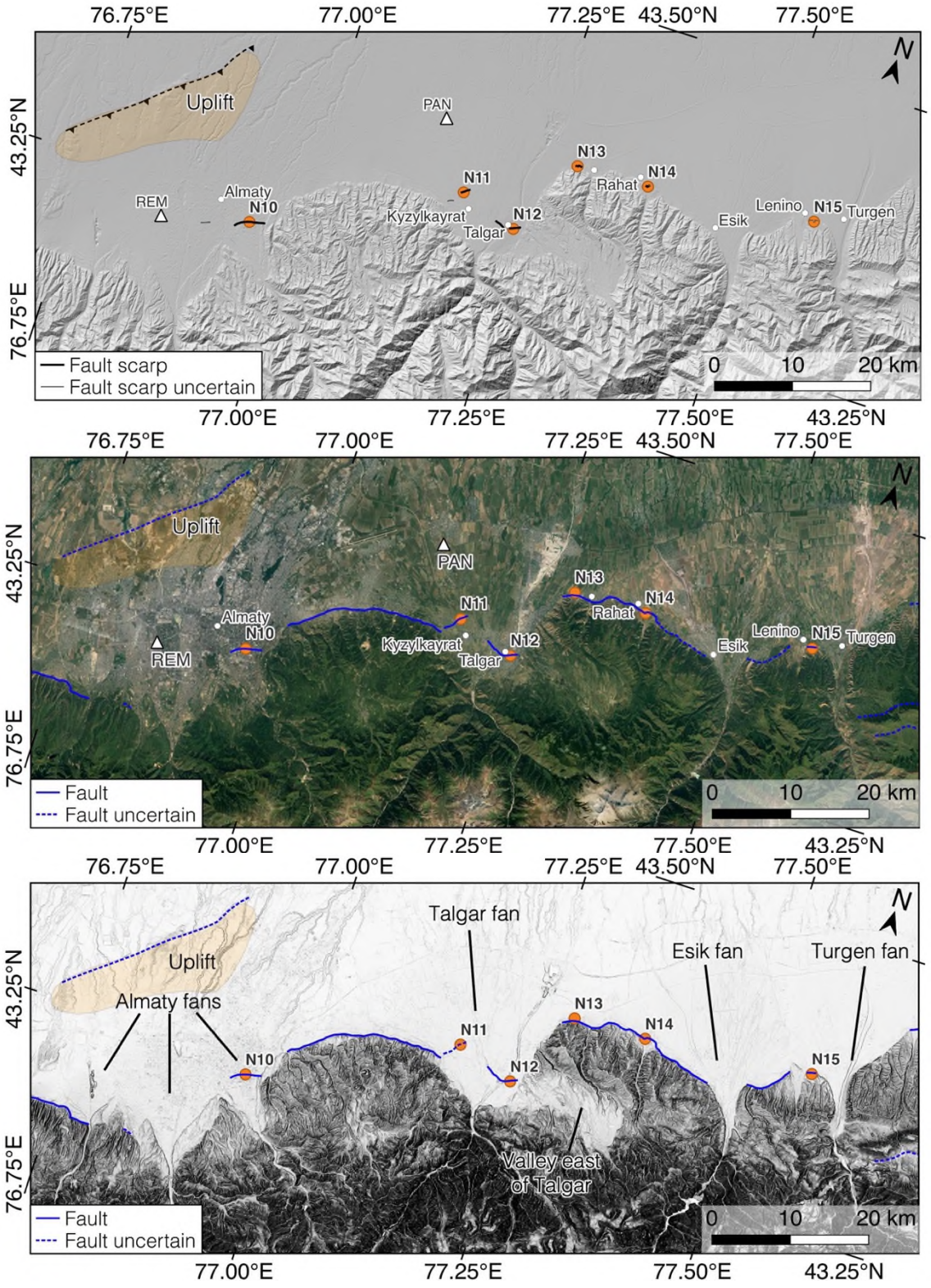

Figure 2.3-15. Overview of Central section. Orange data points are sites discussed in the text; white data points are settlements. White triangles show locations luminescence sample from Dave et al. (2023). Shaded orange polygon shows region of uplift and incision north of Almaty. (a) Scarps

mapped in this study overlain on the Copernicus GLO-30 DEM hill shade. (b) Fault mapping overlain on Google Satellite Imagery (2024 Airbus, 2024 CNES / Airbus, 2024 Maxar Technologies). (c) Fault mapping overlain on slope map derived from Copernicus GLO-30 DEM. Darker colours show steeper slopes. In this panel fan surfaces and geomorphic features are labelled rather than settlements.

Grützner et al. (2017b) and Amey et al. (2021) also map a zone of uplift and incision to the northwest of Almaty, which Amey et al. (2021) interpret as a fold produced by a south-dipping thrust beneath the city – a northern splay of the main ZRF (orange polygon in Figure 2.3-16). Around 30 km to the east of Almaty, another large alluvial fan cuts through the range front and is populated by the town of Talgar and surrounding villages such as Kyzylkayrat (Figure 2.3-17). The Talgar river has incised a channel tens of metres deep in the east of the fan. The DEM and slope map reveal several shallower channels and possible terrace risers dissecting the fan, though distinct surfaces of different ages are difficult to discern due to the presence of the town. Archaeological studies of a medieval fort on the Talgar fan (A5 in Figure 2.3-17) report fissuring in a wall at the site which the researchers interpret as evidence of past seismic activity (Korjenkov et al., 2003). Grützner et al. (2017b) did not observe any scarps in the field, but documented a zone of folding and a ~5 – 6 m offset measured from 30 m resolution data. However, they could not distinguish between a degraded fault scarp or folding. As they do not document any fault scarps, Grützner et al. (2017b) conclude that the surface deformation in Talgar was caused by activity on a blind thrust beneath the city.

We re-examined the Talgar fan using higher resolution Pléiades DEMs and visited two field sites. On the western side of the fan we measure an 8.4 ± 0.3 m scarp offset in the Pléiades DEM across the zone where Grützner et al. (2017b) documented folding (profile A in Figure 2.3-17 and Figure 2.3-18). To the south of Kyzylkayrat at N11, we found a scarp within an active housing development, upon which a telegraph pole and a utility pipe had been built (Figure 2.3-18). A field dGPS survey we collected along a 70 m profile yields a scarp height measurement of 0.5 ± 0.3 m. Remote measurement of the scarp using a Pléiades-derived DEM over several kilometres yields heights of ~2.2 – 3.6 m (Figure

2.3-18a, profiles B and C). We suggest that this larger offset formed in multiple earthquakes and was degraded and smoothed out over time, destroying the shorter wavelength evidence of the scarp. Later, the smaller and sharper ~ 0.5 m scarp was superimposed on top in a more recent earthquake – probably the MRE.

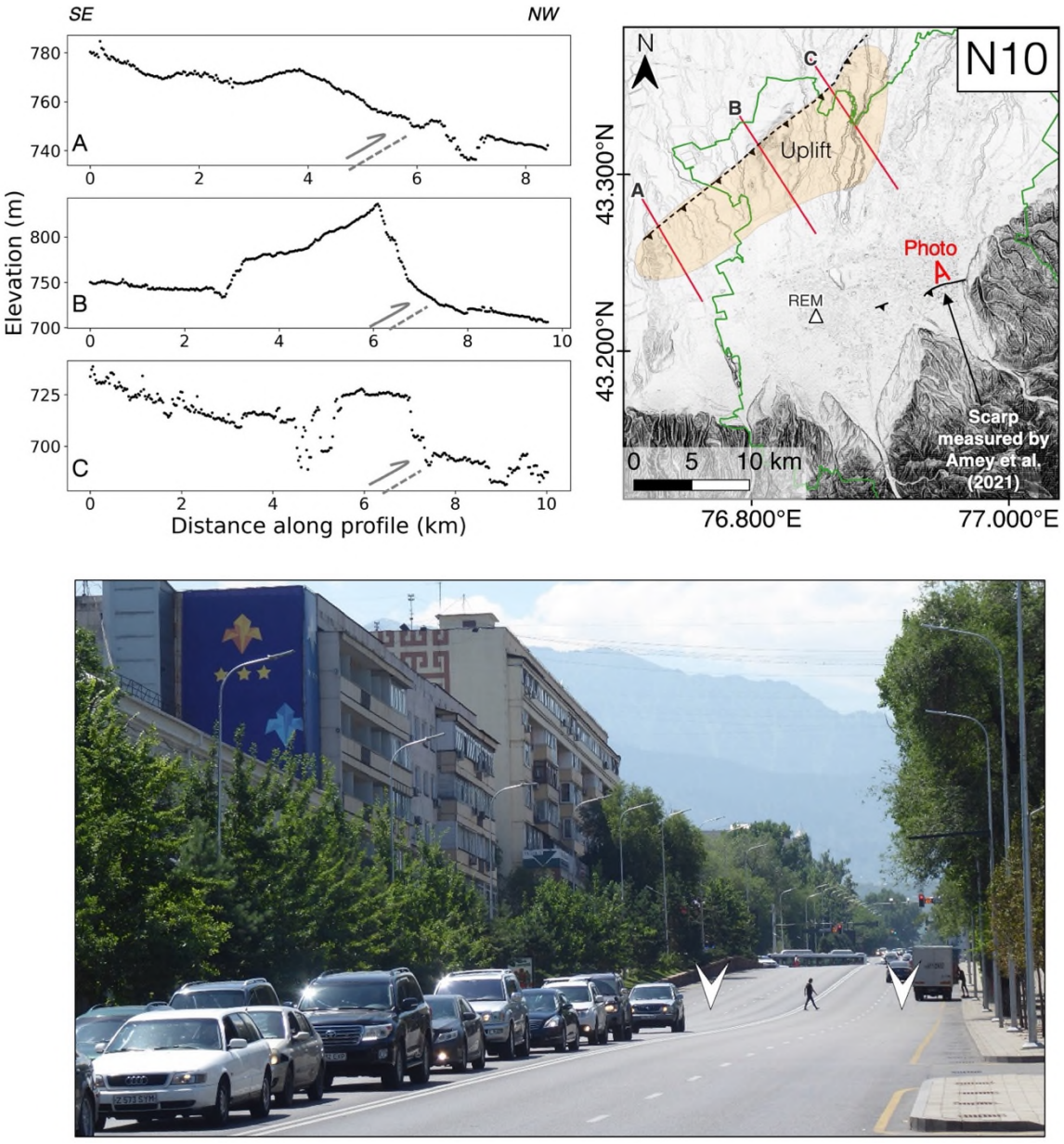

Figure 2.3-16. Top right: Slope map of Copernicus GLO-30 DEM of Almaty. Darker shades correspond to steeper slopes. Almaty city area from Open Street Map outlined in green. Shaded orange polygon marks area of uplift and incision. White triangle is location of REM luminescence sample site from Dave et al. (2023). Red lines show locations of profiles. Top left: Copernicus GLO-30 DEM profiles, sampled every 30 m. Grey dashed line shows inferred thrust fault. Figure after Amey et al.

(2021) and Grützner et al. (2017b). Bottom: Photo courtesy of Ruth Amey showing the mapped fault scarp in Almaty, looking south with the Zailisky Alatau in the background. Base of scarp is marked by white arrows and a pedestrian crossing the road.

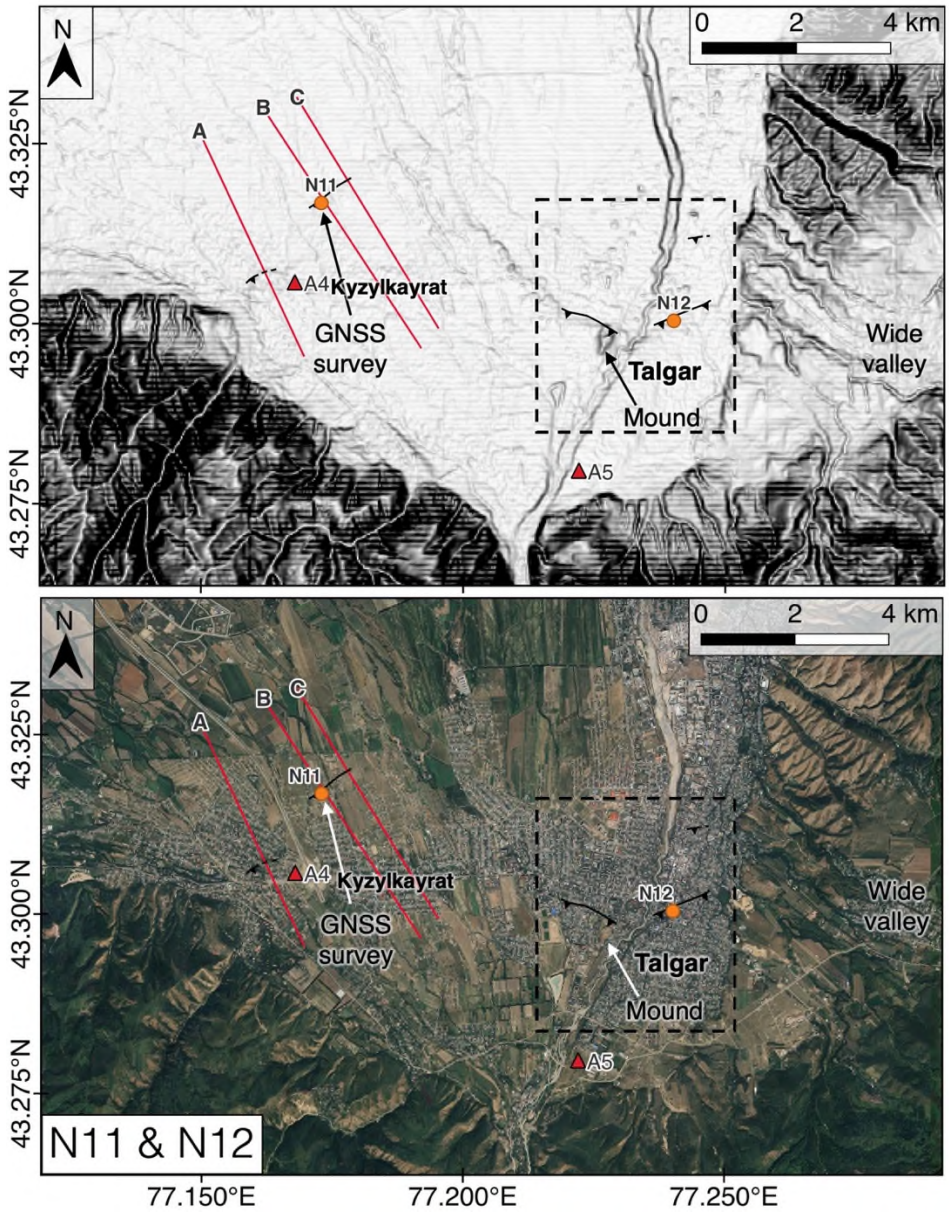

Figure 2.3-17. Overview maps of the Talgar fan. Red triangles A4 and A5 are archaeological sites from Gass (2019). GPS field survey is located at N11. Red lines show profiles corresponding to those in Figure 2.3-18. Box with dashed line corresponds to Figure 2.3-19. Top panel shows slope map derived from Copernicus GLO-30 DEM, with darker colours corresponding to steeper slopes. Lower panel shows same region in Google Satellite imagery (2024 Airbus).

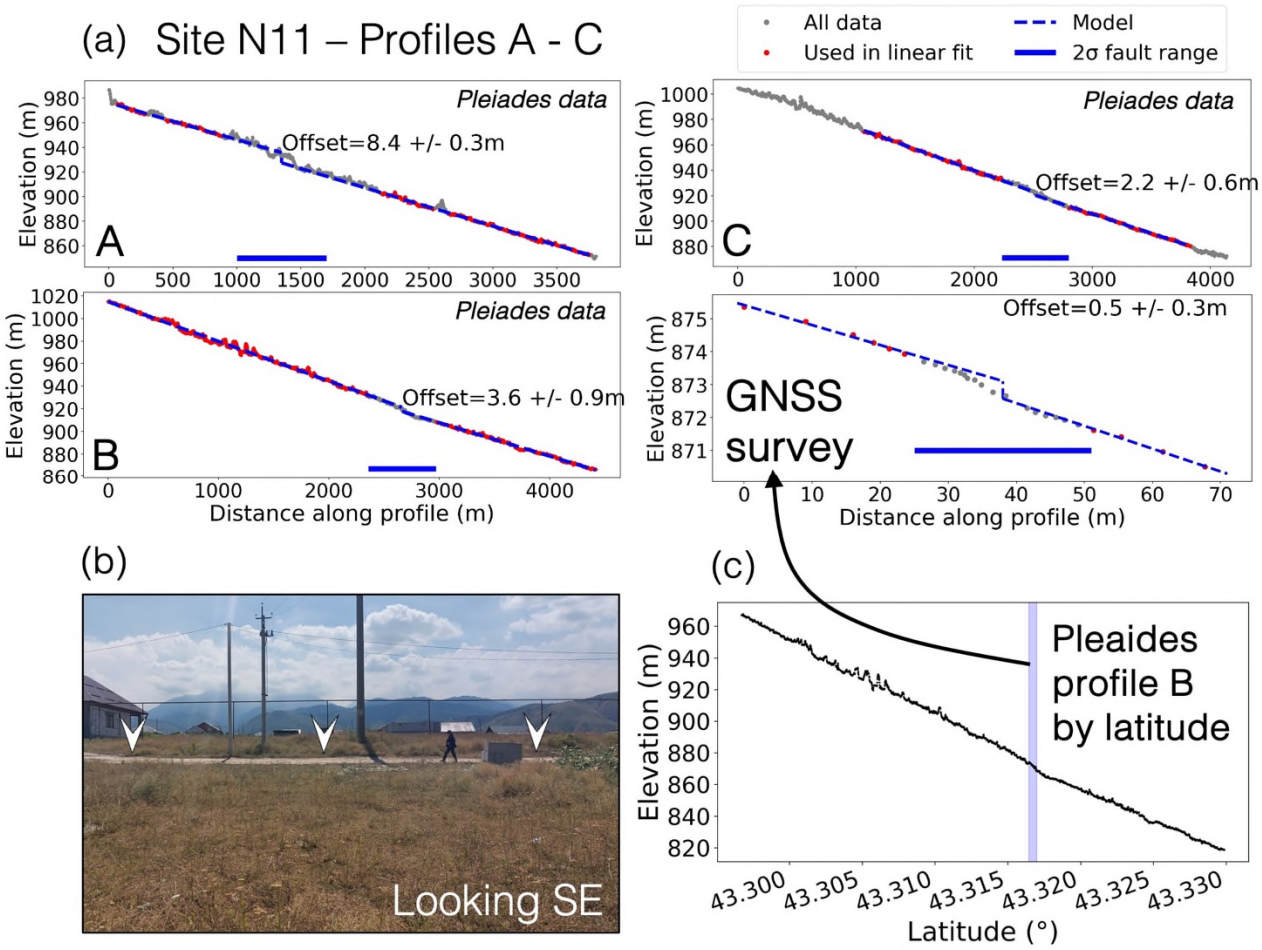

Figure 2.3-18. (a) Scarp profiles and vertical offset measurements for N11. Profiles A, B and C are correspond to the profile lines in Figure 2.3-17, constructed from data sampled every 1.5 m from a Pléiades-derived DEM. Zoomed in plots of the scarp in profiles B and C can be found in Figure 3.3-7. The GPS profile was collected in the field at the point labelled N11 in Figure 2.3-17. (b) Field photo of the scarp near Kyzylkayrat at N11 with geologist for scale. (c) Pleaides-derived elevation profile B (Figure 2.3-17) plotted by latitude with the location of GPS survey highlighted in blue.

Around 5 km to the southeast, close to the river in Talgar town at site N12, we identified possible scarps using Pléiades DEMs, Google Earth, and line mapping from Grützner et al. (2017b). It is difficult to accurately measure scarps within the town using satellite data because the buildings obscure much of the ground surface. Therefore, we carried out a dGPS field survey of this area (Figure 2.3-19, corresponding to the black box in Figure 2.3-17) by securing a receiver to a car and driving around Talgar's road network. We focussed the survey on the set of roads oriented NNE to obtain the highest resolution data in the direction approximately perpendicular to the likely orientation of the

underlying fault. On the east side of the river, we measure scarp heights of ~ 5 m in profiles G and H (smallest measurement is 4.7 ± 0.4 m), and ~9.0 – 12.9 m in profiles C, D and F which lie closer to the river. Profile E is a composite scarp with constituent scarp heights of ~6.3 m and ~ 10.1 m. While no other GPS profiles contain a second scarp, none extend as far to the north as the southern scarp in profile E. On the west side of the river we measure an offset of ~6.1 m ± 0.9 m. It is not clear why the scarps further from the river are significantly larger, and this finding suggests there may be differences in surface age which are not apparent in the topographic data, or some further complexity to the faulting. Due to the proximity of the river, we consider the possibility that some of the scarps have a hydrological rather than tectonic origin. While it is difficult to be certain when the surface is obscured by the town, we support a tectonic interpretation because (a) the scarps strike at a high angle to the present drainage direction, and (b) there is a large mound to the west of the river in Talgar town, ~250 m wide and standing ~30 m higher than the rest of the hanging wall, with its northern edge bounded by our mapped fault trace (Figure 2.3-17). We suggest this mound was uplifted over many earthquake cycles and therefore preserved from erosion.

To the east of Talgar, there is a valley within the mountains, ~4 km wide and extending ~10 km to the east (Figure 2.3-15 bottom panel). The origin of the valley is uncertain, but it is approximately aligned with the scarps in Talgar town and might have formed due to increased erosion along a fault strand. Around 7 km to the north of the scarps in Talgar town, the sharp tectonic (as opposed to hydrological) transition between the mountains and the foreland resumes after its truncation by the Talgar fan. It is unclear whether the fault steps the ~7 km across this gap or whether it is connected to the range front on the western side of the Talgar fan. The location and strike of the scarp near Kyzylkayrat (N11) seems to support the latter interpretation: the fault continues below the northern part of the Talgar fan between N11 and N13, with the Talgar town scarps formed by a separate fault strand (although strands could be connected at depth).

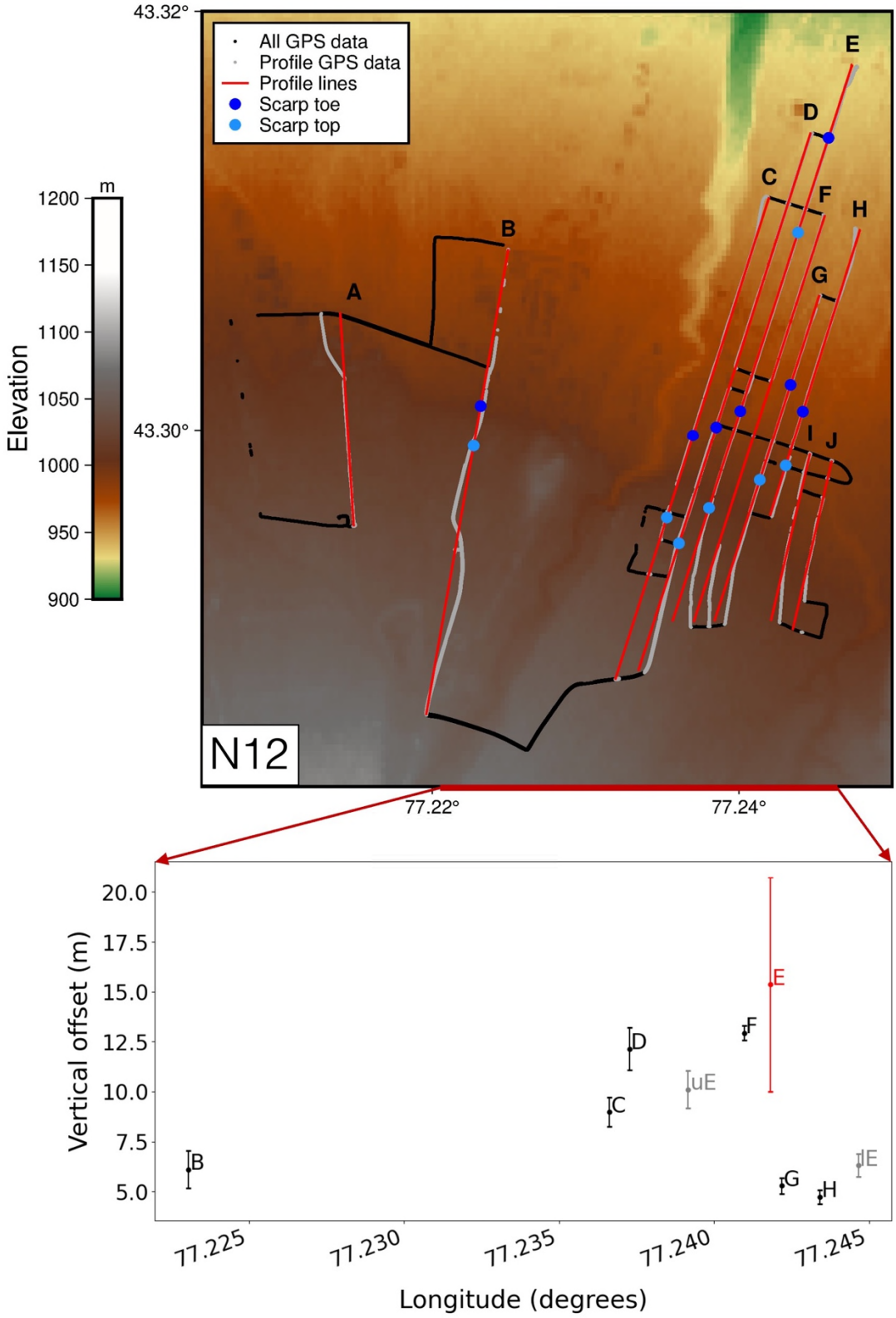

Figure 2.3-19. Top panel:Talgar road surveys, corresponding to box in Figure 2.3-17. Talgar town with ALOS World 3D 30 m (Japan Aerospace Exploration Agency, 2021) elevation map. Cleaned GPS road survey data in black, or grey if used in profiles. Profile lines shown in red, corresponding to Appendix

Figure 2.7-19. Approximate locations of the scarp top and toe are marked with light and dark blue dots, respectively. Lower panel: Vertical offset measurements. Red datapoint is the full offset measurement of scarp E, and the grey datapoints are the uE (upper) and lE (lower) scarps.

At site N13, immediately to the east of the Talgar fan and to the west of the village of Kainazar (Қайназар) we identified some linear discolouration in the satellite images of the fields directly to the north of the range front's topographic step. The site has been heavily modified, consisting of ploughed fields with a major road running along the southern edge (Figure 2.3-20). Ceramic artefacts from the Early Iron Age and Middle ages have been found scattered in the surrounding fields by archaeologists (Gass, 2016), suggesting the site has probably been utilised and modified by humans for millennia. A drone survey of the fields revealed two scarps striking ~E-W, each only a few hundred metres long with offsets of ~ 2.3 – 4.1 m on the western scarp and ~ 1.6 – 2.9 m on the eastern scarp measured from the DEM. The strike and morphology of these features suggests they are earthquake scarps, but due to the modification of the surface we cannot be completely certain that they do not have another origin (e.g. spoil heaps or archaeological features).

Moving ~6.5 km to the east along the range front, Grützner et al. (2017b) documented scarps in a suite of river terraces next to the village of Rahat (Рахат; site N14; Appendix Figure 2.7-21). They measured offsets of ~5 m in the youngest deformed terrace (T2) and a composite scarp of ~3.5 m and ~11 m in terrace T3. We re-measured the site to obtain formal errors consistent with the rest of our analyses and found scarps of 4.7 ± 0.1 m and 4.7 ± 0.1 m for T2 and 12.7 ± 0.2 m for T3. We map a single scarp rather than a double scarp in T3 and suggest that the double scarp measured by Grützner et al. (2017b) was in fact an artefact of measuring across multiple terraces.

To the east of N14, the sharp change in elevation at the range front continues, but it is not always clear whether the break in slope represents offset at the fault or erosion at the edge of a fan. The next two large fans to cross the range front host the towns of Esik (Есік) and Turgen (Тургень; Figure 2.3-15).

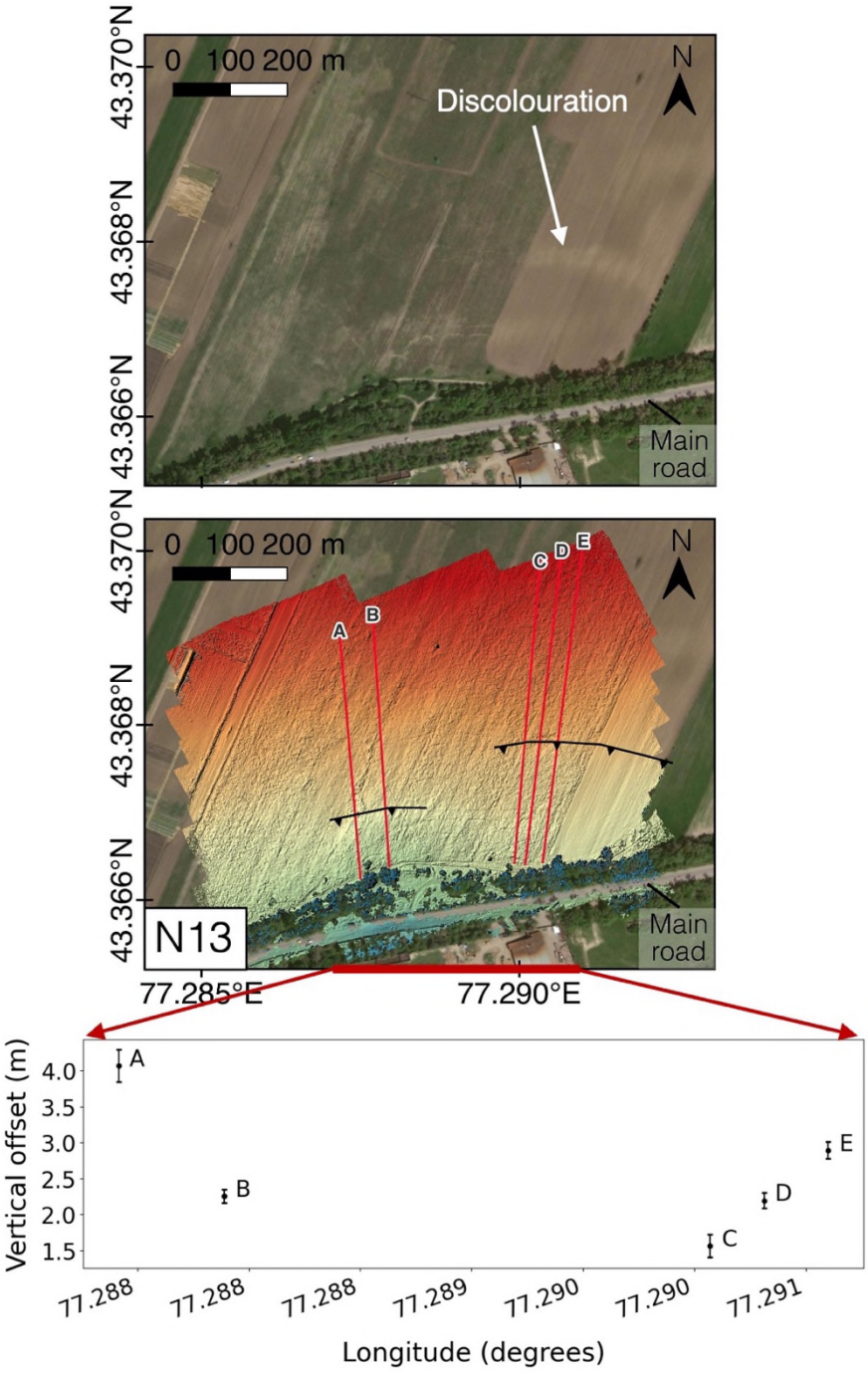

Figure 2.3-20. Site N13. Top panel: Bing Aerial imagery (2023 TomTom, 2023 Maxar). Middle panel: hill shade of drone DEM. Lower panel: vertical offset measurements corresponding to the profile measurements in Appendix Figure 2.7-20

We did not identify any scarps within these fans surfaces in our remote mapping, although we did not visit them in the field and the surfaces have been modified by urbanisation and agriculture. Between

the two fans near the village of Lenino (Ленино), a drainage channel exits the mountains forming a valley a few hundred metres wide (Figure 2.3-21). A graveyard occupies the mouth of the valley and a road runs along its base at the edge of the hills. At study site N15 (Figure 2.3-21), using a Pléiades-derived DEM we identified vertical offsets near the valley mouth. The transition between the hills and the lowlands runs at a high angle to the drainage direction, supporting a tectonic interpretation for the scarp. The oldest (highest elevation) material either side of the valley is offset by ~30 m compared to the foreland. We map a young channel draining to the NNW down the valley as well as several small topographic steps approximately parallel to it. These features are probably terrace risers or the remains of other drainage channels, but we were unable to comprehensively map the surface as a coherent suite of terraces and channels using the available dataset. We measure offsets of ~3.0 – 5.1 m in the valley sediments but no offset in the youngest channel within the resolution of the data (Figure 2.3-21). Most of the mapped scarps are located at the road, coincident with the main topographic step, but the central scarp (profile C, 3.0 ± 0.5 m offset) is located further south, nestled within the valley. This step in the scarp location could be a hydrological feature rather than a tectonic scarp. A field visit and the collection of a drone survey would be required to distinguish between the two, but unfortunately we identified this scarp site after returning from the field.

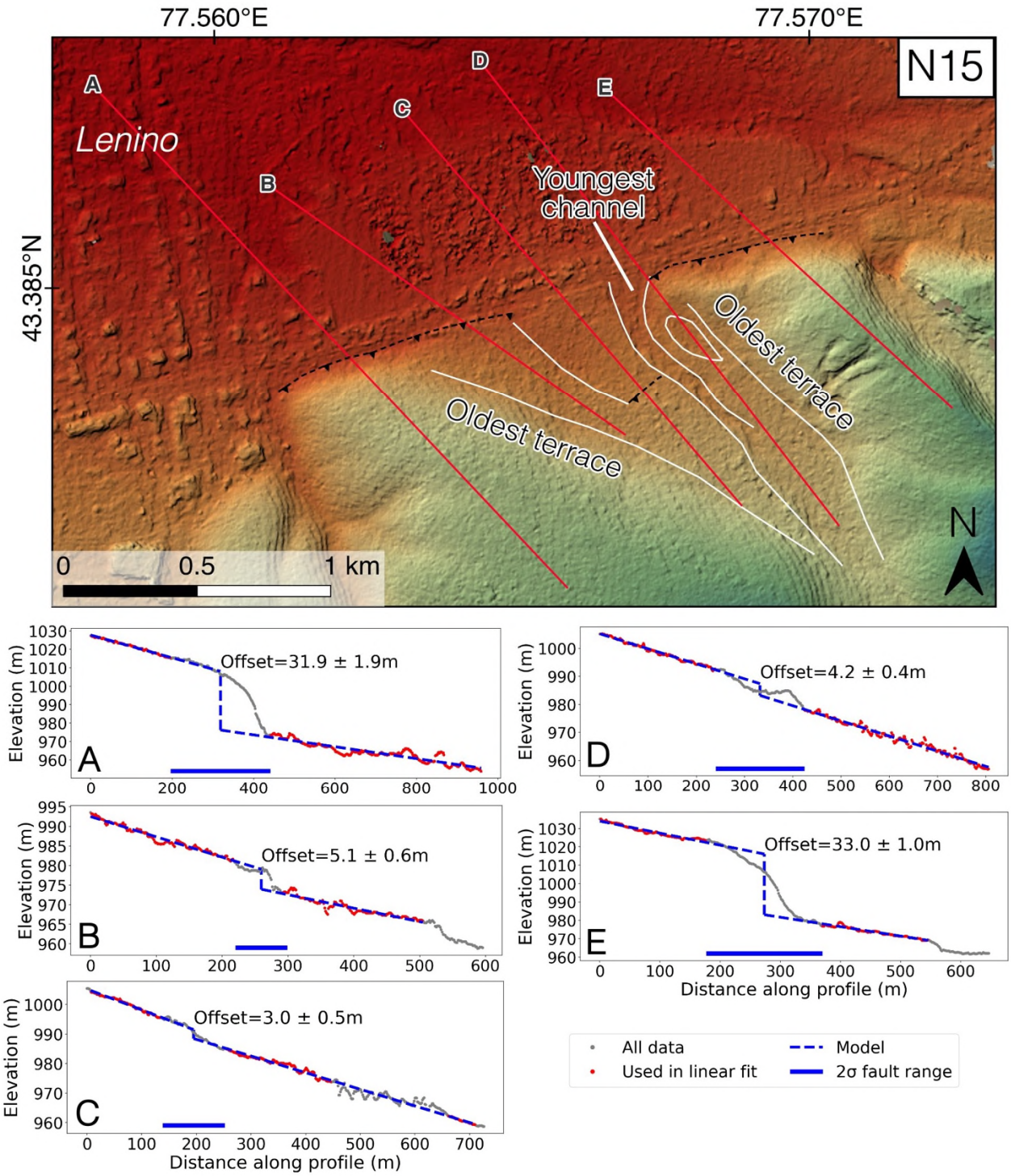

Figure 2.3-21. Site N15 between Lenino and Turgen. Top panel: Hill shaded Pléiades-derived DEM coloured by elevation. White lines mark the edges of topographic features in the stream valley with the oldest terrace and youngest channel labelled. Red lines correspond to profiles A to E in lower panels, sampled from Pléiades-derived DEM every 1.5 m.

2.3.4. East Section (N16 – N20)

To the east of Turgen the Zailisky Alatau drops in height and the alluvial fans along the range front become smaller, their hydrological and sediment input draining from lower elevations and a smaller catchment (Figure 2.3-22). The alluvial fans are no longer populated by large towns. Instead, they are dominated by agricultural land and a few smaller villages. We collected speculative drone surveys to check for smaller scarps within three of these young fans which have been mapped as late Quaternary to modern deposits (Parshina, Zolotokrylina and Semenova, 1979), but we find no evidence of faulting (Appendix Figure 2.7-22). For the ~25 km between N15 and the next scarp site at N16, we find no unequivocal signs of faulting. There is a linearity to the range front in the west which might be tectonic (mapped with a dotted line in Figure 2.3-22) but there is no sharp step in elevation. The several younger fans which cross the range front (whiter surfaces in Figure 2.3-22b) might have destroyed evidence of faulting, but we also find no offsets within surfaces near Ashchybulak (Ащыбұлақ) village which appear older from their incised morphologies. However, between the Turgen fan and site N16, ~10 km to the south of the range front on the northern slopes of the Zailisky Alatau there is a ridge of uplifted material running ENE for ~17 km with a depression on its southern side (Figure 2.3-22). Whilst we did not find fresh scarps in Google or Bing Aerial satellite imagery around the edges of this block, we infer that it was probably uplifted by faulting and could be accommodating the slip in this ~25 km portion of the range front where no faulting is apparent in the geomorphology further to the north.

To the east of Ashchybulak, we map scarps within an older, heavily incised surface which sits between two younger fans at site N16 (Figure 2.3-23). The scarps are at a low angle to the drainage direction so we consider whether they might in fact be a terrace riser. While this is possible, the scarps are stepped rather than forming a smooth line, which seems inconsistent with erosion at the edge of the alluvial fan but could be consistent with faulting. We measure a range of scarp heights between ~8.7 – 21.1 m. The

different offset magnitudes might correspond to surfaces of different ages, but we were unable to map these based on the morphology which is heavily incised in the hanging wall.

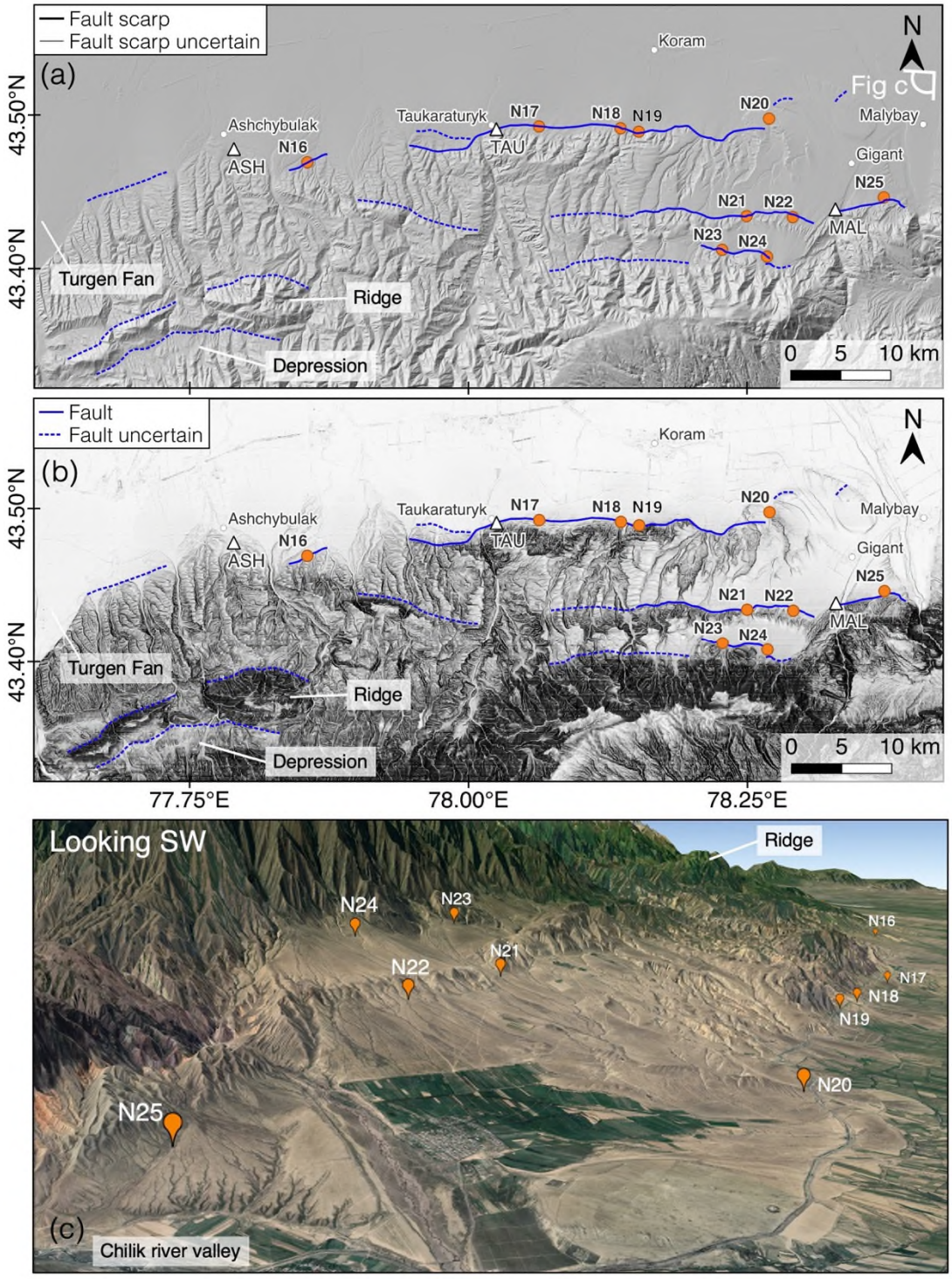

Figure 2.3-22. Overview of east section and parallel strands. Orange data points are sites discussed in the text; white data points are settlements. White triangles are luminescence sampling sites from Dave

et al. (2023). (a) Scarps mapped in this study overlain on the Copernicus GLO-30 DEM hill shade. (b) Fault mapping overlain on slope map derived from Copernicus GLO-30 DEM. Darker colours represent steeper slopes. (c) Satellite imagery overlain on 3 x exaggerated topography from Google Earth (2023 Maxar Technologies, 2023 Airbus, Landsat/Copernicus, 2023 CNES/Airbus), from ~43.5°N 78.4°E, 6.23 km eye altitude, looking southwest.

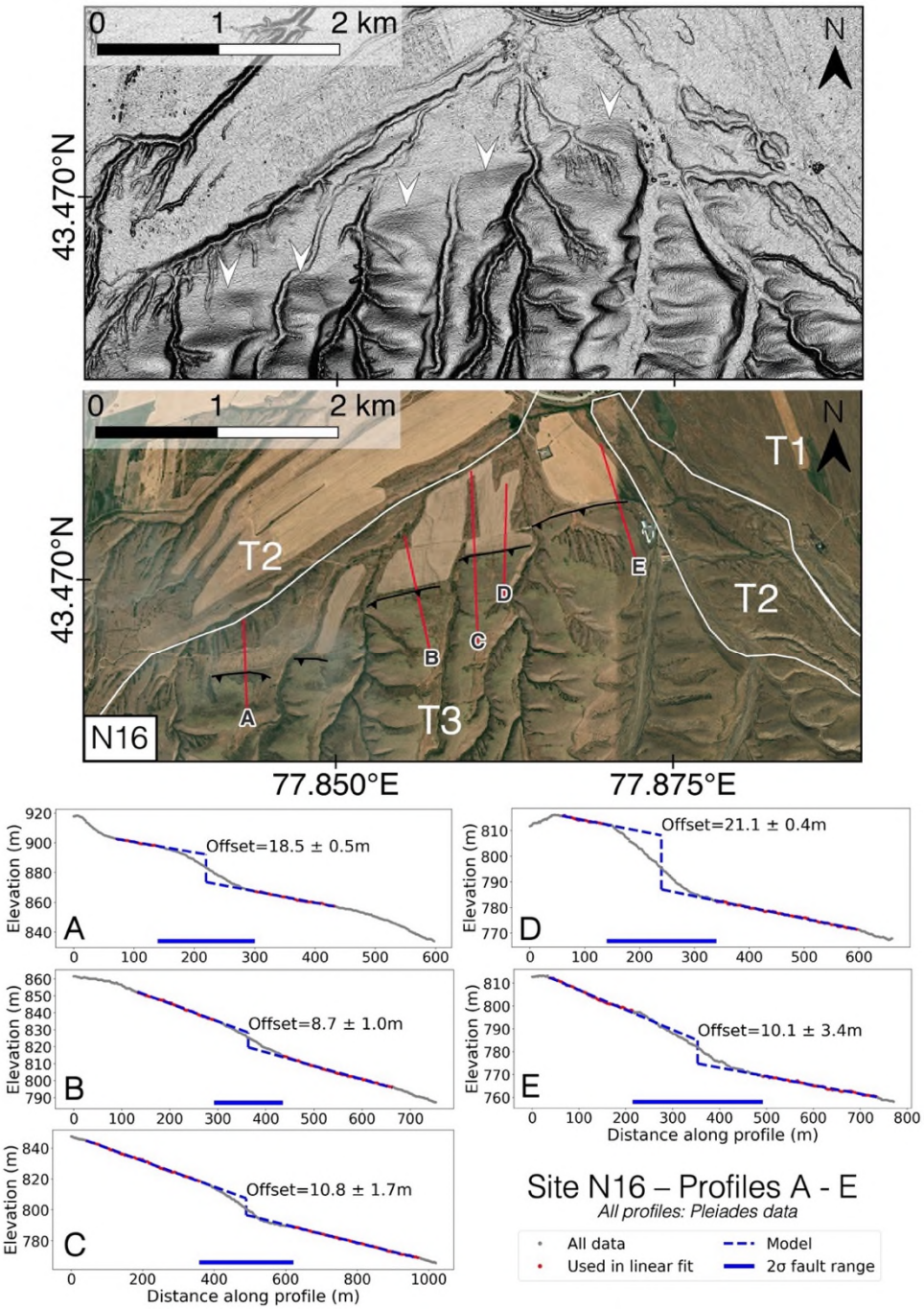

Figure 2.3-23. Site N16 near Ashchybulak. Top panel: Hill shaded Pléiades-derived DEM. White arrows mark base of scarps. Middle panel: Bing Aerial imagery (2023 TomTom, 2023 Maxar). White lines mark

edges of surfaces inferred to be of different ages, T1 – T3, youngest to oldest. Red lines correspond to profiles A to E in lower panels, sampled from Pléiades-derived DEM every 1.5 m.

To the east of N16 we map no scarps for ~17 km, but the Big Almaty Canal runs along much of the range front where we might expect to find a scarp, and in some places it is difficult to distinguish between possible scarps, alluvial features and anthropogenic modification due to the building of roads and the canal. To the east of village of Taukaraturyk (Тауқаратұрық), the canal runs directly along the range front. At site N17 we document evidence of faulting within 500 m of the canal in a set of small alluvial fans (Figure 2.3-24; Figure 2.3-25). The fans have been modified by human activity, including an irrigation ditch and a road. A series of mounds running along the southern edge of the surveyed area are probably spoil-heaps from the digging of the canal. We tentatively map at least three generations of fan, T1 – T3, though the surfaces probably have a range of ages within these classifications. The smallest scarp we measure is ~0.2 – 0.4 m high, profiles L to O (Figure 2.3-24). The surfaces are dissected by many small channels which make the accurate measurement of such small offsets challenging. In some places the scarp is eroded by the channels, such as at profile P where we measure no offset. Satellite imagery also shows an irrigation ditch was built between 2016 and 2018 along the portion of the scarp containing profiles O and P, modification which may also have affected these measurements (Figure 2.3-24). Such activity could be obscuring or destroying small scarps like this one elsewhere on the range front.

The largest scarp offset we measure at N17 is ~0.9 – 1.2 m high (profiles I – K). We attempt to map older and younger surfaces based on cross-cutting relationships and surface texture, but we find only a loose association between inferred surface age and offset: apparently older surfaces have scarps between ~0.3 - 1.2 m in height, whilst apparently younger surfaces have scarps between ~ 0.2 - 0.6 m. There are also locations on surfaces of all inferred ages where we could find no offset at all. Partial erosion of scarps, both natural and from anthropogenic modification, probably explains some of the

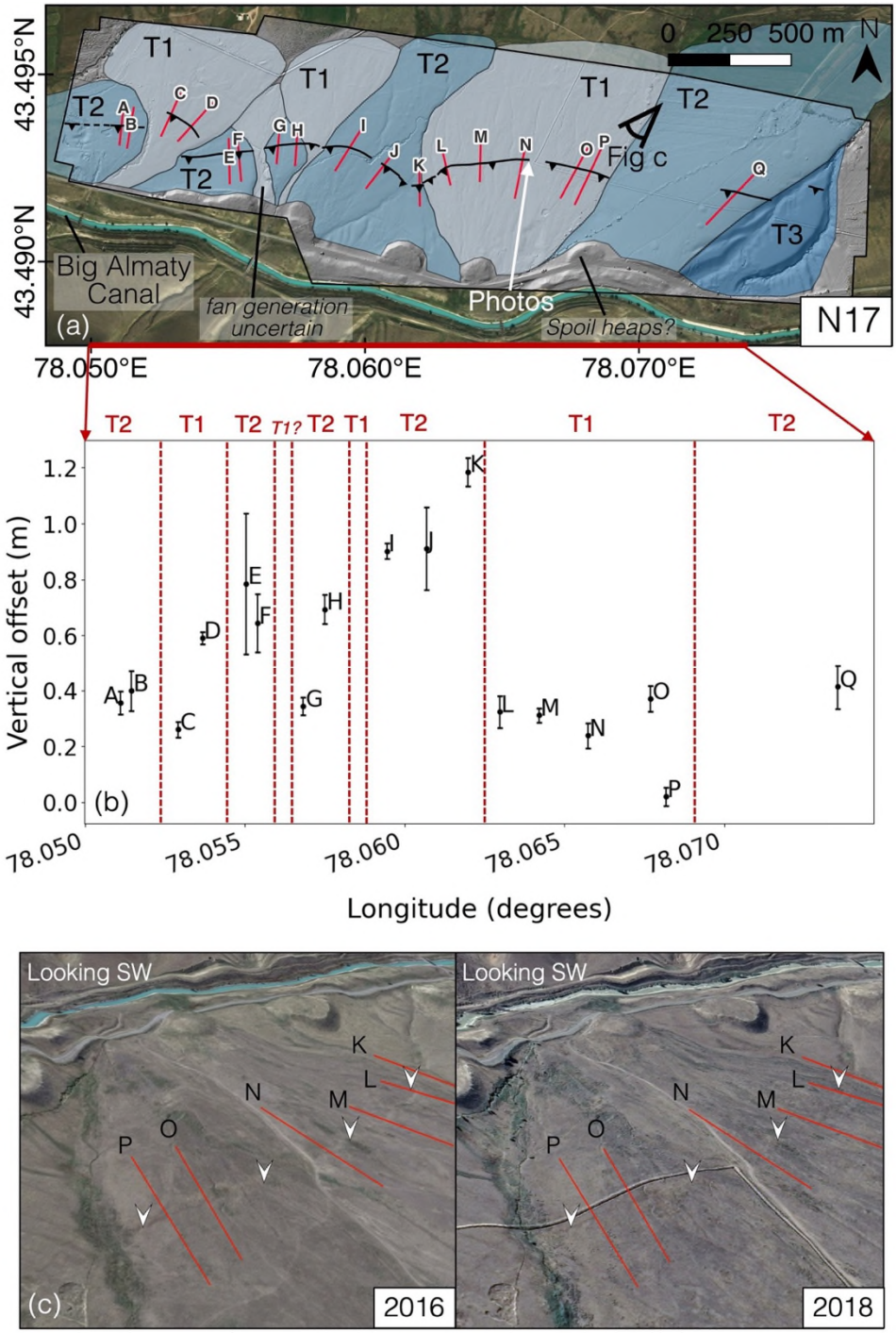

Figure 2.3-24. (a) Site N17 showing hill shade of drone DEM and scarp profiles. Three distinct generations of alluvial fans are mapped (T1-T3). 'Photos' lable corresponds to the location of the images in Figure 2.3-25. (b) Vertical offset measurements plotted by longitude. Dashed lines show estimated locations of transitions between fan generations, labelled above the plot. (c) Satellite imagery overlain on 3 x exaggerated topography from Google Earth (CNES/Airbus, Landsat/Copernicus), 2.37 km eye altitude, looking southwest. Left imagery from December 2016, right from October 2018. Fault scarp is marked by white arrows, labelled red lines are profiles corresponding to those in Appendix Figure 2.7-23 and Appendix Figure 2.7-24.

Figure 2.3-25. Scarp photos from site N17, location labelled in Figure 2.3-24.

variability in the offsets we measure. We suggest the smallest offsets at this site were formed in the MRE. The scarps mapped at this site could not be identified in the Pléiades imagery, only from a drone DEM. This highlights that there are probably other scarp sites with small offsets which we were unable to identify remotely and therefore could not map.

A few kilometres to the west of N17 at the village of Taukararuryk, Dave et al. (2023) sampled the loess foothills for luminescence dating (TAU in Figure 2.3-22). They found ~1 m of ~11.4 – 13.3 ka

loess overlying much older loess of >180 ka. Such a large jump in age suggests there may have been an erosional event here at some point before ~11.4 – 13.3 ka. This might explain why only relatively small scarps are preserved at site N17, if previous topography was eroded.

To the east of N17, two additional fault strands appear ~6 km and ~10 km south of the main range front (Figure 2.3-22). These strands run ~E-W through the foothills of the Zailisky Alatau, and are discussed in detail in section 2.3.5. On the main range front, the Big Almaty Canal and road continue to follow the sharp break in slope between the uplifted foothills and the foreland. At site N18, Grützner et al. (2017b) (site S7 therein) document a scarp offsetting a suite of stream terraces. We reassessed the site and measured offsets of 3.5 ± 0.5 m for the youngest offset terrace (T2), 38.6 ± 0.7 m for the second oldest terrace (T3) and 52.3 ± 0.4 m for the oldest terrace (T4; Appendix Figure 2.7-25). Our results differ from Grützner et al. (2017b), in particular for the youngest terrace, due to a difference in terrace mapping which we explain in detail in Chapter 3.

Around 1 km to the east of the offset terraces, Grützner et al. (2017b) (site S8 therein) identify fault scarps in the declassified Corona imagery from before the Big Almaty Canal was built. They map potential scarps at the latitude of the present-day canal and within the shallow sloping foothills to the south of it. We visited this section of the range front at N19 and confirmed the presence of multiple scarps. Using a drone DEM we map at least four generations of surface (T1 – T4, youngest to oldest) at the site, though we are unable to assign relative ages to surfaces in the east as the cross-cutting relationships are inconclusive (Figure 2.3-26). We measure several distinct scarp heights across the site. Scarps with ~0.3 – 0.6 m vertical offset occupy a surface of unknown age between profiles K to N in the east of the site. We suggest this scarp probably formed in the MRE. In surface T2 (profiles F to J) we measure a ~1.3 – 1.6 m offset. In the west of the study site, the two oldest surfaces (T3 and T4) host larger scarps which have an undulating morphology indicating they are composite scarps with total offsets of ~5.7 – 7.7 m measured in profiles B and C. In profiles A and B the lower scarp seems to

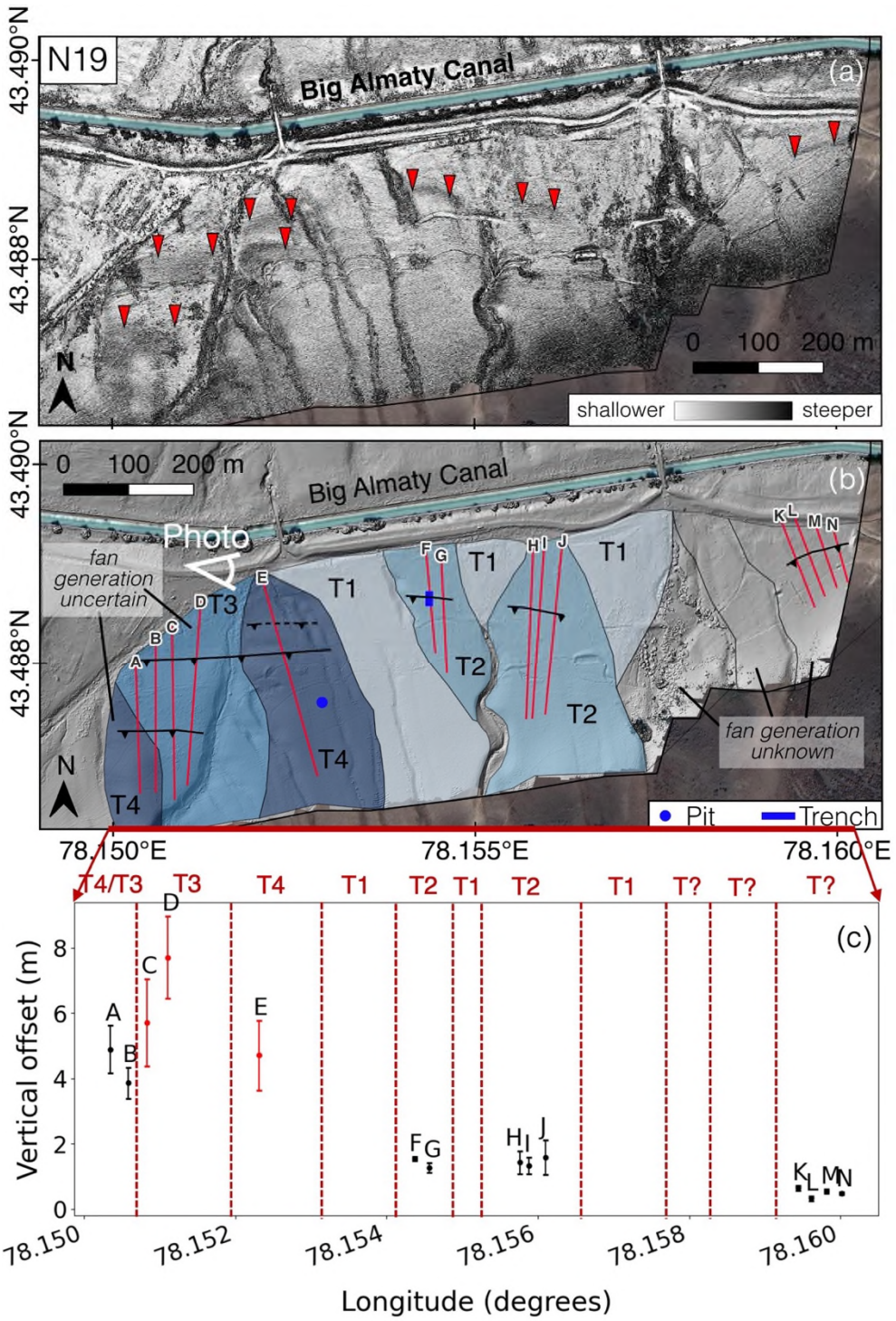

Figure 2.3-26. Koram trench site, N19, corresponding to site S8 in Grützner et al. (2017b). (a) Slope map derived from drone DEM. Red triangles indicate scarps. (b) Hillshade of drone DEM with four inferred fan generations overlain, T1 – T4, youngest to oldest (different colours indicate different inferred fan ages, darker = older). Photo viewing angle corresponds to Figure 2.4-1. (c) Vertical offset measurements plotted by longitude. Red data points are from composite scarps. Dashed lines show estimated locations of transitions between fan generations, labelled above the plot. Profiles are plotted in Appendix Figure 2.7-26.

be truncated by another fan, but we measure offsets of ~3.9 – 4.9 m on the upper scarp. Scarp profile E in surface T4 has an offset of 4.7 ± 1.1 m and also undulates so may be a composite scarp, although its shape could also have been produced by anthropogenic modification of the surface (e.g. a vehicle or herding track). We excavated a paleoseismic trench on the T2 surface which hosts profiles F and G, and a pit on the T4 surface of profile E, both of which are presented in detail in Section 2.4.

For around 10 km to the east of N19 there is an abrupt change in elevation between the foothills and the foreland along which we infer the fault runs, but we do not identify any fresh scarps, including in a drone survey DEM we collected of the area ~2 km to the east of the trench site survey area. It is possible that scarps have been covered by the canal or road in some of this section.

As the fault progresses eastwards from N19, the foothills drop in elevation and become more heavily incised by deep gorges. At site N20, Grützner et al. (2017b) (S9 therein) documented alluvial fan sediments exposed in a river cutting dipping 18° to the north and infer folding due to an underlying thrust, but they do not map a scarp. Around 800 m to the northeast of this river cutting we identify a large scarp within a set of terraces lying between two deeply incised river valleys (Figure 2.3-27). We measure a 40.4 ± 0.8 m scarp in the oldest terrace along profile A and a 13.6 ± 1.5 m scarp in the second oldest terrace along profile B. However, in order to remain approximately perpendicular to the scarp, profile B crosses over into a younger terrace which may have modified the footwall, introducing some further uncertainty to its measurement in addition to the formal error.

To the east of N20, alluvial fans and rivers have removed most of the hanging wall topography and we find only sporadic evidence for a topographic step at the range front with a tectonic origin. All indicators of faulting have disappeared within ~5 km of N20 where the Chilik river exits the range front.

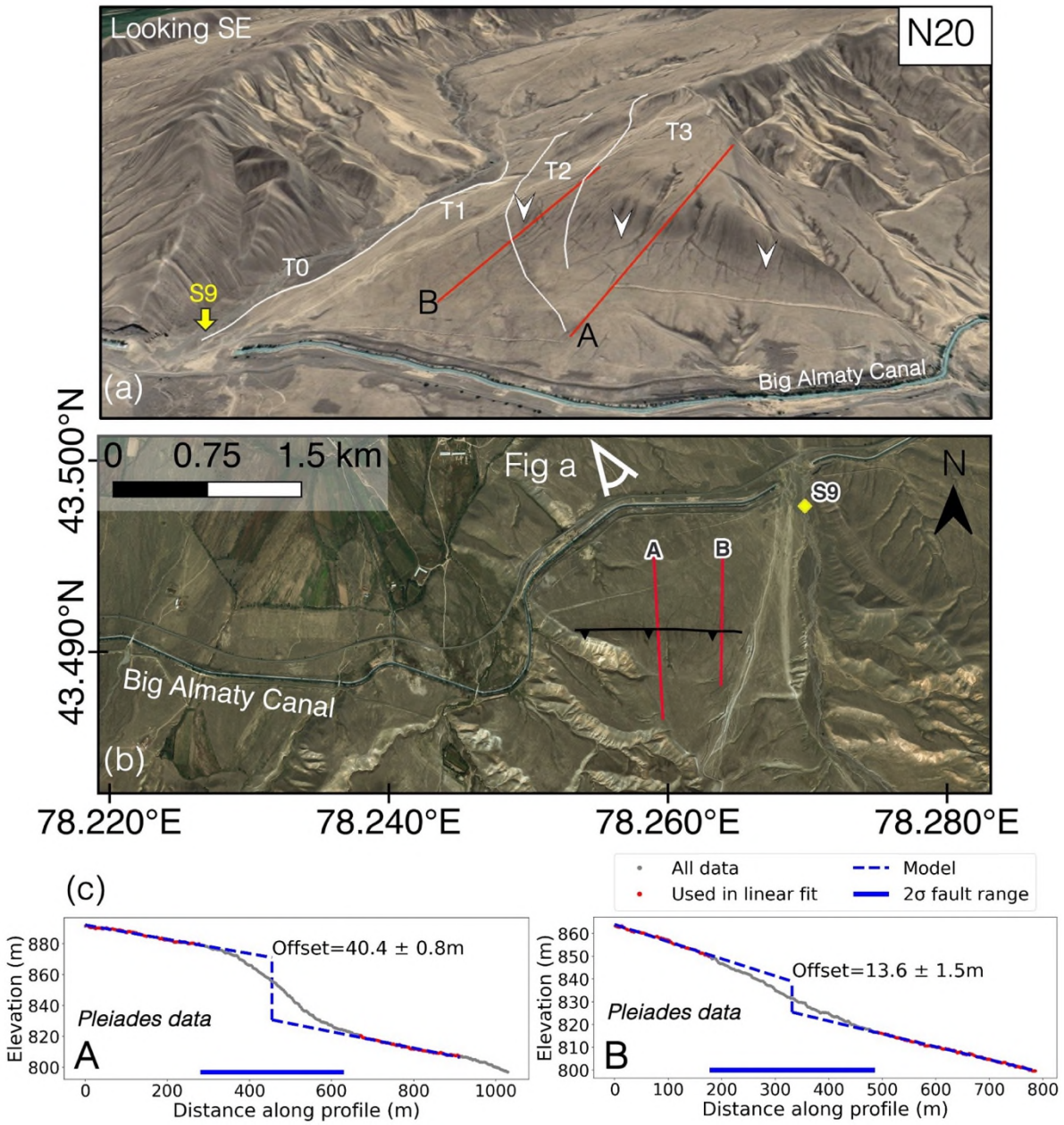

Figure 2.3-27. N20, scarp near site S9 from Grützner et al. (2017b). (a) satellite imagery overlain on 3 x exaggerated topography from Google Earth (2023 Maxar Technologies, Landsat/Copernicus, 2023 CNES/Airbus), at 43.472010°N 78.297892°E, 3.27 km eye altitude, and looking southeast. Fault scarp marked by white arrows, labelled red lines show profiles. White lines are approximate boundaries of river terraces. (c) Bing Aerial satellite imagery (2023 TomTom, 2023 Maxar) of the S9 site and scarp. (d) Scarp profiles measured from a Pléiades-derived DEM sampled every 1.5 m.

2.3.5. Parallel Strands (N21 – N25)

In the eastern section of the Zailisky Alatau, we map three parallel ~E-W striking faults: the main range front fault and two further strands ~6 km and ~9 km to the south, as documented by Grützner et al. (2017b) (Figure 2.3-22). To the west, the strands bound a heavily incised plateau with two topographic steps, which transitions to the east into a suite of smoother alluvial fans cut by a central ridge. Fault scarps run through the alluvial fans along the base of this ridge. At site N21 (Figure 2.3-28), we map 3 generations of fan and a possible fourth generation (T1) as well as modern river channels (T0). We measure three distinct ranges of scarp height, corresponding to surfaces of different generations. In T2 fans scarps are ~2.2. – 2.9 m high. In T3 fans scarps are mostly ~ 10.0 – 16.4 m with one measurement of 7.5 ± 0.4 m (profile G) at the edge of the fan surface where the scarp may have been partially eroded by the neighbouring fan. The oldest terrace hosts a large scarp of ~22.4 – 23.6 m but the footwall is cut by a younger fan, so the scarp may have been modified since its formation.

The scarps continue to the east along the base of the central ridge, documented at site S11 in Grützner et al. (2017b), corresponding to N22 in this study (Figure 2.3-29). Grützner et al. (2017b) mapped four different generations of fan (T1 to T4, youngest to oldest) at the site and measured offsets between ~0.5 – 24 m in three of them data using dGPS surveys along 8 scarp profiles. We produced a similar but more detailed fan mapping based on a DEM from a drone survey we collected, which we used to comprehensively measure the scarp across 27 profiles (Figure 2.3-29). The distinction between fans of different generations is not always clear at this site and we map fans with some uncertainty. Within fans inferred to be generation T1, we map scarps of ~0.4 – 0.7 m and ~0.9 – 1.1 m. The former or possibly both of these scarps are probably single event offsets from the MRE. In the two fans inferred to be of generation T2 in the west of the study site we measure scarps of ~1.0 – 3.2 m. In the most

easterly fan inferred to be T2 we map two ~parallel scarps ~ 100 – 200 m apart, with total offsets across both scarps measuring between 3.8 – 9.9 m. Profile X reveals a large ~9.1 m upper scarp and a

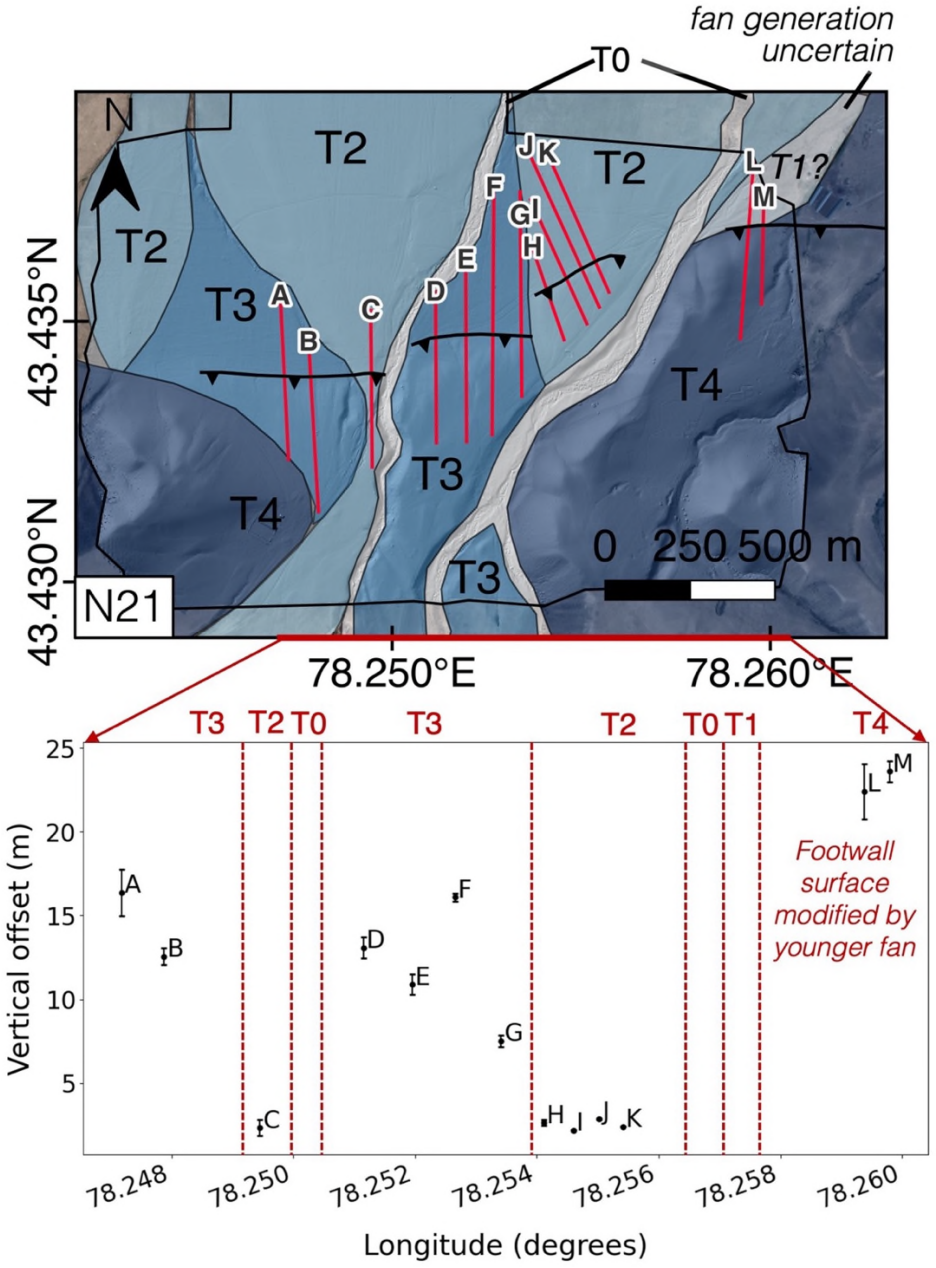

Figure 2.3-28. Site N21. Top: Hillshade of drone DEM from with four inferred fan generations overlain, T1 – T4, youngest to oldest as well as the modern drainage surfaces, T0, which we map only in places where they are wide enough to be significant to our mapping (different colours indicate different inferred surface ages, darker = older). (b) Vertical offset measurements plotted by longitude corresponding to profiles in Appendix Figure 2.7-27. Dashed lines show estimated locations of transitions between fan generations, labelled above the plot.

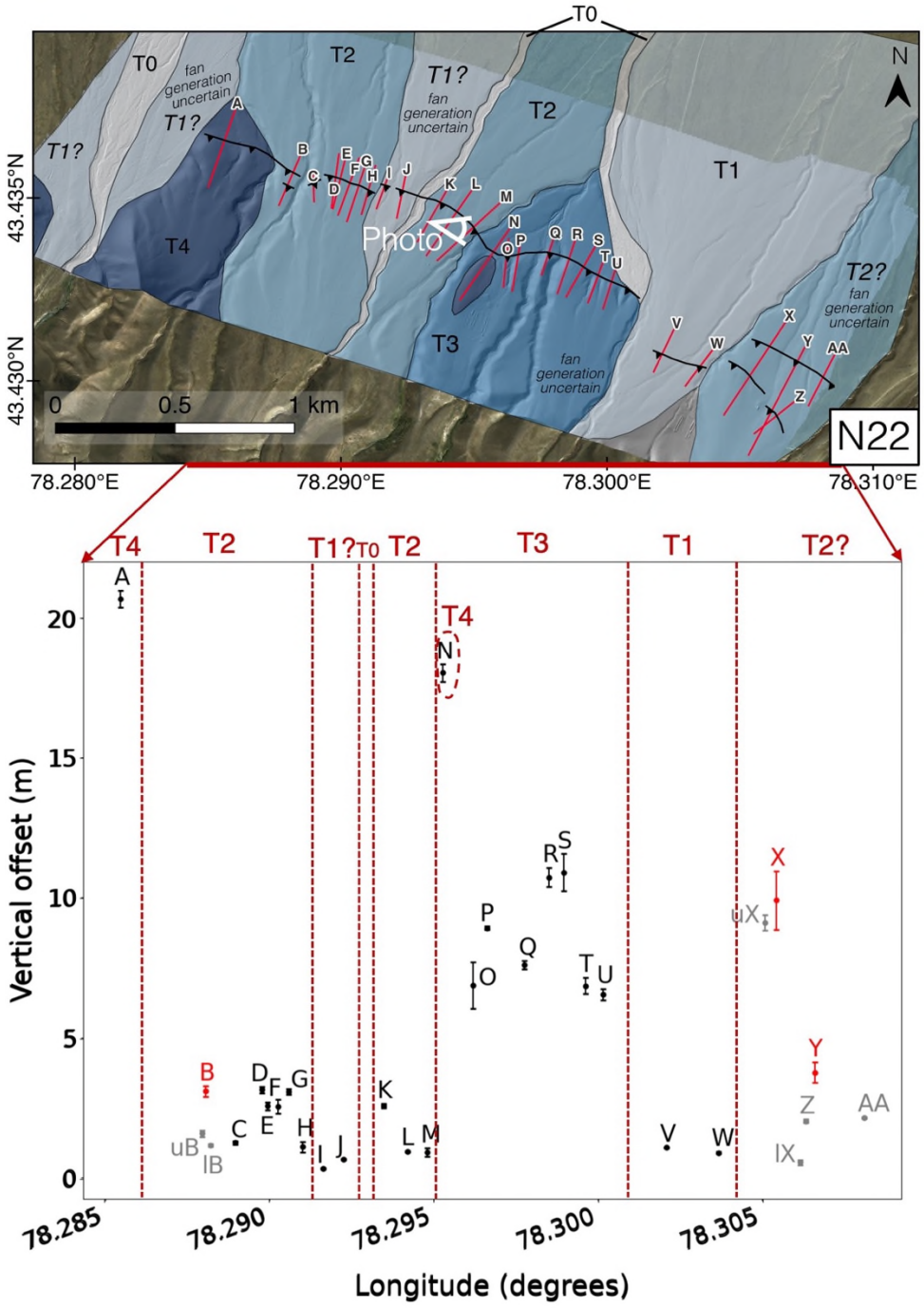

Figure 2.3-29. Site N22. Top: Hillshade of drone DEM with four inferred fan generations overlain, T1 – T4, youngest to oldest as well as the modern drainage surfaces, T0 (different colours indicate different inferred surface ages, darker = older). Photo viewpoint corresponds to Figure 2.3-30. (b) Vertical offset measurements plotted by longitude corresponding to measurements in Appendix Figure 2.7-28, Appendix Figure 2.7-29, Appendix Figure 2.7-30. Dashed lines show estimated locations of transitions between fan generations, labelled above the plot. Red points are total offsets for double scarps. Grey points are offsets for single scarps which are part of a double scarp. uY and lY represent the upper and lower scarps in the Y profile respectively. uB and lB represent the upper and lower scarps in the B profile respectively.

Figure 2.3-30. Photograph of scarps at site N22 from viewpoint marked in Figure 2.3-29. Note geologist standing at scarp base for scale.

~0.6 m lower scarp ~ 150 m to the south (Figure 2.3-29; Appendix Figure 2.7-29). This ~0.6 m lower scarp is the same size as the smallest single offset scarp and might have ruptured in the MRE. In the fan we map as generation T3 we find scarps of ~ 6.6 – 10.9 m (profiles O to U, photographed in Figure 2.3-30), and in the T4 surfaces offsets are on the order of ~ 20 m (profiles A and N, though N crosses into a younger fan and is therefore more uncertain). Our measurements are broadly consistent with Grützner et al. (2017b), but measuring a higher frequency of profiles over a larger area we find rather a lot of variation in height between surfaces inferred to be of the same age and even within a single fan surface in some places. With some exceptions, fans inferred to be older seem to show larger offsets.

Around 3 km to the south of the central fault strand, we also document scarps within the fans at the very edge of the mountains at sites N23 and N24 (Figure 2.3-31). We did not visit these sites in the field, but the scarps are visible in Google Earth and we measure offsets using Pléiades DEMs or Copernicus GLO-30 DEM where the Pléiades data is unavailable due to cloud cover. We measure offsets of ~6.2 – 8.5 m at site N23 across a curved fault trace. At site N24 we measured a 17.6 ± 7.4 m

scarp using 30 m DEM data. Although we map no further scarps along this southern fault strand, there is a sharp change in elevation at the foot of the mountains suggesting the fault probably extends for ~20 km laterally (Figure 2.3-22).

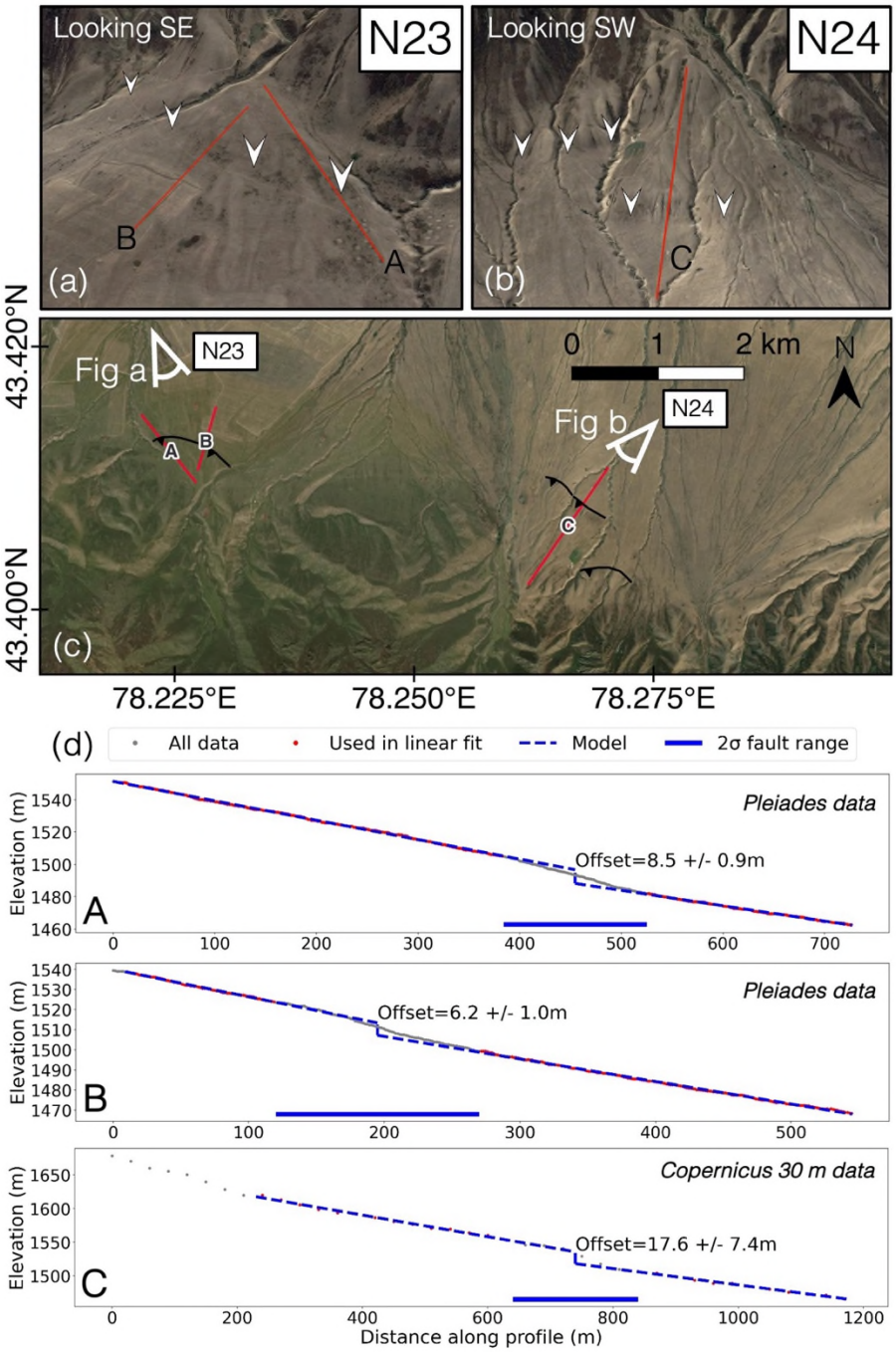

Figure 2.3-31. Sites N23 and N24. Scarps at Malybay south strand. Top panels show satellite imagery overlain on 3 x exaggerated topography from Google Earth (2023 Maxar Technologies, Landsat/Copernicus, 2023 CNES/Airbus), with (a) at 5.31 km eye altitude, and looking southeast, and

(b) at 5.60 km eye altitude, and looking southwest. Fault scarps marked by white arrows, labelled red lines show profiles. (c) Bing Aerial satellite imagery (2024 TomTom, 2024 Maxar) of the south Malybay strand. (d) Scarp profiles. Profiles A and B are measured from a Pléiades-derived DEM sampled every 1.5 m, whilst Profile C is measured from the Copernicus GLO-30 DEM sampled every 30 m.

To the east, the southern fault strands terminates at ~73.33°E where a small river exits the range front and flows down the alluvial fans to the east of Gigant village (Figure 2.3-22). At this point the mountains feeding the range front drop significantly in height. To the east of the small river, we map further scarps at site N25, which seems to be a continuation of the central strand (Figure 2.3-32). Here, we map at least five generations of fan (T1 to T5, youngest to oldest) and modern drainage surfaces (T0), although the relative ages of some fans are unclear where there are no cross-cutting relationships to be assessed and surface morphologies are indistinct. The break in slope which follows the edge of the main alluvial fan (dashed red line in Figure 2.3-32) could be interpreted as a scarp, but we suggest this is a terrace riser because it runs parallel to the drainage in the large main fan and the drone DEM reveals an erosional ditch along most of its length. The main fan is not deformed, but we map scarps in the smaller fans adjacent to it. T1 fans contain no offsets and truncate scarps. There are three distinct sets of scarp heights: ~0.6 – 1 m (profiles A to E) in T3, ~2.3 – 3.9 m (profiles F to I) in T4 and 17.8 ± 0.4 m (profile J) in T5. Based on its small size, we suggest that the T3 scarp probably formed in the MRE.

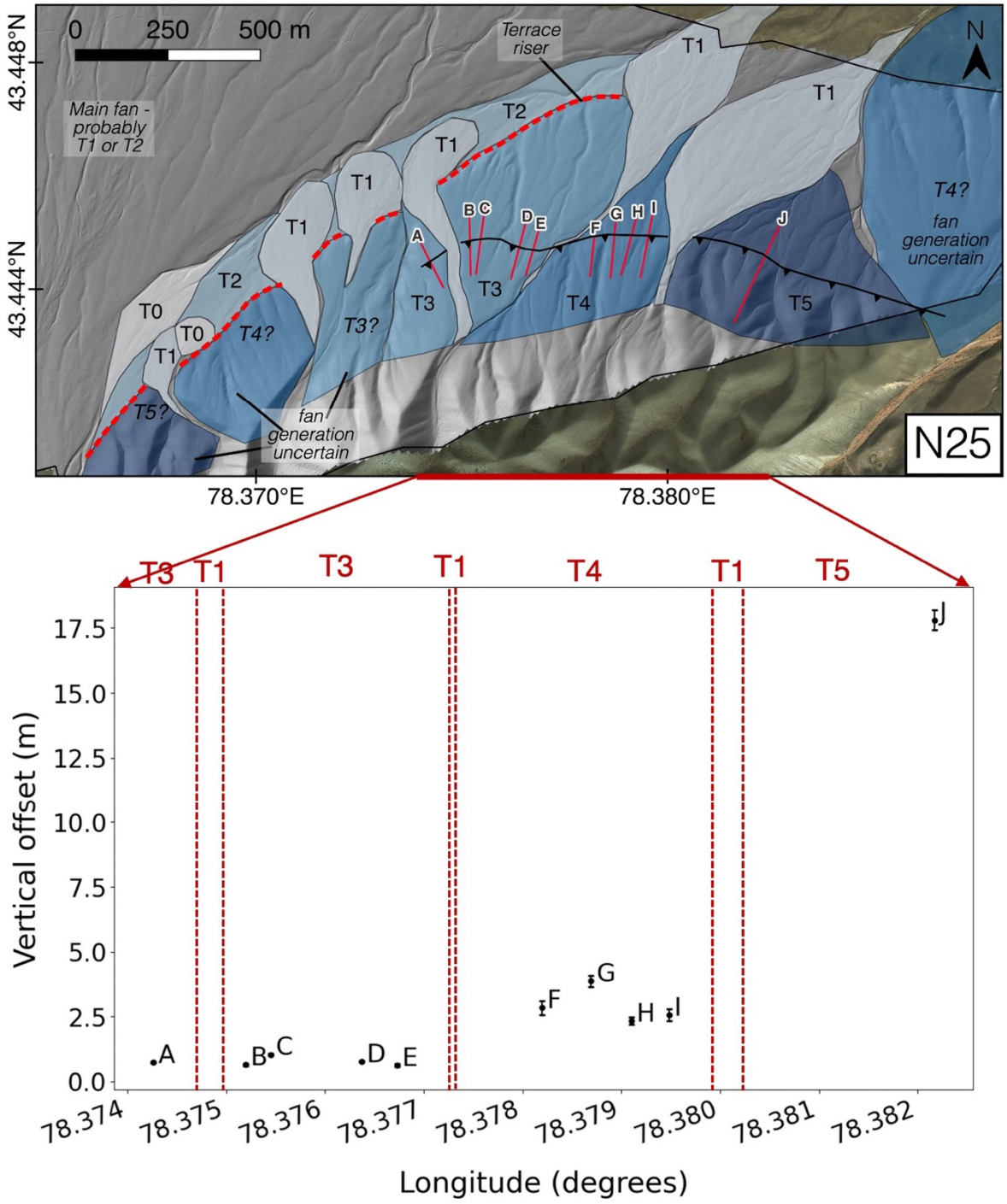

Figure 2.3-32. Site N25. Top: Hillshade of drone DEM with five inferred fan generations overlain, T1 – T5 (youngest to oldest), as well as the modern drainage surfaces, T0 (different colours indicate different inferred surface ages, darker = older). Thick red dashed line shows edge of inferred stream terrace. (b) Vertical offset measurements plotted by longitude corresponding to Appendix Figure 2.7-31. Dashed lines show estimated locations of transitions between fan generations, labelled above the plot.

2.3.6. Malybay Section (N26 – N33)

To the east of site N25, we reach the low-lying eastern end of the mountain range, which stands less than 1 km above the forelands. Here, the Chilik river emerges from the range front having carved a deep gorge on its descent through the mountains, as well as multiple terraces in the piedmont and foreland sediments (Figure 2.3-33). The village of Malybay (Малыбай) lies within the Chilik river valley. We performed a drone survey in the fields south of Malybay along a small portion of the inferred fault trace between N25 and N26, but found no evidence of scarps. To the east of the Chilik river valley, scarps within the alluvial fans extend for ~6.5 km to the east. These scarps were identified in Grützner et al. (2017b) (site S10 therein) – from a field visit they estimated scarp heights to be between < 1 m to several metres depending on fan age, but did not formally measure the scarps. We comprehensively map and measure scarps along this section using drone and Pléiades data.

At site N26 we collected a drone survey from which we map four generations of fan (T1 to T4, youngest to oldest) and a modern drainage surface (T0; Figure 2.3-34). T1 fans have a very distinctive texture and are mapped with high certainty. We find scarps in T3 and T4 fans truncated by the two youngest fans which are undeformed. The smallest scarp is ~1.3 – 3.6 m within a single T3 fan. Largest scarps are ~14 – 21.1 m within T4 fans (Appendix Figure 2.7-32). To the east of our drone survey at N26, scarps continue for ~5 km and we measure offsets using a Pléiades-derived DEM along this section (site N27; Appendix Figure 2.7-33; Appendix Figure 2.7-34; Appendix Figure 2.7-35). Here we again map at least four generations of fan (T1 to T4, youngest to oldest). We find scarps of ~3.5 – 13.2 m in fans we infer to be second oldest (T3), with the smallest scarp ~3.5 – 4.5 m high (profiles I and J). We make one measurement of 38.2 ± 3.6 m in a small surface which is probably of generation T4, though its relative age is uncertain.

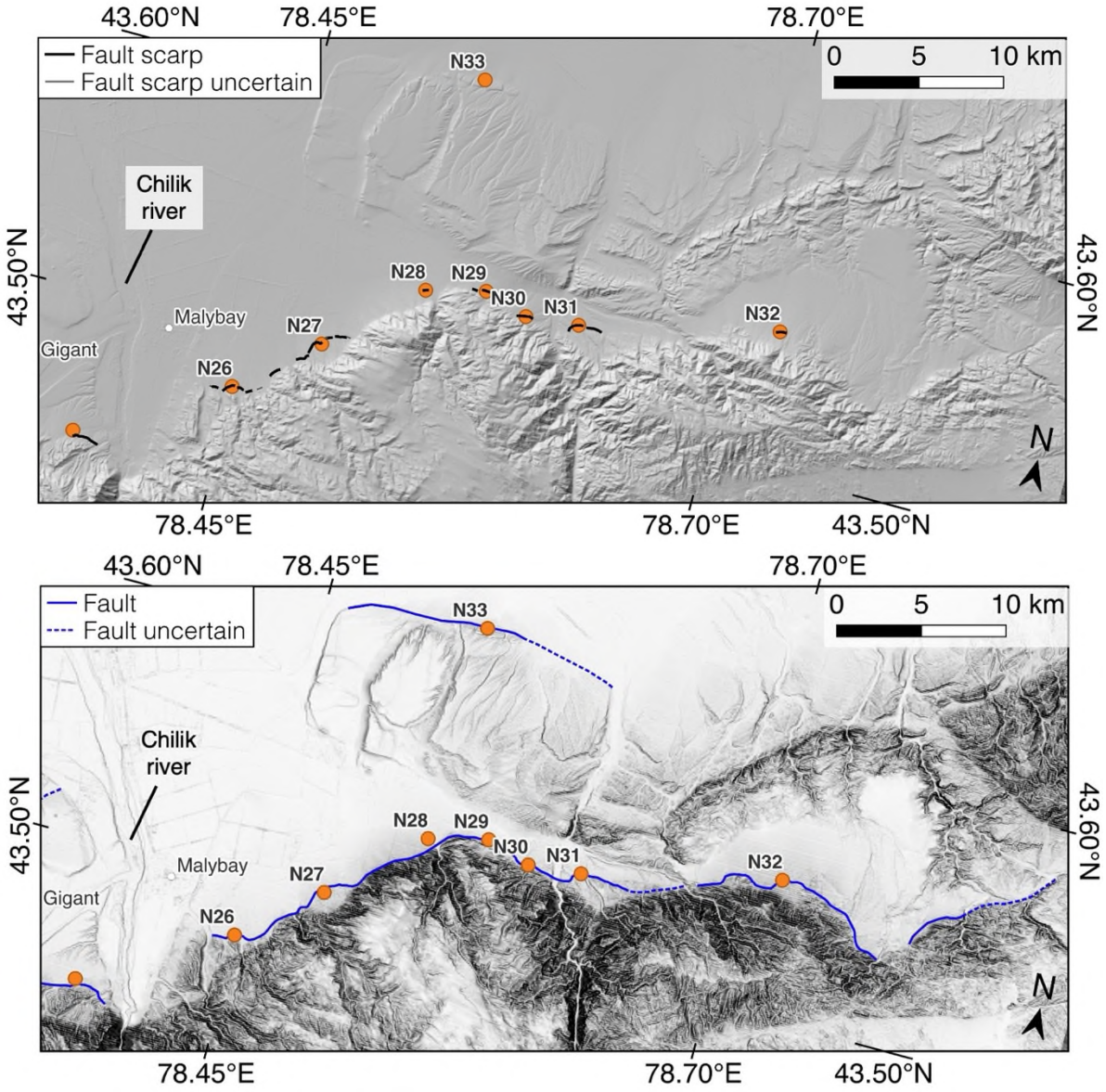

Figure 2.3-33. Overview of Malybay section. Orange data points are sites discussed in the text; white data points are settlements. Top panel: Scarps mapped in this study overlain on the Copernicus GLO-30 DEM hill shade. Lower panel: Fault mapping overlain on slope map derived from Copernicus GLO-30 DEM. Darker colours represent steeper slopes.

At ~78.50°E these scarps terminate (Figure 2.3-33). A sharp change in elevation at the base of the mountains continues for ~ 5 km to the ~northeast, although no scarps are visible in the range front fans until ~78.53°E (site N28) where we measure a ~ 5.3 – 6.4 m offset in one fan surface using a Pléiades DEM (Appendix Figure 2.7-36). At ~78.55°E the fault turns a corner and begins to strike ~E-W along

the south side of a valley. We are uncertain whether the change in elevation on the northern side of this valley was formed by a hydrological process or by activity on another fault. On the south side of the valley, we document several scarps over ~7 km at sites N29 – N31 (Appendix Figure 2.7-37; Appendix Figure 2.7-38; Appendix Figure 2.7-39). Offsets measured from Pléiades data are between 2.5 – 25.5 m, and at all three sites scarps are truncated by at least one generation of younger fan. The smallest scarps measured at sites N29, N30 and N31 are 4.1 ± 0.5 m, ~6.6 – 15.7 m, and ~2.5 – 4.2 m respectively. At site N31, it is not always clear whether breaks in slope are scarps or terrace risers (Appendix Figure 2.7-39). To the east of N31, a sharp step in the topography continues to run along the edge of the low-lying mountains until they die away at ~78.86°E (Figure 2.3-33). We do not have Pléiades or drone data covering this final section of the fault, but we identify a small scarp in Google Earth imagery at site N32 (Figure 2.3-35). Reddish-pink patches along strike of the small scarp are similar in colour to exposures in the mountains and could be basement rocks which have been uplifted and exposed by faulting.

To the north of the valley which hosts sites N28 – N31, the foreland is heavily incised with several terraces running ~N-S (presumably related to the Chilik river) as well as smaller drainage channels cutting into the sediments (Figure 2.3-36). Around site N33 an E-W-striking topographic step forms a northern boundary to these incised sediments, which are uplifted by tens to ~100 m above the sediments to the north. Further to the east the incised sediments continue but the slope break has been flattened by the large alluvial fan which crosses its path (profile C in Figure 2.3-36). We suggest that these sediments have been uplifted by a south-dipping thrust fault.

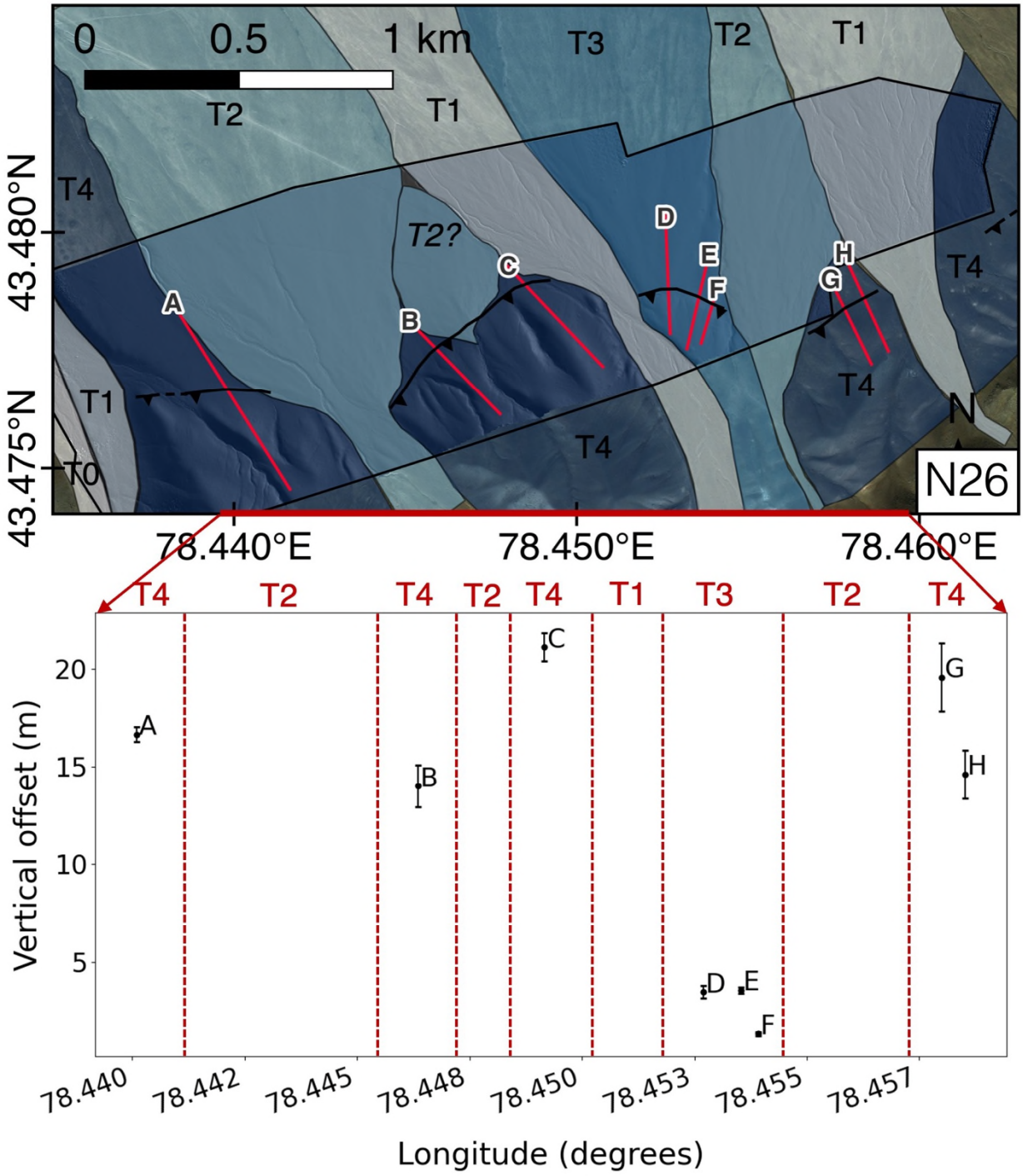

Figure 2.3-34. Site N26. Top: Hillshade of drone DEM with five inferred fan generations overlain, T1 – T4, youngest to oldest as well as the modern drainage surfaces, T0 (different colours indicate different inferred surface ages, darker = older). Thick red dashed line shows edge of inferred stream terrace. (b) Vertical offset measurements plotted by longitude corresponding to Appendix Figure 2.7-32. Dashed lines show estimated locations of transitions between fan generations, labelled above the plot.

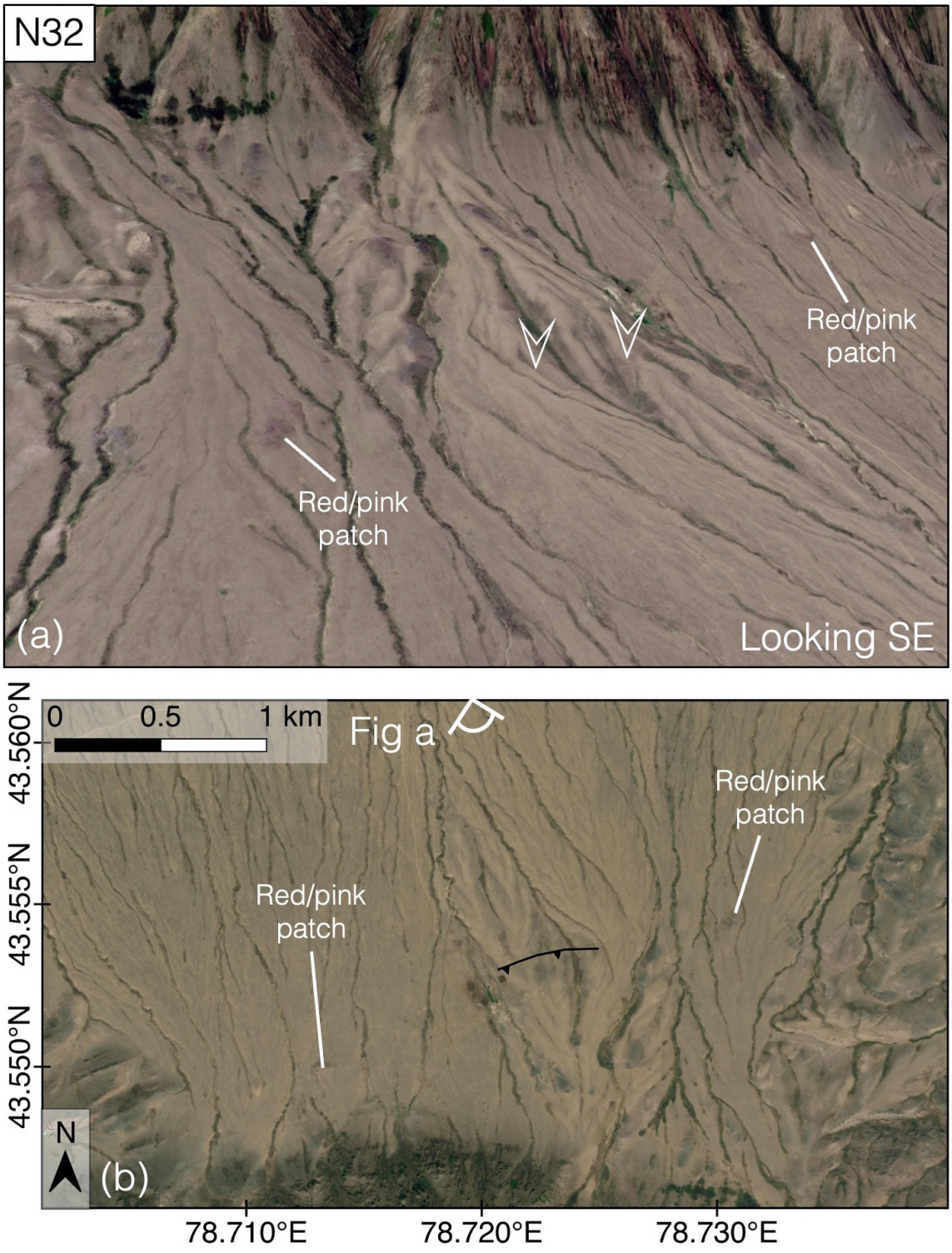

Figure 2.3-35. Site N32. (a) Satellite imagery overlain on 3 x exaggerated topography from Google Earth (2023 Maxar Technologies, Landsat/Copernicus), at 4.29 km eye altitude, and looking southeast. White arrows show location of scarp. (b) Bing Aerial imagery (2024 TomTom, 2024 Maxar). Black line shows location of scarp.

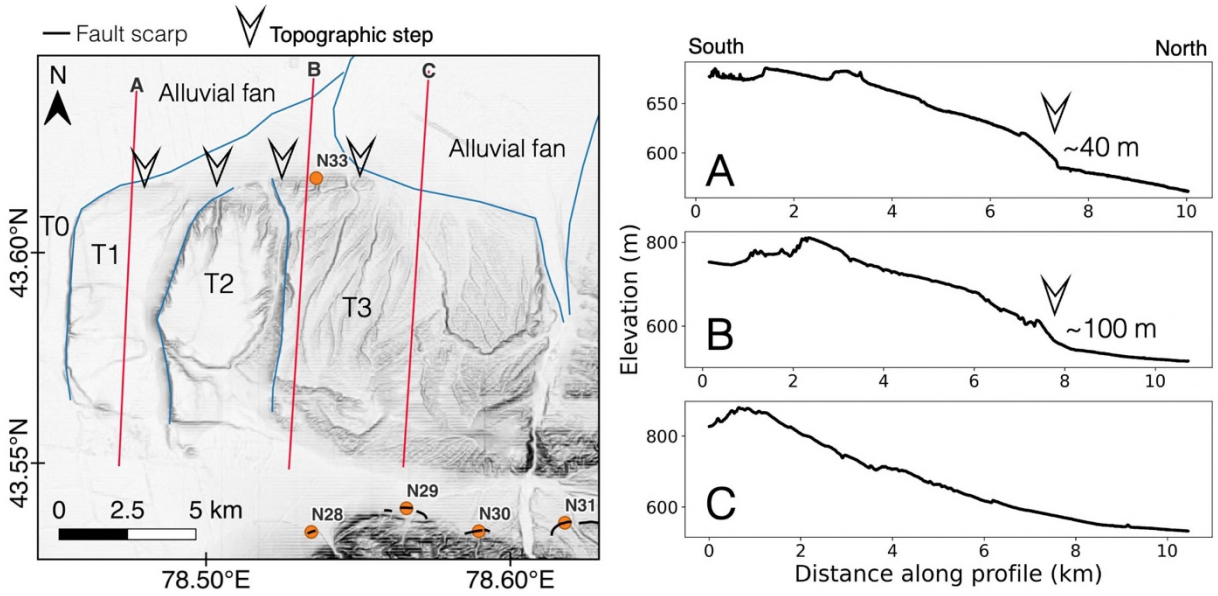

Figure 2.3-36. Elevated and incised sediments around N33. Map shows slope derived from Copernicus GLO-30 DEM. Blue lines mark boundaries of major hydrological features which include three river terraces (T1 – T3) and two large alluvial fans. Study sites marked with orange circles. For site N33, arrows mark a topographic step which we infer to be tectonic. Fault scarps mapped at other sites are marked with black lines. Red lines show locations of profiles A, B and C, which are plotted on the right.

2.4. Paleoseismology of the Zailisky Range Front Fault

We excavated a trench at 43.48867°N 78.15431°E within field site N19, ~100 km ENE of Almaty, ~6 km south of the village of Koram (Корам) and ~100 m south of the Big Almaty Canal (Figure 2.4-1; Figure 2.3-26). We trenched a ~1.3 – 1.6 m high scarp within the loess-blanketed alluvial deposits of the piedmont. We also excavated a pit ~170 m to the southwest of the trench at 43.48764N 78.15273E on the hanging wall of a 4.7 ± 1.1 m high scarp (Figure 2.3-26).

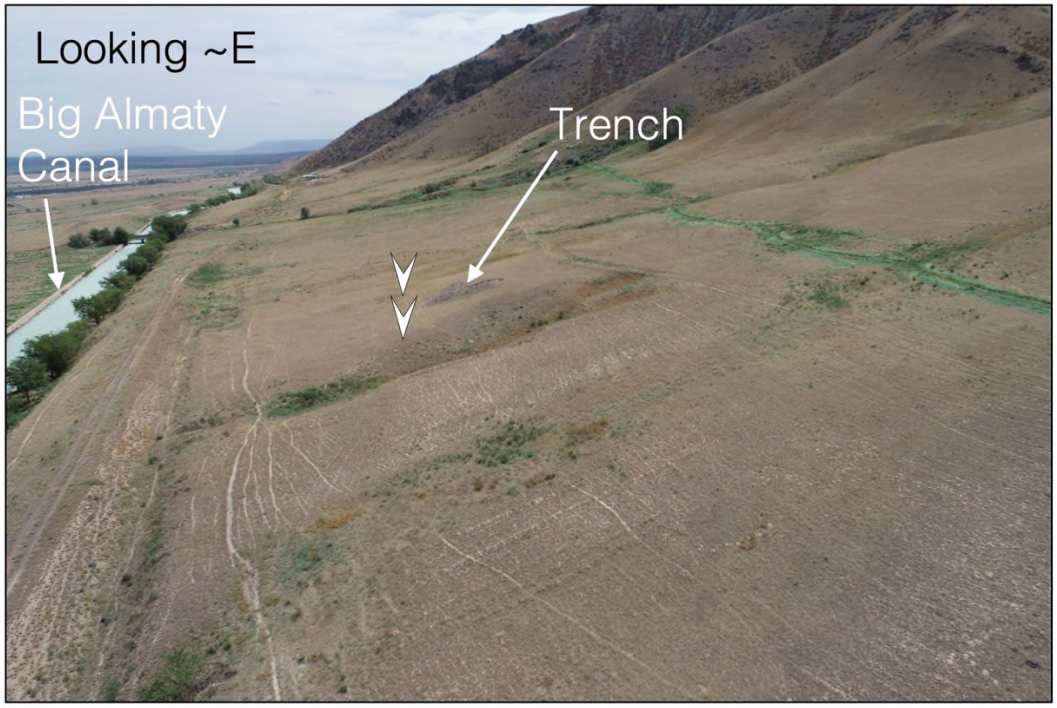

Figure 2.4-1. Oblique aerial photo of trench site (N19). Photo viewpoint marked in Figure 2.3-26b. White arrows show location of scarp.

2.4.1. Trench

2.4.1.1. Stratigraphy and Structure

The trench exposed a sequence of gently northwards-dipping sediments which have been offset vertically by a fault (Figure 2.4-2). Although cementation levels vary, all units are relatively loose,

unconsolidated deposits. All units contain gravels, indicating an alluvial or colluvial origin, though some also contain a high proportion of silt, much of which was probably wind-blown loess (Dave et al., 2023).

Unit 1, the lowest stratigraphic unit, comprises poorly sorted coarse gravels in a silty matrix with occasional lenses of medium gravel and has a curved (concave down) upper boundary. It is overlain by unit 2, well-sorted light-yellow silt with a few sandy lenses and occasional medium to coarse gravel clasts. Unit 1 is present in the footwall below a thin (~ 15 - 40 cm) layer of unit 2, but it is absent in the hanging wall where unit 2 extends up from the base of the trench with a thickness of ~1.4 m. We suggest that unit 1 is a discrete lens or a winding channel deposit with longitudinal variation which appears discontinuous in the 2D section. Within unit 2 in the hanging wall there is also a thin lens of fine gravel approximately parallel to the fault plane, which may be a minor fault strand, although the extent of such a strand cannot be determined due to the homogeneity of the surrounding silt.

The next stratigraphic layer, unit 3, has an undulating, erosive base and is grey in colour. It comprises well-sorted sub-angular to sub-rounded gravels with some lenses of sand. There is an internal stratigraphy of interbedded fine-medium and coarse gravels, with two full cycles visible in the footwall. Unit 3 is thinner in the hanging wall and, while some interbedding is visible, two full cycles are not expressed. We therefore infer that the top of unit 3 was eroded in the hanging wall. While unit 3 is continuous throughout the exposed footwall, in the hanging wall it stops abruptly ~60 cm from the fault. This gap is filled with unit 2, incorporating two irregular clumps of unit 3 which appear to be aligned with the gravel lens in unit 2. This structure may have formed from folding or faulting on the minor fault strand described above.

Unit 4 appears only in the footwall and is wedge-shaped, tapering to a point ~ 5 m away from the fault. It is composed of poorly sorted, angular clasts of all grain sizes up to gravels, with some clasts

seemingly reworked from the underlying units. We interpret this as a colluvial wedge, formed from the collapse and reworking of the overhang produced in a reverse earthquake.

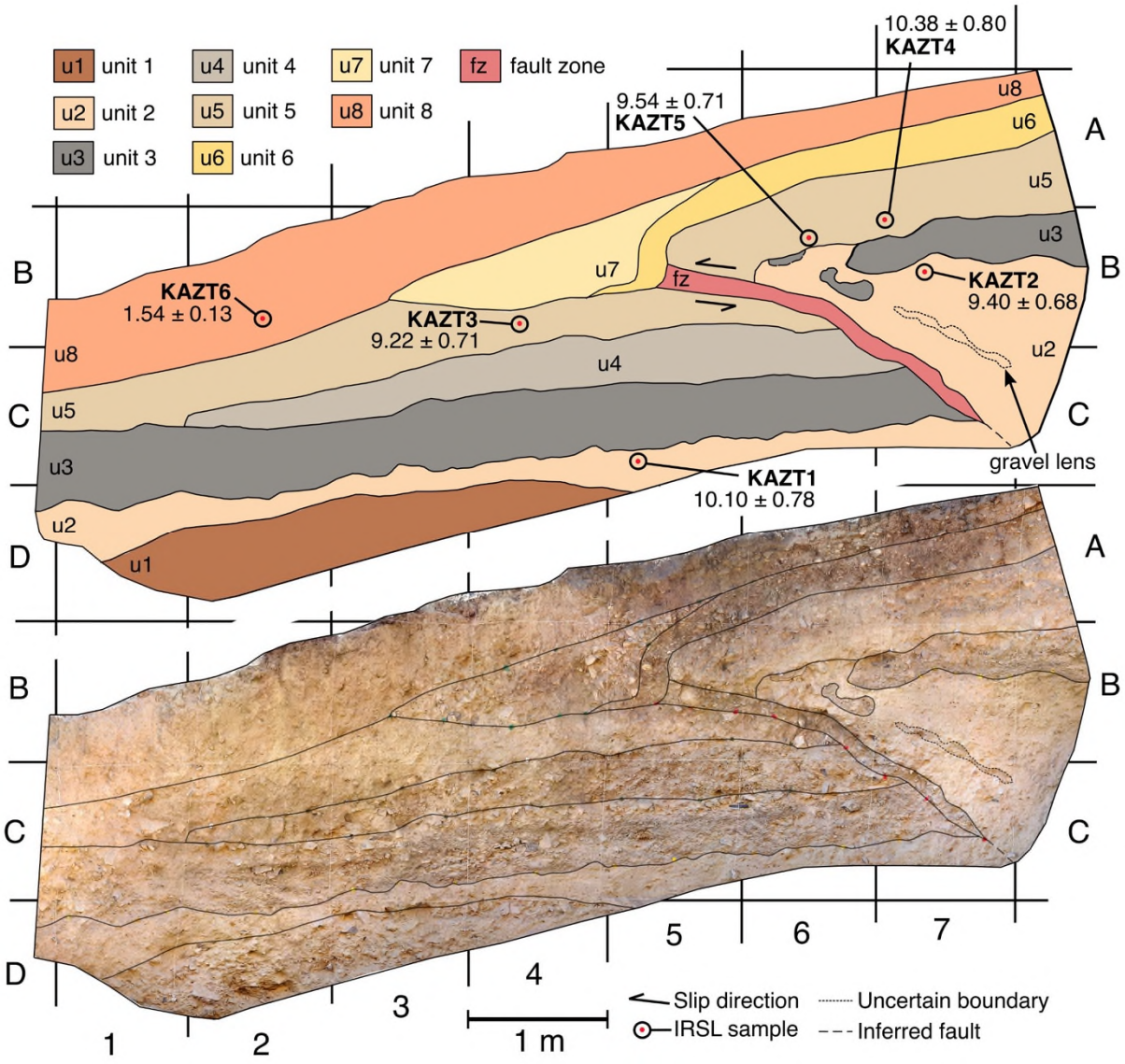

Figure 2.4-2. Paleoseismic trench at site N19. IRSL sample ages are given in kyrs. An unannotated orthophoto is provided in Appendix Figure 2.7-40.

Unit 5 is a well-cemented, cream-coloured silt with fine-medium gravels and occasional larger clasts of coarse gravel and angular cobbles. In the hanging wall, unit 5 is capped by unit 6, a darker gravelly layer, which we interpret as a paleosol. Unit 6 curves into the fault and covers the fault tip. Any discontinuous offset in unit 6 has been masked by the collapse or reworking of the layer. Unit 6 is

absent from most of the footwall. In the hanging wall, units 5 and 6 have been deformed and dragged downwards close to the fault.

Unit 7 is a clast-supported wedge-shaped unit composed of poorly sorted angular gravels of all sizes in an uncemented silty matrix. Some clasts appear to be reworked from unit 6. The wedge is thickest above the fault tip and tapers to a point in the footwall, forming an erosive contact with unit 5 below. We interpret unit 7 as a second colluvial wedge. Unit 8 is the modern soil – an uncemented, light-brown, silty unit with poorly sorted medium to coarse sub-angular gravels and roots. The layer thickens and becomes less gravelly from the hanging wall into the footwall and is undeformed across the fault.

The offset layers lie on either side of a thin fault zone of poorly sorted clasts from adjacent units, except at the base of the trench where the fault is not visible within the homogeneous silt of unit 2. In the lower half of the trench, the fault dips ~ 35° to the south. It remains at this angle moving up through the stratigraphy until it reaches unit 5 in the hanging wall where it shallows abruptly to ~ 8°. To obtain the displacement of units across the fault, we approximate hanging wall boundaries as linear horizons (excluding the folded sections close to the fault), project these onto the ~ 35° fault plane, and then measure the vertical and along-fault distance to where the footwall boundaries intersect the fault (Appendix Figure 2.7-41). The base of unit 3 is vertically offset by ~ 1.2 m and has an along-fault slip of ~ 2 m, while the base of unit 5 is offset by ~ 0.8 m with a slip of 1.3 m. Due to the irregularity of the horizons (particularly unit 3) and the folding close to the fault, uncertainties for these measurements are likely on the order of 10s of centimetres.

2.4.1.2. Inferred Stratigraphic and Earthquake Chronology

We find strong evidence for two earthquakes in the trench and suggest the following chronological interpretation (Figure 2.4-3): The first earthquake, E1, occurred after the deposition of unit 3, offsetting units 2 and 3 across the fault. Movement on a minor fault strand in the hanging wall may have dragged down a clump of unit 3 close to the fault. The subsequent hanging wall collapse, erosion and re-deposition of material from the top of unit 3 formed the first colluvial wedge (unit 4). Next, units 5 and 6 were deposited, then a second earthquake (E2) ruptured the fault, offsetting units 2 to 5 and deforming unit 6. A second colluvial wedge (unit 7) formed, and unit 6 (and probably also the top of unit 5) was eroded from the footwall. Finally, the modern soil, unit 8, was deposited. By differencing the along-fault offsets of the bases of unit 3 and unit 5, we estimate a fault slip of ~ 0.7 m for E1 and ~ 1.3 m for E2, with uncertainties on the order of 10s of centimetres.

We sampled silt-bearing units 2, 5 and 8 to constrain the timing of the earthquakes – all other units were too coarse to be sampled for luminescence dating. Our luminescence dating results (Table 2.4-1) suggest that units 2 and 5, which bracket E1, both formed around 10 ka. Unit 8 post-dates both earthquakes and formed around 1.5 ka. To better constrain the timings of the earthquakes we model the trench chronology with OxCal.

Table 2.4-1. IRSL dating results for samples collected from site N19 and processed at the University of Sheffield, UK. HW = hanging wall. FW = footwall. ka = kyrs before AD 2023.

Sample type	**Sample name**	**Layer sampled**	**Lat (°)**	**Lon (°)**	**Equivalent dose, D_E (Gy)**	**Dose rate (Gy/kyr)**	**Age (ka)**
Trench	KAZT6	Unit 8	43.48867	78.15431	6.59 ± 0.31	4.28 ± 0.28	1.54 ± 0.13
	KAZT1	Unit 2 (FW)			39.70 ± 1.63	3.93 ± 0.30	10.10 ± 0.78
	KAZT2	Unit 2 (HW)			37.83 ± 1.41	4.03 ± 0.25	9.40 ± 0.68
	KAZT3	Unit 5 (FW)			37.49 ± 1.53	4.07 ± 0.26	9.22 ± 0.71
	KAZT4	Unit 5 (HW)			40.67 ± 1.71	3.92 ± 0.24	10.38 ± 0.80
	KAZT5	Unit 5 (HW)			37.08 ± 1.36	3.89 ± 0.24	9.54 ± 0.71
Pit	KAZ19PIT1	Layer 1	43.48764	78.15273	136.14 ± 6.42	4.72 ± 0.28	28.85 ± 2.24
	KAZ19PIT2	Layer 4			101.50 ± 8.01	5.20 ± 0.32	19.54 ± 2.00

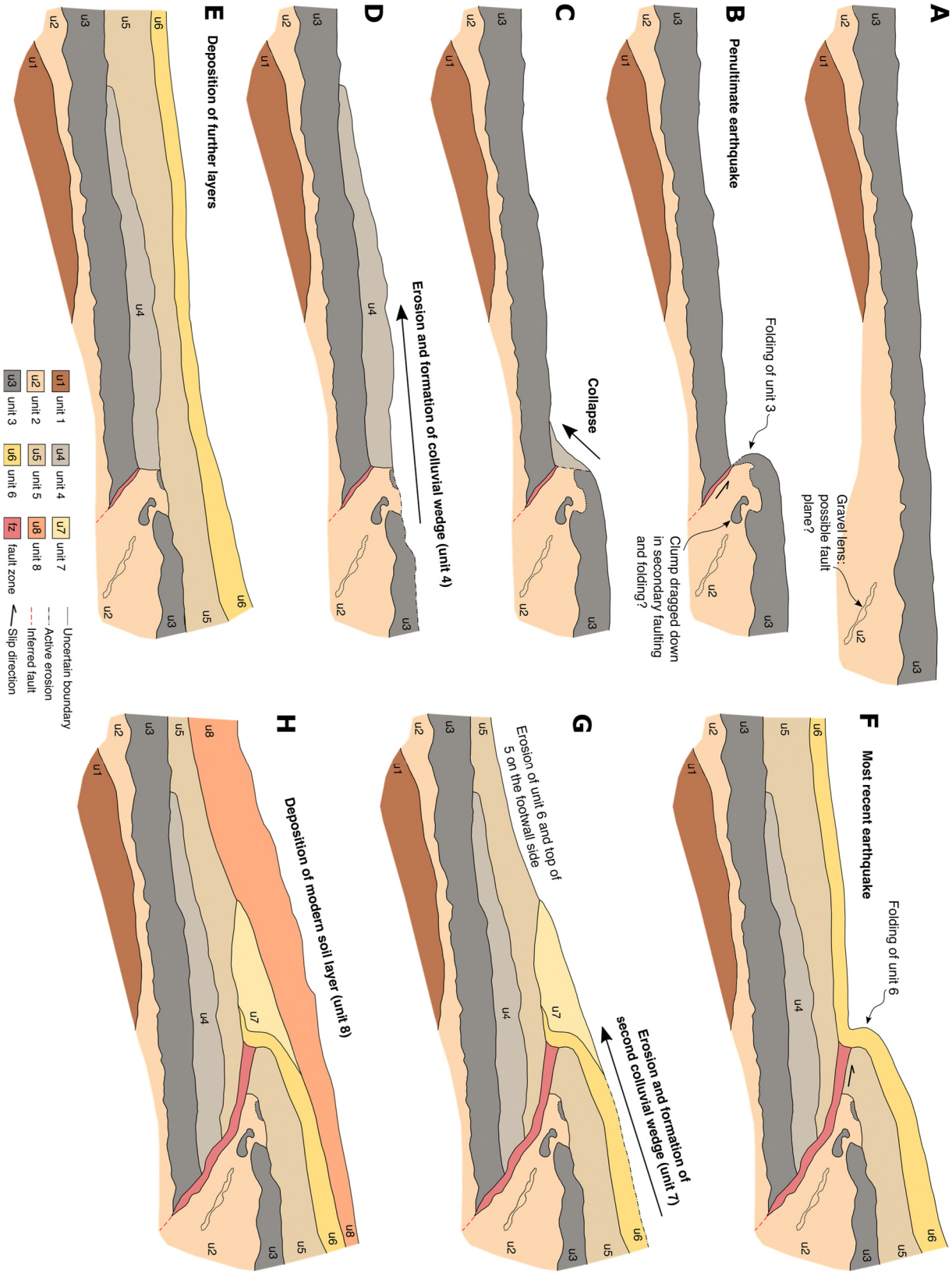

Figure 2.4-3. Chronological interpretation of stratigraphy and structures in the trench at N19.

2.4.1.2.1. OxCal Modelling

We tested several prior models to represent the trench stratigraphy in OxCal. In our preferred prior model (model A; Appendix Table 2.7-9; Appendix Figure 2.7-7; Appendix Table 2.7-4), we assume all units have contiguous transitions, apart from the unit 2/3 and unit 7/8 transitions which we model as sequential boundaries because there is clear evidence of erosion. We assume the colluvial wedges (unit 4 and unit 7) began to form immediately after the earthquakes and therefore model the earthquakes as the starting boundaries of the colluvial phases. The modelled age of earthquake E1 is tightly constrained to 9.5 ± 0.8 ka (2σ) by the age measurements (Table 2.4-2). The modelled age of E2 is between 8.4 – 2.6 ka (95.4% probability range) – we report a range rather than a mean because the event is poorly constrained by the measurements and there is no evidence to favour a central value.

To investigate the sensitivity of these ages to the choice of prior, we test four other models with slightly different assumptions (detailed in Appendix Section 2.7.3.1. ; results summarised in Figure 2.4-4). For example, in model C we assume there is a hiatus after every unit, modelling all boundaries as sequential (Appendix Table 2.7-6; Appendix Figure 2.7-9). Earthquake E1 is almost insensitive to the prior because it is so well constrained by the measurements – all the models we considered are consistent within 1σ error for E1 and mean ages vary between ~9.7 – 9.5 ka (Figure 2.4-4; Appendix Table 2.7-2). As earthquake E2 is less well constrained by the measurements, its modelled age is more sensitive to the prior: upper bound age estimates vary between ~8.0 – 9.3 ka and lower bound ages between ~2.4 – 3.5 ka across the different models. As part of OxCal's uninformative prior, without any other constraints, groupings are assumed to be uniformly distributed through time, so changing the number of boundaries in the model impacts the age of E2 (Christopher Bronk Ramsey, personal communication).

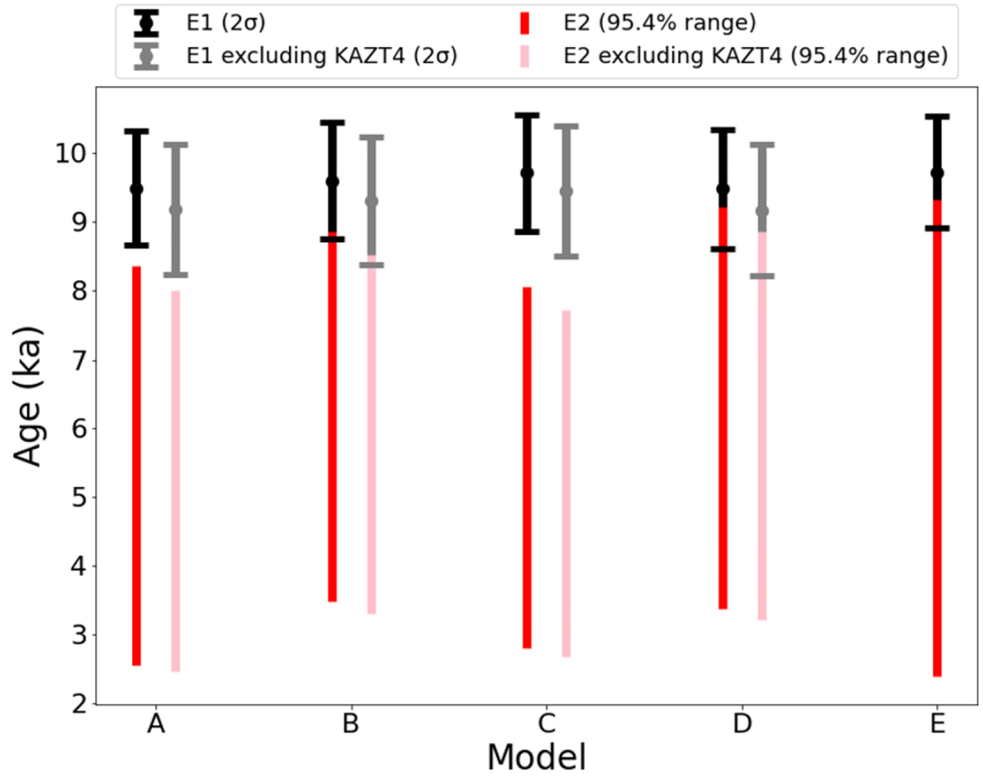

Figure 2.4-4. Age estimates from all OxCal models. Black and grey bars show 2σ error for earthquake E1 ages. Red and light red bars show 95.4% probability ranges for earthquake E2 ages. Black and red bars show model runs including KAZT4. Grey and pink bars show model runs excluding KAZT4.

In four of the models we tested, sample KAZT4 has A_i < 44%, which is below the recommended acceptable threshold of 60% for inclusion (Bronk Ramsey, 2009). Removing this sample age from the models produces earthquake ages which are a few hundred years younger (Figure 2.4-4). However, the KAZT4 luminescence age is consistent with the other two samples from unit 5 within 1σ error and the dose rates from 62% of its measurable grains are in agreement with each other indicating the sample is well-bleached (Appendix Figure 2.7-5). Additionally, the overall agreement indices ($A_{overall}$) for all models are > 60% indicating internal consistency in the model as a whole. Therefore, we conclude that there is insufficient evidence to justify the exclusion of this sample from the model.

Table 2.4-2. Trench measurements and earthquake ages from OxCal (model A). ka = kyrs before AD 2023. Full model results can be found in Appendix Table 2.7-4 and Appendix Figure 2.7-7.

Earthquake	Trench measurements		OxCal model ages						
	Uplift (m)	Slip (m)	Mean (ka)	Median (ka)	1σ (yrs)	2σ (yrs)	95.4% probability range (ka)		Age reported in text (ka)
							From	To	
E2	~0.8	~1.3	5.5	5.6	1.6	3.1	8.4	2.6	8.4 – 2.6
E1	~0.4	~0.7	9.5	9.5	0.4	0.8	10.3	8.7	9.5 ± 0.8

2.4.2. Pit

We also excavated a pit in the hanging wall of the larger scarp (4.7 ± 1.1 m vertical offset) to the southwest of the trench (Figure 2.4-5). In the 2.4 m section we uncovered 11 sedimentary layers, all of which were dominated by loess with only some coarse gravels in a few of the layers (Appendix Table 2.7-11). None of the layers appeared to be alluvial fan sediments and all were probably predominantly wind-deposited, so could have been draped over an existing scarp and might not pre-date the earthquakes which formed it. We dated luminescence samples from 1.70 m and 2.30 m depth to be from ~19.5 ka and ~29 ka respectively (Table 2.4-1). Whilst these dates cannot provide meaningful information regarding the age of the offset, they do confirm that this surface is significantly older than the surface we excavated at the trench. The difference in offset magnitude between the trench scarp (~1.3 – 1.6 m) and the pit scarp (~4.7 m) can therefore be accounted for by their different ages, supporting our inferred fan chronology at site N19 (Figure 2.3-26).

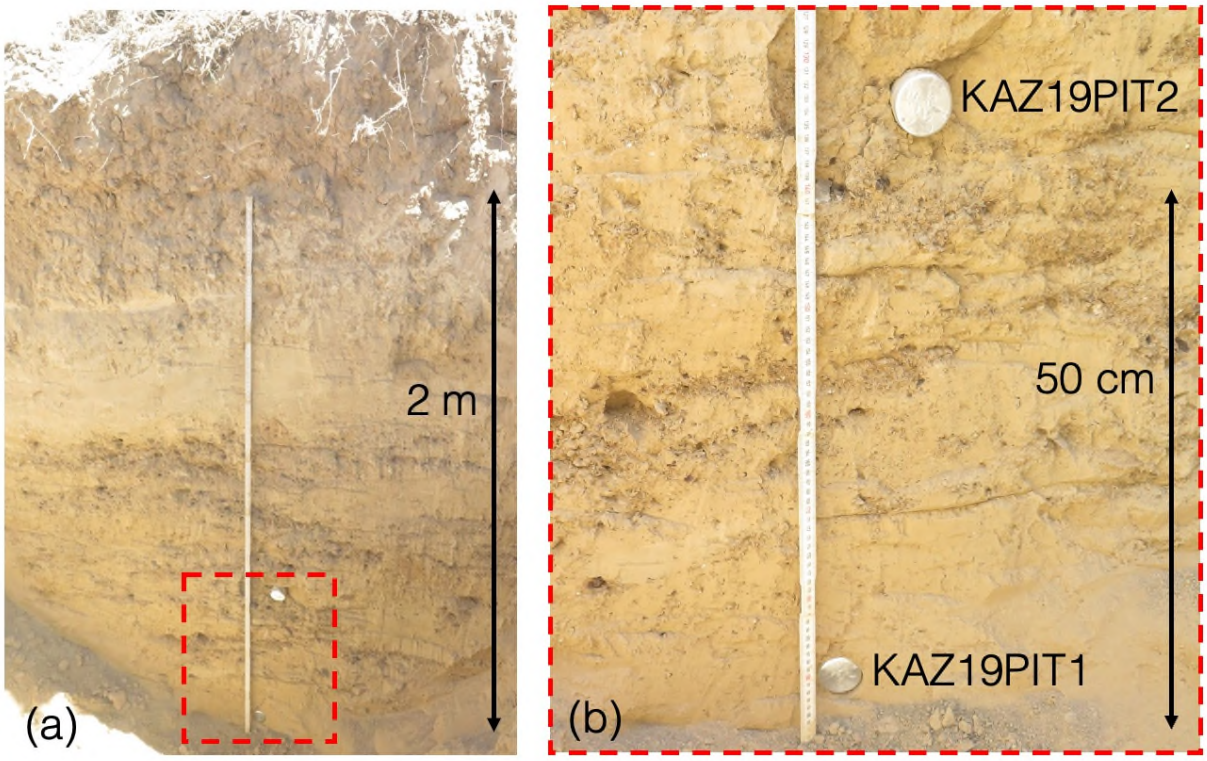

Figure 2.4-5. Photographs of pit excavation at site N19 near Koram. Red dashed box in (a) marks the extent of (b). The two metal luminescence sampling tube caps correspond to samples KAZ19PIT1 and KAZ19PIT2.

2.5. Discussion

2.5.1. Earthquake Chronology

All scarps we map along the ZRF are rather degraded (e.g. Figure 2.4-1; Figure 2.3-6). Like Grützner et al. (2017b), we found no evidence of sharp offsets, fresh scarps or fissuring which would be indicative of a surface rupture within the past few hundred years, such as from the 1887 Verny earthquake. We opened the first paleoseismic trench on the ZRF, revealing two earthquakes which ruptured the east section of the fault at 9.5 ± 0.8 ka (2σ) and again between 8.4 – 2.6 ka (95.4% probability range). The latter estimate is poorly constrained because the ages of the alluvial fan sediments at the trench site are all ~9 – 11 ka. The timing of the MRE could be better constrained by trenching a younger surface.

Our results suggest that, at least at the eastern end of the fault, more than 2 kyrs have passed since the last earthquake. This is qualitatively consistent with geomorphic observations along the ZRF: at many of our study sites one or more generations of undeformed alluvial fans truncate fault scarps, requiring enough time to have elapsed since the MRE for these fans to have formed (probably on the order of hundreds to thousands of years). Furthermore, as highlighted by Grützner et al. (2017b), scarps have a degraded morphology compared to examples of more recent ruptures in the near vicinity such as the 1911 Chon Kemin earthquake scarps mapped by Arrowsmith et al. (2017). The range front scarps have a more similar morphology to the nearby Toraigyr fault, which last ruptured around 3.15 – 3.6 ka BP (Grützner et al., 2017a). With thousands of years since the last earthquake, much of the evidence of faulting along the range front has probably been destroyed or obscured by erosion, burial (e.g. by loess) or anthropogenic activity.

Assuming some regularity to the timing of earthquakes on the ZRF, our results suggest a recurrence interval between ~7 – 5 kyrs, but we cannot rule out a clustering of earthquakes in time (Liu and Stein, 2016). There also may be a higher frequency of earthquakes along the range front as a whole if discrete segments of the fault rupture separately and at different times. Further paleoseismic studies are needed to determine the regularity of the recurrence interval and build a robust chronology for the entire fault. Our results add to a growing body of evidence which suggests major faults in the northern Tian Shan rupture in large but rare earthquakes with thousands of years between events (Deng et al., 1996; Campbell et al., 2015; Abdrakhmatov et al., 2016; Landgraf et al., 2016; Grützner et al., 2017a; Ainscoe et al., 2019; Hu et al., 2021; Tsai et al., 2022).

2.5.2. Past and Future Earthquake Scenarios

2.5.2.1. Slip Magnitudes

In the trench at site N19 we measure uplift of ~0.8 m and slip of ~1.3 m in the MRE, and uplift of ~0.4 m and slip of ~0.7 m in the penultimate earthquake. The slip is nearly twice as big in the MRE than in the penultimate event, demonstrating that there can be significant variation in slip between events in the exact same location. This could correspond to a difference in the event magnitude or might be a result of variations in the slip distribution between two events of a similar magnitude. A few hundred metres to the east of the trench, we measure a scarp of height ~0.3 – 0.6 m (profiles K to N in Figure 2.3-26). From a comparison with the trench measurements, we suggest this is a single event scarp which probably also formed in the MRE. Assuming the slip in the trench represents the average slip on the fault, our measurements corresponds to a rupture length of between 13 – 130 km for the MRE and 8 – 80 km for the penultimate event, applying standard fault slip-to-length ratios from empirical studies which are in the range 10^{-5} – 10^{-4} (Scholz, 1982; Scholz, Aviles and Wesnousky, 1986; Wesnousky, 2008; Tsai et al., 2022).

To determine whether our uplift measurements from the trench are consistent with the rest of the fault, we examine scarp heights from 30 sites along the range front. At most of these sites we measure a range of different vertical offsets, many of which appear to correspond to fans or terraces of different generations and presumably represent different numbers of earthquakes. It is clear that we cannot distinguish between single and multiple event scarps based on morphology alone at a given site – the trench scarp shows a single, smooth break in slope, with no indication that it was produced in two earthquakes rather than one (profiles F and G in Appendix Figure 2.7-26). Instead, we examine the range of smallest scarp heights along the range front and assume that at least some of these must be single event offsets.

Whilst Grützner et al. (2017b) concluded single event scarps were on the order of ~2 – 4 m, our re-analysis of the range front with more sites and higher resolution data shows that smaller offsets are more pervasive. In Figure 2.5-1, we plot the smallest scarp heights along the range front, omitting sites for which we only have 30 m elevation data based on the assumption that single event scarps would not be discernible at this resolution. We include measurements from Pléiades DEMs, but we note that the smallest scarps (less than ~1.5 – 2.5 m) are not identifiable in this dataset. At 8 of the 18 sites with the highest resolution data (drone DEMs or dGPS), we document smallest scarp offsets in the range ~0.2 – 1 m (blue strip in Figure 2.5-1). These sites are distributed throughout much of the fault, in the Akterek section, the central section, the east section and on the parallel strands. In the Malybay section the measured offsets are larger, but most measurements are from Pléiades DEMs so smaller scarps may have been missed. In the west section up on the plateau only 30 m data is available.

We suggest that the ~0.2 – 1 m offsets were produced in the most recent events to rupture the range front, consistent with the ~0.8 m offset documented in the trench. Based on the relatively small size of the scarps, they probably formed in several different ruptures of shorter segments of the fault rather than simultaneously in one rupture of the entire range front (Wells and Coppersmith, 1994). It is

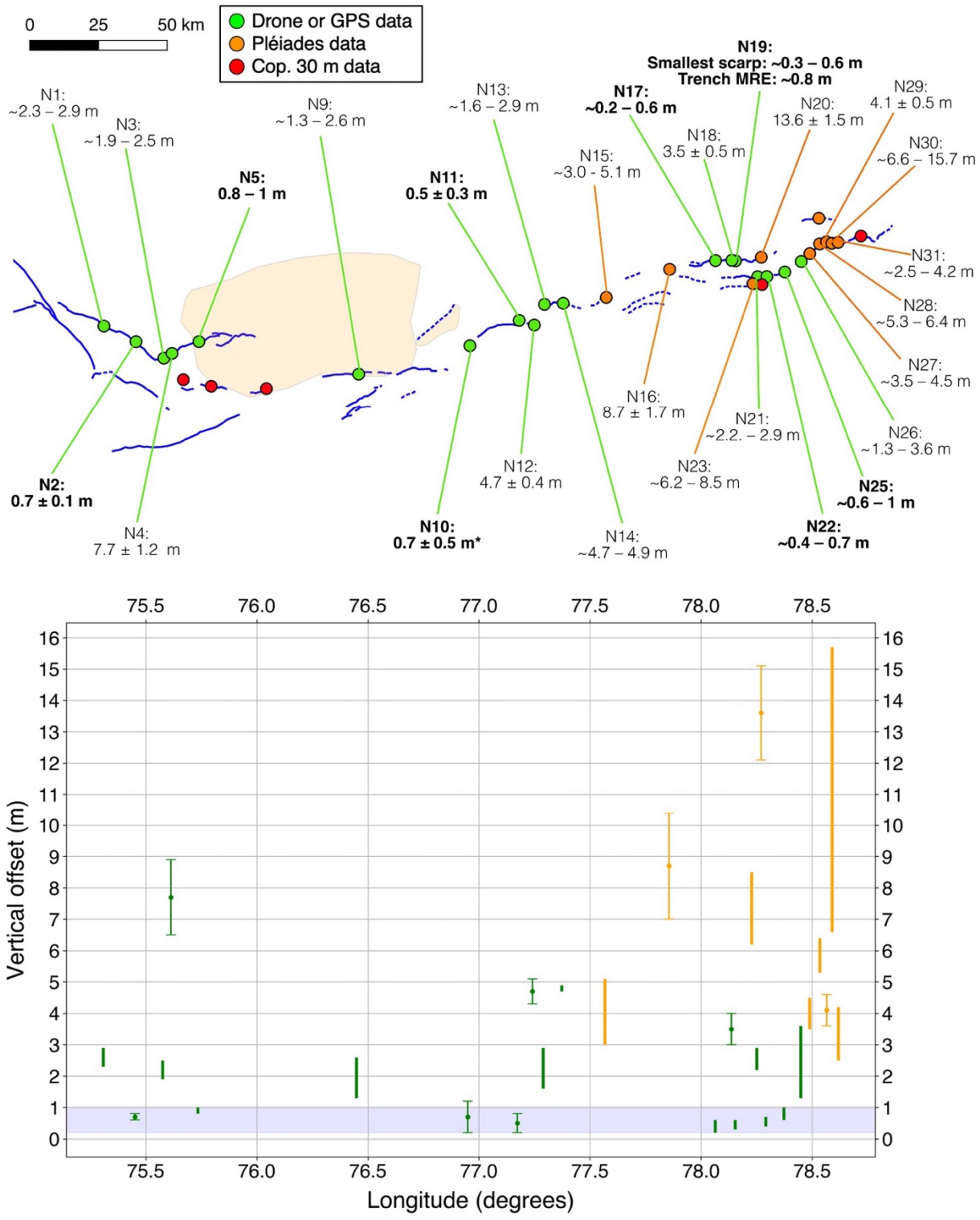

Figure 2.5-1. Summary of smallest scarp offsets measured at study sites. Upper panel: Fault is shown in blue, with uncertain strands shown by dashed lines. Shaded patches show regions of uplift and incision. Circular symbols show study sites colour coded by data type used to measure scarp offsets: green = drone DEM or field GPS survey, orange = Pléiades DEM, red = Copernicus GLO-30 DEM. Sites with drone or GPS data (green) or Pléiades data (orange) are labelled with the vertical offset

measurement from the smallest scarp at the site. Measurements we infer to be of the MRE are labelled in bold. *Data from Amey et al. (2021). Lower panel: Vertical offsets from smallest scarps measured in Pléiades DEMs (orange) and drone DEMs or GPS (green). Thicker lines show data ranges, points with error bars show single offset measurements. Shaded blue region is the ~0.2 – 1 m scarp height range which we interpret to have formed in the most recent event(s).

possible that different sections of the ZRF ruptured with different magnitudes of slip, but the distribution of scarp sites with ≤ 1 m offsets along most of the fault suggests some uniformity. Assuming a fault dip of 30° – 60°, this range of offsets corresponds to a slip of ~0.2 – 2 m. Applying a slip-to-length ratio of 10^{-5} – 10^{-4}, this corresponds to a surface rupture length in the range 2 – 200 km (Scholz, 1982; Scholz, Aviles and Wesnousky, 1986; Wesnousky, 2008; Tsai et al., 2022).

With loess blanketing scarps and large parts of the range front covered by cities and towns, geomorphic studies are inherently biased towards finding larger scarps along the ZRF. For example, it is very unlikely that we would have found the subtle ~0.8 – 1 m scarp at site N5 if it were not located close to larger offsets. We were also fortunate to identify N17 as a potential drone survey target from a slight discolouration in Google Earth images of the fields, as the ≤ 1.2 m offsets could not be measured remotely. It is very unlikely we would have found this site if it were located within one of the urbanised fans. We suggest that there may be many more ≤ 1 m scarps along the range front which we have been unable to identify.

However, slip in surface rupturing earthquakes can be highly variable along strike, as demonstrated by slip distributions in many modern earthquakes – examples can be found in Wesnousky et al. (2008), Arrowsmith et al. (2017), and in Figure 2.5-2, which is after Manighetti et al. (2005) . Therefore, whilst the ~0.2 – 1 m scarps (~0.2 – 2 m slip) appear to form a distinct group of offsets, we cannot rule out the possibility that they represent minimum values in a variable slip distribution rather than the average slip. If this is the case, slip may be better represented by including the ~1 – 5 m scarps that we identify as the smallest offsets at many other sites. Further trenches along the length of the range front

are needed to confirm whether these > 1 m scarps formed in multiple earthquakes or in a single event, to conclusively determine whether the ~0.2 – 1 m scarps best represent the MREs. We therefore suggest that our estimates of characteristic surface slip should be treated as minima until further evidence from trenching is obtained.

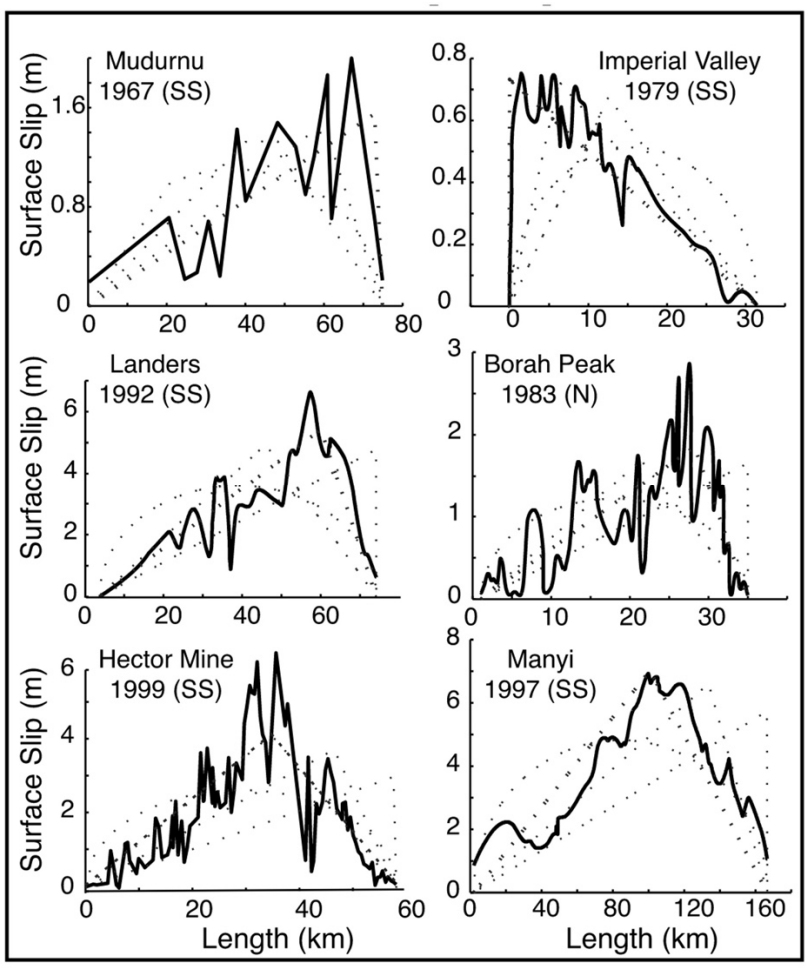

Figure 2.5-2. After Manighetti et al. (2005). Slip distributions in six modern earthquakes. Dotted lines show attempts to model the shape of the distribution.

2.5.2.2. Segmentation of the ZRF

We map scarps for over ~ 300 km along the Zailisky Range Front. The total length of mapped faults is more than 400 km, including overlapping strands. Scarps are separated by gaps or steps ranging

between a few metres to ~40 km in length, but the fault trace inferred from larger topographic features is more continuous. In this section, we use our scarp and geomorphic mapping to assess the possible segmentation of the ZRF and discuss plausible rupture scenarios.

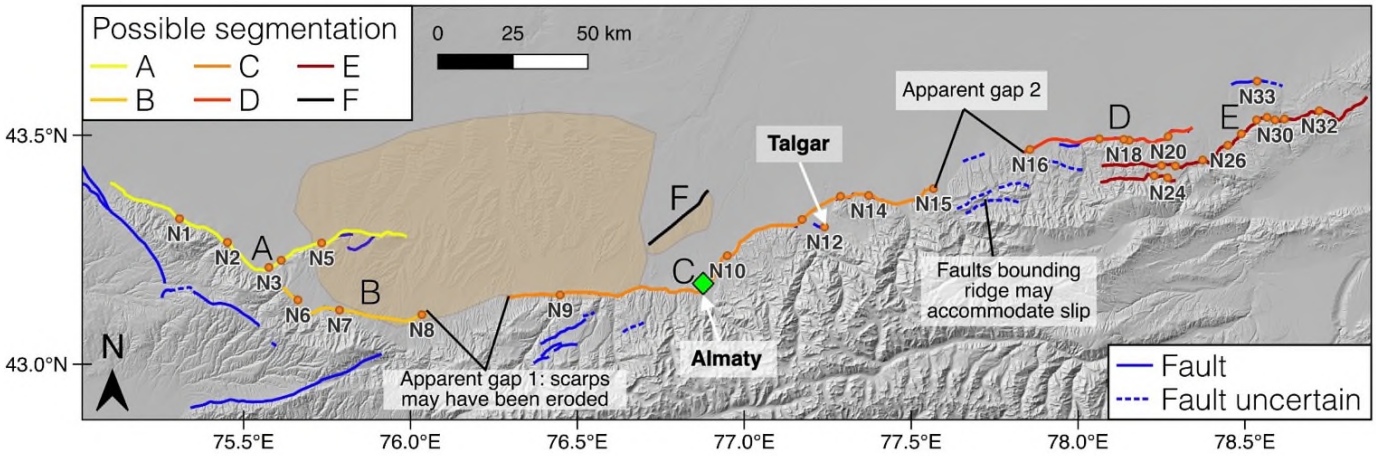

Figure 2.5-3. Possible segmentation and apparent gaps along the ZRF. Orange patches show regions of high incision and inferred uplift. Background map is hill-shaded Copernicus GLO-30 DEM.

At the western end of the fault in the Akterek section, scarps are well preserved in the dry and sparsely populated alluvial fans in front of a relatively low-lying section of the mountains. There are abundant scarps along most of this ~ 80 km section, including where the fault changes strike near Arkhaly (A in Figure 2.5-3). Therefore, we suggest that the fault is continuous and connected in this section and could rupture in a single earthquake. In our analysis of the geomorphology, we discussed the possibility that the fault bounding the plateau could be connected to a buried fault at depth which is causing the uplift and incision of foreland sediments. If there is indeed a buried structure here, a rupture of segment A could be much larger than what can be inferred from surface observations.

In the west section of the fault at the southern edge of the plateau, we document scarps or a sharp slope break along ~ 40 km of the mountain front, which might rupture together as one coherent fault segment (B in Figure 2.5-3). To the east of site N8, we find no evidence of scarps for ~30 km along the range front, and the transition between the mountains and the forelands is relatively gradual (no sharp

slope break) for most of this distance. This might indicate that there is a ~20 – 30 km gap in the fault here (apparent gap 1 in Figure 2.5-3). However, our analysis shows that much of this section is occupied by relatively young fan surfaces and is heavily incised, so scarps may have been eroded (Figure 2.3-12). Furthermore, we do not have high-resolution data for this section to allow the identification of smaller offsets. Therefore, we cannot be certain that this apparent gap reflects a lack of past surface rupture, nor can we rule out activity on a buried fault.

The geomorphology of the central section of the range front is characterised by a series of large alluvial fans, as well as rivers and streams fed by glacial and snow melts from the highest peaks of the Zailisky Alatau. Much of the range front has been extensively modified by towns, villages and agriculture, especially on the slopes of the alluvial fans. There is a prominent and sharp change in elevation for most of the central section of the range front, but only occasional scarps are apparent. We suggest that further scarps in this section have been obscured or destroyed by anthropogenic activity, and that an increased hydrological input from the high mountains compared to the fault's ends may also have led to faster erosion. As such, the difference in scarp abundance between the centre and edges of the fault probably does not reflect a difference in tectonic activity between different segments, rather a difference in preservation. In this central section, we map a ~120 km long inferred fault trace following the sharp slope break at the range front and the occasional scarps which run along it (C in Figure 2.5-3). Any further segmentation is unknown due to the scarcity of scarps and the large fans which have eroded much of the range front topography. Following the mountain front from west to east across the Talgar fan via the scarps in Talgar town at N12, there is an apparent northwards step of ~6 km which could mark a fault segment boundary. However, we find scarps in the northern part of the Talgar fan at N11 which could link the mountain fronts either side of the fan without a significant stepover.

In the eastern section of the ZRF, we find no clear evidence of faulting for ~25 km along the mountain front between N15 and N16, despite minimal anthropogenic modification (apparent gap 2 in Figure 2.5-3). This apparent gap could represent a structural boundary. However, ~10 km to the south of the range front, a ridge within the mountains spans the length of this gap, presumably bounded by fault strands. This structure could be accommodating slip in this portion of the fault zone instead of the range front, potentially allowing ruptures to transfer between the fault segments either side, and accounting for the lack of scarps within the piedmont.

To the east of this apparent gap, we map ~45 km of faulting along the range front (D in Figure 2.5-3). Here, the Zailisky Alatau has a lower elevation, the alluvial fans are small and there is much less modification of surfaces by large settlements. However, the Big Almaty Canal has been built along the range front and has probably obscured some scarps.

We map abundant scarps along the parallel strands and the Malybay section, with individual scarp sites never more than ~9 km apart. Much like the Akterek section, here the range front is rather dry and scarps are not disturbed by anthropogenic modification nor large alluvial fans, except for where the Chilik river exits the mountains. We map a ~75 km fault segment including the Malybay section and the central strand of the three parallel strands (E in Figure 2.5-3). The length of this segment increases to ~90 km if the southern strand of the three parallel strands is also included.

Finally, we map the ~20 km fault splay which lies ~10 – 15 km north of the range front under the northern part of Almaty as segment F ("Northern Splay" in Amey et al. (2021)).

In summary, based on our analysis, we tentatively map a set of possible structural fault segments ranging between ~ 40 – 120 km in length in addition to a ~20 km splay, although further segmentation could be obscured by urbanisation or erosion of the landscape (Figure 2.5-3). Whilst gaps or steps in

faults can halt the propagation of an earthquake, ruptures can also jump across them (Biasi and Wesnousky, 2016). Biasi and Wesnousky (2016) reviewed surface rupture mapping of 14 dip-slip earthquakes and found steps of up to ~12 km, Hamling et al. (2017) report that the 2016 Kaikōura earthquake jumped between faults ~15 km apart, and a 25 km gap in surface ruptures from the 1992 Suusamyr earthquake was mapped by Ghose (1997) and later by Ainscoe et al. (2019). For the purposes of this study, we consider rupture across gaps or steps of < 15 km in the ZRF to be plausible. Most of the possible fault segments we discuss above are separated by small gaps which would not preclude them from rupturing together in a single event. We map only two gaps bigger than 15 km – apparent gaps 1 and 2 in Figure 2.5-3. However, in both cases these gaps might not actually reflect a lack a fault activity, as explained above. Therefore, whilst we map some possible segmentation of the fault, we find no conclusive evidence for significant physical barriers that would prevent multiple segments of the ZRF or even the entire > 400 km length of mapped faults rupturing together in one earthquake. However, based on scarp heights and empirical slip-to-length ratios, typical rupture lengths on the ZRF are more likely < 200 km.

2.5.2.3. Earthquake Magnitude Estimates

Based on our observations, we calculate a range of estimates for earthquake magnitudes on the ZRF using several empirical scaling relationships for thrust faults (Table 2.5-1). These include a relation between average slip (D) and magnitude (M_W) from Wells and Coppersmith (1994) ($M_W = 6.64 + 0.13\log(D)$), and relations between surface rupture length (SRL) and magnitude from Wells and Coppersmith (1994) ($M_W = 5.00 + 1.22\log(SRL)$) and Wesnousky (2008) ($M_W = 4.11 + 1.88\log(SRL)$). Where we have sufficient data, we also calculate M_W from the seismic moment (M_0) using the relation $M_W = \frac{2}{3}\log(M_0) - 6.06$, where $M_0 = \mu AD$, μ is the shear modulus (30 GPa), A (m^2) is the area of the rupture and D (m) is the average slip (Kanamori, 1977; Hanks and Kanamori, 1979).

Table 2.5-1. Earthquake magnitude estimates based on empirical scaling relationships and seismic moment. Empirical scaling relationships are from Wells and Coppersmith (1994), abbreviated to W&C (1994), and Wesnousky (2008), all of which are based on data from thrust faults. Slip is converted from uplift assuming a dip of 30 – 60°, except for trench estimates which are direct measurements. Details of magnitude from seismic moment calculations are given in the text. *1887 M_W range based on Krüger, Kulikova and Landgraf (2018) and Bindi et al. (2014).

Basis for estimation	**Rupture scenario**	**Fault parameters**			**M_W**				
		Uplift (m)	**Slip (m)**	**Length (km)**	**W&C (1994) - slip**	**W&C (1994) - length**	**Wesnousky (2008) - length**	**Seismic moment relation**	**Historical records**
Segmentation	Segment A			~80		7.3	7.7		
	Segment B			~40		7.0	7.1		
	Segment C			~120		7.5	8.0		
	Segment D			~45		7.0	7.2		
	Segment E			~75 – 95		7.3 – 7.4	7.6 – 7.8		
	Segment F			~20		6.6	6.6		
All mapping	Entire length of mapped faults			~400		8.2	9.0		
Scarp offsets	MRE(s)	~0.2 - 1	~0.2 – 2		6.5 – 6.7				
Trench	MRE (E2) segment D	~0.8	~1.3	~45	6.7	7.0	7.2	7.0 – 7.2	
	Penultimate (E1) on segment D	~0.4	~0.7	~45	6.6	7.0	7.2	6.9 – 7.0	
Historical event	1887 Verny earthquake								~7.2 – 7.7*

Using the measurements from the trench to represent the average slip, we obtain estimates of M_W ~ 6.7 and M_W ~ 6.6 for the MRE (E2) and the penultimate event (E1) respectively at the eastern end of the fault. The magnitude-seismic moment relation yields values of M_W ~ 7.0 – 7.2 for E2 and M_W ~ 6.9 – 7.0 for E1, assuming that these events ruptured the full ~45 km of segment D, that the fault dips at 35° as observed in the trench, and that the fault is seismogenic to depths of 15 – 30 km, corresponding to typical earthquake depths in the northern Tian Shan (Figure 2.1-1a; Sloan et al., 2011; Campbell et al., 2013; Alinaghi and Krüger, 2014; Tsai et al., 2022). We note that all the slip in these earthquakes may not have reached the surface and as such these estimates are probably minimum magnitudes. Our estimates of slip magnitudes (at least ~0.2 – 2 m of slip) in the most recent events from measurements along the whole ZRF correspond to minimum magnitudes of M_W 6.5 – 6.7.

Most of the possible fault segments we identify are between ~40 – 120 km in length, corresponding to magnitudes in the range M_W 7.0 – 8.0. The splay beneath the northwest of Almaty, segment F, corresponds to a rupture of M_W ~6.6 based on its length. We find no definitive evidence for physical barriers which would prevent rupture along the entire ~400 km of range front faults, which would correspond to an event of M_W 8.0 – 9.0. While we cannot entirely exclude this possibility, it does not seem to be a likely scenario based on the relatively small scarps which imply that earthquake ruptures should be < 200 km long according to empirical slip-to-length ratios (Scholz, 1982; Scholz, Aviles and Wesnousky, 1986; Wesnousky, 2008; Tsai et al., 2022).

The magnitude estimates based on slip (M_W 6.5 – 6.7) are significantly smaller than magnitudes based on apparent fault segmentation (M_W 7.0 – 8.0). There are a number of possible explanations for this discrepancy: Firstly, the segments we map may be too large. While few barriers to longer ruptures are apparent in our mapping, there may be segmentation we cannot identify with the available data and levels of scarp degradation, especially within the longest segment (C) which is largely obscured by urbanisation. While it might be theoretically possible for the fault to rupture in longer segments, this may not reflect the fault's behaviour in reality – although the M_W ~7.2 – 7.9 Verny earthquake proved that larger magnitude ruptures are possible along a fault at or near the range front. Alternatively, the discrepancy could indicate that our slip estimates for the MREs represent the minimum rather than the average slip, as discussed in the sections above. This can be tested by trenching more > 1 m scarps to confirm whether they are single or multiple event offsets – until such data can be collected, magnitudes based on the smallest scarp offsets should be considered minima. Thirdly, the fault might rupture in events of varying magnitude – a M_W 6.5 – 6.7 rupture in the MREs does not preclude a larger rupture occurring before this or in the future. In the trench we document a doubling of slip between the penultimate earthquake and the MRE, which suggests there is no single characteristic slip magnitude in any given location. Finally, there are examples of earthquakes in which the extent or magnitude of

surface slip was notably smaller than expected for their instrumental magnitude or surface rupture length, both in the Tian Shan (e.g. the 1992 M_W 7.2 Suusamyr earthquake; Dziewonski, Chou and Woodhouse, 1981; Ghose et al., 1997; Ekström, Nettles and Dziewoński, 2012; Ainscoe et al., 2019) and globally (e.g. the 1976 M 7.5 Guatemala earthquake, which had ~1 m average over a length of ~230 km; Plafker, 1976). Some high magnitude earthquakes do not rupture the surface at all, such as the 2015 M_W 7.9 Gorkha earthquake (Zhang et al., 2016), and no scarps from the 1887 M_W ~7.2 – 7.7 Verny earthquake (Bindi et al., 2014; Krüger, Kulikova and Landgraf, 2018) have been found along the Zailisky Range Front (Tatevossian, 2007). Furthermore, earthquake ruptures can occur on complex networks of multiple fault strands, with smaller slip on individual faults combining to produce a larger rupture (e.g. the 2010 El Mayor-Cucapah M_W 7.2 earthquake in Mexico; Fletcher et al., 2014). Therefore, it remains uncertain whether surface geomorphology observations can reflect the full range behaviour of the ZRF, or whether empirical scaling relationships based on global datasets can accurately estimate its past and potential earthquake magnitudes.

2.5.3. Implications for Seismic Hazard

This study builds on the work of Grützner et al. (2017b) to systematically document evidence for active faulting along the entire ~300 km length of the Zailisky Range Front, supporting their conclusion that the fault is a significant source of hazard to local populations. We document new scarps close to population centres, including in the middle of Talgar town. Amey et al. (2021) modelled a range of earthquake scenarios on the ZRF close to Almaty, including the M_W ~7.2 – 7.7 1887 Verny earthquake (modelled as M_W 7.3) and hypothetical M_W 6.5 events on small segments near the city. They found that such events could cause extensive damage and thousands of fatalities. Our analysis suggests that these scenario models should be extended along the entirety of the range front, as paleoearthquakes of at least M_W 6.5– 6.7 have ruptured along most of the length of the ZRF, not only in the vicinity of Almaty. Our fault mapping also demonstrates a continuity to the fault trace

which implies much larger ruptures along hundreds of kilometres of the ZRF might be possible and should also be considered in hazard analyses.

We document the building of houses and infrastructure directly on top of scarps, placing these structures at particular risk of high intensity shaking as well as disruption from co-seismic surface displacements. Grützner et al. (2017b) first documented concerns about the location of the Big Almaty Canal, a major irrigation canal which closely follows and crosses the trace of the ZRF in the eastern section of the range front (Figure 2.5-4). At site N17, we document scarps lying less than 500 m north of the canal, whilst ~5 km to the east at sites N18 and N19, scarps lie less than 200 m south of the canal, and the canal crosses the fault trace several more times (Figure 2.5-4). Our paleoseismic trench proves that this section of the fault has ruptured within the last ~8 kyrs. In a repeat of the MRE that we uncovered at the trench site (N19), the canal would experience differential displacement along its length on the order of ~1 m which could cause significant damage with knock on effects to the water supply downstream.

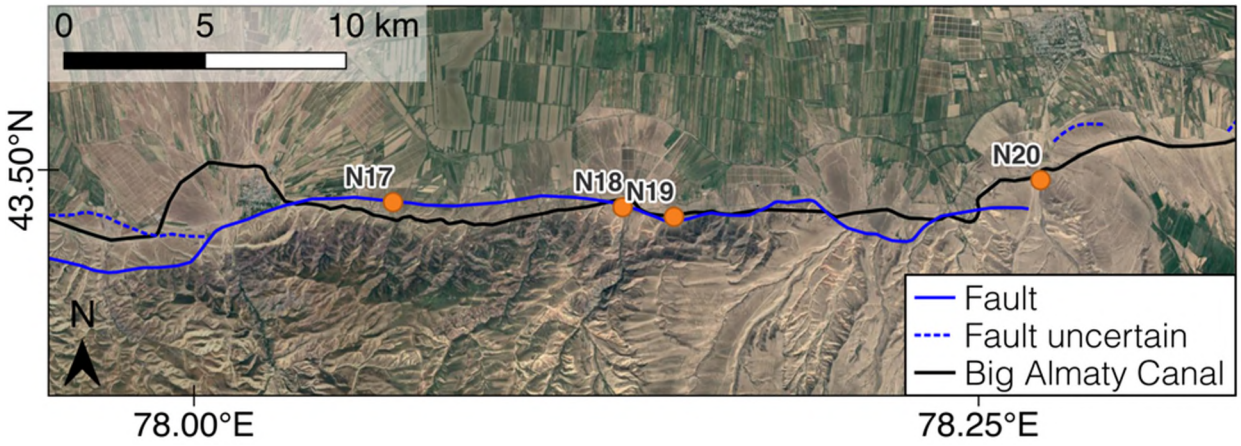

Figure 2.5-4. The Big Almaty Canal intersecting the fault trace within the eastern section of the ZRF. Background imagery is Google Satellite (2023 Airbus, 2024 Maxar Technologies, 2024 CNES / Airbus).

The development and modification of the landscape also present problems for accurately identifying the location and extent of surface ruptures, and there could be more hazardous fault strands or

segments beneath towns that we were unable to map. These challenges will only grow with the population of the range front and further urbanisation. Furthermore, there may be buried seismic sources which are unmappable from surface observations alone: in our analysis of the geomorphology, we identify an ~80 km-wide region of incised foreland sediments along the western part of the range front which could have been uplifted by folding above a blind thrust. Folded foreland sediments near Kosmos (Figure 2.1-1b) dated to ~17 ka (Macklin et al., 2015) are also consistent with deformation extending northwards into the platform (Grützner et al., 2017b). Seismic reflection surveys could help to identify deforming structures in the platform.

Finally, earthquake chronologies are important for assessing the likely frequency and timing of events for hazard analysis. Grützner et al. (2017b) suggested that if the mapped scarps formed thousands of years ago (inferred from a qualitative assessment of scarp morphology) and the ZRF ruptures according to standard models of the seismic cycle, then we might infer that the fault is in the later stages of this cycle – i.e. that it has accumulated strain for thousands of years, is approaching the end of its typical recurrence interval and could rupture again soon. Our analysis shows that more than a thousand years having passed since the last earthquake is not sufficient evidence to indicate that the fault is late in its earthquake cycle, because recurrence intervals could be as large as ~7 kyrs. With the penultimate event and MRE on the eastern section of the ZRF at 9.5 ± 0.8 ka (2σ) and 8.4 – 2.6 ka (95.4% probability range) respectively, we cannot make any inferences about how close the fault may be to rupturing because of the wide range of possible ages of the MRE. The data also cannot clarify whether events on the ZRF rupture at regular intervals or are in fact clustered in time (Liu and Stein, 2016; Grützner et al., 2017b) – if the latter, an average recurrence interval may have limited use in hazard assessment. Further paleoseismic trenching of the ZRF is required to shed light on its temporal behaviour.

2.6. Conclusions

We document active faulting along ~300 km of the Zailisky Range Front at 22 new sites and 11 sites reassessed from Grützner et al. (2017b). All scarps are relatively degraded and there is no evidence for fresh ruptures. We present the first paleoseismic trench on the ZRF, revealing evidence for two paleoearthquakes in its eastern section. At the trench site, the penultimate earthquake (E1) occurred at 9.5 ± 0.8 ka (2σ) and slipped ~0.7 m, and the most recent event (E2) ruptured at some point between 8.4 – 2.6 ka (95.4% probability range), slipping ~1.3 m. These slip measurements correspond to earthquakes of at least M_W ~6.6 and ~6.7 respectively (Wells and Coppersmith, 1994). Our results suggest that consecutive earthquakes on this section of the ZRF are separated by thousands of years (~5 – 7 kyrs, assuming a constant recurrence interval), consistent with observations from other large faults in the northern Tian Shan. From the smallest scarp offsets along the range front, we estimate that the most recent events to rupture the ZRF slipped at least ~0.2 – 2.0 m, corresponding to earthquakes with minimum magnitudes of M_W 6.5 – 6.7 (Wells and Coppersmith, 1994) and consistent with our findings from the trench.

We tentatively map a possible segmentation of the ZRF with segment lengths on the order of ~40 – 120 km, although the extensive urbanisation, erosion and loess cover of the range front may be masking much of the faulting and its true segmentation. Individual ruptures of the proposed segments could produce earthquakes of M_W 7.0 – 8.0 (Wells and Coppersmith, 1994; Wesnousky, 2008), consistent with the 1887 M_W ~7.2 – 7.7 Verny earthquake (Bindi et al., 2014; Krüger, Kulikova and Landgraf, 2018) which is thought to have ruptured on or close to the ZRF (Tatevossian, 2007). We also cannot rule out simultaneous ruptures of multiple segments along hundreds of kilometres of the ZRF producing much larger events.

The combined evidence from this study, Grützner et al. (2017b), and Amey et al. (2021) demonstrates that the ZRF poses significant seismic hazard to populations along the range front. Housing and infrastructure have been built directly on top of scarps, with the notable examples of the Big Almaty Canal, Almaty city and Talgar town. There are probably further scarps beneath urban areas which have been destroyed or obscured. Further paleoseismic trenching of the ZRF is necessary to clarify the magnitude and timing of earthquakes to better inform hazard assessment, but the window of opportunity to comprehensively investigate the densely populated central section of the fault is rapidly closing as the range front becomes more developed.

2.7. Appendix of Chapter 2

2.7.1. dGPS Survey Processing

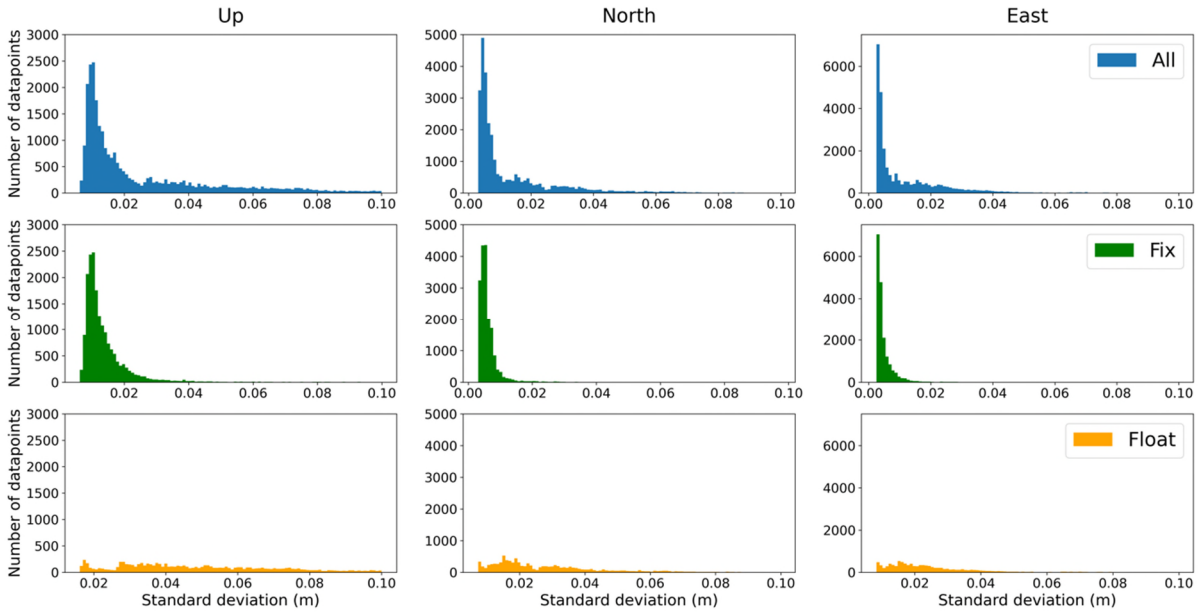

Figure 2.7-1. Histograms (bins = 100) of standard deviation of GPS northings, eastings and up measurements from the Talgar kinematic dGPS road survey (site N12), as output by Emlid Studio v1.4. Top row shows all data points, middle and bottom rows show data points with 'Fix' and 'Float' solutions, respectively. Data with 'Single' solutions represent only 1.6% of points and were discarded.

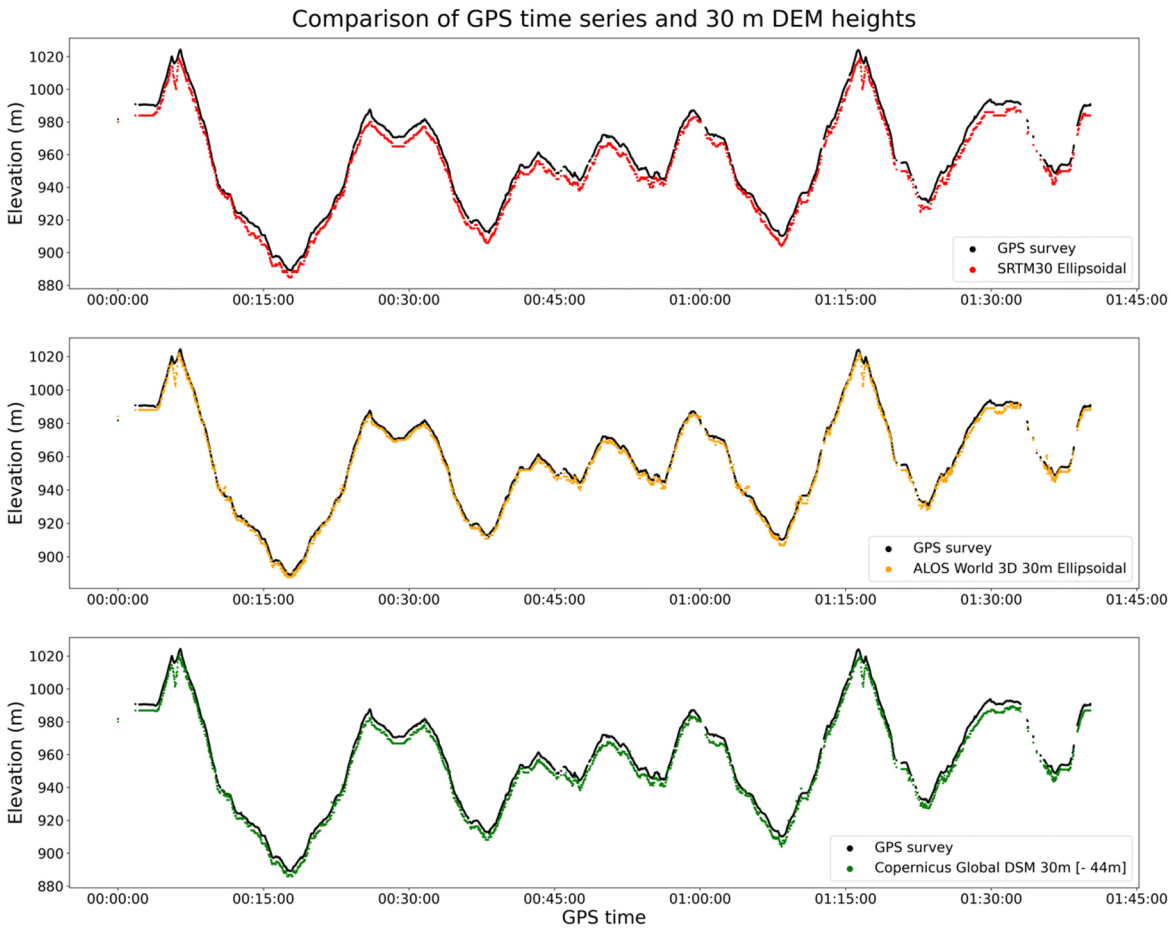

Figure 2.7-2. Talgar (N12) processed dGPS survey data (black) plotted against time since start of survey (GPS time). Elevations extracted from DEMs at the locations of the GPS survey points are also plotted. Top panel: SRTM 30m data (ellipsoidal) in red. Middle panel: ALOS World 3D 30 m (ellipsoidal) data in yellow. Bottom panel: Copernicus GLO-30 DEM orthometric data with 44 m subtracted to give ellipsoidal elevation in green.

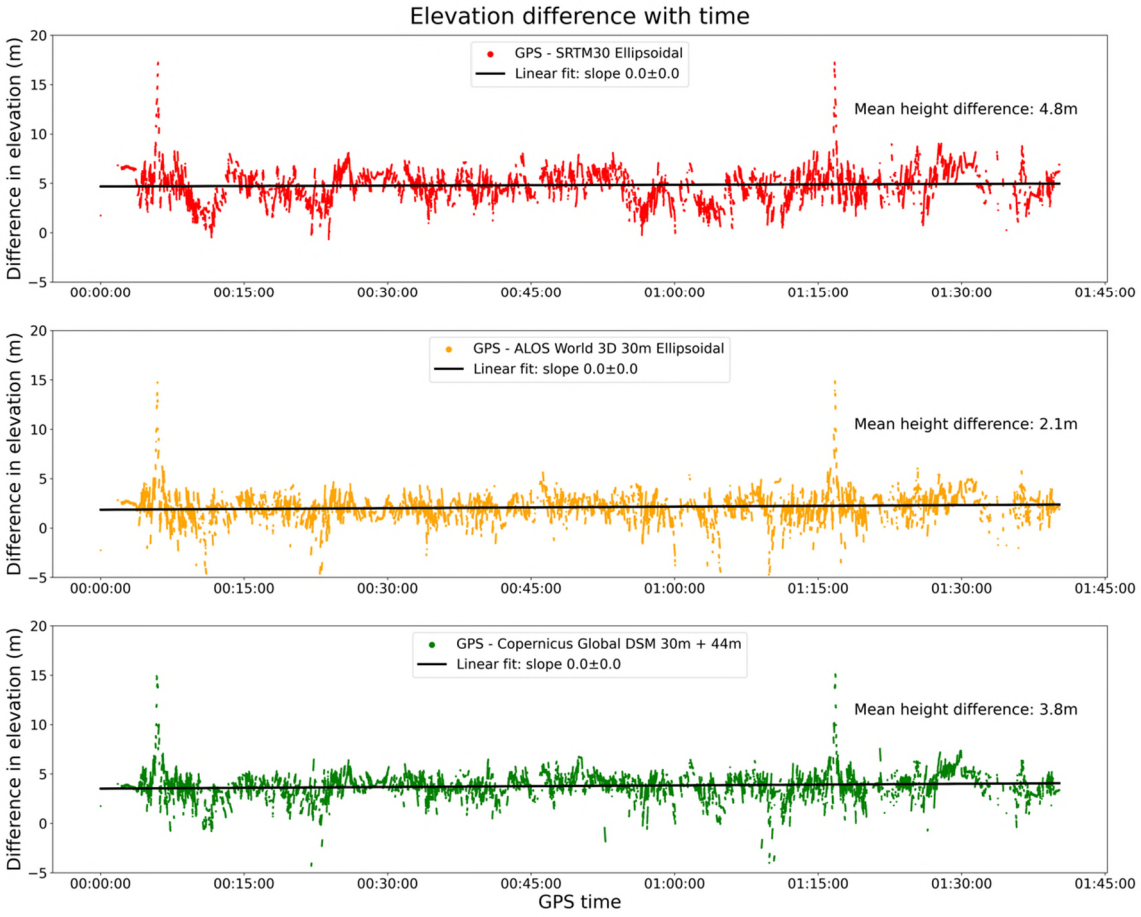

Figure 2.7-3. Difference between dGPS measurements and 30 m DEMs for the Talgar road survey at N12, plotted against time since the start of the GPS survey (GPS time). Black lines show linear fit through the plotted data. Top panel: SRTM 30m data (ellipsoidal) in red. Middle panel: ALOS World 3D 30 m (ellipsoidal) data in yellow. Bottom panel: Copernicus GLO-30 DEM orthometric data with 44 m subtracted to give ellipsoidal elevation in green.

2.7.2. Luminescence Dating Measurements

Table 2.7-1. Summary of analysis parameters and anomalous fading measurements for IRSL samples collected in 2019 and processed in the luminescence laboratory at the University of Sheffield. The average fading measurement was 1.02 ± 0.05.

Site	**Sample name**	**Lab code**	**Depth (m)**	**Grain size (μm)**	**Grains measured**	**Grains accepted (finite D_E)**	**Grains used in D_E calculation**	**Low dose grains excluded**	**Fading measure as a proportion of applied lab dose (±1σ)**
N19 – Koram (trench site)	KAZT1	Shfd19190	2.30	125-212	400	36	25	3	1.06 ± 0.04
	KAZT2	Shfd19191	1.40	125-212	400	52	46	4	1.07 ± 0.06
	KAZT3	Shfd19192	1.08	125-212	400	49	42	3	0.95 ± 0.05
	KAZT4	Shfd19193	0.94	125-212	400	53	33	1	0.94 ± 0.05
	KAZT5	Shfd19194	0.96	125-212	600	28	17	0	1.16 ± 0.10
	KAZT6	Shfd19195	0.62	125-180	200	42	40	2	1.10 ± 0.07
	KAZ19PIT1	Shfd19196	2.30	125-180	200	61	27	0	0.96 ± 0.02
	KAZ19PIT2	Shfd19197	1.70	125-212	400	41	9	0	0.95 ± 0.02

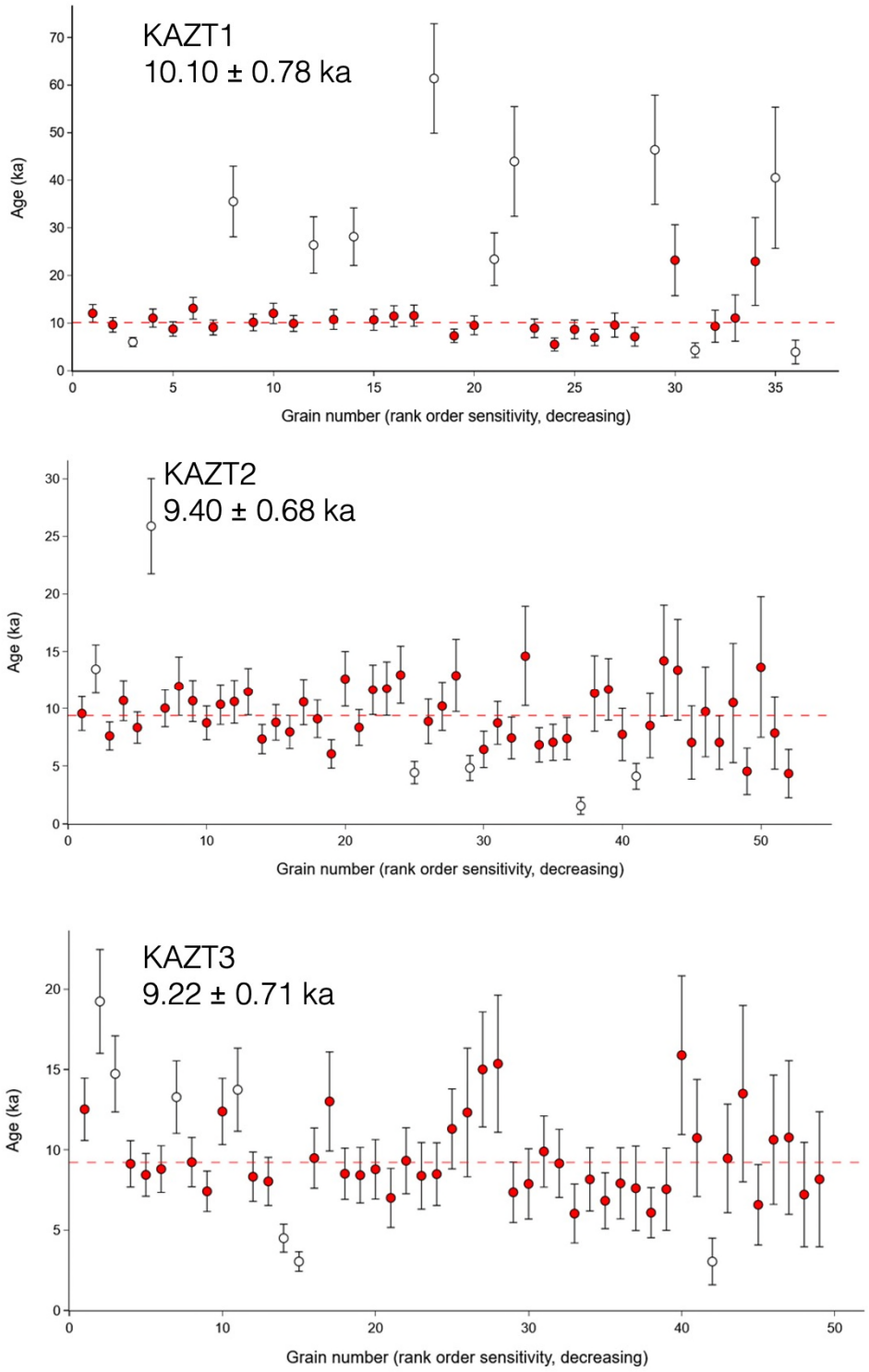

Figure 2.7-4. IRSL age plots for each grain in the KAZT1, KAZT2 and KAZT3 samples from 2019 processed at the University of Sheffield. 400 grains were measured from each sample, grains plotted here had a measurable D_Es, red points represent grains that were included in the final age estimate: 25, 46 and 42 for KAZT1, KAZT2 and KAZT3, respectively.

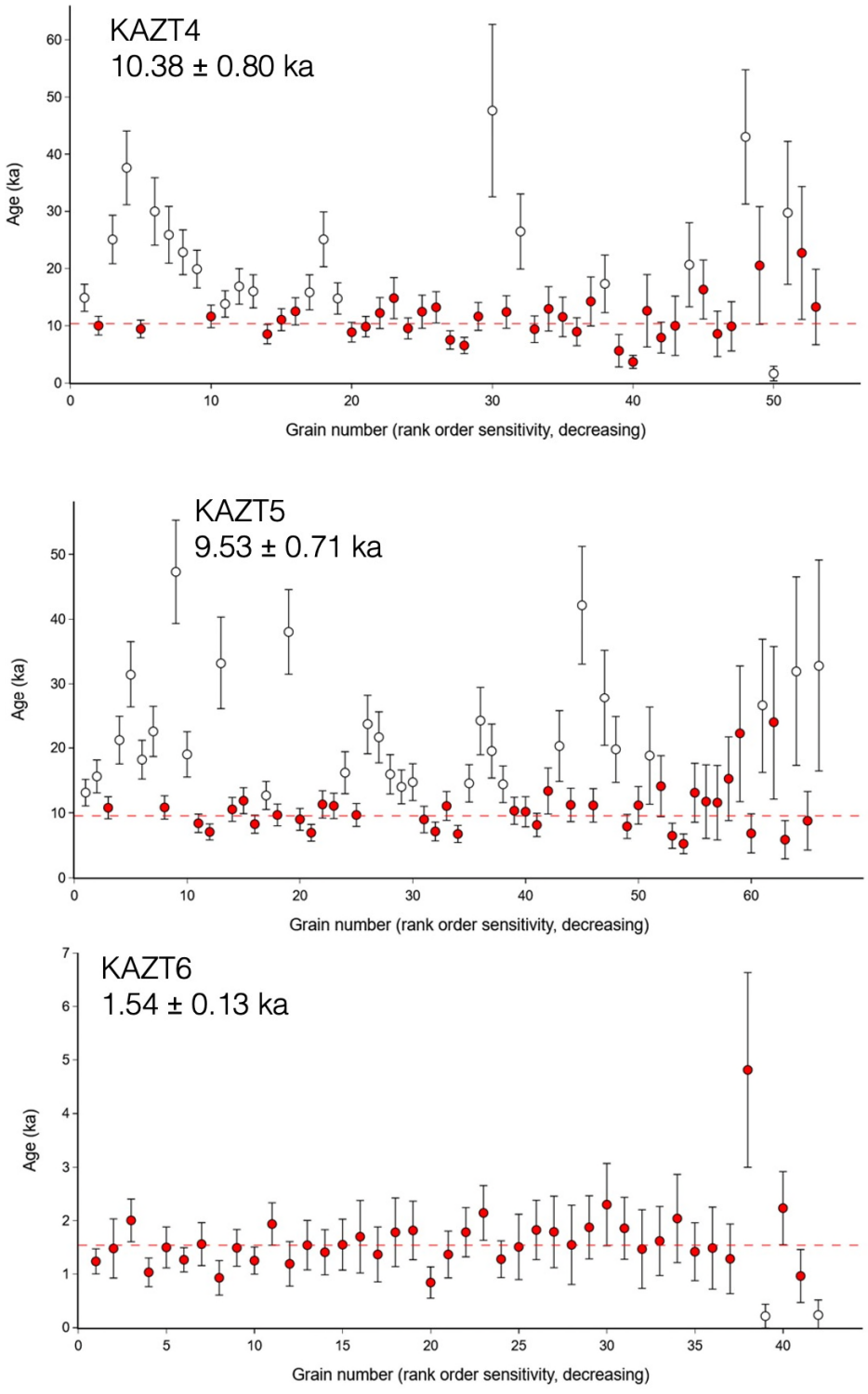

Figure 2.7-5. IRSL age plots for each grain in the KAZT4, KAZT5 and KAZT6 samples from 2019 processed at the University of Sheffield. 400, 600 and 200 grains were measured from KAZT4, KAZT5 and KAZT6, respectively. Grains plotted here had a measurable D_Es, red points represent grains that were included in the final age estimate: 33, 37 and 40 for KAZT4, KAZT5 and KAZT6, respectively.

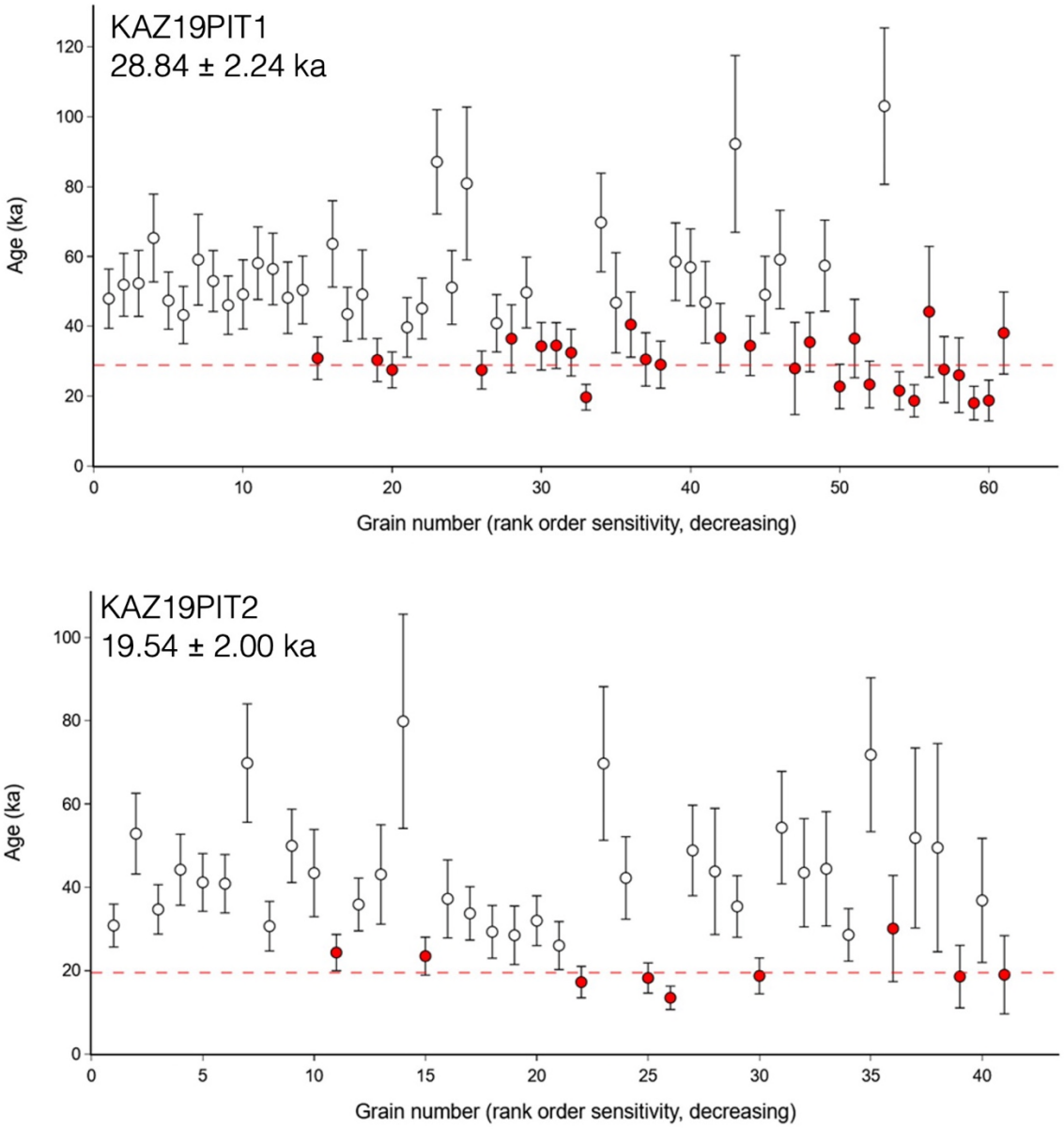

Figure 2.7-6. IRSL age plots for each grain in the KAZ19PIT1 and KAZ19PIT2 samples from 2019 processed at the University of Sheffield. 200 and 400 grains were measured from KAZ19PIT1 and KAZ19PIT2, respectively. Grains plotted here had a measurable D_Es, red points represent grains that were included in the final age estimate: 27 and 9 grains for KAZ19PIT1 and KAZ19PIT2, respectively.

2.7.3. OxCal

2.7.3.1. OxCal Modelling

We test four prior models which make different assumptions about the transitions between the mapped units (Appendix Table 2.7-9). In model A, we assume all units have contiguous transitions, apart from the unit 2/3 and unit 7/8 transitions which we model as sequential boundaries because there is clear evidence of erosion. We assume the colluvial wedges (unit 4 and unit 7) began to form immediately after the earthquakes and therefore model the earthquakes as the starting boundaries of the colluvial phases. Model B is the same as model A, but we model the boundaries between earthquakes and colluvial wedges as contiguous transitions (i.e. the earthquakes mark the start of a continuous depositional sequence) – this model tests the differences induced by different model options rather than different interpretations. In model C we assume there is a hiatus after every unit and model their boundaries as sequential. Model D is the same as model A but units 5 and 6 are modelled as a single phase. Finally, in E, we model only the sampled units (2, 5 and 8) with sequential boundaries, assuming hiatuses between them.

Results for models A to E are presented in the plots and tables below, model are codes reported in Appendix Table 2.7-9, and results are summarised in Table 2.7-2 and Figure 2.4-4. Due to the low agreement index of the sample age from KAZT4 in A, B, C and D, we also ran these models without the KAZT4 measurement (results summarised in Table 2.7-3; Figure 2.4-4). Model A is our preferred model, as it best reflects our interpretation of the trench stratigraphy and event history. Note that the boundaries that begin and end each sequence are required for the model but their posterior dates do not constitute relevant information for this study.

Table 2.7-2. Comparison of earthquake ages for all models including all samples. ka = kyrs before AD 2023.

Model	**Earthquake E1**			**Earthquake E2**		
	μ ± 2σ (ka)	**95.4% probability range (ka)**		**μ ± 2σ (ka)**	**95.4% probability range (ka)**	
		From	**To**		**From**	**To**
A	9.49 ± 0.83	10.33	8.66	5.53 ± 3.12	8.37	2.55
B	9.60 ± 0.84	10.44	8.76	6.36 ± 2.87	8.87	3.48
C	9.71 ± 0.85	10.56	8.87	5.46 ± 2.77	8.06	2.80
D	9.48 ± 0.86	10.32	8.65	6.64 ± 3.20	9.22	3.38
E	9.72 ± 0.81	10.54	8.91	6.22 ± 3.89	9.32	2.40

Table 2.7-3. Comparison of earthquake ages for models A to D excluding sample KAZT4. ka = kyrs before AD 2023.

Model (excluding KAZT4)	**Earthquake E1**			**Earthquake E2**		
	μ ± 2σ (ka)	**95.4% probability range (ka)**		**μ ± 2σ (ka)**	**95.4% probability range (ka)**	
		From	**To**		**From**	**To**
A	9.18 ± 0.94	10.12	8.24	5.29 ± 2.96	8.01	2.47
B	9.31 ± 0.93	10.25	8.38	6.07 ± 2.75	8.53	3.30
C	9.45 ± 0.94	10.40	8.52	5.22 ± 2.64	7.73	2.69
D	9.17 ± 0.95	10.12	8.22	6.30 ± 3.06	8.86	3.22

Table 2.7-4. OxCal modelling results for model A. BP refers to years before the halfway point of 1950. μ is the mean, σ is the standard deviation, m is the median, C is the Convergence Integral.

Model A: $A_{overall}$ = 66.9%										
Name		**Unmodelled Input**		**Modelled Output**						
		μ (yrs BP)	**σ (yrs)**	**μ (yrs BP)**	**σ (yrs)**	**m (yrs)**	**95.4% range (yrs BP)**		**C (%)**	**A_i (%)**
							From	**To**		
Boundary End_8				1039	621	1221	1748	-225	96.7	
Phase Unit_8	KAZT6	1472	128	1487	130	1487	1748	1227	99.9	98.8
Boundary Start_8				2208	873	1898	4176	1222	99.7	
Evidence of erosion										
Boundary End_7				3832	1441	3620	6677	1522	99.6	
Phase Unit_7										
Boundary E2				5455	1560	5486	8298	2479	99.6	
Boundary End_6				7076	1355	7322	9268	4215	99.7	
Phase Unit_6										
Boundary Transition_5/6				8696	533	8749	9696	7620	99.5	
Phase Unit_5	KAZT5	9465	707	8977	393	8984	9754	8192	100	103.4
	KAZT4	10310	799	8997	391	8999	9750	8176	99.8	43.3
	KAZT3	9149	707	8960	398	8965	9757	8152	99.9	120.3
Boundary Transition_4/5				9171	393	9169	9960	8388	99.7	
Phase Unit_4										
Boundary E1				9412	415	9407	10253	8583	99.9	
Boundary End_3				9653	428	9648	10520	8805	99.8	
Phase Unit_3										
Boundary Start_Unit3				9894	432	9889	10774	9036	99.8	
Evidence of erosion										
Boundary End_Unit2				10135	428	10129	10989	9283	99.6	
Phase Unit_2	KAZT2	9331	680	10280	430	10276	11167	9412	99.9	59.8
	KAZT1	10029	779	10313	443	10301	11220	9429	99.9	117.3
Boundary Start_2				10539	563	10490	11676	9471	95.2	

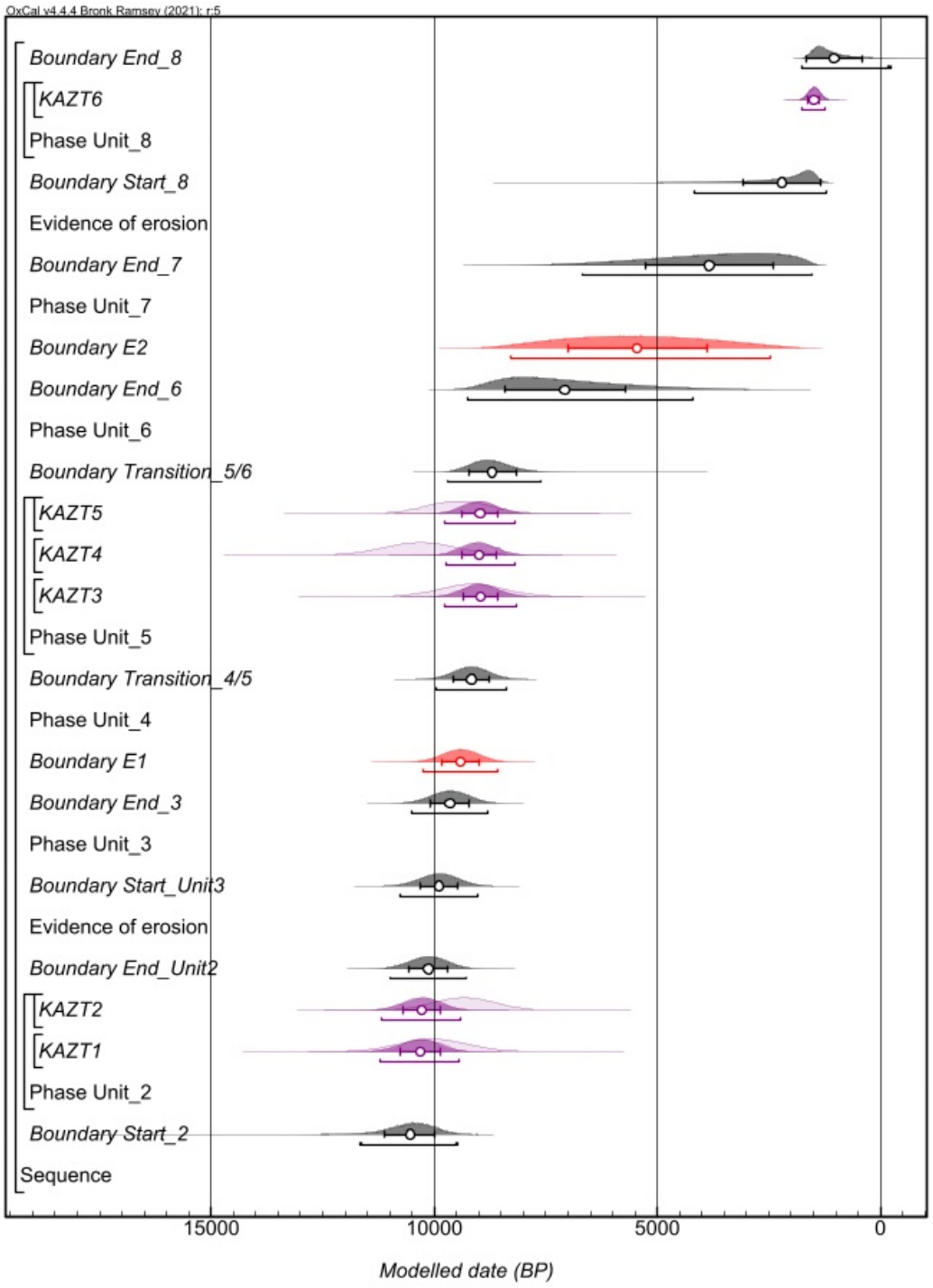

Figure 2.7-7. OxCal trench model A posterior PDFs showing mean, 1σ range and 95.4% probability range. Earthquake PDFs shown in red, sample PDFs in purple with prior PDFs shown in pink. Modelled date is in years before the middle of AD 1950.

Table 2.7-5. OxCal modelling results for model B. BP refers to years before the halfway point of 1950. μ is the mean, σ is the standard deviation, m is the median, C is the Convergence Integral.

Model B: $A_{overall}$ = 67.4%										
Name		**Unmodelled Input**		**Modelled Output**						
		μ (yrs BP)	**σ (yrs)**	**μ (yrs BP)**	**σ (yrs)**	**m (yrs)**	**95.4% range (yrs BP)**		**C (%)**	**A_i (%)**
							From	**To**		
Boundary End_8				1052	605	1229	1754	-213	96.6	
Phase Unit_8	KAZT6	1472	128	1488	129	1488	1749	1228	99.9	99.4
Boundary Start_8				2208	873	1897	4192	1219	99.6	
Evidence of erosion										
Boundary End_7				3841	1443	3631	6697	1523	99.6	
Phase Unit_7										
Boundary Start_7				5474	1558	5507	8314	2508	99.3	
E2				6286	1434	6428	8800	3405	99.6	
Boundary End_6				7097	1342	7344	9262	4209	99.4	
Phase Unit_6										
Boundary Transition_5/6				8694	531	8747	9687	7613	99.2	
Phase Unit_5	KAZT5	9465	707	8974	393	8977	9747	8192	99.9	103.2
	KAZT4	10310	799	8993	392	8999	9790	8200	99.8	43.1
	KAZT3	9149	707	8958	397	8965	9757	8152	99.9	120.2
Boundary Transition_4/5				9167	392	9165	9960	8384	99.7	
Phase Unit_4										
Boundary Start_4				9406	416	9402	10250	8576	99.7	
E1				9526	418	9521	10369	8691	99.8	
Boundary End_3				9646	430	9640	10512	8795	99.7	
Phase Unit_3										
Boundary Start_Unit3				9885	435	9880	10761	9015	99.8	
Evidence of erosion										
Boundary End_Unit2				10124	431	10119	10997	9263	99.6	
Phase Unit_2	KAZT2	9331	680	10268	434	10262	11160	9392	99.7	60.9
	KAZT1	10029	779	10301	448	10293	11220	9405	99.7	117.4
Boundary Start_2				10524	566	10479	11633	9443	94.8	

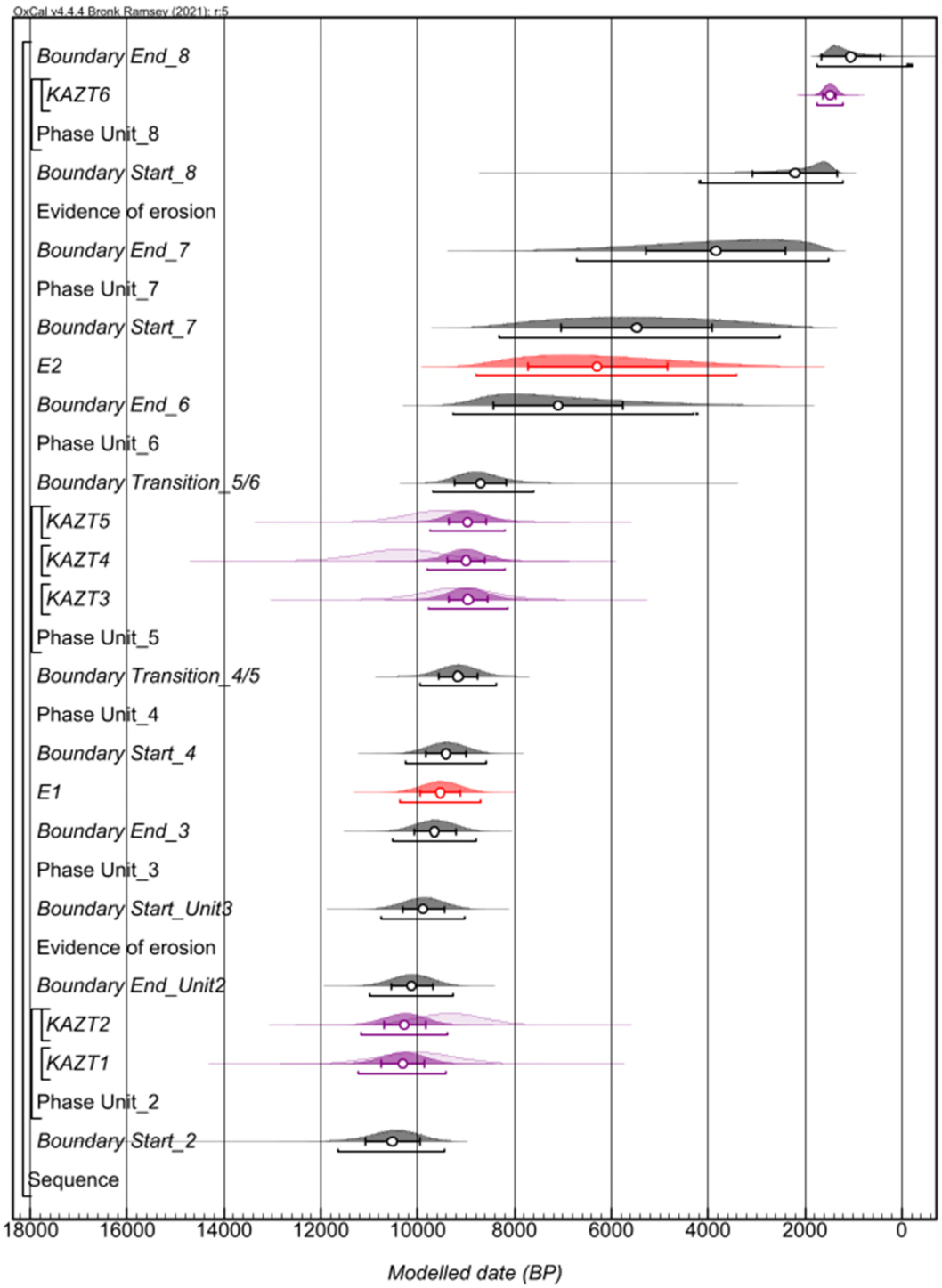

Figure 2.7-8. OxCal trench model B posterior PDFs showing mean, standard deviation and 95.4% probability range. Earthquake PDFs shown in red, sample PDFs in purple with prior PDFs shown in pink. Modelled date is in years before the middle of AD 1950.

Table 2.7-6. OxCal modelling results for model C. BP refers to years before the halfway point of 1950. μ is the mean, σ is the standard deviation, m is the median, C is the Convergence Integral.

Model C: $A_{overall}$ = 61.2%											
Name		**Unmodelled Input**		**Modelled Output**							
		μ (yrs BP)	**σ (yrs)**	**μ (yrs BP)**	**σ (yrs)**	**m (yrs)**	**95.4% range (yrs BP)**		**C (%)**	**A_i (%)**
							From	**To**		
Boundary End_8				1131	500	1268	1762	128	97.5	
Phase Unit_8	KAZT6	1472	128	1490	129	1489	1752	1230	99.9	99.1
Boundary Start_8				2075	727	1826	3708	1223	99.7	
Evidence of erosion										
Boundary End_7				3396	1239	3179	5896	1474	99.7	
Phase Unit_7										
Boundary Start_7				4719	1417	4656	7435	2100	99.3	
E2				5382	1385	5399	7991	2725	99.6	
Boundary End_6				6044	1394	6140	8569	3292	99.3	
Phase Unit_6										
Boundary Start_6				7358	1166	7575	9266	4881	99.7	
Boundary End_5				8672	499	8714	9630	7664	99.4	
Phase Unit_5	KAZT5	9465	707	8922	388	8927	9705	8135	99.9	99.1
	KAZT4	10310	799	8943	388	8943	9734	8152	99.9	38.9
	KAZT3	9149	707	8907	391	8915	9707	8095	99.9	118.6
Boundary Start_5				9095	388	9093	9876	8323	99.7	
Boundary End_4				9312	409	9308	10136	8498	99.8	
Phase Unit_4										
Boundary Start_4				9530	423	9524	10381	8689	99.7	
E1				9639	423	9633	10491	8797	99.8	
Boundary End_3				9748	431	9743	10623	8893	99.7	
Phase Unit_3										
Boundary Start_3				9966	432	9961	10834	9108	99.7	
Evidence of erosion										
Boundary End_2				10184	427	10178	11042	9335	99.5	
Phase Unit_2	KAZT2	9331	680	10314	430	10310	11167	9467	99.7	56.9
	KAZT1	10029	779	10341	441	10332	11228	9468	99.7	116.2
Boundary Start_2										

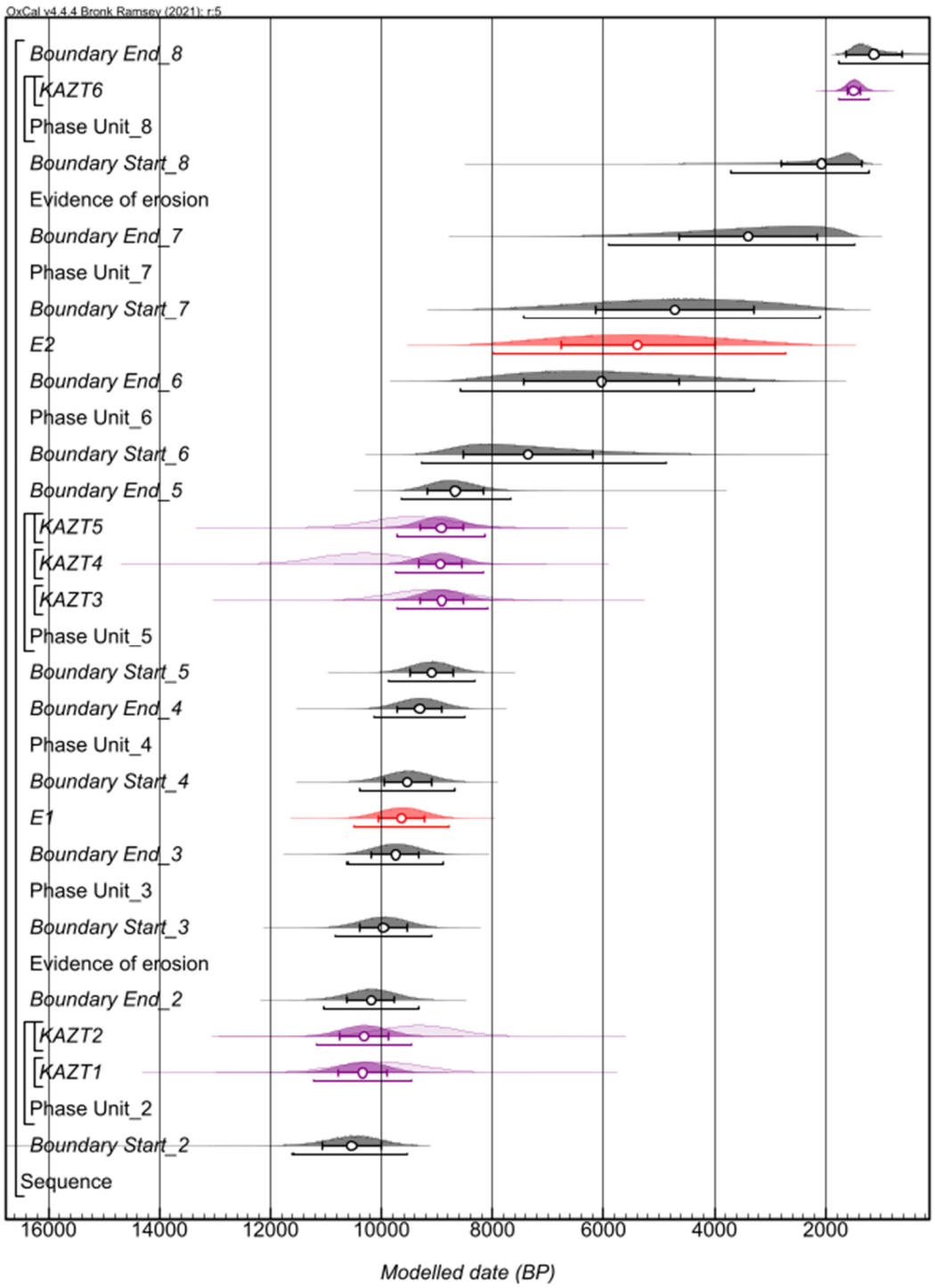

Figure 2.7-9. OxCal trench model C posterior PDFs showing mean, standard deviation and 95.4% probability range. Earthquake PDFs shown in red, sample PDFs in purple with prior PDFs shown in pink. Modelled date is in years before the middle of AD 1950.

Table 2.7-7. OxCal modelling results for model D. BP refers to years before the halfway point of 1950. μ is the mean, σ is the standard deviation, m is the median, C is the Convergence Integral.

Model D: $A_{overall}$ = 65.7%										
Name		**Unmodelled (BP)**		**Modelled (BP)**						
		μ (yrs BP)	**σ (yrs)**	**μ (yrs BP)**	**σ (yrs)**	**m (yrs)**	**95.4% range (yrs BP)**		**C (%)**	**A_i (%)**
							From	**To**		
Boundary End_8				1002	678	1207	1762	-369	97.5	
Phase Unit_8	KAZT6	1472	128	1489	129	1489	1751	1228	99.9	98.9
Boundary Start_8				2386	1062	1994	4803	1227	99.5	
Evidence of erosion										
Boundary End_7				4477	1678	4327	7606	1631	99.5	
Phase Unit_7										
Boundary E2				6566	1595	6819	9143	3306	99.6	
Boundary End_5				8653	568	8717	9692	7507	99.4	
Phase Unit_5	KAZT5	9465	707	8960	396	8963	9754	8157	100	101.9
	KAZT4	10310	799	8989	396	8991	9782	8184	99.9	42.3
	KAZT3	9149	707	8941	402	8951	9742	8130	99.9	119.4
Boundary Transition_4/5				9161	396	9158	9954	8373	99.7	
Phase Unit_4										
Boundary E1				9404	419	9399	10249	8578	99.8	
Boundary End_3				9647	432	9641	10514	8783	99.8	
Phase Unit_3										
Boundary Start_Unit3				9890	436	9884	10764	9019	99.8	
Evidence of erosion										
Boundary End_Unit2				10133	431	10126	11010	9277	99.6	
Phase Unit_2	KAZT2	9331	680	10280	434	10276	11173	9405	99.8	59.9
	KAZT1	10029	779	10314	448	10301	11236	9421	99.8	117
Boundary Start_2				10546	579	10493	11697	9461	96.1	

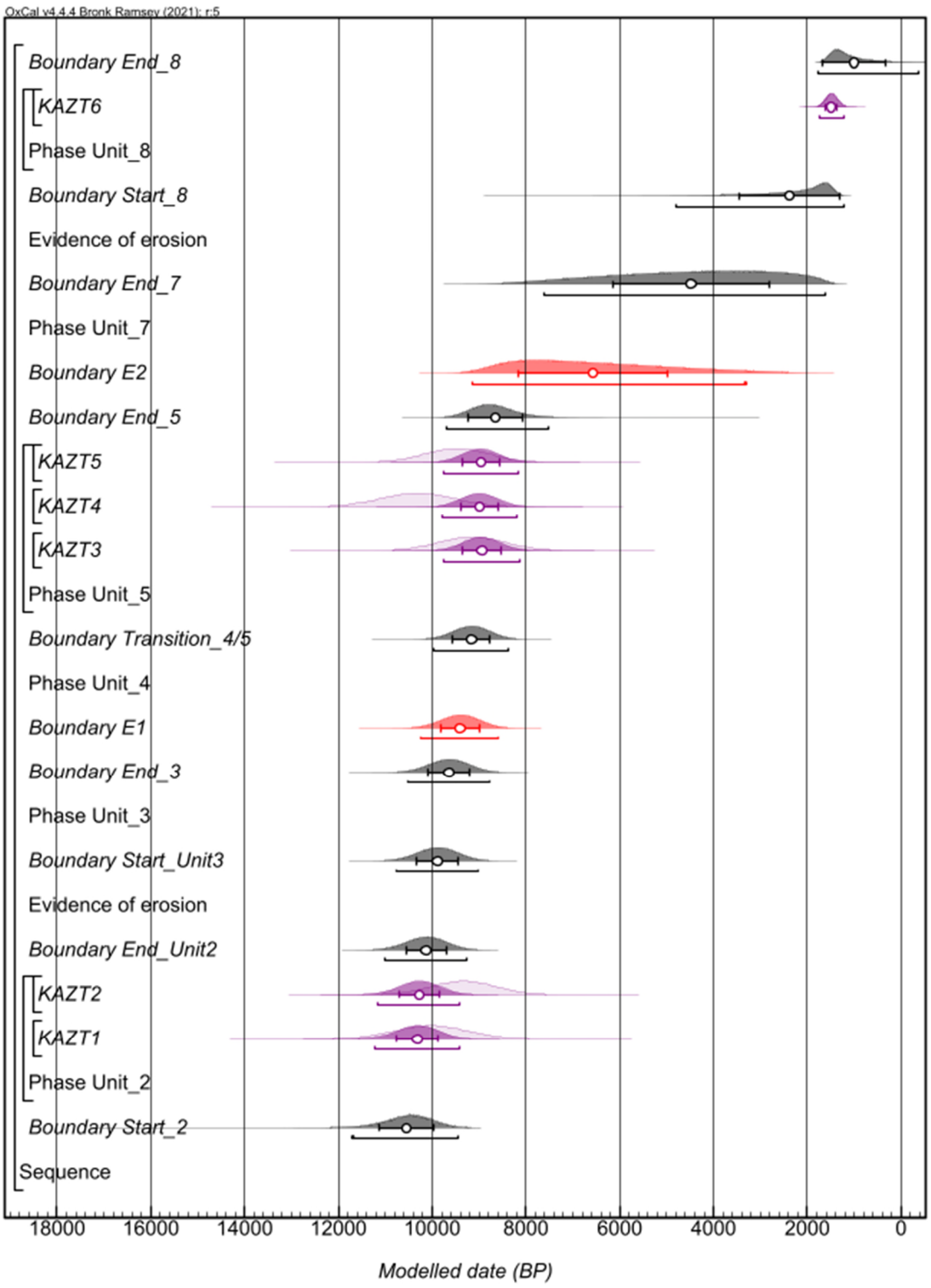

Figure 2.7-10. OxCal trench model D posterior PDFs showing mean, standard deviation and 95.4% probability range. Earthquake PDFs shown in red, sample PDFs in purple with prior PDFs shown in pink. Modelled date is in years before the middle of AD 1950.

Table 2.7-8. OxCal modelling results for model E. BP refers to years before the halfway point of 1950. μ is the mean, σ is the standard deviation, m is the median, C is the Convergence Integral.

Model E: $A_{overall}$ = 93.1%										
Name		**Unmodelled (BP)**		**Modelled (BP)**						
		μ (yrs BP)	**σ (yrs)**	**μ (yrs BP)**	**σ (yrs)**	**m (yrs)**	**95.4% range (yrs BP)**		**C (%)**	**A_i (%)**
							From	**To**		
Boundary End_8				400	1495	913	1781	-2609	97.6	
Phase Unit_8	KAZT6	1472	128	1483	129	1483	1740	1226	99.9	99.5
Boundary Start_8				3634	2038	2948	7897	1276	99.3	
E2				6142	1944	6395	9242	2329	99.4	
Boundary End_5				8652	836	8815	9955	6972	99.4	
Phase Unit_5	KAZT5	9465	707	9167	416	9182	10002	8312	99.9	114.8
	KAZT4	10310	799	9227	410	9231	9990	8384	100	61.0
	KAZT3	9149	707	9129	430	9149	9990	8229	100	121.3
Boundary Start_Unit5				9472	406	9467	10283	8658	99.8	
E1				9649	407	9643	10470	8839	99.9	
Boundary End_Unit2				9826	421	9818	10675	8987	99.8	
Phase Unit_2	KAZT2	9331	680	10041	428	10031	10908	9195	99.9	81.6
	KAZT1	10029	779	10107	461	10083	11065	9195	99.9	121.7
Boundary Start_2				10503	830	10366	12094	9236	95.1	

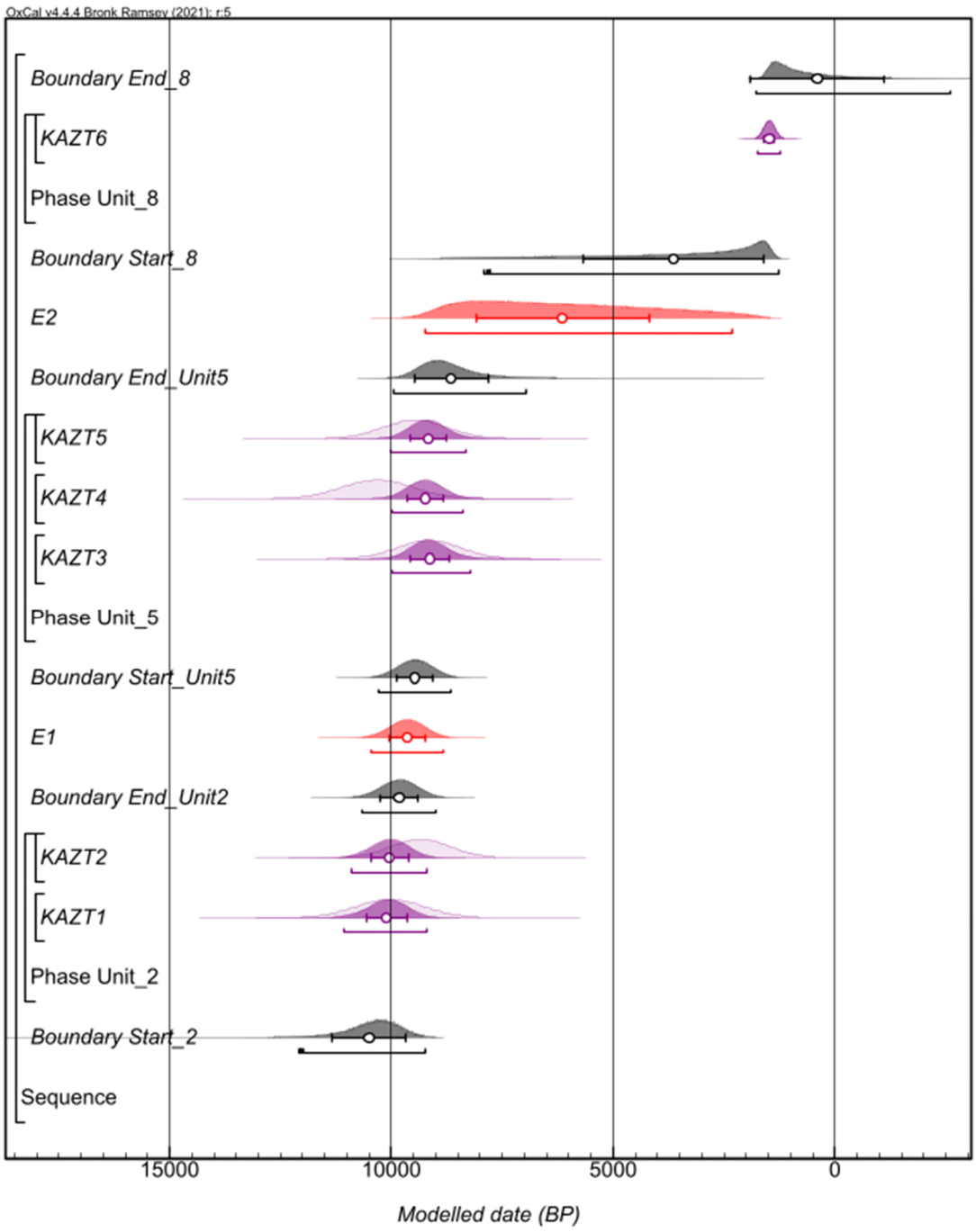

Figure 2.7-11. OxCal trench model E posterior PDFs showing mean, standard deviation and 95.4% probability range. Earthquake PDFs shown in red, sample PDFs in purple with prior PDFs shown in pink. Modelled date is in years before the middle of AD 1950.

Table 2.7-9. OxCal codes for the 4 models tested. To exclude KAZT4, remove the line of code containing the measurement. Note that the luminescence ages are input as years before AD 2020 which was when the measurements were made.

OxCal Model	**Details**	**Code**

A	Contiguous boundaries between all units except unit 2/3 transition and unit 7/8 transition which are treated as sequential. Earthquakes are treated as the base of colluvial wedges.	// A
		Plot()
		{
		Sequence()
		{
		Boundary("Start_2");
		Phase("Unit_2")
		{
		Date("KAZT1",2020-N(10098,779));
		Date("KAZT2",2020-N(9400,680));
		};
		Boundary("End_Unit2");
		Label("Evidence of erosion");
		Boundary("Start_Unit3");
		Phase("Unit_3")
		{
		};
		Boundary("End_3");
		Boundary("E1");
		Phase("Unit_4")
		{
		};
		Boundary("Transition_4/5");
		Phase("Unit_5")
		{
		Date("KAZT3",2020-N(9218,707));
		Date("KAZT4",2020-N(10379,799));
		Date("KAZT5",2020-N(9534,707));
		};
		Boundary("Transition_5/6");
		Phase("Unit_6")
		{
		};
		Boundary("End_6");
		Boundary("E2");
		Phase("Unit_7")
		{
		};
		Boundary("End_7");
		Label("Evidence of erosion");
		Boundary("Start_8");
		Phase("Unit_8")
		{
		Date("KAZT6",2020-N(1541,128));
		};
		Boundary("End_8");
		};
		};

B	Same as model A but with contiguous boundaries between earthquakes and colluvial	// B
		Plot()

	wedges.	{
		Sequence()
		{
		Boundary("Start_2");
		Phase("Unit_2")
		{
		Date("KAZT1",2020-N(10098,779));
		Date("KAZT2",2020-N(9400,680));
		};
		Boundary("End_Unit2");
		Label("Evidence of erosion");
		Boundary("Start_Unit3");
		Phase("Unit_3")
		{
		};
		Boundary("End_3");
		Date("E1");
		Boundary("Start_4");
		Phase("Unit_4")
		{
		};
		Boundary("Transition_4/5");
		Phase("Unit_5")
		{
		Date("KAZT3",2020-N(9218,707));
		Date("KAZT4",2020-N(10379,799));
		Date("KAZT5",2020-N(9534,707));
		};
		Boundary("Transition_5/6");
		Phase("Unit_6")
		{
		};
		Boundary("End_6");
		Date("E2");
		Boundary("Start_7");
		Phase("Unit_7")
		{
		};
		Boundary("End_7");
		Label("Evidence of erosion");
		Boundary("Start_8");
		Phase("Unit_8")
		{
		Date("KAZT6",2020-N(1541,128));
		};
		Boundary("End_8");
		};
		};

C	All unit boundaries treated as sequential – i.e. assuming a hiatus after every distinct depositional layer.	// C
		Plot()
		{
		Sequence()
		{
		Boundary("Start_2");
		Phase("Unit_2")
		{

		Date("KAZT1",2020-N(10098,779));
		Date("KAZT2",2020-N(9400,680));
		};
		Boundary("End_2");
		Label("Evidence of erosion");
		Boundary("Start_3");
		Phase("Unit_3")
		{
		};
		Boundary("End_3");
		Date("E1");
		Boundary("Start_4");
		Phase("Unit_4")
		{
		};
		Boundary("End_4");
		Boundary("Start_5");
		Phase("Unit_5")
		{
		Date("KAZT3",2020-N(9218,707));
		Date("KAZT4",2020-N(10379,799));
		Date("KAZT5",2020-N(9534,707));
		};
		Boundary("End_5");
		Boundary("Start_6");
		Phase("Unit_6")
		{
		};
		Boundary("End_6");
		Date("E2");
		Boundary("Start_7");
		Phase("Unit_7")
		{
		};
		Boundary("End_7");
		Label("Evidence of erosion");
		Boundary("Start_8");
		Phase("Unit_8")
		{
		Date("KAZT6",2020-N(1541,128));
		};
		Boundary("End_8");
		};
		};

D	Same as model A but we treat units 5 and 6 as a single phase.	// D
		Plot()
		{
		Sequence()
		{
		Boundary("Start_2");
		Phase("Unit_2")
		{
		Date("KAZT1",2020-N(10098,779));
		Date("KAZT2",2020-N(9400,680));
		};
		Boundary("End_Unit2");

		Label("Evidence of erosion");
		Boundary("Start_Unit3");
		Phase("Unit_3")
		{
		};
		Boundary("End_3");
		Boundary("E1");
		Phase("Unit_4")
		{
		};
		Boundary("Transition_4/5");
		Phase("Unit_5")
		{
		Date("KAZT3",2020-N(9218,707));
		Date("KAZT4",2020-N(10379,799));
		Date("KAZT5",2020-N(9534,707));
		};
		Boundary("End_5");
		Boundary("E2");
		Phase("Unit_7")
		{
		};
		Boundary("End_7");
		Label("Evidence of erosion");
		Boundary("Start_8");
		Phase("Unit_8")
		{
		Date("KAZT6",2020-N(1541,128));
		};
		Boundary("End_8");
		};
		};

E	Models only the dated units, placing sequential boundaries (i.e. hiatuses) between them.	// E
		Plot()
		{
		Sequence()
		{
		Boundary("Start_2");
		Phase("Unit_2")
		{
		Date("KAZT1",2020-N(10098,779));
		Date("KAZT2",2020-N(9400,680));
		};
		Boundary("End_Unit2");
		Date("E1");
		Boundary("Start_Unit5");
		Phase("Unit_5")
		{
		Date("KAZT3",2020-N(9218,707));
		Date("KAZT4",2020-N(10379,799));
		Date("KAZT5",2020-N(9534,707));
		};
		Boundary("End_Unit5");
		Date("E2");
		Boundary("Start_8");
		Phase("Unit_8")

		{
		Date("KAZT6",2020-N(1541,128));
		};
		Boundary("End_8");
		};
		};

2.7.4. Scarp Offsets: Summary, Profiles and Site Maps

2.7.4.1. Summary of Sites

Table 2.7-10. Site summaries. *Data from Grützner et al (2017b). **Data from Amey et al. (2021).

Site	Highest resolution data set	Largest scarp offset (m)	Smallest scarp offset (m)	Notes	Figures
N1	Drone DEM	~ 13.7 – 14.5	~ 2.3 – 2.9	Distinct scarp heights in three generations of fan (T2 – T4). Scarps truncated by youngest fan (T1) which is undeformed. Smallest scarp in a T2 fan, but another T2 fan has slightly larger 3.1 – 4.4 m scarp.	Figure 2.3-2, Appendix Figure 2.7-13
N2	Drone DEM	~ 3.0 – 7.0	0.7 ± 0.1	Highly variable scarp heights within fans inferred to be of a single generation. Highly curved fault trace. Some folding. Youngest fan (T1) undeformed. Smallest scarp in a T2 fan might have formed in MRE, but further along strike the same T2 fan has another slightly larger ~1.3– 1.7 m scarp.	Figure 2.3-3, Appendix Figure 2.7-14
N3	Drone DEM*	~1.9 – 2.5	~1.9 – 2.5	Corresponds to site S1 from Grützner et al (2017b). Scarp truncated by younger fan.	Figure 2.3-4, Appendix Figure 2.7-15
N4	Drone DEM*	7.7 ± 1.2	7.7 ± 1.2	Corresponds to site S2 from Grützner et al (2017b). One scarp is a composite of ~7.1 m and ~0.7 m offsets, the other is a single scarp of ~7.7 m. We quote the measurement of the single offset scarp to capture large measurement uncertainty. Scarp is truncated by a younger fan with active river channel.	Figure 2.3-4, Appendix Figure 2.7-15
N5	Drone DEM	~ 8.5 ± 1.0	~ 0.8 – 1	Discontinuous scarps with three distinct scarp heights near Beriktas. No distinct fan surfaces are discernible. Smallest scarp might have formed in MRE.	Figure 2.3-5, Appendix Figure 2.7-16
N6	Copernicus GLO-30 DEM	NA	NA	Ridge with at least ~34 m of offset between the two sides.	Figure 2.3-8
N7	Copernicus GLO-30 DEM	57.3 ± 4.2	9.0 ± 3.3	Large scarps in alluvial fans covered in kurgans near Pokrovka. Scarps truncated by youngest fans.	Figure 2.3-9, Appendix Figure 2.7-17, Figure 2.3-9
N8	Copernicus GLO-30 DEM	118.1 ± 14.1	16.2 ± 1.3	Large scarps in heavily incised fans near Talap and Kastek. Scarps truncated by	Figure 2.3-11

				younger fans. Youngest three fan generations appear to be undeformed.	
N9	Drone DEM	~1.3 – 2.6	~1.3 – 2.6	Scarps near Kyzylasker (formerly Fabrichny) first estimated as ~1 m at site S3 in Grützner et al (2017b). Scarp offset measurements across two fans are highly variable over short distances along strike – this might be due to anthropogenic modification or channels we could not identify. Two younger fan generations are undeformed as well as the modern stream bed. Scarps are slightly larger than original ~1 m estimate.	Figure 2.3-13, Appendix Figure 2.7-18
N10	GPS**	2.2 ± 0.5	0.7 ± 0.5	Scarp in the Almaty alluvial fan running through the city. Amey et al. (2021) measured offsets in four road profiles (2.2 ± 0.5 m, 1.6 ± 0.4 m, 0.7 ± 0.5 m and 1.3 ± 0.1 m) spaced at least 700 m apart with GPS. ~0.7 m scarp might represent MRE.	Figure 2.3-16
N11	GPS, Pléiades DEM	8.4 ± 0.3	0.5 ± 0.3	Offsets measured on the western side of the Talgar fan. The 0.5 ± 0.3 m scarp was measured in the field with dGPS, might have formed in MRE. In Pléiades DEMs we measure ~2.2 – 3.6 m across the same scarp.	Figure 2.3-17, Figure 2.3-18.
N12	GPS	15.4 ± 5.4 (total across composite scarp)	4.7 ± 0.4	Scarps within Talgar town identified in dGPS driving survey. ~30 m high mound on hanging wall attests to tectonic origin.	Figure 2.3-17, Figure 2.3-20
N13	Drone DEM	~2.3 – 4.1	~1.6 – 2.9	Scarps near Kainazar at site modified by building of road and ploughing of field. Interpreted as fault scarps but cannot rule out a non-tectonic origin.	Figure 2.3-20, Figure 2.7-20
N14	Drone DEM*	12.7 ± 0.2	~4.7 – 4.9	Scarps in stream terraces, re-measured from Grützner et al (2017b) site S6.	Figure 2.7-21
N15	Pléiades DEM	33.0 ± 1.0	~3.0 – 5.1	Offsets in stream valley, smallest measured scarp is 3.0 ± 0.5 m but we are uncertain of its tectonic origin so we quote the range of values for the smallest set of scarps. We were unable to map a coherent suite of terraces with the available data, a field visit is needed for more clarity.	Figure 2.3-21
N16	Pléiades DEM	21.1 ± 0.4	8.7 ± 1.7	Breaks in slope in surface between two younger fans. It is possible these are hydrological features but their stepped appearance supports a tectonic interpretation.	Figure 2.3-23
N17	Drone DEM	~0.9 – 1.2	~0.2 – 0.6	Small scarps within fields near Taukaraturyk. Scarps have been modified and obscured by anthropogenic activity as well as erosion by fan channels. Smallest scarp might have formed in the MRE.	Figure 2.3-24, Appendix Figure 2.7-23
N18	Drone DEM	52.3 ± 0.4	3.5 ± 0.5	Scarps in suite of terraces reassessed and re-measured from Grützner et al (2017b) site S7	Appendix Figure 2.7-25
N19	Drone DEM	~5.7 – 7.7	~0.3 – 0.6	Trench site to the south of the Big Almaty	Figure 2.3-26,

		(composite scarp)		Canal. Smallest scarps measured from drone DEM is probably the MRE offset and is slightly smaller than the MRE uplift measured in trench which is ~0.8 m.	Appendix Figure 2.7-26
N20	Pléiades DEM	40.4 ± 0.8	13.6 ± 1.5	Large scarp preserved in terraces between two deeply incised river valleys. Some additional uncertainty in 13.6 ± 1.5 m measurement because the footwall may have been modified.	Figure 2.3-27
N21	Drone DEM	~22.4 – 23.6	~2.2. – 2.9	Scarps in three generations of fan surface. Footwall of largest scarp may have been modified since its formation.	Figure 2.3-28, Appendix Figure 2.7-27
N22	Drone DEM	20.7 ± 0.3	~0.4 – 0.7	Re-assessment of site S11 from Grützner et al. (2017b) with new drone data. Our new results are broadly consistent with the original measurements. Scarps deform four generations of fan, with a general trend of larger offsets occupying apparently older fans.	Figure 2.3-29, Figure 2.3-30, Appendix Figure 2.7-28, Appendix Figure 2.7-29, Appendix Figure 2.7-30
N23	Pléiades DEM	~6.2 – 8.5	~6.2 – 8.5	Curved scarp.	Figure 2.3-31
N24	Copernicus GLO-30 DEM	17.6 ± 7.4	17.6 ± 7.4	No Pléiades data available due to cloud cover.	Figure 2.3-31
N25	Drone DEM	17.8 ± 0.4	~0.6 – 1	Three distinct scarp heights in three generations of alluvial fan. Scarps are truncated by a younger fan generation. Smallest scarp might have formed in MRE.	Figure 2.3-32, Appendix Figure 2.7-31
N26	Drone DEM	~14.0 – 21.1	~1.3 – 3.6	Smallest scarp has curved fault trace. Scarps occupy two oldest generations of fan and are truncated by the two youngest which are undeformed.	Figure 2.3-34, Appendix Figure 2.7-32
N27	Pléiades DEM	38.2 ± 3.6	~3.5 – 4.5	~5 km of prominent scarps with offsets varying between ~3.5 – 13.2 m within fans we infer to be of the same generation (T3). Scarps are truncated by two younger generations of fans (T1 & T2), although there is a possible degraded scarp within one T2 surface.	Appendix Figure 2.7-33, Appendix Figure 2.7-34, Appendix Figure 2.7-35
N28	Pléiades DEM	~5.3 – 6.4	~5.3 – 6.4	Short scarp in alluvial fan (T3?) truncated by younger fans and modern drainage.	Appendix Figure 2.7-36
N29	Pléiades DEM	16.7 ± 1.2	4.1 ± 0.5	Scarps in T2 and T3 fans, truncated by younger (T1) fans which are undeformed.	Appendix Figure 2.7-37
N30	Pléiades DEM	~6.6 – 15.7	~6.6 – 15.7	Scarp within what appears to be a single older fan surface, with scarp eroded away in two places by younger channels.	Appendix Figure 2.7-38
N31	Pléiades DEM	~16.5 – 25.5	~2.5 – 4.2	Smallest scarp has curved trace. Scarps in T2 and T3 surfaces which appear to be partially eroded in places by channels. Undeformed T1 wide channels truncate scarps. Uncertain whether largest scarp might be a terrace riser.	Appendix Figure 2.7-39
N32	Copernicus GLO-30 DEM	NA	NA	Scarp in alluvial fan apparent in Google Earth.	Figure 2.7-39
N33	Pléiades DEM	NA	NA	Incised foreland sediments uplifted by tens of metres to ~100 m.	Figure 2.3-36

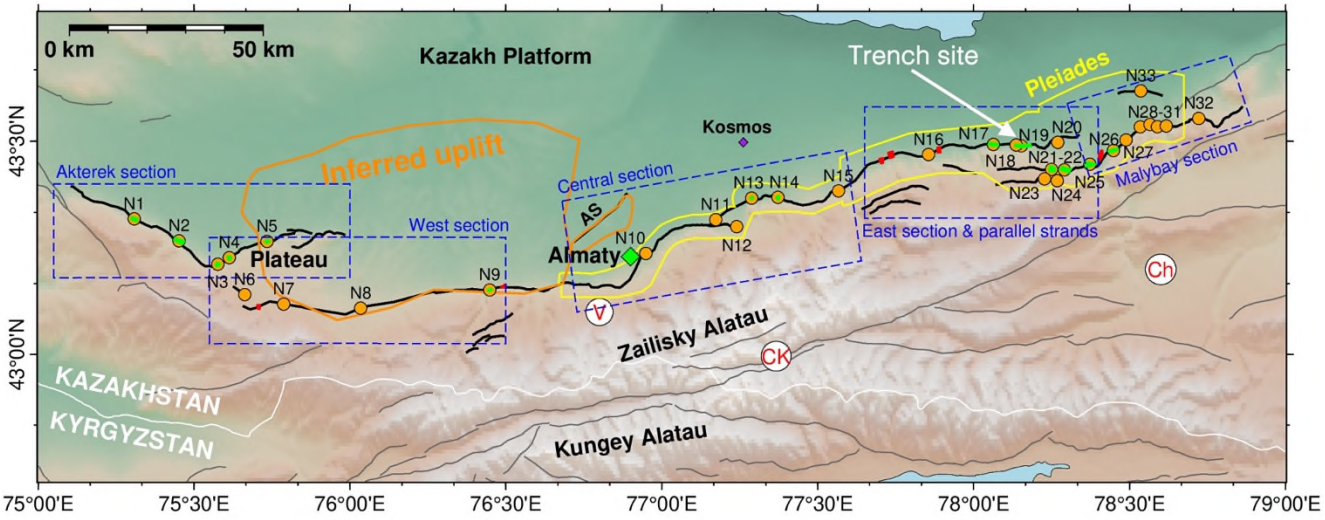

Figure 2.7-12. Scarp site map annotated with additional observations. Symbols and references are as in Figure 2.1-1b with the addition of orange polygons showing areas of inferred uplift. AS = Almaty Splay.

2.7.4.2. Akterek Section

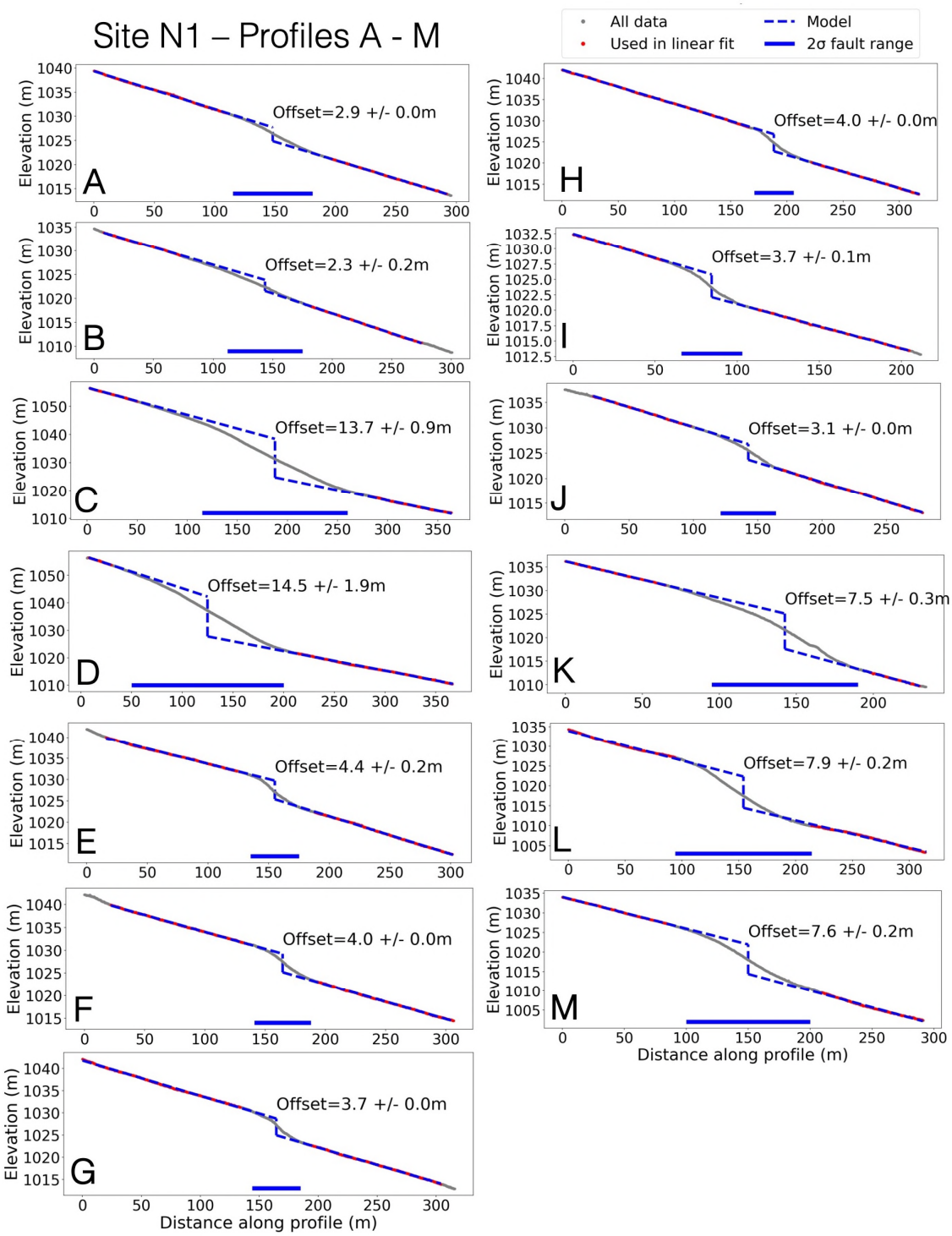

Figure 2.7-13. Vertical offset measurements from site N1 (Figure 2.3-2).

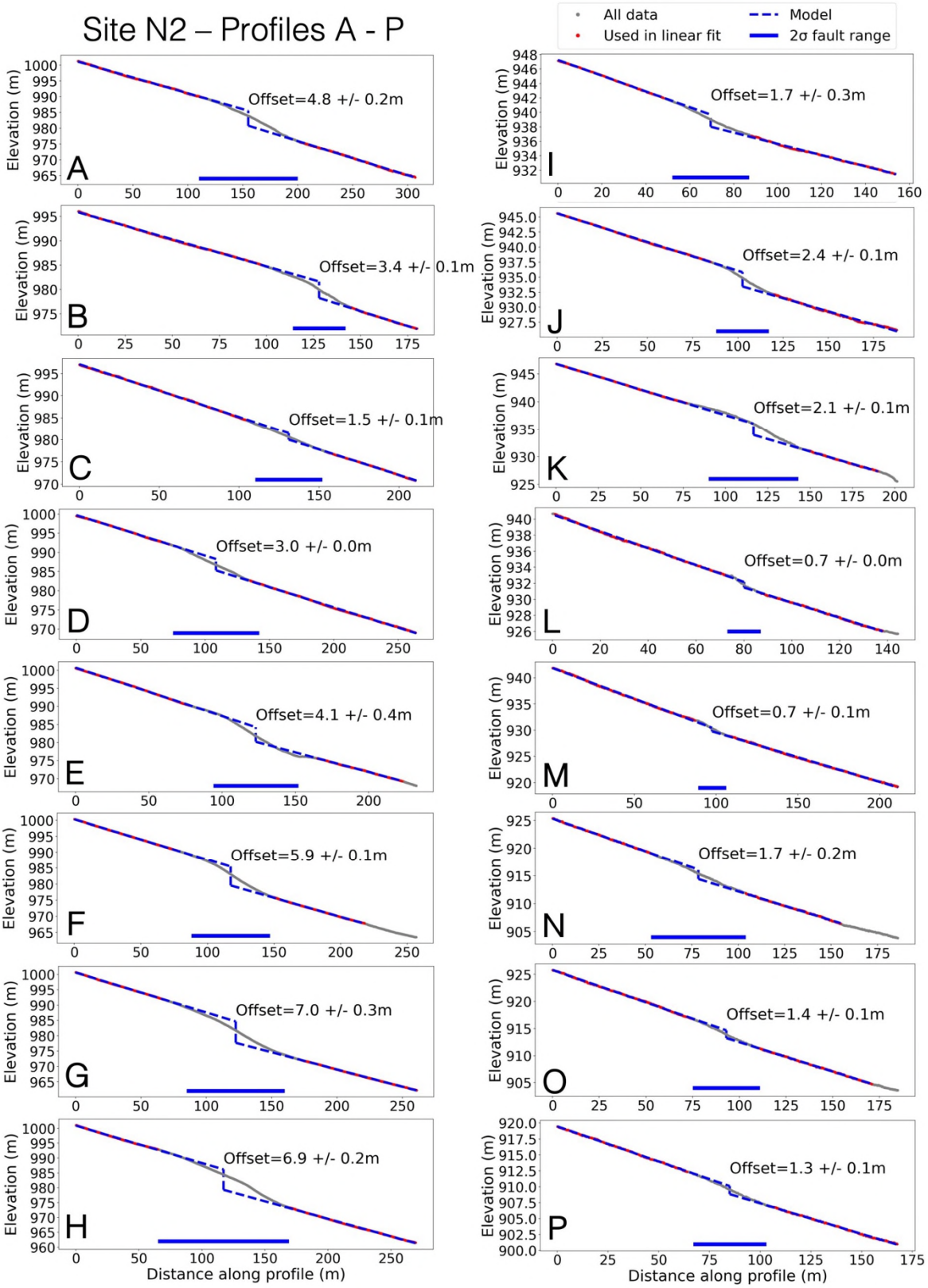

Figure 2.7-14. Vertical offset measurements from site N2 (Figure 2.3-3).

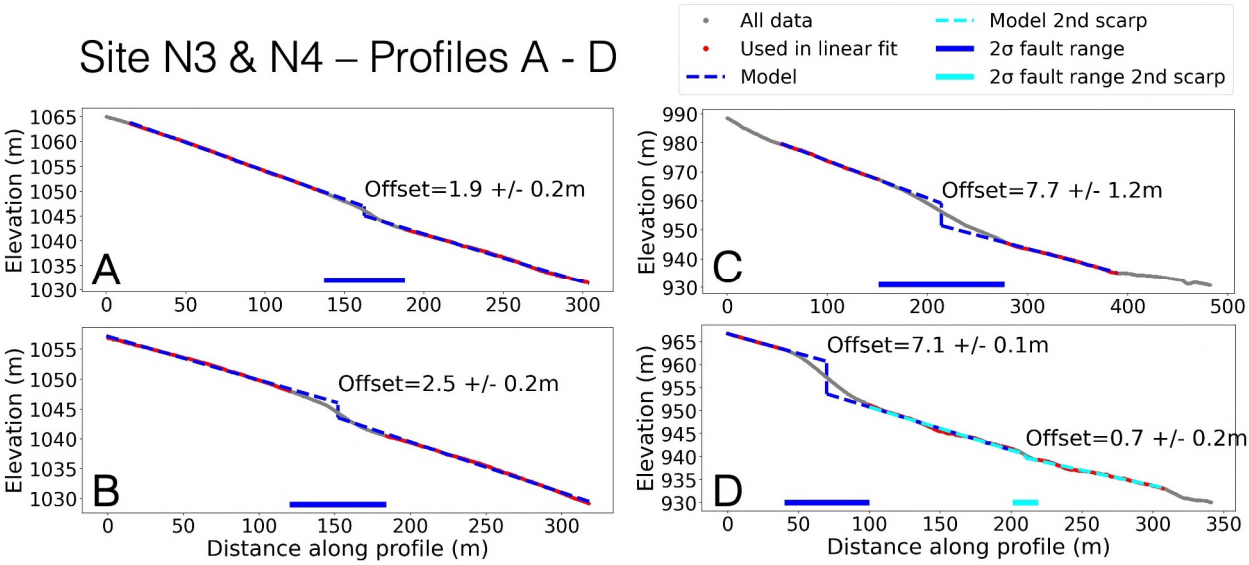

Figure 2.7-15. Vertical offset measurements from sites N3 (A and B) and N4 (C and D), profiles remeasured from Grützner et al. (2017b) sites S1 and S2 (Figure 2.3-4).

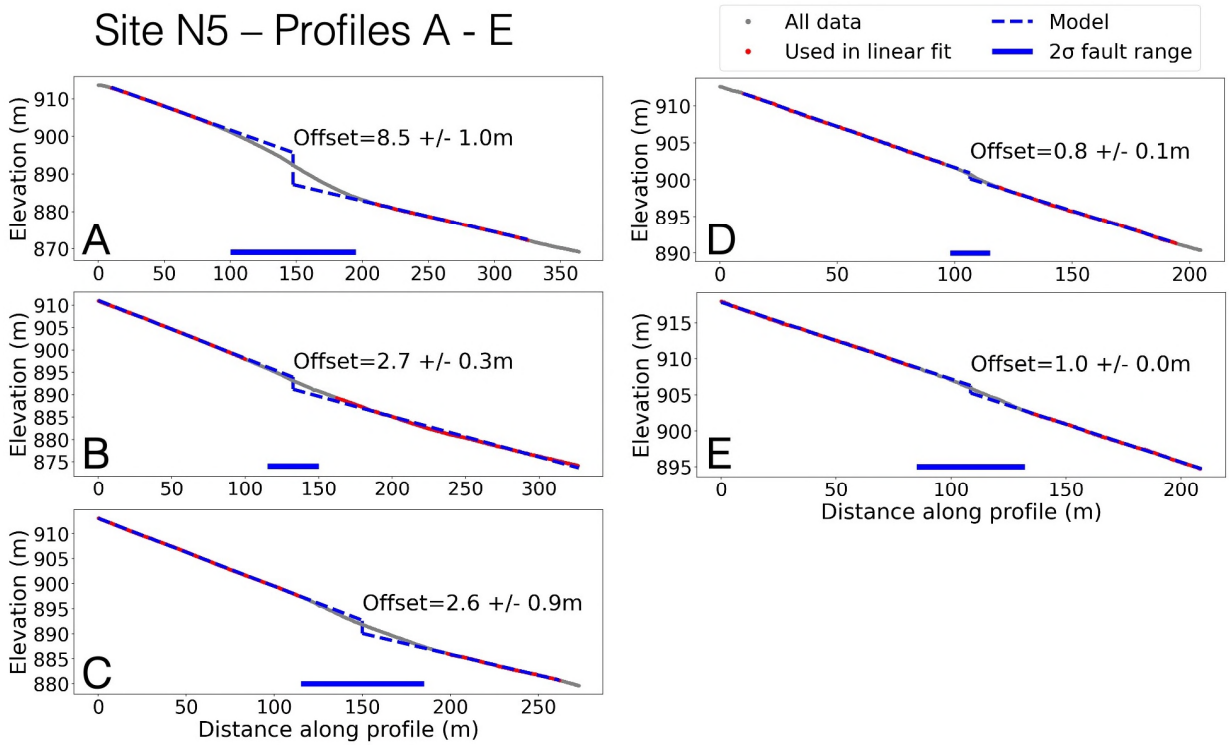

Figure 2.7-16. Vertical offset measurements from site N5 (Figure 2.3-5).

2.7.4.3. West Section

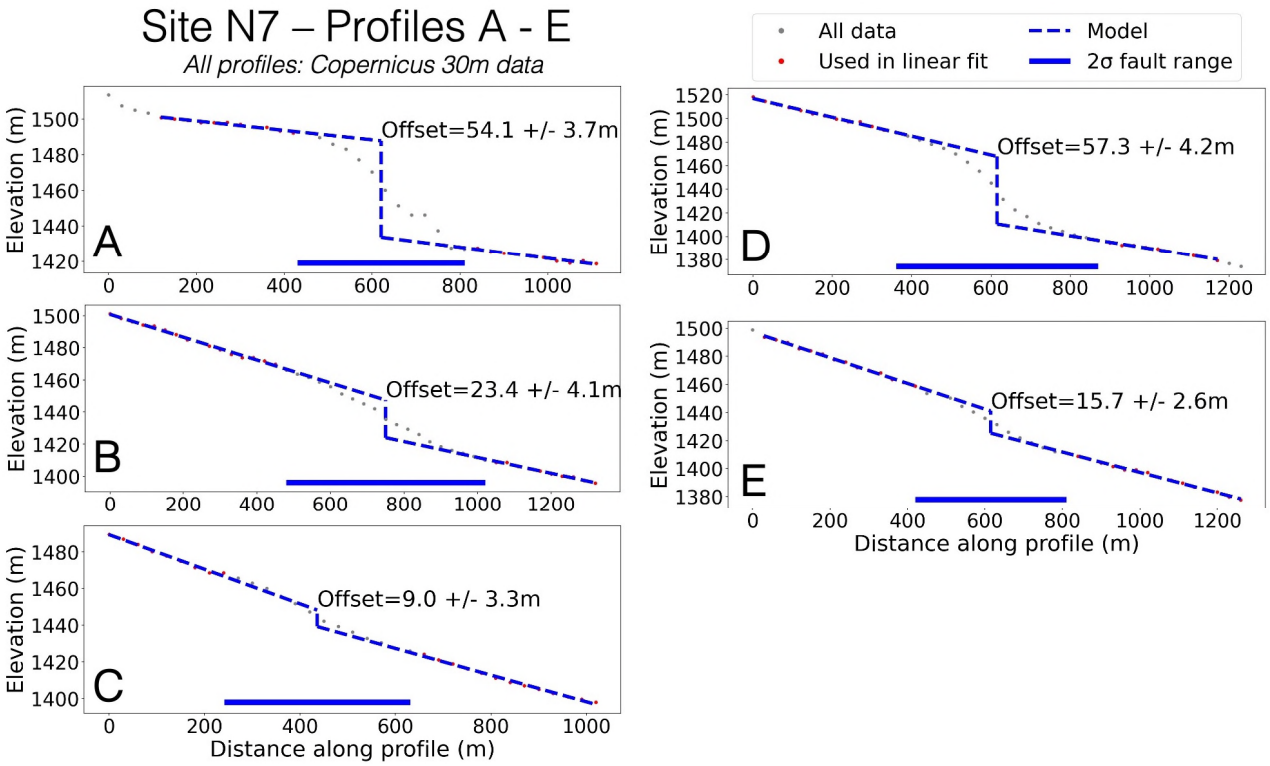

Figure 2.7-17. Vertical offset measurements from site N7 (Figure 2.3-10).

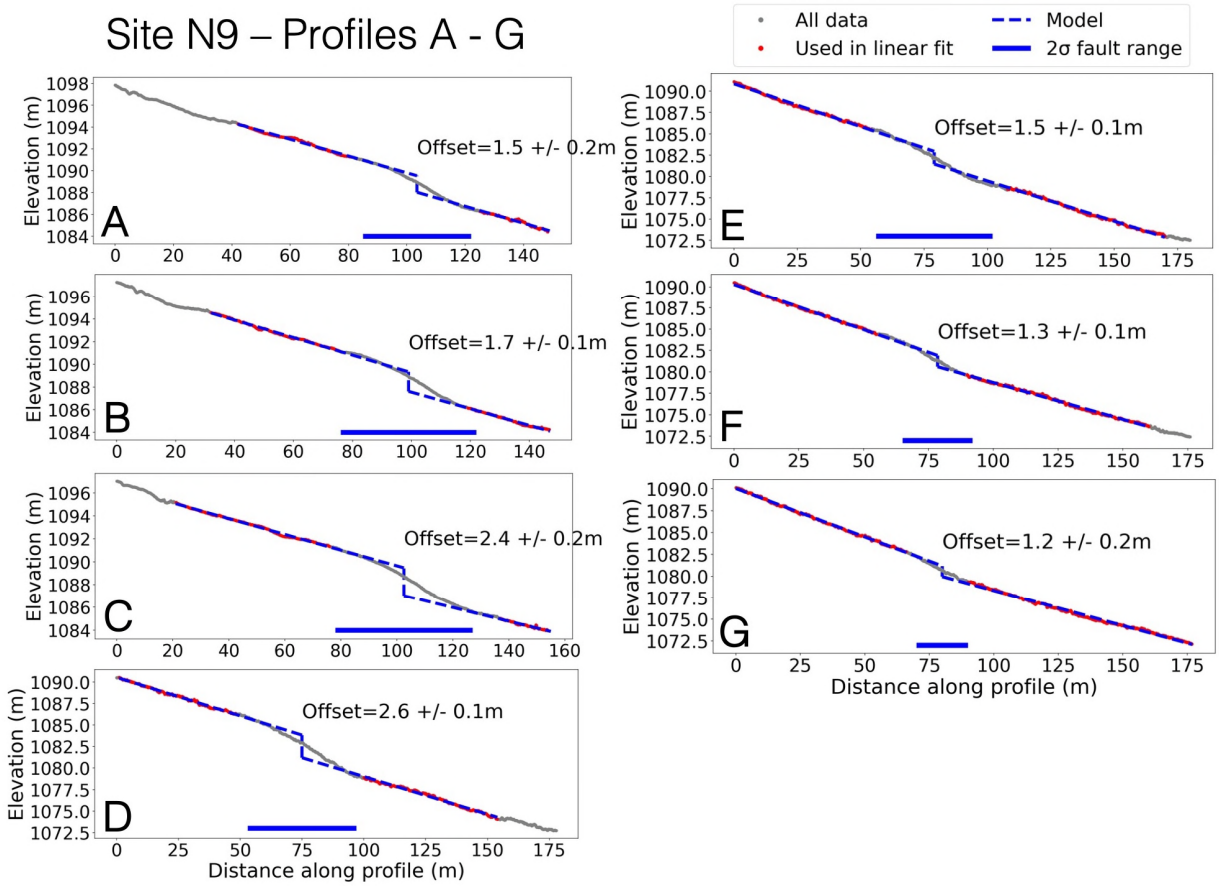

Figure 2.7-18. Vertical offset measurements from site N9 (Figure 2.3-13).

2.7.4.4. Central Section

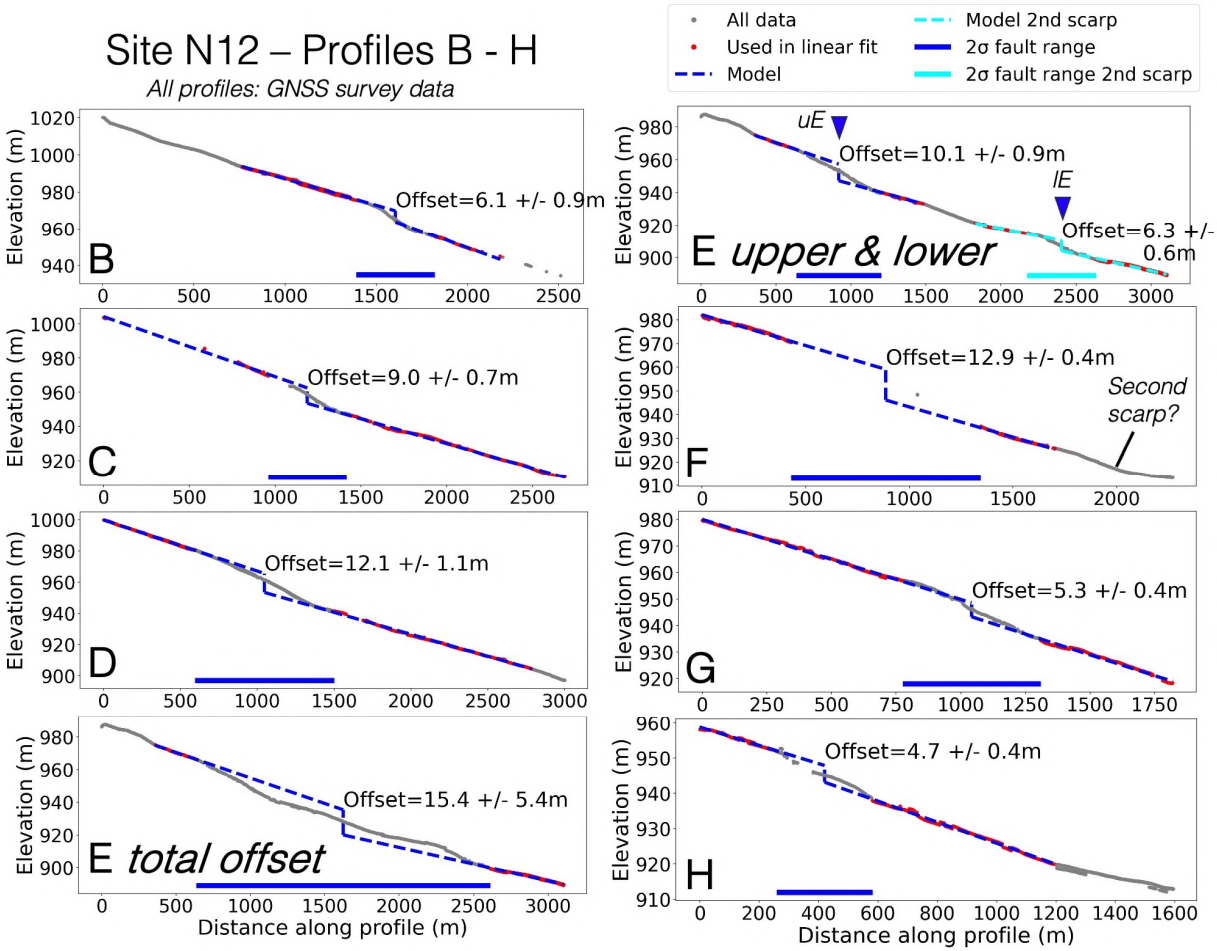

Figure 2.7-19. Vertical offset measurements from site N12 (Figure 2.3-19).

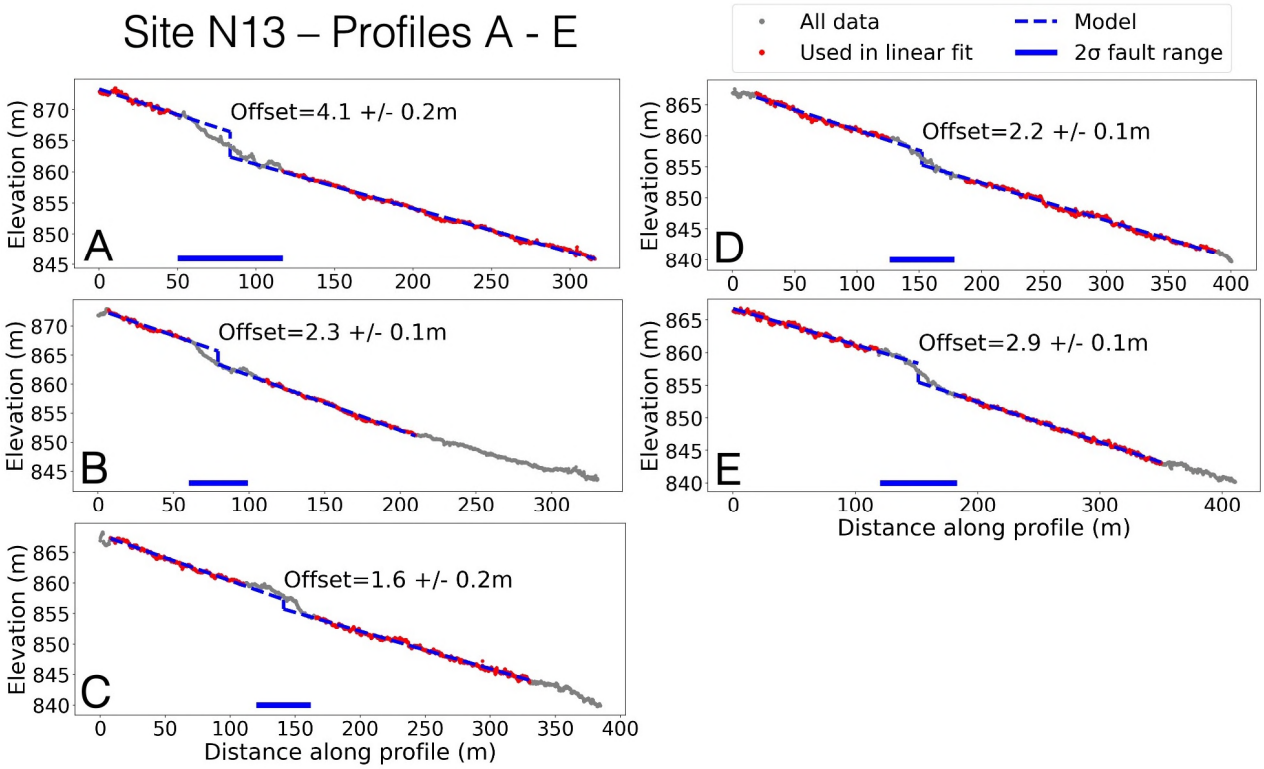

Figure 2.7-20. Vertical offset measurements from site N13 (Figure 2.3-20).

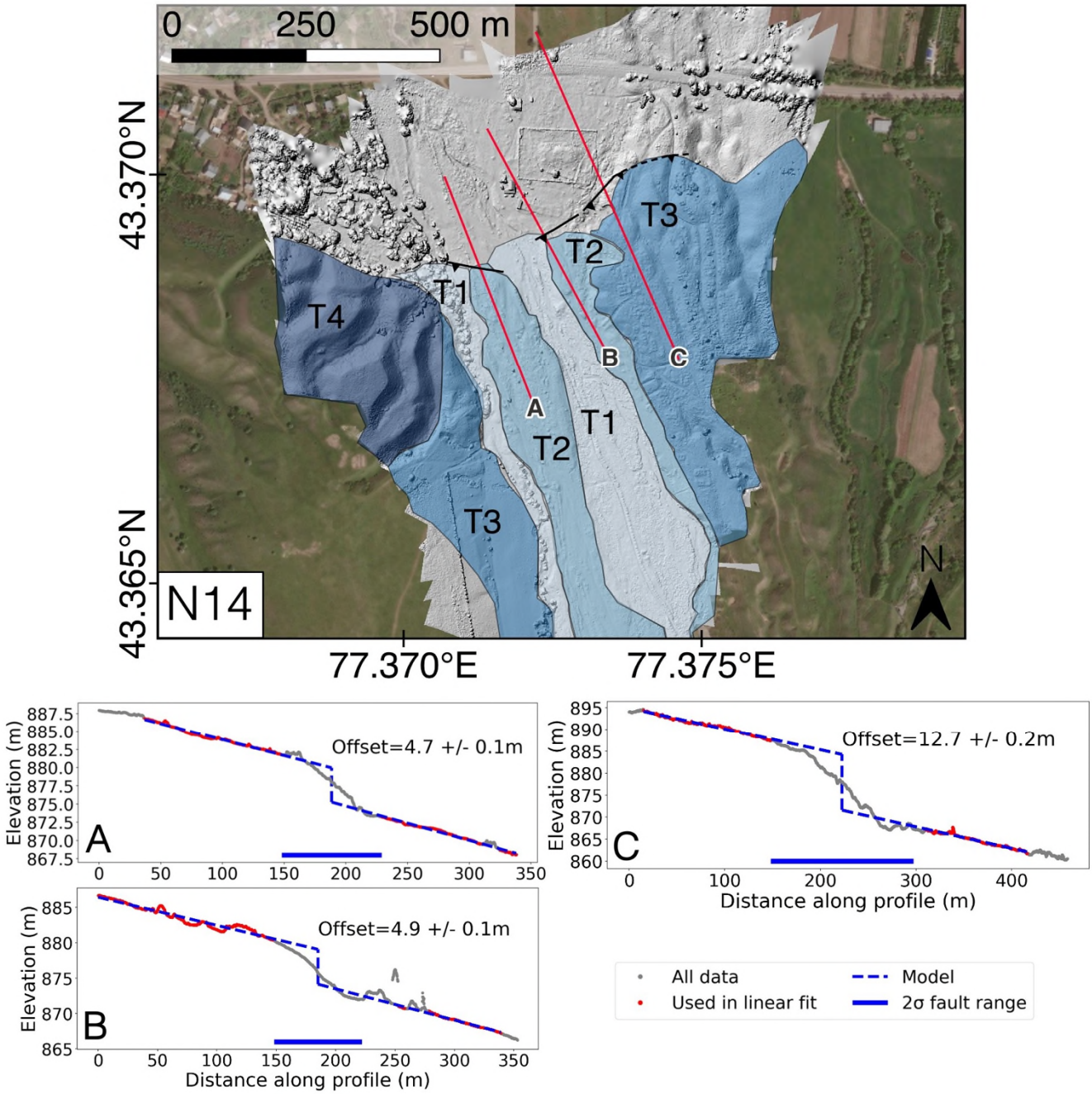

Figure 2.7-21. Site N14 at Rahat, corresponding to site S6 from Grützner et al. (2017b). Top panel: Bing Aerial imagery (2023 TomTom, 2023 Maxar) with hill shade of drone DEM from Grützner et al. (2017b) overlain by terrace mapping (T1 – T4, youngest to oldest; different colours indicate different inferred fan ages, darker = older). Red lines correspond to profiles and vertical offsets in lower panel. Profiles sampled every 15 cm from drone DEM.

2.7.4.5. East Section

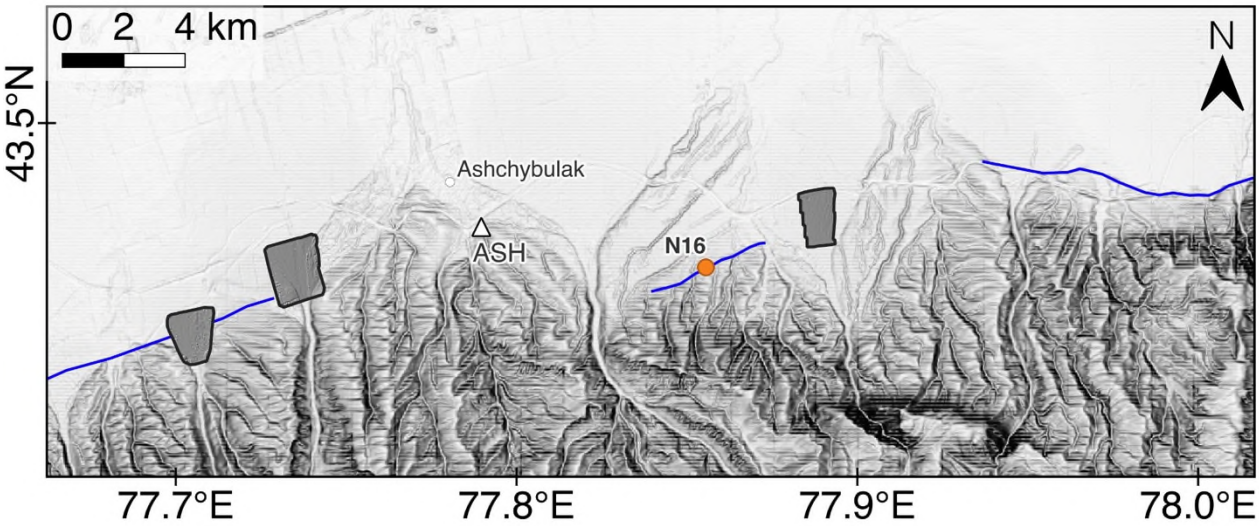

Figure 2.7-22. Map of range front surrounding Ashchybulak showing the locations of three drone surveys of alluvial fans (grey with black outlines) in which we found no evidence of scarps. Background slope map derived from Copernicus GLO-30 DEM, steeper slopes are represented by darker colours. Inferred faults are marked in blue. ASH is the location of a luminescence sampling site from Dave et al. (2023).

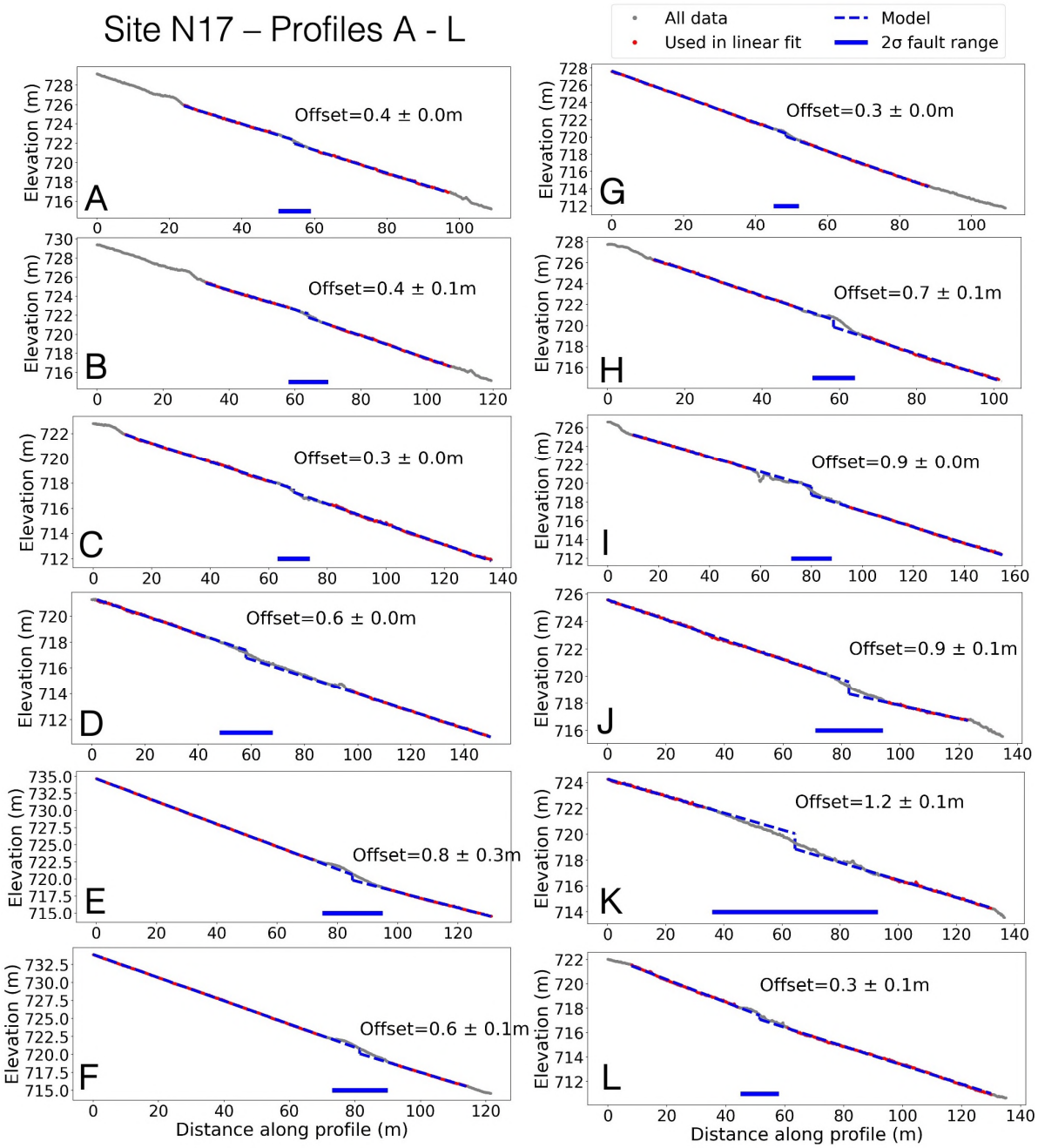

Figure 2.7-23. Vertical offset measurements from site N17 profiles A to L (Figure 2.3-24).

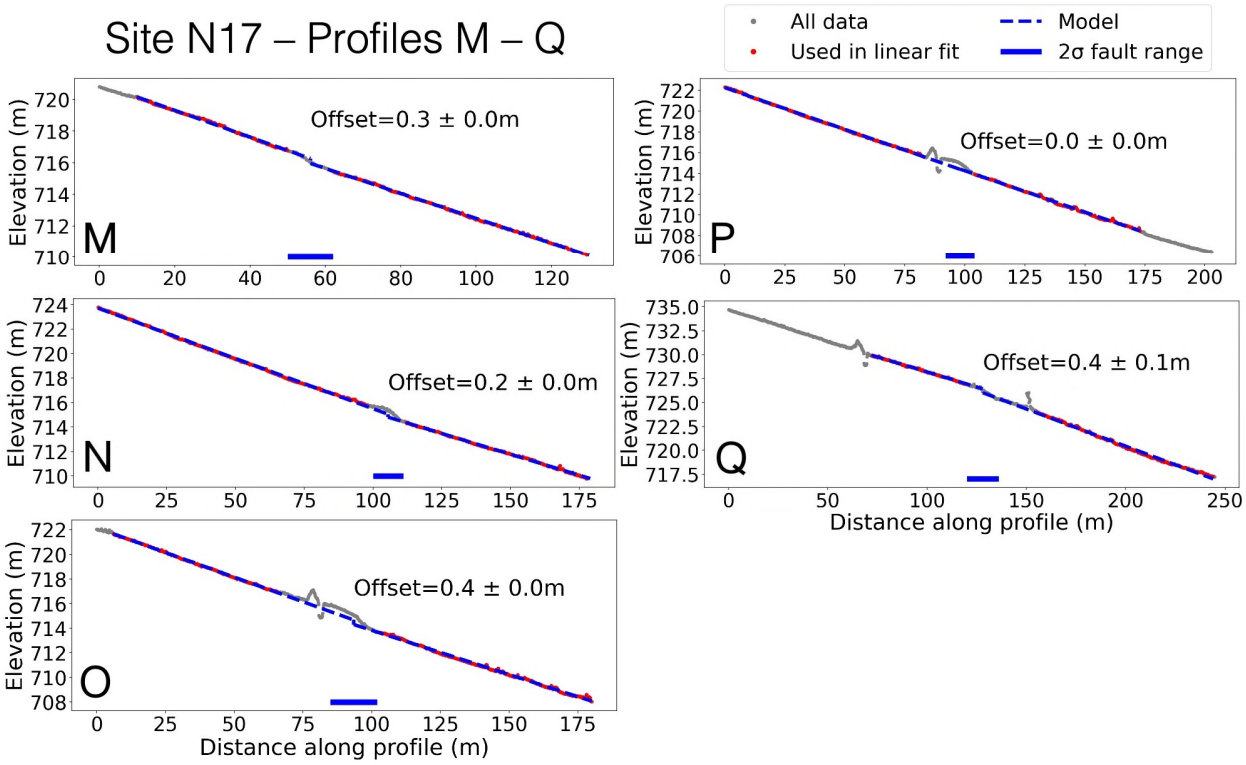

Figure 2.7-24. Vertical offset measurements from site N17 profiles M to Q (Figure 2.3-24).

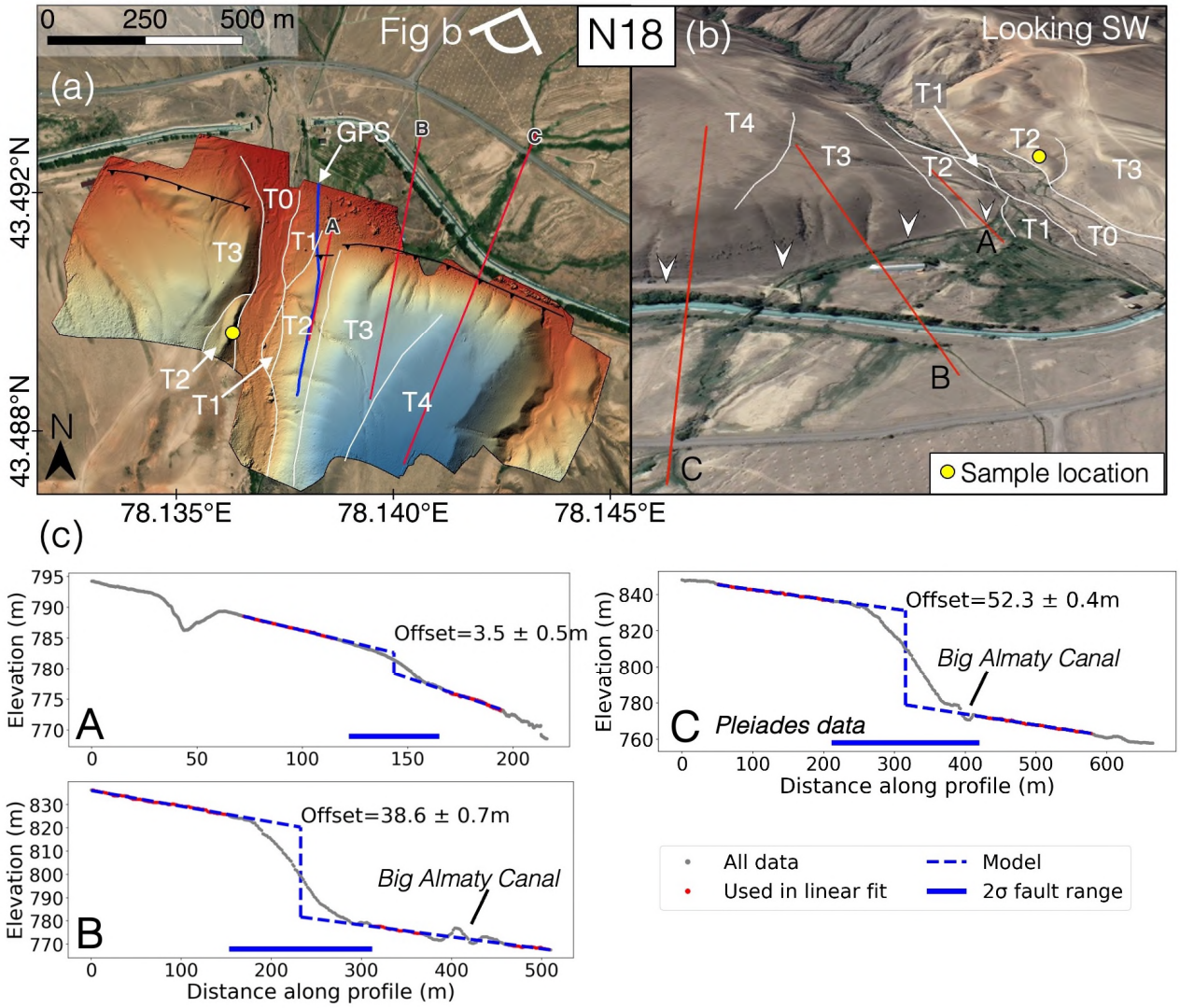

Figure 2.7-25. Koram terraces – reassessment of site S7 from Grützner et al. (2017b). (a) Bing Aerial satellite imagery (2024 TomTom, 2024 Maxar) of the site overlain by a hillshaded DEM collected and processed by Grützner et al. (2017b) . White lines show approximate locations of terrace risers between four terraces (T1 to T4) and the modern river bed (T0). Blue line shows the location of the eastern T2 GPS profile from Grützner et al. (2017b). (b) satellite imagery overlain on topography from Google Earth (2023 Maxar Technologies, Landsat/Copernicus, 2023 Airbus), at 1.10 km eye altitude, and looking southwest. Fault scarp marked by white arrows, labelled red lines show profiles. White lines are approximate boundaries of river terraces. Yellow circle shows approximate sampling location for the samples taken in Grützner et al. (2017b). (c) Scarp profiles. Profile A and B are measured from the drone-derived DEM sampled every 15 cm, whilst C is measured from Pléiades-derived DEM sampled every 1.5 m.

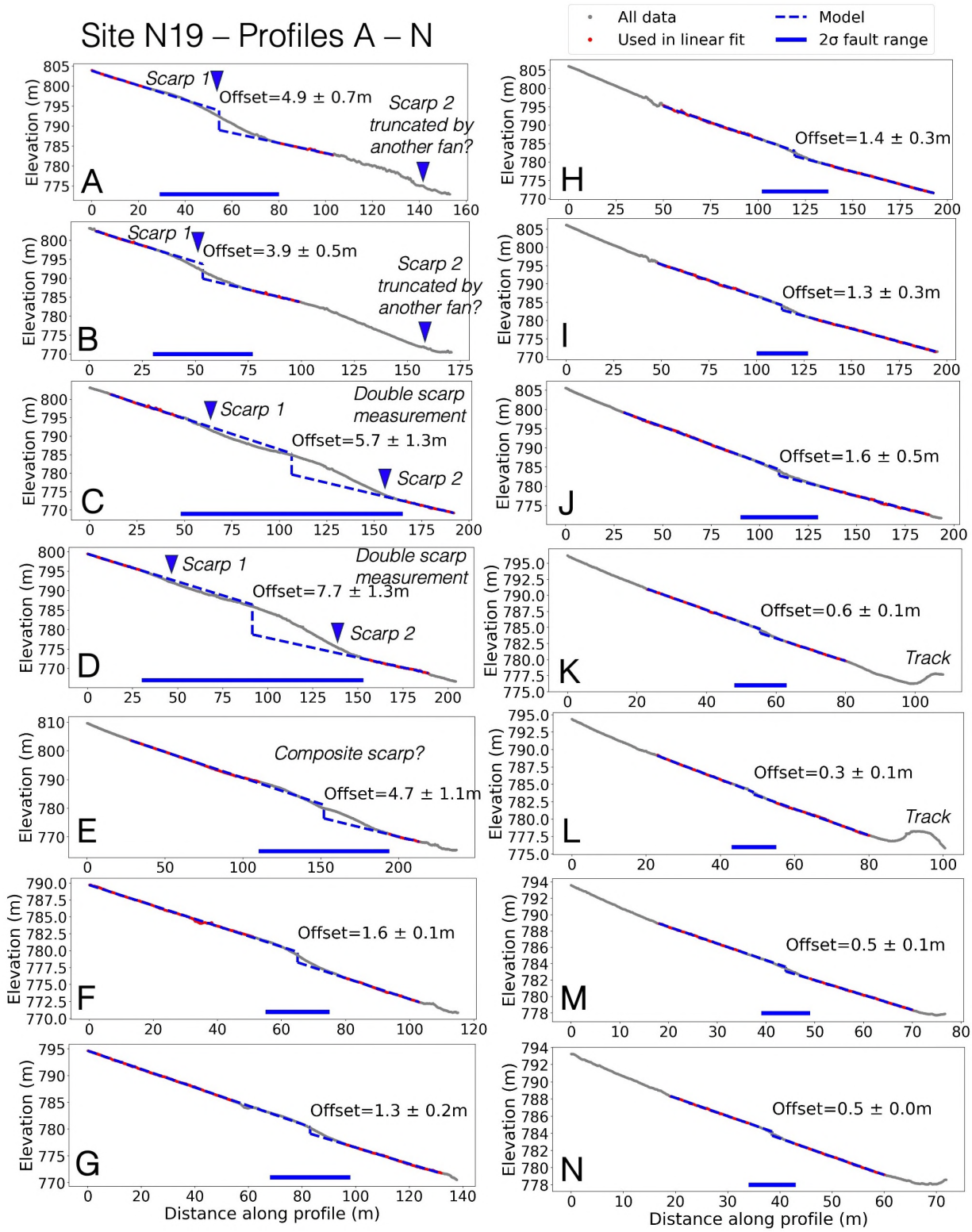

Figure 2.7-26. Vertical offset measurements from site N19 (Figure 2.3-26).

2.7.4.6. Parallel Strands

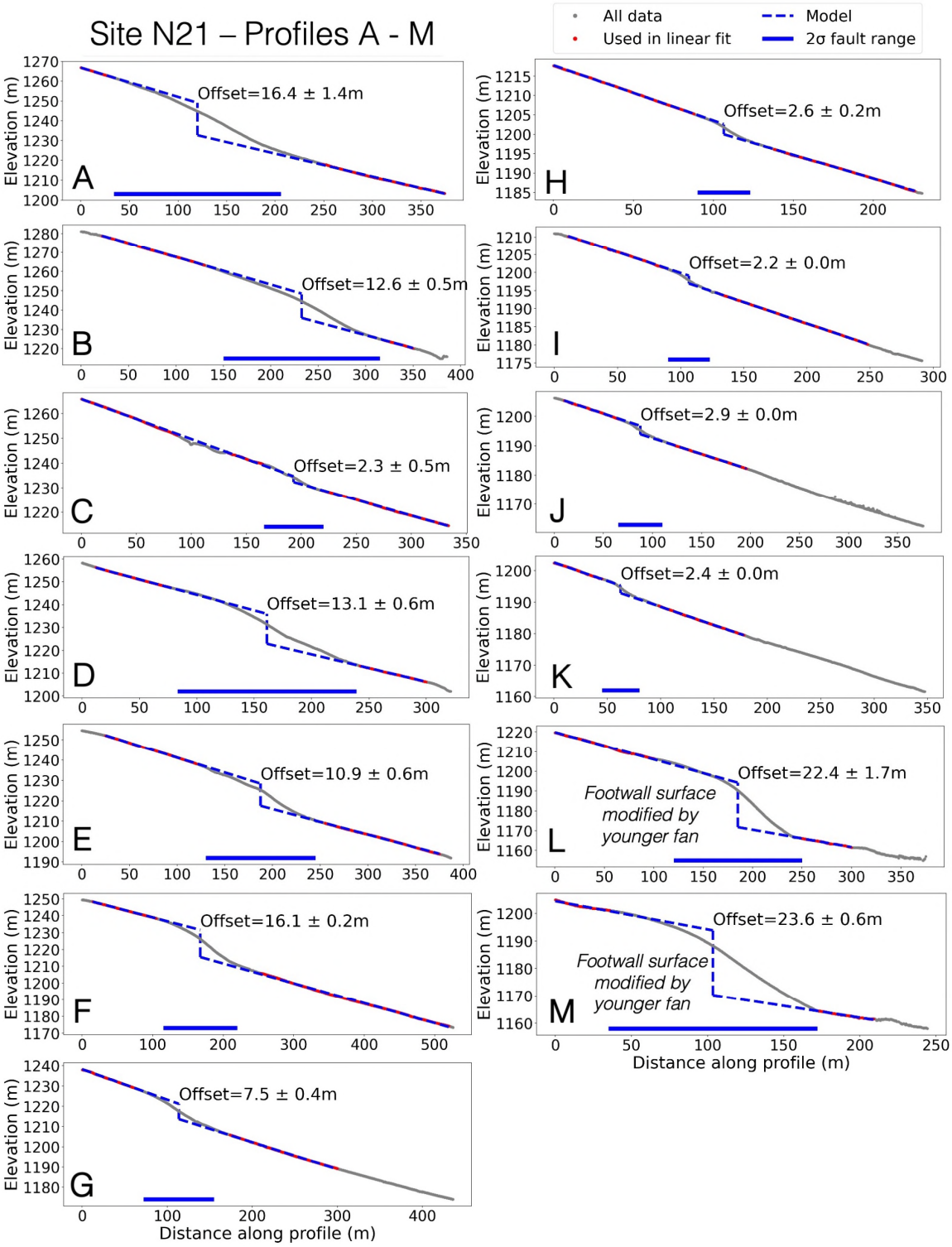

Figure 2.7-27. Vertical offset measurements for site N21 (Figure 2.3-28).

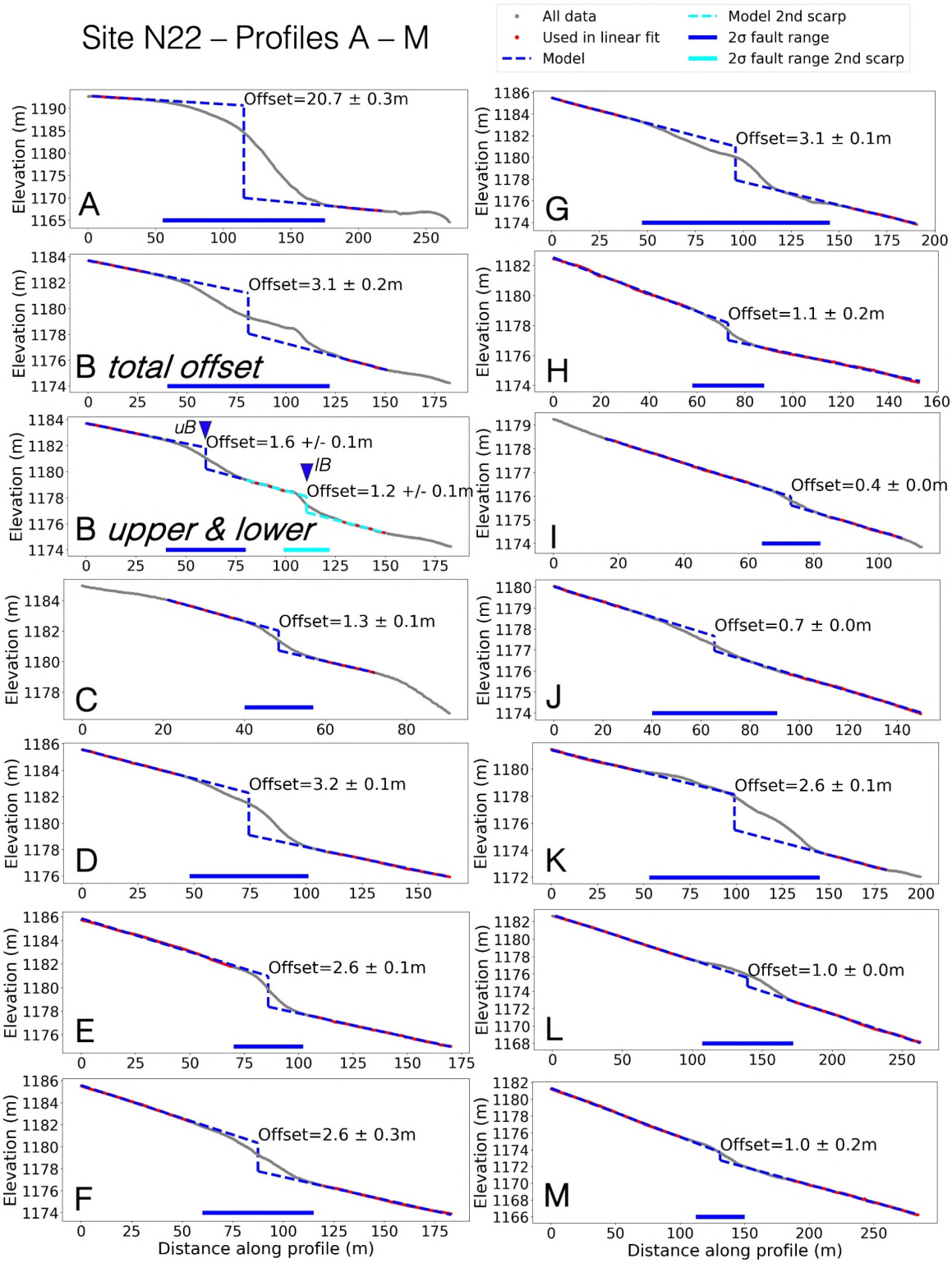

Figure 2.7-28. Vertical offset measurements from site N22 profiles A to M (Figure 2.3-29).

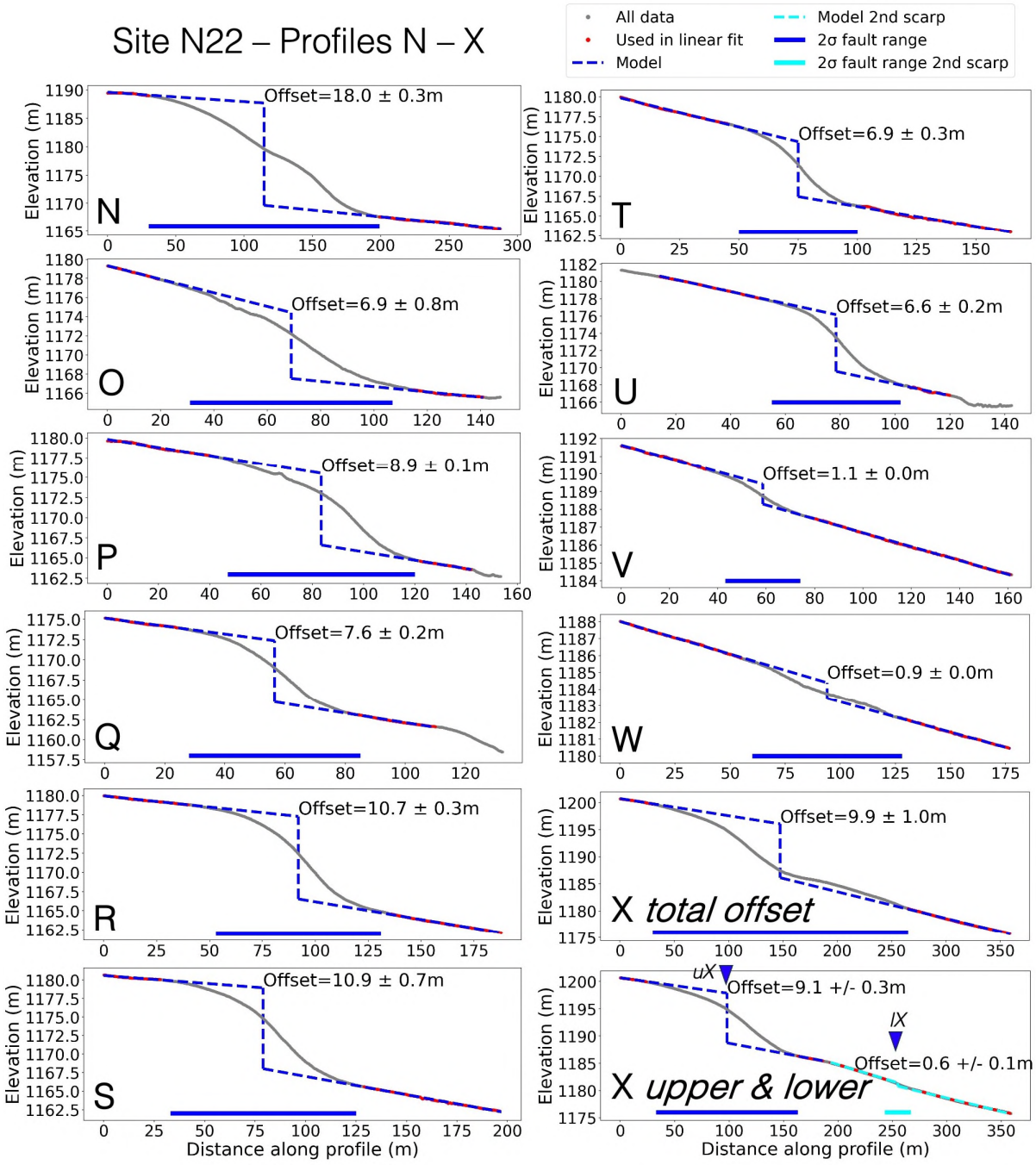

Figure 2.7-29. Vertical offset measurements from site N22 profiles N to X (Figure 2.3-29).

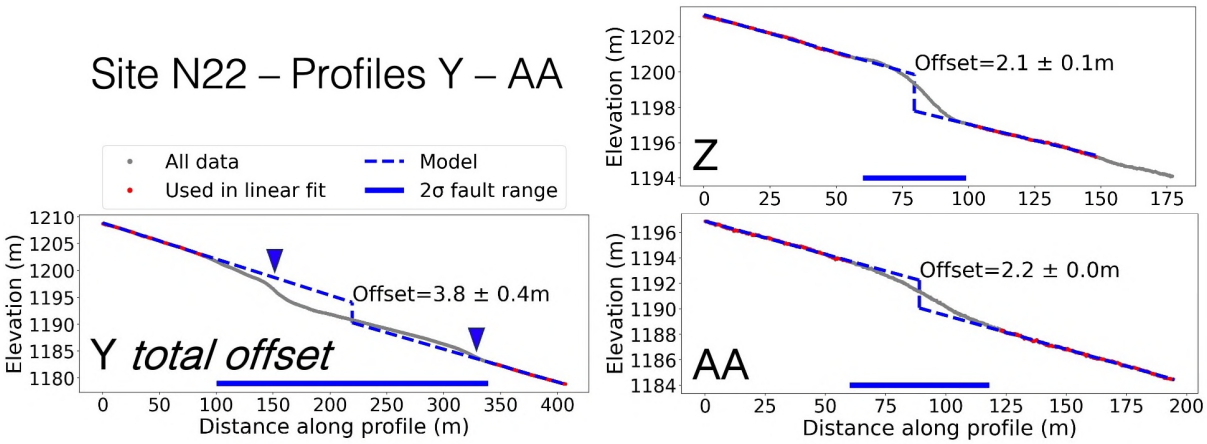

Figure 2.7-30. Vertical offset measurements from site N22 profiles Y to AA (Figure 2.3-29).

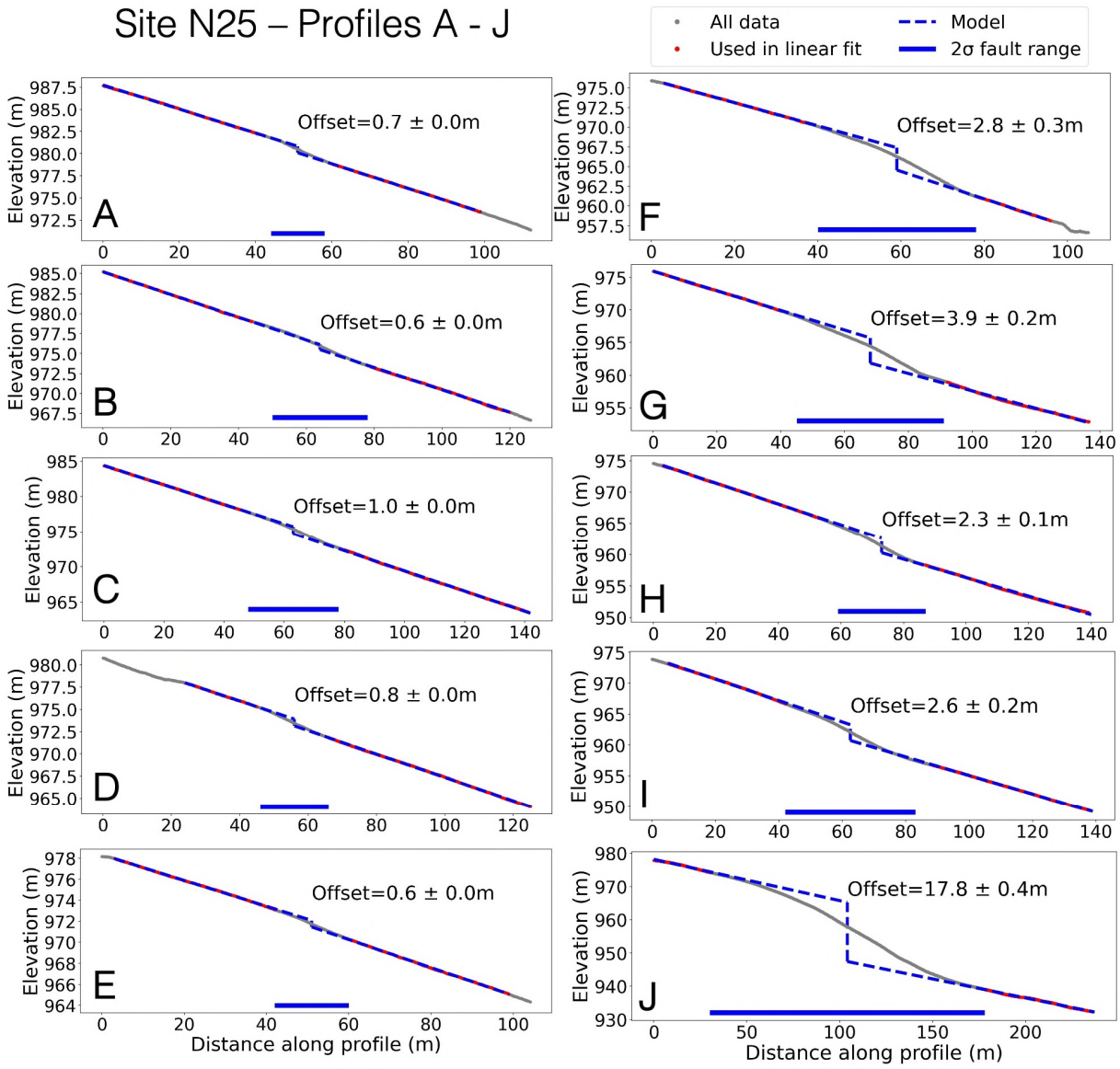

Figure 2.7-31. Vertical offset measurements from site N25 (Figure 2.3-32).

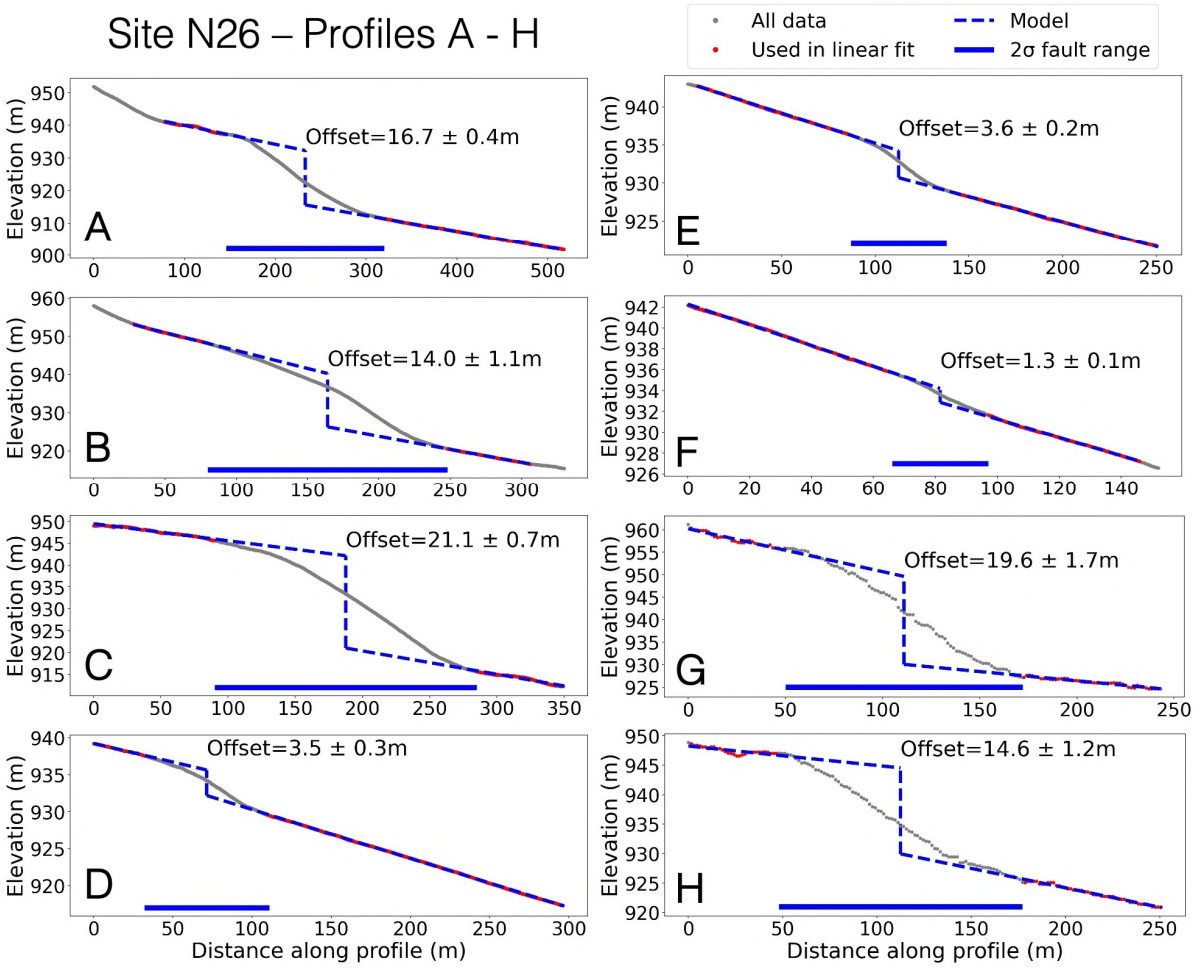

Figure 2.7-32. Vertical offset measurements from site N26 (Figure 2.3-34).

2.7.4.7. Malybay Section

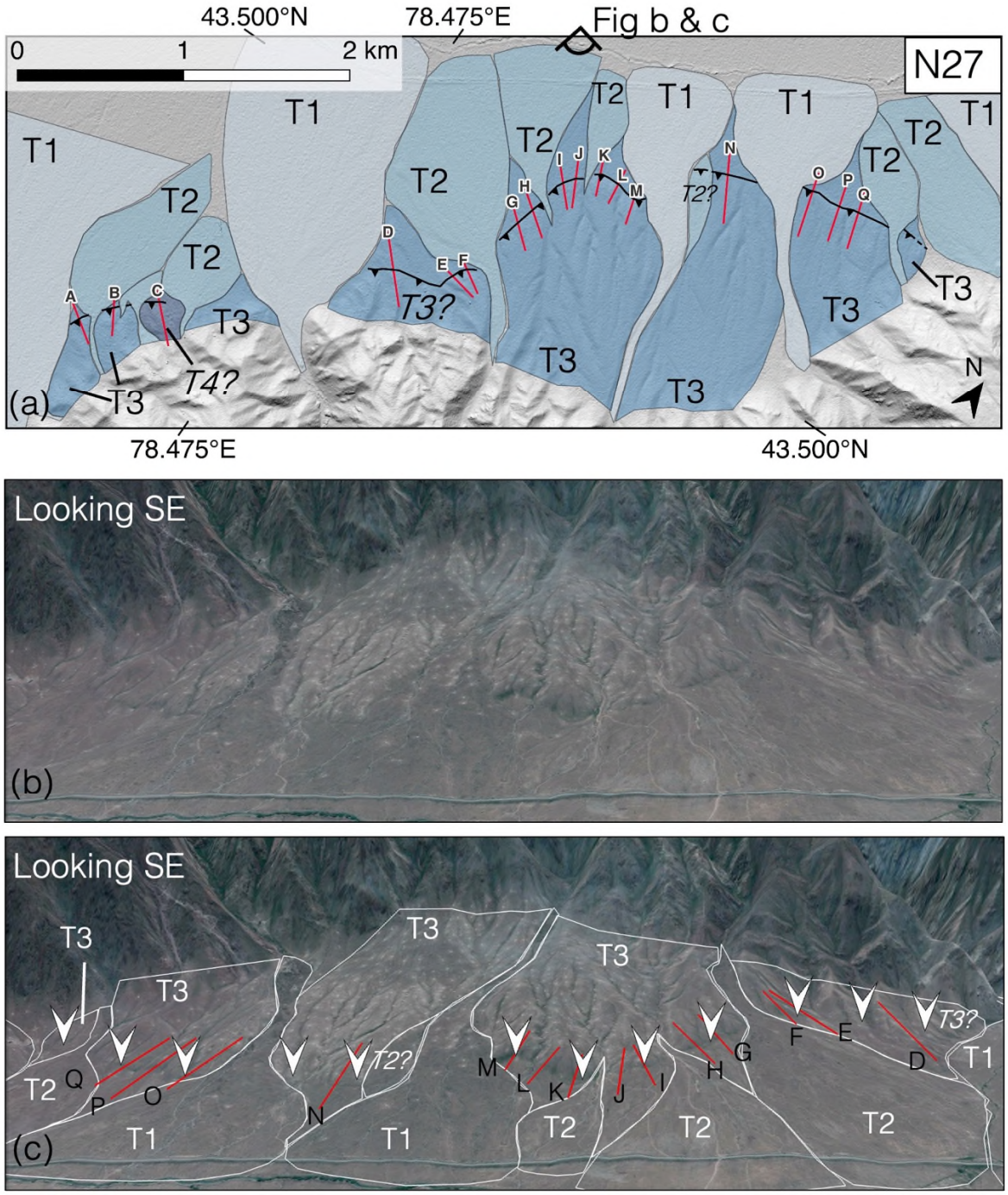

Figure 2.7-33. Site N27. (a) Hill-shaded Pléiades-derived DEM with scarp profiles in red corresponding to Appendix Figure 2.7-34 and Appendix Figure 2.7-35. Four distinct generations of alluvial fans are mapped (T1-T4, youngest to oldest; different colours indicate different inferred fan ages, darker = older). (b) Satellite imagery overlain on 3 x exaggerated topography from Google Earth (Landsat/Copernicus, 2023 Maxar Technologies), at 2.93 km eye altitude, and looking southwest. (c) Imagery from b overlain with fan mapping in white and profile lines in red. White arrows mark scarps.

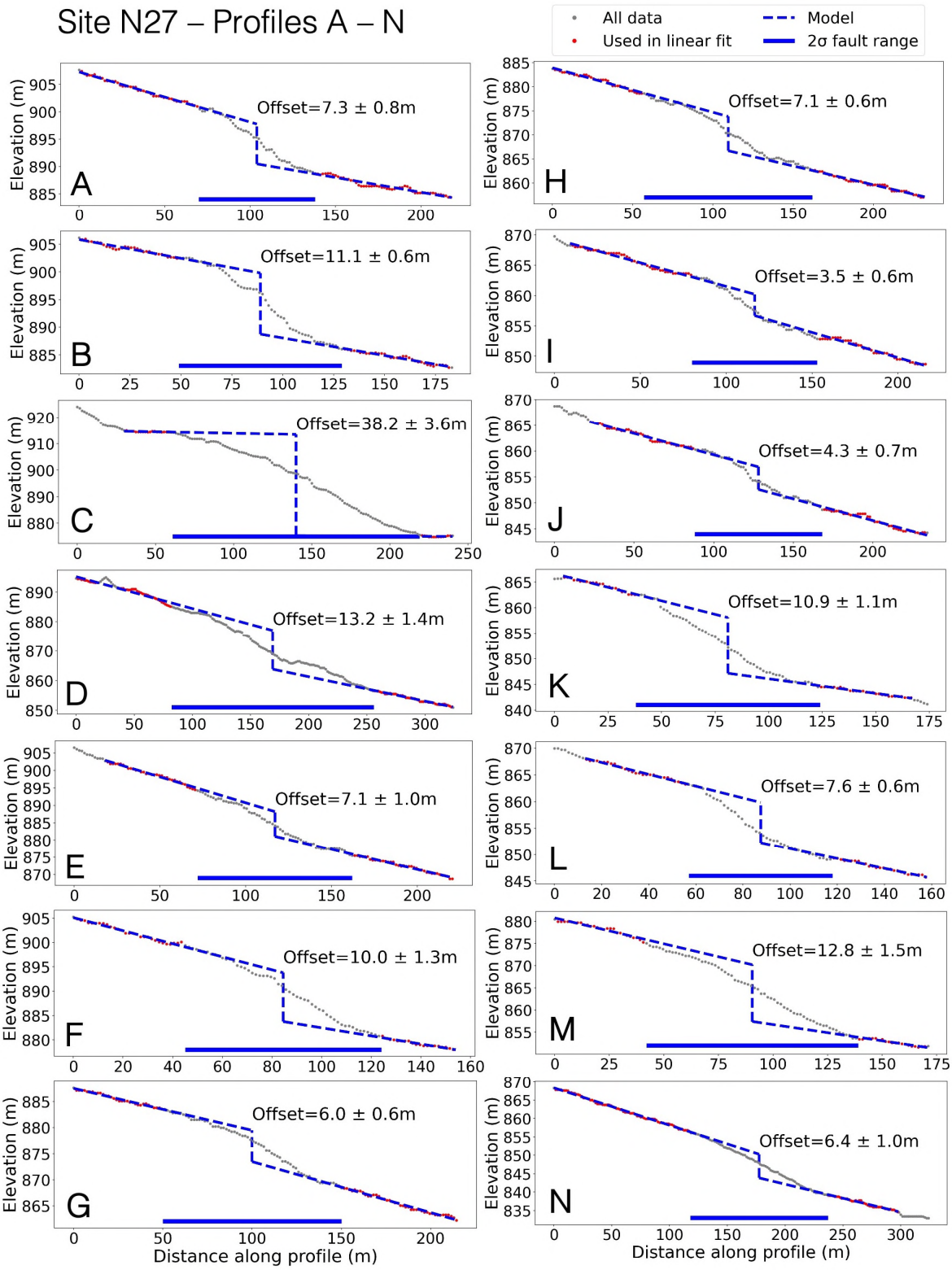

Figure 2.7-34. Vertical offset measurements from site N27, profiles A to N (Appendix Figure 2.7-33).

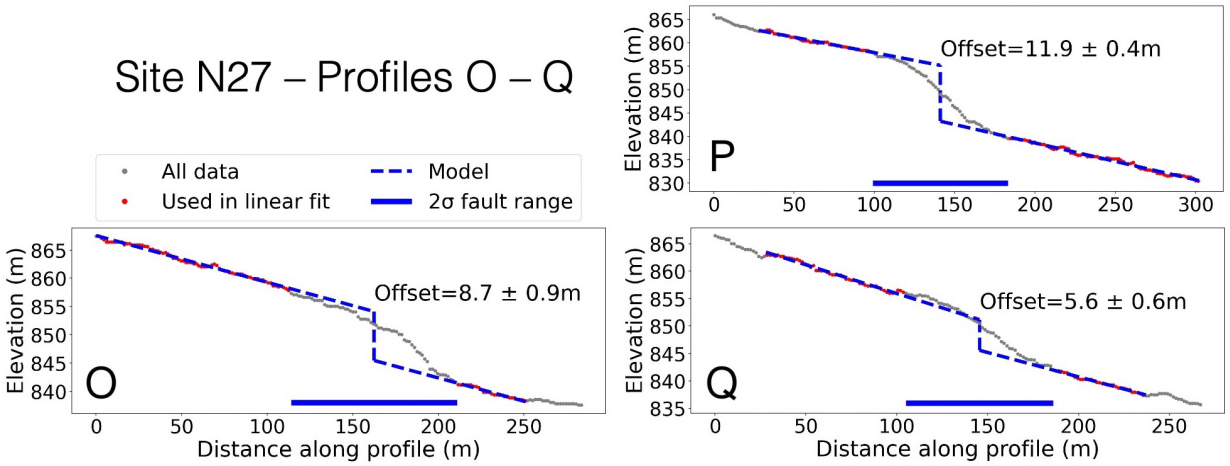

Figure 2.7-35. Vertical offset measurements from site N27, profiles O to Q (Appendix Figure 2.7-33).

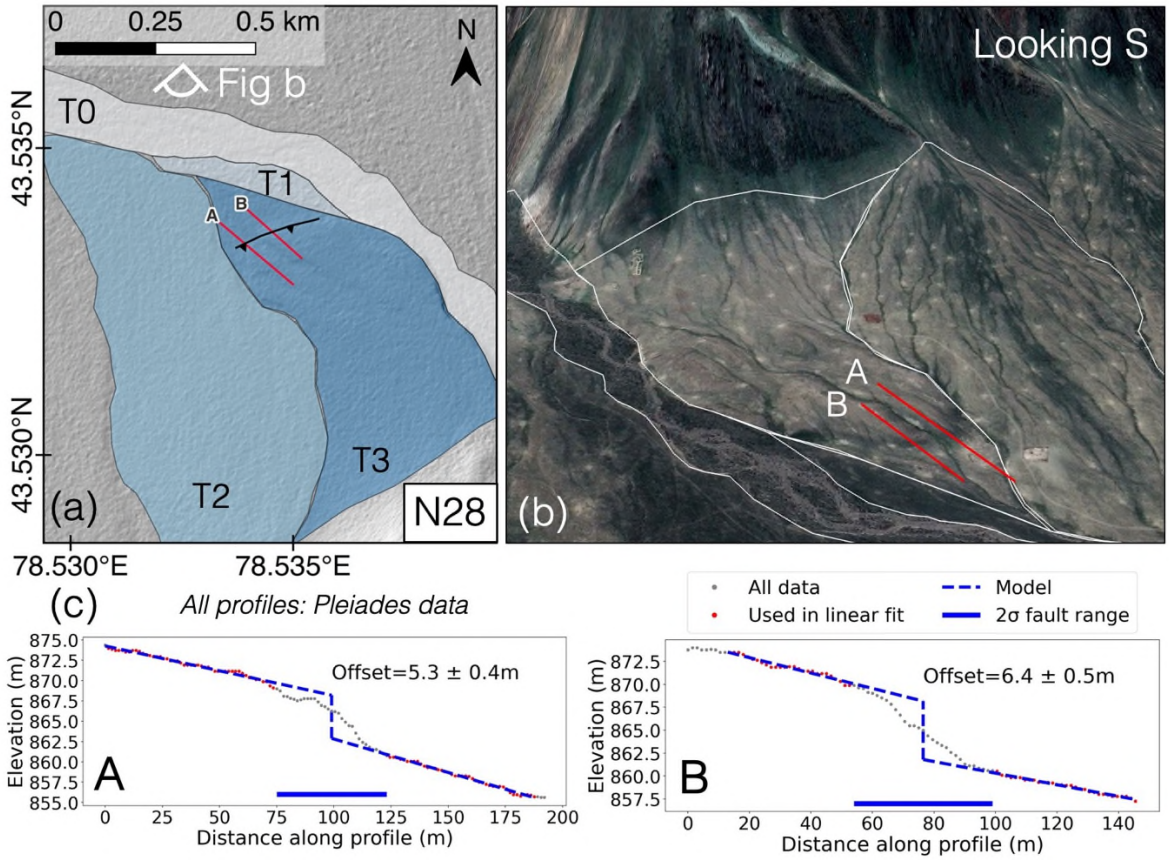

Figure 2.7-36. Site N28. (a) Hill-shaded Pléiades-derived DEM overlain with fan mapping. We infer three generations of fan, T1 to T3 (youngest to oldest), as well as the modern drainage surface, T0 (different colours indicate different inferred surface ages, darker = older). Red lines correspond to profiles in c. (b) Satellite imagery overlain on 3 x exaggerated topography from Google Earth

(Landsat/Copernicus, 2023 Maxar Technologies, 2023 CNES/Airbus), at ~43.5°N 78.5°E, 3.03 km eye altitude, and looking south. White lines show boundaries of mapped fans. Red lines show locations of profiles in c. (c) Vertical offset measurements along profile lines A and B. Elevation sampled every 1.5 m from Pléiades-derived DEM.

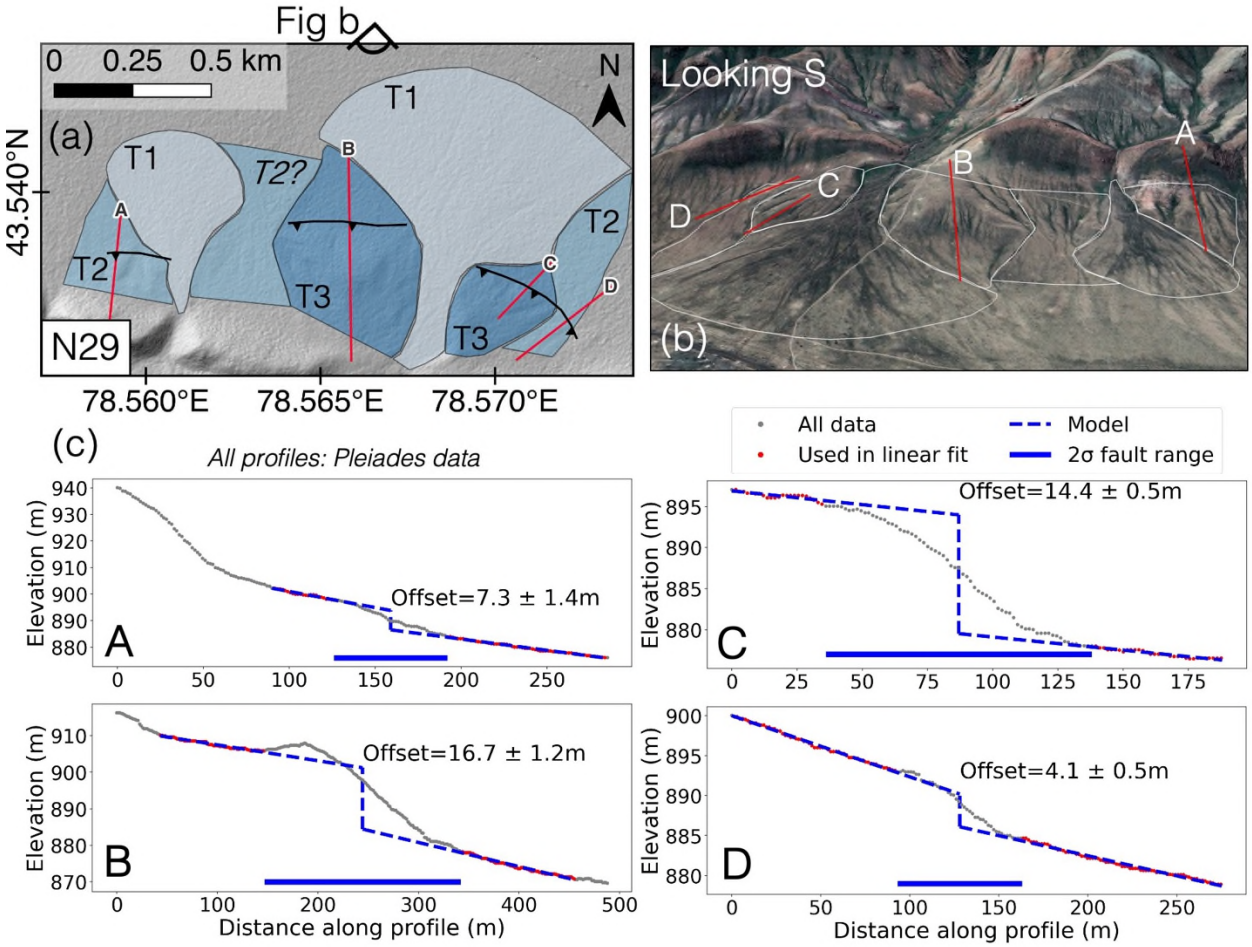

Figure 2.7-37. Site N29. (a) Hill-shaded Pléiades-derived DEM overlain with fan mapping. We infer three generations of fan (T1 to T3, youngest to oldest; different colours indicate different inferred fan ages, darker = older). Red lines correspond to profiles in c. (b) Satellite imagery overlain on 3 x exaggerated topography from Google Earth (Landsat/Copernicus, 2023 Maxar Technologies, 2023 CNES/Airbus), at 3.10 km eye altitude, and looking south. White lines show boundaries of mapped fans. Red lines show locations of profiles in c. (c) Vertical offset measurements along profile lines A to D. Elevation sampled every 1.5 m from Pléiades-derived DEM.

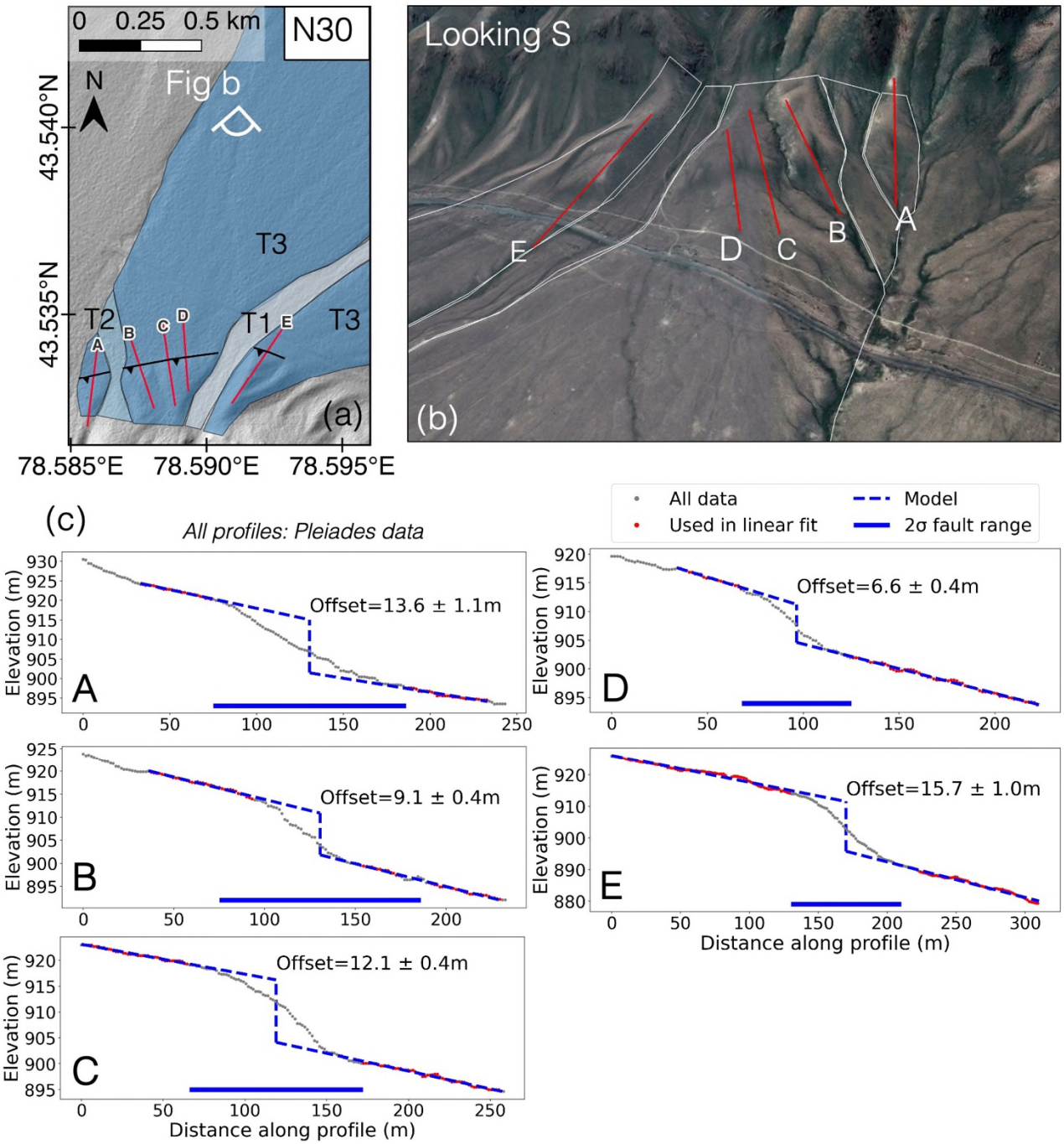

Figure 2.7-38. Site N30. (a) Hill-shaded Pléiades-derived DEM overlain with fan mapping. We infer three generations of fan (T1 to T3, youngest to oldest; different colours indicate different inferred fan ages, darker = older). Red lines correspond to profiles in c. (b) Satellite imagery overlain on 3 x exaggerated topography from Google Earth (2023 Maxar Technologies, 2023 CNES/Airbus), at 3.32 km eye altitude, and looking south. White lines show boundaries of mapped fans. Red lines show locations of profiles in c. (c) Vertical offset measurements along profile lines A to E. Elevation sampled every 1.5 m from Pléiades-derived DEM.

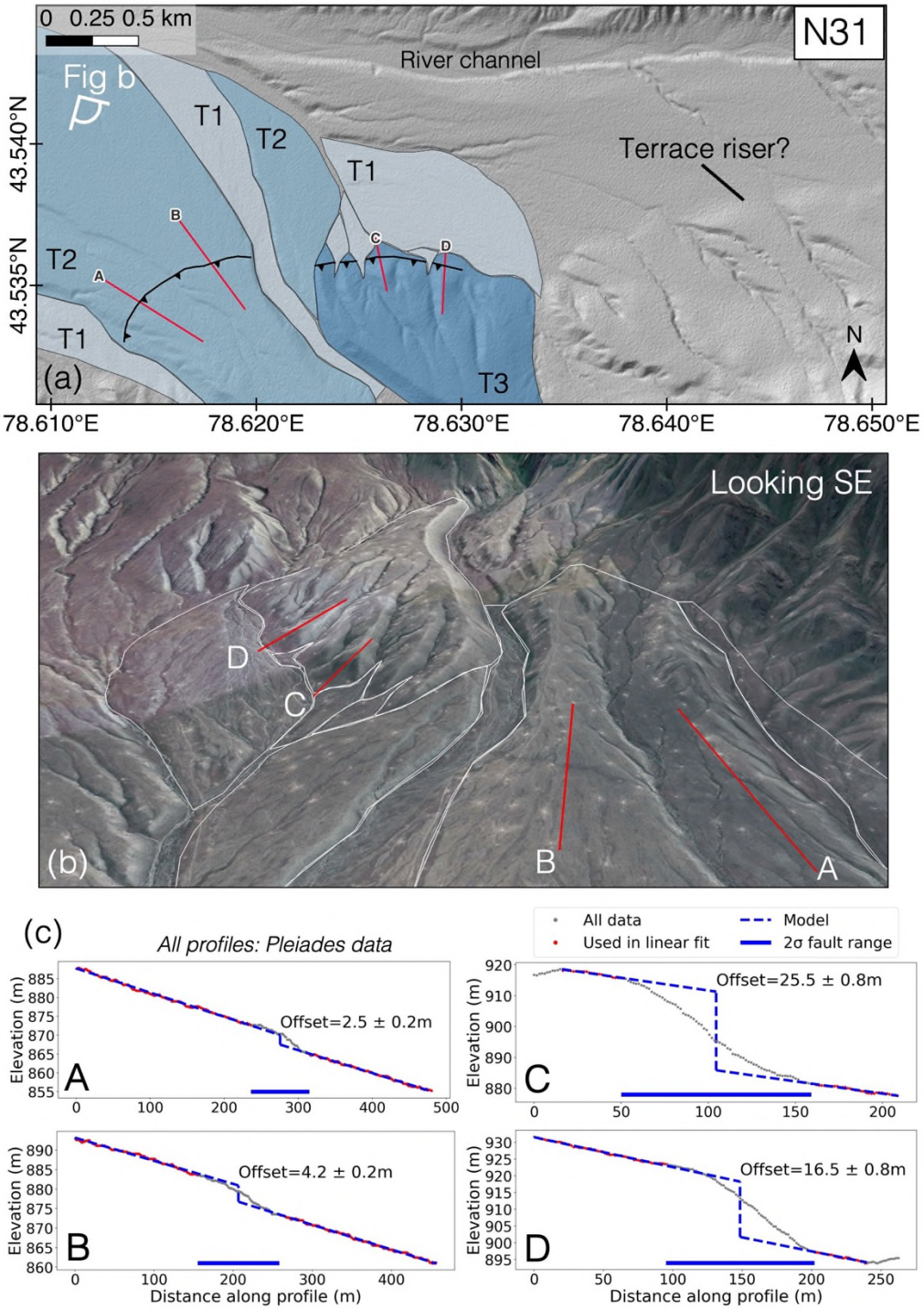

Figure 2.7-39. Site N31. (a) Hill-shaded Pléiades-derived DEM overlain with fan mapping. We infer three generations of fan (T1 to T3, youngest to oldest; different colours indicate different inferred fan ages, darker = older). Red lines correspond to profiles in c. (b) Satellite imagery overlain on 3 x exaggerated topography from Google Earth (Landsat/Copernicus, 2023 Maxar Technologies, 2023 CNES/Airbus), at ~43.5°N 78.6°E, 3.16 km eye altitude, and looking southeast. White lines show boundaries of mapped fans. Red lines show locations of profiles in c. (c) Vertical offset measurements along profile lines A to D. Elevation sampled every 1.5 m from Pléiades-derived DEM.

2.7.5. N19 Trench

Figure 2.7-40. Orthophoto of trench at N19 without annotation.

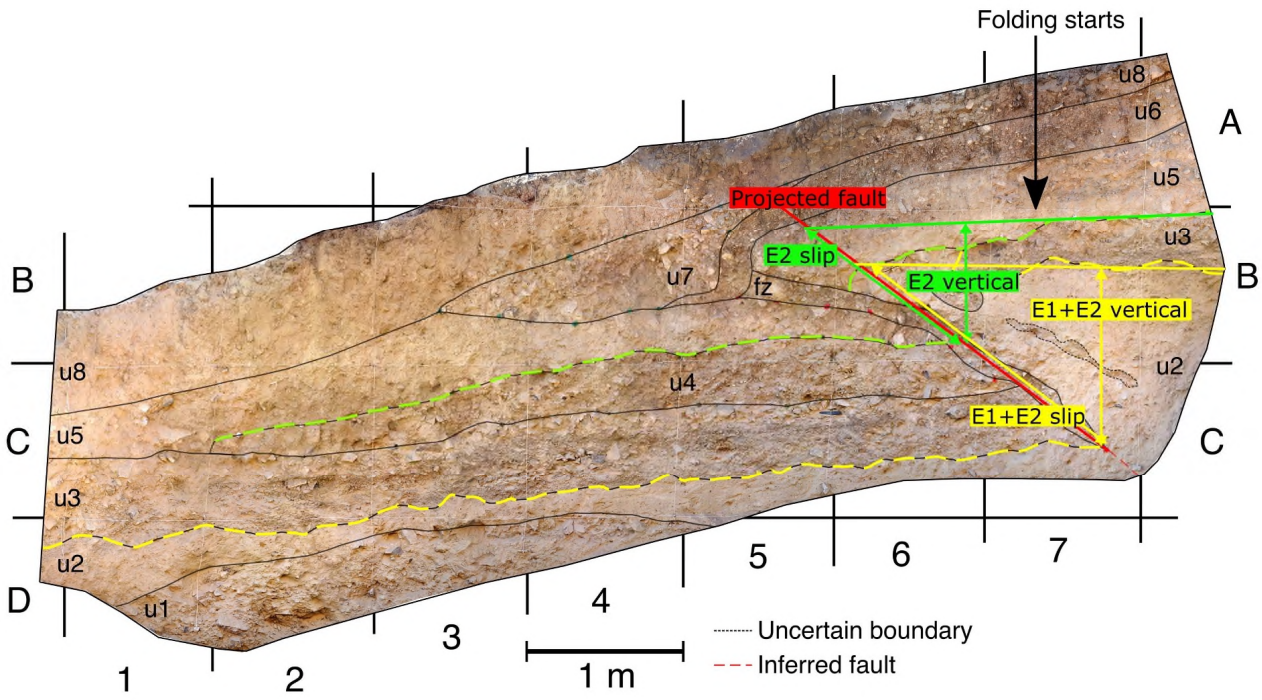

Figure 2.7-41. Annotated trench orthophoto demonstrating measurement methodology for vertical offset and slip. Yellow lines relate to unit 2/unit 3 boundary. Green lines relate to base unit 5 boundary.

2.7.6. N19 Pit

Table 2.7-11. Pit log taken at site N19 near Koram, 43.48764N, 78.15293E, 808m elevation.

Name	Depth (m)	Thickness (m)	Description
Layer 11	0 – 0.40	0.40	Silt with fine to coarse gravel. Poorly sorted. Lots of roots. Modern soil zone.
Layer 10	0.40 – 0.84	0.44	Silt with occasional fine gravels. Well sorted, white and extremely dry. Calcite cementation. A few roots.
Layer 9	0.84 – 1.00	0.16	Pure silt – compact, well sorted loess with no layering. Yellow. Softer than layer 10 above and less calcite cementation. Some soil moisture.
Layer 8	1.00 – 1.18	0.18	Silt with fine gravels with small white carbonate concretions, likely precipitated from rainwater. More fine gravels towards base. Extremely dry. Small cm-sized hole in exposed surface is possible burrow.
Layer 7	1.18 – 1.33	0.15	Medium to coarse angular gravels in a silty loess matrix. Gravels are horizontally layered but not sorted nor imbricated. Gravel clasts are pink-reddish and very weathered, likely volcanic.
Layer 6	1.33 – 1.40	0.07	Loess with coarse sand to fine gravel. Well sorted, not layered. With carbonate concretions as in layer 8. Moist.
Layer 5	1.40 – 1.60	0.20	Silty loess matrix with poorly sorted coarse sand to coarse gravel. Gravels are in lenses and are angular. Gravel clasts are pink-reddish and likely volcanic in origin.
Layer 4	1.60 – 1.77	0.17	Silt with fine gravel – much less gravel than above (i.e. fining from above layer). Only very few calcite concretions. Sample taken at 1.70 m: KAZ19PIT2.
Layer 3	1.77 – 1.87	0.10	Silt with lenses of fine to medium gravel. Rather well sorted. Same volcanic pink-reddish clasts as above.
Layer 2	1.87 – 2.10	0.23	Silt with lenses of fine gravel. Poorly sorted and rather moist.
Layer 1	2.10 – 2.40	0.30	Almost pure silt with the occasional fine gravel but no sand. Sample taken at 2.30 m: KAZ19PIT1.

2.8. Authorship statement for Chapter 2

Contributions: I, Roberta Wilkinson, conducted all the data analysis and wrote the chapter. Discussions with Christoph Grützner and Richard Walker provided direction to the analysis. I collected the field data over two field seasons with Christoph Grützner, Aidyn Mukambayev, Chia-Hsin Tsai, Tamarah King, and Kanatbek Abdrakhmatov. Richard Walker recommended the paleoseismic trenching site. Ian Pierce prepared the drone and dGPS surveying equipment and provided the methodology I used to capture and process my data. Ian Pierce also collected two of the drone surveys presented in this chapter on my behalf in locations selected by me. I processed the drone DEMs and Joshua Smith ran the processing of Pleiades DEMs in Agisoft Metashape according to my instructions. I prepared samples for luminescence dating at the University of Sheffield with the assistance of Chia-Hsin Tsai and under the supervision of Andrew Ivester and Ed Rhodes. Andrew Ivester and Ed Rhodes ran the luminescence measurements and performed the age calculations and corrections.

Acknowledgements: Thank you to Christopher Bronk Ramsey for his advice and pointers on modelling with OxCal, to Anton Gass for providing information on archaeological sites, and to Aditi Dave who kindly talked through her loess datasets with me. Thanks also to Julie Boulliung who taught me how to use some of the field equipment.

Chapter 3

Geodetic and Quaternary Geological Deformation Rates Across the Zailisky Range Front

3.1. Introduction

In the previous chapter we assessed the earthquake potential of the Zailisky Range Front fault (ZRF), which runs along the northern edge of the Western Tian Shan mountains in Central Asia, separating the Zailisky Alatau from the Kazakh Platform (Figure 3.1-1). GPS data show up to ~20 mm/yr of shortening and ~7-8 mm/yr of left-lateral shear across the Western Tian Shan, with deformation distributed across many different faults and shortening rates decreasing from west to east (Zubovich et al., 2016; Wang and Shen, 2020; Wu et al., 2023). This chapter is concerned with how much of the deformation is accommodated across the Zailisky Range Front and on which structures.

Geodetic observations capture surface deformation over periods of years to decades, whilst geological observations provide a record of deformation over thousands of years or more. Time-series InSAR (Interferometric Synthetic Aperture Radar) maps have a high spatial coverage and resolution and can often be used to measure deformation across individual faults, but the technique is largely insensitive to N-S motion, limiting its usefulness in regions dominated by N-S shortening such as the Tian Shan (Elliott, Walters and Wright, 2016). GPS (Global Positioning System) data also cover a large area, so can provide useful measurements across deforming zones, but data points are often too sparse to attribute deformation to individual structures. By contrast, geological slip rates from trenches or dated offset surfaces do provide point measurements of individual fault behaviour but do not contain any contextual information about off-fault deformation in the surrounding area. Therefore, combining both geological and geodetic data allows us to compare rates on individual faults with rates from the

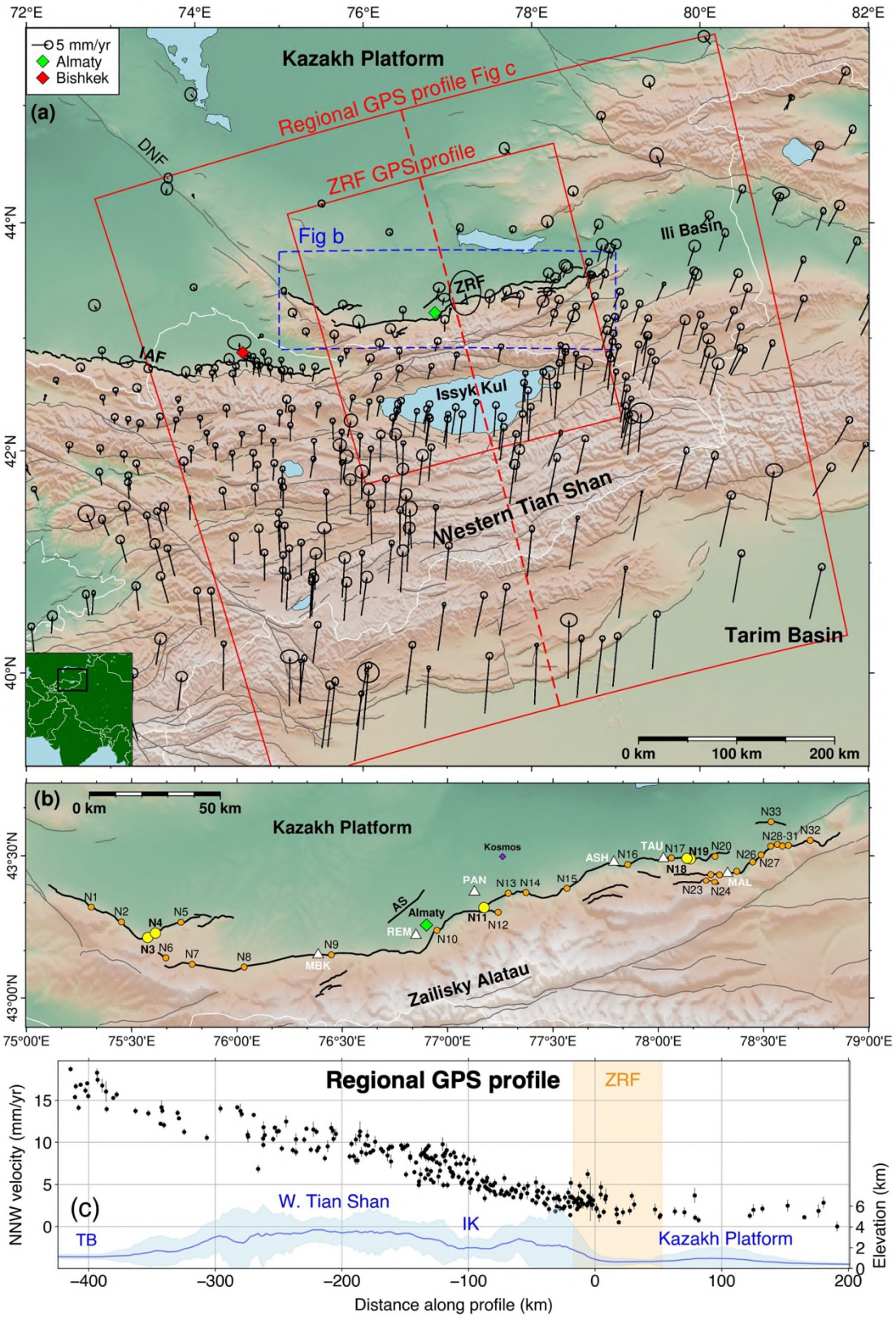

Figure 3.1-1. (a) Overview of Western Tian Shan with GPS velocities referenced to stable Eurasia from the compilation by Wang and Shen (2020) and references therein. Small red box shows location

of ZRF GPS profile in Figure 3.3-1, large red box shows location of regional GPS profile in (c). Faults (dark grey lines) modified after Zelenin et al. (2022) with mapping from this study. Labelled faults: IAF = Issyk-Ata fault, DNF = Dzhalair-Naiman fault, ZRF = Zailisky Range Front fault. IAF and ZRF are highlighted with thicker black lines. White lines mark country borders. Background DEM based on SRTM 30 m data (NASA JPL, 2013). (b) Overview map of the Zailisky Range Front. Faults as in (a) with additional thick black lines showing Zailisky Range Front faults mapped and measured in this study. Yellow circles labelled in bold = slip rate sites. White triangles = luminescence dating sites from Dave et al. (2023) and Fitzsimmons et al. (2017). Orange circles = all sites examined in this thesis. AS = Almaty Splay. (c) GPS velocities (NNW component) along the profile outlined by the largest red box in (a). Positive values indicate motion towards the bearing 345°. SRTM 30 m topography is shown in blue (blue line = median elevation). TB = Tarim Basin, IK = Issyk Kul. Orange region marks the extent of mapped faults along the Zailisky Range Front.

broader deforming zone, and potentially to identify how strain is accommodated and partitioned between structures.

For the majority of faults, geological and geodetic slip rates are thought to be consistent within error (Reilinger et al., 2006; Meade, Klinger and Hetland, 2013; Vernant, 2015). However, for a handful of faults, there is a mismatch between the two measurements. A slightly higher geodetic slip rate is not unexpected for a given fault, as geodetic measurements can capture off-fault deformation in a broader zone as well as fault-specific deformation, as described above (Vernant, 2015). In some cases, a discrepancy between geodetic and geological rates reveals insights into fault behaviour, rheology and regional tectonics – e.g. creep (Chuang and Johnson, 2011), pulsed slip (Gold et al., 2017), or vertical axis rotations (Rizza et al., 2019). However, different studies often disagree on the cause, magnitude or even the existence of the mismatch between rates (e.g. Vernant, 2015; Rust, Korzhenkov and Tibaldi, 2018; Rizza et al., 2019).

Shortening in the Western Tian Shan is highest (~20 mm/yr) between the Pamir and the Kazakh Platform, decreasing to around ~15 mm/yr in our area of interest between the Western Tarim Basin and the Kazakh Platform (Figure 3.1-1c; Wu et al., 2023). Most of this shortening is accommodated on the Tian Shan's southern bounding thrusts and the faults within and between the interior ranges (Figure

3.1-1c; Thompson et al., 2002; Wu et al., 2023). This is apparent in the ~NNW GPS velocity profile plotted in Figure 3.1-1c, in which velocities decrease northwards across the mountains and towards the Range Front. By the northernmost reaches of the Western Tian Shan, only a small proportion of the shortening signal remains: ~0.6 – 1.9 mm/yr according to GPS rates from Wu et al. (2023). Whilst GPS data are too sparse to rule out aseismic slip on the Issyk-Ata and Zailisky Range Front faults (IAF and ZRF in Figure 3.1-1), large historical earthquakes (1885 M_W 6.9 – 7.9 Belovodskoe, 1887 M_W ~7.2 – 7.7 Verny) and paleoseismic studies attest to their seismogenic behaviour (Kondorskaya et al., 1982; Tatevossian, 2007; Bindi et al., 2014; Patyniak et al., 2017; Krüger, Kulikova and Landgraf, 2018). Published Quaternary slip rates from the eastern end of the ZRF are ~1.2 – 2.2 mm/yr (Grützner et al., 2017b) and 0.8 ± 0.5 mm/yr (95% confidence interval; Selander et al., 2012) for the northern fault strand (near N19 and N20 Figure 3.1-1), and 0.43 ± 0.3 mm/yr (95% confidence interval; Selander et al., 2012) for a parallel strand ~6 km to the south.

A full introduction to the regional tectonics and seismicity of the Western Tian Shan can be found in the previous chapter. In the present chapter, we analyse GPS data to obtain a geodetic deformation rate across the Zailisky Range Front. We also reassess previously published geological rates and present new analyses of deformed deposits to obtain a revised Quaternary slip rate for the ZRF. We present new luminescence ages and utilise published age datasets to expand our study. Finally, we compare our geodetic and geological rates to shed light on the distribution of strain between the Zailisky Alatau and Kazakh Platform, with implications for identifying potentially hazardous structures.

3.2. Methods and Datasets

In the sections below we describe our methodologies for estimating the geodetic shortening rate from GPS data and the geological uplift rate from deformed Quaternary features. We convert these estimates to slip rates by assuming a fault dip of between 30° and 60°, except for where we have a direct

observation of slip at the trench site (N19). As some of the parameters used in our rate calculations form uniform distributions between a maximum and minimum value (e.g. dip, some age estimates), whereas other parameters are normally distributed (e.g. offset measurements, some age estimates), we use a Monte Carlo approach to combine these different distributions and obtain a posterior normal distribution with a mean and formal uncertainty estimate for the calculated rates.

3.2.1. GPS Shortening Rate Calculation

We use the compilation of GPS data from Wang and Shen (2020), previously utilised by Wu et al. (2023) to obtain slip rates across the Tian Shan. The GPS data provide north and east velocities, so can be used to constrain shortening and lateral deformation but not uplift. We define a 260 km wide and ~300 km long profile oriented approximately perpendicular to the ZRF (-15° azimuth) (Figure 3.1-1a). We extract profile parallel and profile perpendicular velocity components and project the measurements onto a central profile line. Profile parallel and profile perpendicular velocities represent the shortening and lateral deformation across the ZRF respectively.

To estimate the shortening rate, we difference the average profile parallel GPS velocities either side of the ZRF. To incorporate both the uncertainty in the individual GPS velocities (which we assume to be normally distributed) and the spread of the measurements, we use a Monte Carlo approach. In a single iteration, we randomly select 50% of the GPS measurements with replacement (Figure 3.2-1). We sample a single value from each of the selected measurements' normal distributions (i.e. values closer to a measurement's mean are more likely to be selected). We then calculate the average velocity either side of the fault using this subset of the data. Finally, we difference these averages to obtain a shortening rate for one iteration. We run 100,000 iterations to obtain 100,000 estimates of the change in average velocity across the fault. The mean and standard deviation of these 100,000 measurements is our final estimate of the shortening rate.

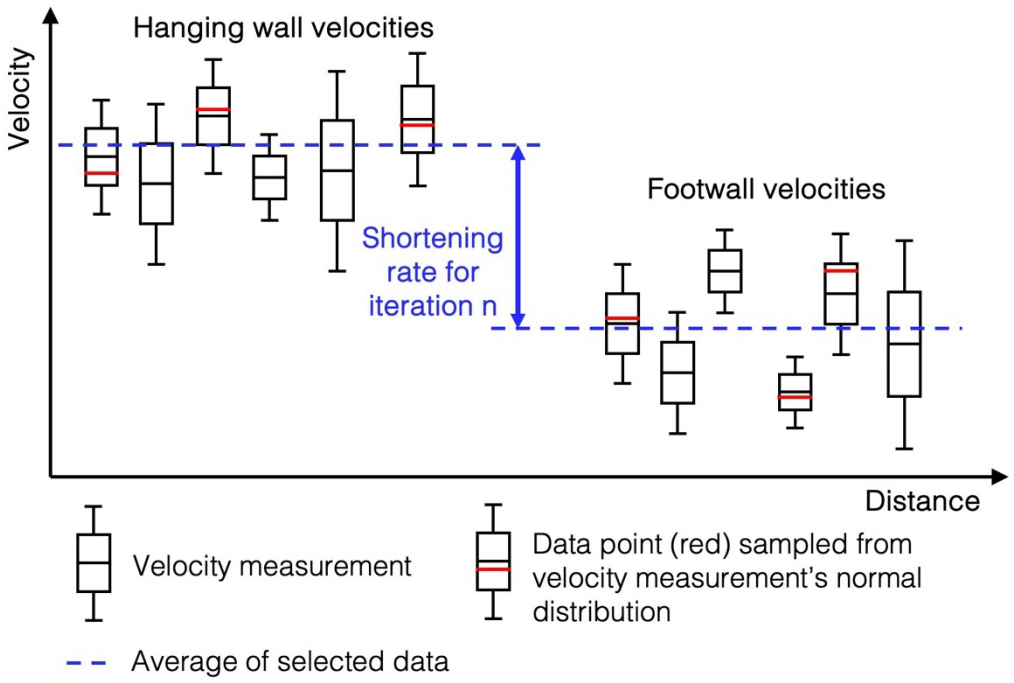

Figure 3.2-1. Schematic diagram of a single iteration of the GPS shortening rate calculation. Half of the velocity measurements (black box and whisker plots) are selected at random and a single value (red line) is sampled from each of their normal distributions. These values are averaged in the hanging wall and footwall (blue dashed lines). The difference between the averages is the shortening rate for this iteration.

3.2.2. Geological Uplift Rate Calculations

To calculate a geological uplift rate, we first identify a geomorphic feature (an alluvial fan or river terrace) which has been deformed by the fault. We measure its vertical offset across the fault according to the methodology outlined in Chapter 2. Next, we estimate the age of the deformed surface either by sampling and dating the sediment, or by using previously published age data. We assume that when an alluvial fan or river terrace is active, pre-existing topography is eroded removing any tectonic scarps. Consequently, any scarps in fans or terraces must have formed since deposition ceased. Dividing the offset magnitude by the abandonment age of the surface yields an uplift rate.

To estimate the abandonment age of a surface, we date samples or use published ages from near the top of the fluvial/alluvial sequence or from the silt which overlies the highest layer of fluvial/alluvial

gravels. However, loess blankets much of the range front and is draped over many of the scarps (Grützner et al., 2017b; Dave et al., 2023). These thick sections of windblown silt could have been deposited at any time since the surface was abandoned, so we only use dates from loess which lies immediately above the fluvial/alluvial gravels to estimate their abandonment age. We assume that loess began accumulating on top of the fan deposits immediately (within the temporal error of the measurements) after the cessation of fan activity.

3.2.3. Dating Methods

3.2.3.1. Luminescence Dating

We utilise luminescence dating to find the age of deformed surfaces. An introduction to this methodology and the concepts discussed below can be found in the Methods section of the previous chapter. In the present chapter, we present new Infrared Stimulated Luminescence (IRSL) dates from samples collected in 2016 from sites N3 and N4. These samples were collected by colleagues before I began my DPhil and were processed in a different laboratory and using a different protocol to that described in the previous chapter.

3.2.3.1.1. IRSL Protocol: 2016 Akterek Samples

Samples collected in 2016 were processed in Germany at the Department of Human Evolution, Max Planck Institute for Evolutionary Anthropology, Leipzig, by Professor Kathryn Fitzsimmons. The IRSL protocol reported to us by Professor Fitzsimmons is summarised below.

The collection and initial preparation of samples was the same as outlined in the previous chapter: samples were collected with metal tubes inserted horizontally into sediment exposures. Samples were opened under subdued red-light conditions and the outermost sediment was removed from the end of the tubes.

After this, the polymineral feldspar-bearing fine-grained (4 – 11 μm) fraction was extracted from the remaining sample material using the methodology of Frechen, Schweitzer and Zander (1996) and each sample was then split into 18 aliquots for measurement. There was insufficient sample to also isolate quartz, so only the polymineral fine fraction was measured. A post-IR infrared high-temperature ($pIR_{50}IRSL_{290}$) SAR protocol was applied in order to isolate the stable signal and minimise the impact of anomalous fading (Buylaert et al., 2009; Thiel et al., 2011; Fitzsimmons et al., 2017).

The IRSL protocol was implemented with a Risø TL-DA-20 reader with stimulation by IR LEDs, the luminescence signal was detected by an EMI 9235QA photomultiplier tube with a D410 filter, and the samples were irradiated with a calibrated $^{90}Sr/^{90}Y$ beta source (Bøtter-Jensen, 1997; Bøtter-Jensen, Mejdahl and Murray, 1999). An initial IR bleach was carried out at 50°C and the post-IR stimulation for luminescence measurement at 290°C, a temperature chosen based on tests run on nearby loess sites by Fitzsimmons et al. (2017). D_E measurements for all samples produced Gaussian distributions, so the Central Age Model of Galbraith et al. (1999) was applied to obtain the final D_E values (Preusser et al., 2008; Fitzsimmons et al., 2017). Three of the samples (AKT1, AKT2 and AKT3) were also measured for residual signals after laboratory bleaching, as low bleachability and a residual component can be a particular issue with feldspar pIR-IRSL measurements (Buylaert et al., 2011; 2012; Fitzsimmons et al., 2017). The residual dose for all three samples was <1% of the equivalent dose, so no correction was applied (Appendix Table 3.6-1). Recycling ratios (produced by repeating the first regenerative dose at the end of the protocol and dividing the resulting luminescence reading by the first luminescence reading from that dose) are all well within 10% of unity, indicating a successful sensitivity correction so no measurements need to be discarded (Appendix Table 3.6-1; Murray and Wintle, 2000; Preusser et al., 2008).

The radioactive isotope (K, Th, U) activity was measured with high-resolution Germanium Gamma Spectrometry at the Felsenkeller of the VKTA in Dresden, Germany. The dose rate was calculated by combining radioactive isotope activity converted to dose rates using factors from Adamiec and Aitken (1998) and Guérin, Mercier and Adamiec (2011), the contribution from cosmic rays calculated from sample density, altitude, location and burial depth as in Prescott and Hutton (1994), and beta dose attenuation corrections due to moisture content (10 ± 5 % for all samples; Mejdahl, 1979). As the samples are fine-grained, an alpha efficiency of 0.08 was applied (Rees-Jones, 1995; Rees-Jones and Tite, 1997).

3.2.3.2. Published Age Datasets

In addition to the new IRSL ages, several published datasets are available which we use to place constraints on the ages of deformed surfaces along the Zailisky Range Front or to contextualise our results.

3.2.3.2.1. Loess Luminescence Ages

To study the mass accumulation rates and past climate dynamics of Central Asia, Dave et al. (2023) and Fitzsimmons et al. (2017) obtained age estimates for loess deposits at five sites along the Zailisky Range Front using Optically Stimulated Luminescence (OSL). The dated sites are marked with white triangles in Figure 3.1-1b, and correspond to the stratigraphic sections and age profiles in Figure 3.2-2 taken from Dave et al. (2023). At four of the five sites no contact between the loess and underlying fluvial or alluvial deposits is visible, so the loess ages cannot be used to date the abandonment of those surfaces. However, at one site (PAN) on the Talgar Fan, the loess overlies a layer of pebbles and gravels and can be used to date fan abandonment.

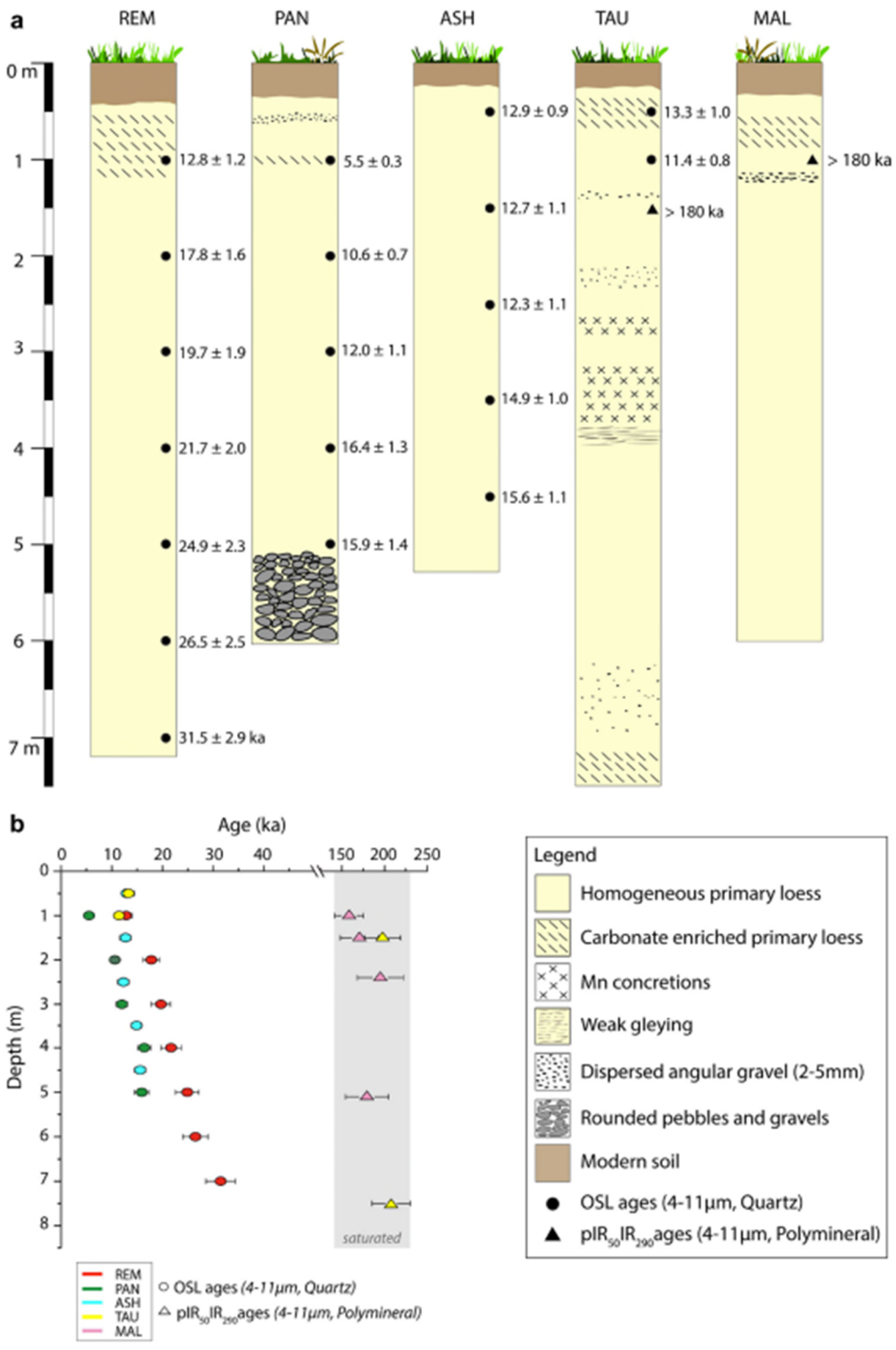

Figure 3.2-2. Figure from Dave et al. (2023) showing loess luminescence ages from five sites along in the foreland of the ZRF. (a) Stratigraphy at each site. (b) Age-depth plots of luminescence dating results (2σ uncertainty).

3.2.3.2.2. Regional River Terraces

Thompson et al. (2002) report dates for Quaternary river terraces across multiple basins within the Kyrgyz Tian Shan. Based on radiocarbon dating of 8 terraces, they suggest a phase of river incision and terrace formation occurred around 13.5 – 15.7 kyrs BP. Based on luminescence dating of 4 terraces, they also suggest that an older suite of terraces formed around 140.7 ± 8.5 ka. Thompson et al. (2002) infer that both phases of terrace formation were caused by concurrent global glacial-interglacial transitions.

The Thompson et al. (2002) terrace ages have previously been used to infer slip rates for tectonically deformed river terraces in the Tian Shan based on their morphologies (e.g. Thompson et al., 2002; Selander et al., 2012). Whilst we do not apply this technique here, we compare the terrace ages to direct dating results to check for consistency, and we review the previous application of these ages to Quaternary deposits on the Zailisky Range Front.

3.2.3.2.3. Archaeology

The Zailisky Range Front and the surrounding region, historically known as ‘Zhetysu’ (‘seven rivers’ in English), has been populated by both nomadic and settled communities for thousands of years and hosts abundant archaeological sites (Gass, 2014). Along the range front there are sites from the Palaeolithic, the Bronze Age, the Early Iron Age and the Middle Ages (Gass, 2014; Fitzsimmons et al., 2017). Early Iron Age sites are most abundant and feature the remains of settlements and burial mounds, many of which were constructed by the Saka people (Gass, 2014). Thousands of these burial mounds, known as ‘Kurgans’, adorn the range front, built into the gentle slopes of the piedmont (Gass, 2014). Most Kurgans have diameters greater than 30 m (Gass, 2014) and many form part of larger burial mounds, so they are easily identified in satellite imagery. The Early Iron Age Saka period probably began around 800 BC and lasted until around 200 BC in our study region (Sala and Deom,

2005; 2013; Gass, 2016), suggesting that surfaces which host Saka archaeology are at least ~2.8 – 2.2 kyrs old.

Based on age data from Dave et al. (2023), Grützner et al. (2017b) and this study, most of the deformed surfaces along the range front probably formed much earlier than ~2.8 – 2.2 ka, so this minimum age constraint is of limited use. However, we identify six archaeological sites with Early Iron Age finds in the literature (Korjenkov et al., 2003; Spengler, Chang and Tourtellotte, 2013; Gass, 2016; 2019; Bekseitov et al., 2019) where the archaeological ages provide a useful cross-check against other datasets and our interpretations. Details of each of the six sites can be found in Appendix Table 3.6-3. Note that not all the site ages are confirmed by direct dating, and some rely on expert interpretation of the artefacts and structures, which introduces some uncertainty to the accuracy of the age estimates.

3.3. Results

3.3.1. Geodetic Rates

From our 260 km wide profile (smallest red box in Figure 3.1-1), we find 1.3 ± 0.4 mm/yr (1σ) of shortening between the Zailisky Alatau and the Kazakh Platform, but no change is apparent in the fault parallel velocities (Figure 3.3-1; Figure 3.3-2). Modelling the two halves of the profile separately yields very similar shortening rates – 1.3 ± 0.5 mm/yr and 1.4 ± 0.7 mm/yr for the eastern and western halves respectively. Assuming a fault dip between 30 – 60°, the shortening rate (1.3 ± 0.4 mm/yr) corresponds to uplift and slip rates of 1.4 ± 0.6 mm/yr and 1.9 ± 0.7 mm/yr respectively. The data are insufficiently dense to constrain a specific model describing the depth or degree of locking.

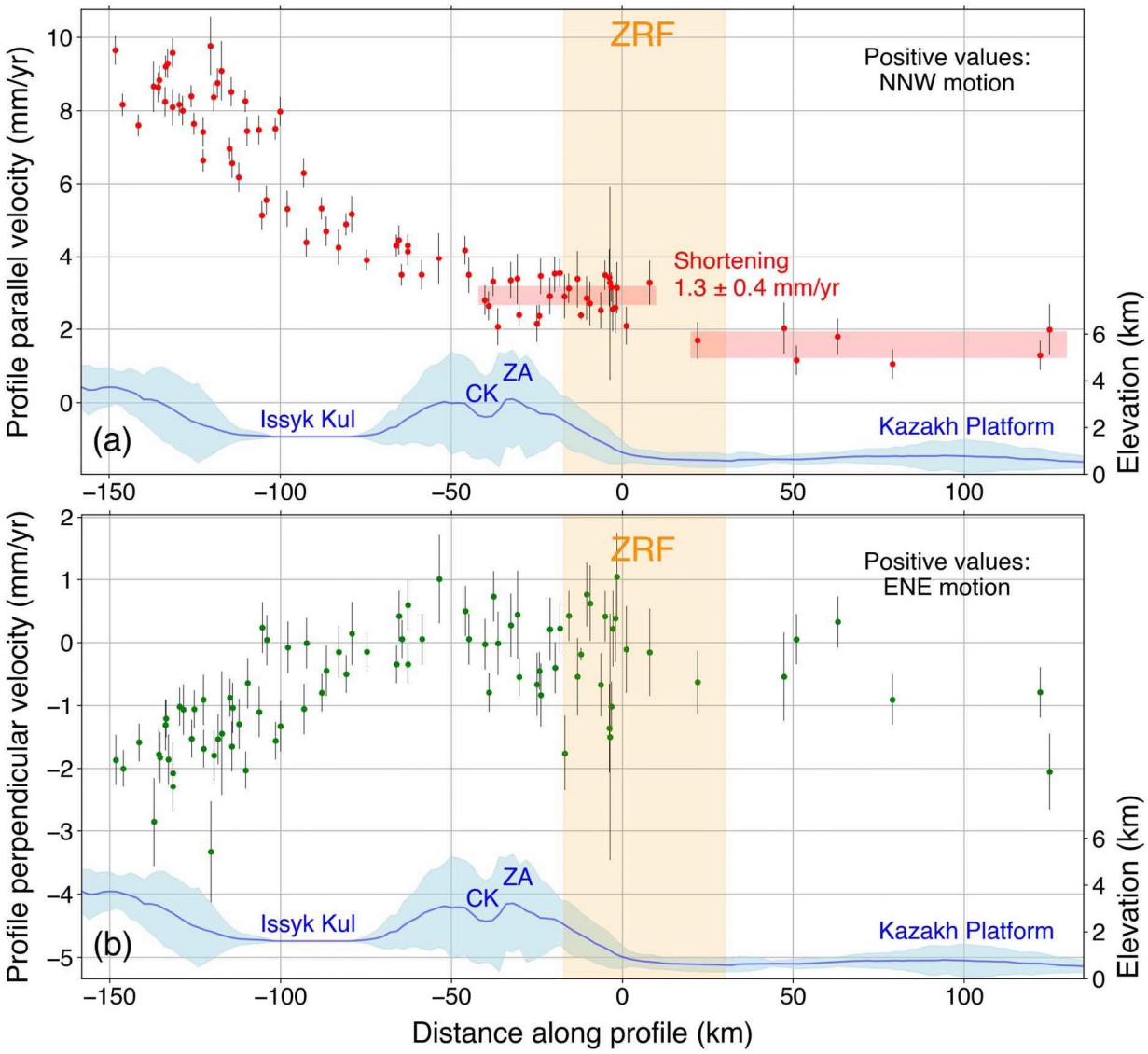

Figure 3.3-1. ZRF GPS profiles corresponding to the smallest red box in Figure 3.1-1, which is 260 km wide. SRTM 30 m topography (NASA JPL, 2013) is shown in blue (blue line = median elevation). GPS velocities (referenced to stable Eurasia) are from the compilation by Wang and Shen (2020) (and references therein). CK = Chon Kemin valley. ZA = Zailisky Alatau. Shaded orange region marks the extent of mapped faults along the Zailisky Range Front. (a) Profile parallel velocities. Red rectangles show the ranges of datapoints in the hanging wall and footwall used calculate the shortening rate across the Range Front, centred on the mean velocities with widths of 2σ. (b) Profile perpendicular velocities.

In Figure 3.3-2 we show the locations of the GPS velocities used to calculate the shortening rate. For most of the width of the profile, data are too sparse to determine whether shortening occurs at the Range Front or within the first ~50 km of the Kazakh Platform or both. We cannot determine whether

deformation is accommodated by a single fault or across multiple faults and folds. Based on observations of incision, in Chapter 2 we mapped an uplifting region within the Kazakh Platform (orange polygon in Figure 2.3-14 and Figure 3.3-2) which could be taking up some of the shortening. Folded sediments dated to ~17kyrs have also been found in the foreland near Kosmos (purple diamond in Figure 3.3-2; Macklin et al., 2015; Grützner et al., 2017b).

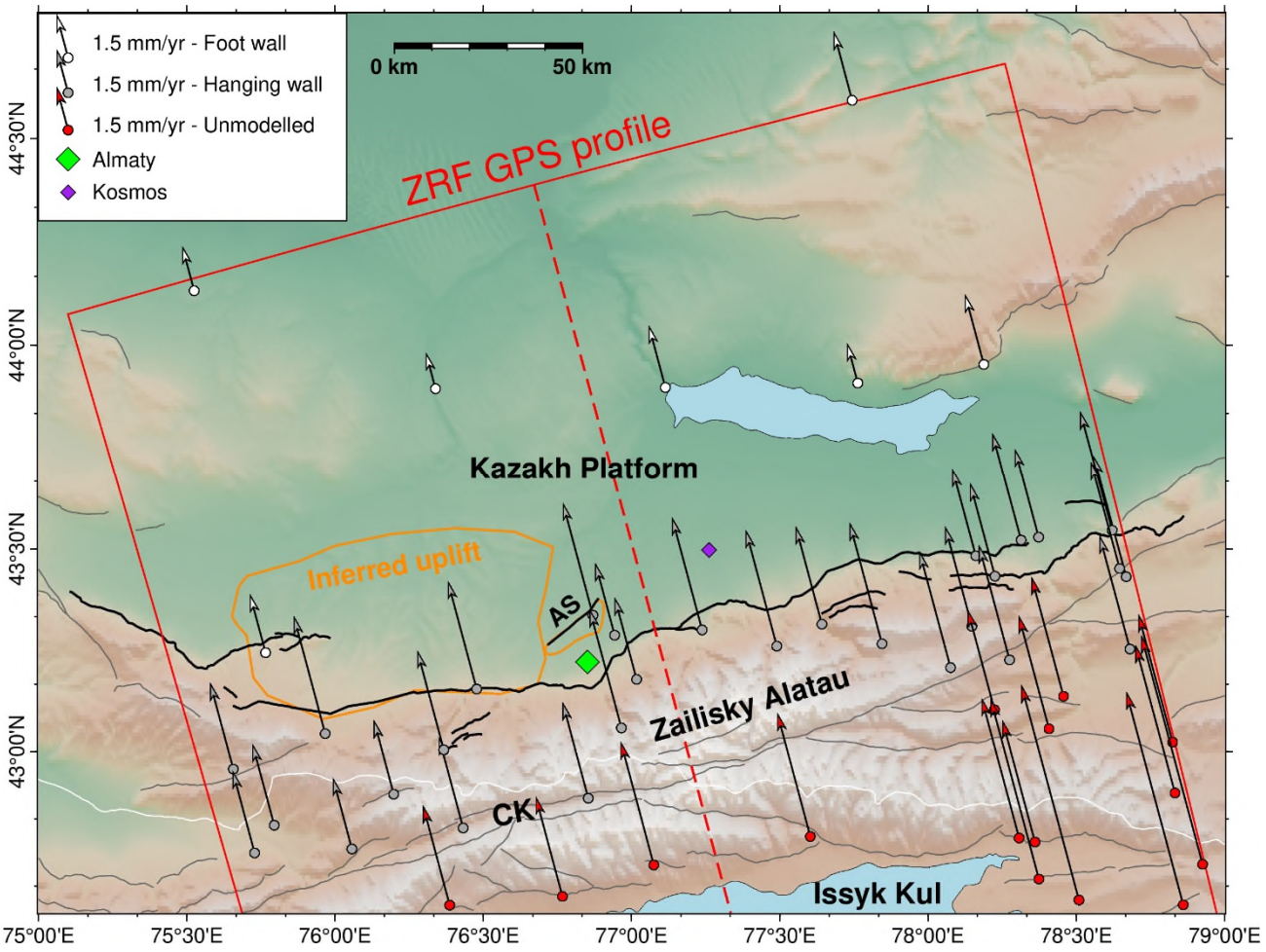

Figure 3.3-2. Profile parallel velocities at GPS stations within the profiled region (red box), focussed on the ZRF (bold black lines). Grey and white GPS data are those used to calculate the average velocities of the hanging wall and foot wall respectively for the purposes of estimating shortening (Figure 3.3-1). Orange polygons show regions where uplift is inferred from geomorphology. CK = Chon Kemin valley. AS = Almaty Splay. SGPS velocities (referenced to stable Eurasia) are from the compilation by Wang and Shen (2020) (and references therein). Faults (dark grey lines) modified after Zelenin et al. (2022) with mapping from this study. White lines mark country borders. Background DEM based on SRTM 30 m data (NASA JPL, 2013).

In the west of the ZRF the fault has two strands with a plateau in between. Here, the GPS data seem to indicate that most of or all the shortening is focussed on the southern fault strand at the main mountain front – but this is based on a single data point at the northern edge of the plateau (Figure 3.3-2). In the centre of the Range Front, a ~25 km long fault splay runs beneath the north of Almaty (AS in Figure 3.3-2). The change in profile parallel velocity occurs to the north of this splay, suggesting that the splay, rather than the main Range Front, may be accommodating a significant amount of the deformation. However, denser velocity measurements are needed to confirm these interpretations and to better resolve the distribution of strain. Everywhere else along the profile, the change in velocity occurs somewhere between the Range Front and ~50 – 80 km into the Kazakh Platform.

Wu et al. (2023) used the same GPS dataset (Wang and Shen, 2020) to estimate deformation rates throughout the Tian Shan. They assign 1.9 ± 1.8 mm/yr of shortening to the eastern half of the Zailisky Range Front (profile C in Wu et al., 2023), which is larger than our estimate of 1.3 ± 0.4 mm/yr. However, Wu et al. (2023) include all GPS measurements between the southern boundary of Issyk Kul and the Zailisky Range Front in their selection of hanging wall GPS stations for the ZRF rate calculation. Our plots reveal that there is ~1 mm/yr of shortening across the Chon Kemin valley (CK in Appendix Figure 3.6-1) which lies in the mountains between Issyk Kul and the Range Front. Therefore, the Wu et al. (2023) shortening estimate of 1.9 ± 1.8 mm/yr overestimates the true rate across the ZRF because they have averaged across an additional step in the velocity which is probably attributable to the Chon Kemin fault. We also note that the uncertainty in the measurement from Wu et al. (2023) is more than four times as large as our measurement uncertainty – they do not state how this uncertainty is calculated or what it represents, so the reason for the large discrepancy is unknown.

A preliminary, unpublished time-series InSAR study of the Tian Shan by Dr Qi Ou (University of Leeds) shows no velocity change at the range front (Qi Ou, personal communication). However,

significant noise in the signal (e.g. from agricultural fields) means small (< ~2 mm/yr) rate changes across faults cannot be resolved in the data (Qi Ou, personal communication). Furthermore, as the InSAR technique is largely insensitive to N-S motion, the absence of a signal does not necessarily reflect a lack of deformation.

3.3.2. Geological rates

3.3.2.1. N3 and N4: Akterek Field Sites

At the western end of the ZRF, sites N3 and N4 lie on the northern fault strand which bounds an uplifted plateau (Figure 3.1-1). First mapped by Grützner et al. (2017b), there are at least four generations of alluvial fan (T1 – T4, youngest to oldest) along this section of the range front, many of which are deformed by scarps (Figure 3.3-3a). Grützner et al. (2017b) collected drone DEMs at both sites.

At site N3, the scarp runs through an alluvial fan surface inferred to be of generation T3 and is truncated in the east by a younger fan (Figure 3.3-3b). A pit was excavated in the hanging wall of the scarp (Figure 3.3-3b; Figure 3.3-4). The top 140 cm of the pit consisted of uniform silt, with the addition of abundant gravels between 140 cm and 160 cm. Below 160 cm depth was a layer of sub-angular to sub-rounded gravels up to ~15 cm in diameter with poorly formed carbonate rinds on the undersides of the clasts. The 20 cm silt and gravel layer between 140 cm and 160 cm could have formed due to silt input into the active alluvial fan or might be the result of reworking of the gravels post-abandonment. Samples AKT1 and AKT2 were collected from the loess at 140 cm depth (20 cm above the alluvium) and yielded luminescence ages of 26.3 ± 1.8 kyrs and 30.5 ± 2.2 kyrs respectively. A third sample, AKT3, was collected at 150 cm depth from within the mixed silt and gravel layer, and yielded a luminescence age of 32.5 ± 2.2 kyrs. We suggest the fan was abandoned around or shortly after the deposition of the gravel and silt layer (AKT3) and before the deposition of the uniform silt

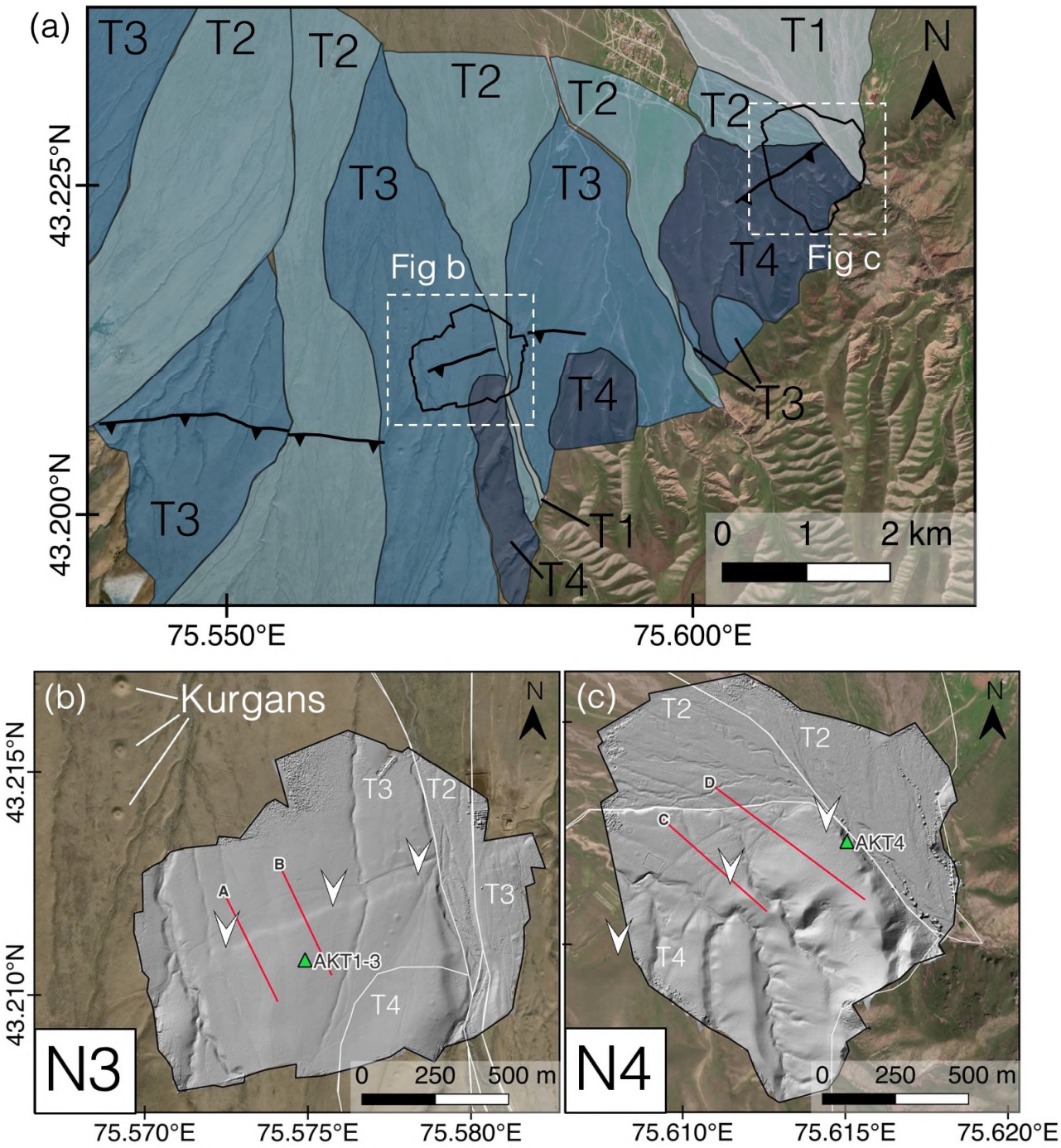

Figure 3.3-3. Overview of sites N3 and N4, corresponding to S1 and S2 in Grützner et al. (2017b). (a) Bing Aerial imagery (2023 TomTom, 2023 Maxar) overlain by alluvial fan mapping of four fan generations (T1-T4, youngest to oldest; different colours indicate different inferred fan ages, darker = older) modified after Grützner et al. (2017b). Figures (b) and (c) show sites N3 and N4 respectively, with Bing Aerial imagery (2023 TomTom, 2023 Maxar) overlain by hill shaded drone DEMs. Red lines are profile locations from Grützner et al. (2017b) which we re-measure (Figure 3.3-5). White arrows mark scarp location. White lines show the boundaries of the mapped fans. Green triangles show luminescence sampling locations.

(samples AKT1 and AKT2). Therefore, we average the three dates to obtain an estimated age for fan abandonment of 29.8 ± 1.8 kyrs. The average of our vertical offset measurements at this site is 2.2 ± 0.3 m (Figure 3.3-5), consistent with the original measurements from Grützner et al (2017b). Using these values, we obtain an uplift rate of 0.07 ± 0.01 mm/yr at site N3, corresponding to a slip rate of 0.11 ± 0.02 mm/yr.

At N4, the scarp runs through a fan inferred to be of generation T4 and is truncated to the east by a large river valley (Figure 3.3-3c, Figure 3.3-6). Luminescence samples from the hanging wall (AKT4, AKT5) were taken from an exposure on the western bank of the river valley from loess lying 0 – 5 cm above the uplifted fluvial gravels, at 5.41 m depth below the ground surface (Figure 3.3-6). In the top ~1 m of the exposed riverbank section were clusters of large (~30 cm) boulders and flat rocks which might be stone tools, implying use of the fan by historical communities. The sampled loess contained some small gravels. No age could be obtained from sample AKT5 due to a power outage during processing. Sample AKT4 yielded a luminescence age of 61.5 ± 4.1 kyrs. Fan activity must have ceased before this date. We measure an offset of 7.7 ± 1.2 m across a single scarp (profile C) and offsets of 7.1 ± 0.1 and 0.7 ± 0.2 across two parallel scarps (profile D) a few hundred metres along strike, similar to Grützner et al (2017b) (Figure 3.3-5). We use the single scarp offset measurement of 7.7 ± 1.2 m in our calculations and obtain an uplift rate of 0.13 ± 0.02 mm/yr for site N4, corresponding to a slip rate of 0.18 ± 0.04 mm/yr.

Table 3.3-1. IRSL dating results for samples collected in 2016 from the Zailisky Range Front and processed at the Max Planck Institute for Evolutionary Anthropology, Leipzig, Germany.

Sample name	**Site**	**Lat (°)**	**Lon (°)**	**Depth (m)**	**Equivalent dose, D_E (Gy)**	**Dose rate (Gy/kyr)**	**Age (kyr)**
AKT1	N3	43.210786	75.574911	1.4	131 ± 4	4.98 ± 0.31	26.3 ± 1.8
AKT2				1.4	131 ± 4	4.39 ± 0.29	30.5 ± 2.2
AKT3				1.5	171 ± 5	5.26 ± 0.31	32.5 ± 2.2
AKT4	N4	43.227308	75.615049	5.41	336 ± 6	5.46 ± 0.35	61.5 ± 4.1
AKT5				5.41	Power outage disrupted measurement, no results		

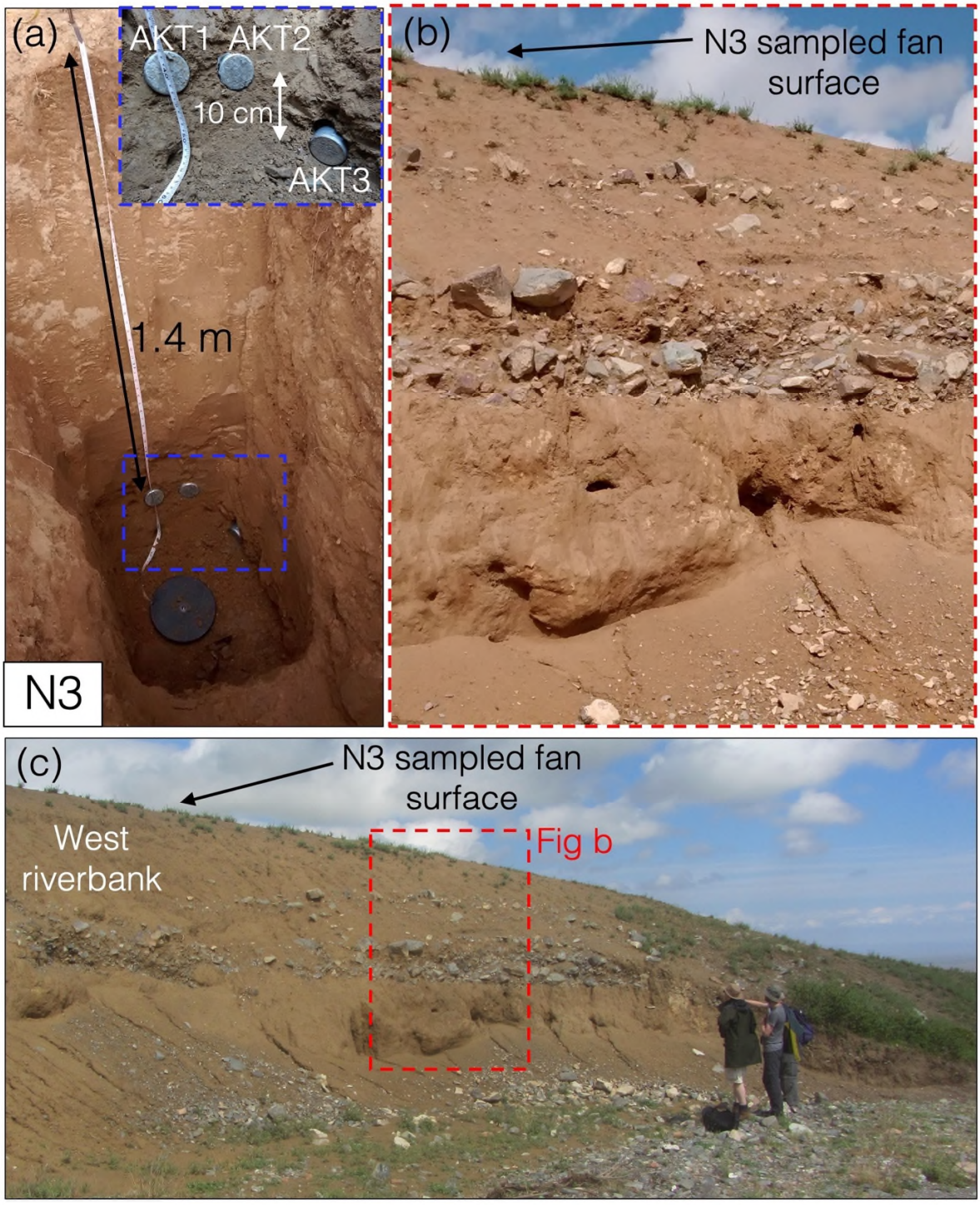

Figure 3.3-4. (a) Pit in fan surface (43.210786°N 75.574911°E) at site N3 which was sampled for luminescence dating. Blue box shows close-up of luminescence samples AKT1, AKT2 and AKT3. (b) Stratigraphy of the fan sampled at N3 exposed in the west bank of the adjacent river. (c) Zoomed-out photograph of the west bank of the river with geologists for scale. Photograph taken at 43.212342°N 75.579160°E.

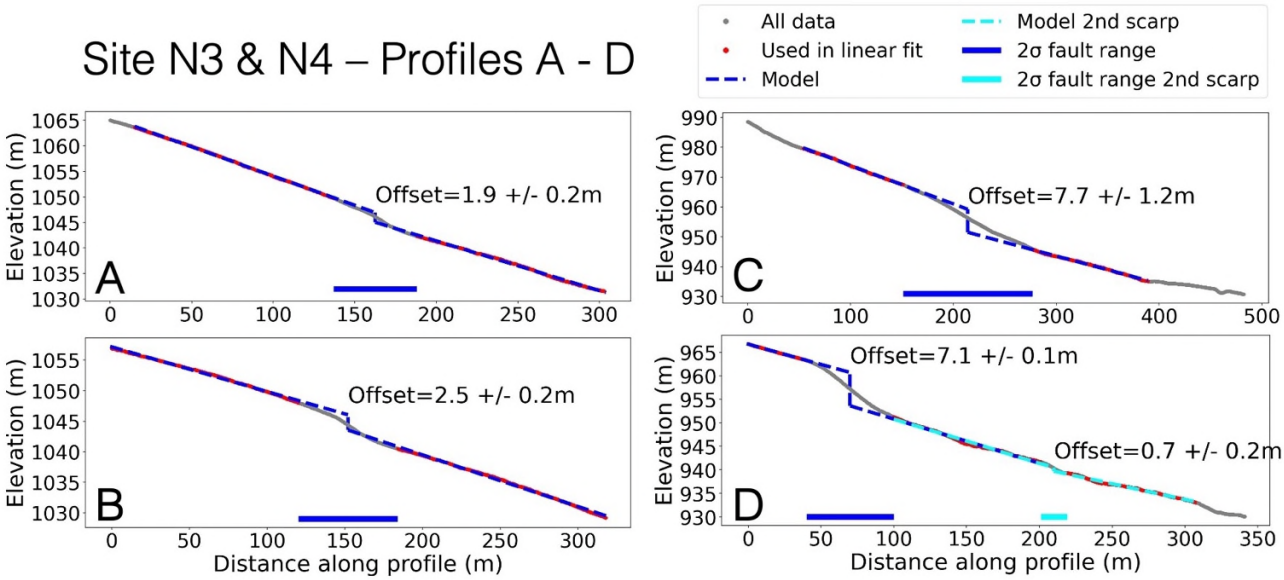

Figure 3.3-5. Vertical offset measurements from sites N3 and N4, profiles remeasured from the drone DEMs collected by Grützner et al. (2017b), corresponding to Figure 3.3-3.

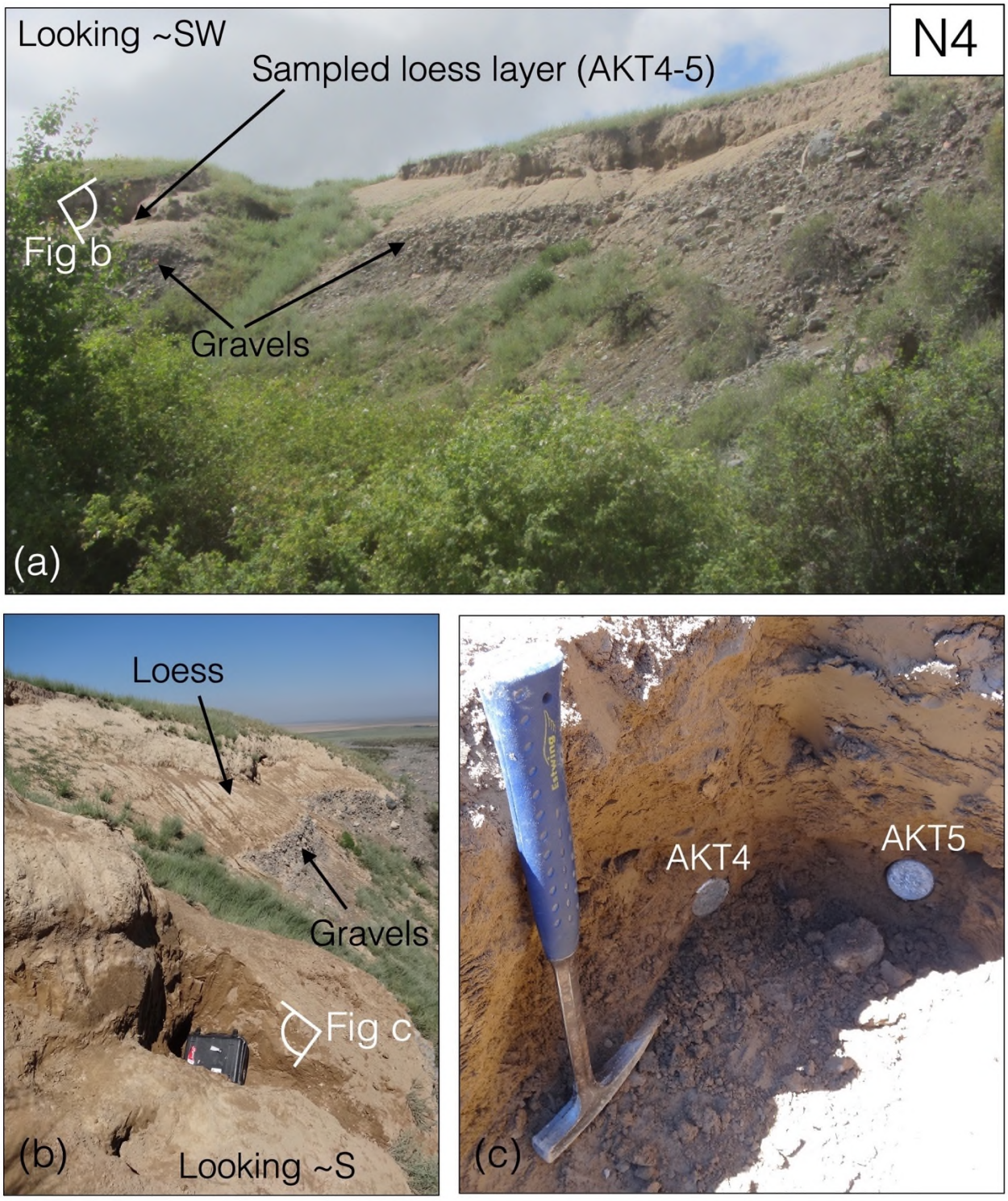

Figure 3.3-6. (a) Photograph of west riverbank taken at 43.227790°N 75.615692°E looking SW towards the sampling site N4, showing gravel deposits overlain by loess. (b) Photo of sampling pit (containing box of equipment) at 43.227308°N 75.615049°E with west riverbank stratigraphy visible in background. (c) Sampling pit with luminescence sampling tubes for samples AKT4 and AKT5.

3.3.2.2. N11: Kyzylkayrat on the Talgar Fan

In Chapter 2, we mapped scarps in the Talgar Fan at sites N11 and N12 (Figure 3.1-1b). The Talgar Fan has been populated for thousands of years (Spengler, Chang and Tourtellotte, 2013; Gass, 2016). Many archaeological finds on the Fan date back to the Early Iron Age Saka period (A1 to A4 in Appendix Table 3.6-3), which suggests the surface must be at least ~2.8 – 2.2 kyrs old (Figure 3.3-7; Korjenkov et al., 2003; Spengler, Chang and Tourtellotte, 2013; Gass, 2016; 2019). A 1979 geological map designates the entire Talgar Fan as upper Quaternary (QIII) in age, apart from the modern deposits surrounding the river (Parshina, Zolotokrylina and Semenova, 1979). In the south of the Talgar Fan, Dave et al. (2023) dated a ~5 m loess section overlying a > 3 m thick gravel bed at the 'PAN' sample site which was exposed by a creek (Figure 3.2-2; Figure 3.3-7). A loess sample from immediately above the gravels at 5 m depth yielded a luminescence age of 15.9 ± 1.4 ka (2σ), whilst a sample from 4 m depth (1 m above the gravels) yielded a luminescence age of 16.4 ± 1.3 ka (2σ) (Dave et al., 2023). These results suggest that this part of the Talgar Fan must have been abandoned before ~16 ka, and we use the average of the two values, 16.2 ± 1.0 ka (1σ), in our rate calculations.

The PAN sample site from Dave et al. (2023) is located ~ 7 km directly down slope of the scarp we mapped in the field at site N11 (near Kyzylkayrat) which we found to be part of a larger offset in the Pleiades DEM, measured along profiles B and C (Figure 3.3-7). We find no significant changes in morphology or major drainage channels between PAN and our offset measurements for B and C (3.6 ± 0.9 m and 2.2 ± 0.6 m) despite the distance between them. Therefore, we assume the abandonment age from PAN is a reasonable estimate for the age of fan abandonment at B and C and we use the average of these two offset measurements (2.9 ± 0.5 m) combined with the luminescence age from Dave et al. (2023) to obtain an uplift rate of ~0.18 ± 0.03 mm/yr and a slip rate of ~0.26 ± 0.06 mm/yr. However, we note that the true uncertainty in these measurements is probably significantly higher than the formal errors due to the distance between the sampling site and the scarp. We do not use the ~8.4 m offset

from profile A (Figure 3.3-7) because it is located further towards the edge of the fan and is not directly up-slope of the PAN dating site.

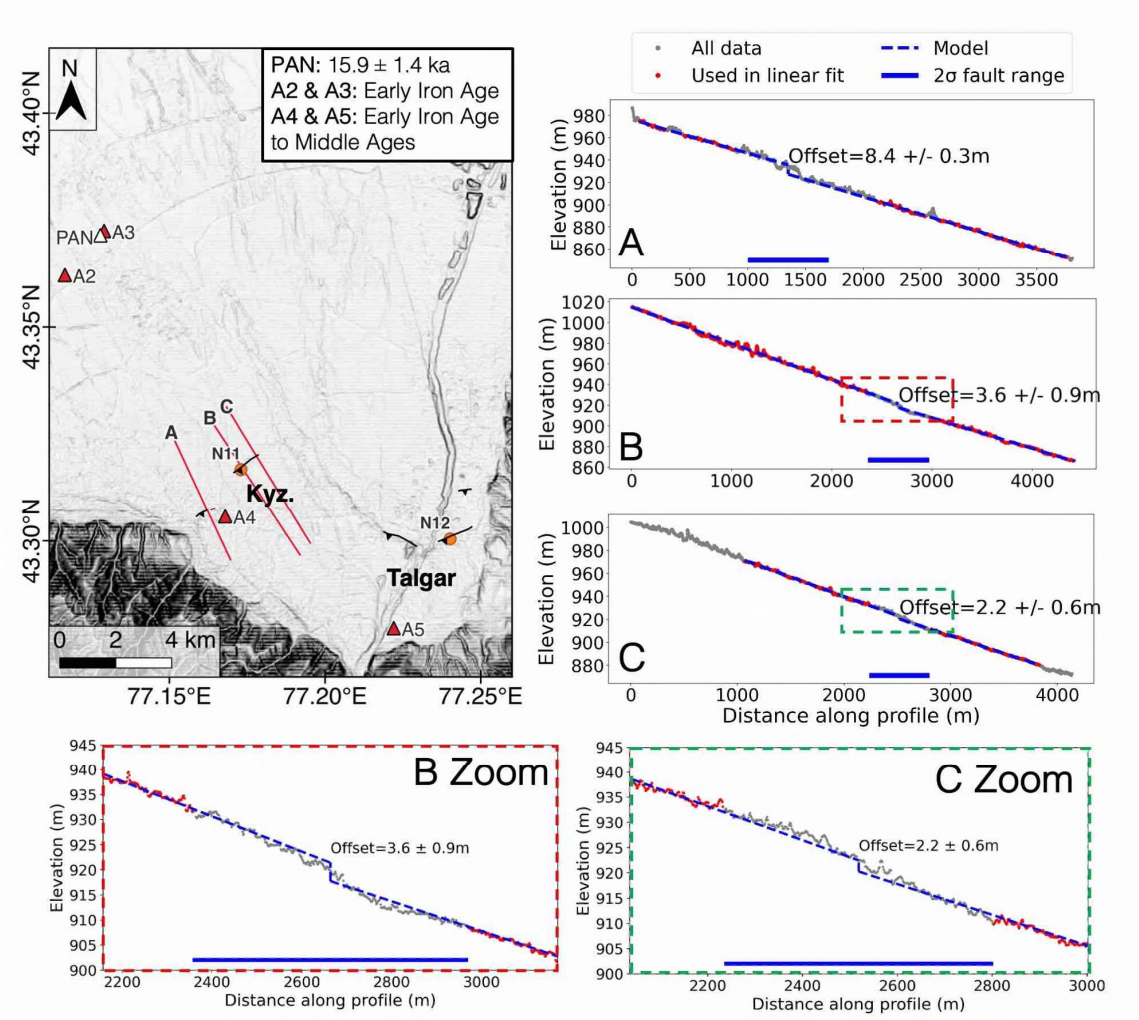

Figure 3.3-7. Top left: Talgar Fan slope map (derived from Copernicus 30 m data) with dating sites labelled, Kyz = Kyzylkayrat. Right top three panels: Vertical offset measurements corresponding to the red profile lines on the slope map. Boxes on profiles B and C correspond to the zoomed in profiles in the bottom two panels which show the data close to the scarp.

3.3.2.3. N19: Trench Site near Koram

In the east of the range front at site N19, scarps offset alluvium < 500 m to the south of the Big Almaty Canal. We excavated a paleoseismic trench at this site which we present in Chapter 2 (Figure 2.4-1; Figure 2.4-2; Figure 2.4-3). We document two earthquakes, offsetting a series of layers which were all deposited within the last ~10 kyrs, dated using IRSL (Table 2.4-1). The penultimate earthquake occurred at 9.5 ± 0.8 ka (2σ), and the total uplift and slip we measure in the trench are ~1.2 m and ~2 m respectively (Table 2.4-2). The oldest stratigraphic layer affected by this offset is Unit 2, which has an age of 9.8 ± 0.5 ka (averaged over two samples), indicating it was deposited shortly before the penultimate earthquake at the very end of the previous earthquake cycle. These values yield an uplift rate of ~0.12 ± 0.01 mm/yr and a slip rate of ~0.20 ± 0.01 mm/yr, averaged over two earthquakes.

We investigate using the modelled ages for Unit 2 from OxCal model A (detailed in Chapter 2) in our calculations rather than the average ages of the samples (Appendix Table 3.6-2), but we find this makes no significant difference to the rates.

3.3.2.4. Reassessment of Published Rates

In this section, we analyse and reassess the previously published geological rates on the ZRF, which are summarised in Table 3.3-2.

3.3.2.4.1. N18: Terraces near Koram from Grützner et al. (2017b)

Site N18, corresponding to the S7 slip rate site in Grützner et al. (2017b), lies ~ 5 km to the south of the village of Koram where a stream exits the Range Front and has formed a series of terraces (Figure 3.3-8). Grützner et al. (2017b) map four terraces, T4 to T1, oldest to youngest, with T1 corresponding to the modern streambed (Figure 3.3-9). They find that terraces T4, T3 and T2 are deformed across the fault scarp with vertical offsets of 50 ± 1.3 m, 30.4 ± 1.6 m, and 9.2 ± 0.4 m (2σ uncertainties)

respectively, all measured on the east side of the stream using dGPS profiles (Figure 3.3-10A). On the western side of the stream, the T2 terrace is present in the hanging wall only and does not cross the fault due to erosion by the stream. Grützner et al. (2017b) find the western T2 terrace to be 14.4 ± 0.6 m (2σ) above the level of the present-day stream bed (Figure 3.3-10B). They estimate an abandonment age of around 13.3 – 15 kyrs for the western T2 terrace based on radiocarbon dating of charcoals from within the fluvial sequence, with additional informal uncertainties relating to possible inheritance and reworking of samples, bulk sediment sampling, and assumptions about deposition rates (Grützner et al., 2017b). Using this age range and the offset between the western T2 terrace and the streambed they calculate an uplift rate of ~1 – 1.1 mm/yr.

We reassessed the mapping and uplift rate calculations from Grützner et al. (2017b) outlined above. The profiles from the east side of the stream where T2 crosses the fault show that the modern streambed lies around 5 m below T2 in the footwall (Figure 3.3-10A). This demonstrates that there has been non-tectonic stream incision since the formation of T2, probably related to climatic changes. Therefore, the offset between the western T2 terrace and the streambed is not a good measure of the tectonic uplift and is probably a significant overestimate. Instead, to calculate the uplift rate, the age of

Table 3.3-2. Previously published geological rates on the ZRF. *Value calculated based on the published data. **95% confidence interval.

Publication	**Location**	**Methodology**	**Offset (m)**	**Age (ka)**	**Uplift rate (mm/yr)**	**Assumed dip (°)**	**Slip rate (mm/yr)**
Grützner et al. (2017b)	N18 (Koram terraces)	Direct dating of river terrace	~14.5	13.3 – 15	1.0 – 1.1	30 - 60	1.2 – 2.2
Selander et al. (2012)	South of Chilik northern strand near N20	Assumed age based on regional terrace correlation	72 ± 30	100 ± 30	0.7 ± 0.4*	45 ± 10	0.8 ± 0.5**
Selander et al. (2012)	South of Chilik southern strand near N21		40 ± 20		0.4 ± 0.2*	30 ± 10	0.43 ± 0.3**

the western T2 terrace should be combined with the offset measure from the eastern T2 terrace which crosses the fault. This method assumes that the terraces inferred to be T2 on either side of the stream are the same age, which we consider to be a reasonable assumption.

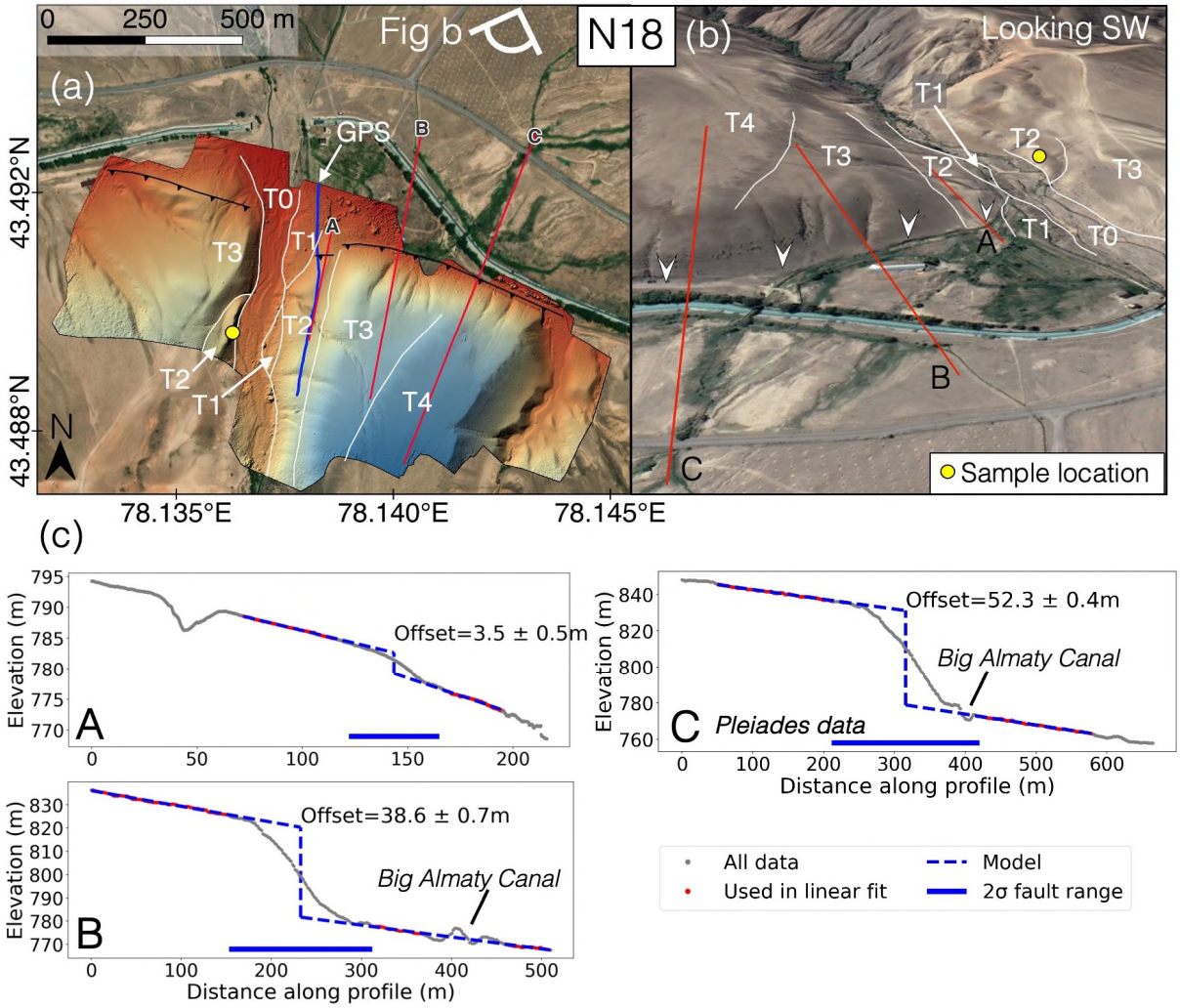

Figure 3.3-8. Koram terraces at site N18 – our reassessment of site S7 from Grützner et al. (2017b). (a) Bing Aerial satellite imagery (2024 TomTom, 2024 Maxar) of the site overlain by a hill shaded DEM collected and processed by Grützner et al. (2017b) . White lines show approximate locations of terrace risers between four terraces (T1 to T4) and the modern river bed (T0). Blue line shows the location of the eastern T2 GPS profile from Grützner et al. (2017b). (b) satellite imagery overlain on topography from Google Earth (2023 Maxar Technologies, Landsat/Copernicus, 2023 Airbus), viewed from 1.10 km eye altitude, and looking southwest. Fault scarp marked by white arrows, labelled red lines show profiles. White lines are approximate boundaries of river terraces. Yellow circle shows approximate sampling location for the samples taken in Grützner et al. (2017b). (c) Scarp profiles. Profile A and B

are measured from the drone-derived DEM sampled every 15 cm, whilst C is measured from Pleiades-derived DEM sampled every 1.5 m.

According to Grützner et al. (2017b), the vertical scarp offset of the eastern T2 terrace is 9.2 ± 0.4 m (2σ), based on a dGPS survey profile. However, upon reassessment of a drone DEM collected by Grützner et al. (2017b), we find that there is an additional terrace below T2, labelled as T1 in Figure 3.3-9 with the streambed re-labelled as T0. T1 does not appear to be offset. The dGPS profile along the eastern T2 terrace from Grützner et al. (2017b) (blue line in Figure 3.3-9a) begins in T2 and then crosses over into T1. Therefore, the 9.2 ± 0.4 m (2σ) value is a measurement of the offset between T1 and the hanging wall of T2 across the terrace riser rather than the offset of T2 across the scarp. Using the drone DEM, we re-measure the T2 offset across the scarp as 3.5 ± 0.5 m (profile A in Figure 3.3-9). Applying the 13.3 – 15 kyrs age range from Grützner et al. (2017b) yields a revised uplift rate of ~0.25 ± 0.04 mm/yr, corresponding to a revised slip rate of ~0.36 ± 0.08 mm/yr. These values are significantly lower than the original estimates.

The T2 terrace age reported by Grützner et al. (2017b) is consistent with 8 other terraces across the Tian Shan dated by Thompson et al. (2002). Whilst we have no direct dates for terraces T3 and T4, one of them might correspond to the 140.7 ± 8.5 ka terraces that Thompson et al. (2002) correlated and dated across the region. We measure offsets of 52.3 ± 0.4 m in T4 and 38.6 ± 0.7 m in T3 (profiles B and C in Figure 3.3-9). Applying an age of 140.7 ± 8.5 ka to T3 yields an uplift rate of 0.27 ± 0.02 mm/yr, consistent with the rate from T2. This might suggest that T3 was abandoned around ~140 ka, but direct dating would be required to confirm this interpretation.

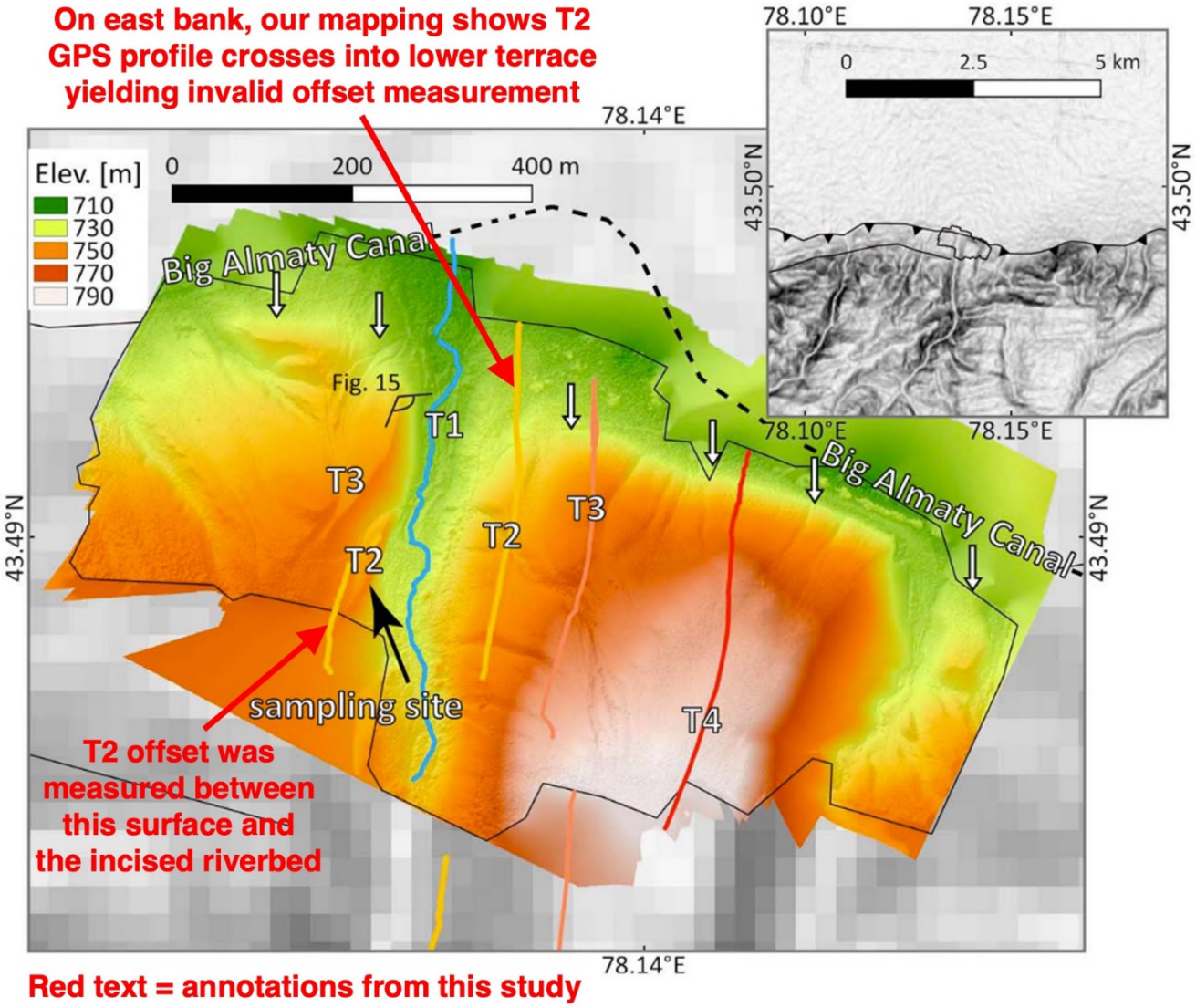

Figure 3.3-9. Figure modified after Grützner et al. (2017b), showing slip rate site S7 (N18 in this study) with hill-shaded drone DEM and terraces labelled in white. Coloured lines are dGPS walking survey profiles across the scarp which is marked by white arrows. Blue profile follows the present-day stream. The label 'Fig. 15' refers to Figure 15 in Grützner et al. (2017b). dGPS profiles are plotted in Figure 3.3-10. Annotations from this study have been added in red.

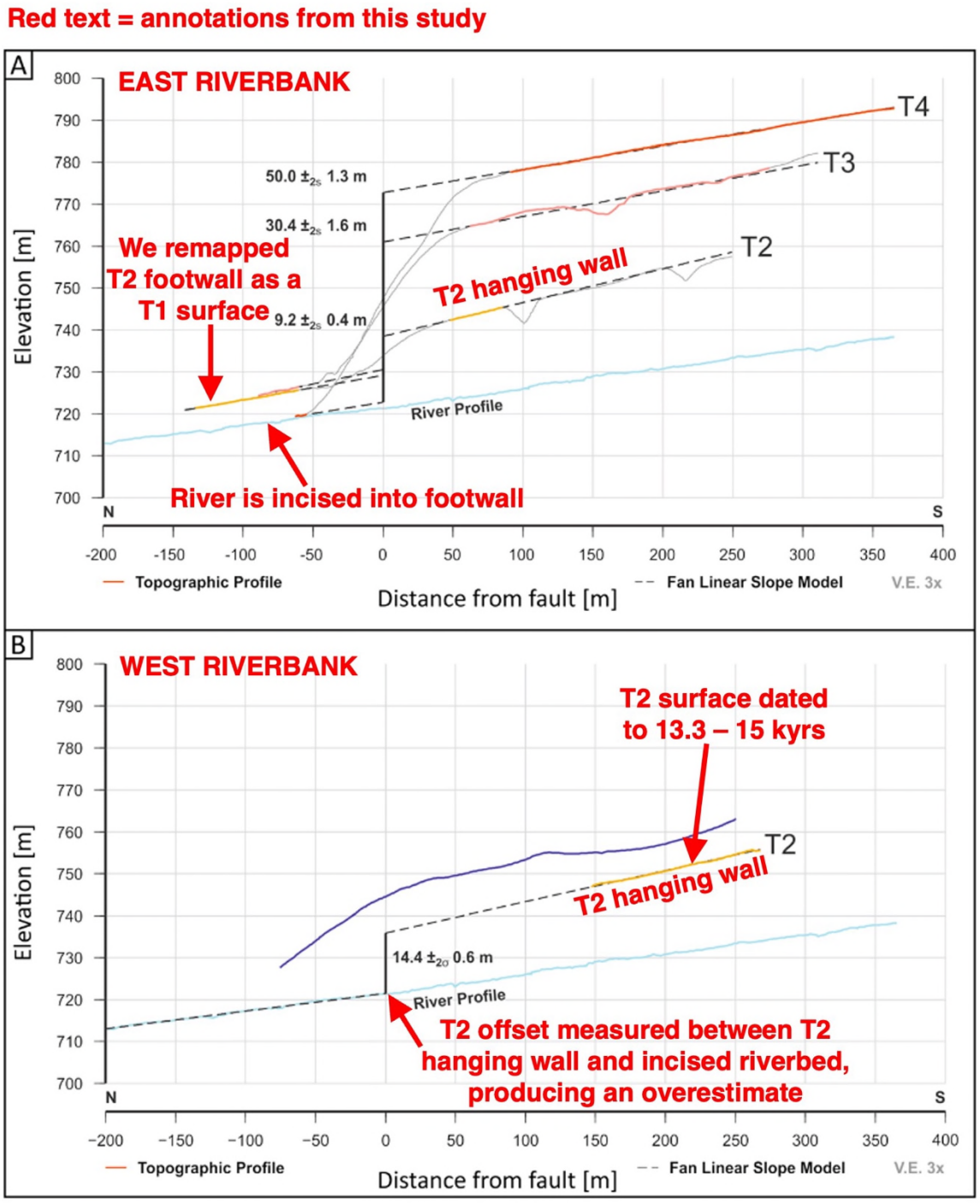

Figure 3.3-10. Figure modified after Grützner et al. (2017b) showing dGPS profiles at slipe rate site S7 (N18 in this study) which correspond to those marked in Figure 3.3-9. (A) Profiles from the east riverbank. (B) Profile from terrace T2 on the west riverbank is in yellow, purple profile is from a surface to the west. Annotations from this study have been added in red.

3.3.2.4.2. Chilik Sites from Selander et al. (2012)

Selander et al. (2012) report two slip-rates from the eastern end of the ZRF to the west of the Chilik river, at sites vi and vii in Figure 3.3-11b, close to our scarp sites N20 and N21. They calculate a slip rate of 0.8 ± 0.5 mm/yr for the northern fault strand at vi, and 0.43 ± 0.3 mm/yr on the strand to the south at vii. They obtained these rates by measuring surface offsets in dGPS profiles, mapping the Quaternary deposits surrounding these sites and then applying ages from other dated surfaces in the region from Thompson et al. (2002). Based on the Thompson et al. (2002) classification of river terraces and their own additional criteria (including morphology, position and soil characteristics), Selander et al. (2012) classify regional Quaternary surfaces as Q1 to Q4 (oldest to youngest), subdividing Q2 into $Q2_1$ and $Q2_2$, and Q3 into $Q3_1$, $Q3_2$ and $Q3_3$ (Figure 3.3-11b). At sites vi and vii, they measure offsets in fans inferred to be of generation Q2 and apply an age based on other Q2 surfaces in the Tian Shan. In the paragraphs below, we reassess this approach.

We compare the Selander et al. (2012) mapping of Quaternary geology to our dataset from the same study area in Figure 3.3-11. According to their mapping, sites N18 and N19 lie within a Q3 surface to the north of the ZRF. Selander et al. (2012) date a Q3 surface elsewhere in the Tian Shan to ~85 ka, but the fluvial and alluvial sediments from sites N18 and N19 have been dated to ~15 – 10 ka (Grützner et al., 2017b; this thesis). Whilst we do not have dates from the Q2 fans at sites vi and vii used in the Selander et al. (2012) rate calculations, the inconsistency of Q3 with direct dating casts doubt on the validity of their inferred Quaternary mapping and inferred regional age correlation. Furthermore, where Selander et al. (2012) map a single Q2 or Q3 fan surface, our detailed studies of high-resolution drone DEMs in this area show that larger fans in fact tend to be composed of ~3 – 5 different generations of cross-cutting surfaces which probably have a large range of different ages (e.g. at N22 in Figure 3.3-11c), with scarp heights ranging from <1 m to >20 m depending on the surface. We suggest it is unlikely that all of the areas mapped by Selander et al. (2012) as Q2 were really

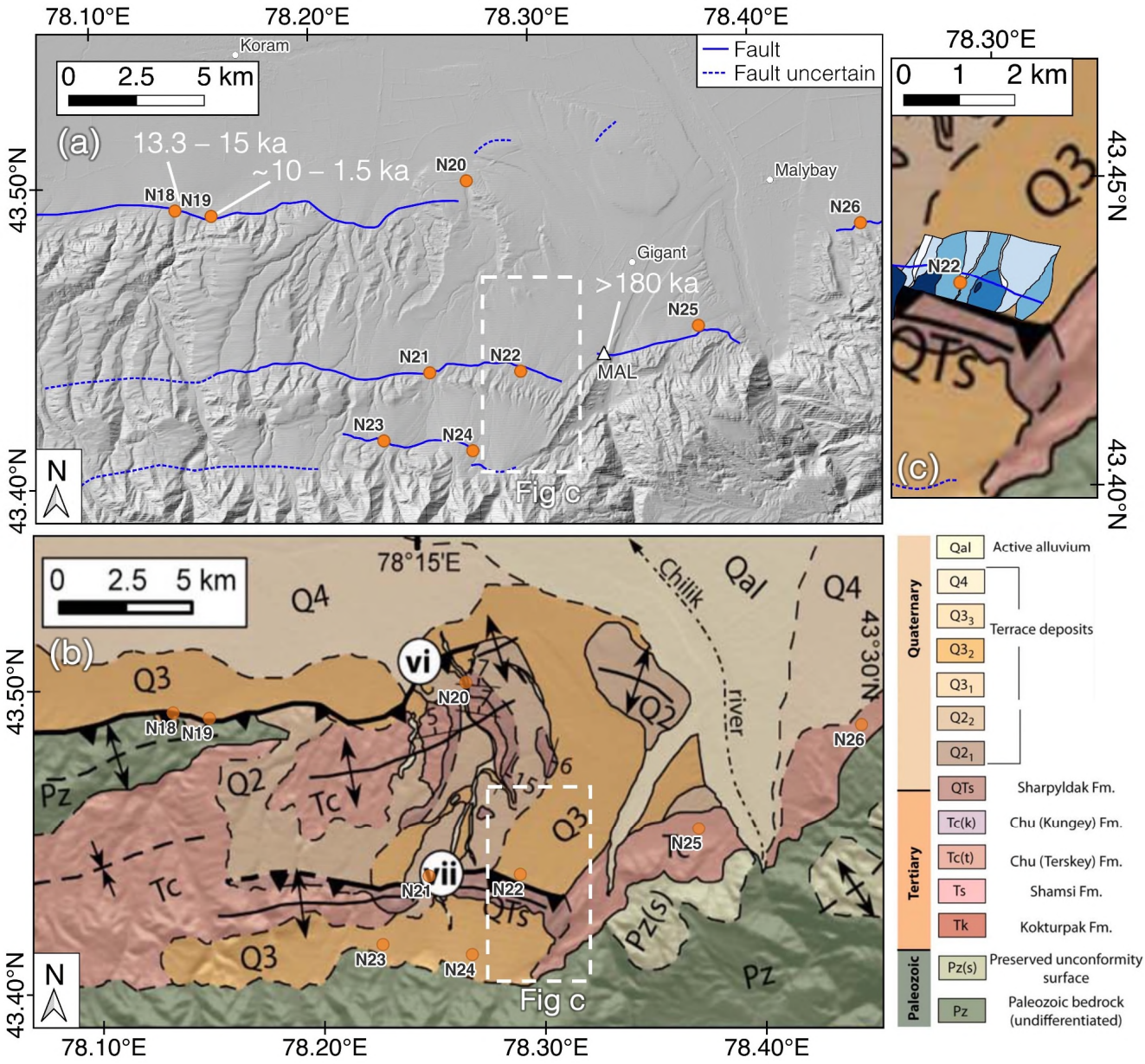

Figure 3.3-11. (a) Hill-shaded Copernicus 30 m DEM. Orange circles show sites from this thesis. White triangle shows location of MAL sampling site from Dave et al. (2023). Sites with which have been dated are labelled with their estimated ages in white. N18 age from Grützner et al (2017b). (b) Neogene and Quaternary geological map and legend modified after Selander et al. (2012). Sites vi and vii show locations of their two slip rate estimates. Map is overlain by orange circles showing sites from this thesis. (c) Zoomed-in map showing Selander et al. (2012) geological map overlain by fan mapping from this thesis at site N22. We map at least 4 generations of fan (darker colours = older fans) in addition to modern channels.

formed around the same time. It is unclear exactly where the dGPS profiles used by Selander et al. (2012) to measure offsets are located and it is therefore difficult to assess the impact of our contrasting mapping on those measurements.

For the slip rate calculation, Selander et al. (2012) use an age for Q2 based on a combination of dated surfaces in the region from Thompson et al. (2002), Bowman et al. (2004) and their own study. Thompson et al. (2002) report a date of 140.7 ± 8.5 ka for $Q2_2$, averaged across four river terraces in the Kyrgyz Tian Shan, > 200 km E or SE of the ZRF slip rate site. Selander et al. (2012) date a $Q2_2$ terrace to 126.4 ± 10.8 ka and a $Q2_1$ terrace to 139.9 ± 6.5 ka from the Toru-Aygir River valley, ~175 km to the SW of ZRF slip rate site. Bowman et al. (2004) also report dates for the Toru-Aygir River valley – we were unable to determine for certain which of these dates correspond to which terraces, but from our best interpretations of the publications, we infer that one or both of 63.8 ± 7.1 ka and 81.7 ± 7.1 ka are considered to apply to Q2 (Selander et al., 2012). Selander et al. (2012) combine the above dates to obtain an age of 100 ± 30 ka for Q2 for the ZRF slip rate calculations. We suggest that such a large range of ages for Q2 may indicate that this is not in fact a surface that can be correlated across the region. Estimates for $Q3_2$ are 85.6 ± 7.6 ka from Selander et al. (2012) and 96.0 ± 8.6 ka from Bowman et al. (2004), lying well within the 100 ± 30 ka estimate for Q2. This calls into question whether these divisions truly represent distinct phases of terrace formation.

We also question the assumption that regional correlations of river terraces can be directly applied to alluvial fans. Terraces and fans form through different, though often connected, hydrological processes and the level of connectivity (or 'coupling') of a fluvial system can vary depending on time and place (Harvey, 2002; Mather, Stokes and Whitfield, 2017). Even if the terrace correlation is applicable locally to alluvial fans, it is unclear that it would still apply at the Selander et al. (2012) slip rate sites which lie at least ~175 km away from all the dated sites in the Kyrgyz Tian, in most cases on the other

side of at least one mountain range. In our own analysis of the ZRF, we are unable to correlate alluvial fan surfaces even over short distances along the fault based on their morphology in satellite imagery, and we find that fan morphology appears to be dependent on a range of factors, including but not limited to age (e.g. uplift, catchment size).

Therefore, while they are not dissimilar from our own rates estimates within error, we are not confident in either the Quaternary mapping or age assumptions behind the Selander et al. (2012) rates. Direct dating of the Quaternary surfaces at sites vi and vii would be required to confirm the robustness of these values and we exclude them from our summary of slip rates on the ZRF.

3.3.2.5. Consistency Checks

Originally mapped by Grützner et al. (2017b), at site N14 (near Rahat) a suite of river terraces (T1 – T4, youngest to oldest) cross the fault (Chapter 2 Appendix Figure 2.7-21). T1 terraces are undeformed, but T2 terraces are offset by 4.7 ± 0.1 m and 4.9 ± 0.1 m, and terrace T3 is offset by 12.7 +/- 0.2 m. As the Thompson et al. (2002) regional terrace age of 13.5 – 15.7 kyrs BP is consistent with direct dating of the youngest deformed terrace at site N18 (see above), we tentatively apply it here at site N14 to the T2 offset. This yields an uplift rate of ~0.33 ± 0.02 mm/yr, slightly larger than the directly dated uplift rates, but broadly consistent within the likely errors. Sample dating would be required to confirm the age of the terrace and the inferred uplift rate, but the Thompson et al. (2002) dataset provides a useful cross check with our measurements.

Archaeological data can also provide constraints on the minimum surface age and therefore the maximum slip rate at some additional sites along the range front (Appendix Table 3.6-3). In the ploughed fields ~1 km north of site N13, no building traces remain but scattered artefacts inferred to be from the Early Iron Age and Middle Ages have been found in a ~200 – 300 x 300 – 400 m area

(A6) (Appendix Figure 3.6-2; Gass, 2016). Although the approximate location of these finds is quite some distance from the scarps at N13, they seem to lie within what appears to be the same surface. As no structural remains were found there is also some uncertainty as to whether the artefacts are definitely in situ. We tentatively suggest that the N13 surface is at least ~2.8 – 2.2 kyrs old. Applying this minimum age to the smallest scarp at N13 (~1.6 – 2.9 m) yields a maximum uplift rate of ~0.7 – 1.0 mm/yr.

At site N7 near the village of Pokrovka, the deformed surfaces are covered in Kurgans. Bekseitov et al. (2019) excavated 3 of these burial mounds and found evidence that two were constructed in the Early Iron Age based on their style and contents (A1 in Appendix Figure 3.6-3). The rest of the Kurgans are very likely to be from the same period (Anton Gass, personal communication). Applying a minimum age of ~2.8 – 2.2 kyrs to the smallest offset (9.0 ± 3.3 m) at site N7 yields a maximum uplift rate of ~3.6 ± 1.3 mm/yr.

While the three uplift rate estimates above are based on speculative assumptions and have high uncertainties, all are consistent with the particularly slow uplift rate estimates we obtain from direct dating of deformed Quaternary surfaces along the range front.

3.4. Discussion

3.4.1. Geological and Geodetic Slip Rates

Our analysis of the ZRF yields uplift rates of ~0.1 – 0.3 mm/yr across five sites (N3, N4, N11, N18 and N19), corresponding to slip rates of ~0.1 – 0.4 mm/yr (Figure 3.4-1; Table 3.4-1). These values are significantly smaller than previously published rates (Selander et al., 2012; Grützner et al., 2017b), which we found to be erroneous. We note that three of the ZRF slip rate estimates (N11, N18, N19) are

averaged over only ~10 – 15 kyrs, corresponding to only two earthquakes at the trench site (N19) and probably only a few more earthquakes at the other two sites (N11 and N18) where scarps are ≤ 3.5 m high. Averaging over so few earthquakes means that some of the variability in slip rate between sites probably reflects variability in slip along strike in individual events (Manighetti et al., 2005; Biasi and Weldon, 2006; Wesnousky, 2008) as well as variability in earthquake recurrence intervals. Hypothetically, if an earthquake occurred tomorrow at the trench site (N19), the slip rate measured from the ~10 ka layer would significantly increase compared to today's value, whereas the slip rates from sites N3 and N4 would be minimally affected by the same scenario as they are averaged over many more earthquakes. The possible temporal clustering of fault activity in this region (e.g. Krüger, Kulikova and Landgraf, 2018) could also mean that slip rates averaged over shorter intervals may not accurately reflect the longer term rate (Vernant, 2015). Nevertheless, the variation in rate estimates between sites is relatively small.

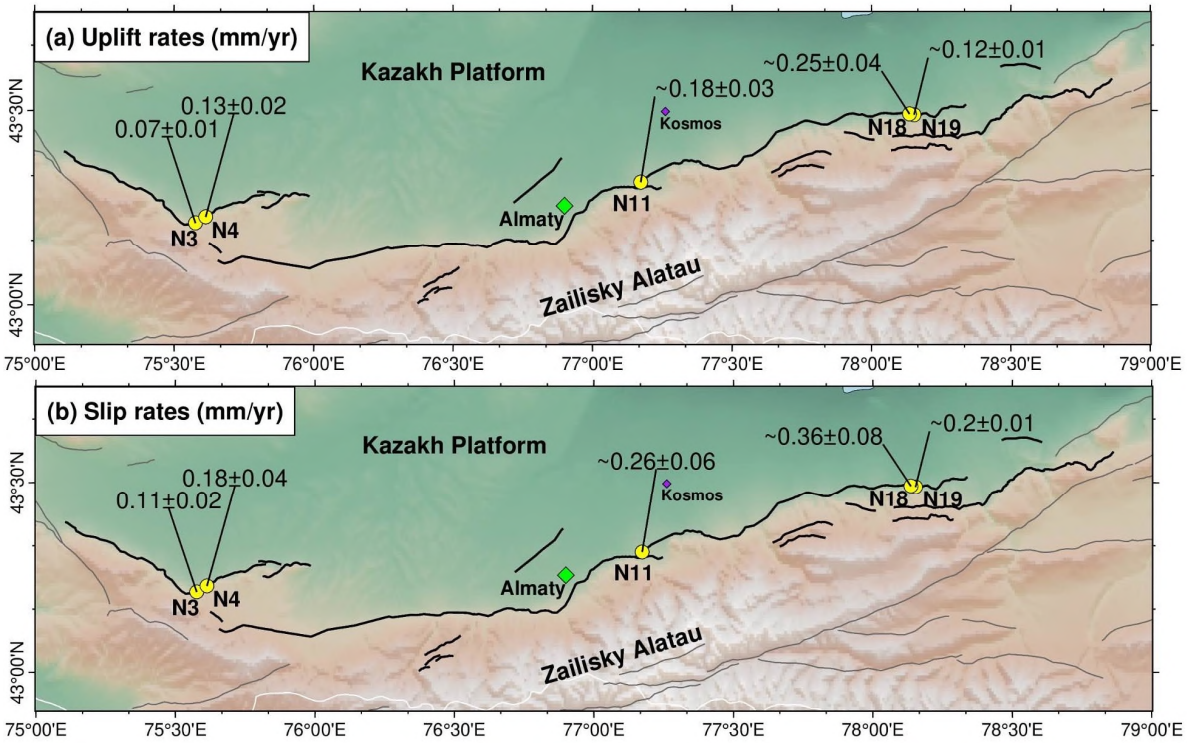

Figure 3.4-1. Summary of (a) uplift rate and (b) slip rate estimates on the ZRF. Thick black lines = ZRF. Other faults (dark grey lines) modified after Zelenin et al. (2022) with mapping from this study. Yellow circles show the locations of rate sites, labelled with their measurements in mm/yr.

Table 3.4-1. Summary of rate estimates. *Average of multiple measurements. All slip rates calculated using a range of slip range of fault dips between ~30º – 60º except N19. '~' indicates significant uncertainties which cannot be captured by the formal error. **N11 estimate is based on age data from ~7 km downslope of the scarp, adding additional uncertainty to the result.

Fault section	**Site**	**Offset (m)**	**Slip (m)**	**Age (kyrs)**	**Uplift rate (mm/yr)**	**Slip rate (mm/yr)**
Akterek (plateau bounding fault)	N3	2.2 ± 0.3*	NA	29.8 ± 1.8*	0.07 ± 0.01	0.11 ± 0.02
	N4	7.7 ± 1.2	NA	61.5 ± 4.1	0.13 ± 0.02	0.18 ± 0.04
Central	N11: Talgar fan	2.9 ± 0.5*	NA	16.2 ± 1.0*	~0.18 ± 0.03	~0.26 ± 0.06**
Eastern	N18: Stream terraces reassessed from Grützner et al. (2017b)	3.5 ± 0.5	NA	~15 – 13.3	~0.25 ± 0.04	~0.36 ± 0.08
	N19: Trench site	~1.2	~2.0	9.8 ± 0.5*	~0.12 ± 0.01	~0.20 ± 0.01

At sites N4 and N11, the dated samples were collected from the loess directly above fan gravels. As discussed in Methods section 3.2.2. , our calculations assume that there is no hiatus in loess deposition after fan abandonment, and therefore that these samples provide a good approximation of the fan abandonment age. We deem this to be a reasonable assumption within the resolution of the age data, which has uncertainties on the order of thousands of years. However, if this assumption is incorrect, the dates from sites N4 and N11 will be underestimates of the fan abandonment age and the resulting slip rates (0.18 ± 0.04 mm/yr and ~0.26 ± 0.06, respectively) will be overestimates. In this scenario, our conclusion still stands: the true slip rates on the along the Zailisky Range Front are smaller than the previously published rates.

In Chapter 2, we found evidence of at least ~0.2 – 1 m of uplift in the most recent earthquakes on the ZRF. Combining this with the uplift rate of ~0.1 – 0.3 mm/yr yields an average recurrence interval of between ~700 yrs and 10 kyrs. This is consistent with our findings from the trench in Chapter 2, which shows thousands of years of inactivity between earthquakes.

Table 3.4-2. Deformation rates between the Zailisky Alatau and the Kazakh Platform from GPS data. Uplift and slip rates are inferred by applying a fault dip of 30 – 60° to the mean shortening rate.

Measured GPS rate	**Inferred GPS rates**	
Shortening rate (mm/yr)	**Uplift rate (mm/yr)**	**Slip rate (mm/yr)**
1.3 ± 0.4	1.4 ± 0.6	1.9 ± 0.7

We find that the geodetic shortening rate between the Zailisky Range Front and the Kazakh Platform is 1.3 ± 0.4 mm/yr based on GPS velocities (Table 3.4-2), accounting for approximately 9% of the ~15 mm/yr of shortening between the western Tarim Basin and the Kazakh Platform (Zubovich et al., 2010; Wu et al., 2023). This corresponds to a slip rate of 1.9 ± 0.7 mm/yr, which is much larger than our geological slip rate estimates. This suggests that the strain between the mountains and the platform is distributed across multiple parallel structures. At the western end of the fault, we measure ~0.1 – 0.2 mm/yr of slip on the northern boundary of the uplifted plateau (N3 and N4), but the change in GPS rate occurs to the south of this fault strand, implying that the fault which runs along the base of the mountains is probably the dominant structure accommodating shortening in this section (Figure 3.3-2). At the eastern end of the ZRF, the fault splits into three parallel strands, and our slip rate sites N18 and N19 (~0.2 – 0.4 mm/yr) are located on the northern-most fault. Here, the other two parallel strands probably also accommodate some of the shortening, although no large velocity changes are apparent across these structures in the sparse GPS data (Figure 3.3-2). In the central section of the fault at site N11, whilst no major parallel faults are apparent, there are scarps a few kilometres to southeast of our slip rate site (N12, Figure 3.3-7) which could potentially form part of another parallel strand.

Whilst these parallel faults might account for some of the discrepancy in slip, the available GPS data are also consistent with shortening occurring in the first ~50 km of the Kazakh Platform (Figure 3.3-2, Figure 3.3-1). There is geomorphic evidence to support foreland deformation, including a large zone of incision in the west (Chapter 2), a ~25 km long fault splay to the north of Almaty (Grützner et al., 2017b; Amey et al., 2021), and folded sediments near Kosmos, labelled in Figure 3.3-2 (Macklin et al., 2015; Grützner et al., 2017b).

With the available data, we cannot conclusively rule out various other explanations for the mismatching geological and geodetic rates such, as an acceleration in slip rate (e.g. Gold et al., 2017; Rust, Korzhenkov and Tibaldi, 2018). However, given that the GPS data do not constrain shortening to a single range front fault, that there are mapped parallel fault strands near our geological slip rate sites, and that there is evidence for shortening in the foreland, it seems more plausible that the discrepancy is due to the shortening being accommodated on multiple structures.

In summary, our results reveal that the shortening between the Zailisky Alatau and the Kazakh Platform is not accommodated on a single fault. The fault strands with geological rate estimates accommodate less than one fifth of the geodetic strain, and the active structures accommodating the remaining shortening might be mapped fault strands along the range front, unmapped faults and folds within the Kazakh Platform, or a combination of both. This highlights that there may be unmapped seismic sources which could pose a hazard to the Zailisky Range Front population. More dense GPS networks and slip rate measurements on parallel structures are needed to better understand which structures are accommodating the deformation. Dense seismic arrays and seismic reflection surveys could also help to identify structures in the foreland and within the Kazakh Platform.

3.4.2. Tectonic History

We measure ~0.1 mm/yr of uplift on the fault which bounds the northern edge of the plateau at the western end of the ZRF. The plateau is uplifted ~ 500 m above the foreland at its highest point. Assuming the uplift rate remained been constant over the past few million years, the plateau must have started uplifting in the late Miocene, around ~ 5 Ma. Exhumation of the Tian Shan began in the late Oligocene to early Miocene, but there is evidence for one or more increases in shortening rate, with the most recent acceleration occurring around the late Miocene (several studies estimate ~11 Ma, with

others ranging between ~15 – 4 Ma; Windley et al., 1990; Hendrix, Dumitru and Graham, 1994; Sobel and Dumitru, 1997; Bullen, Burbank and Garver, 2003; Sobel, Chen and Heermance, 2006; Heermance et al., 2008; Charreau et al., 2009; Macaulay et al., 2014). It is possible that the plateau began uplifting as a result of the increased shortening in the Late Miocene.

3.5. Conclusion

Our analysis suggests Quaternary slip rates on the ZRF are between ~0.1 – 0.4 mm/yr in deposits of ~10 – 60 ka. These rates are consistent with recurrence intervals on the order of thousands of years, as documented in a paleoseismic trench of the ZRF in Chapter 2. The geological slip rates are much smaller than the geodetic slip rate between the Zailisky Alatau and the Kazakh Platform which we find to be 1.9 ± 0.7 mm/yr based on GPS velocities, accounting for ~9% of the shortening across this section of the western Tian Shan. We suggest that geodetic rates are faster because they capture a wider zone of deformation than the geological measurements of individual fault strands. Shortening must be accommodated across multiple parallel structures along the Zailisky Range Front and probably also within the first 50 km of the Kazakh Platform. Such structures could constitute unmapped sources of seismic hazard, and denser geodetic, seismological and geological measurements are needed to identify the dominant active structures.

3.6. Appendix of Chapter 3

3.6.1. Luminescence Dating

Table 3.6-1. Additional parameters from the IRSL analysis of the 2016 samples provided by Kathryn Fitzsimmons, who undertook sample dating in Leipzig, Germany. OD = Overdispersion.

Sample name	**Lab code**	**Site**	**Dose-rate components**				**Additional characteristics**		
			K (%)	**Th (ppm)**	**U (ppm)**	**Cosmic dose rate (Gy/ka)**	**Recycling ratio**	**Residual dose (Gy)**	**OD (%)**
AKT1	EVA1564	N3 – Arkhaly 1	1.74 ± 0.09	9.70 ± 0.49	3.10 ± 0.16	0.20 ± 0.03	1.00 ± 0.01	1.7 ± 0.3	12.2
AKT2	EVA1565		1.75 ± 0.09	9.90 ± 0.50	2.90 ± 0.15	0.20 ± 0.03	1.00 ± 0.02	1.6 ± 0.2	11.8
AKT3	EVA1566		2.22 ± 0.11	10.1 ± 0.5	2.80 ± 0.14	0.20 ± 0.02	1.00 ± 0.01	1.4 ± 0.0	12.3
AKT4	EVA1567	N4 – Arkhaly 2	2.07 ± 0.10	10.4 ± 0.5	3.70 ± 0.19	0.12 ± 0.01	1.00 ± 0.01	N/A	7.2

3.6.2. Geodetic rates

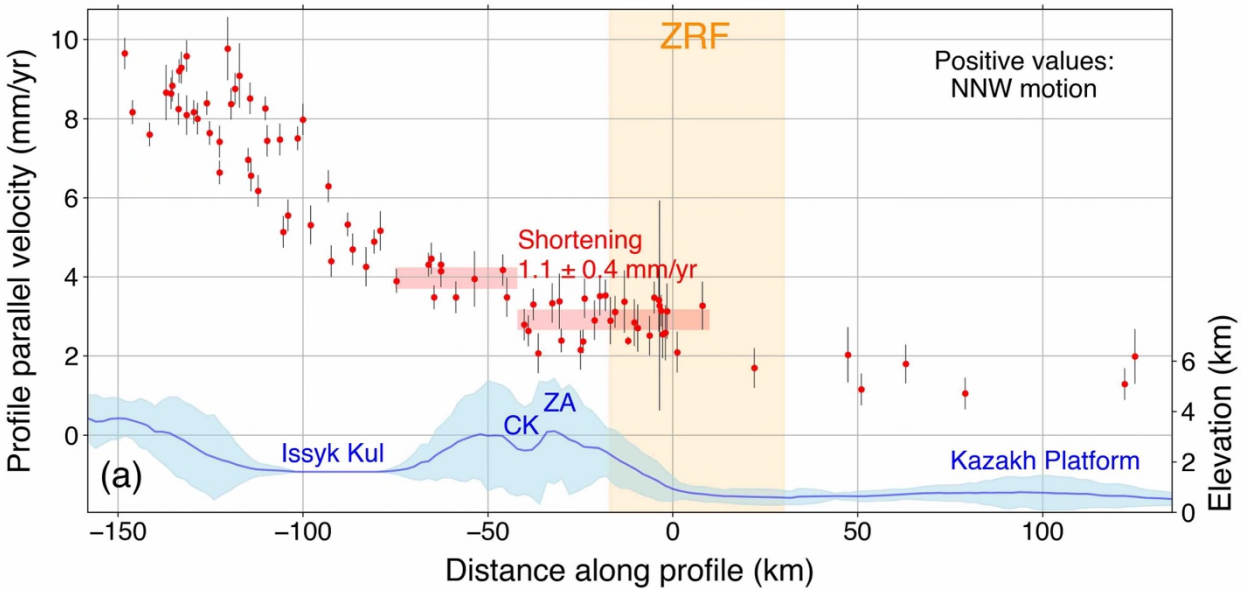

Figure 3.6-1. Profile parallel GPS velocities. Profile extent is marked by red box in Figure 3.1-1, which is 276 km wide. Red rectangles show the ranges of datapoints in the hanging wall and footwall used calculate the shortening rate across the Chon Kemin valley (CK), centred on the mean velocities with widths of 2σ. Topography is shown in blue (blue line = median elevation). GPS velocities (referenced to stable Eurasia) are from the compilation by Wang and Shen (2020) (and references therein). ZA = Zailisky Alatau. Shaded orange region marks the extent of mapped faults along the Zailisky Range Front.

3.6.3. Geological rates

Table 3.6-2. Comparison of uplift rate and slip rate results using the average sample age from the oldest offset layer (unit 2) vs the age obtained from OxCal model A for the same layer, detailed in Chapter 2. ka = kyrs before 2023.

Trench Unit	**Number of earthquakes**	**Slip (m)**	**Uplift (m)**	**Unit age (ka)**	**Uplift rate (mm/yr)**	**Slip rate (mm/yr)**
Unit 2	2	~2 m	~1.2	**Sample average:** 9.8 ± 0.5	~0.12 ± 0.01	~0.20 ± 0.01
				OxCal model A: 10.4 ± 0.3	~0.12 ± 0.00	~0.19 ± 0.01

3.6.3.1. Sites and Offsets

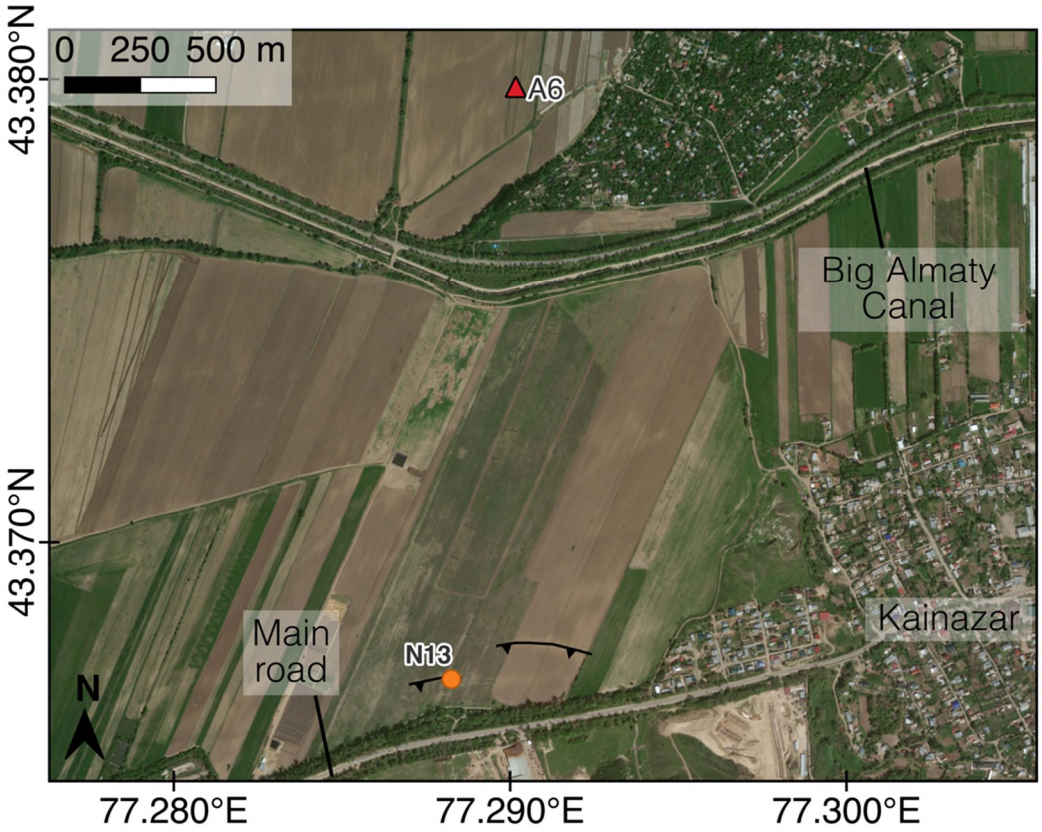

Figure 3.6-2. Map of scarps at N13 and nearby archaeological finds (A6), with imagery from Bing Aerial (2023 TomTom, 2023 Maxar) .

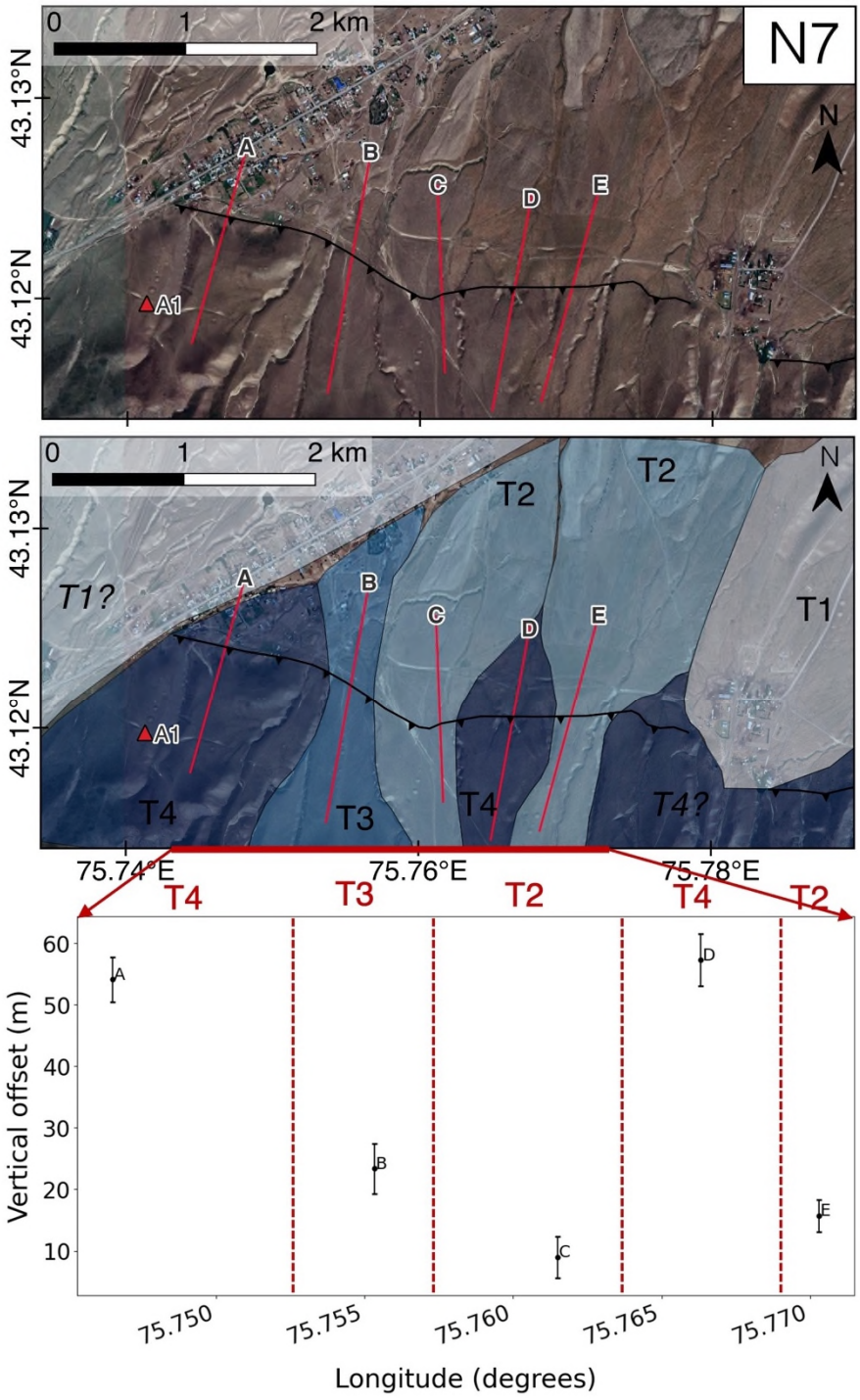

Figure 3.6-3. Site N7 near Pokrovka. A1 is an early Iron Age burial ground (Bekseitov et al., 2019). Top: Google Satellite imagery (2024 Airbus). Middle: Four fan generations overlain on the Google Satellite imagery (2024 Airbus). Bottom: Vertical offset measurements with longitude. Red dashed lines represent transitions between fans of different ages which are labelled above the plot.

3.6.3.2. Archaeological Data

Table 3.6-3 – Archaeological sites along the ZRF. All sites were selected from Gass (2019) apart from the Pokrovka site marked with a *.

Nearest scarp site	Nearby archaeological sites	Age	Details	Likely minimum surface age
N7	A1* (Sunkar burial ground)	Early Iron Age	2 Kurgans characteristic of the Early Iron Age Saka period, contents (e.g. utensils and arrowhead tips) indicate 4th – 3rd centuries BC. Third Kurgan estimated to be younger 2nd Century BC – 5th Century AD. (Bekseitov et al., 2019) Other Kurgans across the site also very likely to be from the Saka period (Anton Gass, personal communication)	~2.8 – 2.2 kyrs
N11	A2 (Tuzusaj settlement)	Early Iron Age	Collection of pit houses on bank of abandoned stream bed. Spengler, Chang, and Tourtellotte (2013) present C-14 dates between 410 BC – 150 BC. Gass (2019) cites C-14 dates in similar range and additional stray finds of from 4th Century BC – 1st Century AD.	~2.8 – 2.2 kyrs
	A3 (Cyganka 8 settlement)	Early Iron Age	Collection of early iron age pit houses and additional stray finds from the same period. One house has been dated to 385-100 BC, another to 775-370 BC with C-14.	
	A4 (Kyzyl-Gajrat settlement)	Early Iron Age – early Middle Ages	Square fortification and protective wall. Ceramics are inferred to be from between the Early Iron Age and the early Middle Ages (Gass, 2016)	
N12	A5 (Talgar settlement)	Early Iron Age to Middle Ages	Building and wall remains from a Middle Ages settlement (thought to be built on the site of an early iron age settlement). Additional stray finds (including a Saka bronze cauldron dated by analogy and Saka ceramics) from the Early Iron Age. Additional reports of Early Iron Age sites from numerous locations around Talgar. (Korjenkov et al., 2003) Fissured wall has been interpreted as evidence of seismic activity (Korjenkov et al., 2003)	~2.8 – 2.2 kyrs
N13	A6 (Kajnazar settlement)	Early Iron Ages and Middle Ages	Settlement area has been ploughed and no building traces remain, but there are various artefacts scattered in the field, including bone fragments and ceramics. Ceramics interpreted as from Early Iron Age and Middle Ages. (Gass, 2016)	~2.8 – 2.2 kyrs

3.7. Authorship Statement for Chapter 3

Contributions: I, Roberta Wilkinson, conducted all the data analysis and wrote the chapter. Discussions with Christoph Grützner and Richard Walker provided direction to the analysis. Luminescence samples from sites N3 and N4 were collected on fieldwork led by Christoph Grützner and Richard Walker before I started my DPhil. Luminescence dating on these samples was conducted by Kathryn Fitzsimmons. All other field data is from the previous Chapter – see authorship statement for Chapter 2.

Acknowledgements: Thank you to Anton Gass for providing information on archaeological sites, and to Aditi Dave who kindly talked through her loess datasets with me. Thank you to Alex Lipp for discussions about best approaches to statistics.

Chapter 4

Aseismic Slip on the Ilyak Fault, Tajikistan, and Active Deformation in the Dushanbe Trough and Tajik Basin

In this chapter, we present a manuscript prepared for submission in which we combine Multi-Temporal InSAR (Interferometric Synthetic Aperture Radar) with a geomorphic analysis to characterise the behaviour of faults around Dushanbe in Tajikistan. The InSAR rate maps we produce cover a larger area of the Tajik Basin (Figure 4.1-1) and contain many signals which warrant further exploration beyond the scope of this thesis. In this manuscript, we focus on the Ilyak fault and other deforming structures close to Dushanbe and their hazard implications, but we discuss possible avenues for further exploration of the entire dataset in the conclusions to this thesis.

4.1. Introduction

Dushanbe, the capital of Tajikistan, sits on the northern edge of the Tajik basin in the Dushanbe Trough (Figure 4.1-1). It is particularly vulnerable to ground shaking due to its rapid expansion over the past few decades onto unconsolidated deposits and landslide-prone slopes (Pilz et al., 2013). The city lies on the Ilyak fault (IF), which runs E-W through the south of the city and has hosted small to medium magnitude earthquakes up to M ~5.5.

Seismic catalogues reveal a cluster of small earthquakes in the centre of the IF occupying a sub-vertical zone ~ 4 – 17 km beneath its surface trace. The focal mechanisms of the two largest events (M_W 4.7 at 17 km and M_W 3.7 at 14.5 km) are consistent with right-lateral strike-slip (Figure 4.1-2; Kufner et al., 2018). Additionally, the M ~5.5 Gissar earthquake (G in Figure 4.1-2) ruptured the western end of the fault in 1989, with a focal mechanism also consistent with right-lateral slip on the IF (Djuraev and Shakirdzanova, 1993). Depth estimates for the Gissar earthquake vary from ~2.5 – 12 km, but modern estimates from the International Seismological Centre suggest a depth of ~12 km and are consistent within their uncertainties (Engdahl, Van Der Hilst and Buland, 1998; Weston et al., 2018; Engdahl et al., 2020; 2020; Storchak et al., 2020; International Seismological Centre, 2022b; 2022a). Despite its moderate magnitude, the Gissar earthquake caused catastrophic landslides in irrigated loess deposits that buried or partially buried several villages and resulted in over 270 fatalities (Ishihara et al., 1990; Djuraev and Shakirdzanova, 1993). These seismic observations suggest that activity on the IF is not limited to the sedimentary cover and indicate the presence of a sub-vertical structure extending into the basement below (Gągała et al., 2020).

The interior of the Tajik basin is characterized by a set of westward-convex folds and thrust sheets trending approximately N-S. In the northern part of the basin most of the thrust sheets curve eastwards as they are dragged into the IF. A notable exception is the westward-dipping Babatag thrust (BT) in the

west of the basin, which intersects the IF at ~90° around ~68.6°E (Figure 4.1-2). Large earthquakes in the region tend to be restricted to the surrounding mountains or their margins, such as the M_W ~7.5 (Chen and Molnar, 1977; Bindi et al., 2014) 1949 Khait earthquake which occurred on the boundary between the Pamir and the Tian Shan (outside the region of Figure 4.1-1; Evans et al., 2009). In 1907 the ~M7.5 Karatog (or Qaratog) thrust earthquake caused damage on the southern slopes of the Tajik Gissar, with reports of more than 1500 fatalities (Kondorskaya et al., 1982; Kalmetieva et al., 2009; Kulikova, 2016). However, the causative fault is unknown, with some sources attributing the event to a thrust bounding the southern edge of the Tajik Gissar, where the macroseismic effects were reported (Nikonov and Shebalina, 1979; Mikhailova et al., 2015) and others placing it >200 km further east within the Peter the 1st range (circles A, B and C in Figure 4.1-1; Kulikova, 2016).

Due to sparse GPS observations and a lack of detailed geomorphic mapping, there is limited knowledge about the strain accumulation on individual faults and folds in the Tajik basin and Tajik Gissar. This lack of comprehensive data makes it challenging to assess the seismic potential of this region accurately. To address this gap, it is essential to conduct continuous mapping of deformation across the basin.

Previous geodetic studies in this region have documented the westward motion of the Tajik basin, with notable deformation occurring on the IF and the BT (Mohadjer et al., 2010; Zubovich et al., 2010; Ischuk et al., 2013; Metzger et al., 2020; 2021). Metzger et al. (2021) generated InSAR (Interferometric Synthetic Aperture Radar) rate maps with a horizontal resolution of ~400 m covering the Tajik basin and the Pamir mountains region. Their findings reveal E-W convergence of about 5 mm/yr on the BT, and a strike-slip rate of around 10 mm/yr in the eastern part of the IF, decreasing to approximately 5 mm/yr in the west. However, the Metzger et al. (2021) dataset has limitations, being of low spatial resolution and strongly filtered, with a low signal-to-noise ratio and poor coverage in some areas. Consequently, it is challenging to ascertain whether the IF is slipping aseismically or

accumulating strain. Additionally, the study does not address whether the observed velocity contrast is localised on a single structure or distributed across multiple faults.

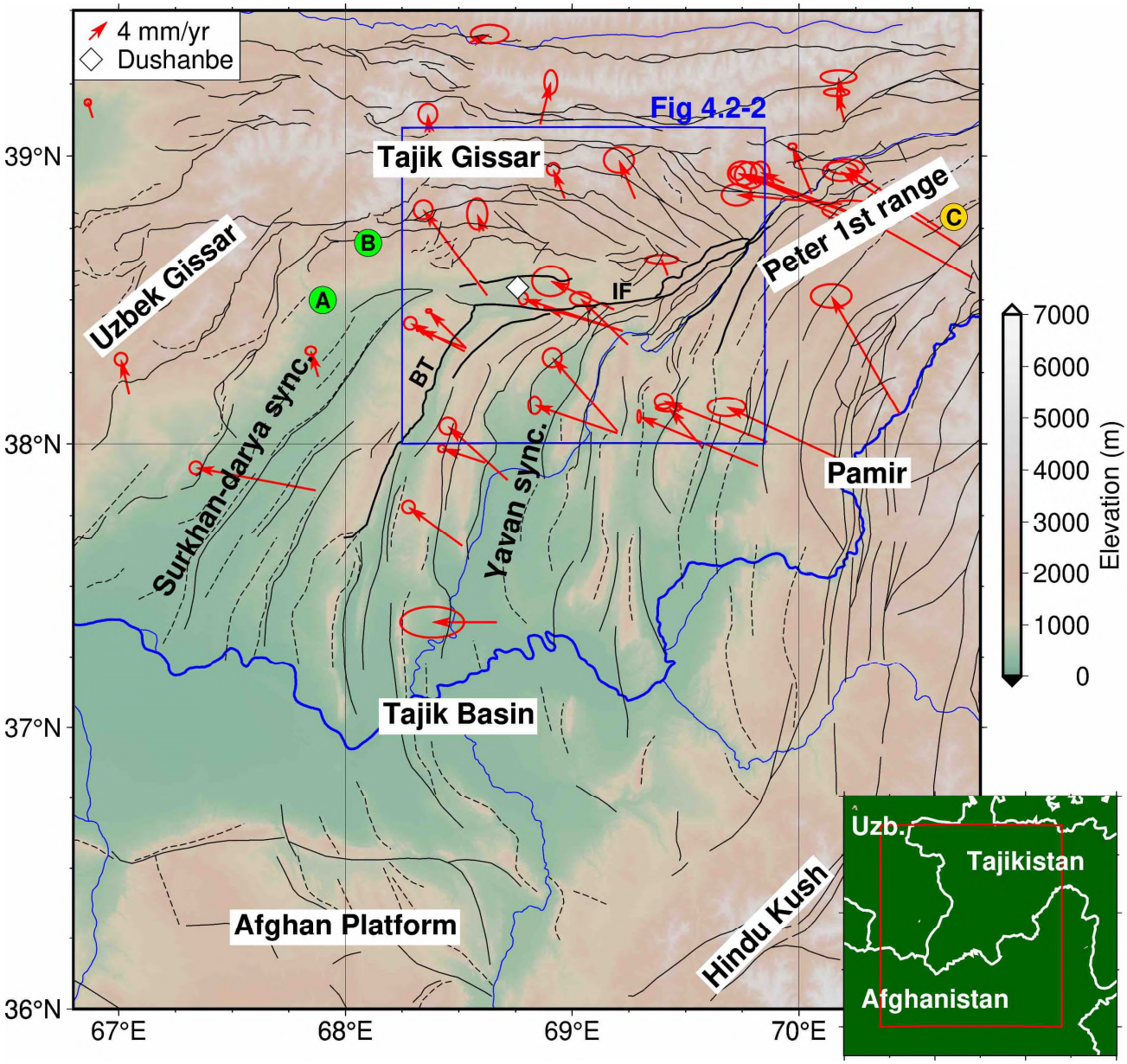

Figure 4.1-1. The Tajik basin and surrounding regions. Topography from 30 m SRTM DEM (NASA JPL, 2013) with major rivers in blue. Solid thin black lines are faults and dashed thin black lines are fold axes, both after Dedow et al. (2020) and Abdulhameed et al. (2020). Thick black lines highlight active faults discussed in this study. IF = Ilyak fault, BT = Bababtag thrust, sync=syncline. GPS (relative to stable Eurasia) from Metzger et al. (2020) and Zubovich et al. (2010) with 70% confidence ellipses. Blue box shows location of Figure 4.1-2. Green circles A and B show the locations of the two 1907 Karatag earthquake events (20 minutes apart) from Mikhailova et al. (2015), while yellow circle C shows the relocation of the 1907 Karatag earthquake by Kulikova (2016) who found only one event.

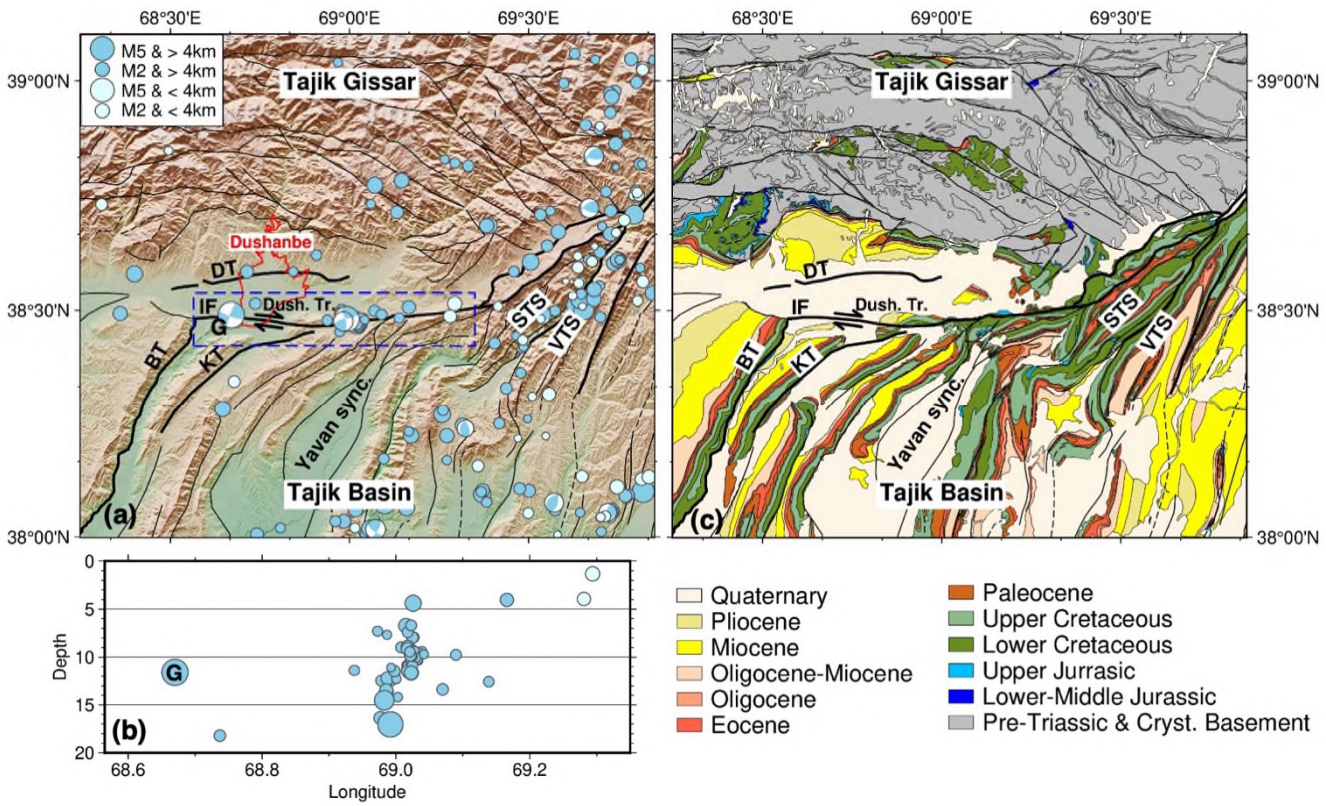

Figure 4.1-2. Maps of the study region: the northern Tajik basin, Dushanbe Trough (Dush Tr.) and southern Tajik Gissar. Solid thin black lines are faults and dashed thin black lines are fold axes, both after Dedow et al. (2020) and Abdulhameed et al. (2020). Thick black lines highlight active faults discussed in this study. IF = Ilyak fault, BT = Bababtag thrust, DT = Dushanbe Trough thrust, STS = Surkhu thrust sheet, VTS = Vakhsh thrust sheet, sync=syncline. (a) Topography from 30 m SRTM DEM. Earthquakes from 2008 – 2014 and focal mechanisms for larger events from Kufner et al. (2018), size corresponds to local magnitude. G = 1989 M5.5 Gissar earthquake (Djuraev and Shakirdzanova, 1993; Maisuradze et al., 1993; Storchak et al., 2020; International Seismological Centre, 2022b). Blue box shows region of earthquakes plotted in (b). Red polygon shows Dushanbe administrative boundary from Open Street Map. (b) Earthquakes in the vicinity of the Ilyak fault plotted by depth. (c) Geological map of the study region from Abdulhameed et al. (2020) and Gągała et al. (2020).

In the present study, we conducted a Multi-Temporal InSAR (MT-InSAR) analysis across the Tajik basin, by analysing networks of 451 (ascending track) and 588 (descending track) interferograms from Sentinel-1 data to produce a continuous and high-resolution mapping of the deformation. We generated ~130 m resolution rate maps with high spatial coverage, which are robustly constrained by redundant interferometric networks (Appendix Figure 4.6-1) corrected with atmospheric delay models (Appendix section 4.6.1.1.3). By adopting this processing method, we determine the extent of aseismic slip and the slip partitioning between the IF and neighbouring structures. Furthermore, we produce the

first rate maps to capture ground deformation in the southern part of the Tajik Gissar and across the thrust sheets in the northeast corner of the Tajik basin. We integrate InSAR measurements with geomorphic mapping, utilizing high-resolution Digital Elevation Models (DEMs) around Dushanbe for further identification and mapping of active faults. Finally, we discuss the implications of the results for seismic hazard in Dushanbe.

4.1.1.1. Seismo-Tectonic Setting

The Tajik basin is a fold and thrust belt in Central Asia, bounded by the Afghan platform to the south, the Tajik Gissar mountains (the southwestern end of the Tian Shan) to the north, the Uzbek Gissar mountains to the west, the Pamir mountains to the east, and the Hindu Kush to the southeast (Figure 4.1-1; Bourgeois et al., 1997; Gągała et al., 2020). The basin stratigraphy consists of ~5 – 10 km of sediments overlying pre-Triassic crystalline basement that also forms the Tajik Gissar and Uzbek Gissar mountains (Gągała et al., 2020). The sedimentary sequence comprises Triassic to Oligocene carbonates and clastic deposits in an epicontinental basin, followed by Neogene synorogenic clastics (mainly conglomerates) derived from the surrounding orogens (Figure 4.1-2; Abdulhameed et al., 2020; Gągała et al., 2020). Near the base of the sedimentary sequence is a layer of upper Jurassic evaporites named the Gaurdak formation (Gągała et al., 2020). In the Neogene, the inversion of the basin initiated the formation of an of E-W shortening and thin-skinned fold and thrust belt which characterises the present day morphology of the basin (Abdulhameed et al., 2020).

The thrust sheets exhibit an eastward dip in the eastern part of the basin and a westward dip in the western part, with the change occurring across the Yavan syncline (Figure 4.1-1; Bourgeois et al., 1997; McNab, Sloan and Walker, 2019; Abdulhameed et al., 2020; Gągała et al., 2020). This E-W shortening is primarily confined to the Jurassic – Neogene sedimentary units situated above the Gaurdak evaporite formation, which acts as a detachment layer throughout the basin and lies at the

base of the thrust sheets (Schurr et al., 2014; Kufner et al., 2018; Gągała et al., 2020). This thin-skinned E-W shortening is caused by the lateral extrusion of the western Pamir, thought to be due to its gravitational collapse (Stübner et al., 2013; Schurr et al., 2014; Kufner et al., 2018). However, other causes of the E-W extension of the Pamir have also been proposed, including radial thrusting on the Main Pamir thrust leading to divergence, and oroclinal bending (Strecker et al., 1995; Yin, Robinson and Manning, 2001; Robinson et al., 2004). Seismic activity within the basin is characterized by earthquakes of generally low magnitude ($M_W < 4.5$), with only a small number of moderate events (M_W ~5-6; Kufner et al., 2018; McNab, Sloan and Walker, 2019). Most earthquakes occur below the evaporitic layer, indicating aseismic deformation may dominate within the sedimentary cover, and some earthquakes occur on the detachment horizon where the evaporites have thinned out due to diapirism (Kufner et al., 2018; Gągała et al., 2020; Metzger et al., 2021).

Based on several deep thrust earthquakes and geomorphic mapping of E-W trending folds at the southern edge of the basin, McNab, Sloan and Walker (2019) suggest that the basement is deforming by N-S compression induced by the India-Asia collision, inferring a mechanical decoupling between the basement and cover. It has also been suggested that stresses relating to lower crustal and mantle delamination and roll back beneath the Pamir and Hindu Kush could be driving deformation within the basement (Sippl et al., 2013; Kufner et al., 2018).

The IF forms the southern edge of the Dushanbe Trough, a topographic depression to the south of the Tajik Gissar with the same stratigraphy as the central basin but a different structural regime, with fold axes striking ~E-W rather than ~N-S (Figure 4.1-2; Gągała et al., 2020). Borehole data, stratigraphic sections and seismic reflection profiles show that the upper Jurassic sediments are much thinner in the Dushanbe Trough and there is no clear evidence for evaporites (Leith, 1985; Gągała et al., 2020). The faults and folds deform the basement and sedimentary cover together, with no evidence of decoupling

(Gągała et al., 2020). Gągała et al. (2020) attribute the location of the Ilyak fault to the tapering out of the Gaurdak evaporites towards the northern edge of the basin.

At the eastern end of the Dushanbe Trough, the ~E-W-striking IF stops abruptly, as a series of overlapping NE-striking basin thrust sheets directly override the Tajik Gissar, including the Surkhu thrust sheet (STS) and Vakhsh thrust sheet (VTS; Figure 4.1-2; Leith and Alvarez, 1985; Bourgeois et al., 1997). Here, sediments are compressed between the Tajik Gissar and the Pamir in a zone of right-lateral transpression and with enhanced seismicity, forming part of the Peter the 1st mountain range (Bourgeois et al., 1997; Kufner et al., 2018).

4.2. Materials and Methods

4.2.1. InSAR Data and Method

Since the 1990s, InSAR has proven fundamental to the mapping and measurement of surface displacements due to earthquakes (e.g. Massonnet et al., 1993; Ainscoe et al., 2017; Hamling et al., 2017). This technique involves analysing the phase difference between two satellite radar images (SAR acquisitions) of the same location acquired at different times. The resulting phase difference, measured in radians, is proportional to the ground motion towards or away from the satellite in its Line Of Sight (LOS). In addition to ground displacement, individual interferograms contain phase contributions from several other sources such as topographic errors, orbital errors, atmospheric phase delays and noise (Osmanoğlu et al., 2016). These phase change maps, or 'wrapped' interferograms, can be 'unwrapped' (converting cyclical phase information to distance) to produce maps of relative surface displacements in the imaged area. In more recent years, Multi-Temporal InSAR (also known as time-series InSAR) has become prevalent for measuring interseismic deformation on the order of millimetres per year. This method involves constructing networks of interferograms spanning several years and inverting for cumulative phase displacements, yielding average velocities for all pixels (e.g.

Hussain et al., 2016; Ou et al., 2022; Watson, Elliott and Walters, 2022; Lemrabet et al., 2023). Surface displacements due to deformation in a single interferogram are usually very small in the interseismic phase and would be obscured by other phase contributions without correction, but the Multi-Temporal InSAR approach proves effective in eliminating contributions unrelated to deformation (Elliott, Walters and Wright, 2016). Tropospheric phase delays often pose a significant challenge, but various techniques, such as atmospheric models or empirical corrections, can be applied to remove them (Doin et al., 2009; Jolivet et al., 2011; Elliott, Walters and Wright, 2016; Yu, Li and Penna, 2018). Given that SAR satellites have near-polar orbits and antennas oriented to the right at high angles of incidence, they are largely insensitive to N-S ground displacements and best-suited to measure E-W and vertical deformation (Ferretti et al., 2007; Pezzo et al., 2014; Elliott, Walters and Wright, 2016).

In this study, we processed data from ESA's Sentinel-1 Synthetic Aperture Radar (SAR) satellites from descending track 151 (D151) and ascending track 71 (A071) acquired in Interferometric Wide (IW) swath mode. These data are freely available at the European Space Agency's Copernicus Open Access Hub (https://scihub.copernicus.eu/) or mirror sites (https://peps.cnes.fr/rocket/#/home). We conducted an MT-InSAR analysis to derive cumulative time series LOS displacement maps and velocity maps over ~ 400 km long swaths in the range direction between ~ 36° and ~ 39.5° latitude (Figure 4.3-1). We process the data with the New Small Baseline Subset (NSBAS) processing chain (Doin et al., 2011; 2015; Grandin, 2015), which is based on the ROIPAC software (Rosen et al., 2004). Our processing approach is based on the methodologies outlined in Daout et al. (2019) and Daout et al. (2023), summarised here and explained in detail in the Supplementary Methods (Appendix section 4.6.1.).

We built robust interferogram networks spanning ~5 years for both the ascending and descending tracks. The networks are a mixture of short and long temporal baseline interferograms, constructed

using acquisitions from October 2014 – December 2020 for the ascending track and October 2014 – March 2021 for the descending track. Pre-unwrapping, the networks contained 464 and 593 interferograms for the ascending and descending tracks, respectively. To prepare the wrapped interferometric phase for unwrapping, we multi-looked the interferograms in 8 looks (i.e. we averaged over 8 pixels in azimuth and 32 pixels in range), filtered them by averaging the phase over a sliding window, and applied empirical phase-elevation corrections (Doin et al., 2011; 2015). These corrections reduce the phase variability and the fringe rate before unwrapping, aiding the unwrapping algorithm and allowing us to successfully unwrap over large areas (Doin et al., 2015; Daout et al., 2019). To avoid the propagation of unwrapping errors, unwrapping paths were imposed which start in areas of high colinearity and progress into areas of lower colinearity (Grandin et al., 2012; Grandin, 2015). For some interferograms, we manually defined high-priority paths to guide the algorithm and reduce unwrapping errors (Grandin et al., 2012; Daout et al., 2016), and a small number interferograms with extensive unwrapping errors were removed from the networks. To reconstruct the full unwrapped phase, the empirical corrections were reintroduced after unwrapping (Daout et al., 2019). Subsequently, following the approach of Dodds et al., (2021), we jointly corrected unwrapped interferograms for a linear phase ramp and tropospheric phase delays using the ECMWF ERA-5 atmospheric model (https://www.ecmwf.int/en/forecasts/dataset/ecmwf-reanalysis-v5). We performed a statistical assessment of this correction and found that the model predicts the tropospheric phase component successfully, with slightly better results than for similar studies (Appendix section 4.6.1.1.3; Dodds et al., 2022). Finally, we performed a time-series analysis to derive the phase-delay time series for both tracks (Doin et al., 2015) and extract the linear and seasonal components with a parametric temporal decomposition (Daout et al., 2017). The final networks used to construct the time-series consisted of 451 interferograms and 588 interferograms for the ascending and descending tracks, respectively.

To address issues of phase bias related to changes in soil moisture and vegetation documented in previous studies (e.g. De Zan et al., 2014; Daout et al., 2020; Ansari, De Zan and Parizzi, 2021; De Luca et al., 2022; Maghsoudi et al., 2022; Purcell et al., 2022), we incorporated longer period interferograms into our networks and removed interferograms with temporal baselines less than 32 days from our final time series analysis (Daout et al., 2020; De Luca et al., 2022; Mathey et al., 2022). We also masked areas potentially affected by bias from the final LOS velocity maps by removing pixels with average temporal baselines of < 3 months (Mathey et al., 2022). We additionally cleaned the final maps based on the posterior uncertainties from the time series inversion and the parametric temporal decomposition to remove high uncertainty pixels.

After this cleaning step, we decomposed the LOS velocity maps (Figure 4.3-1) into vertical and east velocities (V_U and V_E), referencing them to an area of relatively low deformation within the Tajik Basin to the west of the Babatag thrust (Figure 4.3-2). As the available 3D GPS data are sparse and our primary interest is in mapping and measuring velocity contrasts, the final rate maps are internally referenced rather than tied to stable Eurasia and signals are interpreted accordingly in the sections below.

4.2.2. DEM Generation and Scarp Measurement

We constructed Digital Elevation Models (DEMs) from Pléiades satellite imagery of the Dushanbe Trough acquired between 2012 – 2021. We process 8 pairs of panchromatic stereo images using Agisoft Metashape software to build 3-D point clouds and DEMs with a ground resolution of < 1.5 m.

We use these DEMs to map the tectonic geomorphology of the Dushanbe Trough, to identify Quaternary fault scarps and measure their offset. We extract elevation profiles approximately perpendicular to scarps, fit linear models to the hanging wall and footwall, and difference their heights

at the inferred location of the fault (the detailed methodology is available in chapter 2). Within Dushanbe city, we draw profiles along major N-S oriented roads to avoid the impact of buildings on the elevation data.

4.3. Results and Discussion

We produce rate maps with a horizontal resolution of ~130 m, nearly 4 times higher resolution than previously published velocity maps of the region. The LOS velocity maps are presented in Figure 4.3-1. In these maps, negative values (red) indicate relative motion away from the satellite. The LOS velocities have average uncertainties of 0.6 mm/yr and 0.8 mm/yr for the ascending and descending tracks, respectively. Even after cleaning based on uncertainties and the average temporal baseline, we retain very good data coverage, providing an unprecedented continuous estimate of surface deformation in our study area.

The LOS velocity maps (Figure 4.3-1) clearly show the westwards motion of the eastern two-thirds of the Tajik Basin relative to the Tajik Gissar and the Afghan Platform. In the north and west of the basin, these velocity gradients are localised onto the right-lateral Ilyak fault (IF) and the Babatag thrust (BT) respectively. The descending LOS velocity map shows relative motion away from the satellite to the south of the IF (~4 – 5 mm/yr relative to the north) and east of the BT (~2 – 3 mm/yr relative to the west). In contrast, the ascending LOS velocity map shows relative motion towards the satellite to the south of the IF (~4 – 6 mm/yr relative to the north) and east of the BT (~2 – 3 mm/yr relative to the west). The ascending track map also captures the western edge of the Pamir mountains, showing up to ~10 mm/yr of motion towards the satellite relative to the lowlands of the basin. This signal indicates either uplift, westward motion (consistent with the westward collapse of the Pamir) or a combination of the two. Within the basin interior, both tracks show localised patches moving rapidly away from the satellite at several mm/yr and up to ~16 mm/yr within the valley of the Surkhan-darya syncline. These

patches correspond to agricultural areas (see NDVI map in Figure 4.3-1c), so this is likely a subsidence signal caused by water extraction.

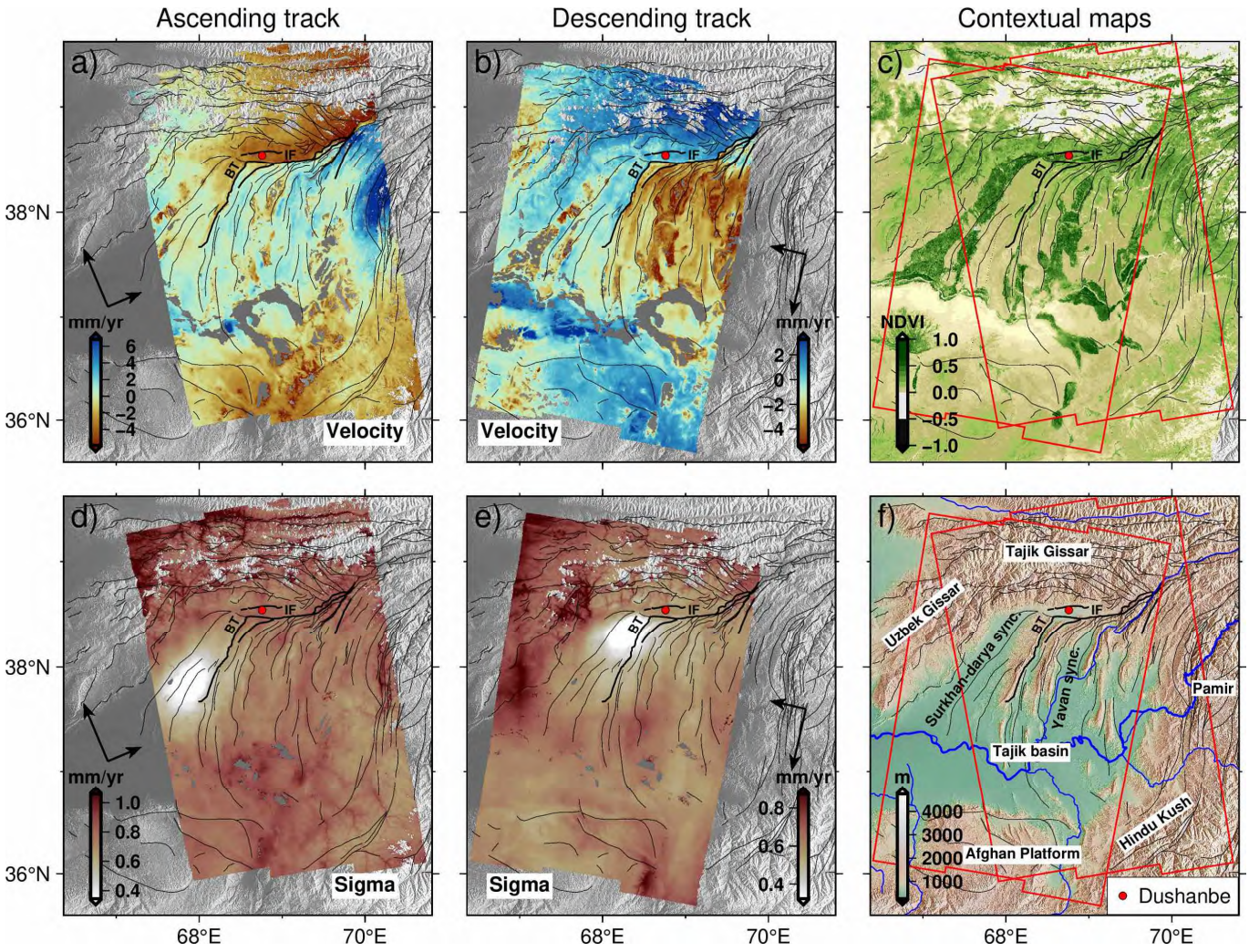

Figure 4.3-1. a) Ascending and b) descending linear LOS velocity maps overlain on 30 m SRTM DEM. Negative (red) values indicate relative motion away from the satellite. BT = Babatag thrust, IF = Ilyak fault. d) and e) show 1σ uncertainties for the ascending and descending LOS velocities respectively. Context maps: processed frames in red. c) Normalised Difference Vegetation Index (NDVI) data from August 2020 (Contains modified Copernicus Sentinel data 2020 processed by Sentinel Hub, accessed through Sentinel Hub EO Browser in 2023). d) Topography (SRTM 30 m DEM) with major rivers in blue, sync=syncline. On all maps, thin black lines are faults after Dedow et al. (2020) and Abdulhameed et al. (2020), and thick black lines highlight active faults discussed in this study.

The derived vertical and east velocity maps are presented in Figure 4.3-2, with average uncertainties of 0.8 mm/yr and 0.6 mm/yr respectively. The east rate map confirms the sharp velocity contrast in the north and west of the basin, corresponding to right-lateral motion across the IF and convergence on the westward-dipping BT. The vertical rate map is dominated by the signal from the subsiding fields (especially within the Yavan syncline in the centre of the basin) but also reveals a longer wavelength signal of relative subsidence of the basin sediments compared to the surrounding mountains.

In the following sections, we further examine tectonic deformation signals in our study region (black box in Figure 4.3-2a and b), the north of the Tajik basin and the Dushanbe Trough, combining our InSAR measurements with geomorphic mapping. We then consider the implications of our results for seismic hazard in Dushanbe.

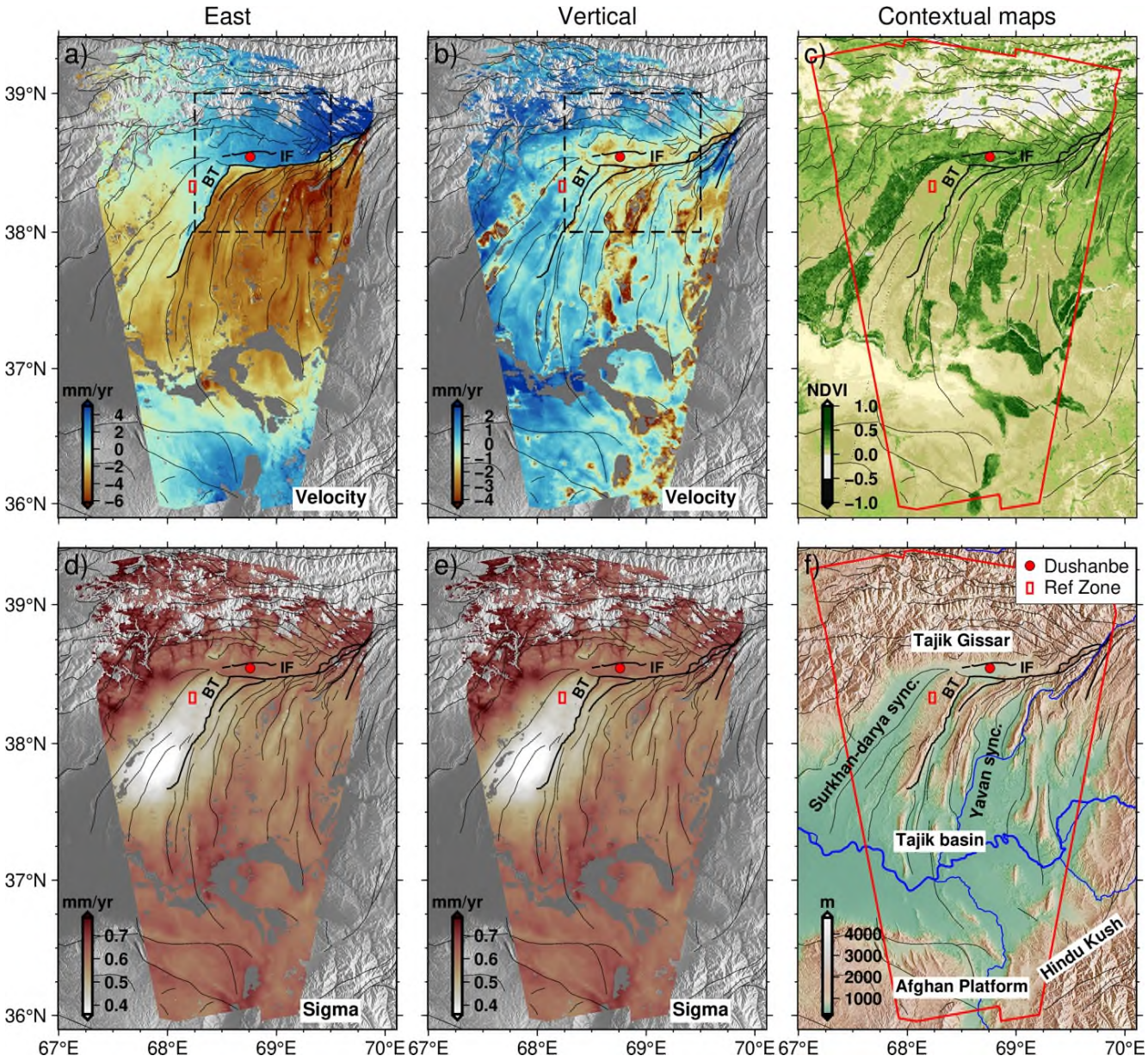

Figure 4.3-2. a) East and b) vertical velocities from the spatial decomposition of the linear LOS velocity fields overlain on 30 m SRTM DEM. Negative (red) values indicate relative westwards motion in a) and subsidence in b). BT = Babatag thrust, IF = Ilyak fault. d) and e) show 1σ uncertainties for the east and vertical velocities respectively. Context maps: velocity map coverage in red. c) Normalised Difference Vegetation Index (NDVI) data from August 2020 (Contains modified Copernicus Sentinel data 2020 processed by Sentinel Hub, accessed through Sentinel Hub EO Browser in 2023). d) Topography (SRTM 30 m DEM) with major rivers in blue, sync=syncline. On all maps, thin black lines are faults after Dedow et al. (2020) and Abdulhameed et al. (2020), and thick black lines highlight active faults discussed in this study. Reference zone for spatial decomposition is marked with a red rectangle.

4.3.1. The Ilyak Fault and the Dushanbe Trough

The eastwards velocity map reveals a sharp change in surface velocity on the IF, consistent with shallow aseismic slip on a right-lateral strike-slip fault (Figure 4.3-3, Figure 4.3-4). To quantify the fault slip rate and its variation along strike, we define nine neighbouring velocity profiles along the IF, each 7.5 km wide and 80 km long. We smooth these velocity profiles using a sliding median filter, then invert the smoothed data to find the parameters of the best fitting arctangent function for each profile (Appendix section 4.6.1.2. ; Savage and Burford, 1973; Turcotte and Schubert, 2014). The modelled strike-slip rate is ~8.7 mm/yr at the eastern end of the IF (profile 9) and decreases to ~6.7 mm/yr in the central part of the fault (profile 5). Modelled locking depths of profiles 5 to 9 are very low, between 0 m and 300 m, confirming very shallow aseismic slip. The evaporite-bearing Gaurdak formation crops out in multiple locations along this part of the IF, suggesting that this layer is the cause of the creep behaviour (Figure 4.3-5; Abdulhameed et al., 2020; Gągała et al., 2020). In our geomorphic analysis, we map a series of streams which cross the IF at the longitude of profile 6. They have been deflected right laterally by between ~100 – 500 m, consistent with localised strike-slip deformation (Figure 4.3-6, Box 2).

The vertical velocity map reveals minimal deformation across the IF compared to the high horizontal velocity changes (Figure 4.3-7, Figure 4.3-8). East and vertical velocities are plotted on the same axes in Appendix Figure 4.6-16 for direct comparison. For the vertical velocity profiles, we estimate the velocity contrast at the fault using a step function which we fit to data very close to the fault (within ~5 – 10 km of the fault trace). In the eastern part of the IF (profiles 7 to 9) we measure a ~1 mm/yr vertical velocity change, with the southern side of the fault uplifting relative to the north. In this eastern section, multiple S or SE dipping thrust sheets are stacked up against the southern side of the IF, forming the high topography on the southern side of the fault (Figure 4.1-2c; Abdulhameed et al., 2020; Gągała et al., 2020). The uplift signal most likely originates from motion on a dipping thrust

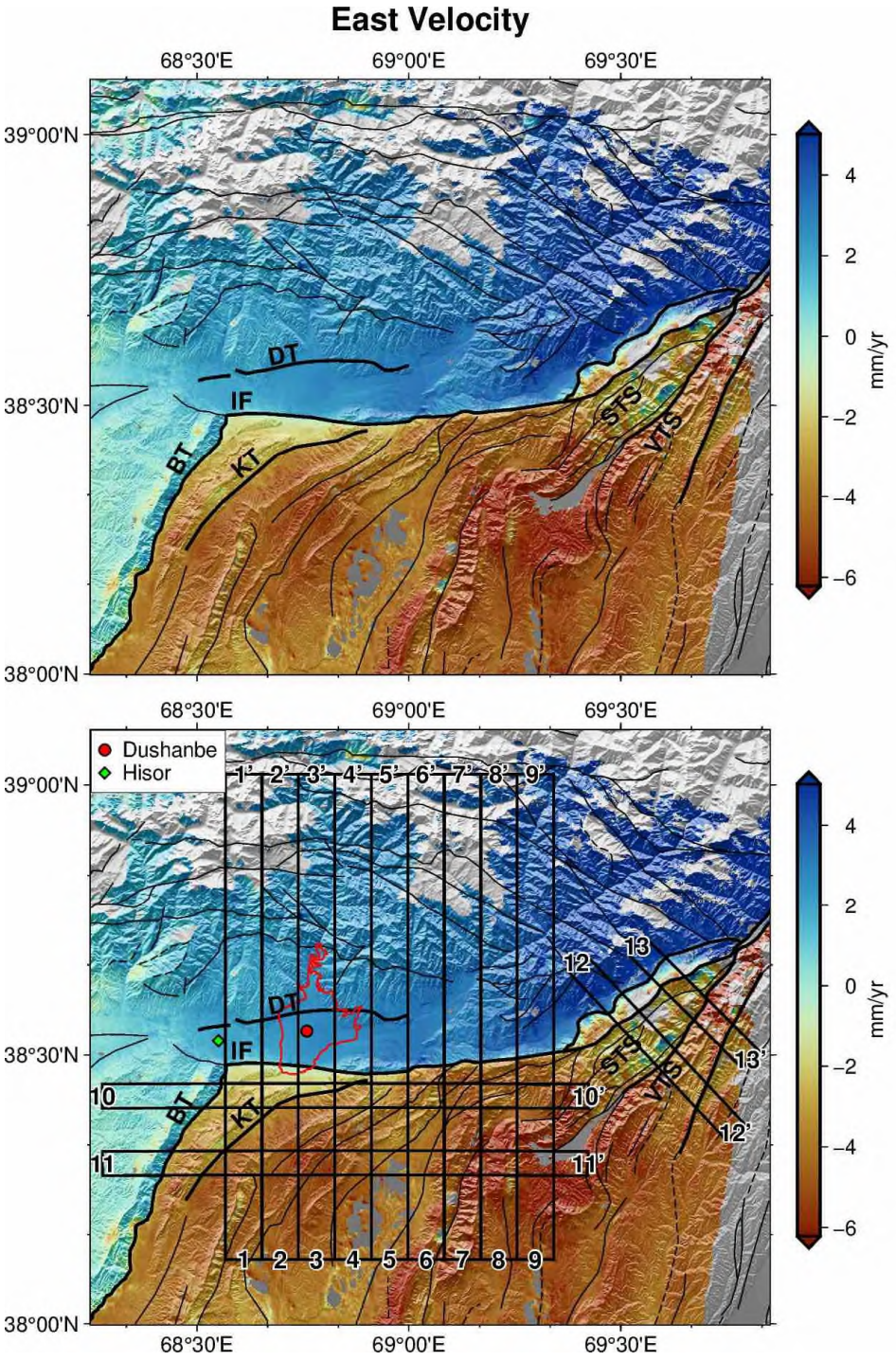

Figure 4.3-3. Eastwards velocity map of the Ilyak fault and surroundings, shaded by the gradient of the SRTM 30 m DEM. Solid and dashed thin black lines are faults and folds after Dedow et al. (2020) and Abdulhameed et al. (2020). Thick black lines = active faults discussed in this study. Rectangles show locations of profiles in Figure 4.3-4. KT = Karchitau thrust, IF = Ilyak fault, DT = Dushanbe Trough thrust, BT = Babatag thrust.

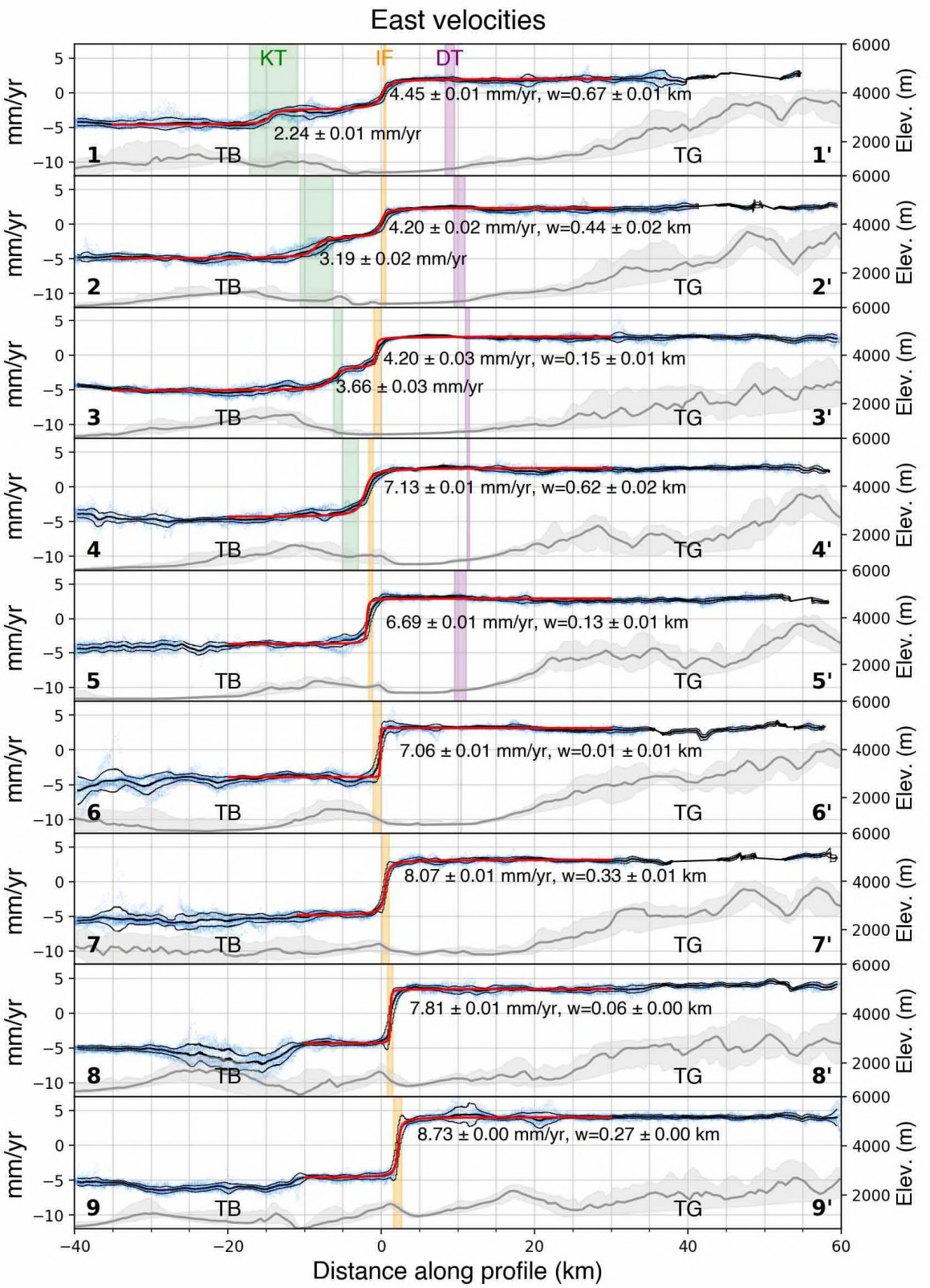

Figure 4.3-4. Eastwards velocity across the Ilyak fault (positive direction indicates relative eastwards motion) corresponding to profiles in Figure 4.3-3. Blue points are data which fall between the 2nd and

98th percentiles for 250 m wide bins. The thick black line is the median and thin black lines show ±1σ for 250 m wide bins. Fault extents of the Karchitau thrust (KT), Ilyak fault (IF), and Dushanbe Trough thrust (DT) are shown in green, orange and purple respectively. Red lines show best fitting models for the Ilyak fault and the Karchitau thrust, labelled with the modelled rate ± 2σ. W = modelled locking depth for the Ilyak fault. SRTM 30 m elevation data is plotted in grey (dark line = median elevation).

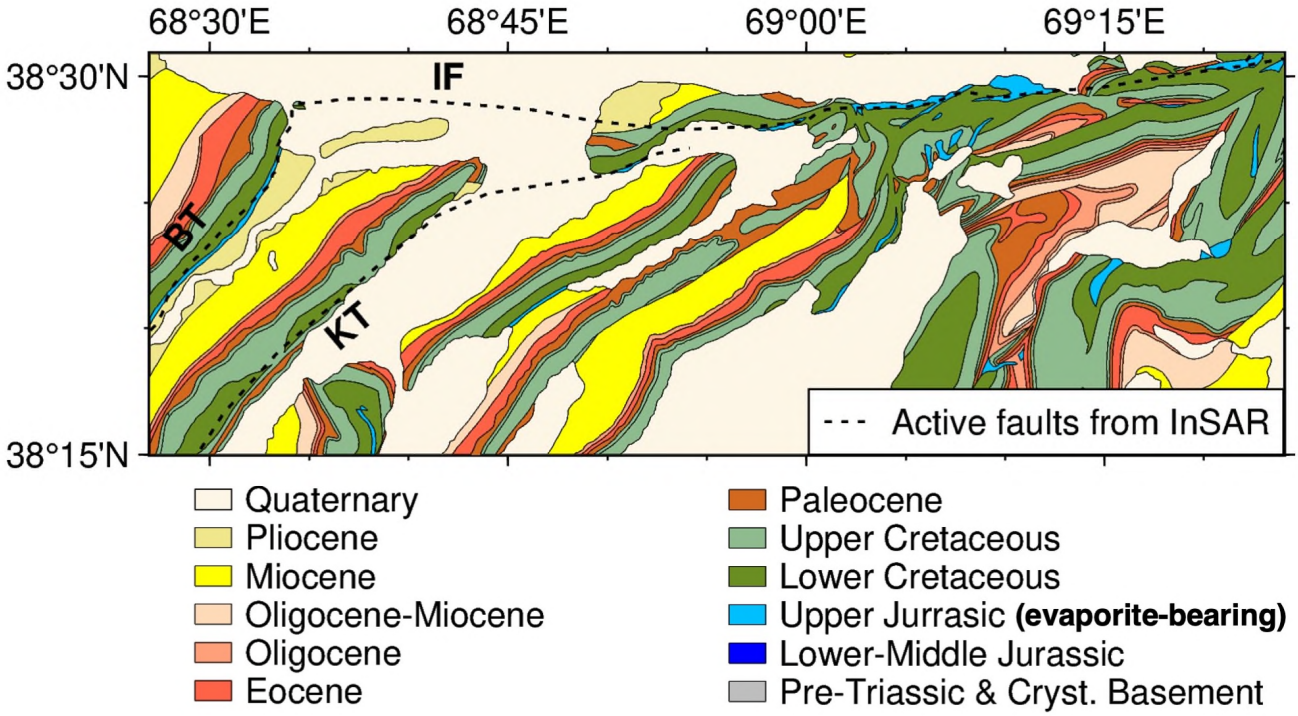

Figure 4.3-5. Zoomed in geological map of the study region from Abdulhameed et al. (2020) and Gągała et al. (2020) overlain with active fault traces mapped in our InSAR rate maps. BT = Babatag thrust, IF = Ilyak fault, KT = Karchitau thrust. The Babatag thrust and the eastern Ilyak fault are coincident with outcrops of the Upper Jurassic evaporite horizon and are found to be slipping aseismically in InSAR rate maps.

which merges with the main strike-slip structure at the surface, as it is correlated with the morphology of the folds at the surface (Figure 4.3-8). In the centre of the IF (profiles 4 to 6) where the basin folds and thrusts are at a higher angle to the fault trace, there are subdued undulations in vertical surface velocities, but there is no measurable vertical offset across the IF, suggesting that the IF does not accommodate shortening.

Further to the west, the IF passes through the southern part of the valley in which Dushanbe is situated. We found no geomorphic evidence of faulting within the youngest fan sediments in this section at the resolution of our DEMs. At the southwestern end of the Dushanbe Trough, the IF forms the sharp northern boundary of a ~180 m high mountain for 5 km, and then enters the southern part of the Hanaka river valley where four small uplifted blocks (~500 m – 2 km wide and tens of metres high) follow the fault trace (Figure 4.3-6, Box 1). We suggest these are compressional push-up structures which were induced by activity on the IF.

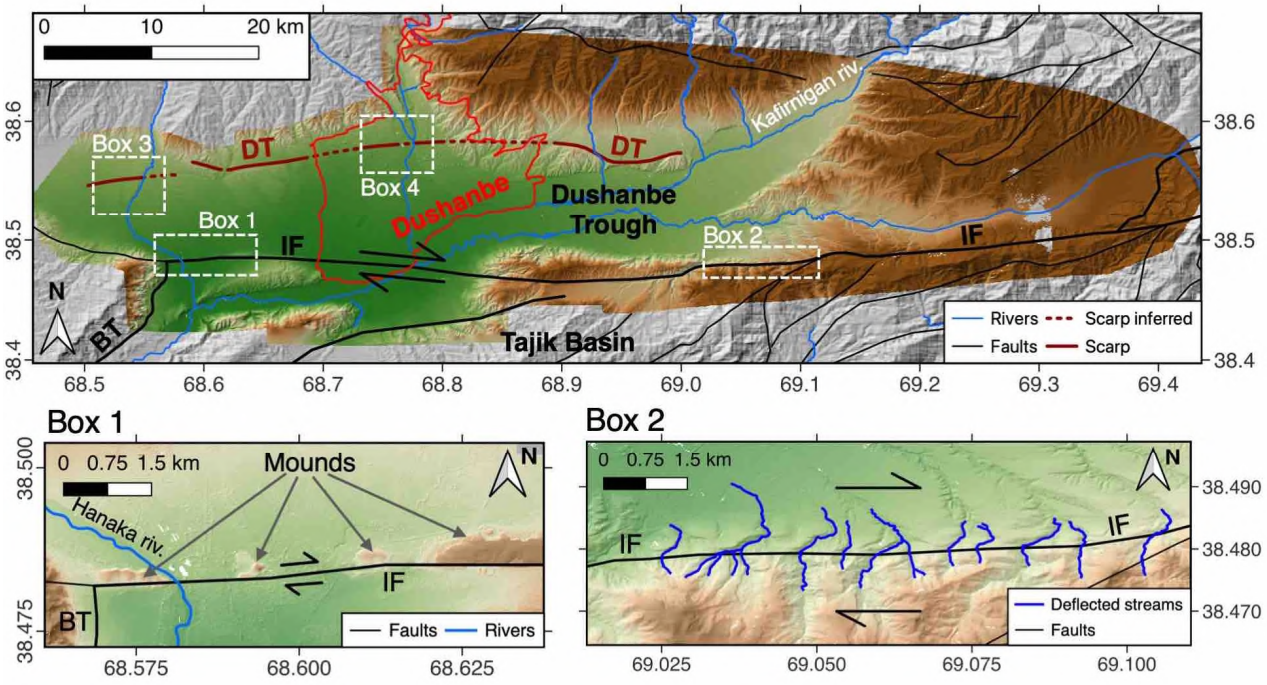

Figure 4.3-6. Pléiades-derived DEM of the Dushanbe Trough. DT = Dushanbe trough thrust, IF = Ilyak fault, BT = Babatag thrust. Background topography (grey) from SRTM 30 m DEM. Rivers and red polygon showing Dushanbe administrative boundary from Open Street Map. Solid thin black lines are faults after Dedow et al. (2020) and Abdulhameed et al. (2020). Thick black lines highlight active faults discussed in this study. Thick red line = scarp mapping for the Dushanbe trough thrust. Box 1: Mounds along the Ilyak fault trace. Box 2: Offset streams along the Ilyak fault trace. Boxes 3 and 4 correspond to Figure 4.3-9.

In most of the profiles 1 to 9, E-W velocity gradients on the Tajik basin folds and faults are apparent to the south of the IF (Figure 4.3-4). To the west of profile 5, the ENE-NNE striking Karchitau thrust (KT) emerges from the IF. The E-W deformation is partitioned between the two faults, and by profile

3, two distinct steps in the surface velocities are clearly visible. These steps become progressively more separated as the trace of the KT moves southwards. The strike-slip rate on the IF decreases to ~4 – 4.5 mm/yr as the KT accommodates ~2 – 4 mm/yr of EW deformation as oblique slip on a NW dipping fault plane. In these western profiles the surface velocity contrast across the IF is less sharp than in the east, and our models yield slightly larger locking depths of ~300 – 700 m. This is probably because the basin folds and thrusts are oblique to the strike of the IF in this section, and the Gaurdak formation does not crop out at the surface along the fault, according to the geological map (Figure 4.3-5; Abdulhameed et al., 2020; Gągała et al., 2020). As such, the creeping evaporite horizon is buried and the creep does not reach the surface.

Vertical velocity profile 3 (Figure 4.3-7) shows ~1 mm/yr of uplift of the sediments to the north of the IF. However, examining the vertical velocity map (Figure 4.3-7), this profile captures the Dushanbe urban area which appears to be subsiding less rapidly than the surrounding fields and the low-lying hills to the NW and NE. We are uncertain if this signal is tectonic or the result of water extraction outside of the urban areas causing increased subsidence. Similarly to the centre of the fault, the other western profiles show subdued undulations with amplitudes of < 1 mm/yr in the vertical velocity near the IF but there is no significant uplift signal associated with shortening.

We also find geomorphic evidence of further active faulting to the north of the IF within the Dushanbe trough (Figure 4.3-6). Two ~E-W trending ridges are apparent in the Quaternary strata to the east and west of Dushanbe. These ridges are asymmetrical with a steeper northern limb, suggesting they may have formed above a south-dipping thrust fault. The ridges are truncated by the alluvial fans associated with the rivers which exit the Tajik Gissar into the Dushanbe Trough. Our analysis of high-resolution DEMs reveals evidence of active faulting within these younger alluvial surfaces along strike of the larger ridges. On the west bank of the Hanaka river, near the town of Hisor, the southern side of the fan is uplifted relative to the north with a vertical offset of up to ~20 m (Figure 4.3-9, Box 3, profiles A-A’

and B-B'). We map a ~250 m wide inactive channel in the hanging wall, which we interpret as a wind gap – a former river channel that was abandoned when hanging wall uplift blocked the flow. The scarp is truncated to the east by a younger fan surface which is undeformed at the resolution of our dataset (profile C-C'). We also map uphill-facing thrust scarps, either side of the Varzob river (Figure 4.3-9, Box 4). We measure the height of these scarps along N-S oriented roads in Dushanbe city and find them to be ~7 – 8 m high (profiles D-D' and E-E'). The Big Gissar Canal is built on top of these scarps. Further to the east in the next valley along, the Kafirnigan river is oriented approximately parallel to the strike of the fault (Figure 4.3-6). Whilst we found some offsets here that could potentially be consistent with faulting, we could not distinguish them from river terracing.

This geomorphic evidence suggests there is a south-dipping thrust fault running through the Dushanbe Trough, which we refer to as the Dushanbe Trough thrust (DT) hereafter. In vertical velocity profile 1 (Figure 4.3-8), there is an apparent ~1 mm/yr of uplift of the sediments to the south of the DT. This might indicate activity on the DT, but the signal does not continue across the other profiles, and it occurs at the transition between the Quaternary trough sediments and the Neogene hills, so we are uncertain whether this is truly a tectonic signal or whether it might relate to other processes such as compaction of the Neogene sediments or water extraction. Alternatively, the DT may be completely locked during the observation period and produce no surface displacements discernible at the resolution and orientation of the rate maps.

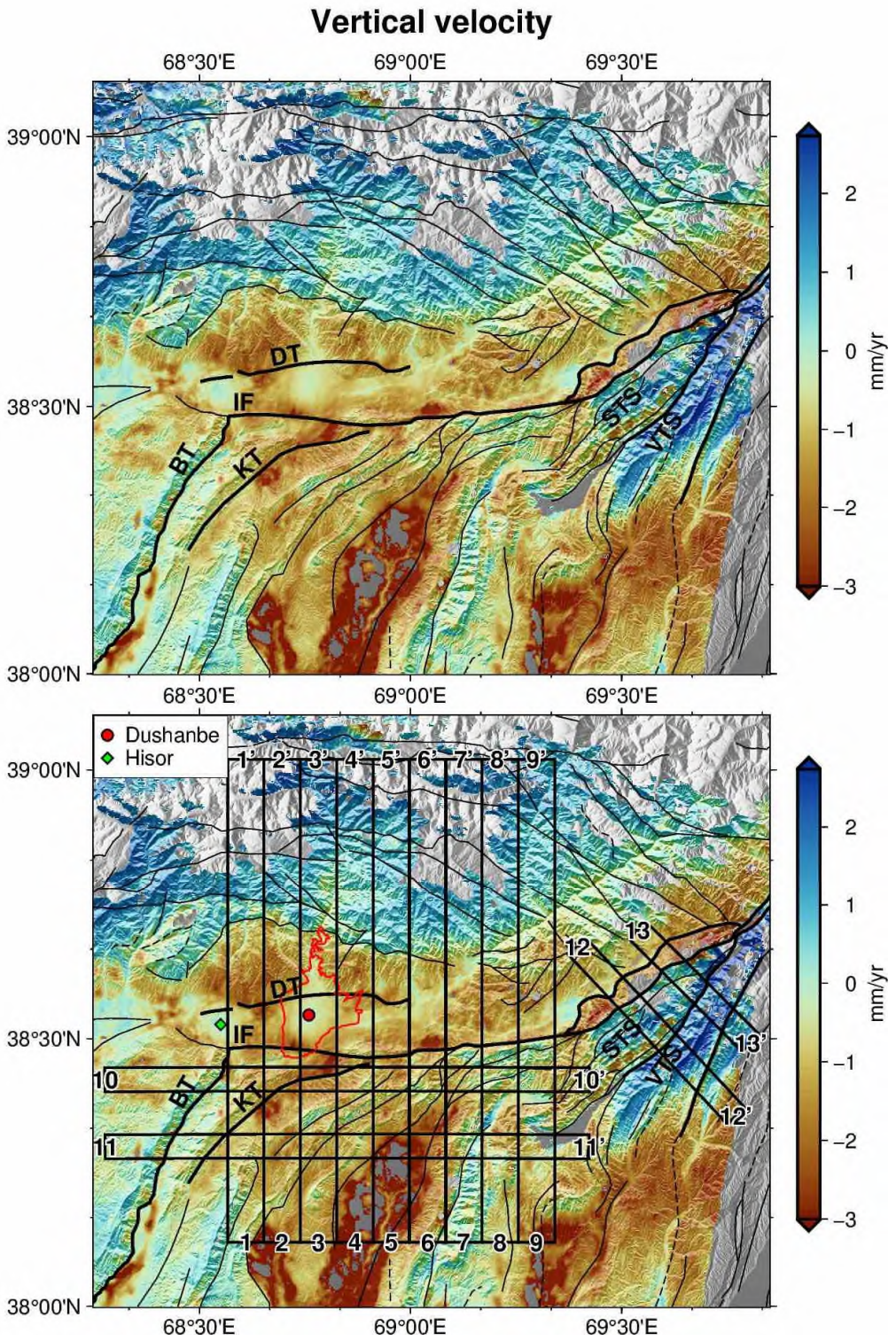

Figure 4.3-7. Vertical velocity map of the Ilyak fault and surroundings, shaded by the gradient of the SRTM 30 m DEM. Solid and dashed thin black lines are faults and folds after Dedow et al. (2020) and Abdulhameed et al. (2020). Thick black lines = active faults discussed in this study. Rectangles show locations of profiles in Figure 4.3-4. Red = Dusahnbe urban area from Open Street Map.

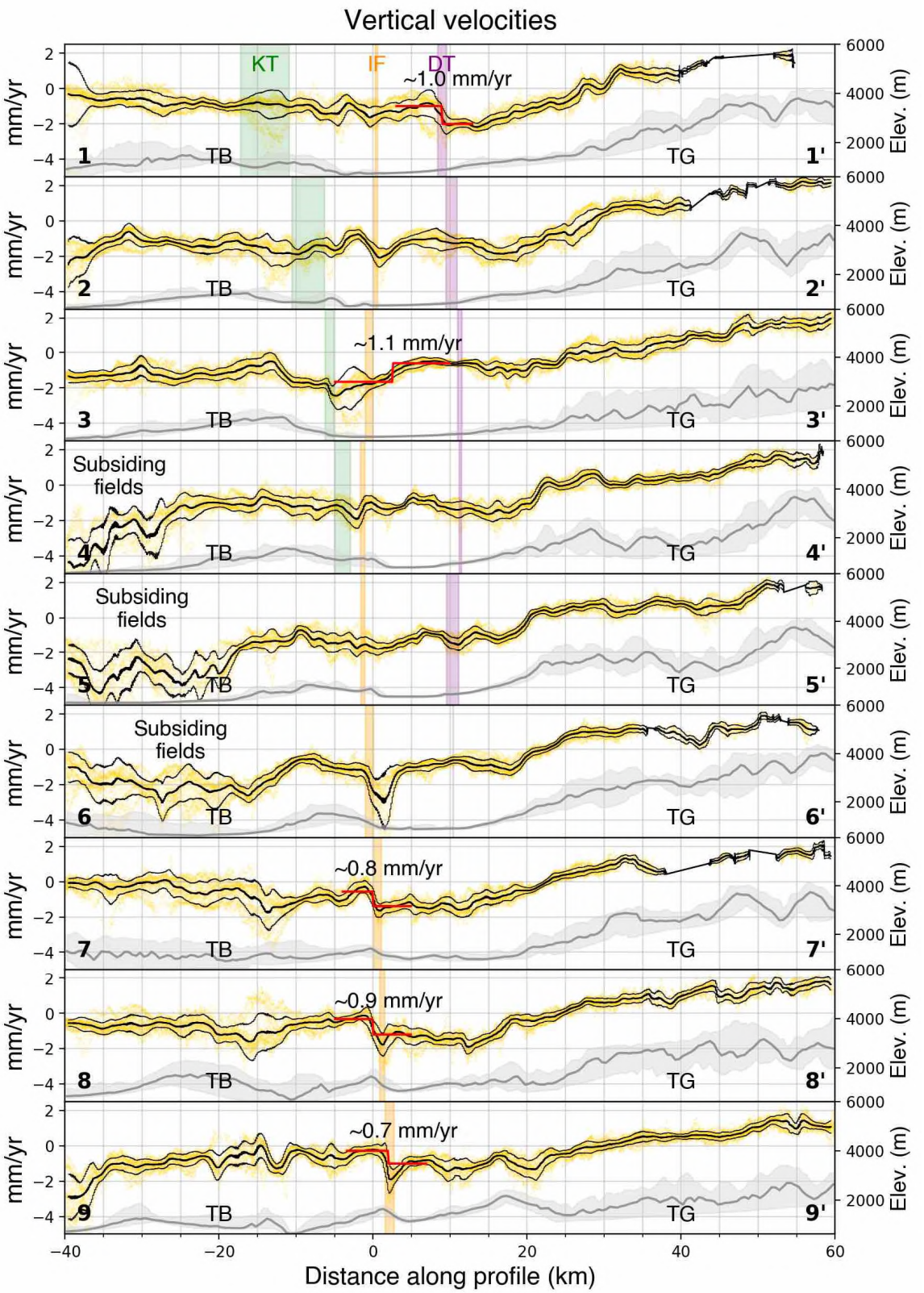

Figure 4.3-8. Vertical velocity across the Ilyak fault (positive direction indicates relative upwards motion) corresponding to profiles in Figure 4.3-7. Yellow points are data which fall between the 2nd

and 98th percentiles for 250 m wide bins. The thick black line is the median and thin black lines show ±1σ for 250 m wide bins. Fault extents of the Karchitau thrust (KT), Ilyak fault (IF), and Dushanbe Trough thrust (DT) are shown in green, orange and purple respectively. Red lines show best fitting step functions, labelled with the modelled rate ± 2σ. SRTM 30 m elevation data is plotted in grey (dark line = median elevation).

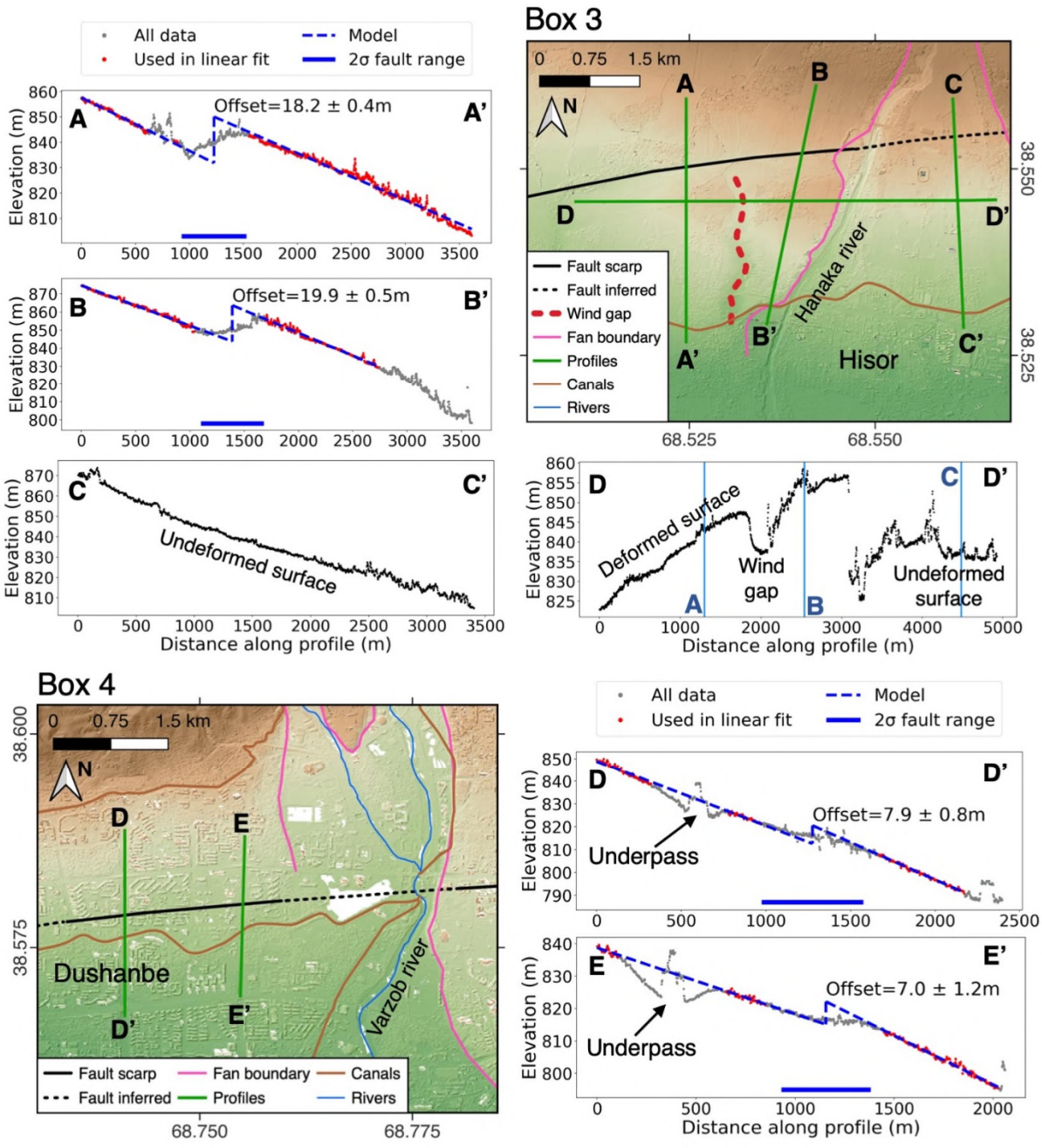

Figure 4.3-9. Scarp geomorphology and profiles in Hisor and Dushanbe from Pléiades-derived DEM, corresponding to boxes 3 and 4 in Figure 4.3-6. Rivers and canals from Open Street Map.

4.3.2. Slip Partitioning Between the Ilyak Fault and the Tajik Fold and Thrust Belt

In the southwestern corner of the Dushanbe Trough, horizontal surface velocities on the IF end abruptly as slip transfers onto the N-NNE striking, westward dipping Babatag thrust (BT). Within our study area situated in the northern part of the basin, there is an abrupt change in E-W surface velocities of ~3 – 4 mm/yr across the mapped trace of the BT, which accommodates more shortening than any of the other basin thrusts (Figure 4.3-3, Figure 4.3-10). The sharpness of the horizontal velocity step reveals very shallow aseismic slip on the evaporite-bearing Upper Jurassic Gaurdak formation, which forms the base of the thrust sheet (Figure 4.3-5; Abdulhameed et al., 2020; Gągała et al., 2020). The short wavelength undulations in the E-W velocities either side of the BT (Figure 4.3-10) likely relate to surficial processes described in Metzger et al. (2021), namely the E-W divergence of ridge crests due to downslope mass movements driven by gravity.

The vertical velocity contrasts are smaller in magnitude and noisier, indicating approximately ~0.5 mm/yr of uplift in the first ~10 km of the hanging wall of the BT at the location of the topographic high, which would correspond to a very low-dipping creeping thrust (Figure 4.3-7; Figure 4.3-10). The particularly low amplitude and undulation of the uplift signal compared to the fast and localised horizontal shortening suggests distributed off-fault deformation within the hanging wall of the folded sediments might play an important role during the interseismic period (e.g. Ainscoe et al., 2017; Johnson, 2018; Daout, Parsons and Walker, 2021).

A profile oriented in the E-W direction across the Tajik Basin, immediately south of the IF reveals a decreasing trend in the westward velocity from the western side of the basin to the BT (profile 10, Figure 4.3-10 and Figure 4.3-3). This decreasing velocity trend is a result of the basin folds and thrusts progressively accommodating a greater portion of the deformation. The velocity undulates around this

overall trend on the individual deforming faults and folds, such as the Karchitau thrust. Slip partitioning and the accommodation of E-W deformation on these thrust structures is the reason for the decline in the strike-slip rate from east to west along the IF (Figure 4.3-4).

At the eastern end of the IF, the Surkhu thrust sheet (STS) and Vakhsh thrust sheet (VTS) overthrust the basement of the Tajik Gissar in a right-lateral transpressional zone (Figure 4.1-2; Leith and Alvarez, 1985). It is unknown whether the IF stops here, merges with the thrust sheets or continues beneath them as separate structure. Figure 4.3-11 shows two profiles across these thrust sheets. The E-W velocity contrast between the basin thrusts and the mountains is ~7 – 9 mm/yr, with the velocity change distributed across a ~ 5 km wide sliver of basin sediments (Figure 4.1-2). The profiles show the thrust sheets uplifting at ~2 – 4 mm/yr, with the VTS over-thrusting the STS as evidenced by the stepped vertical velocity in profile 13. The sharp changes in horizontal surface velocities are consistent with shallow aseismic slip on the basal evaporites. The major steps in vertical and east velocity do not always occur at the same distance along the profiles, suggesting that the thrust and strike-slip components are sometimes partitioned between different structures.

4.3.3. Uplift of the Tajik Gissar

In the vertical velocity map (Figure 4.3-7) and N-S vertical velocity profiles 1 to 9 (Figure 4.3-8), large scale uplift of the Tajik Gissar is apparent, with up to ~3.5 mm/yr of uplift in the highest mountains relative to the Tajik Basin and Dushanbe Trough. Although there could be a basement thrust at the southern edge of the Tajik Gissar, and although additional small-wavelength uplift at the topographic front is also visible, the dominant uplift signal occurs over a much longer wavelength than we would expect from strain accumulation on a thrust fault and does not decay with distance from the fault as we would expect (Simpson, 2015). We suggest that the vertical signal could result from isostatic uplift due

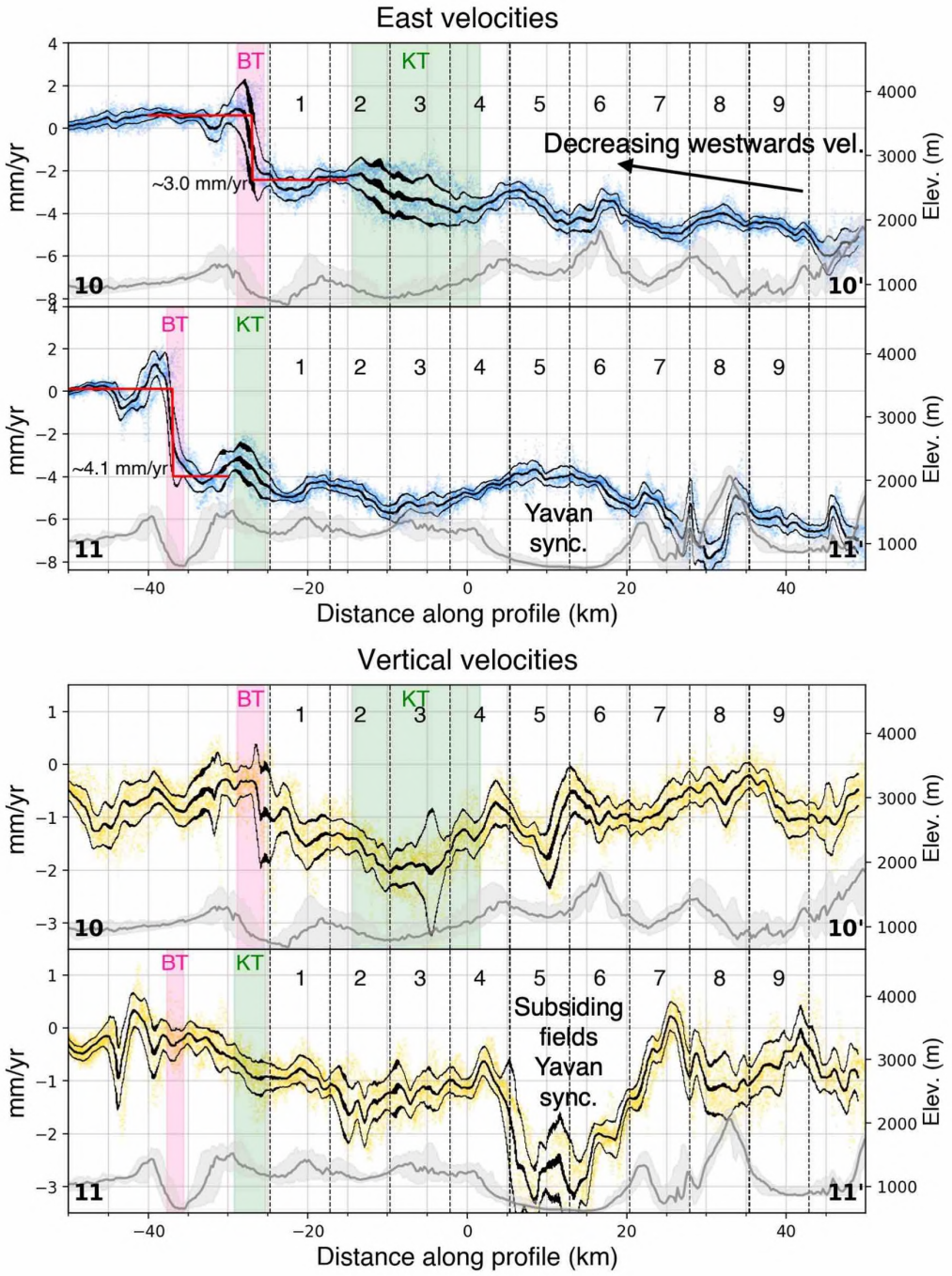

Figure 4.3-10. East (top) and vertical (bottom) velocity profiles across the Tajik basin corresponding to Figure 4.3-3 and Figure 4.3-7 respectively. IF profile extents marked by black dashed lined as labelled with profile number. Fault extents of the Babatag thrust (BT) and Karchitau thrust (KT) are shown in pink and green respectively. Profiles across the Tajik basin. IF profile extents marked by black dashed lined as labelled with profile number. Fault extents of the Babatag thrust (BT) and Karchitau thrust (KT) are shown in pink and green respectively. Elevation data (SRTM 30 m DEM) is plotted in grey (dark line = median elevation).

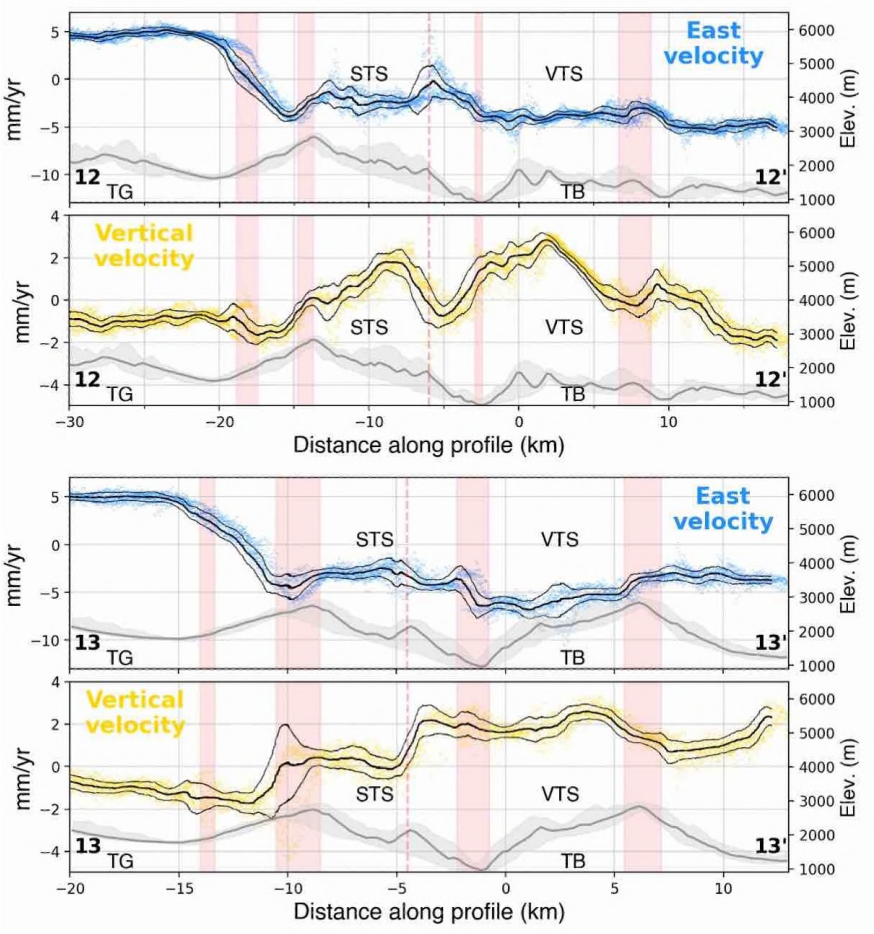

Figure 4.3-11. East and vertical velocity profiles of the Surkhu thrust sheet (STS), Vakhsh thrust sheet (VTS), and Tajik Gissar (TG) corresponding to profiles 12 and 13 in Figure 4.3-3 and Figure 4.3-7. TB = Tajik Basin. Red shaded regions mark the extends of faults mapped in the velocity maps. Red dashed line marks an additional fault identified in the profile. Elevation data (SRTM 30 m DEM) is plotted in grey (dark line = median elevation).

to erosion of the mountains (e.g. Avouac and Burov, 1996; Bullen et al., 2001; Lazear et al., 2013; Vernant et al., 2013). However, there is a rather abrupt change in the uplift rate at the transition between the basin sediments in the Dushanbe Trough and the basement of the Tajik Gissar, particularly apparent in profiles 4, 5, 6 and 8 in Figure 4.3-8, and in the vertical velocity map in Figure 4.3-7. This suggests that the velocity contrast between the mountains and the basin may have additional causes, such as compaction of the basin sediments.

In the north of the east velocity map (Figure 4.3-2) a gradual decrease in the eastwards velocity is apparent from east to west. We are uncertain of the cause of this signal, but it could potentially be long wavelength E-W extension related to gravitational collapse of the mountains. However, as the rate maps are internally referenced to the west of the BT, this signal could also correspond to a decreasing trend in the westwards velocity from west to east across the basin.

4.4. Implications for Seismic Hazard in Dushanbe

Our results show that aseismic slip on the evaporite-bearing layer dominates the deformation in the Tajik basin. The IF, which passes through the south of Dushanbe city, slips aseismically to very shallow depths (~0 – 700 m) at a rate of ~4 – 9 mm/yr. This aseismic slip probably extends to around ~4 – 6 km depth, as this is the approximate thickness of the basin sediments along the IF according to a seismic section interpreted by Gągała et al. (2020). It is unlikely that this shallow creeping structure would pose a significant seismic hazard to Dushanbe. However, earthquake catalogues show events of up to M_L ~5.5 at ~4 – 17 km depth beneath the surface trace of the IF, with available focal mechanisms consistent with right-lateral strike-slip (Figure 4.1-2; Djuraev and Shakirdzanova, 1993; Kufner et al., 2018). Therefore, there must be a seismogenic fault within the basement beneath the IF. Whilst it is possible that the basement fault is also mostly aseismic, hosting earthquakes between creeping patches, as the evaporite-bearing sediments which are responsible for the creep elsewhere are not present in the basement, this is an unlikely scenario.

A locked basement strike-slip fault which is creeping only at shallow depths should produce surface velocity profiles with a smooth, longer wavelength arctangent signal superimposed on a discontinuous step at the fault, as has been documented on the North Anatolian fault (Hussain et al., 2016). We find no longer wavelength signals in our east velocity map indicative of locking and strain accumulation at depth. However, this may be because the slip rate at depth is smaller than the rate of shallow aseismic

slip, such that the aseismic component swamps the locking signal. Furthermore, the decoupling of the sedimentary cover from the basement to the south of the IF could prevent any deformation at depth translating into measurable surface displacements in the southern half of the profiles.

As such, we cannot determine the extent of locking or the slip rate on the basement portion of the Ilyak fault, as the fast, shallow aseismic deformation and/or the two-layer structure of the basin prevents information from depth from reaching the surface. Whilst the creeping signal is indicative of a reduced hazard from the shallow IF, it could be obscuring a greater hazard at depth. It is clear from seismic records that the deep IF can produce earthquakes of at least M_L ~5.5, but the potential for larger events remains unknown.

Through our geomorphic mapping, we also document recent activity on the DT, a south-dipping thrust fault, which we map for ~45 km through the Dushanbe Trough. Whilst we found ~1 mm/yr of possible uplift in one of the surface velocity profiles across the western end of this fault, we were unable to confidently confirm a tectonic origin for the signal. The absence of a surface velocity gradient across this E-W striking fault is not evidence of inactivity, as much of the deformation is likely to be in the N-S direction, to which this technique is insensitive (Elliott, Walters and Wright, 2016), and the thrust may be fully locked during the observation period. We cannot be certain whether the DT is slipping aseismically along an evaporite horizon or whether it may produce earthquakes. However, in contrast to the main part of the Tajik basin and along the IF, borehole data show that the Gaurdak formation is either absent or much thinner in the Dushanbe Trough, and there is no clear evidence for evaporites (Leith and Alvarez, 1985; Gągała et al., 2020). Furthermore, according to interpretations of seismic reflection profiles and borehole data by Gągała et al. (2020), in contrast to the decoupling to the south of the IF, within the Dushanbe Trough, faults and folds deform the basement and sedimentary cover together as one mechanical layer. Therefore, without an evaporite horizon on which to slip aseismically and no evidence of decoupling, we suggest that the DT might be capable of producing

seismic ruptures that could extend into the basement. We have no direct constraints on how large potential earthquakes could be, but a rupture of the entire mapped length (~45 km) would correspond to a M_W 7.0 – 7.2 event according to empirical scaling relations for thrust faults (Wells and Coppersmith, 1994; Wesnousky, 2008). Even a much smaller earthquake on the DT could be very destructive due to its location within the city of Dushanbe and its proximity to major infrastructure. Further investigations of the DT, such as paleoseismic trenching and field mapping, are required to confirm the seismogenic nature of the fault and constrain the size and likelihood of such an event.

Finally, we note that as our data is largely insensitive to N-S motion, it is not optimal for imaging deformation on E-W oriented thrust faults, so there may be additional sources of hazard to Dushanbe we did not identify, such as the source of the ~M7.5 Karatog earthquake.

4.5. Conclusions

We perform an MT-InSAR analysis to produce surface velocity maps of the Dushanbe Trough and the Tajik Basin. We correct interferograms using atmospheric models, to reduce the impact of tropospheric noise on ground deformation estimates. By performing corrections on the wrapped phase and manually guiding the unwrapping algorithm we successfully unwrap an interferogram network including long temporal baselines and excluding shorter baselines, minimising the effect of phase bias. Even after masking the rate maps based on uncertainty and other criteria, we retain very good data coverage in the study area. With this bespoke approach, we produce rate maps with a resolution of ~130 m and average formal uncertainties of < 1 mm/yr.

Our rate maps show the Tajik basin moving westwards relative to its surroundings, with deformation concentrated on the Ilyak fault to the north and the Babatag thrust to the west, both of which are slipping aseismically along an evaporite-bearing horizon. We also document the transpressional uplift

of the Surkhu and Vakhsh thrust sheets in the northeast of the basin, and the relative uplift of the Tajjik Gissar, which we suggest results from isostatic rebound due to erosion with a possible contribution from the compaction of the basin sediments.

In contrast to previous studies, our high-resolution dataset allows us to map and measure short wavelength signals on individual faults such as creep, as well as the partitioning of slip between neighbouring structures. We document shallow right-lateral aseismic slip on the Ilyak fault, with a slip rate of ~8.7 mm/yr at its eastern end, decreasing to ~4.1 mm/yr in the west, due to a transfer of dextral slip to the fold and thrust belt of the Tajik Basin including onto the Karchitau thrust. Whilst the Ilyak fault is creeping within the ~4 – 6 km of sedimentary cover, seismicity indicates that there is a locked fault in the basement below, which is likely a significant source of hazard. However, the deformation at depth is obscured by the rapid deformation and decoupling of the surficial sediments, and little more can be gleaned regarding its earthquake potential from surface measurements alone. Finally, we also find geomorphic evidence for a south-dipping thrust fault within the Dushanbe Trough, including scarps within Dushanbe city. The mapped fault is at least ~45 km long, which could correspond to a M_W earthquake based on its length, and might be a significant source of earthquake hazard to local populations. Further investigation in the field is required to determine its seismic potential.

4.6. Appendix of Chapter 4

4.6.1. Supplementary Methods

4.6.1.1. InSAR Data Processing

Below we outline in detail our Multi-Temporal InSAR processing and post-processing methodology which was undertaken with New Small Baseline Subset (NSBAS) processing chain (Doin et al., 2011; 2015; Grandin, 2015) and the post-processing package PyGdalSAR (https://github.com/simondaout/PyGdalSAR; Daout et al., 2017; 2019; Maubant et al., 2020; Dodds et al., 2022).

4.6.1.1.1. Constructing the Interferograms

The data from each radar acquisition is stored in a Single Look Complex (SLC) image in which each pixel is a complex number, $Z = Ae^{i\varphi}$, where A is the amplitude and φ is the phase. First, using precise orbital data and a 30 m SRTM DEM (NASA JPL, 2013), we co-register the SLC images for all secondary dates to a primary image, to ensure that all images are in the same geometry. To produce an interferogram (IFG), we compute the SLC for date 1 (Z_1) multiplied by the complex conjugate of the SLC for date 2 (Z_2^*). We compute IFGs for dates between October 2014 and March 2021 for D151, and between October 2014 and December 2020 for A071. We include a mixture of shorter and longer period IFGs in our network, with temporal baselines up to 5 months, and small (< 250 m) perpendicular baselines (Figure 4.6-1). Due to the availability of acquisitions, both the ascending and descending IFG networks are less dense in 2015 than in the later years, but there are no significant time gaps in the network that are not covered by multiple interferograms.

In order to reduce speckle (the variation in pixel intensities due to interfering signals from different sub-pixel reflectors; Bamler and Hartl, 1998; Funning, 2005) we multi-look the interferograms in 2

looks. This means averaging over 2 pixels in azimuth and 8 pixels in range, evening out the aspect ratio of the pixels to produce an image with a similar size in both dimensions. The SLCs have a ground pixel resolution of ~ 15 m x 4 m (azimuth x range, to the nearest metre) and the 2-looked IFGs have a resolution of ~ 30 m x 32 m (azimuth x range). We use TOPS (Terrain Observation with Progressive Scans) data which is acquired in bursts, so small errors in the coregistration of SLCs produce steep phase ramps in the IFGs (Grandin, 2015). We remove these ramps using the 'spectral diversity' method outlined in Grandin (2015).

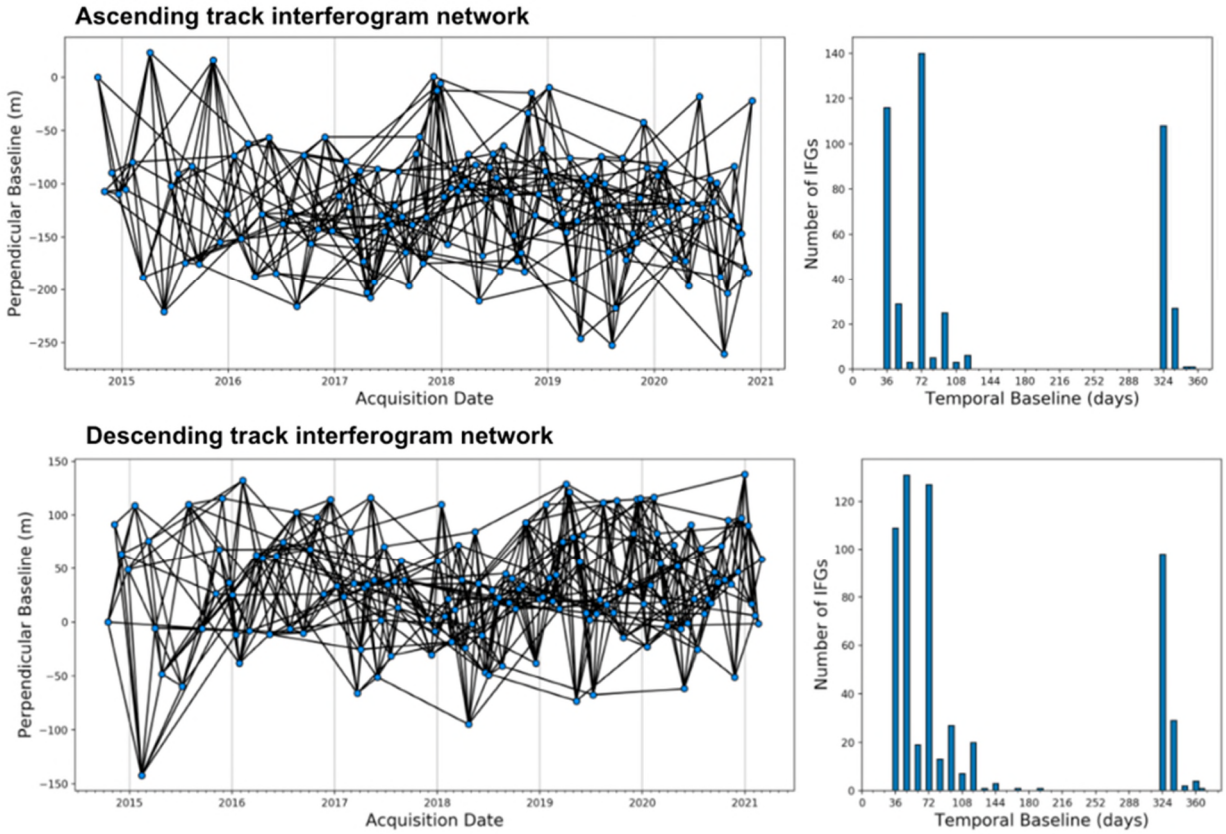

Figure 4.6-1. Interferogram networks and temporal baseline histograms for A151 (top) and D071 (bottom). IFGs = interferograms. Plots after Dodds at el. (2021).

4.6.1.1.2. Unwrapping the Interferograms

First, we perform several pre-unwrapping steps to assist the unwrapping algorithm. For each IFG we replace the amplitude with the coherence measured in 4 x 4 pixel windows. The coherence takes values

between 0 and 1 and is a measure of how statistically similar neighbouring pixels are in terms of both phase and amplitude, with higher coherence indicating more similarity (Rosen et al., 2000; Ferretti et al., 2007). As we expect nearby pixels to have similar properties, the coherence is a better indicator of confidence in the pixel than the amplitude.

Next, we filter the IFGs by taking an average of the complex phase over triangular sliding windows, weighted by the coherence (Doin et al., 2011). We estimate a relationship between the phase of these heavily filtered IFGs and the topography, assuming the phase is a function of the azimuth and the elevation (Figure 4.6-2). We use this empirically determined phase-elevation relationship to remove phase components correlated with topography from the unfiltered IFGs – this part of the signal is likely to be related to atmospheric delays and its removal will reduce the fringe rate before unwrapping. We then replace the coherence with the colinearity, a modified version of the coherence which measures how statistically similar neighbouring pixels are in terms of phase but not in terms of amplitude, as it is better for identifying noisy areas (Pinel-Puyssegur, Michel and Avouac, 2012).

Further multi-looking of the original interferograms can average out deformation signals or high phase/elevation changes in narrow valleys. However, by applying the phase-elevation correction, we reduce the fringe rate sufficiently to enable further multi-looking without smoothing out high fringe rate areas. We multi-look the IFGs in 8 looks (i.e. averaging over 8 pixels in azimuth and 32 pixels in range) to aid the unwrapping algorithm. The 8-looked IFGs have a ground pixel resolution of ~ 120 m x 128 m.

We then run the unwrapping algorithm which starts in regions with the highest colinearity and follows a path through progressively lower colinearity areas (Grandin et al., 2012; Grandin, 2015; Daout et al., 2023). The algorithm is more likely to encounter unwrapping errors (additional cycles of 2π radians incorrectly added to the phase (Yunjun, Fattahi and Amelung, 2019) in regions of lower colinearity, so

unwrapping these regions later on in the process limits the extent to which errors can propagate through the IFG.

Finally, we calculate the unwrapped equivalent of the empirical phase-elevation correction we previously applied to the wrapped phase and add this back to the unwrapped IFGs. While this empirical correction is intended to simulate the stratified atmospheric component of the signal, it may also capture tectonic signals which are correlated to topography, so it is necessary to add it back at this stage.

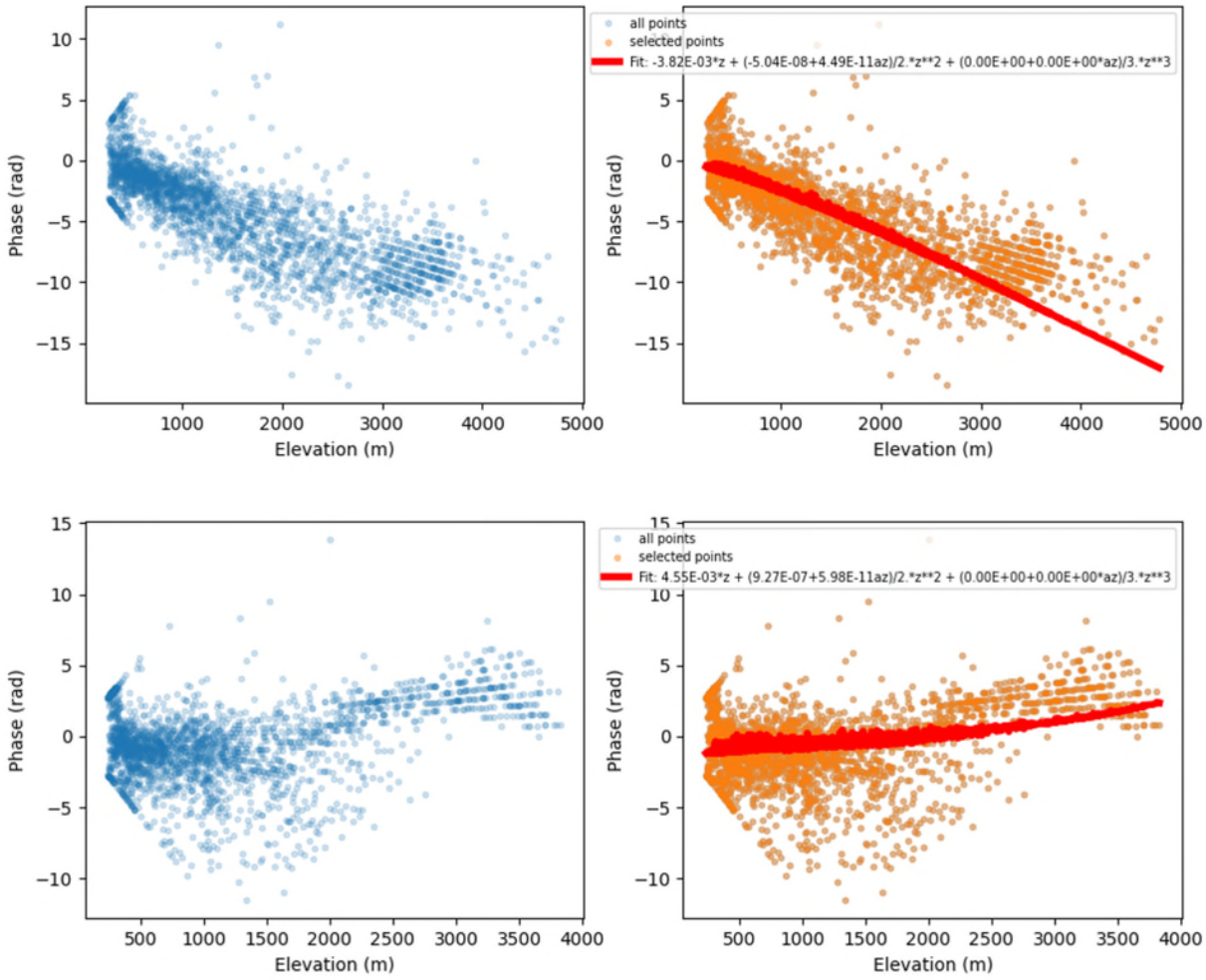

Figure 4.6-2. Examples of phase-elevation relationship estimations on heavily filtered interferograms for pre-unwrapping corrections. Top panel: ascending track IFG 20170714-20170924. Bottom panel: descending track IFG 20201207-20210124.

4.6.1.1.3. Atmospheric Correction

Instead of an empirical correction, to remove tropospheric delays we apply a predictive atmospheric correction to the unwrapped IFGs based on the ECMWF Reanalysis v5 (ERA-5) atmospheric model (https://www.ecmwf.int/en/forecasts/dataset/ecmwf-reanalysis-v5; Jolivet et al., 2011; Daout et al., 2020). To perform this correction, we follow the procedure outlined in Dodds et al. (2021) and Dodds et al. (2022): We estimate a linear phase ramp and offset between each unwrapped IFG and the corresponding ERA-5 phase delay map, $IFG = ERA + ax + by + c$, where x is azimuth, y is range and a, b and c are constants (Dodds, 2021). To impose network closure, we invert for the ramp parameters (a, b and c) for each IFG, then correct the tropospheric delay maps for these ramps and subtract the result from the IFGs (Dodds, 2021). The linear ramps we remove in this step are likely related to residual signals such as ionosphere, unaccounted-for orbital effects, large-scale plate motion, or solid earth tides (Dodds et al., 2022; Lemrabet et al., 2023). These long-wavelength ramps are estimated over the full swath. As such, this step is unlikely to remove any deformation that does not show a linear ramp-like trend and should not affect our interpretation of the regional tectonic activity, which is based on relative velocity gradients within the imaged area. In this step, we also refer the data to a reference area where the spatial and temporal coherence is high. Ideally, the reference area would be in the bedrock of the Tian Shan mountains, but due to the decorrelation of the mountains in many IFGs we choose instead a relatively stable area in the basin interior to the west of the Babatag thrust.

To assess the performance of the ERA-5 atmospheric correction, for each IFG we plot the interferometric phase (with the ramp correction applied) against the modelled atmospheric phase for every pixel and fit a linear model, following the methodology of Dodds et al. (2022). For small temporal baselines, we assume that individual IFGs are dominated by atmospheric phase delays and therefore the atmospheric model should account for the vast majority of the observed signal (Dodds et al., 2022). Under this assumption, a perfectly performing model will have a Pearson correlation coefficient (r) equal to 1 and

gradient equal to 1. Figure 4.6-3 shows analysis of an ascending track IFG for which the modelled atmospheric phase is highly correlated with the de-ramped interferometric phase (r = 0.98) with a gradient of 1. Across our network of IFGs, the performance of the model is variable, as demonstrated by the two further examples in Figure 4.6-5 and Figure 4.6-6 (medium performance, gradient = 0.96 and r = 0.69), and in Figure 4.6-7 and Figure 4.6-8 (poor performance, gradient = -0.03, r = -0.08).

Figure 4.6-9 summarises the model performance across all IFGs for both tracks. The gradients for the ascending track have a mode of 0.79, a mean of 0.71 and a standard deviation of 0.21. The descending track gradients have a mode of 0.85, a mean of 0.74 and a standard deviation of 0.19. For both tracks, the distribution of gradients is close to Gaussian, but with a slight left skew which is more prominent in the descending track. As the correlation (r) is bounded between -1 and 1, to find the mean we rescale the data between 0 and 1 then perform a logit transformation on r ($logit(r) = log(r/(1-r))$). We fit a normal distribution to $logit(r)$ (Figure 4.6-9 c and g), calculate the mean and standard deviation, then transform these values back into the original domain. For the ascending track, the resulting correlations have a mode of 0.85, a mean of 0.78 and a standard deviation of 0.33. For the descending track, the correlations have a mode of 0.86, a mean of 0.81 and a standard deviation of 0.28. For both tracks the correlations (r) and gradients are correlated with each other (Figure 4.6-9 d and h).

This analysis shows that the model predicts the atmospheric component well, but average gradients < 1 suggest a slight underestimation of the amplitude of the signal. Dodds et al. (2022) produced the similar finding that the GACOS atmospheric models (Yu, Li and Penna, 2018) underestimated signal amplitude for Turkmenistan, with a smaller average gradient (i.e. a bigger underestimate) than this study. In our analysis we also find that atmospheric models perform slightly better for the descending track, acquired in the early morning (~06:30 local time/01:30 UTC), than for the ascending track, acquired in the evening (~18:20 local time/13:20 UTC) – Dodds et al. (2022) document the same pattern in their study of Turkmenistan which is at a similar latitude (i.e. similar acquisition times). We suggest the difference

in the performance of the atmospheric prediction between tracks is related to the diurnal cycles of the atmospheric boundary layer, as more turbulence develops in the day compared to the early morning (Stull, 2017), making the evening atmospheric effects harder to predict (Figure 4.6-10).

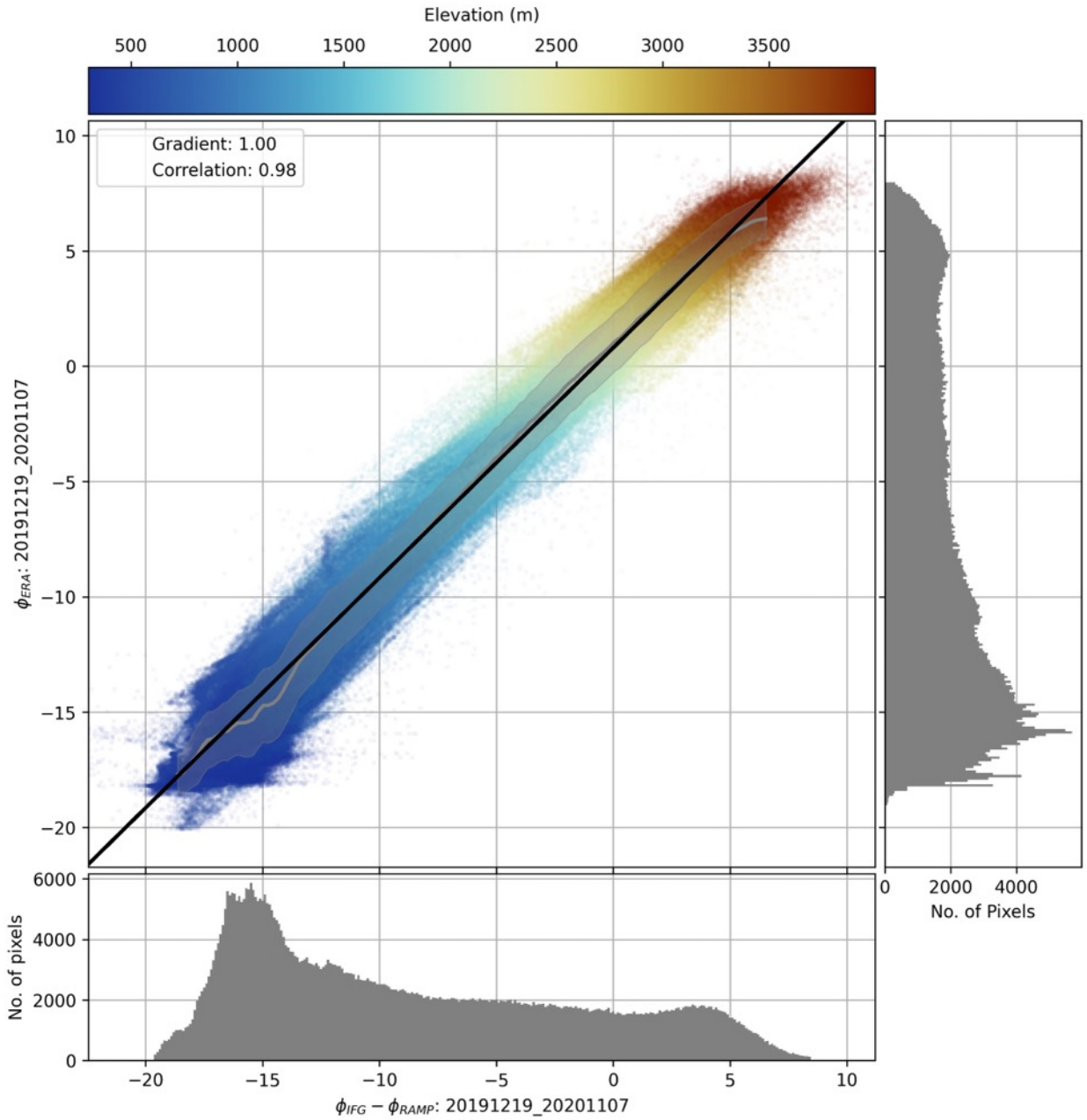

Figure 4.6-3. Interferometric phase with ramp correction plotted against modelled atmospheric phase for Ascending track IFG 20191219 – 20201107. The grey line and grey envelope are the sliding median and standard deviation of the binned data after cleaning to only include the data within the 90th percentile.

The thick black line is the linear model which best fits the sliding mean, weighted by the sliding standard deviation. Methodology and plot after Dodds et al. (2022).

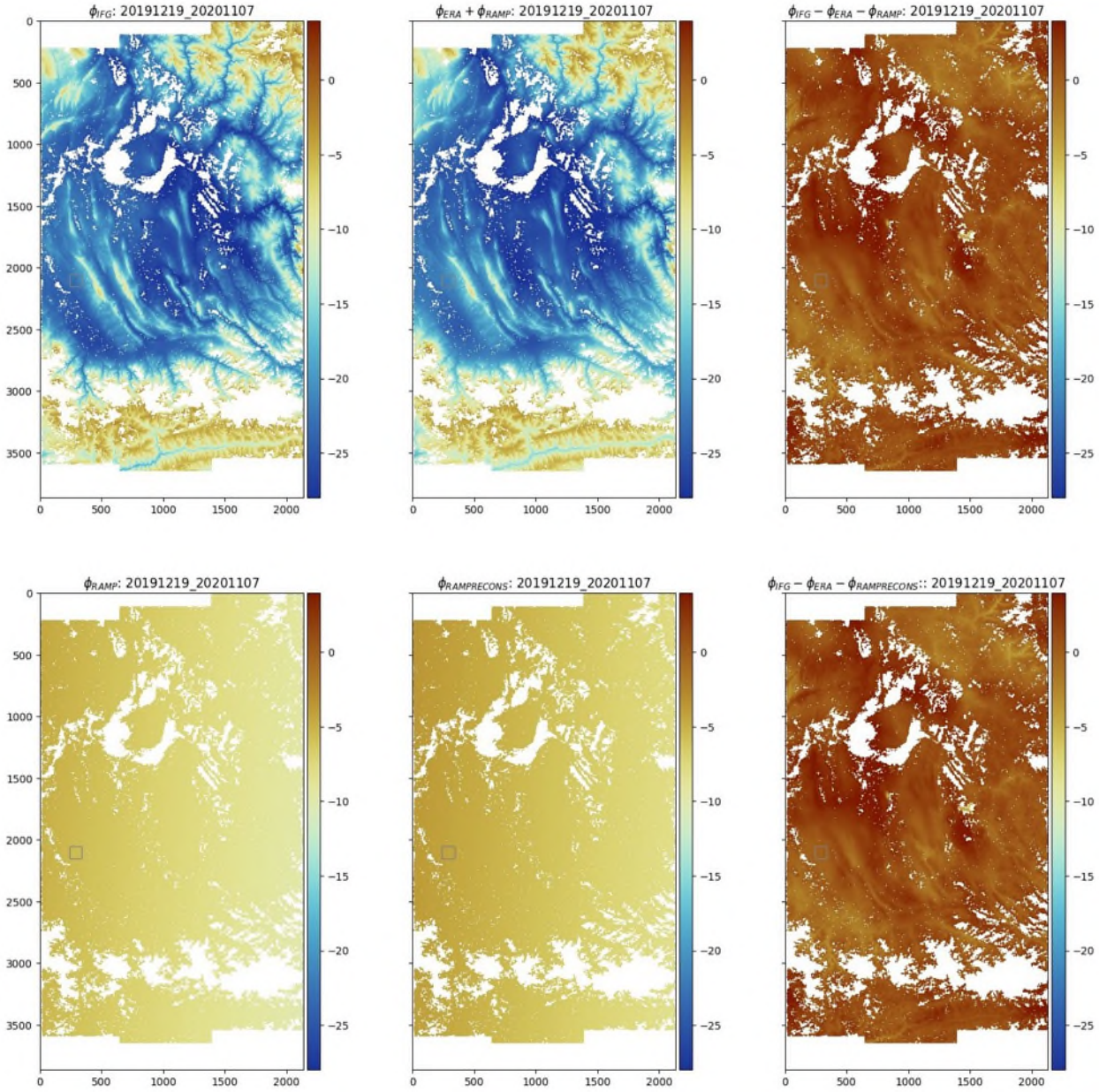

Figure 4.6-4. Maps of atmospheric and ramp corrections for Descending track IFG 20191219 – 20201107. All maps in radar geometry and show phase in mm/yr. Grey square = reference area. Top row from left to right: 1) interferometric phase, 2) atmospheric model + phase ramp, and 3) interferometric phase - atmospheric model – phase ramp. Bottom row from left to right: 1) Phase ramp initial estimate, 2) Reconstructed phase ramp from network inversion, 3) interferometric phase - atmospheric model - phase ramp. Methodology and plot after Dodds et al. (2022).

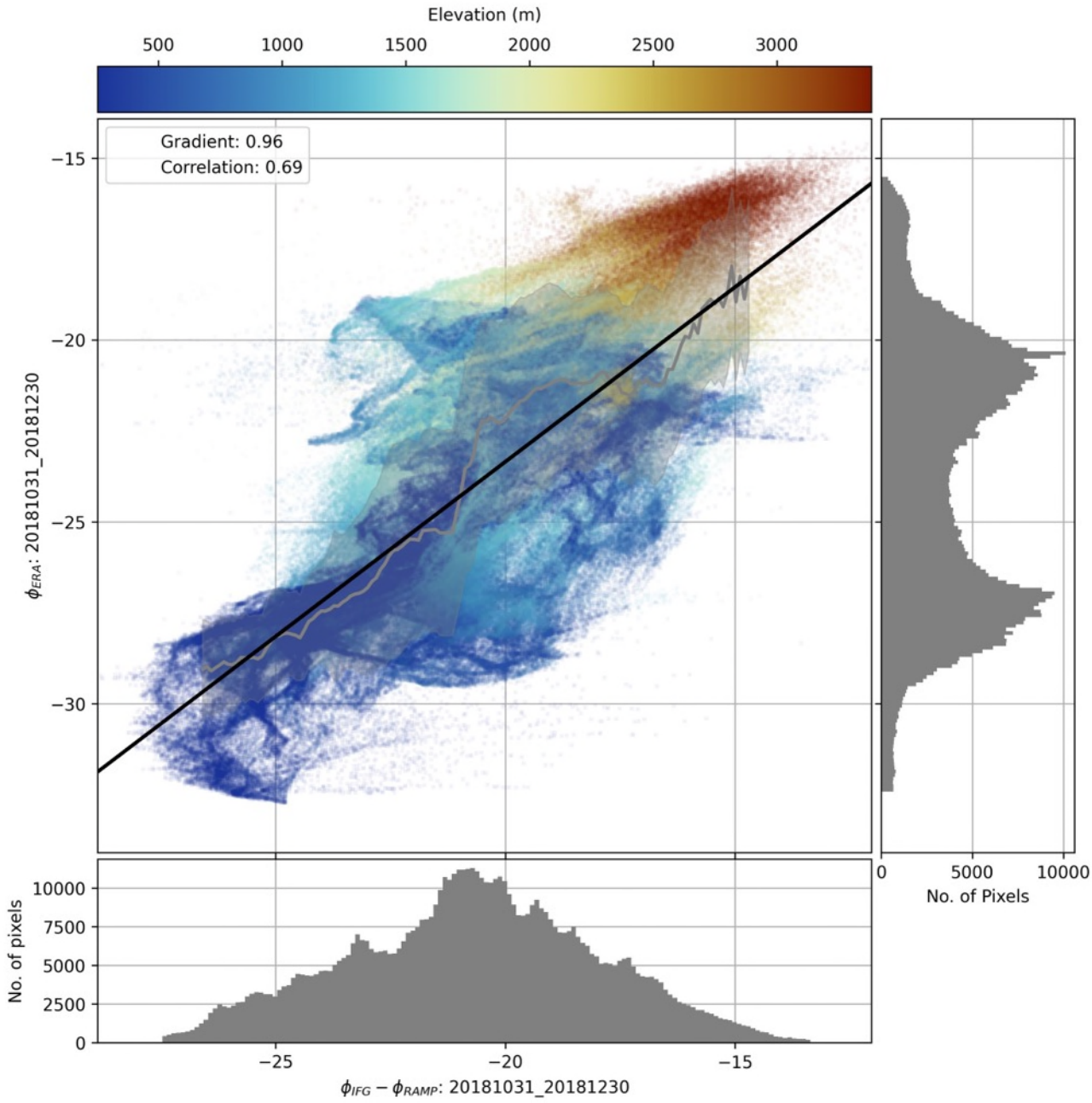

Figure 4.6-5. Interferometric phase with ramp correction plotted against modelled atmospheric phase for Descending track IFG 20181031 – 20181230. The grey line and grey envelope are the sliding median and standard deviation of the binned data after cleaning to only include the data within the 90th percentile. The thick black line is the linear model which best fits the sliding mean, weighted by the sliding standard deviation. Methodology and plot after Dodds et al. (2022).

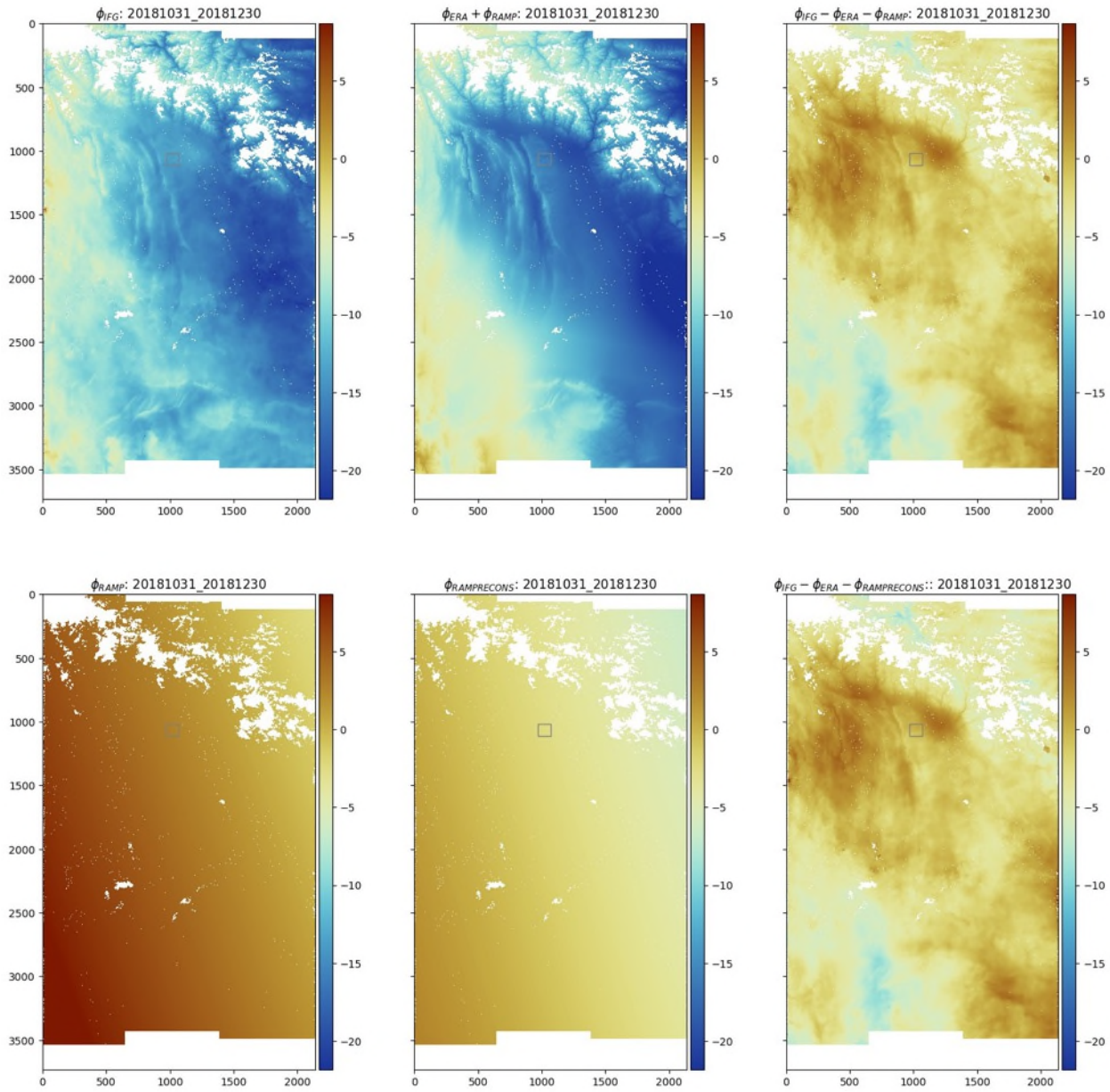

Figure 4.6-6. Maps of atmospheric and ramp corrections for Descending track IFG 20181031 – 20181230. All maps in radar geometry and show phase in mm/yr. Grey square = reference area. Top row from left to right: 1) interferometric phase, 2) atmospheric model + phase ramp, and 3) interferometric phase - atmospheric model – phase ramp. Bottom row from left to right: 1) Phase ramp initial estimate, 2) Reconstructed phase ramp from network inversion, 3) interferometric phase - atmospheric model - phase ramp. Methodology and plot after Dodds et al. (2022).

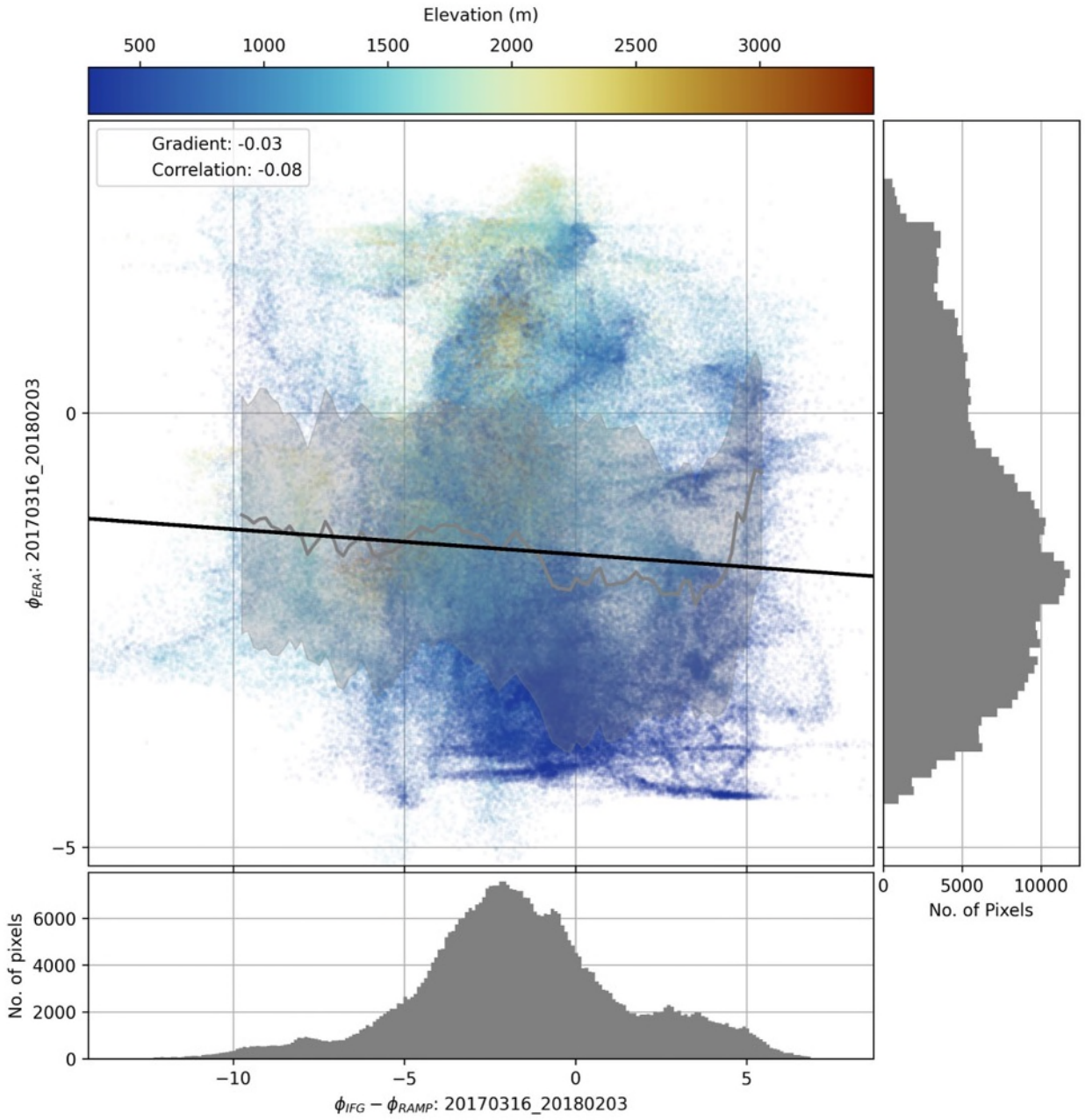

Figure 4.6-7. Interferometric phase with ramp correction plotted against modelled atmospheric phase for Ascending track IFG 20170316 – 20180203. The grey line and grey envelope are the sliding median and standard deviation of the binned data after cleaning to only include the data within the 90th percentile. The thick black line is the linear model which best fits the sliding mean, weighted by the sliding standard deviation. Methodology and plot after Dodds et al. (2022).

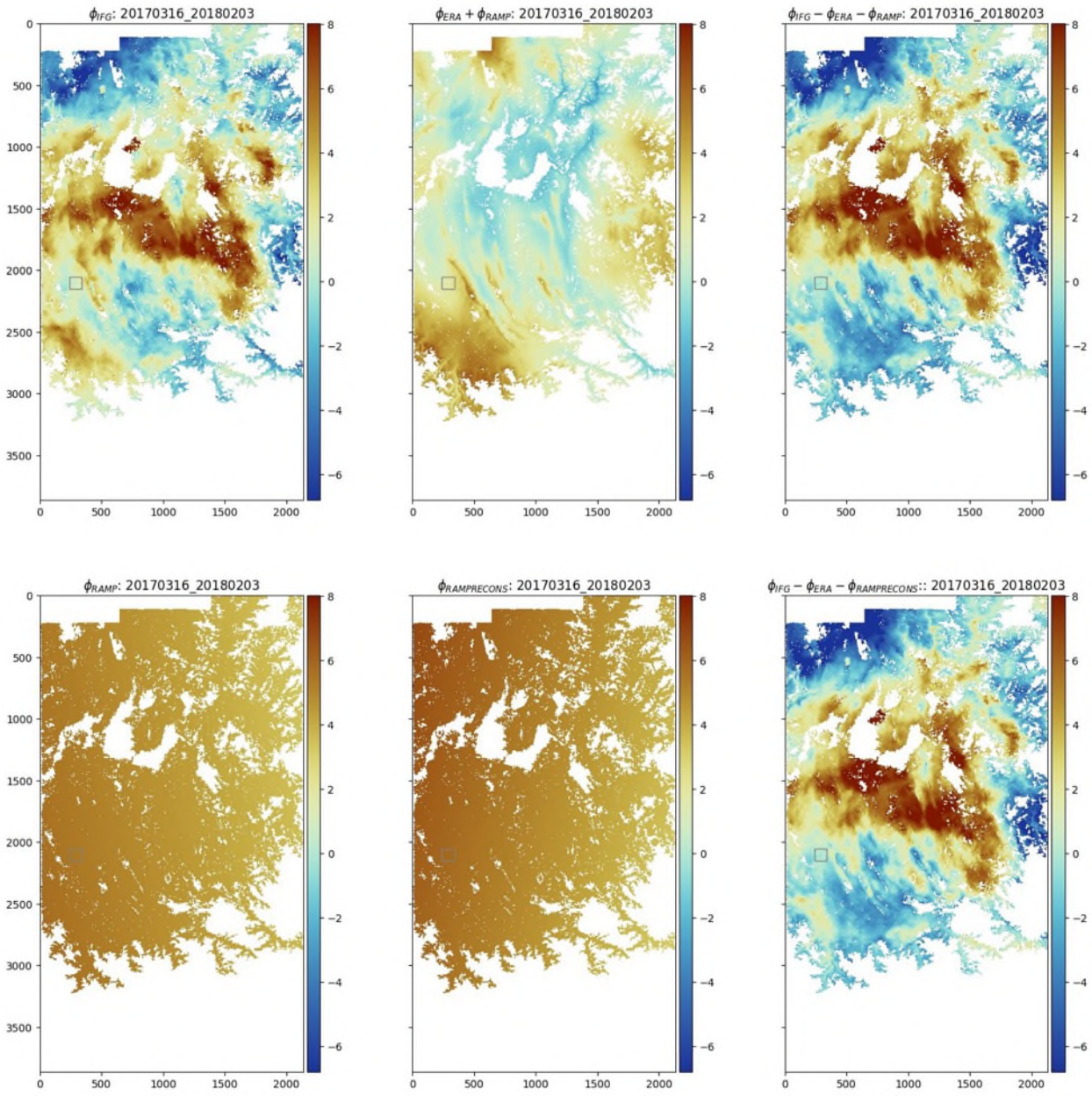

Figure 4.6-8. Maps of atmospheric and ramp corrections for Descending track IFG 20170316 – 20180203. All maps in radar geometry and show phase in mm/yr. Grey square = reference area. Top row from left to right: 1) interferometric phase, 2) atmospheric model + phase ramp, and 3) interferometric phase - atmospheric model – phase ramp. Bottom row from left to right: 1) Phase ramp initial estimate, 2) Reconstructed phase ramp from network inversion, 3) interferometric phase - atmospheric model – phase ramp. Methodology and plot after Dodds et al. (2022).

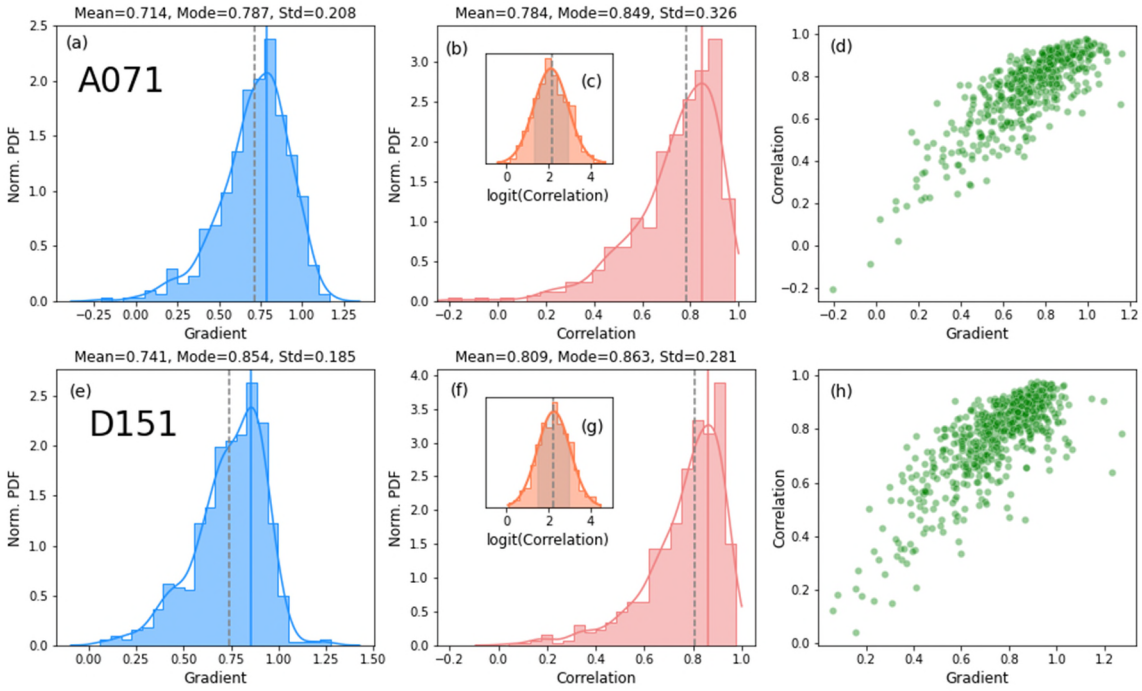

Figure 4.6-9. Results of comparison of individual interferograms after ramp correction with atmospheric phase computed with ECMWF ERA-5 models for the equivalent interferogram. Methodology modified after Dodds et al., (2022). Top row = ascending track, bottom row = descending track. Left plots (a and e) show the gradient between the interferometric and modelled atmospheric phases and middle plots (b and d) show the correlation coefficient (r-value). Blue and pink envelopes show kernel density estimates (KDEs), blue and pink vertical lines mark the modal values and dashed grey vertical lines are the mean values. The insets (c and g) show the histograms of the logit(Correlation) with fitted normal distributions – the mean and standard deviation of the correlation were calculated from the logit(Correlation) dataset and then transformed back into the scaling of the original dataset. The scatter plots on the right (d and h) show the relationship between the gradient and the correlation.

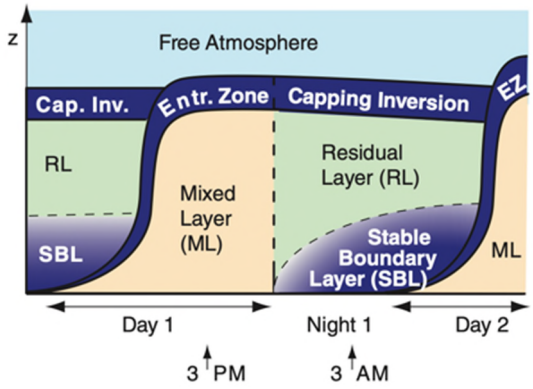

Figure 4.6-10. Diagram from Stull (2017) showing atmospheric boundary layer structure over land in summer in fair weather.

4.6.1.1.4. Time Series Inversion

We perform a pixel-by-pixel time series analysis using the NSBAS method from Doin et al. (2015) and López-Quiroz et al. (2009), which we briefly summarise here. In this method, the total phase delay φ_k between the first and last epochs (i.e. SAR images) is obtained by summing together the incremental phase delay for every epoch, assuming $\varphi_1 = 0$. There are M IFGs in the whole network, but for each individual pixel, l, there are M_l valid interferograms, where $M_l \leq M$. To perform the inversion we set up and solve the linear equation

$$\boldsymbol{d}_l = \boldsymbol{G}_l \boldsymbol{m}_l \tag{4.6-1}$$

where $\boldsymbol{d}_l$ is the data vector containing the IFG phase for pixel l in each of the M_l IFGs, $\boldsymbol{m}_l$ is the vector of unknown incremental phase delays, and $\boldsymbol{G}_l$ is a matrix made up of ones and zeros which defines the connection between $\boldsymbol{m}_l$ and $\boldsymbol{d}_l$ (López-Quiroz et al., 2009). In other words, we solve the system equation

$$\forall q \in [1, M] \quad \sum_{n=i}^{n=j-1} \delta\varphi_n = \Phi_q \tag{4.6-2}$$

pixel by pixel, where $\delta\varphi_n$ is the incremental phase delay for the nth epoch relative to the preceding epoch and Φ_q is the phase of the qth IFG constructed from epochs i and j (López-Quiroz et al., 2009; Doin et al., 2015). The inversion is performed using a least squares regression, which is regularised with the constraints in equations (4.6-3), (4.6-4) and (4.6-5) so that it can be solved for pixels with a missing critical interferogram(s) (i.e. where there is a rank deficiency in $\boldsymbol{G}_l^T \boldsymbol{G}_l$; López-Quiroz et al., 2009). The constraints are:

$$-W_1 \varphi_1^S = 0 \tag{4.6-3}$$

$$\forall k \in [2, N] \quad W_k \left(\sum_{n=1}^{n=k-1} \delta\varphi_n - \varphi_k^S \right) = 0$$

(4.6-4)

$$\forall k \in [1, N] \quad \gamma \omega_k \frac{\partial^2 \varphi_k^S}{\partial t^2} = 0$$

(4.6-5)

(López-Quiroz et al., 2009; Doin et al., 2015). W_k is a weighting accounting for the level of atmospheric turbulence affecting the signal for the kth epoch (Atmospheric Phase Screen). φ_k^S is the evolution of the deformation for the kth epoch, constrained to be smooth in time (equation (4.6-5). N is the total number of epochs and γ is a temporal smoothing coefficient which we set equal to 0.003. ω_k is a weighting for the kth epoch equal to the average time interval between the five epochs from the five-point numerical method used to calculate $\frac{\partial^2 \varphi_k^S}{\partial t^2}$.

To identify unwrapping errors and misclosure of the network, for all the interferograms, M, we calculate the Root Mean Square (RMS) deviation between the observed phase of the IFG, Φ_q, and the equivalent modelled phase (the sum of the incremental phase delay, $\delta\varphi_n$, output from the inversion) for each lth pixel as follows:

$$\Phi_{RMS_{pixel}^l} = \frac{1}{M_l}\left[\sum_{M_l}\left(\Phi_q - \sum_{n=i}^{n=j-1} \delta\varphi_n\right)^2\right]^{1/2}$$

(4.6-6)

(López-Quiroz et al., 2009). To identify which IFGs may be the source of these errors, we also calculate the RMS deviation across all pixels for each individual IFG as follows:

$$\Phi_{RMS_{IFG}} = \frac{1}{P}\left[\sum_{P}\left(\Phi_q - \sum_{n=i}^{n=j-1} \delta\varphi_n\right)^2\right]^{1/2}$$

(4.6-7)

where P is the total number of pixels in the IFG (López-Quiroz et al., 2009). For the interferograms with the highest average $\Phi_{RMS_{IFG}}$, we inspect maps of $\Delta\Phi$, the deviation of the reconstructed phase

from the modelled phase, where $\Delta\Phi = \Phi_q - \sum_{n=i}^{n=j-1} \delta\varphi_n$ (López-Quiroz et al., 2009). Unwrapping errors are marked by abrupt changes in $\Delta\Phi$, as seen in the deviation maps in Figure 4.6-11. If unwrapping errors are extensive, we remove the IFG from the network – 12 and 5 IFGs were removed from the ascending and descending networks, respectively. Otherwise, we manually define high-priority 'paths' in error-prone regions to guide the unwrapping path between areas separated by patches of low coherence and then re-unwrap these IFGs in order to reduce unwrapping errors (Grandin et al., 2012; Daout et al., 2016). We then re-run the time series inversion, performing additional automatic corrections on unwrapping errors as outlined in López-Quiroz (2009). Through this process we improve $\Phi_{RMS_{IFG}}$, $\Delta\Phi$ (Figure 4.6-11) and $\Phi_{RMS^l_{pixel}}$ (Figure 4.6-12), reducing both the number of abrupt changes in RMS and the RMS magnitude. While these iterations remove large network inconsistencies (Doin et al., 2015; Daout et al., 2017; the maximum $\Phi_{RMS_{IFG}}$ is ~ 0.75 radians for the ascending track and ~ 0.6 radians for the descending track) unwrapping errors remain in some areas (Figure 4.6-12b and d). We mask out these remaining errors in later steps.

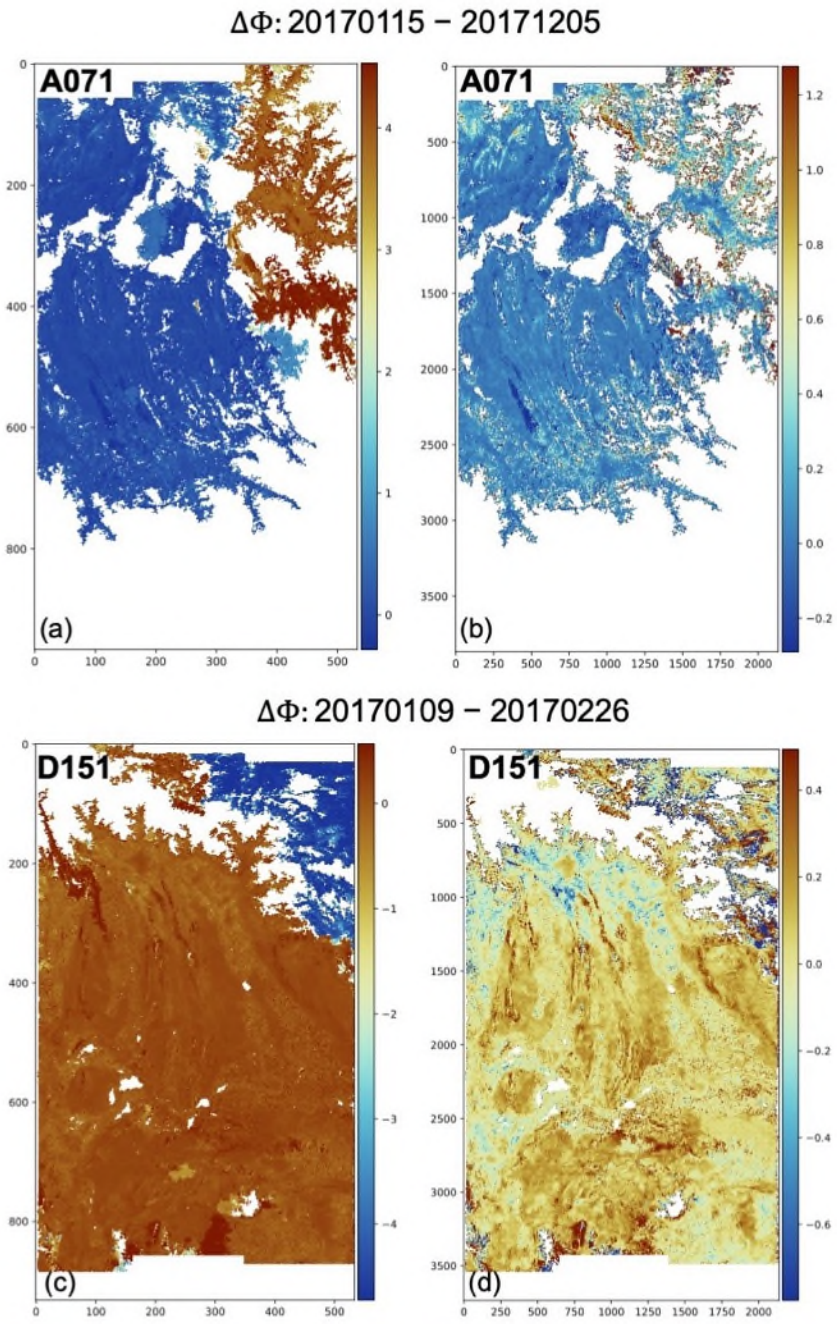

Figure 4.6-11. Deviation maps showing the difference between the modelled and reconstructed phase, ΔΦ, in radar coordinates for 2 different interferograms after the initial time series inversion (left) and the final time series inversion (right).

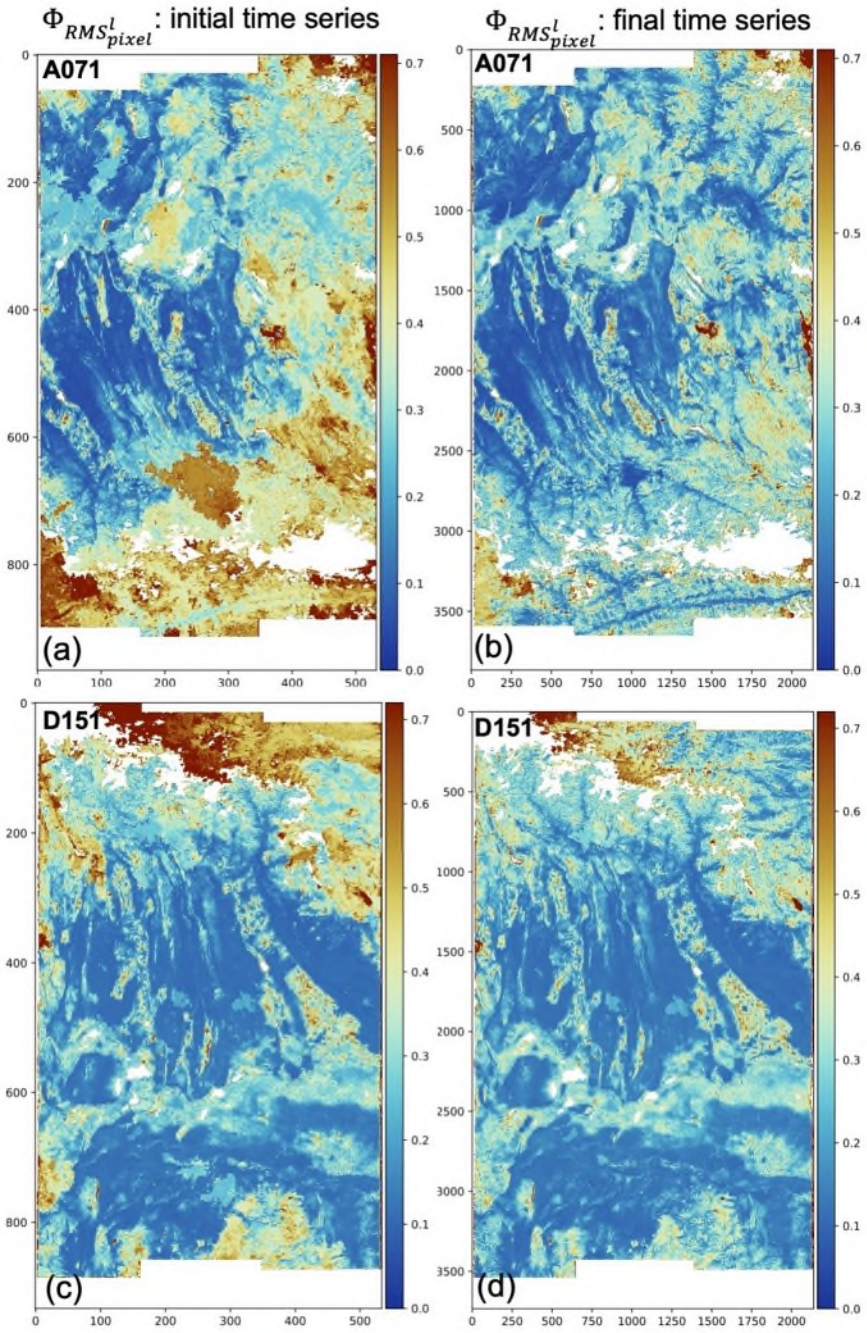

Figure 4.6-12. Maps of $\Phi_{RMS_{pixel}^{l}}$ in radar geometry for the ascending (top row) and descending (bottom row) tracks for the initial time series inversion (left) and the final time series inversion (right). In both tracks the number and magnitude of high RMS patches is reduced as unwrapping errors are removed.

4.6.1.1.5. Temporal Decomposition

To obtain the LOS velocity maps, we perform a temporal decomposition following the scheme detailed in Daout et al. (2017). Again, we solve an inverse problem, $\boldsymbol{d} = \boldsymbol{Gm}$. This time, $\boldsymbol{d}$ is the vector of LOS displacements output from the time series inversion, $\boldsymbol{m}$ is the vector of model unknowns, and $\boldsymbol{G}$ is a matrix defining the relationship between them according to the governing equation:

$$LOS(t) = Acos(wt) + Bsin(wt) + Vt + C, \tag{4.6-8}$$

where $LOS(t)$ is the cumulative displacement over time t, $w = 2\pi/1$ yr, V is the linear rate of motion, and A, B and C are constants. We include sinusoidal and cosinusoidal terms to investigate potential seasonal components from residual atmospheric signals or hydrological processes in snow-covered high mountains, rivers, reservoirs and fields within the study area (Daout et al., 2023).

Using a least squares method (Daout et al., 2017), we perform an initial iteration of the inversion, weighting the data by the residuals of each epoch averaged from the output of the time series inversion, so that epochs with higher misclosure are down-weighted. A second iteration incorporates the misfit between the reconstructed and observed phase from the first iteration of the temporal inversion as a weighting factor (Daout et al., 2023). The uncertainty in the model for each parameter, m, and pixel, l, is defined as

$$\sigma_m^l = \sqrt{\frac{N}{N-M}\left(\Phi_{RMS_{pixel}^l}\right)^2 (\boldsymbol{G}^T\boldsymbol{G})_m^{-1}} \tag{4.6-9}$$

where N is the number of data, M is the total number of parameters, $\Phi_{RMS_{pixel}^l}$ is the RMS for each pixel as calculated from the time series inversion described in Section 4.6.1.1.4, and $(\boldsymbol{G}^T\boldsymbol{G})_m^{-1}$ denotes the mth diagonal element of $(\boldsymbol{G}^T\boldsymbol{G})^{-1}$ and is the variance of the model (Daout et al., 2017; Tsai, 2023).

$\sqrt{A^2 + B^2}$ and $\arctan(B/A)$ represent the amplitude and time lag of the seasonal signal respectively, with corresponding errors of $\sqrt{{\sigma_A^l}^2 + {\sigma_B^l}^2}$ and $\frac{\sigma_B^l|A| + \sigma_A^l|B|}{{\sigma_B^l}^2 + {\sigma_A^l}^2}$ (Daout et al., 2017).

The amplitude of seasonal signals is small for most of the study region, with higher amplitudes associated with rivers, high mountain valleys and a reservoir (Figure 4.6-13). Going forward, we use the linear component of the temporal decomposition, V, in our velocity maps. Due to the minimal seasonal component, this is very similar to the velocity from the time series inversion (Figure 4.6-14). The mean uncertainty in the linear velocity for all pixels is 0.8 mm/yr for the ascending track and 0.6 mm/yr for the descending track (Figure 4.3-1).

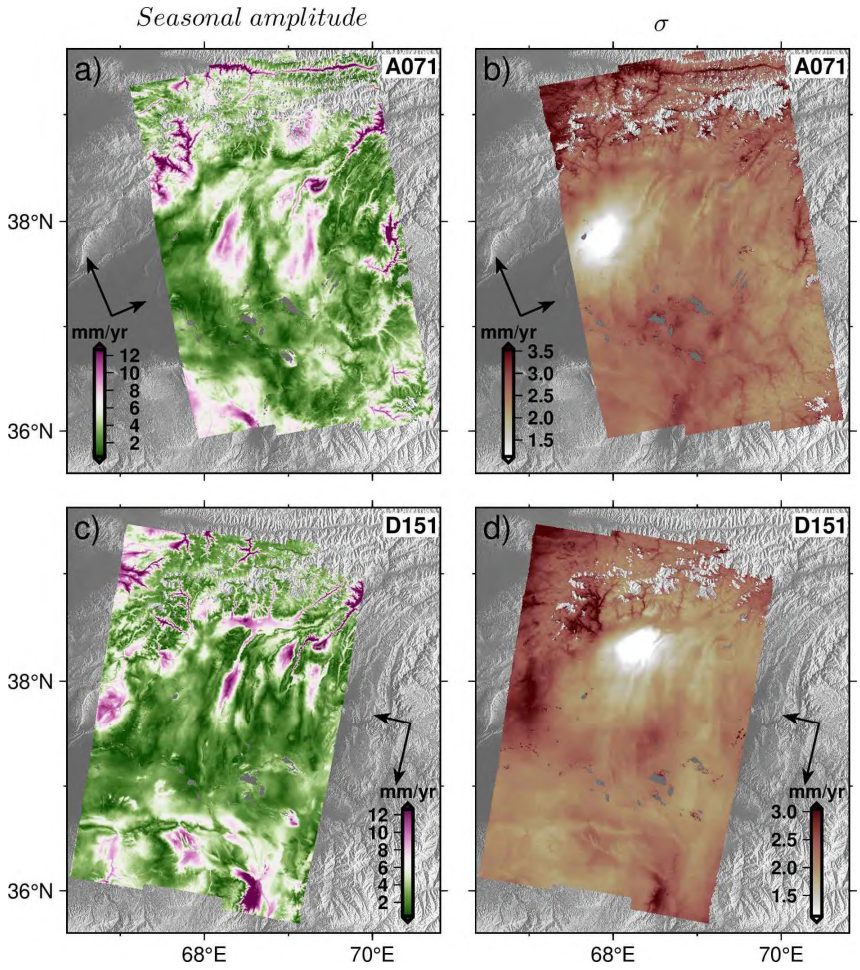

Figure 4.6-13. Amplitude of the seasonal component of the signal from the temporal decomposition (left) and associated uncertainties (right). Background: SRTM 30 m topography.

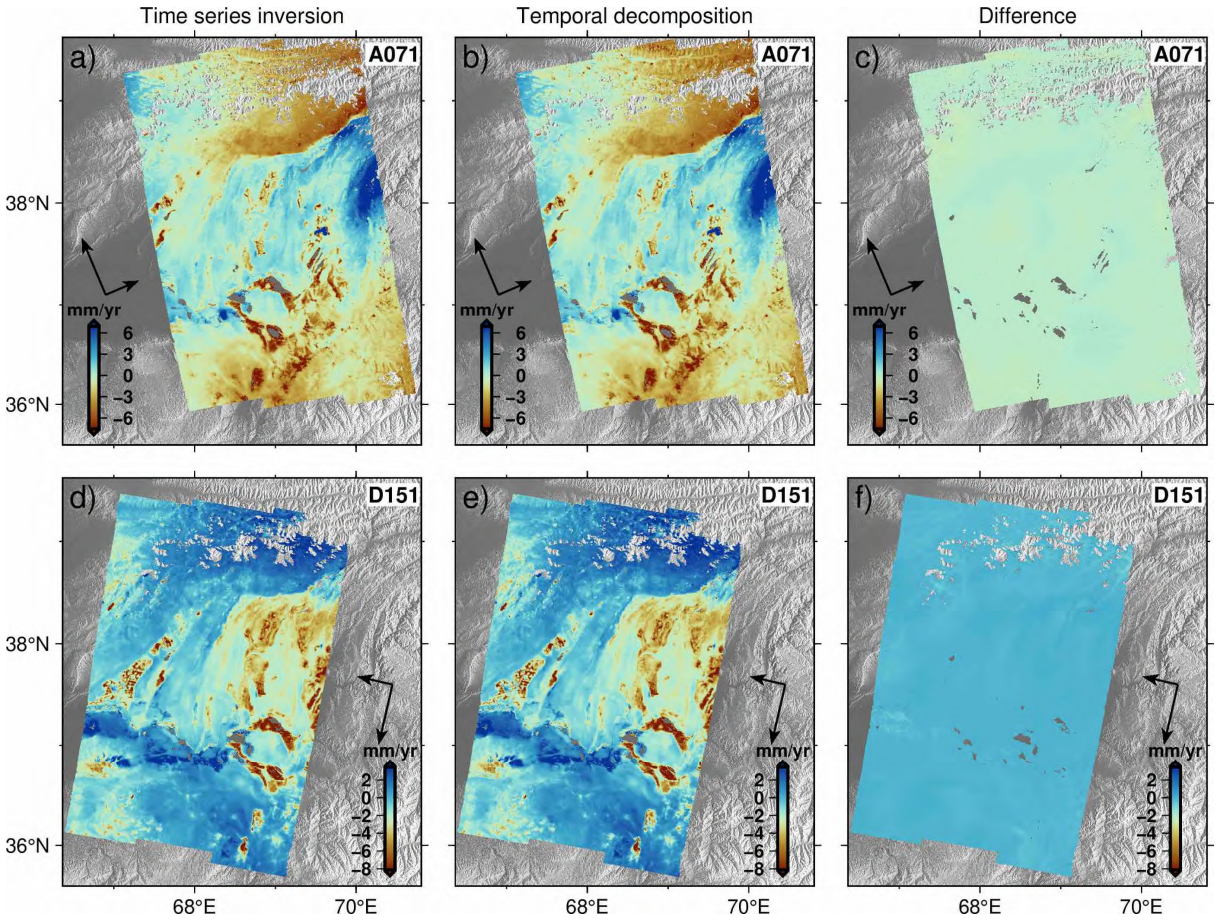

Figure 4.6-14. Linear velocity fields for ascending (top row) and descending (bottom row) tracks. Left: velocity resulting from the time series inversion. Centre: linear component of the temporal decomposition of the time series. Right: difference between the two. Background: SRTM 30 m topography.

4.6.1.1.6. Cleaning the LOS Velocity Maps

Next we clean the linear velocity maps to remove poor quality pixels (Figure 4.6-15). To mitigate phase bias (discussed in section 4.6.1.1.7 below) we follow the method of Mathey et al. (2022) to remove pixels with an average temporal baseline of less than 3 months (mask 1: Figure 4.6-15 a to b and e to f). This step removes the data in many of the agricultural areas. Next, we mask using the uncertainty from the time series inversion, removing pixels with $\Phi_{RMS^{l}_{pixel}}$ > 0.7 rad (~3 mm) for the descending track and > 0.6 rad (~2.6 mm) for the ascending track (mask 2: Figure 4.6-15 b to c and f to g). As $\Phi_{RMS^{l}_{pixel}}$ is low for most pixels, this does not mask much of the velocity map. We then mask

using the uncertainty associated with the linear component of the temporal decomposition (σ_V^l), removing pixels with σ_V^l > 0.20 rad/yr (~0.9 mm/yr) for the descending track and > 0.22 rad/yr (~0.97 mm/yr) for the ascending track (mask 3: Figure 4.6-15 c to d and g to h). This step has a bigger impact, removing what appears to be a remaining unwrapping error in the high mountains as well as multiple river valleys which had high uncertainties, probably due to their high temporal variability and more active surface processes.

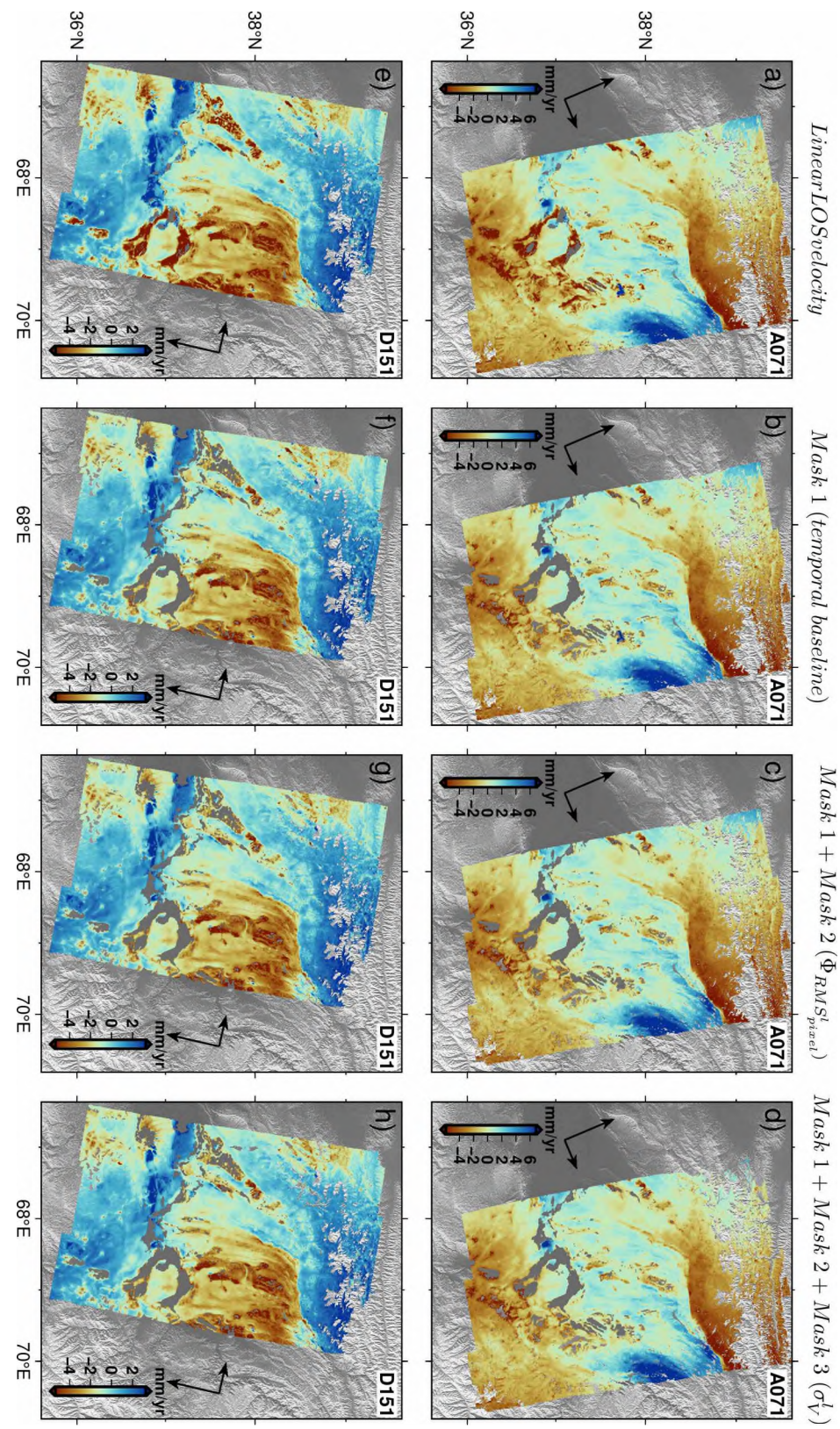

Figure 4.6-15. The cleaning procedure for the ascending (a – d) and descending (e – h) velocity maps. Negative (red) = relative movement away from satellite. The linear LOS velocity output from the

temporal decomposition is in column 1. Column 2 shows the same result after applying mask 1 (removing pixels with an average temporal baseline < 3 months), column 3 shows the result after applying both mask 1 and mask 2 (removing pixels with $\Phi_{RMS_{pixel}^{l}}$ > 0.7 rad (~3 mm) for the descending track and > 0.6 rad (~2.6 mm) for the ascending track), and column 4 shows the result after applying mask 1, mask 2 and mask 3 (removing pixels with σ_V^l > 0.20 rad/yr (~0.9 mm/yr) for the descending track and > 0.22 rad/yr (~0.97 mm/yr) for the ascending track). Background: SRTM 30 m topography.

4.6.1.1.7. Phase Bias Mitigation

Interferograms can be affected by a systematic phase bias, usually in the direction away from the satellite, which can propagate through interferogram networks leading to erroneous subsidence signals in LOS velocity maps (Daout et al., 2020; Ansari, De Zan and Parizzi, 2021; De Luca et al., 2022; Maghsoudi et al., 2022; Purcell et al., 2022). This effect is thought to be related to soil moisture and has been found to correlate with agricultural land use (De Zan et al., 2014; Daout et al., 2020; Maghsoudi et al., 2022; Purcell et al., 2022). Phase bias has been found to have the worst impact on shorter period IFGs and can be effectively mitigated by creating networks based on IFGs with longer temporal baselines (Daout et al., 2020; De Luca et al., 2022; Purcell et al., 2022). Therefore, in our networks we include IFGs with baselines up to 5 months and exclude those with baselines of < 36 days.

Our LOS velocity maps show particularly high subsidence signals in the fields. Whilst this could be a true subsidence signal related to land use, we suspect that this is at least in part a phase bias effect. Therefore, in the cleaning steps outlined above, we mask the LOS velocity maps based on the average temporal baseline of each pixel, removing those pixels with baselines of less than 3 months (Figure 4.6-15 a to b and e to f; Mathey et al., 2022). This step masks out many of the fields, though not all of them.

4.6.1.1.8. Spatial Decomposition

To aid our interpretation of the data and to reduce noise, we decompose the linear component of the ascending and descending LOS velocities into an eastwards horizontal component, V_E, and a vertical component, V_U (Figure 4.3-2; Daout et al., 2023). As the InSAR technique is relatively insensitive to N-S motion (Elliott, Walters and Wright, 2016), we make the assumption that the northward component of the linear velocity, V_N, is zero. We then down sample the data onto 130 m grids. To find V_U and V_E, we perform an inversion for each pixel in the area of overlap of the two tracks using the equation

$$V_{LOS}^{t} = V_U \cos(\theta^t) - V_E \sin(\theta^t) \cos(\phi^t), \tag{4.6-10}$$

where V_{LOS}^{t} is the linear LOS velocity, θ^t is the incidence angle measured from the vertical and ϕ^t is the heading angle measured clockwise from north for track t (Ou, 2020). We use the uncertainties from the temporal decomposition, σ_V^l, as a prior, so that the output uncertainties of the least squares regression are also weighted by σ_V^l (Wright, 2004; Daout et al., 2023).

4.6.1.1.9. Referencing

We attempted to reference the velocity map to stable Eurasia using the 3D GPS rates from Metzger et al. (2020) and the methodology of Ou et al. (2022). However, we found the GPS data to be too sparse and too noisy to produce a meaningful result. Therefore, our final velocity maps are referenced to an area of relatively little deformation within the Tajik Basin to the west of the Babatag thrust.

4.6.1.2. Velocity Profile Modelling

The interseismic deformation measured along a 2-D profiles across a strike-slip fault can be modelled with an arctangent function (Savage and Burford, 1973). We model profiles of the east component of

the velocity on the Ilyak fault (Figure 4.3-4) by inverting for an arctangent function, according to the equation,

$$V = (S/\pi)\tan^{-1}(x/W) + C$$

where V is the velocity, S is the slip rate, x is the distance along the profile, W is the locking depth and C is a constant (Savage and Burford, 1973; Turcotte and Schubert, 2014). If the fault is creeping, the locking depth tends towards zero and the equation tends towards a step function. To prepare the data for inversion, we smooth the profiles using a sliding window median filter with a window size of < 1 km. We use the standard deviations from the sliding window multiplied by two as the prior uncertainties for the inversion. We report posterior uncertainties to two standard deviations.

4.6.2. Additional InSAR figures

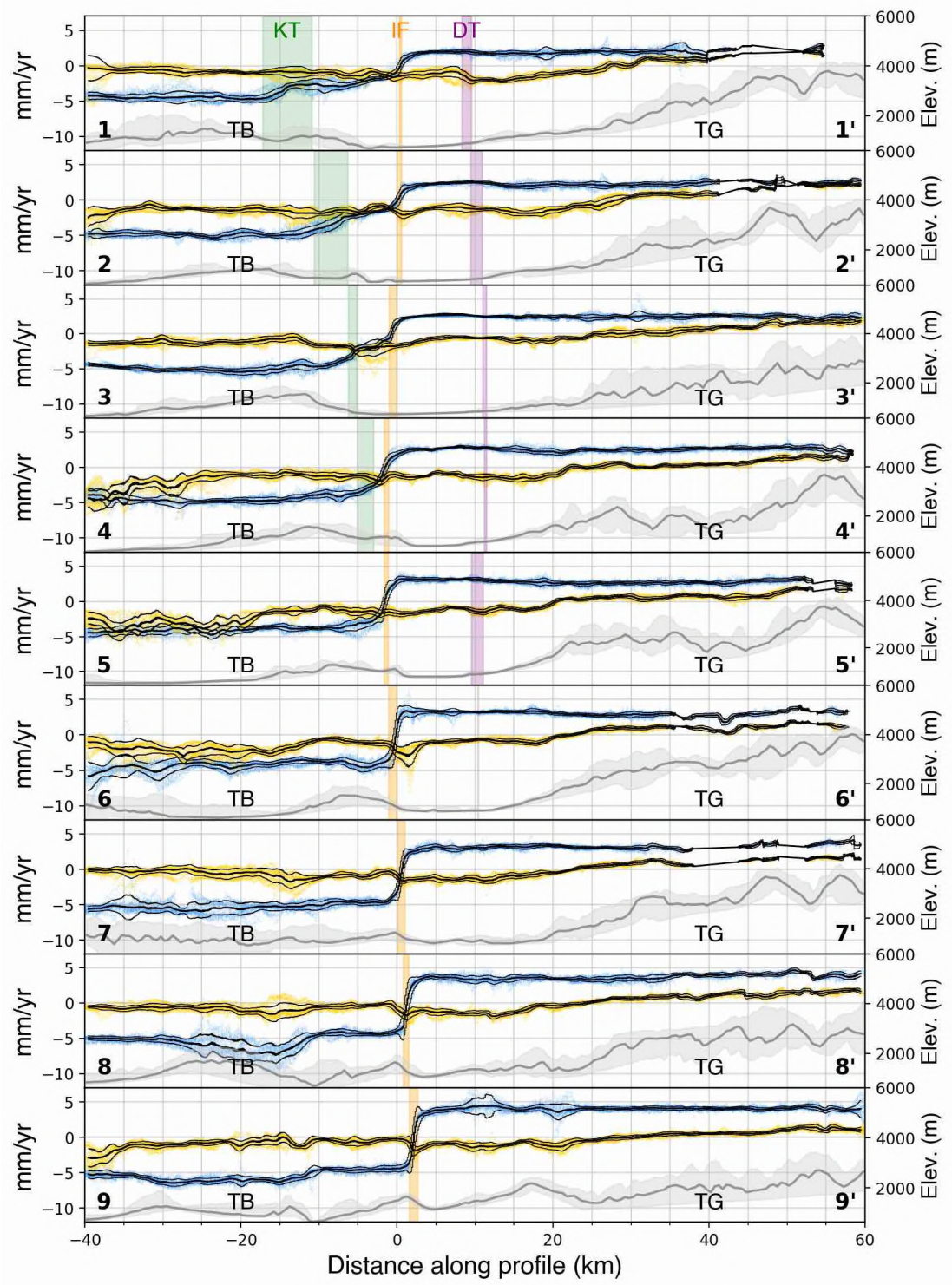

Figure 4.6-16. East (blue) and vertical (yellow) velocities across the Ilyak fault corresponding to profiles in Figure 4.3-3 and Figure 4.3-7. Plotted data fall between the 2nd and 98th percentiles for 250 m wide bins. The thick black line is the median and thin black lines show ±1σ for 250 m wide bins.

Fault extents of the Karchitau thrust (KT), Ilyak fault (IF), and Dushanbe Trough thrust (DT) are shown in green, orange and purple respectively. SRTM 30 m elevation data is plotted in grey (dark line = median elevation).

4.7. Authorship Statement for Chapter 4

Contributions: I, Roberta Wilkinson, wrote the manuscript and conducted the InSAR processing with support and direction from Simon Daout. Simon Daout also contributed comments and suggestions for the structure and wording of the manuscript. I used codes written by Simon Daout and Nick Dodds to process and present the data, as well as my own codes. Nick Dodds also provided advice and technical support with InSAR processing. I processed and analysed the elevation data and discussions with Richard Walker informed interpretations of this data. Richard Walker and Barry Parsons also provided advice on the direction of the research.

Acknowledgements: I would like to thank Sanaa Reuter (né Abdulhameed) for kindly sharing the shapefiles of the geological mapping from Abdulhameed et al. (2020) and Gągała et al. (2020) which I used to make some of the figures of this manuscript. Thank you to Anatoly Ischuk for providing information on local earthquakes and surface processes and to Paul Wordsworth for sharing information on archaeological sites. Thank you also to Aidyn Mukambayev for sending me local earthquake catalogues and to Maria Petrunova for translating them into English. Finally, thank you also to Tom Garth for his advice on interpreting earthquake catalogues and Alex Lipp for discussions about best approaches to statistics.

Chapter 5

Concluding Remarks

In this thesis, I aim to contribute to a better understanding of the typical behaviour of active faults on the continents by mapping, measuring and characterising the deformation in two study regions in Central Asia: the Zailisky Range Front near Almaty in Kazakhstan, and the northern part of the Tajik fold and thrust belt near Dushanbe in Tajikistan. I focus on faults around big cities, in order to improve the available data on seismic sources which informs quantitative seismic hazard assessment, and to obtain qualitative insights into the hazard posed. Despite both study areas being driven by the India-Asia collision, they have strikingly different tectonic regimes: the Zailisky Range Front deforms by slow, N-S thick-skinned shortening by infrequent earthquakes, whilst fast, thin-skinned E-W deformation by aseismic slip dominates in the Tajik basin. As such, these studies provide insights into the range of possible fault behaviour in the region.

5.1. Conclusions from this Thesis

The first part of this thesis pertains to the Zailisky Range Front. In Chapter 2, I present the first paleoseismic trench on the range front, revealing evidence of two earthquakes – the penultimate event at 9.5 ± 0.8 ka (2σ) and the most recent event at some point between 8.4 – 2.6 ka (95.4% probability range). These results add to a growing body of evidence that consecutive earthquakes on large faults in this region are separated by thousands of years (e.g. Landgraf et al., 2016; Ainscoe et al., 2017; Grützner et al., 2017a). Combining results from the trench with scarp mapping at ~30 sites along the Zailisky Range Front indicates slip in the most recent event or events was at least ~0.2 – 2.0 m, corresponding to earthquakes of at least M_W ~6.5 – 6.7 (Wells and Coppersmith, 1994). In my detailed mapping, I find small scarps which have been partially eroded lie very close to infrastructure, or are

actively being built upon, and which I could only identify with the highest resolution datasets. I infer that there are very likely to be more scarps beneath the towns along the range front which have been completely obscured, and consequently an absence of mapped scarps does not indicate an absence of active faulting. This is a significant challenge for characterising hazard along the range front, which will only grow as towns and villages expand. Although the continuity of the fault is difficult to assess due to this urbanisation, erosion and loess deposition, I find minimal evidence for fault gaps or segmentation which would prevent a larger rupture along tens to hundreds of kilometres of the range front, and the 1887 M_W ~7.2 – 7.7 Verny earthquake (Kondorskaya et al., 1982; Tatevossian, 2007; Bindi et al., 2014; Krüger, Kulikova and Landgraf, 2018) indicates that such events are possible. However, even moderate sized events could be destructive to local populations due to their proximity to the fault (Amey et al., 2021).

In Chapter 3, I estimate slip rates on the Zailisky Range Front, from a combination of new data and reassessment of previously published estimates. Offset measurements of deposits from ~10 – 60 ka yield slip rates of ~0.1 – 0.4 mm/yr on fault strands in the west, centre and east of the range front. I derive a shortening rate of 1.3 ± 0.4 mm/yr between the Zailisky Alatau and the Kazakh Platform from GNSS velocities, corresponding to a slip rate of 1.9 ± 0.7 mm/yr. The higher geodetic rate indicates that the individual fault strands, from which I obtain the Quaternary slip rates, only accommodate a small proportion of the shortening. Deformation must therefore occur across multiple parallel fault strands and potentially also within the first ~50 km of the Kazakh Platform, where I also map evidence of uplift in the geomorphology.

The second part of this thesis is concerned with the faulting around Dushanbe, Tajikistan. In Chapter 4, I present InSAR rate maps across the Tajik basin and the Dushanbe Trough with ~130 m resolution and < 1 mm/yr uncertainty. This high-resolution dataset with excellent spatial coverage in the study

region reveals aseismic slip along an evaporite horizon, and slip partitioning, which were not apparent in previously published maps. The data indicate that the Ilyak fault is slipping aseismically to shallow depths at a rate of ~ 6.7 – 8.7 mm/yr in the east and 4.2 – 4.5 mm/yr in the west, with the decrease in rate due to a transfer of slip onto the Karchitau thrust as well as other structures within the basin. The maps also show evidence of aseismic deformation on the Babatag, Surkhu and Vakhsh thrust sheets. Despite moderate magnitude earthquakes in the basement (Kufner et al., 2018; Gągała et al., 2020), no longer wavelength signals indicative of deformation at depth are visible across the Ilyak fault, suggesting that strain accumulation at depth may be obscured by fast surficial velocities and/or decoupling along a detachment horizon. This study highlights the limitations of using geodetic measurements to map and characterise hazardous structures in thin-skinned fold and thrust belts, where deformation at depth may not be expressed in surface measurements. Geomorphic mapping from high-resolution DEMs of the Dushanbe trough also reveals fault scarps in recent alluvial fan deposits, consistent with an active south-dipping thrust running beneath Dushanbe city, which may be capable of producing earthquakes of M_W 7.0 – 7.2 based on its mapped length of ~45 km (Wells and Coppersmith, 1994; Wesnousky, 2008) – field studies will be required to determine its seismogenic potential.

Each of these studies highlights the necessity of combining geological (paleoseismic trenching, geomorphic mapping) and geodetic (GNSS, InSAR) methods, contextualised with seismological data, to comprehensively characterise deformation and identify hazardous faults. In both study regions key findings would have been missed without combining these approaches. Nevertheless, the analyses suggest there are still further unmapped or poorly characterised seismic sources in both regions, and further research is required to build a complete picture of the hazard, suggestions for which I outline below.

5.2. Suggestions for Future Research

5.2.1. Almaty and The Zailisky Range Front

In this thesis I present the only paleoseismic trench to date on the Zailisky Range Front. Whilst this is a useful start to understanding the paleoseismic history, further trenching studies are needed to produce robust earthquake timings and magnitudes. Ideally, future trenching campaigns should be distributed along the length of the fault and across its parallel strands in order to explore the relative importance of the different structures. With limited resources, trenching closer to Almaty should be a priority for informing seismic hazard analyses because of the high potential for loss of life in earthquakes close to the city. Further trenching could better constrain the timing of the most recent event at the eastern end of the fault. Longer paleoseismic records spanning multiple earthquake cycles would extend our earthquake chronology and could be used to determine whether recurrence intervals are regular or whether earthquakes are clustered in time, which has implications for estimating the likely recurrence of large events. The need for such research is pressing given the proximity of the fault to Almaty and other towns along the range front, and the rapid urbanisation which may reduce the number of accessible trenching sites. Seismic reflection profiling would also help to locate the fault where it is obscured beneath Almaty and other towns.

Based on my comprehensive measurement of scarp heights along the range front, a sampling campaign visiting several of those sites could relatively quickly provide robust slip rate estimates for the various fault strands and may also provide insights into the timing of alluvial fan formation. Field investigations in the Kazakh Platform would help to confirm whether the foreland is accommodating some of the geodetically measured strain on buried thrust faults, as our observations seem to suggest. In particular, faults within the subsurface of the foreland could be investigated using seismic reflection surveys and dense seismic arrays. Furthermore, there are a several other faults in the vicinity of Almaty which have not been studied in detail or at all, which warrant further investigation, including

on the Asy Plateau to the southeast and the Dzhalair-Naiman fault to the northwest. Denser GPS networks would be useful to identify the major active structures along the range front and in the surrounding mountains.

Finally, to make the findings from this thesis as useful as possible, future work could include adapting and re-running the scenario-based hazard models of Amey et al. (2021) to incorporate the new fault mapping, extents and earthquake magnitude estimates.

5.2.2. Dushanbe and the Tajik Basin

Chapter 4 demonstrates that even very high-resolution geodetic data are insufficient to characterise deformation on basement faults near Dushanbe. To better understand fault behaviour at depth, the deployment of local seismometers could provide data on low magnitude seismicity which would help to map out basement faulting. For the Dushanbe Trough thrust, paleoseismic studies and sampling of offset surfaces are required to determine its seismogenic potential, earthquake history and slip rate.

The InSAR velocity datasets contain an abundance of interesting and useful signals which warrant further study, a small selection of which we discuss here: Firstly, the results of the time series analysis could be broken down into smaller time slices to study the time dependence of the deformation, such as whether the Ilyak fault creeps in bursts or at a constant rate (e.g. Rousset et al., 2019). Additionally, detailed studies of the deformation on the individual faults and folds within the basin interior could yield interesting insights into how folds grow (e.g. Daout, Parsons and Walker, 2021). The dynamics of mountain building and collapse could also be explored by further analyses of the uplift signal in the Tajik Gissar and the possible uplift and/or westward extrusion of the Pamir imaged in the ascending data. Finally, the rate maps contain several non-tectonic signals, such as hydrologically induced

deformation, soil creep, landsliding and diapirism, all of which could be analysed in detail to better understand the underlying processes (e.g. Metzger et al., 2021).

References

Abdrakhmatov, K.E., Walker, R.T., Campbell, G.E., Carr, A.S., Elliott, A., Hillemann, C., Hollingsworth, J., Landgraf, A., Mackenzie, D., Mukambayev, A., Rizza, M. and Sloan, R.A., 2016. Multisegment rupture in the 11 July 1889 Chilik earthquake (M w 8.0-8.3), Kazakh Tien Shan, interpreted from remote sensing, field survey, and paleoseismic trenching. *Journal of Geophysical Research: Solid Earth*, 121(6), pp.4615–4640. https://doi.org/10.1002/2015JB012763.

Abdulhameed, S., Ratschbacher, L., Jonckheere, R., Gągała, Ł., Enkelmann, E., Käßner, A., Kars, M.A.C., Szulc, A., Kufner, S.K., Schurr, B., Ringenbach, J.C., Nakapelyukh, M., Khan, J., Gadoev, M. and Oimahmadov, I., 2020. Tajik Basin and Southwestern Tian Shan, Northwestern India-Asia Collision Zone: 2. Timing of Basin Inversion, Tian Shan Mountain Building, and Relation to Pamir-Plateau Advance and Deep India-Asia Indentation. *Tectonics*, 39(5), pp.1–26. https://doi.org/10.1029/2019TC005873.

Adamiec, G. and Aitken, M.J., 1998. Dose-rate conversion factors: update. *Ancient TL*, 16(2).

Agisoft LLC, 2023. *Agisoft Metashape User Manual - Professional Edition, Version 2.0*. [online] Available at: <https://www.agisoft.com/downloads/user-manuals/>.

Ainscoe, E.A., Abdrakhmatov, K.E., Baikulov, S., Carr, A.S., Elliott, A.J., Grützner, C. and Walker, R.T., 2019. Variability in surface rupture between successive earthquakes on the Suusamyr Fault, Kyrgyz Tien Shan: Implications for palaeoseismology. *Geophysical Journal International*, 216(1), pp.703–725. https://doi.org/10.1093/gji/ggy457.

Ainscoe, E.A., Elliott, J.R., Copley, A., Craig, T.J., Li, T., Parsons, B.E. and Walker, R.T., 2017. Blind Thrusting, Surface Folding, and the Development of Geological Structure in the M w 6.3 2015 Pishan (China) Earthquake. *Journal of Geophysical Research: Solid Earth*, 122(11), pp.9359–9382. https://doi.org/10.1002/2017JB014268.

Aitken, M.J., 1998. *An introduction to optical dating: the dating of Quaternary sediments by the use of photon-stimulated luminescence*. Oxford: Oxford University Press.

Alinaghi, A. and Krüger, F., 2014. Seismic array analysis and redetermination of depths of earthquakes in Tien-Shan: implications for strength of the crust and lithosphere. *Geophysical Journal International*, 198(2), pp.1111–1129. https://doi.org/10.1093/gji/ggu141.

Amey, R.M.J., Elliott, J.R., Hussain, E., Walker, R., Pagani, M., Silva, V., Abdrakhmatov, K.E. and Watson, C.S., 2021. Significant Seismic Risk Potential From Buried Faults Beneath Almaty City, Kazakhstan, Revealed From High-Resolution Satellite DEMs. *Earth and Space Science*, 8(9), p.e2021EA001664. https://doi.org/10.1029/2021EA001664.

Ansari, H., De Zan, F. and Parizzi, A., 2021. Study of Systematic Bias in Measuring Surface Deformation With SAR Interferometry. *IEEE Transactions on Geoscience and Remote Sensing*, 59(2), pp.1285–1301. https://doi.org/10.1109/TGRS.2020.3003421.

Arrowsmith, J.R., Crosby, C.J., Korzhenkov, A.M., Mamyrov, E., Povolotskaya, I., Guralnik, B. and Landgraf, A., 2017. Surface rupture of the 1911 Kebin (Chon–Kemin) earthquake, Northern Tien

Shan, Kyrgyzstan. *Geological Society, London, Special Publications*, 432(1), pp.233–253. https://doi.org/10.1144/SP432.10.

Avouac, J.P. and Burov, E.B., 1996. Erosion as a driving mechanism of intracontinental mountain growth. *Journal of Geophysical Research: Solid Earth*, 101(B8), pp.17747–17769. https://doi.org/10.1029/96JB01344.

Avouac, J.-P. and Tapponnier, P., 1993. Kinematic model of active deformation in central Asia. *Geophysical Research Letters*, 20(10), pp.895–898. https://doi.org/10.1029/93GL00128.

Avouac, J.P., Tapponnier, P., Bai, M., You, H. and Wang, G., 1993. Active thrusting and folding along the northern Tien Shan and Late Cenozoic rotation of the Tarim relative to Dzungaria and Kazakhstan. *Journal of Geophysical Research: Solid Earth*, 98(B4), pp.6755–6804. https://doi.org/10.1029/92JB01963.

Bamler, R. and Hartl, P., 1998. Synthetic aperture radar interferometry. *Inverse Problems*, 14(4), pp.R1–R54. https://doi.org/10.1088/0266-5611/14/4/001.

Bekseitov, G.T., Tulegenov, T.Z., Ivanov, S.S., Kitov, E.P. and Kitova, A.O., 2019. The investigation of burial site Sunkar in Semirechye. *Bulletin of the South Ural State University*, 19(4), pp.29–39. https://doi.org/10.14529/ssh190404.

Benedetti, L., Tapponnier, P., King, G.C.P., Meyer, B. and Manighetti, I., 2000. Growth folding and active thrusting in the Montello region, Veneto, northern Italy. *Journal of Geophysical Research: Solid Earth*, 105(B1), pp.739–766. https://doi.org/10.1029/1999JB900222.

Biasi, G.P. and Weldon, R.J., II, 2006. Estimating Surface Rupture Length and Magnitude of Paleoearthquakes from Point Measurements of Rupture Displacement. *Bulletin of the Seismological Society of America*, 96(5), pp.1612–1623. https://doi.org/10.1785/0120040172.

Biasi, G.P. and Wesnousky, S.G., 2016. Steps and gaps in ground ruptures: Empirical bounds on rupture propagation. *Bulletin of the Seismological Society of America*, 106(3), pp.1110–1124. https://doi.org/10.1785/0120150175.

Bilham, R., 2014. Chapter 5 - Aggravated Earthquake Risk in South Asia: Engineering versus Human Nature. In: J.F. Shroder and M. Wyss, eds. *Earthquake Hazard, Risk and Disasters*, Hazards and Disasters Series. [online] Boston: Academic Press. pp.103–141. https://doi.org/10.1016/B978-0-12-394848-9.00005-5.

Bindi, D., Parolai, S., Gómez-Capera, A., Locati, M., Kalmetyeva, Z. and Mikhailova, N., 2014. Locations and magnitudes of earthquakes in Central Asia from seismic intensity data. *Journal of Seismology*, 18(1), pp.1–21. https://doi.org/10.1007/s10950-013-9392-1.

Bogdanovich, K.I., Kark, I.M., Korol'kov, B.Y. and Mushketov, D.I., 1914. *Earthquake in Northern district of Tien-Shan, 22 December 1910 (4 January 1911)*. St. Petersburg, Russia: Commision of the Geology Committee.

Bondár, I., Engdahl, E.R., Villaseñor, A., Harris, J. and Storchak, D., 2015. ISC-GEM: Global Instrumental Earthquake Catalogue (1900–2009), II. Location and seismicity patterns. *Physics of the Earth and Planetary Interiors*, 239, pp.2–13. https://doi.org/10.1016/j.pepi.2014.06.002.

Bøtter-Jensen, L., 1997. Luminescence techniques: instrumentation and methods. *Radiation Measurements*, 27(5), pp.749–768. https://doi.org/10.1016/S1350-4487(97)00206-0.

Bøtter-Jensen, L., Mejdahl, V. and Murray, A.S., 1999. New light on OSL. *Quaternary Science Reviews*, 18(2), pp.303–309. https://doi.org/10.1016/S0277-3791(98)00063-8.

Bouilhol, P., Jagoutz, O., Hanchar, J.M. and Dudas, F.O., 2013. Dating the India–Eurasia collision through arc magmatic records. *Earth and Planetary Science Letters*, 366, pp.163–175. https://doi.org/10.1016/j.epsl.2013.01.023.

Bourgeois, O., Cobbold, P.R., Rouby, D., Thomas, J.-C. and Shein, V., 1997. Least squares restoration of Tertiary thrust sheets in map view, Tajik depression, central Asia. *Journal of Geophysical Research: Solid Earth*, 102(B12), pp.27553–27573. https://doi.org/10.1029/97JB02477.

Bowman, D., 2019. *Principles of Alluvial Fan Morphology*. [online] Dordrecht: Springer Netherlands. https://doi.org/10.1007/978-94-024-1558-2.

Bowman, D., Korjenkov, A., Porat, N. and Czassny, B., 2004. Morphological response to Quaternary deformation at an intermontane basin piedmont, the northern Tien Shan, Kyrghyzstan. *Geomorphology*, 63(1–2), pp.1–24. https://doi.org/10.1016/j.geomorph.2004.03.007.

Bronk Ramsey, C., 1995. Radiocarbon Calibration and Analysis of Stratigraphy: The OxCal Program. *Radiocarbon*, 37(2), pp.425–430. https://doi.org/10.1017/S0033822200030903.

Bronk Ramsey, C., 2000. Comment on 'The Use of Bayesian Statistics for ^{14}C Dates of Chronologically Ordered Samples: A Critical Analysis'. *Radiocarbon*, 42(2), pp.199–202. https://doi.org/10.1017/S0033822200059002.

Bronk Ramsey, C., 2009. Bayesian Analysis of Radiocarbon Dates. *Radiocarbon*, 51(1), pp.337–360. https://doi.org/10.1017/S0033822200033865.

Bronk Ramsey, C., 2023. *OxCal Analysis Operations and Models*. [online] OxCal 4.4 Manual. Available at: <https://c14.arch.ox.ac.uk/oxcalhelp/hlp_analysis_oper.html> [Accessed 16 September 2023].

Bullen, M.E., Burbank, D.W. and Garver, J.I., 2003. Building the Northern Tien Shan: Integrated Thermal, Structural, and Topographic Constraints. *The Journal of Geology*, 111(2), pp.149–165. https://doi.org/10.1086/345840.

Bullen, M.E., Burbank, D.W., Garver, J.I. and Abdrakhmatov, K.Ye., 2001. Late Cenozoic tectonic evolution of the northwestern Tien Shan: New age estimates for the initiation of mountain building. *GSA Bulletin*, 113(12), pp.1544–1559. https://doi.org/10.1130/0016-7606(2001)113<1544:LCTEOT>2.0.CO;2.

Burtman, V., 1975. Structural geology of Variscan Tien Shan, USSR. *American Journal of Science*, 275-A, pp.157–186.

Burtman, V.S. and Molnar, P., 1993. Geological and Geophysical Evidence for Deep Subduction of Continental Crust Beneath the Pamir. In: *Geological Society of America Special Papers*. [online] Geological Society of America. pp.1–76. https://doi.org/10.1130/SPE281-p1.

Buylaert, J.-P., Jain, M., Murray, A.S., Thomsen, K.J., Thiel, C. and Sohbati, R., 2012. A robust feldspar luminescence dating method for Middle and Late Pleistocene sediments: Feldspar luminescence dating of Middle and Late Pleistocene sediments. *Boreas*, 41(3), pp.435–451. https://doi.org/10.1111/j.1502-3885.2012.00248.x.

Buylaert, J.P., Murray, A.S., Thomsen, K.J. and Jain, M., 2009. Testing the potential of an elevated temperature IRSL signal from K-feldspar. *Radiation Measurements*, 44(5–6), pp.560–565. https://doi.org/10.1016/j.radmeas.2009.02.007.

Buylaert, J.-P., Thiel, C., Murray, A., Vandenberghe, D., Yi, S. and Lu, H., 2011. IRSL and post-IR IRSL residual doses recorded in modern dust samples from the Chinese Loess Plateau. *Geochronometria*, 38(4), pp.432–440. https://doi.org/10.2478/s13386-011-0047-0.

Campbell, G.E., Walker, R.T., Abdrakhmatov, K., Jackson, J., Elliott, J.R., Mackenzie, D., Middleton, T. and Schwenninger, J.-L., 2015. Great earthquakes in low strain rate continental interiors: An example from SE Kazakhstan. *Journal of Geophysical Research: Solid Earth*, 120(8), pp.5507–5534. https://doi.org/10.1002/2015JB011925.

Campbell, G.E., Walker, R.T., Abdrakhmatov, K., Schwenninger, J., Jackson, J., Elliott, J.R. and Copley, A., 2013. The Dzhungarian fault: Late Quaternary tectonics and slip rate of a major right-lateral strike-slip fault in the northern Tien Shan region. *Journal of Geophysical Research: Solid Earth*, 118(10), pp.5681–5698. https://doi.org/10.1002/jgrb.50367.

Charreau, J., Chen, Y., Gilder, S., Barrier, L., Dominguez, S., Augier, R., Sen, S., Avouac, J.-P., Gallaud, A., Graveleau, F. and Wang, Q., 2009. Neogene uplift of the Tian Shan Mountains observed in the magnetic record of the Jingou River section (northwest China). *Tectonics*, [online] 28(2). https://doi.org/10.1029/2007TC002137.

Chen, K.H. and Bürgmann, R., 2017. Creeping faults: Good news, bad news? *Reviews of Geophysics*, 55(2), pp.282–286. https://doi.org/10.1002/2017RG000565.

Chen, W.-P. and Molnar, P., 1977. Seismic moments of major earthquakes and the average rate of slip in central Asia. *Journal of Geophysical Research (1896-1977)*, 82(20), pp.2945–2969. https://doi.org/10.1029/JB082i020p02945.

Chuang, R.Y. and Johnson, K.M., 2011. Reconciling geologic and geodetic model fault slip-rate discrepancies in Southern California: Consideration of nonsteady mantle flow and lower crustal fault creep. *Geology*, 39(7), pp.627–630. https://doi.org/10.1130/G32120.1.

Clark, D. and McCue, K., 2009. Australian paleoseismology: towards a better basis for seismic hazard estimation. *Annals of Geophysics*, [online] 46(5). https://doi.org/10.4401/ag-3447.

Daout, S., D'Agostino, N., Pathier, E., Socquet, A., Lavé, J., Doin, M.-P., Riesner, M. and Benedetti, L., 2023. Along-strike variation of the strain partitioning within the Apenines as seen from large-scale multi-temporal InSAR analysis. https://doi.org/10.1016/j.tecto.2023.230076.

Daout, S., Dini, B., Haeberli, W., Doin, M.P. and Parsons, B., 2020. Ice loss in the Northeastern Tibetan Plateau permafrost as seen by 16 yr of ESA SAR missions. *Earth and Planetary Science Letters*, 545, p.116404. https://doi.org/10.1016/j.epsl.2020.116404.

Daout, S., Doin, M.P., Peltzer, G., Socquet, A. and Lasserre, C., 2017. Large-scale InSAR monitoring of permafrost freeze-thaw cycles on the Tibetan Plateau. *Geophysical Research Letters*, 44(2), pp.901–909. https://doi.org/10.1002/2016GL070781.

Daout, S., Jolivet, R., Lasserre, C., Doin, M.P., Barbot, S., Tapponnier, P., Peltzer, G., Socquet, A. and Sun, J., 2016. Along-strike variations of the partitioning of convergence across the Haiyuan fault system detected by InSAR. *Geophysical Journal International*, 205(1), pp.536–547. https://doi.org/10.1093/GJI/GGW028.

Daout, S., Parsons, B. and Walker, R., 2021. Post-Earthquake Fold Growth Imaged in the Qaidam Basin, China, With Interferometric Synthetic Aperture Radar. *Journal of Geophysical Research: Solid Earth*, 126(3), pp.1–15. https://doi.org/10.1029/2020JB021241.

Daout, S., Sudhaus, H., Kausch, T., Steinberg, A. and Dini, B., 2019. Interseismic and Postseismic Shallow Creep of the North Qaidam Thrust Faults Detected with a Multitemporal InSAR Analysis. *Journal of Geophysical Research: Solid Earth*, 124(7), pp.7259–7279. https://doi.org/10.1029/2019JB017692.

Dave, A.K., 2022. *Understanding Quaternary aeolian landscape-climate interaction in the piedmonts of Central Asia using luminescence and electron spin resonance techniques*. [Ph.D. Thesis] Johannes Gutenberg-University. https://doi.org/10.25358/OPENSCIENCE-6387.

Dave, A.K., Lisá, L., Scardia, G., Nigmatova, S. and Fitzsimmons, K.E., 2023. The patchwork loess of Central Asia: Implications for interpreting aeolian dynamics and past climate circulation in piedmont regions. *Journal of Quaternary Science*, p.jqs.3493. https://doi.org/10.1002/jqs.3493.

De Luca, C., Casu, F., Manunta, M., Onorato, G. and Lanari, R., 2022. Comments on "Study of Systematic Bias in Measuring Surface Deformation With SAR Interferometry". *IEEE Transactions on Geoscience and Remote Sensing*, 60, pp.1–5. https://doi.org/10.1109/TGRS.2021.3103037.

De Zan, F., Parizzi, A., Prats-Iraola, P. and Lopez-Dekker, P., 2014. A SAR Interferometric Model for Soil Moisture. *IEEE Transactions on Geoscience and Remote Sensing*, 52(1), pp.418–425. https://doi.org/10.1109/TGRS.2013.2241069.

Dedow, R., Franz, M., Szulc, A., Schneider, J.W., Brückner, J., Ratschbacher, L., Gągała, Ł., Ringenbach, J.C., Rajabov, N., Gadoev, M. and Oimahmadov, I., 2020. Tajik Basin and Southwestern Tian Shan, Northwestern India-Asia Collision Zone: 3. Preorogenic to Synorogenic Retro-foreland Basin Evolution in the Eastern Tajik Depression and Linkage to the Pamir Hinterland. *Tectonics*, 39(5). https://doi.org/10.1029/2019TC005874.

Delvaux, D., Abdrakhmatov, K. and Lemzin, I., 2001. Landslides and surface breaks of the 1911 M8.2 Kemin earthquake (Kyrgystan). *Russian Geology and Geophysics*, 42(10), pp.1583–1592.

Deng, Q., Zhang, P., Xu, X., Yang, X., Peng, S. and Feng, X., 1996. Paleoseismology of the northern piedmont of Tianshan Mountains, northwestern China. *Journal of Geophysical Research: Solid Earth*, 101(B3), pp.5895–5920. https://doi.org/10.1029/95JB02739.

Di Giacomo, D., Bondár, I., Storchak, D.A., Engdahl, E.R., Bormann, P. and Harris, J., 2015. ISC-GEM: Global Instrumental Earthquake Catalogue (1900–2009), III. Re-computed M and m, proxy M, final magnitude composition and completeness assessment. *Physics of the Earth and Planetary Interiors*, 239, pp.33–47. https://doi.org/10.1016/j.pepi.2014.06.005.

Di Giacomo, D., Engdahl, E.R. and Storchak, D.A., 2018. The ISC-GEM Earthquake Catalogue (1904–2014): status after the Extension Project. *Earth System Science Data*, 10(4), pp.1877–1899. https://doi.org/10.5194/essd-10-1877-2018.

Djuraev, R.U. and Shakirdzanova, G.N., 1993. The Gissar earthquake 22.01.1989. In: *Earthquakes in the USSR in 1989 (in Russian)*. Nauka. pp.76–84.

Dodds, N., Daout, S., Walker, R.T., Begenjev, G., Bezmenov, Y., Mirzin, R. and Parsons, B., 2022. Interseismic deformation and strain-partitioning along the Main Köpetdag Fault, Turkmenistan, with Sentinel-1 InSAR time-series. *Geophysical Journal International*, 230(3), pp.1612–1629. https://doi.org/10.1093/gji/ggac139.

Dodds, N.W., 2021. *The mechanical properties of fault zones and earthquake cycle dynamics along the northern margins of the Iranian Plateau*. Ph.D. Thesis. University of Oxford.

Doin, M.-P., Lasserre, C., Peltzer, G., Cavalié, O. and Doubre, C., 2009. Corrections of stratified tropospheric delays in SAR interferometry: Validation with global atmospheric models. *Journal of Applied Geophysics*, 69(1), pp.35–50. https://doi.org/10.1016/j.jappgeo.2009.03.010.

Doin, M.-P., Lodge, F., Guillaso, S., Jolivet, R., Lasserre, C., Ducret, G., Grandin, R., Pathier, E. and Pinel, V., 2011. Presentation of the small baseline NSBAS processing chain on a case example: the Etna deformation monitoring from 2003 to 2010 using Envisat data. In: *Proceedings of Fringe 2011: Advances in the Science and Applications of SAR Interferometry*. Frascati, Italy: European Space Agency.

Doin, M.-P., Twardzik, C., Ducret, G., Lasserre, C., Guillaso, S. and Jianbao, S., 2015. InSAR measurement of the deformation around Siling Co Lake: Inferences on the lower crust viscosity in central Tibet. *Journal of Geophysical Research: Solid Earth*, 120(7), pp.5290–5310. https://doi.org/10.1002/2014JB011768.

Durcan, J.A., King, G.E. and Duller, G.A.T., 2015. DRAC: Dose Rate and Age Calculator for trapped charge dating. *Quaternary Geochronology*, 28, pp.54–61. https://doi.org/10.1016/j.quageo.2015.03.012.

DuRoss, C.B., Personius, S.F., Crone, A.J., Olig, S.S. and Lund, W.R., 2011. Integration of Paleoseismic Data from Multiple Sites to Develop an Objective Earthquake Chronology: Application to the Weber Segment of the Wasatch Fault Zone, Utah. *Bulletin of the Seismological Society of America*, 101(6), pp.2765–2781. https://doi.org/10.1785/0120110102.

Dziewonski, A.M., Chou, T.-A. and Woodhouse, J.H., 1981. Determination of earthquake source parameters from waveform data for studies of global and regional seismicity. *Journal of Geophysical Research: Solid Earth*, 86(B4), pp.2825–2852. https://doi.org/10.1029/JB086iB04p02825.

Ekström, G., Nettles, M. and Dziewoński, A.M., 2012. The global CMT project 2004-2010: Centroid-moment tensors for 13,017 earthquakes. *Physics of the Earth and Planetary Interiors*, 200–201, pp.1–9. https://doi.org/10.1016/j.pepi.2012.04.002.

Elliott, J.R., Walters, R.J. and Wright, T.J., 2016. The role of space-based observation in understanding and responding to active tectonics and earthquakes. *Nature Communications*, 7, p.13844. https://doi.org/10.1038/ncomms13844.

Emlid Studio, 2023. *Glossary*. [online] Available at: <https://docs.emlid.com/emlid-studio/reference/glossary> [Accessed 10 February 2023].

Engdahl, E.R., Di Giacomo, D., Sakarya, B., Gkarlaouni, C.G., Harris, J. and Storchak, D.A., 2020. ISC-EHB 1964–2016, an Improved Data Set for Studies of Earth Structure and Global Seismicity. *Earth and Space Science*, 7(1). https://doi.org/10.1029/2019EA000897.

Engdahl, R., Van Der Hilst, R. and Buland, R., 1998. Global Teleseismic Earthquake Relocation with Improved Travel Times and Procedures for Depth Determination. *Bulletin of the Seismological Society of America*, 88(3), pp.722–743.

England, P. and Jackson, J., 2011. Uncharted seismic risk. *Nature Geoscience*, 4(6), pp.348–349. https://doi.org/10.1038/ngeo1168.

European Space Agency and Airbus, 2022. *Copernicus DEM*. https://doi.org/10.5270/ESA-c5d3d65.

Evans, S.G., Roberts, N.J., Ischuk, A., Delaney, K.B., Morozova, G.S. and Tutubalina, O., 2009. Landslides triggered by the 1949 Khait earthquake, Tajikistan, and associated loss of life. *Engineering Geology*, 109, pp.195–212. https://doi.org/10.1016/j.enggeo.2009.08.007.

Feng, X.Y., 1990. The Nilka earthquake fault zone in Xinjiang. *Inland earthquake.*, 4(3), pp.273–277.

Ferretti, A., Monti-Guarnieri, A., Prati, C. and Rocca, F., 2007. *InSAR principles: guidelines for SAR interferometry processing and interpretation*. The Netherlands: ESA Publications, ESTEC.

Fitzsimmons, K.E., Iovita, R., Sprafke, T., Glantz, M., Talamo, S., Horton, K., Beeton, T., Alipova, S., Bekseitov, G., Ospanov, Y., Deom, J.-M., Sala, R. and Taimagambetov, Z., 2017. A chronological framework connecting the early Upper Palaeolithic across the Central Asian piedmont. *Journal of Human Evolution*, 113, pp.107–126. https://doi.org/10.1016/j.jhevol.2017.07.006.

Fletcher, J.M., Teran, O.J., Rockwell, T.K., Oskin, M.E., Hudnut, K.W., Mueller, K.J., Spelz, R.M., Akciz, S.O., Masana, E., Faneros, G., Fielding, E.J., Leprince, S., Morelan, A.E., Stock, J., Lynch, D.K., Elliott, A.J., Gold, P., Liu-Zeng, J., González-Ortega, A., Hinojosa-Corona, A. and González-García, J., 2014. Assembly of a large earthquake from a complex fault system: Surface rupture kinematics of the 4 April 2010 El Mayor-Cucapah (Mexico) Mw 7.2 earthquake. *Geosphere*, 10(4), pp.797–827. https://doi.org/10.1130/GES00933.1.

Fraser, J., Vanneste, K. and Hubert-Ferrari, A., 2010. Recent behavior of the North Anatolian Fault: Insights from an integrated paleoseismological data set. *Journal of Geophysical Research: Solid Earth*, [online] 115(B9). https://doi.org/10.1029/2009JB006982.

Frechen, M., Schweitzer, U. and Zander, A., 1996. Improvements in sample preparation for the fine grain technique. *Ancient TL*, 14, pp.15–17.

Funning, G.J., 2005. *Source parameters of large shallow earthquakes in the Alpine-Himalayan belt from InSAR and waveform modelling*. [Ph.D. Thesis] University of Oxford. Available at: <https://solo.bodleian.ox.ac.uk/permalink/f/89vilt/oxfaleph016632892>.

Gągała, Ł., Ratschbacher, L., Ringenbach, J., Kufner, S., Schurr, B., Dedow, R., Abdulhameed, S., Le Garzic, E., Gadoev, M. and Oimahmadov, I., 2020. Tajik Basin and Southwestern Tian Shan, Northwestern India-Asia Collision Zone: 1. Structure, Kinematics, and Salt Tectonics in the Tajik

Fold-and-Thrust Belt of the Western Foreland of the Pamir. *Tectonics*, 39(5), p.e2019TC005871. https://doi.org/10.1029/2019TC005871.

Galbraith, R.F., Roberts, R.G., Laslett, G.M., Yoshida, H. and Olley, J.M., 1999. Optical Dating of Single and Multiple Grains of Quartz from Jinmium Rock Shelter, Northern Australia: Part 1, Experimental Design and Statistical Models. *Archaeometry*, 41(2), pp.339–364. https://doi.org/10.1111/j.1475-4754.1999.tb00987.x.

Gass, A., 2014. Das Land der sieben Flüsse im 2. bis 1. Jahrtausend v.Chr. *eTopoi Journal for Ancient Studies*, 3, pp.87–106.

Gass, A., 2016. *Das Siebenstromland zwischen Bronze- und Früheisenzeit: Eine Regionalstudie*. Topoi - Berlin Studies of the Ancient World. [online] Berlin, Boston: De Gruyter. https://doi.org/10.1515/9783110311198.

Gass, A., 2019. *Pyramids of the Steppe / Kazakhstan, Land of Seven Rivers*. https://doi.org/10.17171/2-13.

Ghose, S., Mellors, R.J., Korjenkov, A.M., Hamburger, M.W., Pavlis, T.L., Pavlis, G.L., Omuraliev, M., Mamyrov, E. and Muraliev, A.R., 1997. The MS = 7.3 1992 Suusamyr, Kyrgyzstan, earthquake in the tien shan: 2. Aftershock focal mechanisms and surface deformation. *Bulletin of the Seismological Society of America*, 87(1), pp.23–38. https://doi.org/10.1785/BSSA0870010023.

Gizzi, F.T., 2015. Worldwide trends in research on the San Andreas Fault System. *Arabian Journal of Geosciences*, 8(12), pp.10893–10909. https://doi.org/10.1007/s12517-015-1878-4.

Gold, R.D., Cowgill, E., Arrowsmith, J.R. and Friedrich, A.M., 2017. Pulsed strain release on the Altyn Tagh fault, northwest China. *Earth and Planetary Science Letters*, 459, pp.291–300. https://doi.org/10.1016/j.epsl.2016.11.024.

Grandin, R., 2015. Interferometric Processing of SLC Sentinel-1 TOPS Data. In: *Proceedings of Fringe 2015: Advances in the Science and Applications of SAR Interferometry and Sentinel-1 InSAR Workshop*. [online] European Space Agency. https://doi.org/10.5270/Fringe2015.pp116.

Grandin, R., Doin, M.-P., Bollinger, L., Pinel-Puysségur, B., Ducret, G., Jolivet, R. and Sapkota, S.N., 2012. Long-term growth of the Himalaya inferred from interseismic InSAR measurement. *Geology*, 40(12), pp.1059–1062. https://doi.org/10.1130/G33154.1.

Green, O.R., Searle, M.P., Corfield, R.I. and Corfield, R.M., 2008. Cretaceous-Tertiary Carbonate Platform Evolution and the Age of the India-Asia Collision along the Ladakh Himalaya (Northwest India). *The Journal of Geology*, 116(4), pp.331–353. https://doi.org/10.1086/588831.

Grützner, C., Carson, E., Walker, R.T., Rhodes, E.J., Mukambayev, A., Mackenzie, D., Elliott, J.R., Campbell, G. and Abdrakhmatov, K., 2017a. Assessing the activity of faults in continental interiors: Palaeoseismic insights from SE Kazakhstan. *Earth and Planetary Science Letters*, 459, pp.93–104. https://doi.org/10.1016/j.epsl.2016.11.025.

Grützner, C., Walker, R.T., Abdrakhmatov, K.E., Mukambaev, A., Elliott, A.J. and Elliott, J.R., 2017b. Active Tectonics Around Almaty and along the Zailisky Alatau Rangefront. *Tectonics*, 36(10), pp.2192–2226. https://doi.org/10.1002/2017TC004657.

Guérin, G., Mercier, N. and Adamiec, G., 2011. Dose-rate conversion factors: update. *Ancient TL*, 29(1), pp.5–8.

Hamburger, M.W., Sarewitz, D.R., Pavlis, T.L. and Popandopulo, G.A., 1992. Structural and seismic evidence for intracontinental subduction in the Peter the First Range, Central Asia. *Geological Society of America Bulletin*, 104(4), pp.397–408. https://doi.org/10.1130/0016-7606(1992)104<0397:SASEFI>2.3.CO;2.

Hamling, I.J., Hreinsdóttir, S., Clark, K., Elliott, J., Liang, C., Fielding, E., Litchfield, N., Villamor, P., Wallace, L., Wright, T.J., D'Anastasio, E., Bannister, S., Burbidge, D., Denys, P., Gentle, P., Howarth, J., Mueller, C., Palmer, N., Pearson, C., Power, W., Barnes, P., Barrell, D.J.A., Van Dissen, R., Langridge, R., Little, T., Nicol, A., Pettinga, J., Rowland, J. and Stirling, M., 2017. Complex multifault rupture during the 2016 M_w 7.8 Kaikōura earthquake, New Zealand. *Science*, 356(6334), p.eaam7194. https://doi.org/10.1126/science.aam7194.

Hanks, T.C. and Kanamori, H., 1979. A moment magnitude scale. *Journal of Geophysical Research: Solid Earth*, 84(B5), pp.2348–2350. https://doi.org/10.1029/JB084iB05p02348.

Harris, R.A., 2017. Large earthquakes and creeping faults. *Reviews of Geophysics*, 55(1), pp.169–198. https://doi.org/10.1002/2016RG000539.

Harvey, A.M., 2002. Effective timescales of coupling within fluvial systems. *Geomorphology*, 44(3–4), pp.175–201. https://doi.org/10.1016/S0169-555X(01)00174-X.

Heermance, R.V., Chen, J., Burbank, D.W. and Miao, J., 2008. Temporal constraints and pulsed Late Cenozoic deformation during the structural disruption of the active Kashi foreland, northwest China. *Tectonics*, [online] 27(6). https://doi.org/10.1029/2007TC002226.

Hendrix, M.S., Dumitru, T.A. and Graham, S.A., 1994. Late Oligocene-early Miocene unroofing in the Chinese Tian Shan: An early effect of the India-Asia collision. *Geology*, 22(6), pp.487–490. https://doi.org/10.1130/0091-7613(1994)022<0487:LOEMUI>2.3.CO;2.

Hollingsworth, J., Walker, R.T., Abdrakhmatov, K., Campbell, G., Mukambayev, A., Rhodes, E. and Rood, D.H., 2016. Active fault slip and potential large magnitude earthquakes within the stable Kazakh Platform (Central Kazakhstan). [online] AGU Fall Meeting 2016 Abstracts. San Francisco: American Geophysical Union. Available at: <https://ui.adsabs.harvard.edu/abs/2016AGUFM.T32B..05H> [Accessed 28 August 2023].

Hu, Z., Yang, X., Yang, H., Huang, W., Wu, G., Miao, S. and Zhang, L., 2021. Slip Rate and Paleoseismology of the Bolokenu-Aqikekuduk (Dzhungarian) Right-Lateral Strike-Slip Fault in the Northern Tian Shan, NW China. *Tectonics*, 40(8), p.e2020TC006604. https://doi.org/10.1029/2020TC006604.

Huntley, D.J. and Baril, M.R., 1997. The K content of the K-feldspars being measured in optical dating or in thermoluminescence dating. *Ancient TL*, 15(1), pp.11–13.

Hussain, E., Hooper, A., Wright, T.J., Walters, R.J. and Bekaert, D.P.S., 2016. Interseismic strain accumulation across the central North Anatolian Fault from iteratively unwrapped InSAR measurements. *Journal of Geophysical Research: Solid Earth*, 121(12), pp.9000–9019. https://doi.org/10.1002/2016JB013108.

Ingleby, T. and Wright, T.J., 2017. Omori-like decay of postseismic velocities following continental earthquakes. *Geophysical Research Letters*, 44(7), pp.3119–3130. https://doi.org/10.1002/2017GL072865.

International Seismological Centre, 2022a. *ISC-EHB dataset*. https://doi.org/10.31905/PY08W6S3.

International Seismological Centre, 2022b. *On-line Bulletin*. https://doi.org/10.31905/D808B830.

International Seismological Centre, 2023. *On-line Bulletin*. https://doi.org/10.31905/D808B830.

Ischuk, A., Bendick, R., Rybin, A., Molnar, P., Khan, S.F., Kuzikov, S., Mohadjer, S., Saydullaev, U., Ilyasova, Z., Schelochkov, G. and Zubovich, A.V., 2013. Kinematics of the Pamir and Hindu Kush regions from GPS geodesy. *Journal of Geophysical Research: Solid Earth*, 118(5), pp.2408–2416. https://doi.org/10.1002/jgrb.50185.

Ishihara, K., Okusa, S., Oyagi, N. and Ischuk, A., 1990. Liquefaction-induced flow slide in the collapsible loess deposit in Soviet Tajik. *International Journal of Rock Mechanics and Mining Sciences & Geomechanics Abstracts*, 28(5), p.282. https://doi.org/10.1016/0148-9062(91)90223-9.

Ivester, A.H., Rhodes, E.J., Dolan, J.F., Van Dissen, R.J., Gauriau, J., Little, T., McGill, S.F. and Tuckett, P.A., 2022. A method to evaluate the degree of bleaching of IRSL signals in feldspar: The 3ET method. *Quaternary Geochronology*, 72, p.101346. https://doi.org/10.1016/j.quageo.2022.101346.

Jackson, D.D. and Kagan, Y.Y., 2006. The 2004 Parkfield Earthquake, the 1985 Prediction, and Characteristic Earthquakes: Lessons for the Future. *Bulletin of the Seismological Society of America*, 96(4B), pp.S397–S409. https://doi.org/10.1785/0120050821.

Jackson, J., 2008. Surviving natural disasters. In: E. Shuckburgh, ed. *Survival*. Cambridge: Cambridge University Press.

Jackson, J. and McKenzie, D., 1988. The relationship between plate motions and seismic moment tensors, and the rates of active deformation in the Mediterranean and Middle East. *Geophysical Journal International*, 93(1), pp.45–73. https://doi.org/10.1111/j.1365-246X.1988.tb01387.x.

Japan Aerospace Exploration Agency, 2021. *ALOS World 3D 30 meter DEM V3.2*. Available at: <https://opentopography.org/meta/OT.112016.4326.2> [Accessed 18 January 2023].

Johnson, K.M., 2018. Growth of Fault-Cored Anticlines by Flexural Slip Folding: Analysis by Boundary Element Modeling. *Journal of Geophysical Research: Solid Earth*, 123(3), pp.2426–2447. https://doi.org/10.1002/2017JB014867.

Jolivet, M., Dominguez, S., Charreau, J., Chen, Y., Li, Y. and Wang, Q., 2010. Mesozoic and Cenozoic tectonic history of the central Chinese Tian Shan: Reactivated tectonic structures and active deformation. *Tectonics*, [online] 29(6). https://doi.org/10.1029/2010TC002712.

Jolivet, R., Grandin, R., Lasserre, C., Doin, M.-P. and Peltzer, G., 2011. Systematic InSAR tropospheric phase delay corrections from global meteorological reanalysis data. *Geophysical Research Letters*, 38(17), pp.1–6. https://doi.org/10.1029/2011GL048757.

Kalmetieva, Z.A., Mikolaichuk, A.V., Moldobekov, B.D., Meleshko, A.V., Jantaev, M.M. and Zubovich, A.V., 2009. *Atlas of Earthquakes in Kyrgyzstan*. [online] Bishkek: The European Commission's Humanitarian Aid Department, The Secretariat of the United Nations International Strategy for Disaster Reduction, The Central Asian Institute for Applied Geosciences. Available at: <https://www.caiag.kg/en/projects/114-atlas-zemletryasenij-kyrgyzstana>.

Kanamori, H., 1977. The energy release in great earthquakes. *Journal of Geophysical Research (1896-1977)*, 82(20), pp.2981–2987. https://doi.org/10.1029/JB082i020p02981.

Kars, R.H., Reimann, T., Ankjaergaard, C. and Wallinga, J., 2014. Bleaching of the post-IR IRSL signal: new insights for feldspar luminescence dating: Feldspar luminescence dating. *Boreas*, 43(4), pp.780–791. https://doi.org/10.1111/bor.12082.

Kitis, G., Polymeris, G.S., Pagonis, V. and Tsirliganis, N.C., 2013. Anomalous fading of OSL signals originating from very deep traps in Durango apatite. *Radiation Measurements*, 49, pp.73–81. https://doi.org/10.1016/j.radmeas.2012.11.011.

Kondorskaya, N.V., Shebalin, N.V., Khrometskaya, Ye.A. and Gvishiani, A.D. eds., 1982. *New Catalog of Strong Earthquakes in the U.S.S.R. from Ancient Times Through 1977*. Boulder: World Data Center A for Solid Earth Geophysics.

Korjenkov, A., Baipakov, K., Chang, C., Peshkov, Y. and Savelieva, T., 2003. Traces of ancient earthquakes in medieval cities along the Silk Road, northern Tien Shan and Dzhungaria. *Turkish Journal of Earth Sciences*, 12(3), pp.241–261.

Krüger, F., Kulikova, G. and Landgraf, A., 2017. Instrumental magnitude constraints for the 11 July 1889, Chilik earthquake. In: A. Landgraf, S. Kübler, E. Hintersberger and S. Stein, eds. *Seismicity, Fault Rupture and Earthquake Hazards in Slowly Deforming Regions*. [online] London: The Geological Society. pp.41–72. https://doi.org/10.1144/SP432.8.

Krüger, F., Kulikova, G. and Landgraf, A., 2018. Magnitudes for the historical 1885 (Belovodskoe), the 1887 (Verny) and the 1889 (Chilik) earthquakes in Central Asia determined from magnetogram recordings. *Geophysical Journal International*, 215(3), pp.1824–1840. https://doi.org/10.1093/gji/ggy377.

Kudriavtseva, A., 2023. *Interactions between tectonics, climate, and surface processes in the Kyrgyz Tian Shan*. [Ph.D. Thesis] University of Potsdam. p.15841 KB, XV, 164 pages. https://doi.org/10.25932/PUBLISHUP-60372.

Kufner, S.-K., Schurr, B., Ratschbacher, L., Murodkulov, S., Abdulhameed, S., Ischuk, A., Metzger, S. and Kakar, N., 2018. Seismotectonics of the Tajik Basin and Surrounding Mountain Ranges. *Tectonics*, 37(8), pp.2404–2424. https://doi.org/10.1029/2017TC004812.

Kulikova, G., 2016. *Source parameters of the major historical earthquakes in the Tien-Shan region from the late 19th to the early 20th century*. [Ph.D. Thesis] University of Potsdam. Available at: <http://nbn-resolving.de/urn:nbn:de:kobv:517-opus4-88370> [Accessed 3 April 2019].

Kulikova, G. and Krüger, F., 2015. Source process of the 1911 M8.0 Chon-Kemin earthquake: investigation results by analogue seismic records. *Geophysical Journal International*, 201(3), pp.1891–1911. https://doi.org/10.1093/gji/ggv091.

Landgraf, A., Dzhumabaeva, A., Abdrakhmatov, K.E., Strecker, M.R., Macaulay, E.A., Arrowsmith, JR., Sudhaus, H., Preusser, F., Rugel, G. and Merchel, S., 2016. Repeated large-magnitude earthquakes in a tectonically active, low-strain continental interior: The northern Tien Shan, Kyrgyzstan. *Journal of Geophysical Research: Solid Earth*, 121(5), pp.3888–3910. https://doi.org/10.1002/2015JB012714.

Lazear, G., Karlstrom, K., Aslan, A. and Kelley, S., 2013. Denudation and flexural isostatic response of the Colorado Plateau and southern Rocky Mountains region since 10 Ma. *Geosphere*, 9(4), pp.792–814. https://doi.org/10.1130/GES00836.1.

Leith, W., 1985. A mid-Mesozoic extension across Central Asia? *Nature*, 313, pp.567–570. https://doi.org/10.1038/313567a0.

Leith, W. and Alvarez, W., 1985. Structure of the Vakhsh fold-and-thrust belt, Tadjik SSR: Geologic mapping on a Landsat image base. *Geological Society of America Bulletin*, 96(7), pp.875–885. https://doi.org/10.1130/0016-7606(1985)96<875:SOTVFB>2.0.CO;2.

Lemrabet, L., Doin, M.-P., Lasserre, C. and Durand, P., 2023. Referencing of Continental-Scale InSAR-Derived Velocity Fields: Case Study of the Eastern Tibetan Plateau. *Journal of Geophysical Research: Solid Earth*, 128(7), p.e2022JB026251. https://doi.org/10.1029/2022JB026251.

Liu, M. and Stein, S., 2016. Mid-continental earthquakes: Spatiotemporal occurrences, causes, and hazards. *Earth-Science Reviews*, 162, pp.364–386. https://doi.org/10.1016/j.earscirev.2016.09.016.

López-Quiroz, P., Doin, M.-P., Tupin, F., Briole, P. and Nicolas, J.-M., 2009. Time series analysis of Mexico City subsidence constrained by radar interferometry. *Journal of Applied Geophysics*, 69(1), pp.1–15. https://doi.org/10.1016/j.jappgeo.2009.02.006.

Macaulay, E.A., Sobel, E.R., Mikolaichuk, A., Kohn, B. and Stuart, F.M., 2014. Cenozoic deformation and exhumation history of the Central Kyrgyz Tien Shan. *Tectonics*, 33(2), pp.135–165. https://doi.org/10.1002/2013TC003376.

Macklin, M.G., Panyushkina, I.P., Toonen, W.H.J., Chang, C., Tourtellotte, P.A., Duller, G.A.T., Wang, H. and Prins, M.A., 2015. The influence of Late Pleistocene geomorphological inheritance and Holocene hydromorphic regimes on floodwater farming in the Talgar catchment, southeast Kazakhstan, Central Asia. *Quaternary Science Reviews*, 129, pp.85–95. https://doi.org/10.1016/j.quascirev.2015.10.020.

Maghsoudi, Y., Hooper, A.J., Wright, T.J., Lazecky, M. and Ansari, H., 2022. Characterizing and correcting phase biases in short-term, multilooked interferograms. *Remote Sensing of Environment*, 275, p.113022. https://doi.org/10.1016/j.rse.2022.113022.

Mahan, S.A., Rittenour, T.M., Nelson, M.S., Ataee, N., Brown, N., DeWitt, R., Durcan, J., Evans, M., Feathers, J., Frouin, M., Guérin, G., Heydari, M., Huot, S., Jain, M., Keen-Zebert, A., Li, B., López, G.I., Neudorf, C., Porat, N., Rodrigues, K., Sawakuchi, A.O., Spencer, J.Q.G. and Thomsen, K., 2022. Guide for interpreting and reporting luminescence dating results. *GSA Bulletin*, 135(5–6), pp.1480–1502. https://doi.org/10.1130/B36404.1.

Maisuradze, V.V., Kulakova, E.N., Moroz, E.D., Ulzhaeva, L.T., Kuzmina, E.G., Bokina, T.Yu., Zubkova, N.V., Gordeeva, N.I., Sergeeva, N.I., Poroshenko, L.A., Maklakova, N.I., Lukk, A.A., Leonova, V.G., Yunga, S.L., Matasova, L.M., Karimova, M., Abdukadyrov, A.A., Vlasova, A.A.,

Koichmanova, N.I., Akmatalieva, U. and Gaipov, B.N., 1993. Mechanisms of earthquake focus by region: Central Asia and Kazakhstan. In: *Earthquakes in the USSR in 1989 (in Russian)*. Nauka. p.371.

Manighetti, I., Campillo, M., Sammis, C., Mai, P.M. and King, G., 2005. Evidence for self-similar, triangular slip distributions on earthquakes: Implications for earthquake and fault mechanics. *Journal of Geophysical Research*, 110, pp.1–25. https://doi.org/10.1029/2004JB003174.

Massonnet, D., Rossi, M., Carmona, C., Adragna, F., Peltzer, G., Feigl, K. and Rabaute, T., 1993. The displacement field of the Landers earthquake mapped by radar interferometry. *Nature*, 364(6433), pp.138–142. https://doi.org/10.1038/364138a0.

Mather, A.E., Stokes, M. and Whitfield, E., 2017. River terraces and alluvial fans: The case for an integrated Quaternary fluvial archive. *Quaternary Science Reviews*, 166, pp.74–90. https://doi.org/10.1016/j.quascirev.2016.09.022.

Mathey, M., Doin, M. -P., André, P., Walpersdorf, A., Baize, S. and Sue, C., 2022. Spatial Heterogeneity of Uplift Pattern in the Western European Alps Revealed by InSAR Time-Series Analysis. *Geophysical Research Letters*, 49(1), p.e2021GL095744. https://doi.org/10.1029/2021GL095744.

Maubant, L., Pathier, E., Daout, S., Radiguet, M., Doin, M.-P., Kazachkina, E., Kostoglodov, V., Cotte, N. and Walpersdorf, A., 2020. Independent Component Analysis and Parametric Approach for Source Separation in InSAR Time Series at Regional Scale: Application to the 2017–2018 Slow Slip Event in Guerrero (Mexico). *Journal of Geophysical Research: Solid Earth*, 125(3), pp.1–24. https://doi.org/10.1029/2019JB018187.

McKenzie, D. and Jackson, J., 1983. The relationship between strain rates, crustal thickening, palaeomagnetism, finite strain and fault movements within a deforming zone. *Earth and Planetary Science Letters*, 65(1), pp.182–202. https://doi.org/10.1016/0012-821X(83)90198-X.

McNab, F., Sloan, R.A. and Walker, R.T., 2019. Simultaneous orthogonal shortening in the Afghan-Tajik Depression. *Geology*, 47(9), pp.862–866. https://doi.org/10.1130/G46090.1.

Meade, B.J., Klinger, Y. and Hetland, E.A., 2013. Inference of Multiple Earthquake-Cycle Relaxation Timescales from Irregular Geodetic Sampling of Interseismic Deformation. *Bulletin of the Seismological Society of America*, 103(5), pp.2824–2835. https://doi.org/10.1785/0120130006.

Mejdahl, V., 1979. Thermoluminescence dating: beta-dose attenuation in quartz grains. *Archaeometry*, 21(pt1), pp.61–72.

Metzger, S., Gągała, Ł., Ratschbacher, L., Lazecký, M., Maghsoudi, Y. and Schurr, B., 2021. Tajik Depression and Greater Pamir Neotectonics From InSAR Rate Maps. *Journal of Geophysical Research: Solid Earth*, 126(12), p.e2021JB022775. https://doi.org/10.1029/2021JB022775.

Metzger, S., Ischuk, A., Deng, Z., Ratschbacher, L., Perry, M., Kufner, S., Bendick, R. and Moreno, M., 2020. Dense GNSS Profiles Across the Northwestern Tip of the India-Asia Collision Zone: Triggered Slip and Westward Flow of the Peter the First Range, Pamir, Into the Tajik Depression. *Tectonics*, 39(2), p.e2019TC005797. https://doi.org/10.1029/2019TC005797.

Mikhailova, N., Poleshko, N.N., Aristova, I.L., Mukambayev, A.S. and Kulikova, G.O., 2015. *EMCA Central Asia Earthquake catalogue v1.1*. https://doi.org/10.5880/GFZ.EWS.2015.001.

Mohadjer, S., Bendick, R., Ischuk, A., Kuzikov, S., Kostuk, A., Saydullaev, U., Lodi, S., Kakar, D.M., Wasy, A., Khan, M.A., Molnar, P., Bilham, R. and Zubovich, A.V., 2010. Partitioning of India-Eurasia convergence in the Pamir-Hindu Kush from GPS measurements. *Geophysical Research Letters*, [online] 37(4). https://doi.org/10.1029/2009GL041737.

Molnar, P. and Tapponnier, P., 1975. Cenozoic tectonics of Asia: Effects of a continental collision. *Science*, 189(4201), pp.419–426. https://doi.org/10.1126/science.189.4201.419.

Murray, A.S. and Wintle, A.G., 2000. Luminescence dating of quartz using an improved single-aliquot regenerative-dose protocol. *Radiation Measurements*, 32(1), pp.57–73. https://doi.org/10.1016/S1350-4487(99)00253-X.

Murray, A.S. and Wintle, A.G., 2003. The single aliquot regenerative dose protocol: potential for improvements in reliability. *Radiation Measurements*, 37(4–5), pp.377–381. https://doi.org/10.1016/S1350-4487(03)00053-2.

Mushketov, I.V., 1890. The Verny earthquake of May 28 (June 9), 1887. *Proceedings of the Geological Committee*, X(1).

NASA JPL, 2013. *NASA Shuttle Radar Topography Mission Global 1 arc second*. https://doi.org/10.5067/MEASURES/SRTM/SRTMGL1.003.

Nikonov, A.A. and Shebalina, T.Yu., 1979. Lichenometry and earthquake age determination in central Asia. *Nature*, 280, pp.675–677. https://doi.org/10.1038/280675a0.

Osmanoğlu, B., Sunar, F., Wdowinski, S. and Cabral-Cano, E., 2016. Time series analysis of InSAR data: Methods and trends. *ISPRS Journal of Photogrammetry and Remote Sensing*, 115, pp.90–102. https://doi.org/10.1016/j.isprsjprs.2015.10.003.

Ou, Q., 2020. *Crustal Strain and Seismic Hazard of the NE Tibetan Plateau*. Ph.D. Thesis. University of Oxford.

Ou, Q., Daout, S., Weiss, J.R., Shen, L., Lazecky, M., Wright, T.J. and Parsons, B.E., 2022. Large-Scale Interseismic Strain Mapping of the NE Tibetan Plateau From Sentinel-1 Interferometry. *Journal of Geophysical Research: Solid Earth*, [online] 127(6). https://doi.org/10.1029/2022JB024176.

Pagani, M., Monelli, D., Weatherill, G., Danciu, L., Crowley, H., Silva, V., Henshaw, P., Butler, L., Nastasi, M., Panzeri, L., Simionato, M. and Vigano, D., 2014. OpenQuake Engine: An Open Hazard (and Risk) Software for the Global Earthquake Model. *Seismological Research Letters*, 85(3), pp.692–702. https://doi.org/10.1785/0220130087.

Parshina, G.N., Zolotokrylina, E.E. and Semenova, A.A., 1979. *Geological Map of the Kazakh SSR, K-43-B (Alma-ata)*.

Patyniak, M., Landgraf, A., Dzhumabaeva, A., Abdrakhmatov, K.E., Rosenwinkel, S., Korup, O., Preusser, F., Fohlmeister, J., Arrowsmith, J.R. and Strecker, M.R., 2017. Paleoseismic Record of Three Holocene Earthquakes Rupturing the Issyk-Ata Fault near Bishkek, North Kyrgyzstan. *Bulletin of the Seismological Society of America*, 107(6), pp.2721–2737. https://doi.org/10.1785/0120170083.

Pezzo, G., Merryman Boncori, J.P., Atzori, S., Antonioli, A. and Salvi, S., 2014. Deformation of the western Indian Plate boundary: insights from differential and multi-aperture InSAR data inversion for

the 2008 Baluchistan (Western Pakistan) seismic sequence. *Geophysical Journal International*, 198(1), pp.25–39. https://doi.org/10.1093/gji/ggu106.

Picotti, V., Romano, M.A., Ponza, A., Guido, F.L. and Peruzza, L., 2022. The Montello Thrust and the Active Mountain Front of the Eastern Southern Alps (Northeast Italy). *Tectonics*, 41(12), p.e2022TC007522. https://doi.org/10.1029/2022TC007522.

Pierce, I., Guliyev, I., Yetirmishli, G.J., Muradov, R., Kazimova, S., Javanshir, R., Johnson, B., Marshall, N., Walker, R.T. and Wordsworth, P., 2022. Surface Rupturing Earthquakes of the Greater Caucasus Frontal Thrusts, Azerbaijan. *ESS Open Archive*. [online] https://doi.org/10.22541/essoar.167152213.30022523/v1.

Pilz, M., Bindi, D., Boxberger, T., Hakimov, F., Moldobekov, B., Murodkulov, S., Orunbaev, S., Pittore, M., Stankiewicz, J., Ullah, S., Verjee, F., Wieland, M., Yasunov, P. and Parolai, S., 2013. First Steps toward a Reassessment of the Seismic Risk of the City of Dushanbe (Tajikistan). *Seismological Research Letters*, 84(6), pp.1026–1038. https://doi.org/10.1785/0220130040.

Pinel-Puyssegur, B., Michel, R. and Avouac, J.-P., 2012. Multi-Link InSAR Time Series: Enhancement of a Wrapped Interferometric Database. *IEEE Journal of Selected Topics in Applied Earth Observations and Remote Sensing*, 5(3), pp.784–794. https://doi.org/10.1109/JSTARS.2012.2196758.

Plafker, G., 1976. Tectonic Aspects of the Guatemala Earthquake of 4 February 1976. *Science*, 193(4259), pp.1201–1208. https://doi.org/10.1126/science.193.4259.1201.

Prescott, J.R. and Hutton, J.T., 1994. Cosmic ray contributions to dose rates for luminescence and ESR dating: Large depths and long-term time variations. *Radiation Measurements*, 23(2), pp.497–500. https://doi.org/10.1016/1350-4487(94)90086-8.

Preusser, F., Degering, D., Fuchs, M., Hilgers, A., Kadereit, A., Klasen, N., Krbetschek, M., Richter, D. and Spencer, J.Q.G., 2008. Luminescence dating: basics, methods and applications. *E&G Quaternary Science Journal*, 57(1/2), pp.95–149. https://doi.org/10.3285/eg.57.1-2.5.

Purcell, V., Reddin, E., Ebmeier, S., González, P.J., Watson, A., Morishita, Y. and Elliott, J., 2022. Nearly Three Centuries of Lava Flow Subsidence at Timanfaya, Lanzarote. *Geochemistry, Geophysics, Geosystems*, 23(10), p.e2022GC010576. https://doi.org/10.1029/2022GC010576.

QGIS.org, 2023. *QGIS Geographic Information System*. Available at: <http://qgis.osgeo.org>.

Rees-Jones, J., 1995. Optical Dating of Young Sediments Using Fine-Grain Quartz. *Ancient TL*, 13, pp.9–14.

Rees-Jones, J. and Tite, M.S., 1997. Optical Dating Results for British Archaeological Sediments. *Archaeometry*, 39(1), pp.177–187. https://doi.org/10.1111/j.1475-4754.1997.tb00797.x.

Reid, H.F., 1910. *The California Earthquake of April 18, 1906, Report of the State Earthquake Investigation Commission, in Two Volumes and Atlas: Volume 2 The Mechanics of the Earthquake*. [online] Washington D.C.: The Carnegie Institution of Washington. Available at: <http://archive.org/details/californiaearthq1969cali> [Accessed 18 December 2023].

Reilinger, R., McClusky, S., Vernant, P., Lawrence, S., Ergintav, S., Cakmak, R., Ozener, H., Kadirov, F., Guliev, I., Stepanyan, R., Nadariya, M., Hahubia, G., Mahmoud, S., Sakr, K., ArRajehi, A., Paradissis, D., Al-Aydrus, A., Prilepin, M., Guseva, T., Evren, E., Dmitrotsa, A., Filikov, S.V., Gomez, F., Al-Ghazzi, R. and Karam, G., 2006. GPS constraints on continental deformation in the Africa-Arabia-Eurasia continental collision zone and implications for the dynamics of plate interactions. *Journal of Geophysical Research: Solid Earth*, [online] 111(B5). https://doi.org/10.1029/2005JB004051.

Rhodes, E.J., 2011. Optically Stimulated Luminescence Dating of Sediments over the Past 200,000 Years. *Annual Review of Earth and Planetary Sciences*, 39(1), pp.461–488. https://doi.org/10.1146/annurev-earth-040610-133425.

Rhodes, E.J., 2015. Dating sediments using potassium feldspar single-grain IRSL: Initial methodological considerations. *Quaternary International*, 362, pp.14–22. https://doi.org/10.1016/j.quaint.2014.12.012.

Rhodes, E.J., Bronk Ramsey, C., Outram, Z., Batt, C., Willis, L., Dockrill, S. and Bond, J., 2003. Bayesian methods applied to the interpretation of multiple OSL dates: high precision sediment ages from Old Scatness Broch excavations, Shetland Isles. *Quaternary Science Reviews*, 22(10–13), pp.1231–1244. https://doi.org/10.1016/S0277-3791(03)00046-5.

Rizza, M., Abdrakhmatov, K., Walker, R., Braucher, R., Guillou, V., Carr, A.S., Campbell, G., McKenzie, D., Jackson, J., Aumaître, G., Bourlès, D.L. and Keddadouche, K., 2019. Rate of Slip From Multiple Quaternary Dating Methods and Paleoseismic Investigations Along the Talas-Fergana Fault: Tectonic Implications for the Tien Shan Range. *Tectonics*, 38(7), pp.2477–2505. https://doi.org/10.1029/2018TC005188.

Robinson, A.C., Yin, A., Manning, C.E., Harrison, T.M., Zhang, S.-H. and Wang, X.-F., 2004. Tectonic evolution of the northeastern Pamir: Constraints from the northern portion of the Cenozoic Kongur Shan extensional system, western China. *GSA Bulletin*, 116(7–8), pp.953–973. https://doi.org/10.1130/B25375.1.

Rosen, P.A., Hensley, S., Joughin, I.R., Li, F.K., Madsen, S.N., Rodriguez, E. and Goldstein, R.M., 2000. Synthetic aperture radar interferometry. *Proceedings of the IEEE*, 88(3), pp.333–382. https://doi.org/10.1109/5.838084.

Rosen, P.A., Hensley, S., Peltzer, G. and Simons, M., 2004. Updated repeat orbit interferometry package released. *Eos, Transactions American Geophysical Union*, 85(5), pp.47–47. https://doi.org/10.1029/2004EO050004.

Rousset, B., Fu, Y., Bartlow, N. and Bürgmann, R., 2019. Week-Long and Year-Long Slow Slip and Tectonic Tremor Episodes on the South Central Alaska Megathrust. *Journal of Geophysical Research: Solid Earth*, 124(12), pp.13392–13403. https://doi.org/10.1029/2019JB018724.

Royer, J.-Y., Gordon, R.G. and Horner-Johnson, B.C., 2006. Motion of Nubia relative to Antarctica since 11 Ma: Implications for Nubia-Somalia, Pacific–North America, and India-Eurasia motion. *Geology*, 34(6), p.501. https://doi.org/10.1130/G22463.1.

Rust, D., Korzhenkov, A. and Tibaldi, A., 2018. Geologic Slip-Rate Determinations on the Talas-Fergana Fault: Mismatch With Geodetic Slip Rate. *Geophysical Research Letters*, 45(9), pp.3880–3888. https://doi.org/10.1002/2017GL076990.

Rutte, D., Ratschbacher, L., Schneider, S., Stübner, K., Stearns, M.A., Gulzar, M.A. and Hacker, B.R., 2017. Building the Pamir-Tibetan Plateau—Crustal stacking, extensional collapse, and lateral extrusion in the Central Pamir: 1. Geometry and kinematics. *Tectonics*, 36(3), pp.342–384. https://doi.org/10.1002/2016TC004293.

Sala, R. and Deom, J., 2013. Geografie und Kulturlandschaften in Kasachstan. In: Th. Stöllner and Z. Samašev, eds. *Unbekanntes Kasachstan. Archäologie im herzen Asiens Katalog der Ausstellung des Deutschen Bergbau-Museums vom 26. Januar bis zum 30. Juni 2013*. Bochum: German Mining Museum Bochum. pp.41–54.

Sala, R. and Deom, J.-M., 2005. *Petroglyphs of South Kazakhstan*. Almaty: Laboratory of Geoarchaeology.

Savage, J.C. and Burford, R.O., 1973. Geodetic determination of relative plate motion in central California. *Journal of Geophysical Research*, 78(5), pp.832–845. https://doi.org/10.1029/JB078i005p00832.

Scholz, C.H., 1982. Scaling laws for large earthquakes: Consequences for physical models. *Bulletin of the Seismological Society of America*, 72(1), pp.1–14. https://doi.org/10.1785/BSSA0720010001.

Scholz, C.H., 2010. Large earthquake triggering, clustering, and the synchronization of faults. *Bulletin of the Seismological Society of America*, 100(3), pp.901–909. https://doi.org/10.1785/0120090309.

Scholz, C.H., Aviles, C.A. and Wesnousky, S.G., 1986. Scaling differences between large interplate and intraplate earthquakes. *Bulletin of the Seismological Society of America*, 76(1), pp.65–70. https://doi.org/10.1785/BSSA0760010065.

Schurr, B., Ratschbacher, L., Sippl, C., Gloaguen, R., Yuan, X. and Mechie, J., 2014. Seismotectonics of the Pamir. *Tectonics*, 33(8), pp.1501–1518. https://doi.org/10.1002/2014TC003576.

Segall, P., 2002. Integrating Geologic and Geodetic Estimates of Slip Rate on the San Andreas Fault System. *International Geology Review*, 44(1), pp.62–82. https://doi.org/10.2747/0020-6814.44.1.62.

Selander, J., Oskin, M., Ormukov, C. and Abdrakhmatov, K., 2012. Inherited strike-slip faults as an origin for basement-cored uplifts: Example of the Kungey and Zailiskey ranges, northern Tian Shan. *Tectonics*, 31(4), pp.1–22. https://doi.org/10.1029/2011TC003002.

Şengör, A.M.C., Tüysüz, O., İmren, C., Sakınç, M., Eyidoğan, H., Görür, N., Le Pichon, X. and Rangin, C., 2005. The North Anatolian Fault: A New Look. *Annual Review of Earth and Planetary Sciences*, 33(1), pp.37–112. https://doi.org/10.1146/annurev.earth.32.101802.120415.

Simpson, G., 2015. Accumulation of permanent deformation during earthquake cycles on reverse faults. *Journal of Geophysical Research: Solid Earth*, 120(3), pp.1958–1974. https://doi.org/10.1002/2014JB011442.

Sippl, C., Schurr, B., Yuan, X., Mechie, J., Schneider, F.M., Gadoev, M., Orunbaev, S., Oimahmadov, I., Haberland, C., Abdybachaev, U., Minaev, V., Negmatullaev, S. and Radjabov, N., 2013. Geometry of the Pamir-Hindu Kush intermediate-depth earthquake zone from local seismic data. *Journal of Geophysical Research: Solid Earth*, 118(4), pp.1438–1457. https://doi.org/10.1002/jgrb.50128.

Sloan, R.A., Jackson, J.A., McKenzie, D. and Priestley, K., 2011. Earthquake depth distributions in central Asia, and their relations with lithosphere thickness, shortening and extension: Earthquake depth distributions in central Asia. *Geophysical Journal International*, 185(1), pp.1–29. https://doi.org/10.1111/j.1365-246X.2010.04882.x.

Smedley, R.K. and Skirrow, G.K.A., 2020. Luminescence Dating in Fluvial Settings: Overcoming the Challenge of Partial Bleaching. In: J. Herget and A. Fontana, eds. *Palaeohydrology: Traces, Tracks and Trails of Extreme Events*, Geography of the Physical Environment. [online] Cham: Springer International Publishing. pp.155–168. https://doi.org/10.1007/978-3-030-23315-0_8.

Sobel, E.R., Chen, J. and Heermance, R.V., 2006. Late Oligocene–Early Miocene initiation of shortening in the Southwestern Chinese Tian Shan: Implications for Neogene shortening rate variations. *Earth and Planetary Science Letters*, 247(1), pp.70–81. https://doi.org/10.1016/j.epsl.2006.03.048.

Sobel, E.R. and Dumitru, T.A., 1997. Thrusting and exhumation around the margins of the western Tarim basin during the India-Asia collision. *Journal of Geophysical Research: Solid Earth*, 102(B3), pp.5043–5063. https://doi.org/10.1029/96JB03267.

Spengler, R.N., Chang, C. and Tourtellotte, P.A., 2013. Agricultural production in the Central Asian mountains: Tuzusai, Kazakhstan (410–150 B.C.). *Journal of Field Archaeology*, 38(1), pp.68–85. https://doi.org/10.1179/0093469012Z.00000000037.

Steier, P. and Rom, W., 2000. The Use of Bayesian Statistics for ^{14}C Dates of Chronologically Ordered Samples: A Critical Analysis. *Radiocarbon*, 42(2), pp.183–198. https://doi.org/10.1017/S0033822200058999.

Storchak, D.A., Harris, J., Brown, L., Lieser, K., Shumba, B. and Di Giacomo, D., 2020. Rebuild of the Bulletin of the International Seismological Centre (ISC)—part 2: 1980–2010. *Geoscience Letters*, 7(1), pp.1–21. https://doi.org/10.1186/S40562-020-00164-6/FIGURES/16.

Strecker, M.R., Frisch, W., Hamburger, M.W., Ratschbacher, L., Semiletkin, S., Zamoruyev, A. and Sturchio, N., 1995. Quaternary deformation in the Eastern Pamirs, Tadzhikistan and Kyrgyzstan. *Tectonics*, 14(5), pp.1061–1079. https://doi.org/10.1029/95TC00927.

Stübner, K., Ratschbacher, L., Rutte, D., Stanek, K., Minaev, V., Wiesinger, M., Gloaguen, R. and Members, P.T., 2013. The giant Shakhdara migmatitic gneiss dome, Pamir, India-Asia collision zone: 1. Geometry and kinematics. *Tectonics*, 32(4), pp.948–979. https://doi.org/10.1002/tect.20057.

Stull, R.B., 2017. *Practical meteorology: an algebra-based survey of atmospheric science*. Version 1.02b ed. Vancouver, BC, Canada: University of British Columbia.

Tatevossian, R.E., 2007. The Verny, 1887, earthquake in Central Asia: Application of the INQUA scale, based on coseismic environmental effects. *Quaternary International*, 173–174, pp.23–29. https://doi.org/10.1016/j.quaint.2007.02.006.

Thatcher, W., 2009. How the Continents Deform: The Evidence From Tectonic Geodesy. *Annual Review of Earth and Planetary Sciences*, 37(1), pp.237–262. https://doi.org/10.1146/annurev.earth.031208.100035.

Thiel, C., Buylaert, J.-P., Murray, A., Terhorst, B., Hofer, I., Tsukamoto, S. and Frechen, M., 2011. Luminescence dating of the Stratzing loess profile (Austria) – Testing the potential of an elevated temperature post-IR IRSL protocol. *Quaternary International*, 234(1–2), pp.23–31. https://doi.org/10.1016/j.quaint.2010.05.018.

Thompson, S.C., Weldon, R.J., Rubin, C.M., Abdrakhmatov, K., Molnar, P. and Berger, G.W., 2002. Late Quaternary slip rates across the central Tien Shan, Kyrgyzstan, central Asia. *Journal of Geophysical Research: Solid Earth*, 107(B9), p.ETG 7-1-ETG 7-32. https://doi.org/10.1029/2001JB000596.

Tibaldi, A., Graziotto, E., Forcella, F. and Gapich, V.H., 1997. Morphotectonic indicators of Holocene faulting in central Tien Shan, Kazakstan, and geodynamic implications. *Journal of Geodynamics*, 23(1), pp.23–45. https://doi.org/10.1016/S0264-3707(96)00021-X.

Tsai, C.-H., 2023. *Active Tectonics and Palaeoseismicity of the Northern Tien Shan and Dzhungaria*. Ph.D. Thesis. University of Oxford.

Tsai, C.-H., Abdrakhmatov, K., Mukambayev, A., Elliott, A.J., Elliott, J.R., Grützner, C., Rhodes, E.J., Ivester, A.H., Walker, R.T. and Wilkinson, R., 2022. Probing the Upper End of Intracontinental Earthquake Magnitude: A Prehistoric Example From the Dzhungarian and Lepsy Faults of Kazakhstan. *Tectonics*, 41(10), p.e2022TC007300. https://doi.org/10.1029/2022TC007300.

Turcotte, D.L. and Schubert, G., 2014. *Geodynamics*. Third edition ed. Cambridge: Cambridge University Press.

U.S. Geological Survey, 2023. *Tectonic Plate Boundaries*. Available at: <https://www.usgs.gov/programs/earthquake-hazards/google-earthtmkml-files> [Accessed 20 December 2023].

Vernant, P., 2015. What can we learn from 20 years of interseismic GPS measurements across strike-slip faults? *Tectonophysics*, 644–645, pp.22–39. https://doi.org/10.1016/j.tecto.2015.01.013.

Vernant, P., Hivert, F., Chéry, J., Steer, P., Cattin, R. and Rigo, A., 2013. Erosion-induced isostatic rebound triggers extension in low convergent mountain ranges. *Geology*, 41(4), pp.467–470. https://doi.org/10.1130/G33942.1.

Wang, M. and Shen, Z., 2020. Present-Day Crustal Deformation of Continental China Derived From GPS and Its Tectonic Implications. *Journal of Geophysical Research: Solid Earth*, 125(2), p.e2019JB018774. https://doi.org/10.1029/2019JB018774.

Watson, A.R., Elliott, J.R. and Walters, R.J., 2022. Interseismic Strain Accumulation Across the Main Recent Fault, SW Iran, From Sentinel-1 InSAR Observations. *Journal of Geophysical Research: Solid Earth*, 127(2), p.e2021JB022674. https://doi.org/10.1029/2021JB022674.

Wells, D.L. and Coppersmith, K.J., 1994. New Empirical Relationships among Magnitude, Rupture Length, Rupture Width, Rupture Area, and Surface Displacement. *The Journal of Geology*, 84(4), pp.974–1002.

Wesnousky, S.G., 1986. Earthquakes, quaternary faults, and seismic hazard in California. *Journal of Geophysical Research: Solid Earth*, 91(B12), pp.12587–12631. https://doi.org/10.1029/JB091iB12p12587.

Wesnousky, S.G., 2008. Displacement and Geometrical Characteristics of Earthquake Surface Ruptures: Issues and Implications for Seismic-Hazard Analysis and the Process of Earthquake Rupture. *Bulletin of the Seismological Society of America*, 98(4), pp.1609–1632. https://doi.org/10.1785/0120070111.

Wessel, P., Luis, J.F., Uieda, L., Scharroo, R., Wobbe, F., Smith, W.H.F. and Tian, D., 2019. The Generic Mapping Tools Version 6. *Geochemistry, Geophysics, Geosystems*, 20(11), pp.5556–5564. https://doi.org/10.1029/2019GC008515.

Wesson, R.L., 1988. Dynamics of fault creep. *Journal of Geophysical Research: Solid Earth*, 93(B8), pp.8929–8951. https://doi.org/10.1029/JB093iB08p08929.

Westoby, M.J., Brasington, J., Glasser, N.F., Hambrey, M.J. and Reynolds, J.M., 2012. 'Structure-from-Motion' photogrammetry: A low-cost, effective tool for geoscience applications. *Geomorphology*, 179, pp.300–314. https://doi.org/10.1016/j.geomorph.2012.08.021.

Weston, J., Engdahl, E.R., Harris, J., Di Giacomo, D. and Storchak, D.A., 2018. ISC-EHB: reconstruction of a robust earthquake data set. *Geophysical Journal International*, 214(1), pp.474–484. https://doi.org/10.1093/gji/ggy155.

Windley, B.F., Alexeiev, D., Xiao, W., Kröner, A. and Badarch, G., 2007. Tectonic models for accretion of the Central Asian Orogenic Belt. *Journal of the Geological Society*, 164(1), pp.31–47. https://doi.org/10.1144/0016-76492006-022.

Windley, B.F., Allen, M.B., Zhang, C., Zhao, Z.-Y. and Wang, G.-R., 1990. Paleozoic accretion and Cenozoic redeformation of the Chinese Tien Shan Range, central Asia. *Geology*, 18(2), pp.128–131. https://doi.org/10.1130/0091-7613(1990)018<0128:PAACRO>2.3.CO;2.

Wright, T.J., 2002. Remote monitoring of the earthquake cycle using satellite radar interferometry. *Philosophical Transactions of the Royal Society of London. Series A: Mathematical, Physical and Engineering Sciences*, 360(1801), pp.2873–2888. https://doi.org/10.1098/rsta.2002.1094.

Wright, T.J., 2004. Toward mapping surface deformation in three dimensions using InSAR. *Geophysical Research Letters*, 31(1), p.L01607. https://doi.org/10.1029/2003GL018827.

Wu, C., Ren, G., Yu, J., Zheng, W., Li, X., Liu, J., Wang, S., Li, C., Zhang, Z., Yang, H. and Zhang, D., 2020. Oblique Right-Lateral Faulting Along the Northern Margin of the Ili Basin in the Northern Tian Shan, Northwest China. *Tectonics*, 39(10), p.e2020TC006061. https://doi.org/10.1029/2020TC006061.

Wu, C., Zhang, P., Zhang, Z., Zheng, W., Xu, B., Wang, W., Yu, Z., Dai, X., Zhang, B. and Zang, K., 2023. Slip partitioning and crustal deformation patterns in the Tianshan orogenic belt derived from GPS measurements and their tectonic implications. *Earth-Science Reviews*, 238, p.104362. https://doi.org/10.1016/j.earscirev.2023.104362.

Yin, A., Robinson, A. and Manning, C.E., 2001. Oroclinal Bending and Slab-Break-Off Causing Coeval East-West Extension and East-West Contraction in the Pamir-Nanga Parbat Syntaxis in the Past 10 m.y. [online] AGU Fall Meeting. San Francisco: American Geophysical Union. Available at: <https://ui.adsabs.harvard.edu/abs/2001AGUFM.T12F..03Y> [Accessed 21 December 2023].

Youngs, R.R. and Coppersmith, K.J., 1985. Implications of fault slip rates and earthquake recurrence models to probabilistic seismic hazard estimates. *Bulletin of the Seismological Society of America*, 75(4), pp.939–964. https://doi.org/10.1785/BSSA0750040939.

Yu, C., Li, Z. and Penna, N.T., 2018. Interferometric synthetic aperture radar atmospheric correction using a GPS-based iterative tropospheric decomposition model. *Remote Sensing of Environment*, 204(August 2017), pp.109–121. https://doi.org/10.1016/j.rse.2017.10.038.

Yunjun, Z., Fattahi, H. and Amelung, F., 2019. Small baseline InSAR time series analysis: Unwrapping error correction and noise reduction. *Computers & Geosciences*, 133, p.104331. https://doi.org/10.1016/j.cageo.2019.104331.

Zelenin, E., Bachmanov, D., Garipova, S., Trifonov, V. and Kozhurin, A., 2022. The Active Faults of Eurasia Database (AFEAD): the ontology and design behind the continental-scale dataset. *Earth System Science Data*, 14(10), pp.4489–4503. https://doi.org/10.5194/essd-14-4489-2022.

Zhang, D. and Wang, G., 2007. Study of the 1920 Haiyuan earthquake-induced landslides in loess (China). *Engineering Geology*, 94(1–2), pp.76–88. https://doi.org/10.1016/j.enggeo.2007.07.007.

Zhang, H., Aldana-Jague, E., Clapuyt, F., Wilken, F., Vanacker, V. and Van Oost, K., 2019. Evaluating the potential of post-processing kinematic (PPK) georeferencing for UAV-based structure-from-motion (SfM) photogrammetry and surface change detection. *Earth Surface Dynamics*, 7(3), pp.807–827. https://doi.org/10.5194/esurf-7-807-2019.

Zhang, L., Li, J., Liao, W. and Wang, Q., 2016. Source rupture process of the 2015 Gorkha, Nepal Mw7.9 earthquake and its tectonic implications. *Geodesy and Geodynamics*, 7(2), pp.124–131. https://doi.org/10.1016/j.geog.2016.03.001.

Zinke, R., Dolan, J.F., Rhodes, E.J., Van Dissen, R. and McGuire, C.P., 2017. Highly Variable Latest Pleistocene-Holocene Incremental Slip Rates on the Awatere Fault at Saxton River, South Island, New Zealand, Revealed by Lidar Mapping and Luminescence Dating. *Geophysical Research Letters*, [online] 44(22). https://doi.org/10.1002/2017GL075048.

Zubovich, A., Schöne, T., Metzger, S., Mosienko, O., Mukhamediev, Sh., Sharshebaev, A. and Zech, C., 2016. Tectonic interaction between the Pamir and Tien Shan observed by GPS. *Tectonics*, 35(2), pp.283–292. https://doi.org/10.1002/2015TC004055.

Zubovich, A.V., Wang, X.Q., Scherba, Y.G., Schelochkov, G.G., Reilinger, R., Reigber, C., Mosienko, O.I., Molnar, P., Michajljow, W., Makarov, V.I., Li, J., Kuzikov, S.I., Herring, T.A., Hamburger, M.W., Hager, B.H., Dang, Y.M., Bragin, V.D. and Beisenbaev, R.T., 2010. GPS velocity field for the Tien Shan and surrounding regions. *Tectonics*, 29(6), p.TC6014. https://doi.org/10.1029/2010TC002772.